UNCLASSIFIED

AD NUMBER
AD377315
CLASSIFICATION CHANGES
TO: unclassified
FROM: confidential
LIMITATION CHANGES
TO: Approved for public release, distribution unlimited
FROM: Distribution authorized to U.S. Gov't. agencies and their contractors; Administrative/Operational Use; NOV 1966. Other requests shall be referred to Air Force Rocket Propulsion Lab., AFSC, Edwards AFB, CA.
AUTHORITY
DoD 5200.1-r, 31 Dec 1972; AFRPL ltr 7 May 1973

THIS PAGE IS UNCLASSIFIED

GENERAL DECLASSIFICATION SCHEDULE

IN ACCORDANCE WITH

DOD 5200.1-R & EXECUTIVE ORDER 11652

THIS DOCUMENT IS:

Subject to General Declassification Schedule of Executive Order 11652-Automatically Downgraded at 2 Years Intervals- DECLASSIFIED ON DECEMBER 31,1972

BY

Defense Documentation Center
Defense Supply Agency
Cameron Station
Alexandria, Virginia 22314

SECURITY

MARKING

The classified or limited status of this report applies to each page, unless otherwise marked.

Separate page printouts MUST be marked accordingly.

THIS DOCUMENT CONTAINS INFORMATION AFFECTING THE NATIONAL DEFENSE OF THE UNITED STATES WITHIN THE MEANING OF THE ESPIONAGE LAWS, TITLE 18, U.S.C., SECTIONS 793 AND 794. THE TRANSMISSION OR THE REVELATION OF ITS CONTENTS IN ANY MANNER TO AN UNAUTHORIZED PERSON IS PROHIBITED BY LAW.

NOTICE: When government or other drawings, specifications or other data are used for any purpose other than in connection with a definitely related government procurement operation, the U. S. Government thereby incurs no responsibility, nor any obligation whatsoever; and the fact that the Government may have formulated, furnished, or in any way supplied the said drawings, specifications, or other data is not to be regarded by implication or otherwise as in any manner licensing the holder or any other person or corporation, or conveying any rights or permission to manufacture, use or sell any patented invention that may in any way be related thereto.

CONFIDENTIAL

AERONUTRONIC LOG No. [redacted]

[redacted]

AFRPL-TR-66-205

372315

(UNCLASSIFIED TITLE)

BERYLLIUM EROSION CORROSION INVESTIGATION FOR SOLID ROCKET NOZZLES

Third Technical Progress Report

W. L. Smallwood, et al.
Aeronutronic Division of Philco-Ford Corporation

TECHNICAL REPORT AFRPL-TR-66-205

November 1966

In addition to security requirements which must be met, this document is subject to special export controls and each transmittal to foreign governments or foreign nationals may be made only with prior approval of AFRPL (RPPR-STINFO), Edwards, California 93523.

D D C
DEC 6 [illegible]
A

Air Force Rocket Propulsion Laboratory
Research and Technology Division
Air Force Systems Command
Edwards Air Force Base, California

NOTICE: This material contains information affecting the National Defense of the United States within the meaning of the Espionage Laws, Title 18 U.S.C., Sections 793 and 794, the transmission or revelation of which in any manner to an unauthorized person is prohibited by law.

DOWNGRADED AT 3 YEAR INTERVALS; DECLASSIFIED AFTER 12 YEARS

CONFIDENTIAL

Best
Available
Copy

Secondary Publication No. C-3706

(UNCLASSIFIED TITLE)

BERYLLIUM EROSION CORROSION INVESTIGATION FOR SOLID ROCKET NOZZLES

Third Technical Progress Report

W. L. Smallwood, et al.
Aeronutronic Division of Philco-Ford Corporation

In addition to security requirements which must be met, this document is subject to special export controls and each transmittal to foreign governments or foreign nationals may be made only with prior approval of AFRPL (RPPR-STINFO), Edwards, California 93523

NOTICE: This material contains information affecting the National Defense of the United States within the meaning of the Espionage Laws, Title 18 U.S.C., Sections 793 and 794, the transmission or revelation of which in any manner to an unauthorized person is prohibited by law.

DOWNGRADED AT 3 YEAR INTERVALS; DECLASSIFIED AFTER 12 YEARS

FOREWORD

This report is submitted in accordance with the requirements of Contract AF04(611)-10753, sponsored by the Air Force Rocket Propulsion Laboratory, Edwards Air Force Base, Edwards, California. The Air Force Technical Monitor is Mr. W. F. Payne/RPMCH. The contract is under the administrative control of Defense Contract Administration Services, Anaheim Region Office, 1548 State College Boulevard, Anaheim, California. The contract is being performed by Aeronutronic Division of Philco-Ford Corporation, Ford Road, Newport Beach, California. A major propellant manufacturing subcontract is being performed by Atlantic Research Corporation, Shirley Highway at Edsall Road, Alexandria, Virginia. This report describes the program technical progress from 15 March 1966 through 10 October 1966. The report covers a specific segment of work rather than work accomplished during a calendar quarter.

This report has been assigned a secondary report number for internal recording and control purposes. The secondary designation is Aeronutronic Technical Report C-3706 abbreviated as ADP-TR-C-3706.

In addition to the principal author, the authors listed in alphabetical order below have made major contributions to the report sections as indicated:

Section II:	H. L. Moody
Section III:	J. K. Hall
Section IV:	R. D. Hackett
Section V:	J. G. Baetz R. D. Hackett
Section VI:	J. P. McMullen

This report contains classified information extracted from (1) confidential attachments to the basic contract AF04(611)-10753 dated 14 May 1965, (2) Aeronutronic Proposal, Beryllium Erosion Corrosion Investigation for Solid Propellant Rocket Nozzles (U), Volume 1, Applied Research Laboratories Publication No. P-14355(C), dated 20 November 1964, and (3) references marked with an asterisk.

Publication of this report does not constitute Air Force approval of the report's findings or conclusions. It is published only for the exchange and stimulation of ideas.

Approving Authority: AFRPL/RPMC

UNCLASSIFIED ABSTRACT

This is the third technical progress report for Contract AF04(611)-10753, covering the period 15 March to 10 October 1966. The program is directed toward understanding the basic mechanisms of corrosion and erosion of graphite, tungsten and ablative plastic materials exposed to state-of-the-art beryllium propellant exhausts. The results of 18 solid propellant firings are presented and evaluated. The 100-pound grains were in end burner, center perforated and key configurations. Submerged, steep inlet and conventional nozzle contours were tested. Four of the nozzles used dense tungsten inserts; the others were edge grain pyrolytic graphite. Carbon cloth and asbestos phenolics were used as aft closure, nose cap and entrance cone insulation. Three beryllium formulations and one aluminum analog (one test) were used. Pressure, thrust, and thermocouple data are included. Photographs of the tested hardware, analyses of nozzle deposits and analyses of exhaust plume particle samples are presented. Nozzle throat thermal histories and convective heat transfer coefficients were calculated. Oxide deposition effects provided extensive thermal insulation and corrosion protection of the nozzle contour. Throat corrosion occurred on only 9 tests. The key grains produced two axial grooves in the nozzles. Almost no evidence of physical erosion was found. Corrosion, deposition, heat transfer and ballistic performance are discussed in terms of physical and analytical models. The motor test results tend to confirm the original hypotheses concerning the beryllium nozzle erosion problem. Designs for the 500-pound grain motor tests and progress in the development of analytical design techniques are also discussed.

CONTENTS

SECTION PAGE

I INTRODUCTION 1

II ANALYTICAL STUDIES

2.1 Objectives, Scope, and Summary. 5
2.2 Propellant Chemistry and Performance. 6
2.3 Nonideal Propellant Chemistry and Performance . . 22
2.4 Fluid Mechanics 41
2.5 Heat Transfer 58
2.6 Conclusions, Recommendations and Future Work . . 108

III LABORATORY STUDIES

3.1 Objectives, Scope and Summary 116
3.2 Condensed Phase Reaction Studies. 117
3.3 Condensed Phase Impaction and Deposition. 121
3.4 Post Test Analysis. 122
3.5 Conclusions, Recommendations, and Future Work . . 228

IV CORRELATION STUDIES

4.1 Objectives, Scope and Summary 231
4.2 Correlation 234
4.3 Motor Test Instrumentation 261
4.4 Conclusions, Recommendations, and Future Work . . 273

V MOTOR DESIGN, FABRICATION AND TEST

5.1 Objectives, Scope and Summary 276
5.2 Small Motor Tests 278
5.3 Development Motor Tests 305
5.4 Conclusions, Recommendations, and Future Work . . 310

CONTENTS (Continued)

SECTION PAGE

VI INDUSTRIAL HYGIENE AND SAFETY. 316

VII PROGRAM INTEGRATION AND DEMONSTRATION

7.1 Program Integration 319
7.2 Program Demonstration 325

APPENDIX 327

REFERENCES 362

DISTRIBUTION 363

ILLUSTRATIONS

FIGURE		PAGE
1	Key to Exhaust Gas Stay Time Calculations	35
2	Slotted Grain Designs for Small Motor Tests	42
3	Estimated Flow Field - Type II Slotted Grain.	47
4	Estimated Effects of Multiple Grain Slots on Flow Field.	51
5	Streamlines and Impingement Profile - Remote Endburner with Conventional Nozzle.	52
6	Streamlines and Impingement Profile - Close End Burning Grain with a Submerged Nozzle	53
7	Streamlines and Impingement Profiles - Close End Burning Grain with Steep Inlet Nozzle	54
8	Streamlines and Impingement Profiles - Type I Grain with Conventional Nozzle.	55
9	Streamlines and Impingement Profiles - Type I Grain with Submerged Nozzle	56
10	Throat Temperature Response with Deposition - Test T-1. .	69
11	Throat Temperature Response with Deposition - Test T-2. .	70
12	Throat Temperature Response with Deposition - Test T-3. .	71
13	Throat Temperature Response with Deposition - Test T-4. .	72

ILLUSTRATIONS (Continued)

FIGURE PAGE

14 Throat Temperature Response with Deposition - Test T-5. . . 73

15 Throat Temperature Response with Deposition - Test T-7. . . 74

16 Throat Temperature Response with Deposition - Test T-9. . . 75

17 Throat Temperature Response with Deposition - Test T-10 . . 76

18 Throat Temperature Response with Deposition - Test T-11 . . 77

19 Throat Temperature Response with Deposition - Test T-12 . . 78

20 Throat Temperature Response with Deposition - Test T-14 . . 79

21 Throat Temperature Response with Deposition - Test T-15 . . 80

22 Throat Temperature Response with Deposition - Test T-16 . . 81

23 Temperature Response with Deposition at Upstream Area Ratio of 1.03 - Test T-16 82

24 Temperature Response with Deposition at Upstream Area Ratio of 1.37 - Test T-16 83

25 Throat Temperature Response with Deposition - Test T-17 . . 84

26 Temperature Response with Deposition at Upstream Area Ratio of 1.37 - Test T-17 85

27 Throat Temperature Response with Deposition - Test T-18 . . 86

28 Throat Temperature Response with Deposition - Test T-19 . . 87

29 Throat Temperature Response with Deposition - Test T-20 . . 88

30 Throat Temperature Response with Deposition - Test T-21 . . 89

31 Throat Temperature Response with Deposition - Test T-22 . . 90

32 Throat Temperature Response with Deposition - Test T-23 . . 91

33 Throat Temperature Response with Deposition - Test T-25 . . 92

34 Nozzle Throat Insulation Density and Temperature Profiles . 93

ILLUSTRATIONS (Continued)

FIGURE PAGE

35 Nozzle Throat Insulation Heat Absorption 94

36 Aft Closure Insulator - Test T-8 124

37 ATJ Graphite Entrance Cone - Test T-8. 125

38 Nozzle From Test T-8 - Throat Approach View. 126

39 Nozzle From Test T-8 - Exit Cone View. 127

40 Nozzle From Test T-8 - Cross Section 128

41 Aft Closure Insulator - Test T-9 130

42 Nozzle From Test T-9 - Exit Cone View. 131

43 ATJ Graphite Entrance Cone - Test T-9. 132

44 Aft Closure Insulator Cross Section - Test T-9 133

45 Nozzle From Test T-9 - Cross Section 134

46 Aft Closure Insulator - Test T-10. 137

47 Nozzle From Test T-10 - Exit Cone View 138

48 ATJ Graphite Entrance Cone - Test T-10 139

49 Aft Closure Insulator Cross Section - Test T-10. 140

50 Nozzle From Test T-10 - Cross Section (Top Half) 141

51 Nozzle From Test T-10 - Cross Section (Bottom Half). . . . 142

52 Aft Closure Insulator - Test T-11. 144

53 ATJ Graphite Entrance Cone - Test T-11 145

54 Aft Closure Insulator Cross Section - Test T-11. 146

55 Nozzle From Test T-11 - Cross Section. 148

56 Aft Closure Insulator and Nozzle - Test T-12 (As Received). 150

ILLUSTRATIONS (Continued)

FIGURE PAGE

57 Nozzle From Test T-12 - Exit Cone View 151

58 Aft Closure Insulator and Nozzle - Test T-12 (Soot Removed) 152

59 Submerged Nozzle From Test T-12 (Soot Removed) 153

60 ATJ Graphite Entrance Cone - Test T-12 154

61 Nozzle Throat Section - Test T-12 (Throat Approach View) . 155

62 Nozzle Throat Cross Section - Test T-12. 156

63 Aft Closure Insulator and Nozzle Entrance - Test T-13 (As Received) 159

64 Nozzle From Test T-13 - Exit Cone View 160

65 Aft Closure Insulator Damage - Test T-13 161

66 Nozzle From Test T-13 - Damaged Area 162

67 Nozzle From Test T-13 - Entrance Cone View (Loose Deposits Removed). 163

68 Steel Aft Closure Damage - Test T-13 164

69 Nozzle End Support Ring Damage - Test T-13 165

70 Pyrolytic Graphite Throat Insert From Test T-13. 168

71 Aft Closure Insulator From Test T-14 (As Received) 169

72 Nozzle From Test T-14 - Entrance Cone View (As Received) . 170

73 Nozzle From Test T-14 - Exit Cone View (As Received) . . . 171

74 Nozzle From Test T-14 - Cross Section. 172

75 Aft Closure Insulator - Test T-15. 175

76 Nozzle From Test T-15 - Throat Approach View 176

77 Nozzle From Test T-15 - Exit Cone View 177

ILLUSTRATIONS (Continued)

FIGURE		PAGE
78	ATJ Graphite Entrance Cone - Test T-15	178
79	Nozzle From Test T-15 - Cross Section.	179
80	Tungsten Insert - Test T-16.	182
81	Tungsten Insert for Test T-17 - Before Test.	185
82	Tungsten Insert From Test T-17 - After Test (Trailing Edge).	186
83	Tungsten Insert From Test T-17 - After Test (Leading Edge)	186
84	Nozzle From Test T-17 - Entrance View.	187
85	Tungsten Insert From Test T-17 (Before Deposit Removal). .	188
86	Tungsten Insert From Test T-17 (Deposits Removed, Etched).	189
87	Carbon Cloth Phenolic Entrance Cone - Cross Section. . . .	190
88	Nozzle From Test T-18 - Nose Cap View (Loose Deposits Removed).	192
89	Tungsten Insert From Test T-18 (Before Deposit Removal). .	193
90	Tungsten Insert From Test T-18 (Loose Deposits Removed). .	195
91	Nozzle From Test T-19 - Nose Cap View.	196
92	Nozzle From Test T-19 - Exit Cone View	197
93	Nozzle From Test T-19 - Cross Section.	198
94	Tungsten Insert From Test T-19 (Loose Deposits Removed). .	199
95	Nozzle From Test T-19 - Entrance Cone View	202
96	Nozzle From Test T-20 - Cross Section.	203
97	Aft Closure Insulator From Test T-21 (As Received)	205
98	Nozzle From Test T-21 - Throat Approach View	206

ILLUSTRATIONS (Continued)

FIGURE PAGE

99 ATJ Graphite Entrance Rings - Test T-21 207

100 Nozzle From Test T-21 - Cross Section 208

101 Layout of Holes in Aft Closure for Test T-21. 209

102 Aft Closure Insulator From Test T-21 (Loose Deposits Removed). 210

103 Aft Closure Insulator From Test T-22 (As Received). 212

104 Nozzle From Test T-22 - Entrance View (As Received) 213

105 ATJ Graphite Entrance Rings - Test T-22 (Loose Deposits Removed) 214

106 Nozzle From Test T-22 - Cross Section 215

107 Submerged Nozzle From Test T-23 - Entrance View 217

108 Submerged Nozzle From Test T-23 - Cross Section 218

109 Aft Closure Insulator and Nozzle From Test T-24 219

110 Nozzle From Test T-24 - Cross Section 221

111 Nozzle From Test T-25 - Entrance Cone View. 222

112 Nozzle From Test T-25 - Exit Cone View. 223

113 Nozzle From Test T-25 - Cross Section 224

114 Tungsten Ring From Pallas Scale Motor 226

115 Propellant Effects on Throat Deposit History (I). 243

116 Propellant Effects on Throat Deposit History (II) 244

117 Propellant Effects on Throat Deposit History (III). 245

118 Propellant Effects on Throat Deposit History (IV) 246

119 Propellant Effects on Throat Deposit History (V). 247

ILLUSTRATIONS (Continued)

FIGURE PAGE

120 Propellant Effects on Throat Deposit History (VI) 248

121 Effect of Stay Time on Throat Deposit History (I) 249

122 Effect of Stay Time on Throat Deposit History (II). . . . 250

123 Effect of Grain Type on Throat Deposit History (I). . . . 251

124 Effect of Nozzle and Grain Type on Throat Deposit History 252

125 Effect of Grain Type on Throat Deposit History (II) . . . 253

126 Nozzle Effects on Throat Deposit History. 254

127 Effects of Heat Sink on Throat Deposit History. 255

128 Effect of Carbon Cloth Entrance on Throat Deposit History 256

129 Thermocouple Locations for Nozzle T-25. 262

130 Thermocouple Locations for Nozzle T-54. 269

131 Thermocouple Locations for Nozzle T-53. 270

132 Thermocouple Locations for Nozzles T-51 and T-52. 271

133 Motor Case Design - Close End Burning Grains. 280

134 Nozzle Design for Test T-23 281

135 Nozzle Design for Test T-25 282

136 Chamber Pressure and Thrust Versus Firing Time Test T-8 . 285

137 Chamber Pressure and Thrust Versus Firing Time Test T-9 . 285

138 Chamber Pressure and Thrust Versus Firing Time Test T-10. 286

139 Chamber Pressure and Thrust Versus Firing Time Test T-11. 286

ILLUSTRATIONS (Continued)

FIGURE PAGE

140 Chamber Pressure and Thrust Versus Firing Time Test T-12. . 287

141 Chamber Pressure and Thrust Versus Firing Time Test T-13. . 287

142 Chamber Pressure and Thrust Versus Firing Time Test T-14. . 288

143 Chamber Pressure and Thrust Versus Firing Time Test T-15. . 288

144 Chamber Pressure and Thrust Versus Firing Time Test T-16. . 289

145 Chamber Pressure and Thrust Versus Firing Time Test T-17. . 289

146 Chamber Pressure and Thrust Versus Firing Time Test T-18. . 290

147 Chamber Pressure and Thrust Versus Firing Time Test T-19. . 290

148 Chamber Pressure and Thrust Versus Firing Time Test T-20. . 291

149 Chamber Pressure and Thrust Versus Firing Time Test T-21. . 291

150 Chamber Pressure and Thrust Versus Firing Time Test T-22. . 292

151 Chamber Pressure and Thrust Versus Firing Time Test T-23. . 292

152 Chamber Pressure and Thrust Versus Firing Time Test T-24. . 293

153 Chamber Pressure and Thrust Versus Firing Time Test T-25. . 293

154 Change in Nozzle Throat Radius Versus Firing Time Test T-8. 295

155 Change in Nozzle Throat Radius Versus Firing Time Test T-9. 296

156 Change in Nozzle Throat Radius Versus Firing Time Test T-10 297

157 Change in Nozzle Throat Radius Versus Firing Time Test T-11 297

158 Change in Nozzle Throat Radius Versus Firing Time Test T-12 298

159 Change in Nozzle Throat Radius Versus Firing Time Test T-13 298

ILLUSTRATIONS (Continued)

FIGURE PAGE

160 Change in Nozzle Throat Radius Versus Firing Time Test T-14 299

161 Change in Nozzle Throat Radius Versus Firing Time Test T-15 299

162 Change in Nozzle Throat Radius Versus Firing Time Test T-16 300

163 Change in Nozzle Throat Radius Versus Firing Time Test T-17 300

164 Change in Nozzle Throat Radius Versus Firing Time Test T-18 301

165 Change in Nozzle Throat Radius Versus Firing Time Test T-19 301

166 Change in Nozzle Throat Radius Versus Firing Time Test T-20 302

167 Change in Nozzle Throat Radius Versus Firing Time Test T-21 302

168 Change in Nozzle Throat Radius Versus Firing Time Test T-22 303

169 Change in Nozzle Throat Radius Versus Firing Time Test T-23 303

170 Change in Nozzle Throat Radius Versus Firing Time Test T-24 304

171 Change in Nozzle Throat Radius Versus Firing Time Test T-25 304

172 500 Pound Internal Burning Grain. 307

173 Motor Case Design - Development Tests 308

174 Nozzle Design for Tests T-51 and T-52 309

175 Nozzle Design for Test T-53 311

ILLUSTRATIONS (Continued)

FIGURE PAGE

176 Nozzle Design for Test T-54 312

177 Measured Heat Sink Temperatures, Test T-8 328

178 Measured Heat Sink Temperatures, Test T-9 330

179 Measured Heat Sink Temperatures, Test T-10. 333

180 Measured Heat Sink Temperatures, Test T-11. 336

181 Measured Heat Sink Temperatures, Test T-12. 338

182 Measured Heat Sink Temperatures, Test T-13. 339

Measured Heat Sink Temperatures, Test T-14. 340

184 Measured Heat Sink Temperatures, Test T-15. 342

185 Measured Heat Sink Temperatures, Test T-16. 345

186 Measured Heat Sink Temperatures, Test T-17. 348

187 Measured Heat Sink Temperatures, Test T-18. 349

188 Measured Heat Sink Temperatures, Test T-19. 351

189 Measured Heat Sink Temperatures, Test T-20. 352

190 Measured Heat Sink Temperatures Test T-21. 354

191 Measured Heat Sink Temperatures, Test T-22. 355

192 Measured Heat Sink Temperatures, Test T-23. 358

193 Measured Heat Sink Temperatures, Test T-25. 360

TABLES

TABLE		PAGE
I	Chamber Compositions and Flame Temperature	9
II	Experimental Corrosion Parameter Data	13
III	Comparison of Corrosion Threshold With Test Results	14
IV	Predicted and Measured Corrosion Rates	16
V	Uncorrected Ballistic Performance Efficiency Data	30
VI	Adjusted Ballistic Performance Efficiencies	32
VII	Exhaust Gas Stay Time Data	36
VIII	Slotted Grain Tests - Design Parameters	43
IX	Comparison of Groove Depth and Temperature-Slotted Grain Tests	44
X	Material Thermal Properties	60
XI	Small Motor Test Heat Transfer Parameters	66
XII	Asbestos Phenolic Thermal Properties	67
XIII	Asbestos Phenolic Characterization and Performance	68
XIV	Influence of Grain Geometry on Throat Heat Transfer	102
XV	Influence of Nozzle Geometry on Throat Heat Transfer	103
XVI	Influence of Propellant Formulation on Throat Heat Transfer	105

TABLES (Continued)

TABLE PAGE

XVII Influence of Nozzle Material on Throat Heat Transfer. . . . 107

XVIII Motor Test T-8 Deposit Analysis 129

XIX Motor Test T-9 Deposit Analysis 135

XX Motor Test T-10 Deposit Analysis. 143

XXI Motor Test T-11 Deposit Analysis. 149

XXII Motor Test T-12 Deposit Analysis. 157

XXIII Motor Test T-13 Deposit Analysis. 166

XXIV Motor Test T-14 Deposit Analysis. 173

XXV Motor Test T-15 Deposit Analysis. 180

XXVI Motor Test T-16 Deposit Analysis. 183

XXVII Motor Test T-17 Deposit Analysis. 191

XXVIII Motor Test T-18 Deposit Analysis. 194

XXIX Motor Test T-19 Deposit Analysis. 200

XXX Motor Test T-20 Deposit Analysis. 204

XXXI Motor Test T-23 Deposit Analysis. 216

XXXII Motor Test T-25 Deposit Analysis. 220

XXXIII Thermal Instrumentation List. 263

XXXIV Post Test Thermocouple Examination Comments 265

XXXV Quality of Thermocouple Data. 266

XXXVI Motor Design Summary 277

XXXVII Ballistic Data, Tests T-8 Through T-25. 283

XXXVIII General Nozzle Throat Performance 294

XXXIX Cumulative Beryllium Sampling Program Results (To 1 October 1966) 317

SECTION I (C)

INTRODUCTION

This report describes the technical progress made under Contract AF04(611)-10753, "Beryllium Erosion Corrosion Investigation for Solid Rocket Nozzles," during the calendar period 15 March to 10 October 1966. Serious delays in the rocket motor testing phase of the program have occurred during this period. The normal quarterly coverage system has been abandoned in favor of providing coverage of a logical segment of the program plan. Therefore, the primary objective of this report is to present and analyze the results of a series of 18 motor tests which, together with the 7 tests conducted during the preceding reporting period, constitute Task III, Small Motor Testing, of the program. The second objective of this report is to summarize the progress made in the supporting analytical, laboratory, correlation and motor design study areas of the program through the end of the reporting period.

The technical effort on the contract began on 1 June 1965. The original program plan called for completion of the technical effort on 30 June 1966. As a result of schedule slippage and an expansion of the scope of work, the contractual completion date was advanced to 17 October 1966, with distribution of the final report to be completed by 30 December 1966. However, the current estimate of the actual completion date is 1 December 1966, with distribution of the final report by 15 February 1967.

This report is the third of three progress reports required by the contract. The first report, Reference 1, described the technical achievements during the first four months of the contract and described the over-all program objectives, scope and plan. Briefly, the program objectives are:

(1) Provide an understanding of the mechanisms of erosion and corrosion with beryllium propellants.

(2) Determine which nozzle materials and designs can be used with beryllium propellants.

(3) Successfully demonstrate the performance of a test weight nozzle system with a beryllium propellant.

The bulk of the program effort has been allocated to the design, fabrication of hardware, test and analysis of the results of two major series of solid propellant rocket motor tests. The first series of 25 small motor tests utilizes 100-pound grains (one inch nozzle throat diameter) and is divided into several subseries. Each of the subseries has the objective of exposing the influence of the following major motor design parameters on nozzle materials corrosion-erosion: (1) propellant formulation, (2) grain design, (3) nozzle contour, (4) motor configuration, (5) nozzle materials, and (6) nozzle thermal capacity. The second major series of 4 development motor tests utilizes 500-pound grains (2.4 inch nozzle throat diameter). These tests are intended to contribute to the understanding of the influence of the following effects on nozzle corrosion: (1) nozzle scale, (2) grain design, (3) motor configuration, and (4) nozzle submergence. In addition to these motor testing tasks, the results of the program are to be demonstrated by means of a prediction of the nozzle performance for a beryllium motor test to be conducted under another contract.

Generally speaking, the program plan also provides for the performance of specific analytical, laboratory and data correlation studies. The objectives of these studies are to: (1) support the motor testing phases of the program, (2) provide bases for interpreting the motor test results, (3) establish the points of similarity and difference of beryllium with respect to aluminum propellant systems, and (4) provide reasonable analytical techniques which can be used in the design of nozzles for use with beryllium propellants. Wherever possible, these studies have been extended to consider or utilize the results of other programs using beryllium propellants.

The over-all scope of this research contract is limited in a number of important ways. The primary materials of interest are the commonly used graphite, dense tungsten and reenforced ablative insulation. Cooled nozzle concepts are excluded from consideration and all designs must be capable of direct conversion to a flight weight configuration. Both composite and composite-modified-double base beryllium propellants, with theoretical specific impulse (1000/14.7 psia) in range of 280 to 285 seconds are being used. Beryllium propellant formulations have been limited to four, two of each type. Two double base and one composite aluminum analog propellants have been selected for testing. All solid propellant grains have been manufactured by the Atlantic Research Corporation to Aeronutronic specifications. Finally, all rocket motor tests are being conducted by the Air Force Rocket Propulsion Laboratory.

The program technical approach is based on two major assumptions. In the first place, it is expected that the important differences between comparable beryllium and aluminum propellants are confined to: (1) metal phase combustion mechanics and (2) condensed phase impaction, deposition, and flow. The second major assumption is that presently used design and analysis techniques fail to accurately characterize some or all of the following phenomena: (1) convective heat transfer, (2) corrosive species and reaction products mass transport, (3) ablative materials pyrolysis products mass addition to the nozzle boundary layer, and (4) the character and behavior of condensed phases in the exhaust. The second assumption is not restricted to beryllium propellants. It is expected that an advanced understanding of the beryllium erosion and corrosion mechanisms cannot be achieved unless the important heat and mass transfer processes are well characterized.

During the period covered by Reference 1, emphasis was placed on the analysis, laboratory study, and motor design areas. Four beryllium and three aluminum analog propellant formulations were selected for use in the testing phases of the program. The theoretical and nonequilibrium performance and corrosivity characteristics of the propellants were calculated. Progress was made toward improving convective heat transfer theory and procedures were established for nozzle post-test thermal analysis. Cold·flow modeling and condensed phase reaction studies were completed in the laboratory. Arc plasma impingement experiments and a low melting beryllium compound survey were initiated as part of the laboratory studies. Propellant grain, motor configuration, and nozzle designs were completed for the early 100-pound motor tests. Four propellant grains and several sets of motor hardware were delivered to AFRPL for test. However, no motor tests were completed during the first reporting period.

Motor testing was initiated during the period covered by the second progress report, Reference 2. Four beryllium and three aluminum analog propellants were used in identical tests to provide a direct comparison of their corrosion, heat transfer and oxide deposition characteristics. The motor configuration was selected to insure that complete combustion would be achieved. Ballistic and nozzle thermal response data were obtained and analyzed. Exhaust plume particle samples and all hardware (without being decontaminated) were returned to Aeronutronic for post-test laboratory analysis. The motor test results generally confirmed the expectation that completely burned aluminum and beryllium propellant exhausts would have extensively similar effects on nozzle materials performance. Nozzle throat deposit thickness histories were established for each test by means of ballistic performance analyses. The oxide deposits provided more thermal insulation and corrosion protection of the nozzle throat than was anticipated. Pyrolytic graphite throat surface temperatures reached the design goal of 5000°F in only two tests. In the other five tests, contour temperatures reached only about 4000°F. No nozzle corrosion occurred at all on two of the beryllium propellant tests (composite formulations). In addition to the test results, Reference 2 also summarized progress in the following areas: (1) design of small motor tests through T-22, (2) preliminary design of the development motor tests, (3) laboratory survey for low melting tungsten compounds, (4) arc plasma condensed phase impaction study, (5) laboratory production of beta-beryllia, (6) cold flow modeling study being conducted under another contract, (7) characterization of non-equilibrium propellant exhausts, and (8) development of heat transfer and oxide deposit flow analyses. No results were obtained during the second reporting period which contradicted the basic premises of the program technical approach.

The present report is organized, as in the past, in parallel with the division of the program technical effort. Advancements in the analytical, laboratory, data correlation and motor design efforts are covered in Sections II through V, respectively. Each of these sections also covers an appropriate segment of the analysis and evaluation of the motor test results. Thus, the measured pressure and thrust data, along with the derived throat deposition/erosion histories, may be found in Section 5.2. Photographs of the tested hardware and the results of the condensed phase deposit and exhaust plume particle analyses are given in Section 3.4. Results of attempts to correlate the measured throat deposit histories are reported in Section 4.2. All thermocouple temperature data has been isolated in the Appendix. Finally, the results of all post-test nozzle corrosion, ballistic performance and heat transfer analyses are presented in Section 2.2, 2.3 and 2.5, respectively. Section VI contains a summary of the industrial hygiene program results. Section VII presents a brief discussion which attempts to interpret the individual task results in terms of the over-all program objectives. Section 7.2 describes the plan which has been established for accomplishing the Program Demonstration Phase.

Although several of the 500-pound development motor tests were conducted while this report was in preparation, no results of these tests have been included. It is currently expected that all testing will be complete by 31 October 1966. The test results will be presented in the Final Report. However, analysis of the test results should be complete by about 1 December 1966. Interested parties should contact the Air Force Technical Monitor to obtain such information in advance of the distribution of the Final Report.

SECTION II (C)

ANALYTICAL STUDIES

2.1 (U) OBJECTIVES, SCOPE, AND SUMMARY

a. Objectives

The primary objectives of the Analytical Studies Task of the program were described in Section 2.1 of Reference 1 and have not significantly changed. During the third reporting period, the primary objectives have been (1) to complete the nozzle thermal and corrosion performance analyses for Tests T-8 through T-25, (2) to compare the results with the qualitative and quantitative heat transfer and corrosion models, and (3) to provide analytical support for the development motor nozzle design effort.

b. Scope

The original scope of work planned for the Analytical Studies Task was described in Section 2.1 of Reference 1. During this reporting period, the number of motor tests to be conducted was increased. The scopes of the thermal and corrosion post-test analysis subtasks were modified accordingly. Efforts to empirically determine the gas side and effective convection heat transfer coefficients, other than at the nozzle throat, have been abandoned. It has not been possible to measure or otherwise determine the transient variation of the oxide deposit thickness with axial position. Emphasis has been shifted to the development of an analytical deposit flow model. Adequate funds are not available to complete the checkout of this model or apply it in the analysis of the small motor test results. Planned efforts, to analytically characterize condensed beryllia particle flow in the motor chambers tested, have also been reduced. It is believed that such an effort would not provide sufficiently accurate or useful results at the present time. Correlation of theoretical convection heat transfer predictions with program measurements has been deferred to the final reporting period.

c. Summary of Progress

The specific elements of work completed during the third reporting period are summarized below:

(1) Consideration of metal particle ignition and combustion models has continued.

(2) Measured motor ballistic performance data obtained from the small motor test firings have been compared with the ideal performance.

(3) Flow fields and condensed phase impaction areas along the small motor contours have been estimated.

(4) Uniform and nonuniform corrosion of nozzle components has been evaluated for the small motor test nozzles.

(5) Nozzle throat thermal histories and convective heat transfer coefficients have been determined for 15 of the 18 tests conducted during the reporting period. Similar results, for six of the first seven motor tests (reported in Reference 2), have been recalculated using new thermal conductivity data for pyrolytic graphite.

(6) Nozzle throat deposit history data, derived by ballistic analysis (Section 5.2), have been used in all heat transfer and corrosion analyses.

(7) Preliminary calculations, using the analytical wall deposit flow model, have been performed with encouraging results.

2.2 (C) PROPELLANT CHEMISTRY AND PERFORMANCE

a. (C) Propellant Selection

The criteria for selecting propellants, for use in this program, and propellant formulations (four beryllium and three aluminum analogs) were presented in Section 2.2a of Reference 1. The selection of propellants for each of the program motor tests was completed during the second reporting period. This information has been presented in Section 5.2, Reference 2, and in Section 5.2 of this report.

It has been hypothesized that grouping of beryllium propellants according to specific formula characteristics, ideal flame temperature, oxidation ratio and/or ideal performance will not provide direct clues to nozzle erosion or ballistic performance problems with beryllium propellants. Slow or incomplete combustion of the beryllium metal particles or agglomerates is believed to be at the root of both high nozzle erosion and low delivered performance for beryllium, compared to aluminum, propellants. The consideration of the problem of metal particle combustion suggests that two other ideal characteristics of propellants should be examined in selecting propellants and interpreting their performance. These are obtained by assuming that none of the metal additive burns (at chamber pressure). The ideal flame temperature and the ideal flame composition, without metal combustion, are then calculated in the usual manner by assuming thermodynamic equilibrium. Low formulation flame temperatures (no metal combustion), especially if they fall below the beryllium oxide melting point (about 2800°K), suggest that achieving complete combustion and high performance will be difficult. If formulation flame temperatures should approach or fall below about 1900°K, the beryllium may not burn at all. If the formulation flame temperature exceeds about 2800°K, metal combustion should be no more difficult for beryllium than aluminum. Agglomeration at the grain surface is likely to occur when flame temperature are above 2800°K. Within the range 1900 to 2800°K, the quantity of particular oxygen-bearing species may be very significant. Thus, the reaction of water with beryllia is expected to drive the apparent metal particle ignition temperature downward from 2800°K. On the other hand, species like CO_2 and NO would presumbably have to diffuse into or through the beryllia shell on the metal particle to react with beryllium.

The additional propellant evaluation parameters described above have not been examined for a wide variety of propellants. The formulation flame temperatures for the beryllium propellants used in this program fall below 2400°K. In comparison, the propellant to be used in the Program Demonstration Phase (see Section 7.2) has a formulation flame temperature which is above 3000°K. Other advanced propellants, using high energy additives or binders (TAZ, TAG, NF_2, etc.), are also expected to have high formulation flame temperatures. It will be most interesting to see whether the ballistic and nozzle performance problems, attributed to the state-of-the-art beryllium propellants, will prevail for the advanced propellants. Metal particle agglomeration, rather then oxide shell interference, should be the cause of metal combustion problems if they occur. In contrast, the beryllium hydride propellants can have quite low formulation flame temperatures. While there have been obvious ballistic performance problems with the hydride system, it is not known whether a nozzle erosion problem also exists.

It is conceivable, then, that both nozzle erosion and ballistic performance problems can be predicted in advance. As long as the beryllium metal combustion argument is accepted, the results of this program indicate that it may eventually be possible to circumvent performance problems. According to Reference 3, beryllium propellant evaluation motor firings have already shown up the dependence of measured performance on motor residence time and flame temperature (for a particular motor-grain design). Similarly, Aerojet and Hercules have apparently observed the effects of oxidation ratio and formula variation on the performance of particular types of propellants. It is speculated that these observations will appear to be more reasonable when interpreted in terms of the temperature and composition of the propellant exhaust without metal combustion.

The obvious dividends, to be obtained in introducing these new and possibly more fundamental parameters, are simply that propellant tailoring and evaluation motor design efforts may be guided more directly to achieving optimum delivered performance. Eventually, it would be logical to establish relationships between performance and burning particle residence time and between residence time and flame composition or temperature. However nozzle erosion problems would not necessarily disappear for such high performance propellant systems which would evolve. Nozzle materials, upstream of the throat, may still be exposed to the flame before complete combustion is achieved. The results of the present program suggest that the encouragement of oxide deposition protection coupled with appropriate grain and contour designs could effectively minimize the erosion problem.

b. (C) Propellant Characterization

(1) (U) Ballistic Performance

The ideal ballistic performance parameters, calculated for the seven propellants being used in this program, are given in Table VI of Reference 1. Such data has been repeated in this report as required in the evaluation of the ballistic performance efficiency.

(2) (U) Ideal Exhaust Composition

No data have been generated during the reporting period to supplement the ideal exhaust compositions which were given in Table VII of Reference 1. The ideal composition and flame temperature of the four beryllium propellants are compared in Table I for the cases of zero and 100 percent metal combustion. Only the most prevalent gaseous species have been included for convenience. This data is used in the discussion of beryllium metal particle combustion in Section 2.3 following.

TABLE I. CHAMBER COMPOSITIONS AND FLAME TEMPERATURE (C)

(Specie Concentration - Moles/100 Grams of Propellant)

	Arcocel 191F		Arcocel 319 BRF		Arcane 54F		Arcane 24F	
Specie	100% Be	100% BeX	100% Be	100% BeX	100% Be	100% BeX	100% Be	100% BeX
CHO	0.00113	0.000055	0.00122	0.000109	0.00079	0.000028	0.00073	0.000032
CO	1.2464	0.71225	1.6119	1.25695	1.0071	0.68272	0.9974	0.67932
CO_2	0.02309	0.55852	0.01059	0.36760	0.01622	0.34157	0.0261	0.34497
$HC\ell$	0.16847	0.26408	0.04281	0.06815	0.4252	0.5702	0.4653	0.57886
H	0.26816	0.00187	0.1841	0.00176	0.16667	0.00027	0.1506	0.000392
OH	0.02275	0.00161	0.00473	0.000462	0.00932	0.00006	0.0141	0.000102
H_2	1.0806	0.24701	1.2654	0.5478	1.5775	0.56113	1.4750	0.54256
H_2O	0.16600	1.1204	0.0666	0.8774	0.2006	1.24864	0.3032	1.2804
NO	0.00220	0.00012	0.00048	0.000026	0.00058	0.0000015	0.00085	0.000003
N_2	0.40100	0.40233	0.6568	0.6576	0.3006	0.301051	0.3049	0.30546
O	0.00315	0.000008	0.00039	0.000001	0.00059	-	0.00083	-
O_2	0.00019	0.000015	0.000008	-	0.000030	-	0.000068	-
B_eO	1.4062	-	1.1378	-	1.1330	-	1.1240	-
Flame Temperature (°K)	3758	2393	3517	2287	3429	1978	3400	2034

Note: (1) All data calculated at 800 psia.

(2) BeX is unburned beryllium.

(3) (C) Ideal Corrosion Theory

Throat corrosion was measured in the post-test examination of 15 of the 21 pyrolytic graphite nozzles tested. Measurements for the other 6 graphite nozzles indicated that no positive change in throat diameter had occurred. Because of throat shrinkage due to plastic deformation, no corrosion data could be obtained for the 4 tests using tungsten inserts. The objectives of this section are to present the corrosion data and to discuss these results in terms of simplified corrosion theory.

The total measured change in throat radius ranged from 1 to 20 mils. Before presenting the data in detail, the errors associated with these relatively small values should be considered. The most important error is a result of thermal expansion induced deformation of the throat washer. During Contract AF 04(611)-9904, it was concluded that the throat should shrink from 1 to 3 mils on the radius, depending on the axial constraint of the throat washer and the maximum surface temperature level attained in the test. In nine of the program tests for which net average throat corrosion did not occur, the final throat diameters were less than the original values (see Section 5.2). The net shrinkage varied from 0 to 9 mils on the radius, with 7 of the 9 measurements falling into the 0 to 3 mil range. The nozzles, for which 6.5 and 9 mil shrinkage were measured, were examined more closely and it was concluded that all of the deposit had not been removed and probably could not be without removing some of the graphite. The nozzles showing the low shrinkage usually had no beryllia deposits on the throat washer. On removal of the amorphous carbon deposit, the original machining marks could often be seen in the pyrolytic graphite surface. In view of these observations, the measured radial erosion has been corrected by adding 2 to 3 mils to account for the estimated throat shrinkage. The corrected and uncorrected values are given separately in the discussions which follow. The magnitudes of the corrections applied are obviously questionable in view of other potential measuring and deposit removal errors. However, the correction is physically realistic.

The second major problem, or error, in the characterization of corrosion is that circumferentially nonuniform oxide deposition leads to nonuniform surface regression. On Tests T-3, T-6 and T-20, corrosion occurred before the deposits arrived to cover the throat surface. The throat measurements, taken at 4 to 6 positions, showed no variation. On all other tests, corrosion either did not occur, was very nonuniform (slotted grain tests), or was slightly nonuniform with a net throat shrinkage. While the axial grooving of the nozzle with the slotted grains constituted the greatest nonuniformity, it is also obvious that the top sector of the throat washer corroded more than the bottom. This is believed to be due entirely to gravity effects on the flow of the liquid oxide deposits.

The third source of error is related to the deposit nonuniformity problem. The deposit histories are developed (see Section 5.2) by assuming uniform deposit thickness. This data is then used in the thermal analysis which produces the throat surface temperature history (see Section 2.5e). Significant errors are almost certainly involved in the indicated time of arrival or departure of the deposit. The deposit coverage of the throat will be most nonuniform during these times. Consequently, errors will be transmitted to the determination of the time during which corrosion occurs and the graphite surface temperatures prevailing during the corrosion period.

Table II presents the corrosion data obtained for all of the small motor tests except for those which used tungsten inserts or had no corrosion. The column headings in this table are explained below except where the meaning is obvious.

$\bar{P}$: Average chamber pressure over the period when throat corrosion actually occurred. The average nozzle throat pressure can be obtained by multiplying $\bar{P}$ by 0.575.

$\bar{h}_c$: Average gas side, throat heat transfer coefficient over the entire firing from Section 2.5e. The value given is corrected to the average coefficient over the time when corrosion actually occurred by multiplying by the ratio of $\bar{P}$ to the average pressure over the entire firing, raised to the 0.8 power.

$\bar{C}_p$: Average equilibrium boundary layer specific heat, at the wall temperature when corrosion occurred, taken from Figures 2 and 3, Reference 2.

$\bar{B}$: Average thermodynamic saturation parameter, at the wall temperature when corrosion occurred, for the particular propellant, taken from Figures 14 and 15, Reference 1, and from similar plots which have not been published. Note that these B values are for the case of inert condensed oxides.

ΔT: Range of throat surface temperature during period when corrosion occurred.

$\overline{\Delta r}$: Average change in throat radius. Average of at least four measurements of the throat diameter after removal of soot and beryllia deposits.

Δr_{max}: One half of the maximum measurement of post-test throat diameter change.

Δr_{min}: One half of the minimum measurement of post-test throat diameter change.

ΔR: One half of the measured throat diameter change which most logically represents the corrosion for each particular nozzle. One or more diameter measurements, excluding those which reflect grooves and/or minimum values, were selected or averaged. Then, the throat regression values were corrected by adding two mils to account for the thermal expansion effect. Since these numbers no longer represent circumferential averages, they do not agree precisely with similar data (averages) given in Section 5.2.

$\mathring{R}$: Average corrosion rate over the estimated time period when corrosion occurred, based on ΔR.

It should be noted that the corrosion rates for nozzles T-2, T-15 and T-25 are based on the arbitrary assumption that the corrosion occurred over a period of one second. The actual corrosion time period could not be determined since the deposition-erosion histories (see Section 5.2) indicate that the average throat area was always less than the original area. It should also be noted that the nozzle throats were elliptical on Tests T-1, T-5, T-7 and T-25. If it is assumed that the bottom section of the nozzle was protected by oxide deposits and only the top half corroded, the $\mathring{R}$ values could reasonably be doubled. This argument also applies, to a lesser degree, to the other tests except when corrosion occurred before the deposits arrived. However, the actual throat diameter measurements tended to be more uniform as the total throat regression increased above 3 or 4 mils on the radius.

Thermodynamic analysis of the various propellant exhausts with respect to graphite indicates that the exhausts are saturated with carbon at all temperature levels below some critical or threshold value. The threshold is defined as the carbon wall temperature for which the B value is zero (see Figures 12 through 15, Reference 1). The value of this critical temperature has been shown to depend on the degree of combustion of the metal additive and is not very sensitive to the unrealistic assumption that the metal oxides are free to react with the wall material.

The theoretical threshold temperatures are given in Table III. The range indicated represents the 0 and 100 percent metal combustion extremes, with the low threshold value corresponding to the 0 percent metal combustion case. This table also gives graphite throat surface temperatures, at the time

TABLE II. EXPERIMENTAL CORROSION PARAMETER DATA (C)

Propellant	Test	$\overline{P}$	$\overline{h_c}$	$\overline{c_p}$	$\overline{B}$	ΔT	$\overline{\Delta r}$	Δr_{max}	Δr_{min}	Corrected ΔR	$\dot{R}$	Grain Type, Nozzle Contour
-	-	psig	Btu/in^{2}sec°F	Btu/lb°F	-	°F	Mils	Mils	Mils	Mils	Mils/sec	-
Arcane 24F	T-2	740	0.0056	0.80	0.08	3800-3900	-1		-	1	1*	REB-Conv
Arcane 54F	T-11	830	0.0060	0.90	0.09	4320-4400	2	2.5	-1.5	4	2	CP-Conv
Arcane 60	T-5	860	0.0040	0.50	0.07	3480-3880	3	5	1	6	1.3	REB-Conv
Arcocel 191F	T-1	700	0.0075	0.95	0.13	4840-4880	5	6	4	7	4	REB-Conv
Arcocel 191F	T-9	740	0.0090	1.03	0.26	5240-5280	4	4	3.5	6	4.3	CP-Conv
Arcocel 191F	T-10	1300	0.0100	1.10	0.32	5240-5500	6	10	1.5	7	2.3	Key II-Conv
Arcocel 191F	T-12	1000	0.0120	1.10	0.32	5260-5480	19	22.5	16	21	9.5	Key II-Subm
Arcocel 191F	T-13	960	-	-	-	-	8	35	2	5	1.7	Key II-Steep
Arcocel 191F	T-20	740	[illegible]	0.85	0.06	4340-4400	7	-	-	9	6	CP-Conv
Arcocel 191F	T-25	760	0.0072	0.93	[illegible]	4700-4800	-0.3	-	-	1	1*	CP-Conv
Arcocel 389	T-7	950	0.0080	0.60	0.22	5040-5150	3	3	2	5	3	REB-Conv
Arcocel 319BRF	T-3	1060	0.0073	0.75	0.01	2500-4000	3	5	1	6	2	REB-Conv
Arcocel 319BRF	T-14	800	0.0074	0.80	0.12	4680-4840	12	-	-	14	2.5	CP-Conv
Arcocel 319BRF	T-15	900	0.0053	0.70	0.002	2200-2500	-1.5	22	-9	3	3*	Key III-Conv
Arcocel 390	T-6	500	0.0060	0.46	0.01	2000-3000	1	2	1	3	2	REB-Conv

---

*Estimated, assuming corrected corrosion occurred over 1 second period

TABLE III. COMPARISON OF CORROSION THRESHOLD WITH TEST RESULTS (C)

		Surface Temperature of Graphite Throat at:		
Test	Propellant	Deposit Arrival (°F)	Start of Corrosion (°F)	Theoretical Corrosion Threshold (°F)
T-1	191F	2500	-	1000-1900
T-2	24F	1700	-	600-1700
T-3	319BRF	-	2500	1400-2300
T-4	54F	2600	-	900-1900
T-5	60	2150	-	800-1900
T-6	390	-	2000	1500-2300
T-7	389	4200	-	1000-1800
T-8	389	-	-	-
T-9	191F	3400	-	1000-1900
T-10	191F	2000	-	1000-1900
T-11	54F	1800	-	900-1900
T-12	191F	5000	-	1000-1900
T-13	191F	-	-	-
T-14	319BRF	2900	-	1400-2300
T-15	319BRF	-	2200	1400-2300
T-20	191F	-	4000	1000-1900
T-21	191F	1900	-	1000-1900
T-22	54F	2800	-	900-1900
T-23	191F	2800	-	1000-1900
T-24	319BRF	-	-	-
T-25	191F	2300	-	1000-1900

when the protective oxide deposits first arrived or when corrosion began (prior to deposit arrival), for each of the nozzle tests. Examination of the calculated graphite surface temperatures, Section 2.5e, indicates that the rate of temperature rise was very high on Tests T-7, T-9, T-10, T-12, T-14 and T-20. Note in the table that the surface temperatures when deposits arrived (or corrosion started for T-20) are well above the theoretical corrosion threshold temperatures. (Test T-10 is not regarded as an exception since the throat deposit appeared within about 0.1 second of ignition; the deposit history analysis cannot be that accurate.) While there may actually be an induction time for corrosion, it is more likely that greater error is to be associated with the surface temperature calculation during the time when the rate of rise is the highest. Tests T-4, T-22 and T-23 had intermediate surface temperature rise rates, compared to the other tests which had slow rates. With these considerations in mind, it appears that the threshold temperature, for the case of complete metal combustion, most closely fits the observations. There is no positive indication that incomplete metal combustion has occurred. It is also doubtful that experimentally measured corrosion threshold temperatures could be used to indicate the degree of metal combustion unless the initial surface temperature rise rates were very slow. The low accuracy with which the start of corrosion can be determined would also be a problem.

Considering the reasonably high C* efficiencies (see Section 2.3b) and the corrosion threshold observations, it was concluded that nonequilibrium combustion effects could be neglected in analyzing the corrosion results. The predictions of ideal corrosion theory are compared with the measured corrosion rates (adjusted) in Table IV. As previously discussed, four of the rates could be as much as twice the selected rate if the corrosion was limited to the top half of the throat. Thus, a range is given for the appropriate tests. Fictitious rates are given for one of these tests and two others (corrosion period not known).

The first set of predictions, R, were obtained using Equation 17 of Reference 1. This equation rather accurately predicts the results of Tests T-3, T-6 and T-20. It is interesting to note that the surface temperatures were in the range where little or no contribution to corrosion is expected from hydrogen. These three tests also produced corrosion prior to deposition. In general, it is expected that this technique would always overestimate the corrosion rate because it necessarily overestimates the availability of reactive species and does not account for boundary layer blowing effects. Since the predictions are rather extreme in the temperature range where the hydrogen reactions are important, the B value technique cannot be recommended for use above about 4000°F. Below this temperature level, where the carbon-oxygen reactions prevail, it appears to be reasonably accurate and could be used. There is not sufficient data available to attempt an empirical correction. By artificially reducing the stability of the products of carbon-hydrogen reactions, the B value technique could be used to calculate only the effect of the carbon-oxygen reactions.

TABLE IV. PREDICTED AND MEASURED CORROSION RATES (C)

Propellant	Test	$\mathring{R} = \frac{h_c \bar{B}}{C_p W}$ (mils/sec)	$\mathring{R}_{H_2O}$ (mils/sec)	$\mathring{R}_{H_2}$ (mils/sec)	$\mathring{R}_{Measured}$ (mils/sec)
Arcane 24F	T-2	7	4.6	0.1	1*
Arcane 54F	T-11	7	2.9	0.6	2
Arcane 60	T-5	7	4.6	0.1	1.3-2.6
Arcocel 191F	T-1	10	2.9	1.3	4-8
Arcocel 191F	T-9	16	3.2	2.6	4.3
Arcocel 191F	T-10	28	5.0	4.7	2.3
Arcocel 191F	T-12	30	5.3	5.1	9.5
Arcocel 191F	T-13	-	-	-	1.7
Arcocel 191F	T-20	8	3.7	0.5	6
Arcocel 191F	T-25	9	2.8	1.0	1*-2*
Arcocel 389	T-7	24	6.4	3.2	3-6
Arcocel 319BRF	T-3	2.8	1.3	0	2
Arcocel 319BRF	T-14	9	1.2	1.2	2.5
Arcocel 319BRF	T-15	0	0.9	0	3*
Arcocel 390	T-6	1.5	1.9	0	2

---

*Estimated, assuming corrected corrosion occurred over a one second period.

Another way of doing this is to calculate the corrosion contribution for each reasonable chemical reaction. The assumptions of the heat and mass transfer similarity argument and thermodynamic equilibrium prevails at the graphite-boundary layer gas interface are retained. Examination of the exhaust compositions of all the propellants indicates that H_2O and H_2 will be the dominant reactants. While oxygen is also available as CHO, CO_2, NO, OH, O and O_2, these species exist in considerably lower concentrations than the H_2O. The gaseous beryllium hydroxide and suboxide species, while more significant than comparable aluminum species, also exist in small concentrations in the exhausts. In reality, many of these species will tend to disappear as they diffuse through the boundary layer, forming more water and some condensed beryllia. Atomic and molecular hydrogen are found in large quantities in all exhausts. Additional hydrogen is produced via the reaction of water with carbon.

The objective of the alternate prediction approach is to consider each reaction separately. This permits the consideration of nonunity specie Lewis numbers. Otherwise, if all reactions were to be added up, the net result would be equivalent to the B value method. The immediate objective is to consider only the reactions due to water and hydrogen.

The water-graphite reaction is presumed to proceed as follows:

$$C(s)+H_2O(g) = CO(g)+H_2(g)$$

Then the linear graphite surface regression rate can be written as

$$R_{H_2O} = \frac{12}{18}\frac{m_{H_2O}}{W} = \left(\frac{12}{18}\right)\left(\frac{1}{W}\right)\left(\frac{h_c}{C_p}\right)\left(\frac{18}{\overline{M}}\right)\left(\frac{P_o-P_s}{P_t}\right)\left(\frac{Di}{\alpha}\right)$$

which reduces to

$$R_{H_2O} = \frac{150}{\overline{M}}\left(\frac{h_c}{C_p}\right)\left(\frac{D_i}{\alpha}\right)\left(\frac{P_o-P_s}{P_t}\right)$$

for the graphite density, W, set equal to 0.08 lb/in.^{3}. $\overline{M}$ is the average boundary layer gas molecular weight; (h_c/C_p) is the ratio of the convective heat transfer coefficient to the boundary layer equilibrium specific heat; (D_i/α) is the Lewis number for water diffusing in the boundary layer; p_t is the throat or local static pressure, p_o is the partial pressure of water vapor in the free stream and p_s is the partial pressure of water at the wall. Noting that $\overline{M}$ ranges from 17.9 to 18.8 for the seven propellants of interest, the Lewis number (water) is taken to be unity. Also, at temperatures above about 4000°R, the equilibrium partial pressure of water vapor at the wall was found to be negligible compared to the free stream value (i.e., $p_s = 0$). Thus, the particularly simple result

$$R_{H_2O} = \frac{150}{\bar{M}} \left(\frac{h_c}{C_p}\right)\left(\frac{p_o}{p_t}\right)$$

is obtained. Similar reasoning for the case of the hydrogen reaction,

$2C(s)+H_2(g)=C_2H_2(g)$

leads to the expression,

$$\dot{R}_{H_2} = \frac{300}{\bar{M}} \left(\frac{h_c}{C_p}\right)\left(\frac{Di}{\alpha}\right)\left(\frac{p_{H_2}}{p_t}\right) K_p$$

where; (Di/α) is the Lewis number for the acetylene diffusing in the boundary layer, p_{H2} is the free stream partial pressure of hydrogen, and K_p is the equilibrium constant for the hydrogen reaction at the wall temperature of interest. The Lewis number for acetylene should be significantly less than unity (unless the boundary layer should become fully turbulent). A value of 0.5 was chosen for the present calculations.

If it is presumed that both the hydrogen and water reactions proceed simultaneously, then the sum of R_{H_2O} and R_{H_2} would serve as a first approximation of the corrosion rate. The actual situation is more complex, since water may react with acetylene within the boundary layer. This would tend to eliminate the wall-water reaction, but it would accelerate the wall-hydrogen reaction by a nearly equivalent amount. Some investigators have previously concluded that the hydrogen-graphite reaction is subject to severe chemical kinetic restrictions, even at temperatures in the range being examined. Such reaction rate restrictions would be most likely to appear when the heat and mass transfer coefficients are high, as is the case here. However, a low Lewis number for acetylene could at least partially account for this observation.

In comparing the results in Table IV, it would appear that the water reaction, when augmented to account for the CO_2, $Be(OH)_2$, etc., rather accurately predicts the measured values. There appears to be a trend involving the composite and double base division of the propellants. The predicted water reaction rates are uniformly higher than measured for the composites and are uniformly lower (except T-7 and T-10) for the double base propellants. The composites also have the lowest theoretical and formulation flame temperatures. (Thus, it could be argued that excess amounts of beryllium hydroxide gas could exist in the composite exhaust.) However, the amount of the oxygen available for reaction with the graphite (H_2O, CO_2, $Be(OH)_2$, etc.) is divided differently in the two propellant types. The composite exhausts have 83 to 89 percent of the available oxygen in the form of water while the double base exhausts have only 68-70 percent of the available oxygen in the form of water. (Of course, these figures pertain only to the ideal combustion case.) It should be noted that the division of the oxygen, among the various species, will depend most strongly on (1) the amount of carbon in the formulation, (2) the oxidation ratio, and (3) the ideal flame temperature. The beryllium particle combustion model suggests that relatively large amounts of the beryllium hydroxide gases could form during the combustion process in the chamber. These species might then persist, in higher than ideal concentrations, to the nozzle throat and beyond. Clearly, more detailed study of the actual beryllium hydroxide gas formation mechanics would be necessary before any conclusions could be reached concerning its relative importance in double base and composite systems. In any case, it does not appear likely that larger concentrations of $Be(OH)_2$ or BeOH would alter the graphite corrosion picture extensively. It will be more difficult for these molecules to diffuse to the wall than it will be for water and the concentration of other oxygen bearing species will diminish proportionately. The only new factor will be the appearance of molecular beryllia at the wall. The beryllia-carbon reaction will proceed, depending on the wall temperature, to form either beryllium carbide or beryllium vapor. Either of these new species would be available to react with the oxygen bearing species diffusing toward the wall. It is speculated, then, that ballistic performance would be a more logical indicator of the excessive hydroxide formation than nozzle corrosion.

While it would not be logical to assume that hydrogen plays no role in the corrosion of pyrolytic graphite, it is quite evident that consideration of only the carbon-oxygen reactions will provide a suitable first approximation of the corrosion rate. Since corrosion was experienced over a wide range of surface temperatures, and since the hydrogen reaction is "not necessary" to explain the measured corrosion, it would be reasonable to neglect the hydrogen contribution below surface temperatures of about 5200°F. Chemical kinetic rate restriction probably also pertains above this temperature level. It is generally not recommended that pyrolytic graphite be designed to operate at surface temperatures above about 5500°F. Within this rather narrow range, 5200 to 5500 F, the corrosion rate should accelerate, but probably would never reach the equilibrium (B value) rate. In the vicinity of 5500 F, it is expected that the pyrolytic graphite surface would begin to break down physically (nodule erosion).

Except for the carbide formation and plastic deformation problems, the tungsten inserts do not appear to have been corroded. No conclusions have been reached concerning the source of the carbon. It had been assumed that gaseous graphite reaction and insulation ablation products would be the source. This cannot be demonstrated until the deposit history upstream of the throat can be estimated and additional microprobe analyses of the tungsten surfaces are performed.

Physical erosion was not observed in any significant amount on any of the tests. Local surface spallation was noted occasionally on the ATJ graphite exit cones. The appearance of the pits suggested that the majority occurred at the end of firing or during cool down. In a few instances (with the Arcocel 191F propellant) the erosion pits were axially elongated to as much as 1/2 inch. In the absence of the protective beryllia deposits, polycrystalline graphite is expected to corrode and erode simultaneously. While a detailed model describing this process has not been formulated as yet, it is apparent that the erosion behavior of ATJ, Graphitite-G90, etc., will not be similar to that of pyrolytic graphite. Furthermore, the high effective surface area of the polycrystalline graphites (compared to pyrolytic graphite) will change the corrosion picture considerably. Consequently, none of the results obtained for pyrolytic graphite in this program should be extended to the polycrystalline graphite materials.

The grooving of the nozzle inlet and throat sections, which occurred on the tests using slotted grains, is discussed in Section 2.4 following. The simplified corrosion model is based on diffusional mass transport through a boundary layer which is not fully turbulent. Whenever reactive species are convectively transported to the wall or the reaction products are convectively removed from the nozzle surface, the corrosion rate will increase. Abnormally high local turbulence may be introduced due to contour irregularities, nonuniform free stream flow or localized condensed phase inpingement. As the turbulent convection mass transport rates increase beyond the diffusional mass transport rates which would otherwise prevail, chemical kinetic reaction rate restrictions should appear. Otherwise, the corrosion rate could increase by many orders of magnitude. As the original turbulent convection disturbance dissipates in the axial direction, the groove should become shallower and narrower, provided that the groove itself does not promote secondary turbulence. Convective transport of reactants and products will also occur at boundary layer reattachment points. Clearly, both situations should be anticipated and avoided.

c. (U) Propellant Thermal Properties

Average boundary layer specific heat data, for the seven propellants being used in this program, were presented in Section 2.2 of Reference 2. These data were generated for the case of 100 percent metal combustion and it is assumed that condensed beryllia is uniformly distributed in the exhaust flow and nozzle boundary layer. Examination of the nozzle surface temperature histories (see Section 2.5e) suggests that the "wall temperature" of interest, in defining the average boundary layer specific heat, is that of the oxide deposit surface. In most tests, the oxide surface or the exposed throat surface exceeded the beryllia fusion temperature over a major portion of the firing period. Consequently, concern over whether beryllia actually exists or solidifies within the nozzle boundary layer may not be warranted (see page 10, Reference 2). If the beryllia actually does not exist in the boundary layer, significant errors would still be incorporated in the calculated enthalpy and density profiles. The potential magnitude of these errors has not been determined.

When the Bartz type equation is used to predict convective heat transfer coefficients, it has been recommended that the equilibrium specific heats, averaged over the boundary layer between the stagnation enthalpy and wall surface enthalpy, be substituted for the frozen specific heat. In the more complicated numerical boundary layer analyses, the enthalpy-temperature data are used directly, without converting to specific heat. (In either case, it should be recalled that complete combustion has been assumed.) Consideration is currently being given to the determination of the other important properties, namely the viscosity and Prandtl number. It appears that the Prandtl number has been overestimated significantly. Recommended values for these properties will be given in the Final Report.

2.3 (C) NONIDEAL PROPELLANT CHEMISTRY AND PERFORMANCE

a. (C) Solid Propellant Combustion

One of the major hypotheses, adopted in the formulation of the program technical approach, was that incomplete combustion of beryllium metal particles would induce both abnormal corrosion and low performance. A qualitative combustion model was formulated and it was concluded that beryllium and aluminum metal particles would generally not burn in the same manner. In fact, it is fairly well agreed that neither aluminum nor beryllium will burn in the same way in different propellant formulations. In spite of the fact that the program motor firings have produced little direct evidence of combustion-corrosion coupling, data from other programs continue to indicate that incomplete and nonideal metal combustion actually occur. When this happens, the availability of oxygen, for reaction with motor insulation and nozzle materials, may increase by a factor of ten or more. In addition, tungsten could be exposed to beryllium metal with equally serious consequences. It is of general interest, then, to be able to identify those propellant formulation and motor design parameters which adversely influence metal combustion. Obviously, the motor designer must be aware of both the potential consequences of the combustion problem and the ways to avoid extreme erosion.

It has been suggested that the metal particles are ejected into the combustion gas stream when the burning surface receeds far enough to permit the release of the particle. It is thought that the most important parameters which would have a pronounced influence on this ejection process would be those which also govern the particle agglomeration phenomenon. Even though the flame stand off distance is of the order of the metal particle diameter, the particle surface temperature should always be less than the ideal flame temperature without any metal combustion. However, the particle surface temperature will not be low enough to prevent surface oxidation. The oxide film or coating that develops might contain some nitride and carbide impurities. In any case, the refractory coating cannot be expected to melt while the beryllium particles reside on the propellant surface since a large fraction of the metal must have already burned before the local flame temperatures can exceed the beryllia melting point. Since the melting point of beryllium metal is about 1500°K, it is likely that the metal will remain solid until ejection unless: (1) the particles reside at the propellant surface for a long time or (2) the flame temperature without metal combustion is well above 1500°K. On the other hand, aluminum particles are likely to melt before ejection. Even when the metal particle has partially melted and is free to collide with other metal particles on the propellant surface, the solid oxide shell will be partially effective in preventing agglomeration of particles. This should occur to a greater degree for beryllia than alumina, considering their respective melting points. Consequently, the beryllium particles are expected to leave the grain surface without agglomeration, while some of the aluminum particles may agglomerate. This will not necessarily hold for the higher energy advanced propellants which will characteristically have higher grain surface and formulation flame (no metal combustion) temperatures.

An interesting example of beryllium surface agglomeration has been reported in Reference 4. In this case the particles are beryllium hydride. The authors, after observing agglomeration, speculated that the particle surface temperatures must have exceeded 1500°K (without complete dissociation of the hydride) and may have been at or above the beryllia melting point. While it is agreed that the beryllium must melt to permit agglomeration, there is an alternate explanation of the observed sticking. That is, as long as hydrogen is being evolved from the particle surface, it is considerably less likely that a protective oxide coating will be formed. Without the oxide shell, agglomeration could proceed without temperatures significantly exceeding the beryllium melting point.

Whether or not agglomeration of the metal particles occurs on the grain surface would also depend on the other propellant ingredients. The spacing and size of the ammonium perchlorate, RDX, HMX, etc., particles would have a strong influence on the local convective currents, temperature chemistry and flame stand off distances. In general, it would be logical to assume that these factors would have about the same influence on particle movement on the grain surface for either beryllium or aluminum. However, beryllium should always be less likely to agglomerate, for a given particle collision frequency, simply because of the metal and oxide melting point differences. It is worth noting that thermal expansion stresses induced during particle heating and metal phase change would tend to break up the oxide shell. Once the particle has begun to melt, such stresses, particle collision forces and gas shear forces may minimize the effectiveness of the oxide to prevent agglomeration.

Once the metal particle or agglomerate leaves the propellant surface it will continue to be heated by surface reactions and convective heating (velocity lag effect). As long as a solid oxide shell remains, only two types of reactions are anticipated. The diffusion of oxidizing species into the oxide shell to react with the beryllium or aluminum may occur, but at a rather low rate. If the exhaust essentially reaches equilibrium (without metal combustion) water vapor and carbon dioxide will be available in very high concentrations. If these species diffuse through the oxide shell and react with the metal, they may produce a larger number of gas molecules than are consumed. The build up of metallic suboxide, H_2 and CO gases would eventually lead to explosion or fragmentation of the particle. If the reactions proceed after the oxide shell melts, the particle may become a hollow sphere. If the metal suboxides should condense to the oxide, the bubble could collapse (cavitate) as opposed to bursting. Some excellent experimental observations of aluminum particle fragmentation may be found in Reference 5. It is interesting to note that beryllium particles have not been observed to fragment significantly, if at all. The higher oxide melting point, lack of stable beryllium suboxides or beryllia-water reactions might account for this.

The second possibility for reaction while a solid oxide shell remains has already been mentioned above. That is, according to our previous speculations and Reference 6 (for example), the water vapor may react directly with the beryllia to form the gaseous hydroxides. Even if the thermodynamic data for the BeOH and $Be(OH)_2$ species are significantly in error, a diffusion controlled reaction could proceed at the particle surface. This reaction would not consume the entire oxide shell but would tend to keep it at a relatively constant thickness. The oxide thickness would stabilize as a consequence of the migration of beryllium metal atoms to the reaction zone (at the surface or within the oxide shell) and the diffusion of the hydroxide products away from the particle surface. Apparently the aluminum hydroxides are considerably less stable than the beryllium hydroxides. It is also possible that the chlorides play a part in the early stages of metal particle combustion. However, this seems somewhat less likely simply because two molecules of HCL are required to complete the conversion of BeO to $BeCL_2$ and because the quantity of HCL is significantly lower than that of water.

Both types of reactions postulated above will accelerate the metal particle heating rate. Once the oxide melting point is reached, surface tension forces may cause the oxide to withdraw to one side of the particle. Of course, this has been observed in some detail for aluminum. The resulting change in particle shape and the limitation of oxidation reactions to only a portion of the particle surface apparently promotes spinning and, in some cases, fragmentation of the particles. It is postulated that this will not occur for the beryllium propellants unless the theoretical flame temperatures are well above the beryllia melting point (4635^oF). That is, it should not be required that a large fraction of the available beryllium actually react before the average exhaust temperature can be raised to the beryllia melting point. Note that the melting point of alumina (2300^oK) is below the formulation flame temperatures (no metal combustion) of the Arcocel 389 (2513^oK) and Arcocel 390 (2390^oK) aluminum analogs. On the other hand, the Arcane 60 analog propellant has a formulation flame temperature of only 2066^oK. This, plus the fact that the heat transfer and throat deposit history obtained on Test T-5 were "unusual", strongly suggests that even aluminum may not burn well under the conditions where berylliim usually must burn.

Consider, then, some additional consequences of incomplete metal combustion. The largest beryllium particles (20 - 50 microns) will be the most difficult to burn, provided only that the particle velocity lag heating diminishes with decreasing particle area to volumn ratio. Similarly, the largest aluminum particles and/or agglomerates will be most difficult to burn. Such large particles will be primary contributors to deposition where the flow direction is changed along the motor closure or nozzle inlet. The end burning grain tests (T-1 through T-7 and T-21 through T-24) provided an unusually good opportunity for this to occur. On the aluminum analog tests (T-5 through T-7), aluminum metal was actually found in the asbestos phenolic aft closure insulator char material. No beryllium metal was found, but the amount of beryllium carbide was above expectations. Because the chamber velocities were below 10 ft/sec and the metal particles leave the grain surface in the normal direction, the velocity lag heating would be at a minimum for the tests conducted in this program. Even the long gas stay times (see Section 2.3b) for the remote end burners may not have been sufficient to complete the combustion of aluminum particles in Test T-5 and possibly T-6 (low chamber pressure and hang fire).

Recalling that it has been speculated that the beryllium will not agglomerate on the grain surface, it follows that the partially burned particles will be limited to something close to the largest diameter of the original metal particles (40-50 microns). If surface agglomeration of aluminum occurs, the particles could be considerably larger (NOTS, China Lake, has reported agglomerates up to 1500 microns with fuel rich grains). Under the appropriate combination of circumstances, it would be possible for oxygen enrichment of the exhaust to be greater for an aluminum propellant than for its beryllium analog. If, under these same circumstances, surface deposits did not protect the contour materials, the aluminum propellant would appear to be the most corrosive. Note that if significant amounts of metal are deposited on the contour, this may not have a major effect on performance. The reasoning here is that the metal would continue to vaporize and/or burn and may be consumed before it flows past the nozzle throat or is ejected from the nozzle. However, it should also be noted that rather large amounts of aluminum metal were found in the chamber residue (see Section 4.3, Reference 1) while beryllium metal was found only on Test T-13 (see Section 4.3 following).

Turning to the internal burning grain configuration, two interesting factors arise. First the metal particles are ejected from the grain surface in the normal direction which is 90 degrees from the axial gas flow direction. The particles should experience considerable slip and the heating will be much greater than the parallel injection case (end burner). Secondly, the largest particles are likely to have the largest turning radius and penetrate farther into the core of the flow. The gases nearest the axis of the grain port should have achieved a higher temperature. Unless they are already fuel rich as a result of particle stratification, the combustion of the large metal particles may be accelerated. However, at the end of the grain, the gases at the outside of the port may be somewhat oxygen rich. Again, the agglomeration of aluminum, producing very large particles, could lead to higher nozzle corrosion than a beryllium analog. It is interesting to compare the throat deposit histories obtained on Tests T-4 and T-11 (see Section 5.2). Test T-4 used the Arcane 54F propellant in the remote end burning configuration while the same propellant was used in the Type I (7 inch circular port). There was almost no throat deposition on T-11 while deposits reached a maximum of 45 mils on T-4. Then, on Test T-22, the deposition increased beyond that obtained on Test T-5. It would be interesting to see the results of using the Arcane 60 analog in the close end burning grain configuration of Test T-22.

It is generally worth noting that in any propellant, especially at low oxidation ratios, the last metal particles to burn will have the least oxygen available to them. Such particles could pass beyond the throat without burning significantly unless the oxide shell melts and accumulates on one side of the particle, exposing the liquid metal and accelerating the vaporization process. The low pressures in the exit cone would also tend to accelerate metal vaporization. It is speculated, then, that for each beryllium metal size distribution (and possibly grain configuration) there will be a minimum theoretical flame temperature for which good performance can be achieved. The higher the number of the large particles, the greater must be the difference between the theoretical flame temperature and the beryllia melting point. In the extreme, if only one micron particles were used, the required minimum flame temperature would approach the beryllia melting point (or go below if it the hydroxide gas reactions are important enough). Apparently, ordinary beryllium powder has not been successfully used in propellants with theoretical flame temperatures below about 3200°K. Even then, these levels are reached with only small percentages of beryllium metal in the propellant. Similar conclusions were reached by Kuehl, Reference 7.

Under the appropriate conditions, it is expected that either beryllium or aluminum (and even beryllium hydride) can be burned completely. The evidence available suggests that aluminum will undergo rapid combustion, after a short ignition delay, as long as sufficient oxygen (H_2O, CO_2, etc.) is available. The vapor diffusion flame model is expected to apply, except that is will be complicated by particle spinning effects. The alumina apparently will appear as a fog of very small particles and one or more relatively large particles deriving from the original oxide shell. It is currently argued that acceleration effects in the nozzle throat region will cause the large particles to grow when the smaller particles catch up (less velocity lag) and hit the larger ones. Evidently, some of the hollow spheres may be formed in the combustion process in the chamber. However, it also seems reasonable that the dissolution of gases (CO, H_2, etc.) in the molten oxide during depressurization in the exit cone may be an important effect. Usually the alumina particles do not freeze within the nozzle so that the hollow sphere may be preserved simply as a result of freezing the outer surface first.

It is most interesting to observe that the beryllia particles are predominately in the size range of 0.01 to 0.2 micron. There are also larger particles (about 1 to 8 microns) found in small numbers. If the large particle sweeping model applies for alumina it should presumably also occur with beryllia. Apparently the large beryllia particles could also be the residue of the original oxide shell formed on the metal particle. Since there are relatively few large metal particles to begin with and fragmentation may not occur during the slower and more stable beryllium particle combustion, it does not appear that the beryllia particles obey the sweeping model. Aside from the possibility that neither this observation nor the alumina growth model are correct, there are few logical explanations. It is conceivable that the very small beryllia particles were condensed from beryllium hydroxide gases in the exit cone (below the beryllia fusion temperature) where the acceleration effects are less important. This has been suggested in Reference 6. (This hypothesis could probably be examined to establish its validity by several means.) The companion observation (few if any hollow beryllia spheres) would not be surprising if the CO, H_2, etc. gases were not as soluble in beryllia as they may be in alumina. Any alternate explanation of the apparent failure of beryllia to grow in size would probably have to involve either electrostatic charge effects or continuing burning (outgasing) of the large particles as they pass through the throat pressure gradient. In any case, the presence of the larger particles seems necessary to explain the deposition results obtained on this program. It is speculated that certain advanced propellants will have high enough flame temperatures to permit the beryllium to burn primarily in the vapor diffusion flame mode. If the reaction between beryllium vapor and water should produce beryllia (as opposed to the water-beryllia reaction producing the hydroxide), then exhaust plume particle sampling could provide important new evidence.

It is reasonably obvious that the problem of beryllium combustion should be the subject of continued study. For the present, the qualitative combustion model and condensed phase flow (deposition) theory can be employed to guide the designer in the right direction. Unfortunately, each grain design, propellant formulation and motor contour must be examined separately. Generalization of rules concerning chamber residence time appears to be unwarranted as a substitute for determining the actual velocity slip heating of the metal particles. Since high velocity particle impact (leading to splatter or rebound) may preclude the establishment of protective oxide deposits, the combination of submerged nozzles and high propellant mass fraction appears to provide the most dangerous situation. However, deep submergence should be beneficial in that mass generated behind the nozzle will flow along a relatively long path and will tend to shield the nose cap and inlet section from the more dangerous port flow. Basically, the designer must choose between the alternatives of achieving nearly complete combustion or encouraging deposition. The encouragement of the deposition of unburned particles of beryllium may not be desirable if the throat insert happens to be tungsten. While the formation of the low melting alloys of tungsten has not actually been observed in this program, it continues to be a logical possibility.

b. (C) Nonideal Ballistic Performance

The effects of poor metal combustion on C-star and impulse efficiency were examined for the seven propellants being used in this program. The results may be found in Sections 2.3 of References 1 and 2. These data were to have been used in conjunction with the measured ballistic performance efficiency to obtain an estimate of the degree of metal combustion achieved in each small motor test. This goal has not been satisfactorily reached as is explained in the discussions which follow.

Table V summarizes the average chamber pressure, C-star and impulse data obtained for the entire series of small motor tests. The C-star values were calculated in the manner described on Page 237, Reference 2. This technique utilizes an integral average throat area to include the effects of deposition and erosion which cannot be accounted for by averaging the measured initial and final (with or without deposit) throat diameters. The action times used in the computation of the C-star data were obtained in the manner indicated in Figure 117, Reference 2. The specific impulse data were calculated using the same action time, the original propellant weight and the integral average thrust. None of the data presented have been corrected in any way. The C-star and impulse efficiencies were computed using the ideal ballistic performance at the nominal design pressure (800 psia) irrespective of the actual average motor pressure. These ficticious efficiency numbers will be corrected for presentation in the final report. For the present, it will be noted that the average pressures were quite close (within 50 psi) to the nominal value on 14 of the tests. The minimum pressure, 275 psi below nominal, occurred on Test T-6 which was a hang fire. The maximum pressure, 186 psi above nominal, occurred on Test T-15. Obviously, the pressure correction effects will be rather large at these extremes.

Several other major errors must be considered in addition to the pressure effect. It is apparent that the propellant weight should be adjusted to account for the surface deposits and chamber residue which did not pass through the throat or flowed along the contour as a liquid deposit. Unfortunately, no attempt was made to obtain motor residue weights. However, for beryllium propellant tests, it is estimated that the retained oxides amounted to about 1/2 to 2 pounds, the lower number being associated with the submerged nozzle tests (except T-23) and the higher number being associated with the end burning grains. The relatively high porosity of the deposits has been considered in making these estimates. In addition, the movies of the firings suggest that 1/2 to 2 pounds of slag flowed along the wall and was expelled at the exit cone lip. There appears to be a definite correspondence between the throat deposit thickness history and the amount of material expelled. The retention of thick, solid deposits or very low deposit thicknesses (e.g., Tests T-4, T-5, T-7, T-11, T-14, T-21, T-22, T-23 and T-24) corresponds to the low estimate of slag expulsion. When thick deposits formed at the nozzle throat and subsequently melted and

TABLE V. UNCORRECTED BALLISTIC PERFORMANCE EFFICIENCY DATA (C)

Propellant	Grain Type	Nozzle Type	Test Number	Chamber Pressure (average) (psig)	C* (measured average) (ft/sec)	C* Efficiency (percent)	ISP Measured (sec)	ISP Efficient (percent)
191F	I	Conv PG	9	774.6	5168	95.0	235	84.5
191F	I	Conv PG	20	826.8	5163	95.0	244	87.8
191F	I	Conv PG	25	828.2	5167	95.0	237	85.3
191F	I	Conv W	16	835.9	5083	93.3	235	84.5
191F	I	Conv W	17	798.4	5040	92.5	227	81.7
191F	I	Sub W	18	841.0	4920	90.4	233	83.9
191F	EB (remote)	Conv PG	1	804.2	5164	95.0	235	84.5
191F	EB (close)	STP PG	21	933.3	4669	85.8	236	85.0
191F	EB (close)	Sub PG	23	811.2	4784	87.9	232	83.5
191F	II	Conv PG	10	822.6	5317	97.7	252	90.7
191F	II	Sub PG	12	729.9	5065	93.1	237	85.3
191F	II	STP PG	13	726.8	5026	92.3	224	80.6
319BRF	I	Conv PG	14	812.7	5204	94.5	254	90.3
319BRF	I	Sub W	19	895.8	5222	95.0	238	84.6
319BRF	EB (remote)	Conv PG	3	894.9	5494	99.6	245	87.0
319BRF	EB (close)	STP PG	24	636.1	5267	95.6	228	81.1
319BRF	III	Conv PG	15	986.2	5583	101.2	249	88.5
54F	I	Conv PG	11	775.2	5233	96.5	254	91.1
54F	EB (remote)	Conv PG	4	788.8	4898	90.3	231	82.8
54F	EB (close)	STP PG	22	857.1	5017	92.5	234	83.9
24F	EB (remote)	Conv PG	2	706.3	5041	93.5	236	85.1
389	EB (remote)	Conv PG	7	962.8	5087	98.2	223	85.5
389	II	Conv PG	8	799.2	-	-	238	91.3
390	EB (remote)	Conv PG	6	525.3	4918	93.2	222	84.2
60	EB (remote)	Conv PG	5	814.6	4882	95.2	226	87.6

flowed away, large amounts of slag are expelled. Evidently, then the C-star efficiencies could logically be corrected by 1 to 4 percent to account for slag effects. The same corrections would not apply as well to the impulse efficiency, since the expelled oxide will contribute significantly to the measured thrust. Such contributions can actually be seen on some of the thrust curves.

The heat transfer and skin friction losses are estimated to be of the order of 1 to 2 percent, depending on the length of the motor contour actually exposed to the combustion gases. These losses are partially countered by pyrolysis gas mass addition effects. The minimum effect should apply to the submerged nozzles without a carbon cloth entrance cone (Tests T-12, T-18, and T-23) and the maximum effect would apply to the tests using the end burning grains. The corrections should be somewhat larger for impulse efficiency to account for exit cone heating. The additional correction would be of the order of 1/2 percent.

The impulse efficiencies should also be corrected for divergence losses. The usual nozzle half angle correction would apply to each test. However, when large amounts of deposit pass the nozzle throat, it has been observed (motion pictures) that the plume may actually detach and reattach at the bottom sector of the nozzle. This is thought to be the result of the gravity effect causing significant deposit buildup along the cool exit cone surface (at the bottom). Post-test examination of the exit cones bears this out. Step discontinuities in the exit cone have varied up to a maximum of about one eighth of an inch. The resulting side thrust loss should be approximately additive to the divergence loss. It is estimated that the sum of these losses will range from 3 to 4 percent for the 20 degree half angle nozzles used. Again, the minimum correction applies to Tests T-4, T-5, T-7, T-11, T-14, T-21, T-22, T-23 and T-24.

It would normally be necessary to correct the C-star efficiencies to account for the nozzle throat curvature effect on the throat area. Since a large curvature has been used, the correction will be less than about 1/4 percent and is neglected. It is presumed that the throat deposits will not have a significant influence on the throat curvature.

The estimated corrections are listed separately in Table VI along with upgraded performance efficiency figures. Note that the chamber pressure effect has not been included. Any difference between the roughly corrected C-star efficiencies and 100 percent should be associated with condensed phase particle lag and combustion efficiency losses. These two losses would be complimentary since unburned metal particles or agglomerates would create the greater drag losses. The submerged and steep inlet nozzle contours probably cause the concentration of the condensed particles to be higher near the nozzle axis than near the wall contour, contributing to higher particle drag losses. Considering these factors and the directional effect of the chamber pressure correction, the following tests appear to

TABLE VI. ADJUSTED BALLISTIC PERFORMANCE EFFICIENCIES

	Estimated Losses Due to:						Adjusted Efficiency	
	Slag Effect		Heat Transfer		Divergence			
Test	C* (percent)	ISP (percent)	C* (percent)	ISP (percent)	20° Angle (percent)	Side Thrust (percent)	C* (percent)	ISP (percent)
T-1	3	3	2	2-1/2	3	1	100.0	94.0
T-2	3	3	2	2-1/2	3	1	98.5	94.6
T-3	2	2	2	2-1/2	3	1/2	103.6	95.0
T-4	3	3	2	2-1/2	3	1/2	95.3	91.8
T-5	3	3	1-1/2	2	3	1	99.7	96.6
T-6	2	2	1-1/2	2	3	1/2	96.7	91.7
T-7	2	2	2	2-1/2	3	0	102.2	93.0
T-8	2-1/2	2-1/2	1-1/2	2	3	1	-	99.8
T-9	2	2	1-1/2	2	3	1	98.5	92.5
T-10	2-1/2	2-1/2	1-1/2	2	3	1/2	101.7	98.7
T-11	-	1	1-1/2	2	3	0	99.0	97.0
T-12	2-1/2	2-1/2	1	1-1/2	3	1	96.6	93.3
T-13	2-1/2	4-1/2	1-1/2	2	3	1	96.3	91.1
T-14	1-1/2	1-1/2	1-1/2	2	3	0	97.5	96.8
T-15	1	1	1	1-1/2	3	0	103.2	94.0
T-16	2	2	1-1/2	2	3	1	96.8	92.5
T-17	2	2	1-1/2	2	3	1	96.0	89.7
T-18	1	1	1	1-1/2	3	1	92.4	90.4
T-19	1	1	1-1/2	2	3	0	97.5	90.6
T-20	2	2	2	2-1/2	3	1/2	99.0	95.8
T-21	3	3	2	2-1/2	3	0	90.8	93.5
T-22	3	3	2	2-1/2	3	0	97.5	92.4
T-23	1	1	1	1-1/2	3	1/2	89.9	89.5
T-24	3	3	2	2-1/2	3	0	100.6	89.6
T-25	1-1/2	1-1/2	1-1/2	2	3	1	98.0	92.8

have produced incomplete metal combustion: T-4, T-16, T-17, T-18, T-21, T-23 and, possibly, T-14, T-19 and T-22.

The heat transfer results (see Section 2.3.d, following) agree with the observation concerning Test T-4. Thus, the Arcane 54F propellant deposition on Tests T-4 and T-22 could be reflecting some unburned particle deposition. (Compare the deposition curve on Test T-2, Arcane 24F propellant at apparently high efficiency, with those of Tests T-4 and T-22.) There is no obvious reason why the tungsten nozzles, Tests T-16 through T-19, should have given low C-star efficiencies. The throat shrinkage effect appears to be the only immediate source of error. Note that the throat heat transfer coefficients were uniformly low by 60 to 80 percent, compared to Tests T-9, T-20 and T-25. The isotropic nature of tungsten accounts for part of the tungsten thermal behavior. However, throat shrinkage during the firing would lead to lower deposit thicknesses and a lower heat transfer coefficient. The tungsten nozzle tests will, consequently be examined more closely during the remaining period of the program. Tests T-21 and T-23 (Arcocel 191F propellant) definitely have low C-star efficiencies. The heat transfer and deposition data agree with this finding. It is speculated that the high temperature 191F propellant may be burning in a regime where surface agglomeration of beryllium is occurring. The relatively higher performance of the 319BRF and 54F propellants in Tests T-22 and T-24 suggests that either agglomeration does not occur or a smaller number or size of agglomerates are formed.

The lowest C-star efficiency for the Arcane 54F propellant occurred on Test T-22. This is interpreted as an indication that the metal combustion efficiency could have been lower during the first portion of the firing. On Test T-19, Arcocel 319BRF, the tungsten throat contraction problem could account for the C-star efficiency being well below 100 percent. If this is true, then the performance on Test T-14 (identical to Test T-19 except for the throat insert material) will be higher after pressure and area ratio effects are accounted for. For the present then, Tests T-3, T-15 and T-24 (end burning and Type III grains) which had efficiencies over 100 percent, appear to be the unusual ones (Arcocel 319BRF only). Unless some reasonable explanation can be found for these "super" efficiencies, it is logical to assume that the particle drag losses are near zero for the 319BRF propellant. It appears that this would also apply to the other propellants.

No attempt has been made to explain the behavior of the impulse efficiencies. These figures should be quite sensitive to the accuracy of the thrust measurement. It is possible that a systematic error has been introduced by using the highest of the two thrust measurements. In some cases there was a significant difference between the thrust curves. The raw data will be re-examined on this basis and any results will be included in the final report. In no case will the change, from one thrust measurement to another, influence the throat deposit history by more than a few percent.

In connection with the ballistic performance analysis, exhaust gas residence times have been estimated for the end burning and center perforated (Type I) grains. Figure 1 shows cross sections of these grains. Two stations are indicated for the end burner, representing the initial and final location of the burning surface. For the Type I grain, Stations 1 and 2 are the points closest to and farthest from the nozzle throat at grain ignition. Stations 3 and 4 represent the same extremes at burnout. A one-dimensional analysis was used to determine an average flow velocity along the most direct streamline path connecting each station and the nozzle throat plane. The length of the path and average velocity provide the stay time estimate. Such stay times do not necessarily represent the residence time for burning metal particles. The results of the calculations are presented in Table VII. Note that the remote end burning grains are located approximately 12 inches farther from the throat than the close end burner grains (see Section 5.2).

Clearly, the stay times are respectably large for the remote end burning grains. It should be remembered, however, that the low chamber velocities (about 10 ft/sec axially) severely limit the burning metal particle convective heating rate. The portion of the exhaust products which follows the motor contour is expected to achieve a higher degree of combustion than the portion which flows along the motor axis. From a ballistic performance point of view, the velocity, acceleration, temperature and particle concentration along the axis from the grain surface to the nozzle throat are critical. Thus, measured performance should correlate with such parameters as: (1) grain diameter to throat contraction ratio, (2) aft closure and nozzle entrance cone angles, (3) initial axial distance from grain surface to the nozzle throat, (4) formulation and ideal flame temperatures relative to the oxide melting point, (5) metal loading, and (6) propellant oxidation ratio. From the oxide deposition point of view, the most significant parameters should be (1) the stay time along a stream line path from the grain outer radius to the point along the aft closure contour where impaction will occur (also nearly an axial path), and (2) all of the parameters listed above. If metal actually should deposit on the aft closure, there would be an indirect effect on ballistic performance. From the corrosion point of view, the aft closure insulation would potentially be exposed to a fuel rich exhaust. The nozzle throat (unless protected by deposits) may be exposed to either a fuel or oxidizer rich exhaust depending on the behavior of deposited beryllium metal and the slip experienced (away from the wall) by unburned particles as they approach the throat.

The close end burning grain design was originally selected to obtain an initial stay time (with respect to the aft closure insulator at its outer diameter) of essentially zero. At the same time, the axial stay time (to the throat) was reduced by a factor of five. This resulted in lower performance, higher deposition and lower nozzle throat heat transfer. The steep inlet nozzle contour was selected because it should have forced the particles (metal or oxide) towards the center of the flow. This would have increased the relative oxygen content of the gases flowing over the nozzle

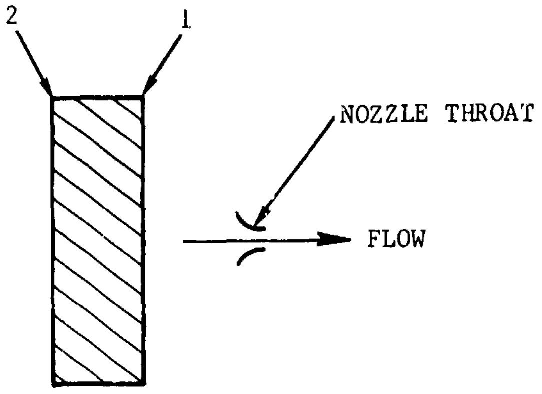
2
1
NOZZLE THROAT
FLOW

END BURNING GRAIN

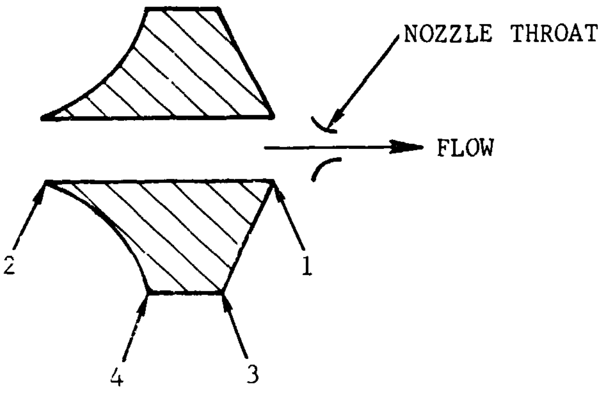
NOZZLE THROAT
FLOW
2
1
4
3

CENTER PERFORATED
GRAINS (TYPE I)

F08183 U

FIGURE 1. KEY TO EXHAUST GAS STAY TIME CALCULATIONS

TABLE VII. EXHAUST GAS STAY TIME DATA (C)

Test	Nozzle Configuration	Throat Diameter (inches)	Grain Type	Calculated Stay-Times (seconds)* Station (1)	Station (2)	Station (3)	Station (4)
T-1	Conventional	1.165	Remote End-Burner	0.19	0.27	-	-
T-2	Conventional	1.030	Remote End-Burner	0.25	0.36	-	-
T-3	Conventional	1.190	Remote End-Burner	0.18	0.25	-	-
T-4	Conventional	1.030	Remote End-Burner	0.25	0.36	-	-
T-9	Conventional	1.214	I	0.0035	0.017	0.042	0.097
T-11	Conventional	1.080	I	0.0044	0.013	0.060	0.14
T-14	Conventional	1.218	I	0.0035	0.017	0.042	0.097
T-16	Conventional	1.214	I	0.0035	0.017	0.042	0.097
T-17	Conventional	1.214	I	0.0035	0.017	0.042	0.097
T-18	Submerged	1.214	I	0.0019	0.016	0.035	0.092
T-19	Submerged	1.214	I	0.0019	0.016	0.035	0.092
T-20	Conventional	1.214	I	0.0035	0.017	0.042	0.097
T-21	Steep Inlet	1.165	Close End-Burner	0.044	0.12	-	-
T-22	Steep Inlet	1.030	Close End-Burner	0.056	0.16	-	-
T-23	Submerged	1.165	Close End-Burner	0.040	0.12	-	-
T-24	Steep Inlet	1.217	Close End-Burner	0.040	0.11	-	-
T-25	Conventional	1.222	I	0.0035	0.017	0.042	0.097

---

* See Figure 1 for station locations

throat, causing higher corrosion. If this actually occurred, it was well obscured by the deposits which reached the throat before surface temperatures exceeded the corrosion threshold. Unfortunately, the attempt to capture the early deposits at the outer radius of the aft closure insulator also failed (see Section 4.3, Tests T-21 and T-22). Consequently, the question as to whether the axial stay time or beryllium deposition may have been the dominant cause of the ballistic performance losses on the close end burning grain tests has not been answered. It will be observed by comparing the performance on Tests T-1, T-21 and T-23, that the submerged nozzle gave significantly lower performance. From this and a comparison of the throat deposit histories, it is speculated that both effects are important.

It has been generally concluded that it would be almost impossible to demonstrate the relationship between high nozzle corrosion and low ballistic performance with an end burning grain. Since this derives from the deposition protection phenomenon, the one chance would be to fire the motor vertically up. However, it might be more profitable to depend on the internal burning grain. In comparison with the end burners, the center perforated (Type I) grains always have shorter stay times, either along the grain axis or along the wall to the throat. Yet, the ballistic performance of Type I grains is significantly better than the close end burners. In this case the flow along the motor axis should achieve the highest degree of combustion. Initially, the port flow will be turned by the nozzle inlet section, causing significant deposition and higher concentrations of particles (metal or oxide) near the wall. Rather high throat corrosion was experienced before deposition on Test T-20. This may have been a result of excess oxygen availability while the stay time was near 5 milliseconds (Station 1). As the grain burns, the particle deposition point should move upstream to the steep section of the aft closure insulator. Then, unburned particles will tend to be thrown away from the contour. By then, the stay times have increased and deposits protect the throat. Again, short stay time effects on corrosion cannot be derived. It is probable that the big factor in achieving the high performance is the change in the direction of mass injection from the grain surface. The metal particles may be sheared from the grain or may be injected normally to the main flow direction. In either case, velocity slip heating of the particles will be much greater than for parallel injection (end burners).

It is generally concluded that gas stay time is not a valid correlation parameter when grain design and motor contour are allowed to vary. Furthermore, poor metal combustion will not usually constitute a hazard to motor materials in designs which encourage deposition. However, it is speculated that beryllium alloying of tungsten and extreme corrosion of graphite could and have occurred under the appropriate conditions. Thus, high velocity impaction, low impact angle and high surface temperatures will discourage deposition. It can be expected that appropriately corrected C-star efficiency and the measured throat heat transfer coefficient data will provide a good qualitative indication of low metal combustion efficiency.

c. (C) Nonideal Exhaust Composition

Examination of the chamber gas composition (Table I), as a function of degree of metal combustion, has shown that CO_2 concentrations vary by more than an order of magnitude. Water vapor concentrations vary by a factor of about 4 to 12 depending on the propellant oxidation ratio. Atomic and molecular hydrogen concentrations vary in accordance with the water concentration and flame temperature. The CO concentration varies inversely as the CO_2 while the $HC\ell$ and N_2 concentrations vary only slightly.

Metal particles or agglomerates, according to the combustion model, must undergo surface oxidation, ignition and vapor phase combustion in the nonideal exhaust environment. Evidently, water and CO_2 must be the primary oxidants during the surface oxidation and ignition stages. Particle ignition temperatures, unless strongly influenced by the CO_2, will be close to 1900°K (Reference 7). Combustion would be relatively slow while the particle temperature rises from the ignition limit to the beryllia melting point. The smallest particles and/or agglomerates should burn first, depleating the supply of H_2O and CO_2. Evidently, enough of the smaller particles must burn to cause the flame temperature to rise above the beryllia melting point. When this occurs, the large particles should burn in a vapor diffusion mode. However, rapid burning would only occur if the concentrations of the oxidants is relatively high. The $HC\ell$ may have an important role during this stage of burning since beryllium chloride gas is a stable equilibrium exhaust product. It is not obvious that the inerts, H_2, CO and N_2, play a major role in the metal combustion process, except as they are involved in the diffusion flame or influence the beryllium-beryllia particle structure via adsorption or solution.

A serious situation is expected to arise when the chamber exhaust flows in such a way as to create a high concentration of burning particles in some portion of the flow. The relative availability of oxygen (H_2O, CO_2, etc) will be abnormally low and particle combustion in any mode will be repressed. Conversely, where particle concentrations are below average, the gas phase will have an abnormally high oxygen content, which will accelerate combustion of the particles. Clearly, it is not desirable to complicate the combustion of the particles before they reach the beryllia melting temperature. For any particular grain design, the flow field can be estimated and the possibility of burning metal particle stratification can be qualitatively evaluated. Then, it should be possible to anticipate beryllium metal deposition, high oxygen availability near the motor contour, and ballistic performance losses.

One advantage of the advanced beryllium propellant systems appears to be that the particles will not be forced to burn in the 1900 to 2800°K temperature range. The primary effect in determining ignition delay times should be the particle heat capacity. Thus, particle agglomeration at the grain surface will be important. Rapid, vapor diffusion controlled, combustion of the particles will minimize the tendency for particle stratification to occur. Nearly ideal oxygen concentrations may be established as the rule rather than the exception. Such exhausts will be hotter but materials temperature control should be adequate to control corrosion and erosion. The primary danger would be that designs might be based on heat transfer data which has been derived from systems where poor metal combustion has occurred. Such heat transfer data could be quite low. Then, in the advanced systems, material temperatures would exceed design levels, inducing poor nozzle and insulation materials performance.

It is recommended, therefore, that careful consideration be given to the nonideal exhaust composition in any studies of beryllium metal particle combustion. Degree of metal combustion and exhaust stratification effects must be considered in selecting nozzle heat transfer design data or predictions.

d. (C) Nonideal Exhaust Corrosivity

It was observed, in Paragraph b. above, that the adjusted C-star efficiencies on Tests T-21 and T-23 were particularly low (90.8 and 89.9 percent, respectively). Since the efficiencies are average values, little can be done in the case of Test T-20, where poor metal combustion may have influenced the corrosion. It is interesting to speculate that the 10 percent loss in efficiency on Tests T-21 and T-23 was due solely to poor metal combustion. From Figure 4 of Reference 1, it is found that only half of the metal burned. The corresponding impulse efficiency (50 percent metal combustion) would be 91 percent. Since the estimated impulse efficiency was about 94 percent, it is possible that the 50 percent metal combustion figure applies to the C-star efficiency while 60 percent would be more appropriate for impulse. Note that the particle drag losses have been neglected.

Based on 50 percent metal combustion, Figure 8 (Reference 1) indicates that the concentration of oxidizing species in the exhaust is more than tripple the amount in the ideal exhaust. Figure 10 (Reference 1) indicates that the flame temperature would drop from $3758^{\circ}K$ to $3230^{\circ}K$. If this were accounted for in the calculation of the throat heat transfer coefficient (Section 2.5.e, Test T-21), the new value would be about twice that obtained. Thus, the true heat transfer coefficient would be about 0.0089 Btu/in^{2}sec$^{\circ}$F instead of the 0.0040 value presented. (This manipulation neglects changes in the average boundary layer specific heat.) This result agrees rather well with the heat transfer data obtained on Tests T-1, T-9, T-20 and T-25. Figures 12 and 14 of Reference 1 suggest that the nonideal exhaust would have been about 3 times more corrosive to graphite at the 50% metal combustion level. Obviously, the extreme deposition protection experienced on the low performance firings prevents a test of the corrosion prediction.

2.4 (C) FLUID MECHANICS

One of the objectives of the Analytical Studies Task has been to assess the influence of nonuniform and two-phase flow effects on the behavior of the motor materials. Phenomena affecting the gas-side surface behavior and directly related to the combustion chamber exhaust flow field can be identified from basic fluid mechanics arguments. For the present, interest is confined to the following elements of the overall materials-exhaust interaction problem:

(1) Boundary layer heat and mass transfer dependence on free stream turbulence, boundary layer edge properties (velocity, pressure, temperature), flow separation, reattachment, and boundary layer starting point.

(2) Particle impingement and subsequent deposition dependence on particle slip across gas streamlines.

(3) Degree of combustion dependence on stay time and grain port velocities.

The manner in which these factors can be incorporated in the convection and deposition analyses has been discussed in Sections 2.5a and 2.5b of Reference 2.

a. (C) Slotted Grain Flow Field Effects

In characterizing the boundary layer heat and mass transfer phenomena, the corresponding analytical models (Section 2.5a) require assuming an axisymmetric flow field. For many grain designs, this condition does not necessarily apply (i.e., star grain). Therefore, due to the inadequacies of the analytical boundary layer model, and the complexities involved in describing particle slip for the unsymmetrical flow field, an experimental investigation was pursued. In this investigation, the unsymmetrical flow field was produced by employing a center perforated grain with a single axial slot (see Figure 2). The basis for selecting a single slotted grain was, in part, to eliminate the flow field interaction caused by multiple slots.

The slotted grains were used in Tests T-8, 10, 12, 13, and 15. Within this series, detailed design variations included changes in the metal additive propellant formulation, grain port velocity, and nozzle contour. Table VIII compares appropriate slotted grain test design parameters. It can be seen, using Test T-10 as a reference, that: T-8 introduces a change in propellant metal type; T-12 and T-13 introduce changes in nozzle contour; and T-15 introduces changes in grain port velocity and propellant formulation. In each motor the aft closure, throat insert and exit cone gas side surface materials were asbestos phenolic, ATJ graphite, pyrolytic graphite washers and ATJ graphite, respectively.

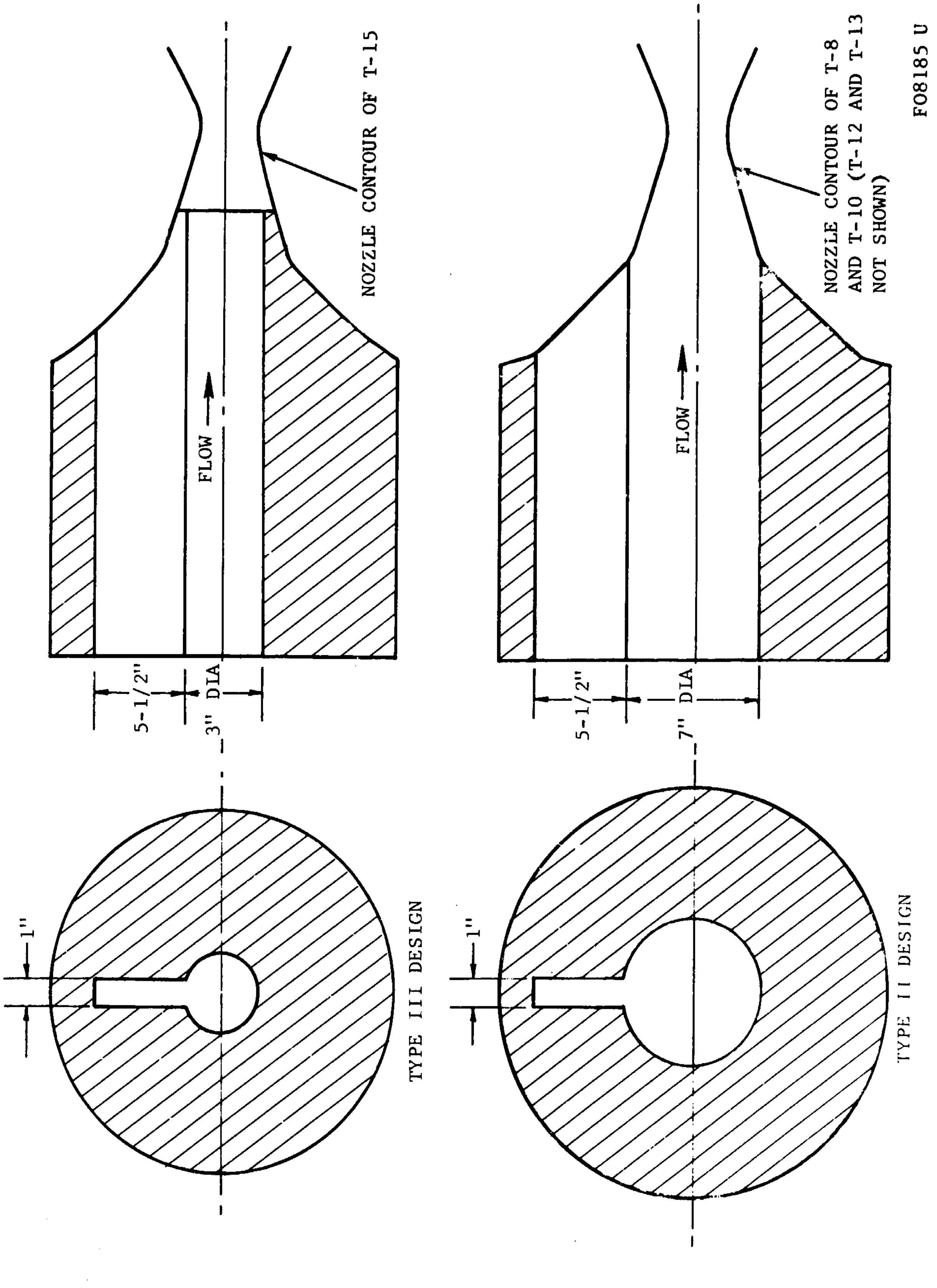
NOZZLE CONTOUR OF T-15
FLOW
5-1/2"
3" DIA
1"
TYPE III DESIGN
NOZZLE CONTOUR OF T-8 AND T-10 (T-12 AND T-13 NOT SHOWN)
FLOW
5-1/2"
7" DIA
1"
TYPE II DESIGN
F08185 U

FIGURE 2. SLOTTED GRAIN DESIGNS FOR SMALL MOTOR TESTS

TABLE VIII. SLOTTED GRAIN TESTS - DESIGN PARAMETERS (U)

Test Number	Grain Design	Initial Port to Throat Area Ratio*	Propellant	Nozzle Contour
T-8	7 in. CP-single slot	38	389 (Aluminum analog of 191F)	Conventional 18 degree entrance
T-10	7 in. CP-single slot	37	191F (Beryllium)	Conventional 18 degree entrance
T-12	7 in. CP-single slot	37	191 (Beryllium)	Submerged nozzle
T-13	7 in. CP-single slot	37	191F (Beryllium)	Conventional 55 degree entrance
T-15	3 in. CP-single slot (Same slot dimensions as 7 in. CP-single slot)	11.5	319 (Beryllium)	Conventional 180 degree entrance

---

*Includes slot area

In each of the slotted grain tests, the nozzle was instrumented with thermocouples (see Section 4.3). In tests T-10, T-12 and T-15, thermocouple data at identical axial positions were obtained at various circumferential positions relative to the grain slot location. The thermocouple data, together with post-test inspection of circumferential and axial variations in nozzle surface regression, were used to assess the influence of the unsymmetrical flow field. The results of the slotted grain tests are summarized in Table IX. The surface regression described in Table IX is based on a qualitative physical examination of the motor. The actual measurement of the circumferential variation in regression would require cross-sectioning the nozzle at four circumferential locations. Nozzle photographs in Section 3.4 should be examined.

From Table IX it can be concluded that, in all cases, grooving occurred at 0 and 180 degree positions relative to the 90 degree and 270 degree positions. It is also evident that the highest temperature corresponds to the location experiencing the highest surface regression. In all of the symmetrical

TABLE IX. COMPARISON OF GROOVE DEPTH AND TEMPERATURE-SLOTTED GRAIN TESTS (C)

Test Number	Variation in Circumferential Surface Regression*			Circumferential Temperature Variation**	
	Aft Closure	Entrance	Throat Insert	Entrance	Throat Insert
T-8	Slight grooving at 0° and 180°, fairly uniform at other positions.	Slight grooving at 180°, uniform at other positions.	Uniform at all positions.	—	—
T-10	Slight grooving at 0° and medium at 180°, uniform at other positions.	Slight grooving at 0° and medium at 180°, uniform at other positions.	Medium grooving at 180° decreasing at throat, uniform at other positions.	$T_{180} > T_{90} > T_0$ @ 15 seconds $T_{180} = 2650°F$ $T_{90} = 1780°F$ $T_0 = 1330°F$	—
T-12	Slight grooving at 0° and very slight at 180°, uniform at other positions.	At 0°, medium groove at nose cap stagnation point only, nothing in entrance; at 180°, medium over nose cap and entrance; uniform over other positions.	Medium grooving at 180° decreasing at throat; uniform at other positions.	—	$T_{180} > T_{90}$ @ 15 seconds $T_{180} = 2460°F$ $T_{90} = 2100°F$
T-13 Burn through at 90° position.	Medium grooving at both 0 and 180°, uniform at other position, except burn through position.	Slight grooving at 0° and heavy at 180°; uniform at other position, except burn through position.	Heavy grooving at 180°, uniform at other position, except burn through position.	—	—
T-15	Medium grooving at 0°, uniform at other positions.	Medium grooving at 0° and 180°, uniform at other positions.	Heavy grooving at 0° and medium at 180°, uniform other positions.	$T_{225} > T_{150}$ @ 14 seconds $T_{225} = 1510°F$ $T_{150} = 1380°F$	—

* Circumferential position of grain slot is at the 0° location, circumferential positions are measured in the clockwise direction looking aft.

** Data obtained from thermocouples positioned at identical nozzle axial positions and located at different circumferential locations. Subscripts on temperature refer to circumferential position (see Section 4.3 for axial location).

grain tests (end burner and center perforated), nearly uniform circumferential surface regression was measured. Therefore, it is concluded that the unsymmetrical flow field caused the nonuniformities.

To explain the observed circumferential variations in surface behavior, consideration must be given to the influence of the flow field on boundary layer heat and mass transfer, the effect of particle impingement, and the degree of combustion.

The slotted grain flow field has been qualitatively characterized by considering the difference between the mass generated in the slot and that generated in center perforation. The magnitude of this difference should be indicative of the relative velocity gradients and jet mixing that occur in the chamber and nozzle. With more mass being generated in the slot, a velocity gradient and free shear layers (or mixing region) will result. This will cause a radial jet type flow disturbance. The reflection of the slot on the grain and nozzle surfaces will appear 180 degrees from the circumferential slot location. A parameter, relating the ideal velocities of the slot and center perforation, can be defined by assuming that (1) the mass generated in the slot does not mix with that of the center perforation and (2) isobaric and isothermal conditions exist in the flow field. That is, the mass generated in the slot and center, respectively, are:

$$\dot m_S = \dot r\, A_{BS}$$

$$\dot m_C = \dot r\, A_{BC}$$

Where $\dot r$ is the propellant burn rate and A_{BS} and A_{BC} are the burn areas for the slot and center perforation. Assuming the two masses do not mix:

$$\dot r\, A_{BS} = \rho_S U_S A_{XS}$$

$$\dot r\, A_{BC} = \rho_C U_C A_{XC}$$

where A_{XS} and A_{XC} are the cross-sectional areas of the slot and center perforation. The velocity ratio in the appropriate flow areas is then:

$$\frac{U_S}{U_C} = \left(\frac{\dot r\, A_{BS}}{\rho_S A_{XS}} \quad \frac{\rho_C A_{XC}}{\dot r\, A_{BC}}\right)$$

Assuming equal burn rates pressure, temperature and molecular weights, the velocity ratio reduces to:

$$\frac{U_S}{U_C} = \frac{A_{BS}\, A_{XC}}{A_{BC}\, A_{XS}}$$

When U_S/U_C is less than, equal to, or greater than unity, the corresponding flow field in the grain port involves: (1) gases originating in the center perforation mixing with the slot gases in the slot, $U_S/U_C < 1$; (2) uniform radial and circumferential velocity profiles in the grain port, $U_S/U_C = 1$; (3) gases originating in the slot mixing with the center perforation gases in the center perforation, $U_S/U_C > 1$. Therefore, when U_S/U_C is greater than unity, a reflection of the slot on the 180 degree surface may be expected, the degree of reflection increasing with increasing U_S/U_C. Actually, the interaction of the grain port flow with the motor aft closure precludes the achievement of completely uniform flow. That is, the mass flowing in the slot will tend to deflect the streamlines toward the 180 degree wall position when a circular cross section is approached beyond the aft end of the grain.

For the slotted grains employed in Tests T-8, 10, 12, and 13, the velocity ratio (U_S/U_C) is 3.4 and for T-15 the ratio is 1.55. Figure 3 represents a schematic of the gas streamlines that can be expected for the slotted grain tests. It can be seen that a semistagnation line type flow interaction occurs on the propellant and nozzle surfaces 180 degrees from the slot. Along this line a relatively high degree of turbulence is induced, causing increased heat and mass transfer. Due to the nature of the jet type flow field this semistagnation line will extend along the nozzle contour with the strength of the disturbance gradually diminishing.

The formation of axial grooves in line with the slot (0 degree relative position) is apparently a more complicated process. The mass flowing in the slot will have both axial and radial velocity components. In the vicinity of the aft closure insulator surface, the flow must parallel the steep contour. Evidently the particle slip will always promote deposition (beryllia and beryllium) at the aft end of the slot. As the radial jet flow emerges from the slot, the symmetrical nozzle contour angles [illegible] considerably. The condensed phases in the flow will tend to be thrown away from the contour. Both the deposition and particle stratification effects will tend to create an oxygen rich wall jet extending along the nozzle contour in line with the slot. The lower the degree of metal combustion at the aft end of the slot the more corrosive will be the wall jet. Since oxides will tend to deposit primarily at the outer radius of the slot-aft closure interface, a significant time will pass between ignition and arrival of deposits in the 0 degree groove. However it is not obvious whether the arrival of deposits or the progressive widening of the grain slot will be most important in arresting the groove development.

Best Available Copy

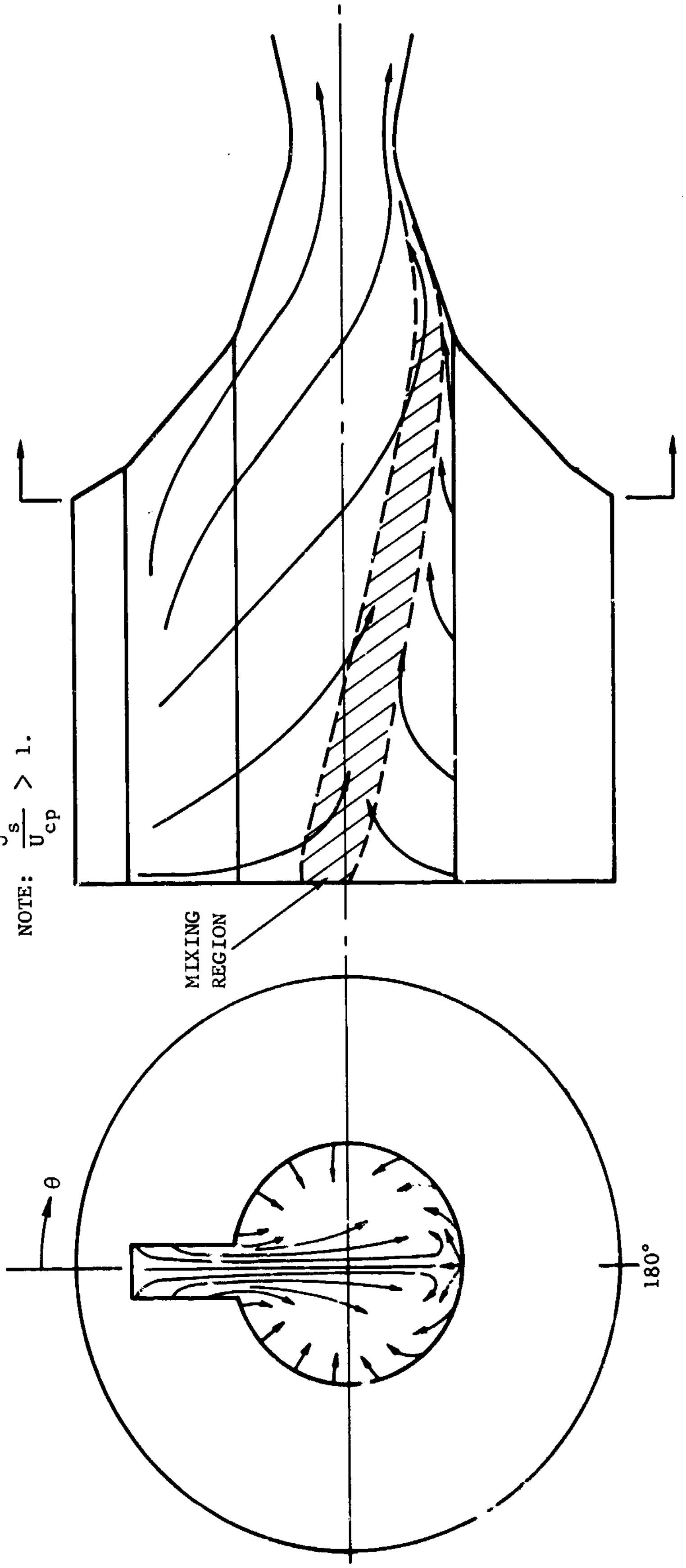
NOTE: $\frac{U_s}{U_{cp}} > 1.$
MIXING REGION
0°
θ
180°

F08179 U

FIGURE 3. ESTIMATED FLOW FIELD - TYPE II SLOTTED GRAIN

It is currently believed that the grooves at both the 0 degree and 180 degree positions are formed during the early portion of the firing. In a long firing, after deposition protection effects have disappeared, the grooves will continue to develop.

The results of unsymmetrical flow effects on surface behavior can be observed by comparing Tests T-10 and T-15 (different grain port area ratio, propellant formulation, and equal slot geometry). In Test T-10, the depth of the groove opposite the grain slot exceeds that at the 0 degree position, whereas, for Test T-15, just the opposite occurs. As stated previously, the ratio U_S/U_C is 3.4 and 1.55 and the grain port area ratio is 37.0 and 11.5 for T-10 and T-15, respectively. Therefore, the radial jet flow effect will be more pronounced for T-10 than T-15, promoting the deeper groove observed at the 180 degree position for T-10. Note that the mixing length of T-15 is less than T-10, approximately 3 compared to 7 inches However, jet flow theory suggests that mixing length is of secondary importance compared to the jet velocity ratio. Hence, the jet velocity ratio is assumed to be the governing parameter in groove formation opposite the slot. The grain port area ratio differences in T-10 and T-15 suggest that the degree of metal combustion or particle stratification is less for T-15 (assuming equal combustion mechanics for the two propellants). Hence, the magnitude of the regression at the 0 degree location for T-15 could be attributed to oxygen enrichment of the 0 degree wall jet.

The effect of nozzle contour on the degree of combustion and jet flow phenomena can be deduced from motors T-10, 12 and 13. The variation of surface regression with circumferential positions for T-10 and T-13 are very similar, the only difference being in magnitude. This may be attributed to differences in aft closure and nozzle contour angles. In Test T-12, the 0 degree groove terminated downstream from the nose cap. This suggests that the gas streamline corresponding to the slot center resembles that of an end burner grain design, thus causing an interferring flow stagnation point at the 0 degree position on the entrance nose cap. At the 180 degree position, however, the jet type flow field is preserved causing localized corrosion.

In Test T-8, representing the aluminum analog of Test T-10, the 0 degree and 180 degree grooves were not as pronounced as on Test T-10. Very slight grooving was noted for T-8 at the 0 degree position in the aft closure and the groove extended into the entrance section at the 180 degree position. This could indicate that the aluminum analog had a higher degree of metal combustion than the beryllium propellant. However, another phenomenon that will influence the correlation between the two propellants is that of deposition With reference to the physical model of deposition presented in the second quarterly report, the buildup and downstream progression of the deposit (for a given propellant, temperature, and nozzle design) is dependent on the metal oxide melting point, impinging particle size, thermal conductivity, viscosity, and surface chemical reactions. In Tests T-8 and T-10, the nozzle contour and gas-side materials were identical.

However, large differences in metal oxide melting point, particle size (see Section 2.5d of Reference 2), and thermal conductivity would probably cause the Al_2O_3 deposit to provide both chemical and thermal protection more effectively during the initial portion of the firing.

The energy transported to the nozzle surface, and the surface regression associated with particle impingement, does not appear to be important for the slotted grains studied in this contract. For the slotted grain and nozzle geometries of Table IX, the 0 degree circumferential location will experience the greatest particle impingement. This is evident from consideration of the slot to center perforation velocity ratios and the gas streamline turning angles (see Section 3.3.4 in Reference 1). From Reference 1, it is noted that, for the 18 degree nozzle entrance geometry, impingement occurs in the aft closure and is terminated just upstream of the entrance section. However, in the 18 degree nozzle entrance geometries (T-8, 10 and 15) grooving was observed at the 0 degree position in the entrance section. This suggests that the aft closure, entrance and throat surface regression at 0 degrees cannot be directly attributed to particle impingement. However, it may be connected with incomplete combustion, burning metal particle stratification effects or impingement induced boundary layer turbulence.

Another phenomenon that may be induced by the slot jet flow is increased propellant burning rate at the 180 degree position. As is evident in Figure 3, the jet-type flow will cause increased heat and mass transfer at 180 degrees, not only on the nozzle, but on the propellant, potentially causing grooving of dishing out of the propellant. This is the best available explanation for the observed progressive-regressive grain burning.

In conclusion, the influence of the slotted grains on nozzle behavior can be described on the basis of the unsymmetrical flow field. Specifically for the slotted grain designs employed in this program, the slot to center perforation velocity ratio indicates a radial jet flow field. This flow field will promote the formation of two axial grooves in the nozzle contour. The groove formed in line with the slot is caused by an artificially oxygen enriched wall jet while the groove formed opposite the slot is a result of higher local boundary layer shear, convection and turbulence. The influence of particle impingement on increased heat transfer and surface regression is thought to be negligible; however, further investigation is required in this area. Both grooves are believed to have formed early in the firing with oxide deposition and grain flow field changes jointly acting to arrest the groove formation during the latter portion of the firing. Nozzle submergence may be effective in eliminating the groove in line with the grain slot.

The above conclusions can be extended to estimate the nozzle behavior of rocket motors employing multiple slotted grains. For example, consider center perforated grains with 2 and 4 axial slots. A schematic of each flow field is shown in Figure 4 for the case where the individual slot mass generation exceeds that of the center perforation. The flow fields of the 2 and 4 slot grains are similar to that of impinging jets. Grooving should occur at 0 degree and 180 degrees for the 2 slot case (0, 90, 180, and 270 degrees for the 4 slot case) due to the increased corrosivity of the wall jet in line with the slots. Grooves will also form at 90 and 270 degrees for the 2 slot case (45, 135, 225 and 315 degrees for the 4 slot case) due to the axial semistagnation line effect. As the number of slots increase, the grooving caused by the semistagnation line jet flow field should decrease due to increased mixing of the masses generated in the slots (i.e., increased number of free shear layers). However, the grooving induced by the increased corrosiveness may not diminish at circumferential positions in line with the slots.

b. (C) Symmetrical Grain Flow Field Effects

The gas streamlines and condensed phase deposition profiles at two burn times have been estimated for the following grain-nozzle designs: (1) the remote end burner-conventional, (2) close end burner-submerged, (3) close end burner-steep inlet, (4) 7 inch center perforated-conventional, and (5) 7 inch center perforated-submerged. Schematic representations of each of these designs are presented in Figures 5 through 9. The variations in the velocity vectors and particle impingement with motor axial position were approximated using the results and conclusions of the cold flow modeling study (see Section 3.3b, Reference 1). The coordinates of the condensed phase deposition profiles are defined as:

> Abscissa ('S') is the distance along the nozzle contour starting at the location A (noted on the sketch of the motor contour) and proceeding downstream.
>
> Ordinate ('$\bar{X}$') is the ratio of the number of particles impinging on the wall per unit wall area to the number of particles in the free stream per unit cross-sectional area of the flow.

The streamlines and impingement profile for the remote end burner-conventional nozzle, presented in Figure 5, will remain essentially constant. Any transients in particle impingement during the firing will result from (1) particle size change, (2) aft closure insulation pyrolysis rate change, (3) nozzle contour change resulting from deposition and/or surface regression or (4) gravitational effects.

The gas streamlines in the close end burner-submerged nozzle will undergo extreme changes during the firing as shown in Figure 6. The submerged nozzle will cause a stagnation point to develop at location 'B' on the inlet. The recirculating flow will deposit particles on the aft closure at a low

Best Available Copy

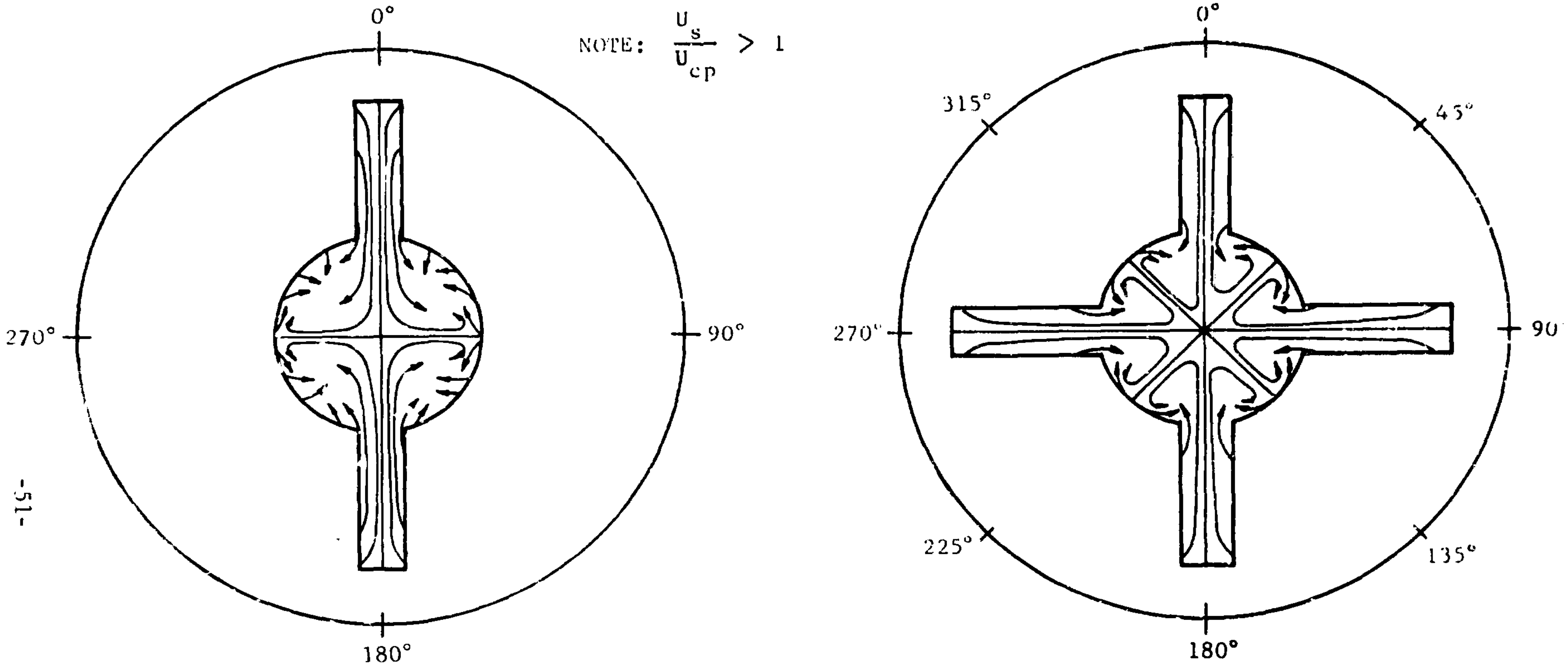
0°
90°
180°
270°
NOTE: $\frac{U_s}{U_{cp}} > 1$
0°
45°
90
135°
180°
225°
270°
315°

SIGNIFICANT AFT CLOSURE INSULATION AND NOZZLE GROOVES
WILL FORM AT EACH ANGULAR POSITION INDICATED

F08178 U

FIGURE 4. ESTIMATED EFFECTS OF MULTIPLE GRAIN SLOTS ON FLOW FIELD

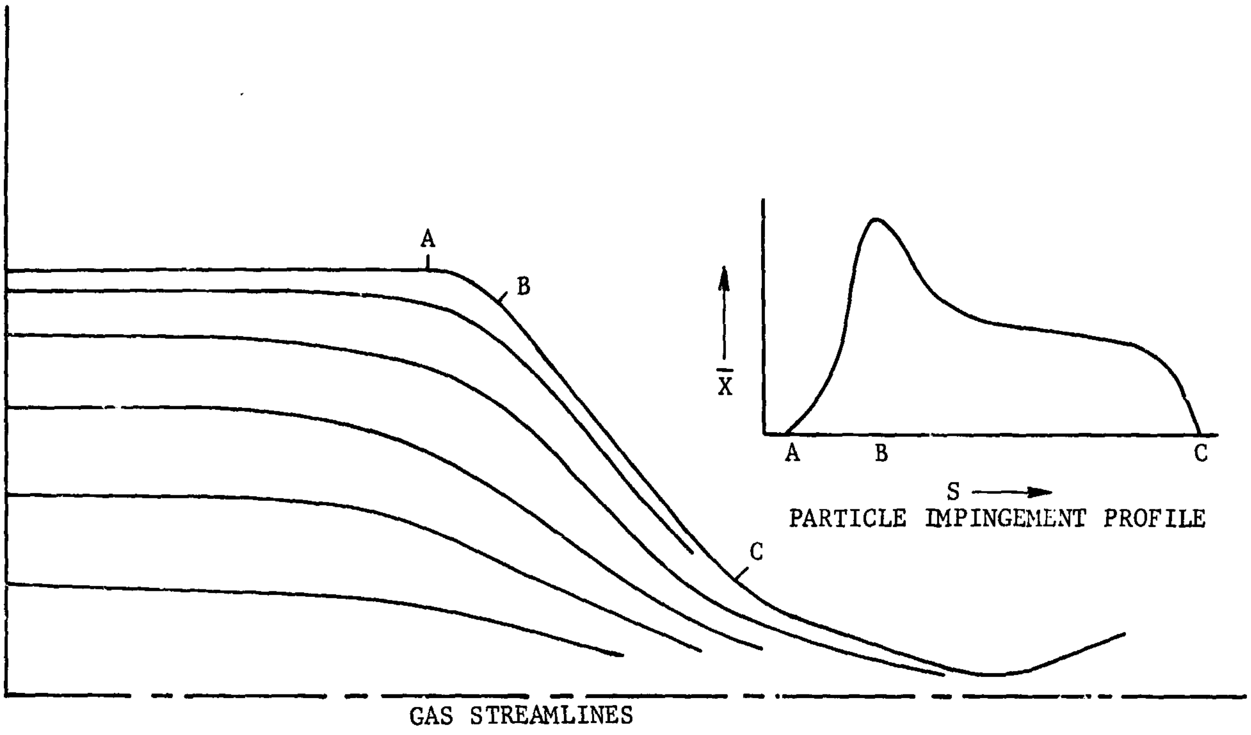
A
B
C
$\bar{X}$
A
B
C
S
PARTICLE IMPINGEMENT PROFILE
GAS STREAMLINES

F08186 U

FIGURE 5. STREAMLINES AND IMPINGEMENT PROFILE - REMOTE ENDBURNER WITH CONVENTIONAL NOZZLE

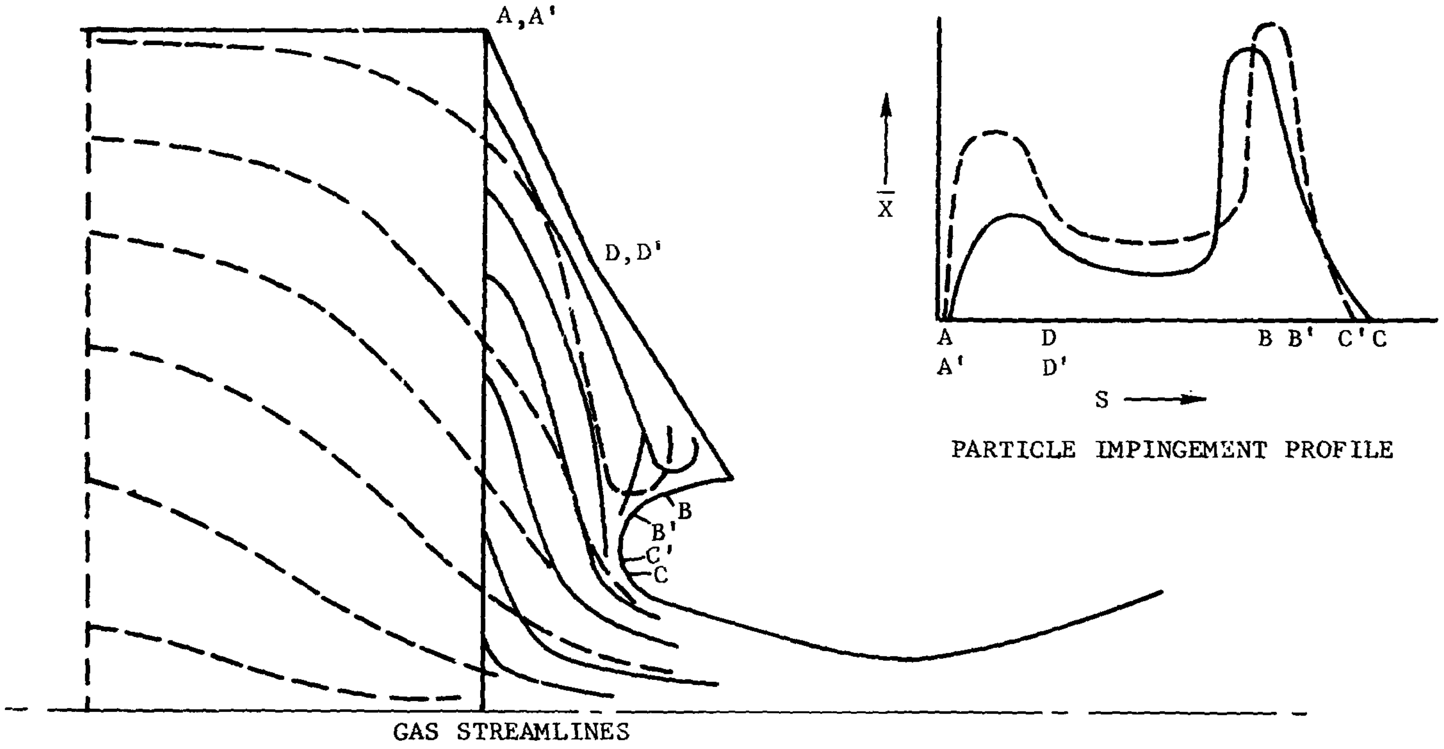
A,A'
D,D'
B
B'
C'
C
X̄
A
A'
D
D'
B B' C'C
S

GAS STREAMLINES

PARTICLE IMPINGEMENT PROFILE

F08187 U

FIGURE 6. STREAMLINES AND IMPINGEMENT PROFILE - CLOSE END BURNING GRAIN WITH A SUBMERGED NOZZLE

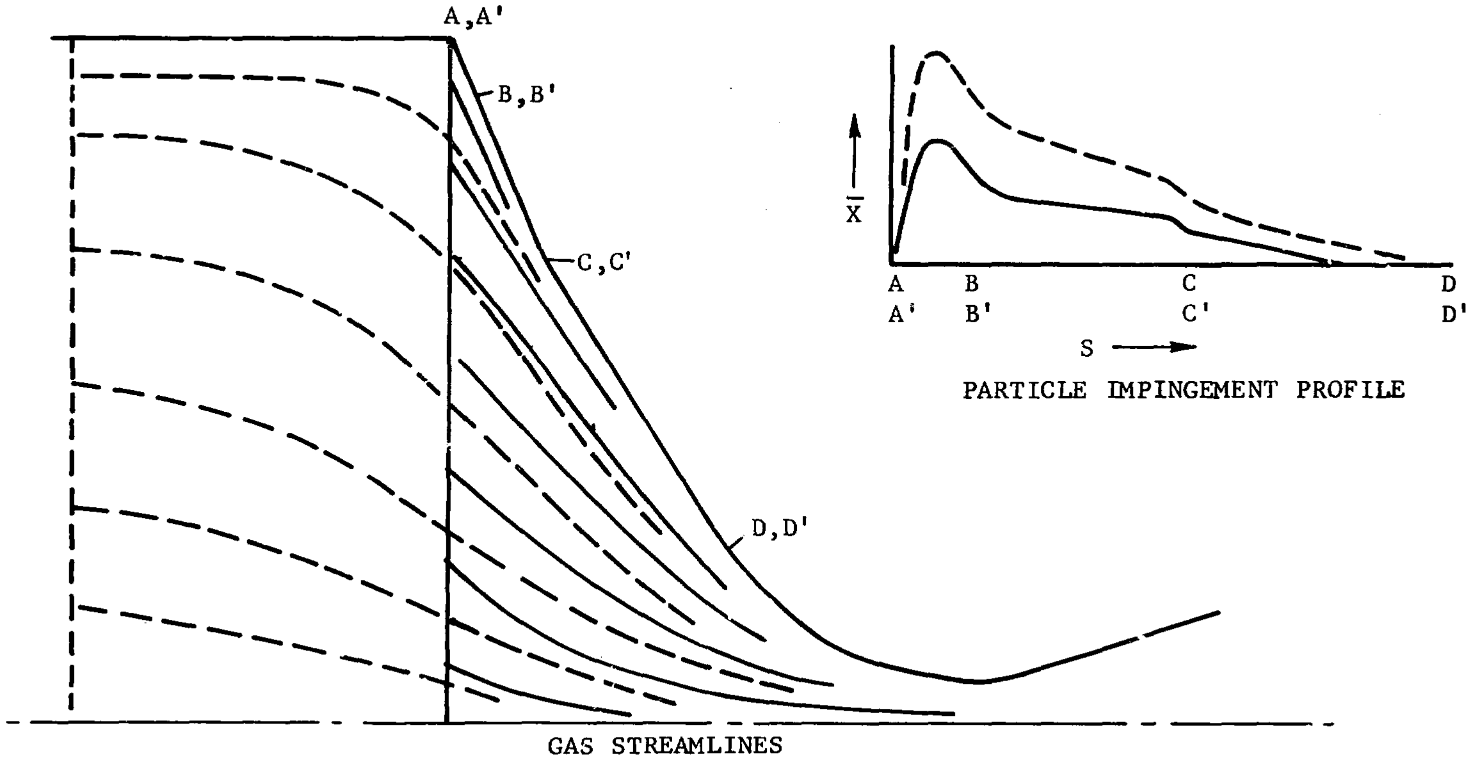
A,A'
B,B'
C,C'
D,D'
GAS STREAMLINES
X̄
A
A'
B
B'
C
C'
D
D'
S
PARTICLE IMPINGEMENT PROFILE

F08188 U

FIGURE 7. STREAMLINES AND IMPINGEMENT PROFILES - CLOSE END BURNING GRAIN WITH STEEP INLET NOZZLE

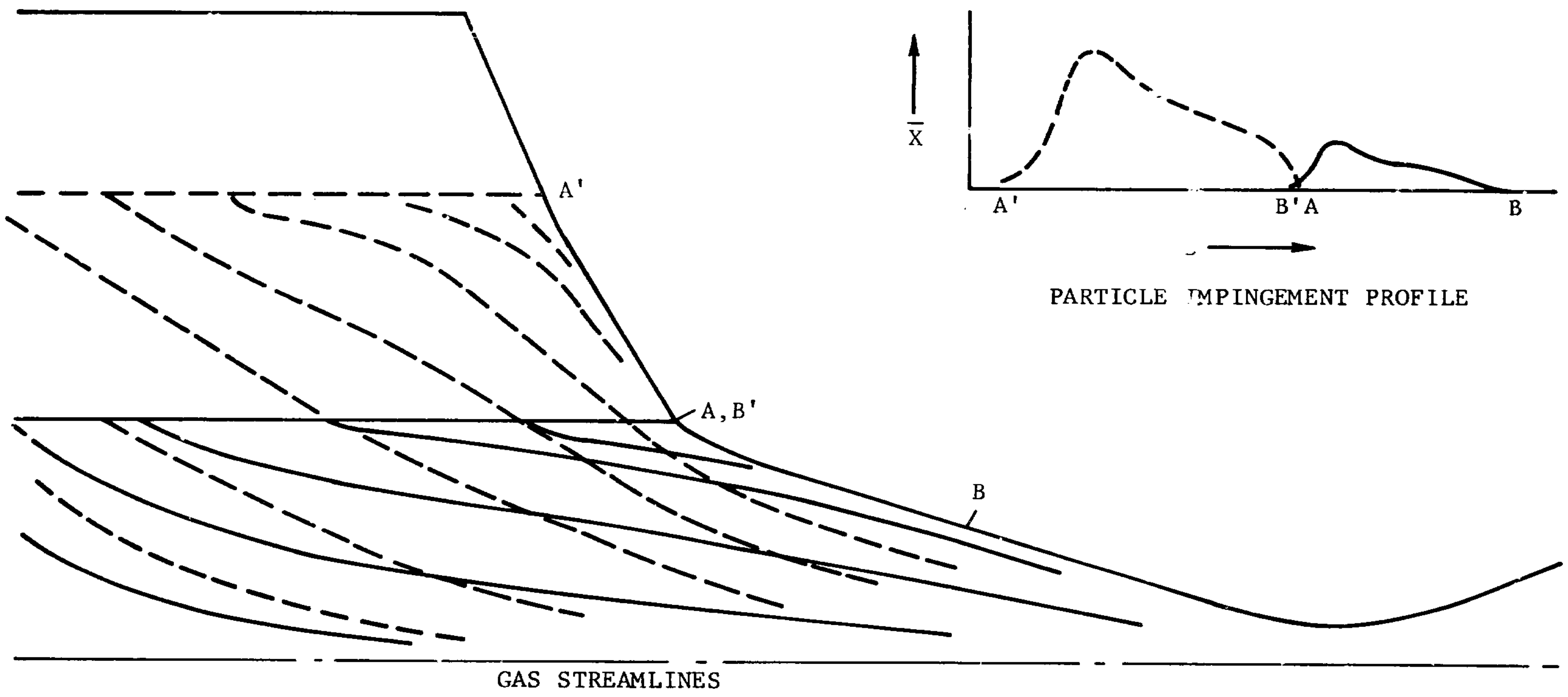
A'
A, B'
B
GAS STREAMLINES
$\overline{X}$
A'
B'A
B
PARTICLE IMPINGEMENT PROFILE
F08190 U

FIGURE 8. STREAMLINES AND IMPINGEMENT PROFILES - TYPE I GRAIN WITH CONVENTIONAL NOZZLE

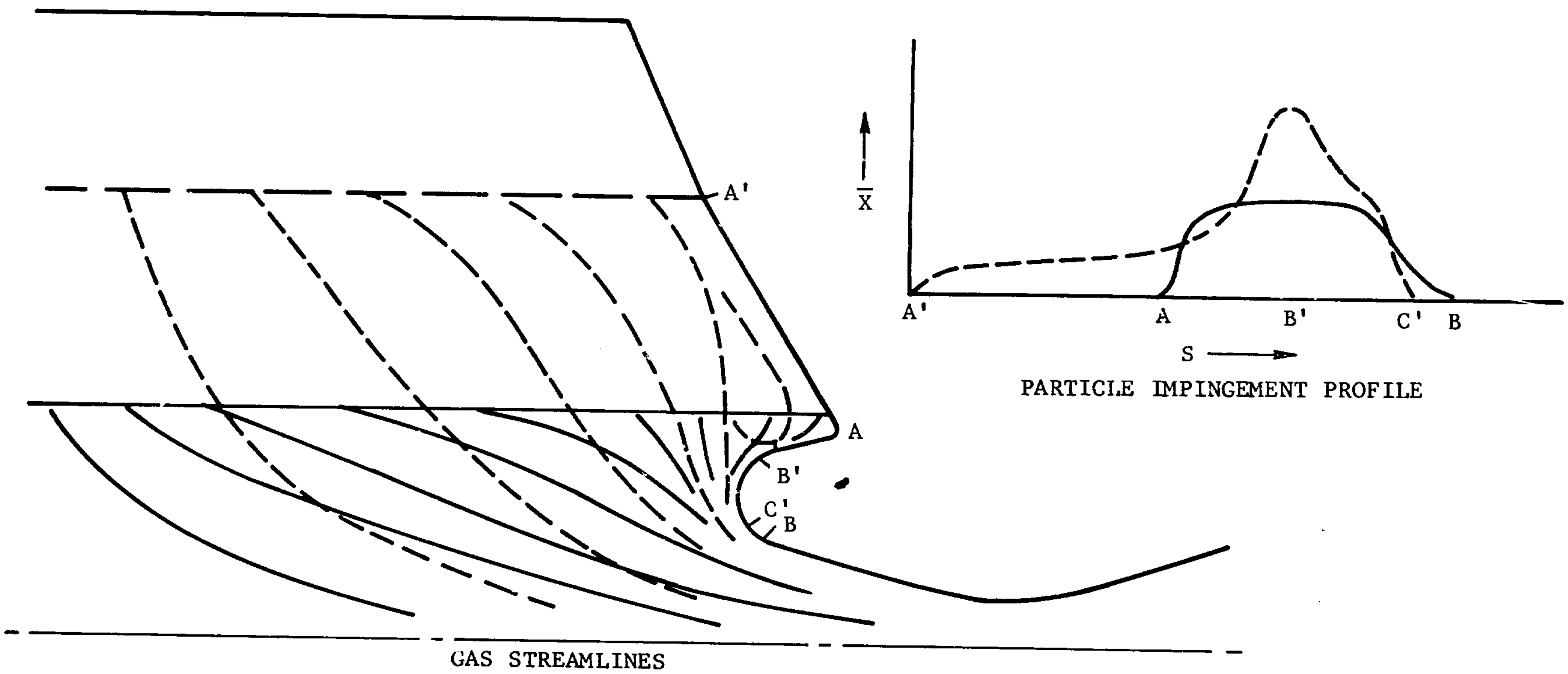
A'
A
B'
C'
B
X̄
S
A'
A
B'
C'
B
PARTICLE IMPINGEMENT PROFILE
GAS STREAMLINES

FIGURE 9. STREAMLINES AND IMPINGEMENT PROFILES - TYPE I GRAIN WITH SUBMERGED NOZZLE

velocity and will mix with the oncoming flow in the region between 'D' and 'B.' The change in aft closure angle at 'D' will result in lower impingement at that position. Particle impingement will diminish to zero in region 'C.'

The gas streamlines for the close end burner-steep inlet nozzle will be transient during the firing, as is shown in Figure 7. The gas vectors and particle impingement rates will, at long firing times, be similar to the vectors and impingement rates of Figure 5. The change in aft closure angle at 'C' will induce a decrease in the impingement on the downstream surfaces. The location at which impingement diminishes to zero is approximately at position 'D'.

The center perforated grain, when used with the conventional nozzle (Figure 8), will initially induce a negligible amount of impingement. Initially, the streamlines are essentially parallel to the wall. However, as the grain burns, exposing the aft closure with the increased contour angle, the increased streamline turning will result in increased impingement.

The gas streamlines and corresponding particle impingement profile for the center perforated-submerged configuration will be extremely transient as shown in Figure 9. As the grain burns the submerged nozzle will induce a stagnation point on the nose cap at 'B' and a recirculation region between 'A' and 'B.' Initially, however, the stagnation along the outer surface of the nose cap will not occur.

2.5 (C) HEAT TRANSFER

The major portion of the analytical studies effort during the reporting period has been devoted to the reduction and analysis of thermal data obtained from the small motor firings T-8 through T-25. The detailed design of the nozzles and the thermocouple instrumentation plan may be found in Sections 5.2 and 4.3, respectively, in this report and References 1 and 2. The actual thermocouple temperature data has been separated and placed in the Appendix. It should be noted that the nozzle thermal response and convective heat transfer, for Tests T-1 through T-7, have been recalculated. These new results supersede the results previously presented in Reference 2. It should be kept in mind that the heat transfer studies have the dual objectives of: (1) characterizing the actual thermal response of the nozzle materials tested in support of the study of beryllium corrosion mechanisms, and (2) establishing reasonable convective and radiative heat transfer prediction techniques for use in the design of nozzle thermal protection systems.

a. (U) Convection

The development of the advanced boundary layer computer program, described in Sections 2.5a of References 1 and 2, has not been emphasized during the third reporting period. Because the oxide deposit thickness could only be measured at the nozzle throat, the axial variation in the gas side convective heat transfer coefficient has not been determined. Furthermore, without the deposit thickness data, the effective heat transfer coefficients should depend on the motor design parameters which influence deposition as well as depending on the axial position along the nozzle. Consequently, direct comparison between the computer program predictions and the calculated test results is still premature.

At the same time, the methods used to compute exhaust properties (viscosity, conductivity and Prandtl number) are being re-examined. It is premature to present the results. However, preliminary indications are that the revised property values will depress the theoretical heat transfer coefficient shown in Figure 6 of Reference 2. Evidently, this will produce improved agreement between the theoretical and experimental values.

The throat heat transfer coefficients calculated for the small motor tests (except Tests T-8, T-13 and T-24) are presented and discussed in Section 2.5e following. These data will be compared with the revised theoretical predictions in the final report.

b. (U) Radiation

Methods of analysis and experimental measurements of the radiation from the chamber exhaust were described and discussed in Section 2.5b of References 1 and 2. No additional work on radiation heat transfer has been performed during the third reporting period. In general, the contribution of radiation to the nozzle throat heating has been shown to be negligible for the small motor nozzles.

c. (U) Conduction/Ablation

The determination of the thermal response and gas side heat transfer coefficient for Tests T-8 through T-25 has been accomplished by employing the thermal analyses described in References 1 and 2. As in Reference 2, the thermal analysis effort has been concentrated at the nozzle throat section. This is a consequence of the presence of BeO or Al_2O_3 deposits on the aft closure, entrance section, and throat insert during the major portion of the firing. Since the deposit thickness is only known at the throat, the axial variation of the gas side convective heat transfer coefficient could not be determined. This situation provides the basis for the development of the analytical deposition flow model.

The throat washer thermal history was recalculated for small motor Tests T-1 through T-7, using temperature dependent thermal conductivity data for pyrolytic graphite obtained from a recently published report (Reference 8). Use of this thermal conductivity data resulted in a better correlation between (1) calculated and measured temperatures, and (2) gas side convective heat transfer coefficients for similar motor firings. The new thermal conductivity data was also employed in the throat thermal analysis of the nozzles from Tests T-9 through T-15 and T-20 through T-25. The analytical techniques described in Sections 2.5 of References 1 and 2, were employed in the analyses of the pyrolytic graphite nozzles.

In Small Motor Tests T-16 through T-19, employing tungsten throat inserts backed with ATJ graphite, the thermal analysis technique has been modified to account for the isotropic nature of tungsten (radial and axial conduction). The gas side boundary condition and the tungsten-ATJ thermal response were obtained by instrumenting the backside of the tungsten and ATJ insert components and then correlating the calculated and measured temperatures. However, in this calculation, it is necessary to estimate the axial variation of the oxide deposit thickness. Two major models have been examined. Thus, it has been assumed that either the measured transient deposit thickness at the throat is identical along the tungsten contour or that the deposit surface temperature is isothermal. In essence, both assumptions specify the deposit thickness on the tungsten both upstream and downstream of the throat. The first assumption is most reasonable if the gas side contour of the tungsten insert is isothermal. An isothermal deposit surface temperature is physically reasonable, once the deposit surface melts. Neither assumption can be accurate at the beginning or end of the deposition pulse.

In the isothermal deposit surface calculation, a trial and error procedure was employed to find the approximate variation in axial deposit thickness that satisfied the isothermal condition. In this calculation, the axial variation of convective heat transfer was determined using the area ratio correction suggested by the simplified Bartz equation:

$$h_{t=0} = \bar{h}\left[\frac{(A/A_*)_I}{(A/A_*)_{t=0}}\right]^{0.9}\left[\frac{P}{\bar{P}}\right]^{0.8}$$

Here, $h_{t=0}$, P and $(A/A^*)_{t=0}$ are the instaneous heat transfer coefficient, chamber pressure and area ratio, respectively; and $\bar{h}$, $\bar{P}$ and $(A/A^*)_I$ are the average heat transfer coefficient, average chamber pressure and initial area ratio, respectively.

The material properties, employed in the thermal analyses and not presented in Reference 2, are shown in Table X. These data consist of the revised pyrolytic graphite a-b direction thermal conductivity and the specific heat, density and thermal conductivity of tungsten.

TABLE X. MATERIAL THERMAL PROPERTIES

Material	Temperature (°F)	Density (lb/in³)	Local Specific Heat (Btu/lb°F)	Thermal Conductivity (Btu/in sec°F)x10⁴
Pyrolytic	250	(Presented in Reference 2)		54.0
Graphite	1750	↓	↓	26.4
(a-b direction)	2500			16.2
	3000			13.0
	4000			11.4
	5000			11.3
Tungsten	500	0.675	0.0335	17.0
	5500		0.0460	11.0

The thermal response and ablation characteristics of the throat insert backup insulation material was evaluated during this period. In all the 100-pound motors, the insert insulation material was asbestos phenolic. The insulation response was analyzed using the charring ablation program described in Reference 9. However, in Reference 9, the ablation behavior of asbestos phenolic was found to be unique in that a large free water content is typical of the material. That is, the approximate chemical formula for asbestos phenolic, excluding the Fe and Al impurities, is:

$$\left.\begin{array}{ll} X\cdot(3MgO \cdot 2SiO_2 \cdot 2H_2O) & \text{- Asbestos} \\ Y\cdot(C_6H_6O) & \text{- Phenolic} \\ Z\cdot(H_2O) & \text{- Free water} \end{array}\right\} \qquad (1)$$

The per cent by weight of asbestos, phenolic and free water (X, Y, Z, respectively) for a given material is a strong function of the techniques and procedures involved in manufacturing. For example, a typical asbestos phenolic with 60% by weight of asbestos, will contain approximately 38.8% phenolic and 1.2% free water. Since water will be released in the temperature range of phenolic decomposition, the pyrolysis gas enthalpy and heat of virgin material decomposition will be a strong function of water content. Also, for asbestos phenolic, a good definition of the materials' thermal properties has not been presented in the literature, complicating the analytical determination of thermal response. Therefore, the analytical characterization of the ablation behavior of asbestos phenolic consisted of a parametric study to determine the property data that best fit the measured char depth, partly degraded material thickness and transient heat absorption by the insulator. The asbestos phenolic boundary condition, at the ATJ-AP interface, was the transient temperature measured during firing and partial soak. In applying the charring ablation program after 300 seconds of soak, the pyrolysis rate of the material decreased to such a small value that further use of the computer to establish the fully soaked char depth was uneconomical. To estimate the pyrolysis rate at soak times greater than 300 seconds and subsequently the final char depth, the effective heat of ablation was employed. The effective heat of ablation (Q^*) is defined as,

$$Q^* = \frac{\dot{Q}}{\dot{m}} \ \text{(Btu/lb)}$$

where: $\dot{Q}$ is the heat flux to the asbestos phenolic surface and $\dot{m}$ is the resulting mass loss rate. However, during the nozzle soak period, Q^* for asbestos phenolic, in the configuration under study, is a function of char depth and radial temperature profile. Therefore, the time dependence of Q^* was determined using the 'charring' ablation analysis for soak times less than 300 seconds and extrapolated to longer soak times, thus permitting determination of final char depth.

The 'measured' heat absorbed by ablation is in reality only approximate since a semi-empirical technique is required for its determination. That is, assuming that (1) the heat lost by the PG-ATJ insert is due solely to the backup insulation ablation-conduction and (2) the PG-ATJ heat sink is isothermal, the heat transferred to the insulator is:

$$\dot{Q}_a = \left(\left[\rho C V \Delta T\right]_{P.G.} + \left[\rho C V \Delta T\right]_{ATJ} \right) \frac{1}{\Delta t} \qquad (2)$$

Heat lost from PG washer

Heat lost from ATJ sleeve

At long soak times, the two assumptions are reasonable. However, the heat losses to the ambient environment and other nozzle components via convection, axial conduction, and radiation during the early portion of the soak period will be significant (Reference 9). This means that the calculated Q_a will be greater than the actual heat transfer to the insulator.

In reviewing the 'charring ablation' program (Reference 9), the thermal properties required as input and/or defined by the program are:

(1) Virgin material density,
(2) Resin mass fraction,
(3) Temperature dependent virgin and fully charred materials' thermal conductivity (K_V and K_C, respectively):

$$K = \left[\frac{K_v - K_c}{\rho_v - \rho_c}\right](\rho - \rho_v) + K_v$$

(4) Temperature dependent virgin and fully charred materials' specific heat (C_V and C_C, respectively):

$$C = \left[\frac{C_v - C_c}{\rho_v - \rho_c}\right](\rho - \rho_v) + C_v$$

(ρ in the above equations is the local, instantaneous material density),

(5) Pyrolysis rate law constants (A, E, and n)

$$\left[\frac{1}{\rho_v - \rho_c}\right]\frac{\delta\rho}{\delta t} = -A\left(\frac{\rho - \rho_c}{\rho_v - \rho_c}\right)^n \exp\left[-E/RT\right] \qquad (3)$$

(6) Resin heat of decomposition,
(7) Pyrolysis gas enthalpy vs temperature.

Of these properties, those lacking accurate characterization and which are of primary importance in the ablation process include: char thermal conductivity, pyrolysis rate law and pyrolysis gas enthalpy. For simplicity, the char thermal conductivity was assumed constant in the temperature range of interest (70 to 1850°F). The pyrolysis rate law based on TGA data, measured for phenolic resins, was assumed to be single valued. (However, for a more accurate characterization of asbestos phenolic decomposition, it is recommended that 3 laws be employed; two characterizing phenolic decomposition (see Reference 10) and one describing the phase change of water. The determination of these three laws will, however, require TGA data on asbestos phenolic, which as yet is not known to exist.) The gas enthalpy versus temperature was analytically determined assuming that:

(1) The pyrolysis gases are in thermochemical equilibrium with the char through which they flow.

(2) Magnesia and magnesium silicate (asbestos decomposition products) do not vaporize or react with the carbon char (most reasonable for char temperatures below 2000°F).

(3) Two chemical formulas are adopted to characterize the phenolic resin (C_6H_6O and $C_9H_{12}O$).

(4) The insulation composition is: 65% asbestos, 34.65% phenolic and 0.35% free water.

The results of this parametric study involving property variation are presented in Section 2.5e-2.

c. (U) Deposition Model

The analytical deposition model, described in Section 2.5 of Reference 2, has been reduced to mathematical form to provide a computerized capability of predicting the deposition flow phenomena and the resulting nozzle material's thermal response. At the close of the reporting period, the deposition computer program was being checked out using motor firing T-4 as a test case. Except for a minor instability problem inherent in the deposit mass balance, the results are very encouraging. The mathematical description of the deposition process, the assumptions employed in the analytical model, and the predictions acquired from the computer program will be presented in the final report.

Initially, the results of the cold flow modeling study (Section 3.3 of Reference 1) will be used to establish a condensed phase deposition profile along the motor contour. It is expected that arbitrary deposition profile inputs will also be used in a trial and error approach. The object will be to eventually predict the measured temperature and deposit history of the nozzle throat washer. Measured temperature histories of other pyrolytic graphite washers will provide an additional check on the computer program results. It should then be possible to evaluate the capabilities of the analytical model and the cold flow modeling technique. Extension of this effort to other grain designs will not be attempted until satisfactory results are obtained for the end burner designs.

Best Available Copy

e. (C) Results of Thermal Analyses

(1) (U) Measured Temperatures

The thermocouple temperature data obtained on Tests T-8 through T-25 are presented in the Appendix. Similar data was included in Section 2.5 of Reference 2 for Tests T-1 through T-7.

(2) (C) Nozzle Thermal Analysis

The gas side convective heat transfer coefficient and the heat sink thermal response, at the throat location, have been determined (for the majority of the firings) using the thermal analyses described in Section 2.5c. The pertinent conditions pertaining to the thermal analyses and the resulting nozzle gas side convective heat transfer coefficients at the nozzle throat are summarized in Table XI. The throat heat sink thermal response corresponding to the coefficients and conditions of Table XI are presented in Figures 10 through 33. At the present time, the effective heat transfer coefficients (see Reference 2, Section 2.5c) for Tests T-8 through T-25, at positions other than the throat, have not been determined. These coefficients were characterized for Tests T-1 through T-7 during the second reporting period. However, lacking the deposition histories at positions other than the throat, the data cannot be used directly in the characterization of the gas side boundary condition. Appreciating the importance of deposition on nozzle thermal behavior and considering the large amounts of deposition encountered in the small motor firings, the effective heat transfer coefficients as reported for T-1 through T-7 at stations other than the throat would have little general value. When and if the analytical deposition model (Section 2.5d) can provide the required deposit history data, the evaluation of the gas side heat transfer can be completed.

The thermal and ablation response of asbestos phenolic, used as the throat insert insulation material for rocket motor T-7, was determined using the thermal analyses described in Section 2.5c. This required a parametric study involving the systematic variation of properties until a best fit was obtained between the calculated and the measured char depth, pyrolysis zone thickness, and transient heat transfer to the insulation. The resulting combination of properties derived from the parametric study are given in Table XII.

A complete characterization of the insulation material, together with the insulator boundary condition employed in the thermal analyses, is presented in Table XIII. As noted in Section 2.5c, the insulator boundary condition consisted of the measured ATJ-asbestos phenolic interface temperature applied as a forcing function to the asbestos phenolic surface.

The radial density and temperature profiles, determined using the 'charring' ablation program with the properties of Table XII, are presented in

Figure 34. Figure 35 compares the predicted and semi-empirically determined heat absorption by the insulation material. The semi-empirical heat absorption is estimated from Equation 2. The heat absorbed in Figure 35 includes the heat stored in the insulation, as ρcVT, and the heat dissipated by the ablation process. The particular value employed for the resin heat of decomposition had little effect on the results, as the heat absorbed by the transpiring pyrolysis gases was over an order of magnitude greater than the heat absorbed by resin decomposition.

(3) (C) Discussion of Results

(a) (C) General Comments

Test T-8: The heat sink thermal response and the gas side heat transfer coefficient at the throat were not calculated for Test T-8. It was not possible to perform the analyses because of insufficient thermocouple data and uncertainties in the calculated throat deposit thickness history. It was also impossible to obtain the throat washer equilibration temperature or backside temperature transient during firing. The calculated throat deposit thickness is uncertain due to suspected errors induced by the presence of a large amount of deposit on the exit cone.

Test T-9: The thermal response of the throat washer is presented in Figure 16. Comparison of the calculated and measured backwall temperatures indicates agreement during the initial part of the firing when the major portion of the deposit is solid (assuming melting point of deposit equal to that of BeO). When the liquid deposit thickness increases (estimated from the difference in BeO and P.G. surface temperatures), the calculated P.G. backwall temperature is significantly less than the measured value. Since the average gas side heat transfer coefficient ($h=0.009$ Btu/in^{2}sec$^\circ$F) was determined from the measured equilibration temperatures (see Section 2.5c), the measured and calculated total heat transferred to the washer are in agreement. This indicates a potential error in the estimate of liquid BeO thermal conductivity, if the transient deposit thickness history, P.G. thermal properties and thermocouple data are assumed to be accurate. Note that the calculated BeO and P.G. surfaces temperatures reach the melting point of BeO at 2.8 and 10 seconds, respectively. The measured deposit thickness decreases at 6 seconds and approaches zero at 14 seconds. Review of the deposition model of Reference 2 will show that the deposit cannot propagate downstream or approach zero thickness until the local BeO and P.G. surface temperatures reach the BeO melting point. The calculated and measured responses are evidently compatible with that model. The fact that the throat BeO deposit thickness increases, when a portion of that deposit is predicted to be in the liquid state, suggests that the increase is due to the upstream BeO mass addition rate being greater than the mass depletion rate, thereby indicating a high rate of melting and flow from positions upstream of the throat.

TABLE XI. SMALL MOTOR TEST HEAT TRANSFER PARAMETERS (C)

Test Number	Initial Throat Diameter (inches)	Firing Time(1) (sec)	Average Chamber Pressure(2) (psia)	Ideal Throat Recovery Temperature (°R)	C*(5) Efficiency (%)	Average Throat Convective Heat transfer Coefficient(3) (Btu/in^{2}sec °F)
T-1	1.166	17.4	870	6610	95.0	0.0075
T-2	1.030	24.5	840	6020	93.5	0.0056
T-3	1.190	16.0	902	6250	99.6	0.0073
T-4	1.030	24.0	834	6050	90.3	0.0067
T-5	1.044	23.0	853	6090	95.2	0.0040
T-6(#1)	1.20	21.6	636	6260	93.2	0.0060
T-7	1.146	16.5	952	6660	98.2	0.0080
T-8	1.215	16.5	812	6660	-	-
T-9	1.212	18.7	778	6610	95.0	0.0090
T-10	1.232	18.0	800	6610	97.7	0.010
T-11	1.080	24.2	780	6060	96.5	0.0060
T-12	1.232	19.0	738	6610	93.1	0.012
T-13	1.238	19.0	727	6610	92.3	-
T-14	1.218	17.1	814	6250	94.5	0.0074
T-15	1.180	16.2	995	6250	101.2	0.0053
T-16	1.24	17.1	846	6610	93.3	0.0062
T-17	1.24	18.0	800	6610	92.5	0.0052(4)
T-18	1.24	17.2	854	6610	90.4	0.0050(4)
T-19	1.24	16.2	910	6250	95.0	0.0046(4)
T-20	1.214	18.2	835	6610	95.0	0.0090
T-21	1.165	16.5	946	6610	85.8	0.0040
T-22	1.030	25.0	865	6050	92.5	0.0062
T-23	1.179	18.9	850	6610	87.9	0.0060
T-24	1.211	23.2	636	6250	95.6	-
T-25	1.222	17.6	830	6610	95.0	0.0072

(1) Firing time is thermal action time (see Reference 2 Table IV).
(2) Average chamber pressure over the thermal action time.
(3) Gas side heat transfer coefficient averaged over action time.
(4) Assumed uniform deposit thickness vs A/A*, see discussion in Section 2.5.e(3).
(5) Uncorrected, see Section 2.3.

TABLE XII. ASBESTOS PHENOLIC THERMAL PROPERTIES* (C)

Property	Value	Comments
Virgin material density	0.0577 lb/in^3	Measured
Char material density	0.0490 lb/in^3	Measured
Virgin material thermal conductivity	$3.0\text{x}10^{-6} \frac{\text{Btu}}{\text{in sec}^\circ\text{F}}$	Measured at 70°F (assumed independent of temperature)
Char thermal conductivity	$3.0\text{x}10^{-6} \frac{\text{Btu}}{\text{in sec}^\circ\text{F}}$	Parametrically determined (independent of temperature)
Virgin material specific heat	$0.28 \frac{\text{Btu}}{\text{lb}^\circ\text{F}}$	Obtained from Reference 9
Char specific heat	$0.38 \frac{\text{Btu}}{\text{lb}^\circ\text{F}}$	Obtained from Reference 9
Pyrolysis rate law constants (Equation 3)	n = 1.2 A - 2.68x10^4 (1/minute) E = 19.8 (Kcal/gm-mole)	Measured for phenolic, Reference 10
Resin heat of decomposition	1000 Btu/lb$_{\text{gas}}$	Parametrically determined (found to be unimportant in ablation process)
Pyrolysis gas enthalpy	Temperature (°F) — Enthalpy (Btu/lb) 620 — -3530 1520 — -466 2420 — +547	Analytically determined with: x = 0.65, Y = 0.3465, z = 0.0035 in Equation 1. Phenolic = $C_9H_{12}O$. Assuming: thermochemical equilibrium and MgO and SiO_2 do not react with carbon

---

* Representing best agreement between calculated and measured ablation parameters

TABLE XIII. ASBESTOS PHENOLIC CHARACTERIZATION AND PERFORMANCE (C)

Material:

RDD 41 Type 9600 Asbestos
MIL R9299 Phenolic Resin
35% by weight resin

Fabrication:

Rolled on 20° bias with 200 lb pressure on roller, roller surface speed = 50 ft/sec. Cured at 100 psig in hydroclave (preheated to 200°F for 2 hours) at 320°F for 24 hours.

Measured ATJ-Asbestos Phenolic Interface Temperature*

Time (sec)	Temperature (°F)
0	100
6	226
10	450
15	930
20	1265
25	1539
28	1644
33	1760
38	1797
49	1830
52	1831
71	1821
88	1787
112	1743
160	1665
200	1610
380	1520
333**	1464

* Data obtained from small motor Test T-7.
** Temperature readings terminated at 333 seconds.

CONDITIONS

$T_{r_*} = 6150°F$

$h_{g.s.} = 0.0075 \left(\frac{P}{870}\right)^{0.8}$

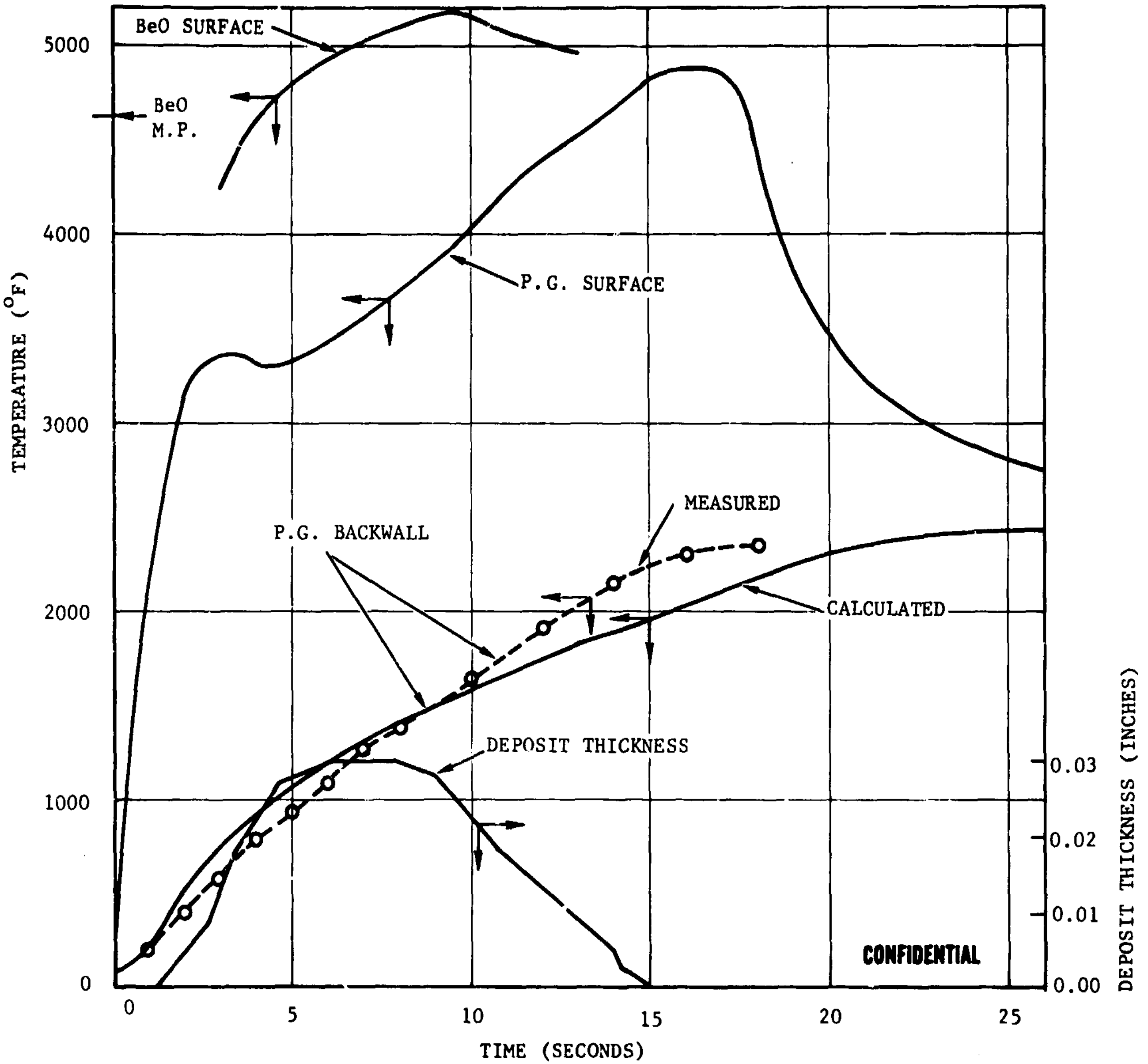

F08192 C

FIGURE 10. THROAT TEMPERATURE RESPONSE WITH DEPOSITION - TEST T-1

CONDITIONS

$T_{r_*} = 5560°F$

$h_{g.s.} = 0.0056 \left(\frac{P}{840}\right)^{0.8}$

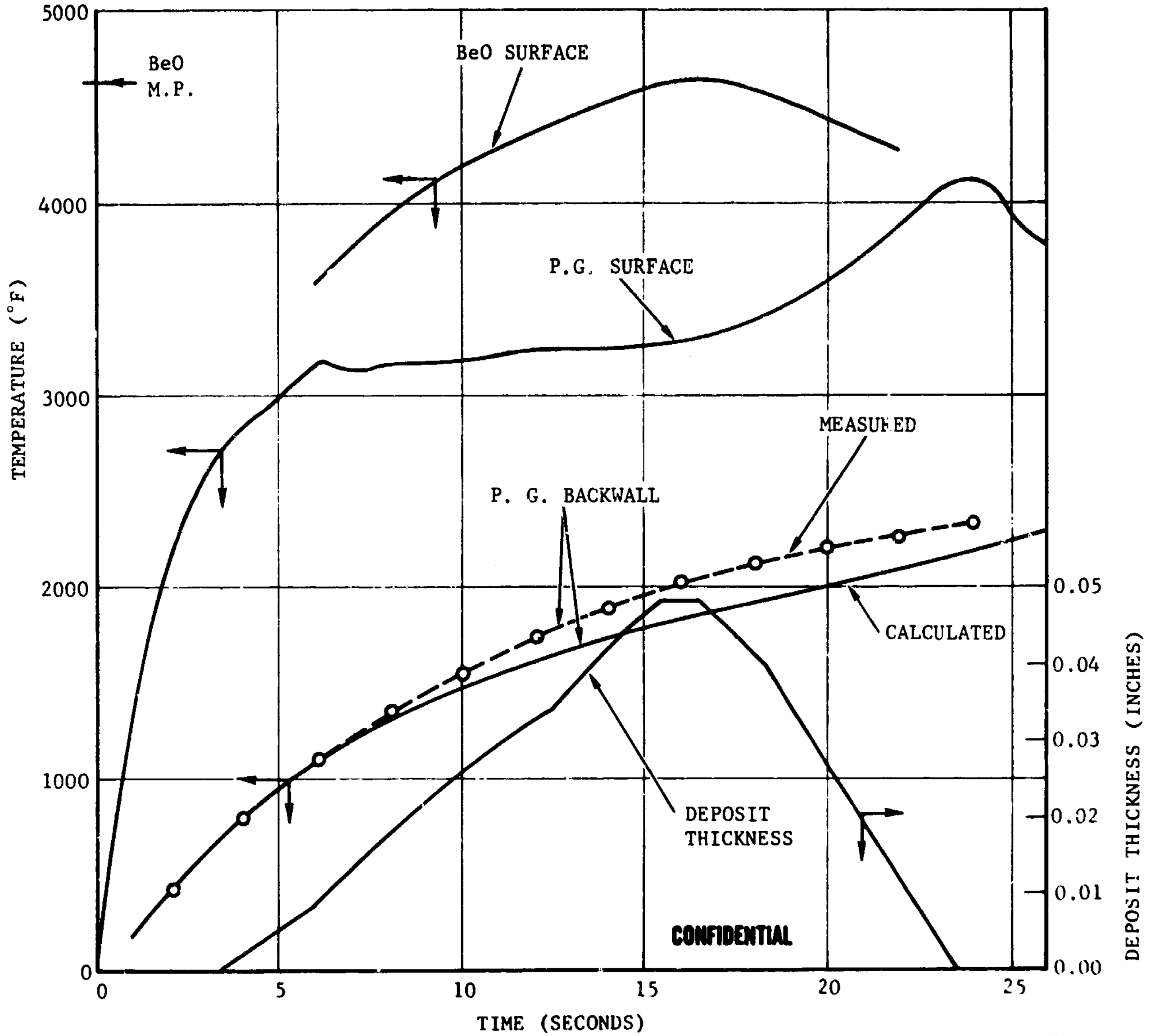

FIGURE 11. THROAT TEMPERATURE RESPONSE WITH DEPOSITION - TEST T-2

CONDITIONS

$T_{r_*} = 5790°F$

$h_{g.s.} = 0.0073 \left(\frac{P}{902}\right)^{0.8}$

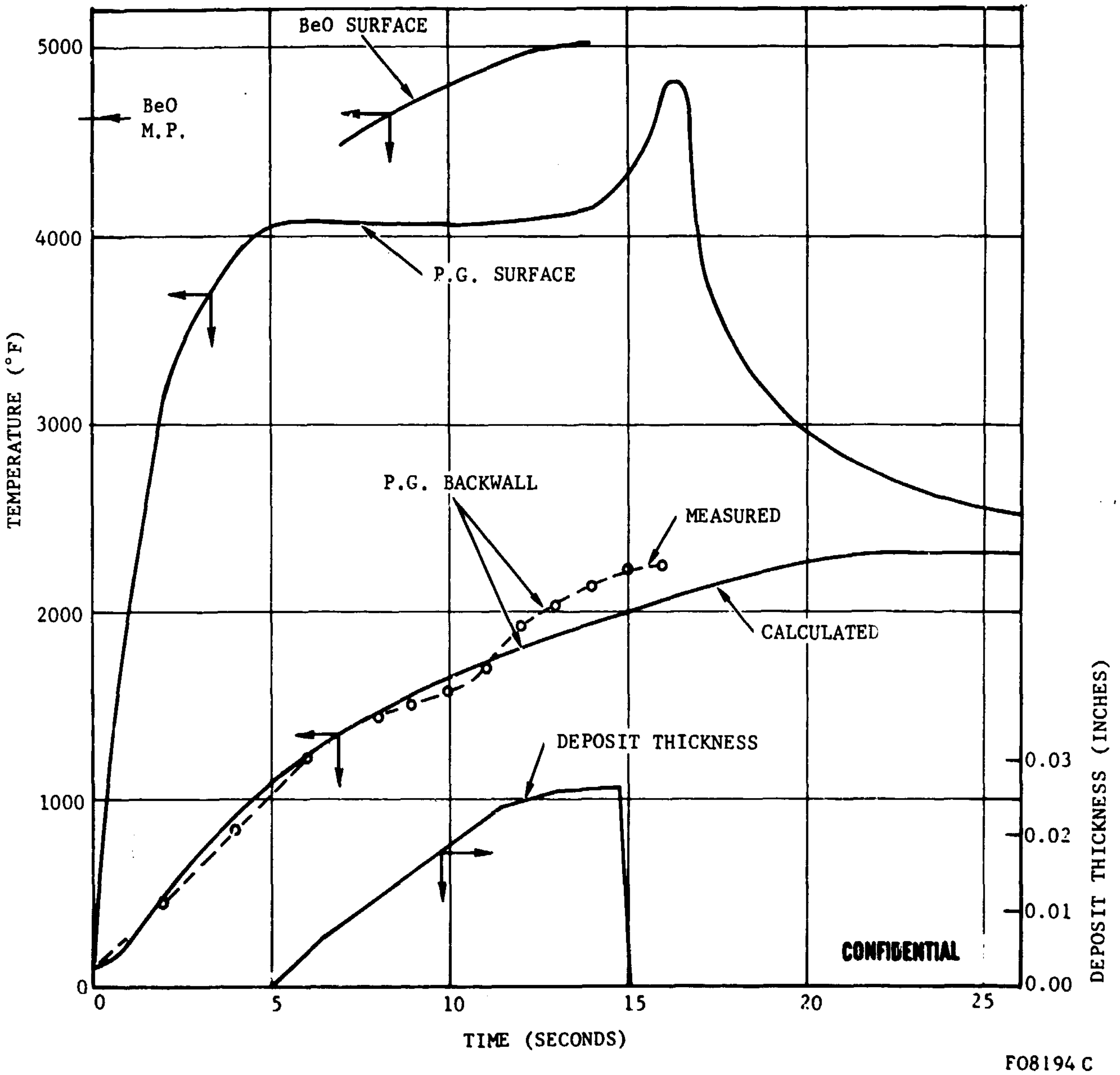

F08194 C

FIGURE 12. THROAT TEMPERATURE RESPONSE WITH DEPOSITION - TEST T-3

CONDITIONS

T_{r_*} = 5590°F

$h_{g.s.} = 0.0067 \left(\frac{P}{834}\right)^{0.8}$

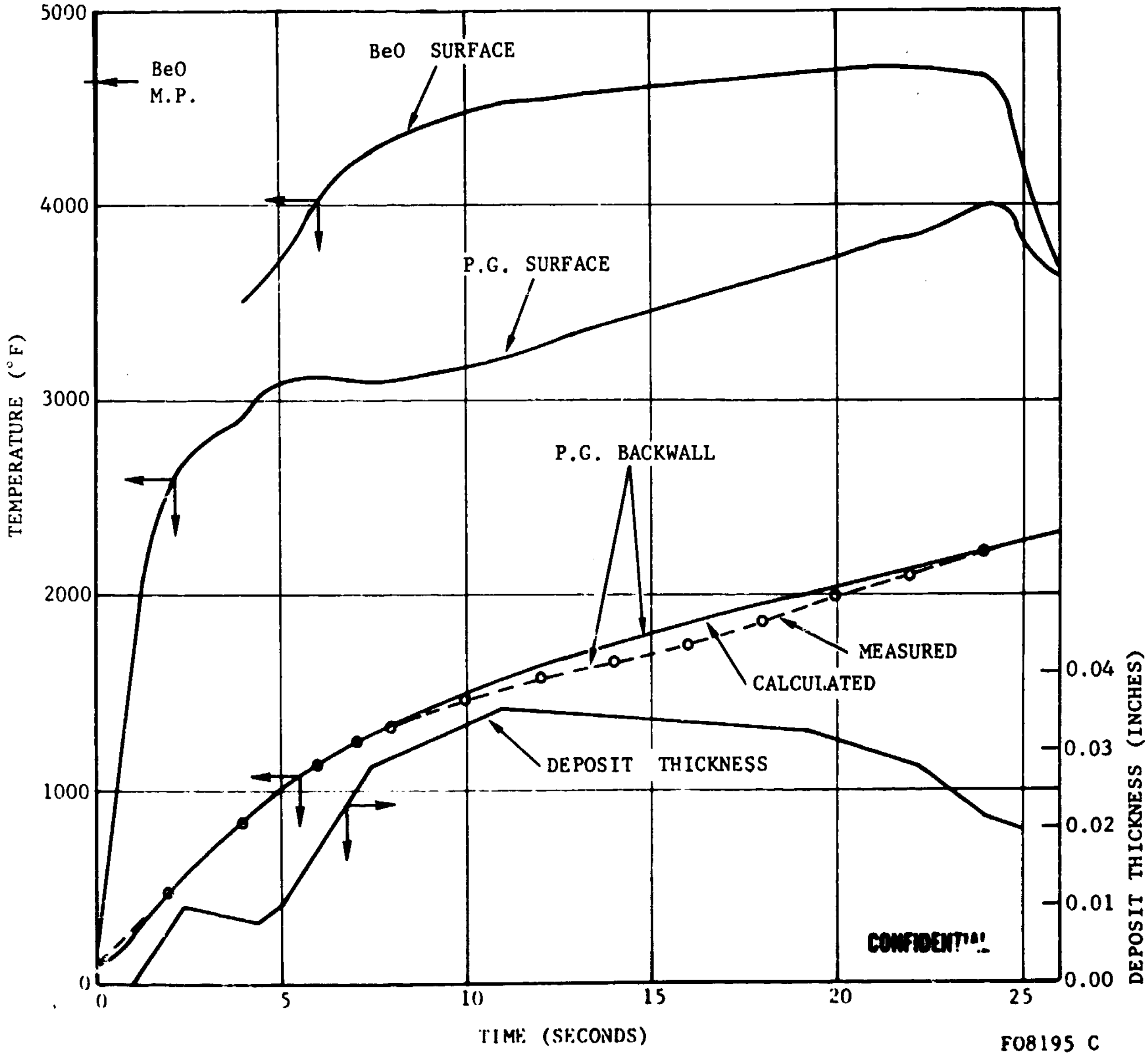

FIGURE 13. THROAT TEMPERATURE RESPONSE WITH DEPOSITION - TEST T-4

CONDITIONS

$T_{r_*} = 5630°F$

$h_{g.s.} = 0.0040 \left(\frac{P}{853}\right)^{0.8}$

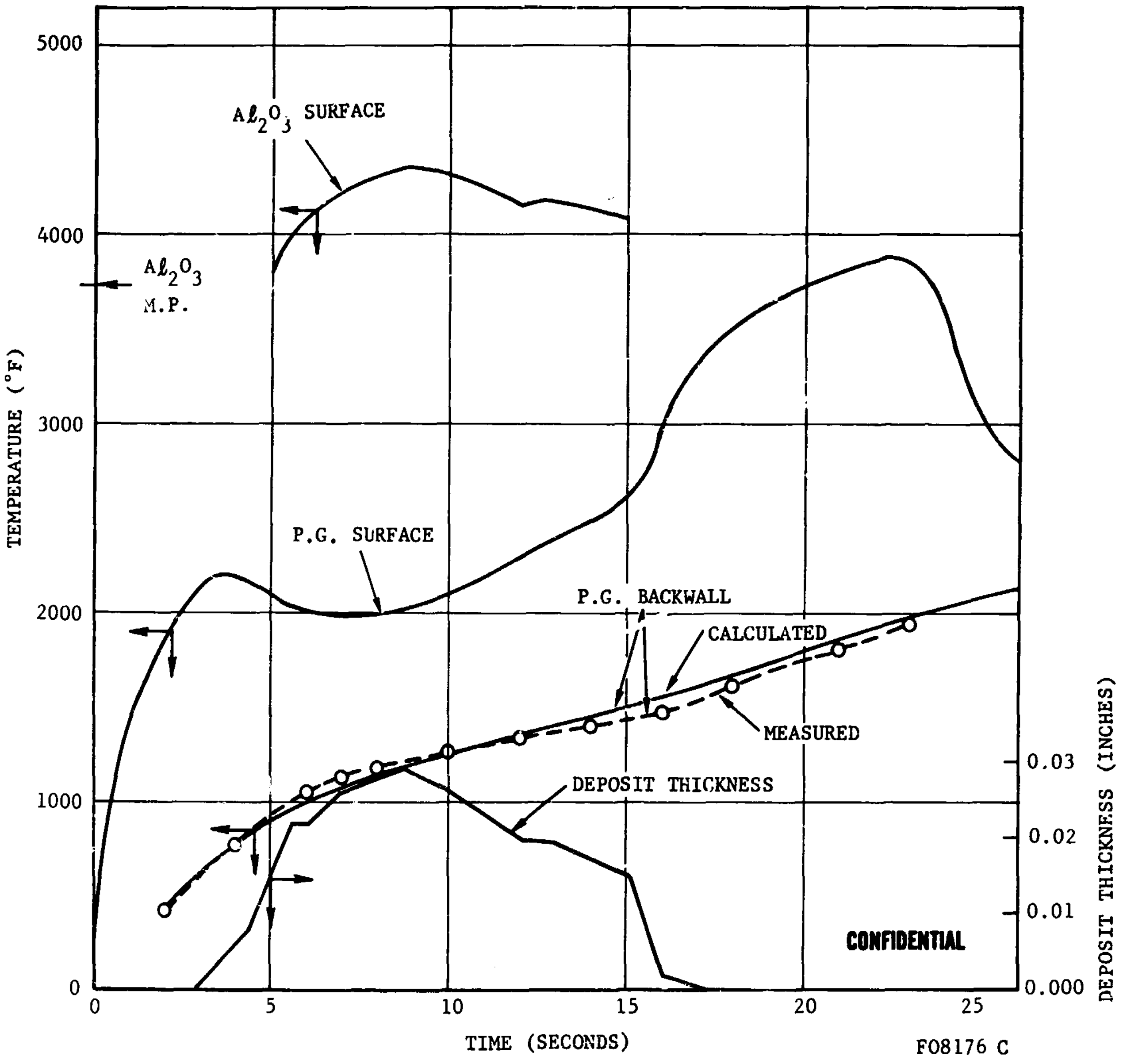

FIGURE 14. THROAT TEMPERATURE RESPONSE WITH DEPOSITION - TEST T-5

CONDITIONS

$T_{r_*} = 6200°F$

$h_{g.s.} = 0.0080 \left(\frac{P}{952}\right)^{0.8}$

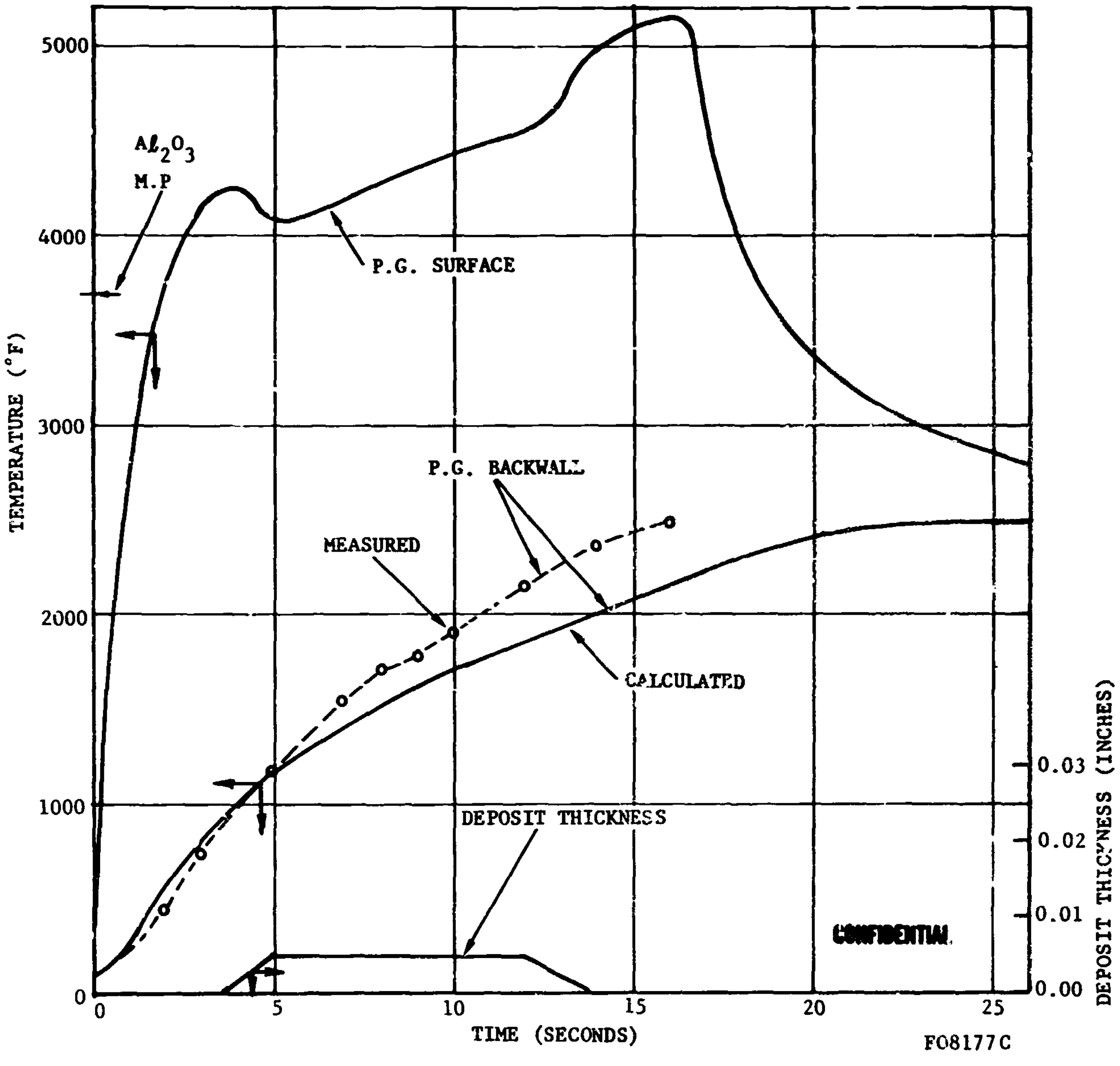

FIGURE 15. THROAT TEMPERATURE RESPONSE WITH DEPOSITION - TEST T-7

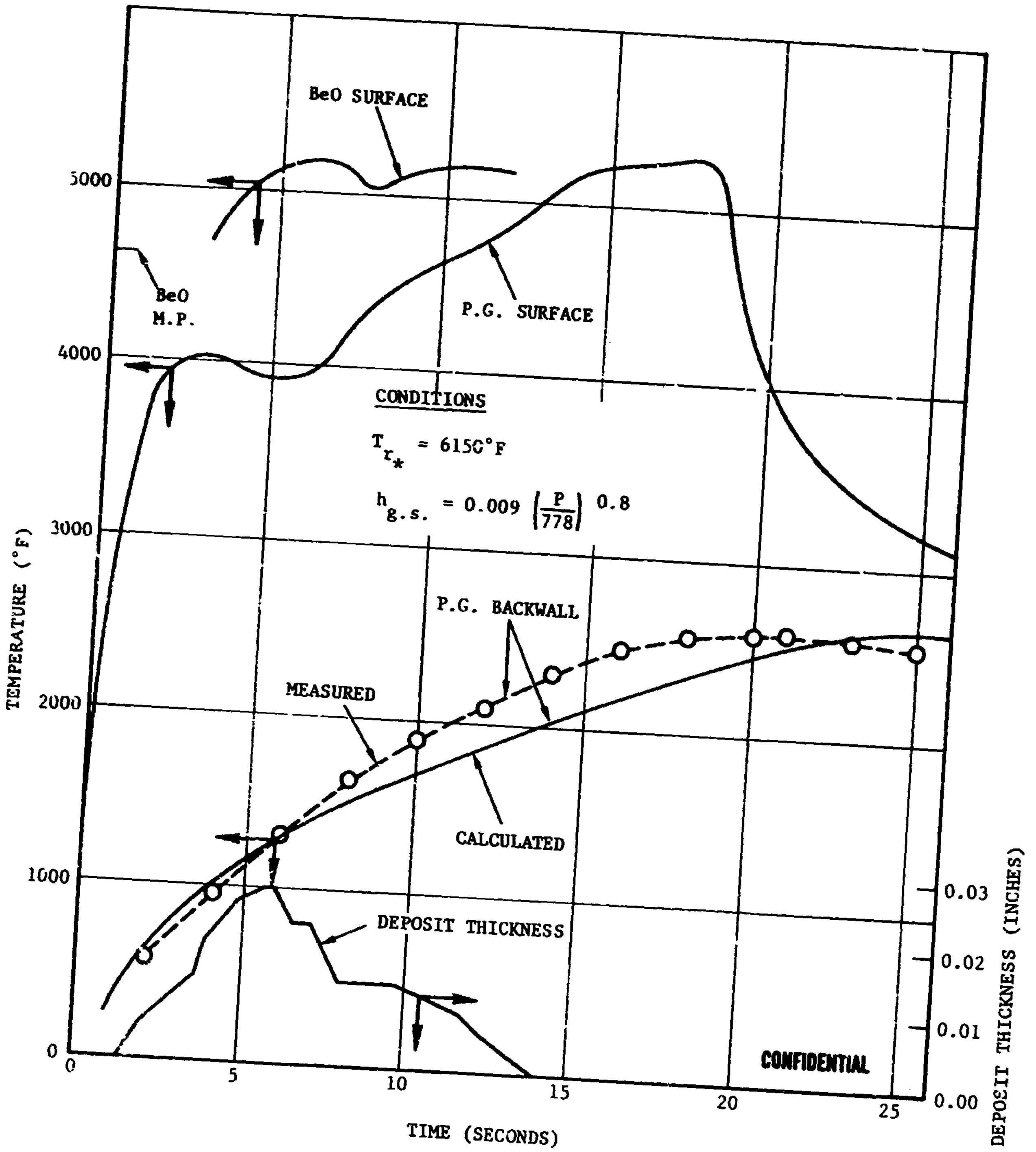

FIGURE 16. THROAT TEMPERATURE RESPONSE WITH DEPOSITION - TEST T-9

F08196 C

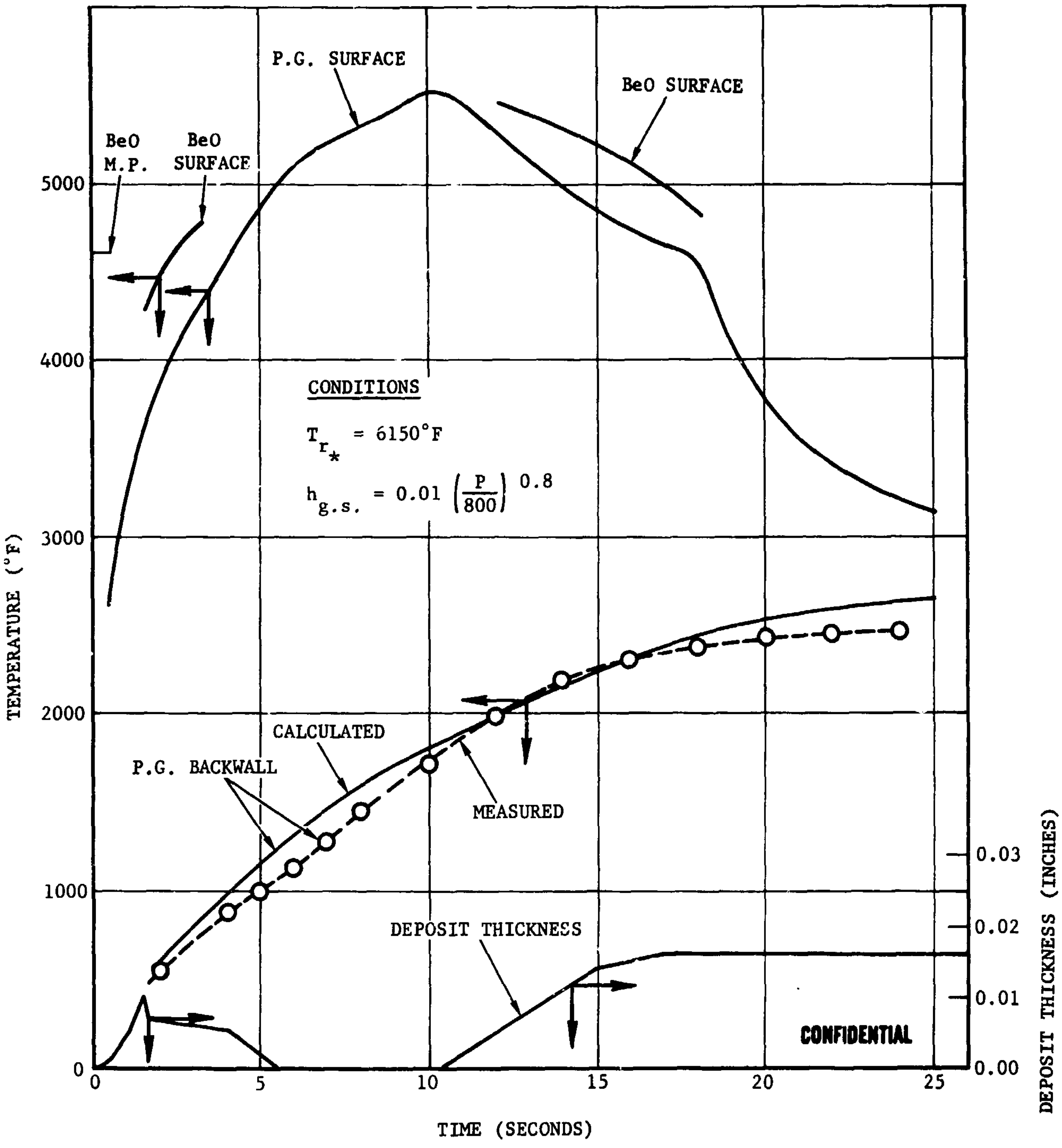

F08198 C

FIGURE 17. THROAT TEMPERATURE RESPONSE WITH DEPOSITION - TEST T-10

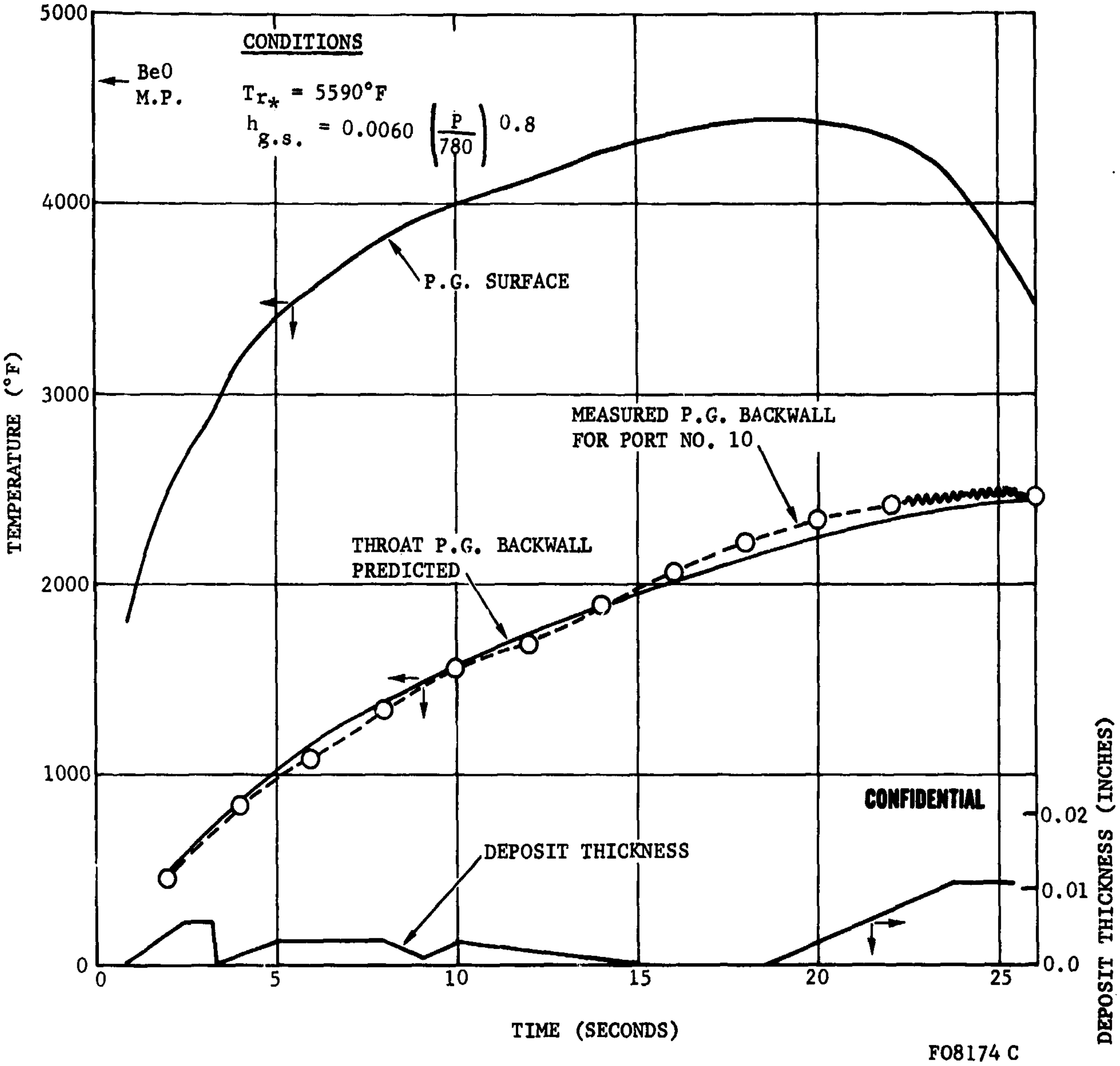

FIGURE 18. THROAT TEMPERATURE RESPONSE WITH DEPOSITION - TEST T-11

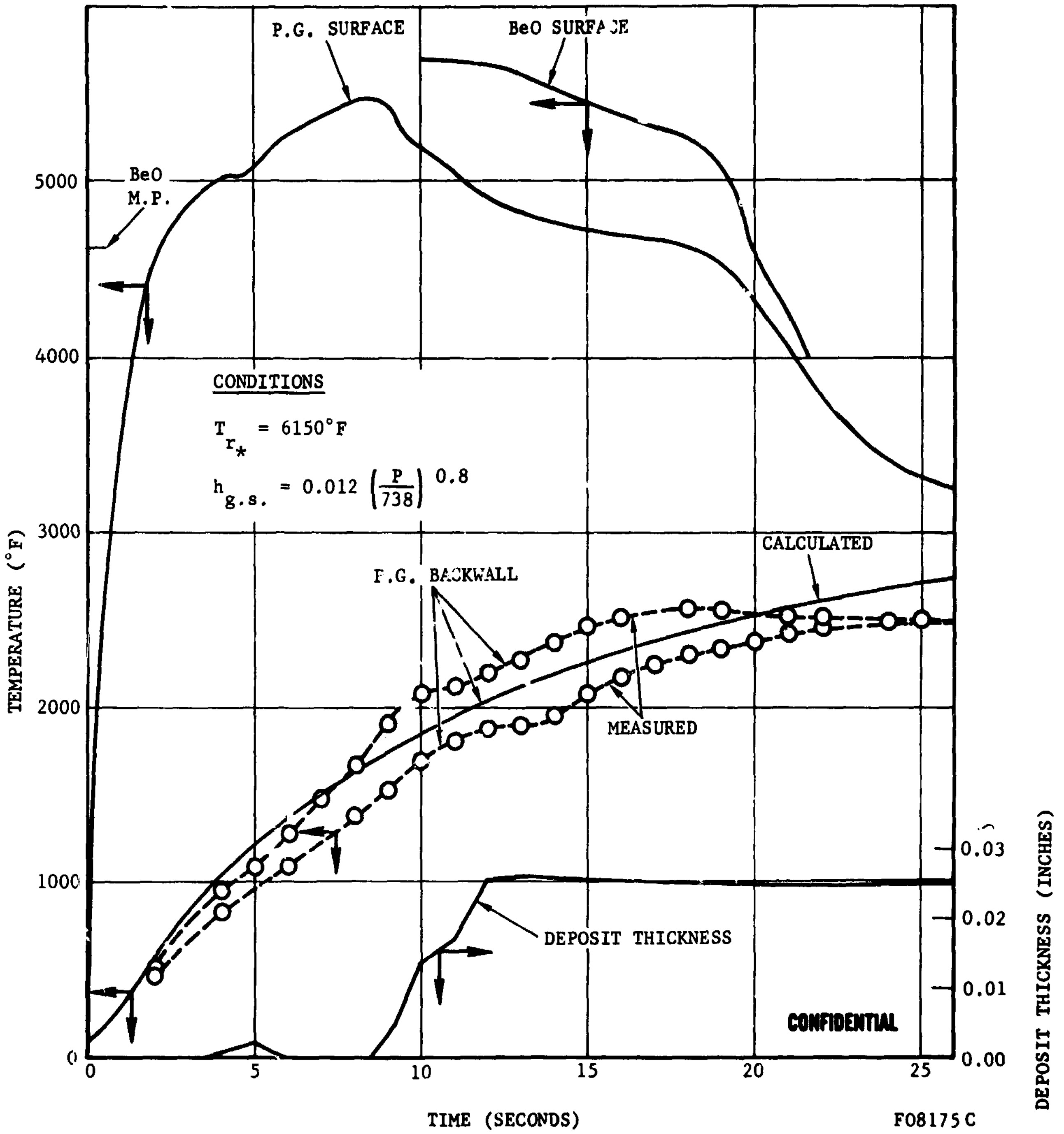

FIGURE 19. THROAT TEMPERATURE RESPONSE WITH DEPOSITION - TEST T-12

CONDITIONS

$T_{r_*} = 5790°F$

$h_{g.s.} = 0.0074 \left(\frac{P}{814}\right)^{0.8}$

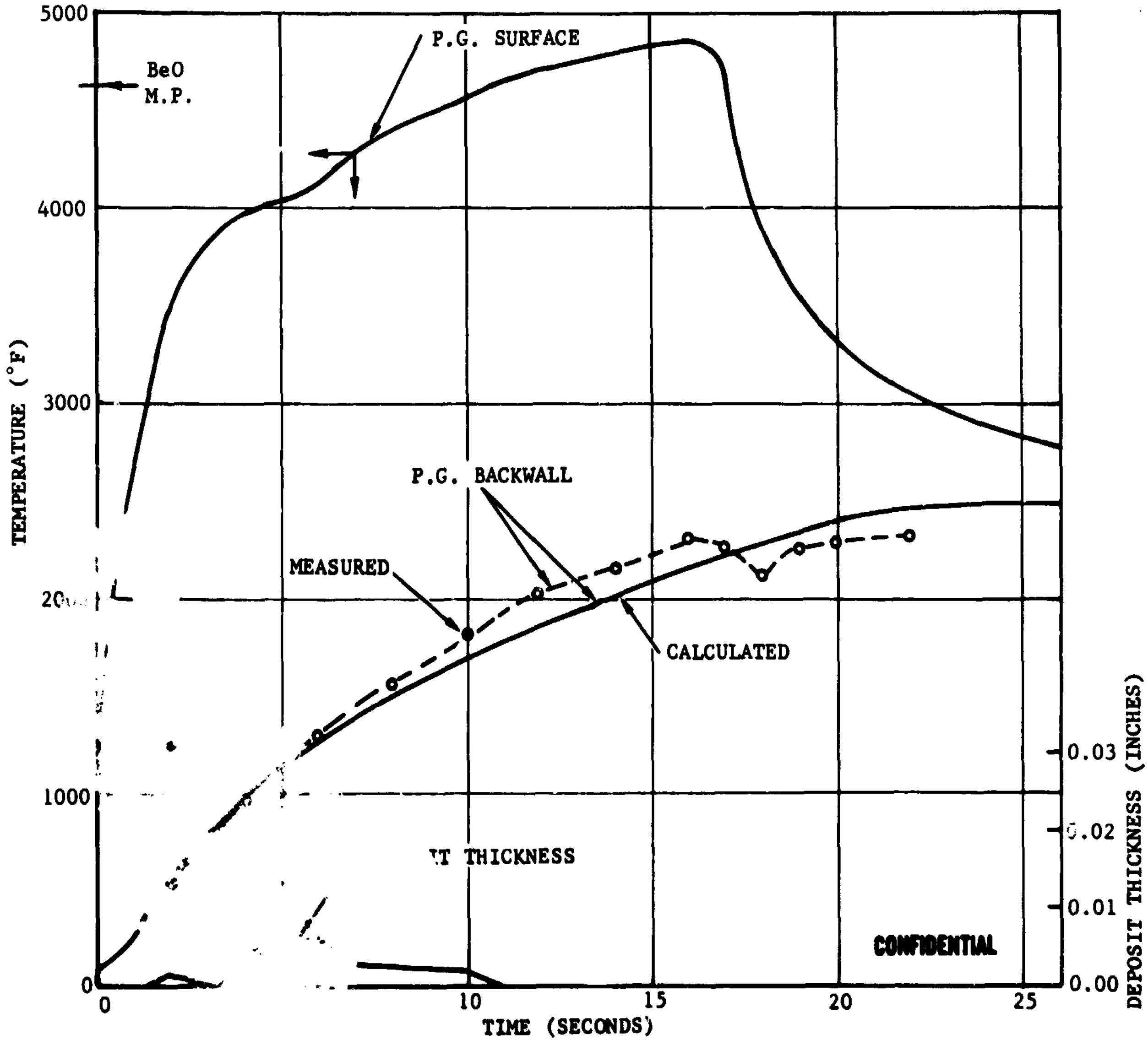

F08202 C

FIGURE 20. THROAT TEMPERATURE RESPONSE WITH DEPOSITION - TEST T-14

CONDITIONS

$T_{r_*} = 5790°F$

$h_{g.s.} = 0.0053 \left(\frac{P}{995}\right)^{0.8}$

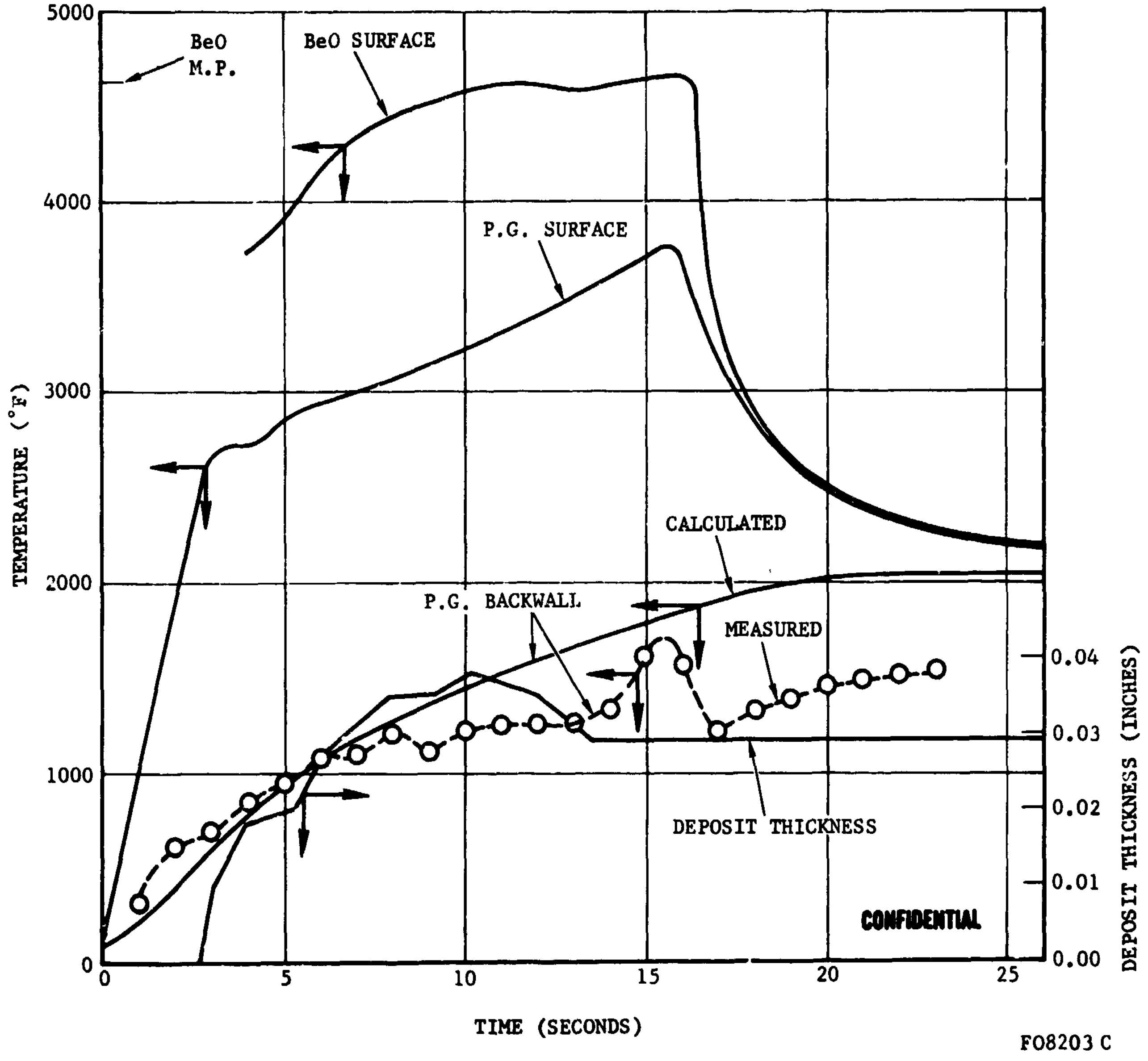

FIGURE 21. THROAT TEMPERATURE RESPONSE WITH DEPOSITION - TEST T-15

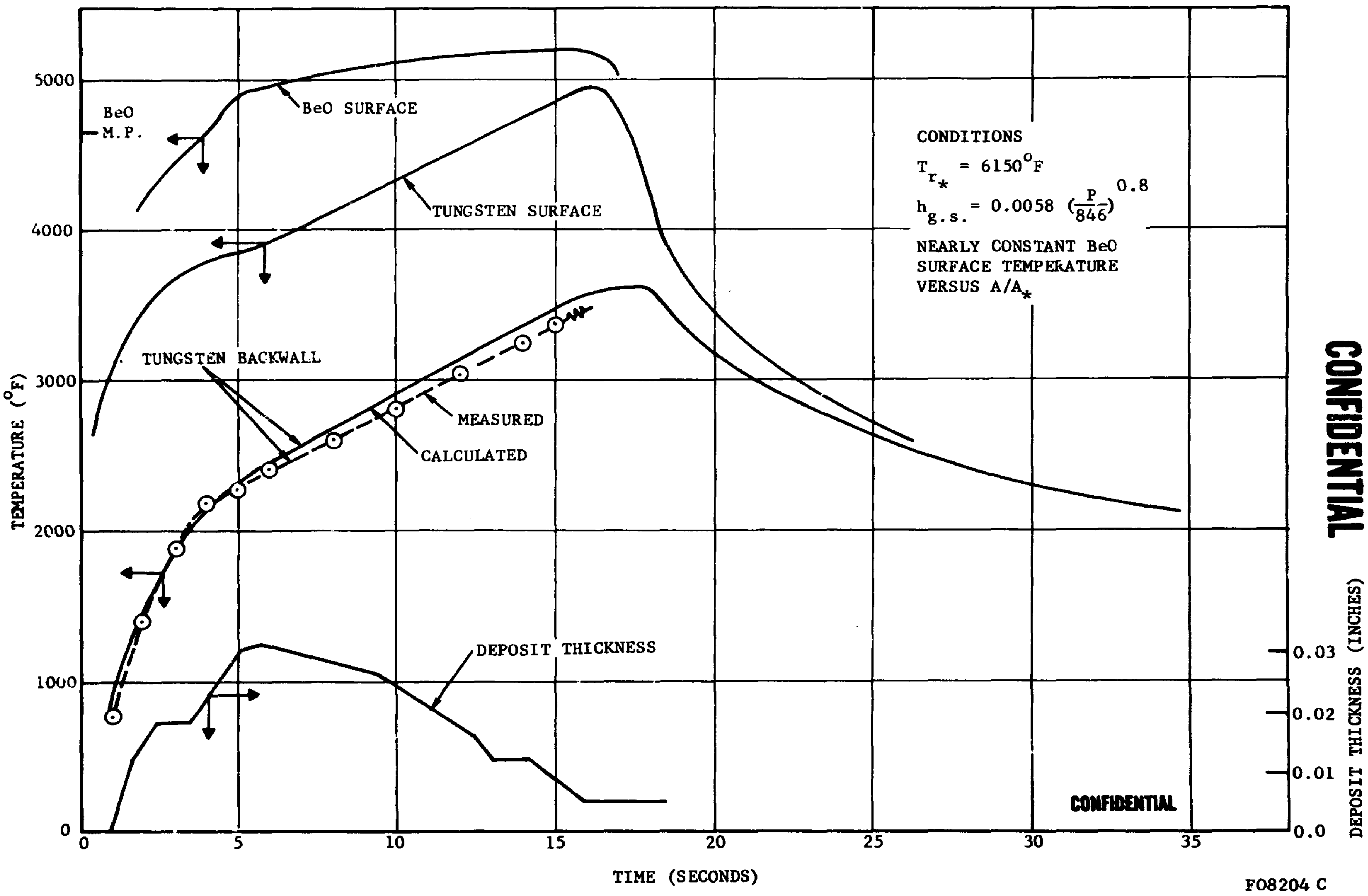

FIGURE 22. THROAT TEMPERATURE RESPONSE W.TH DEPOSITION, TEST T-16

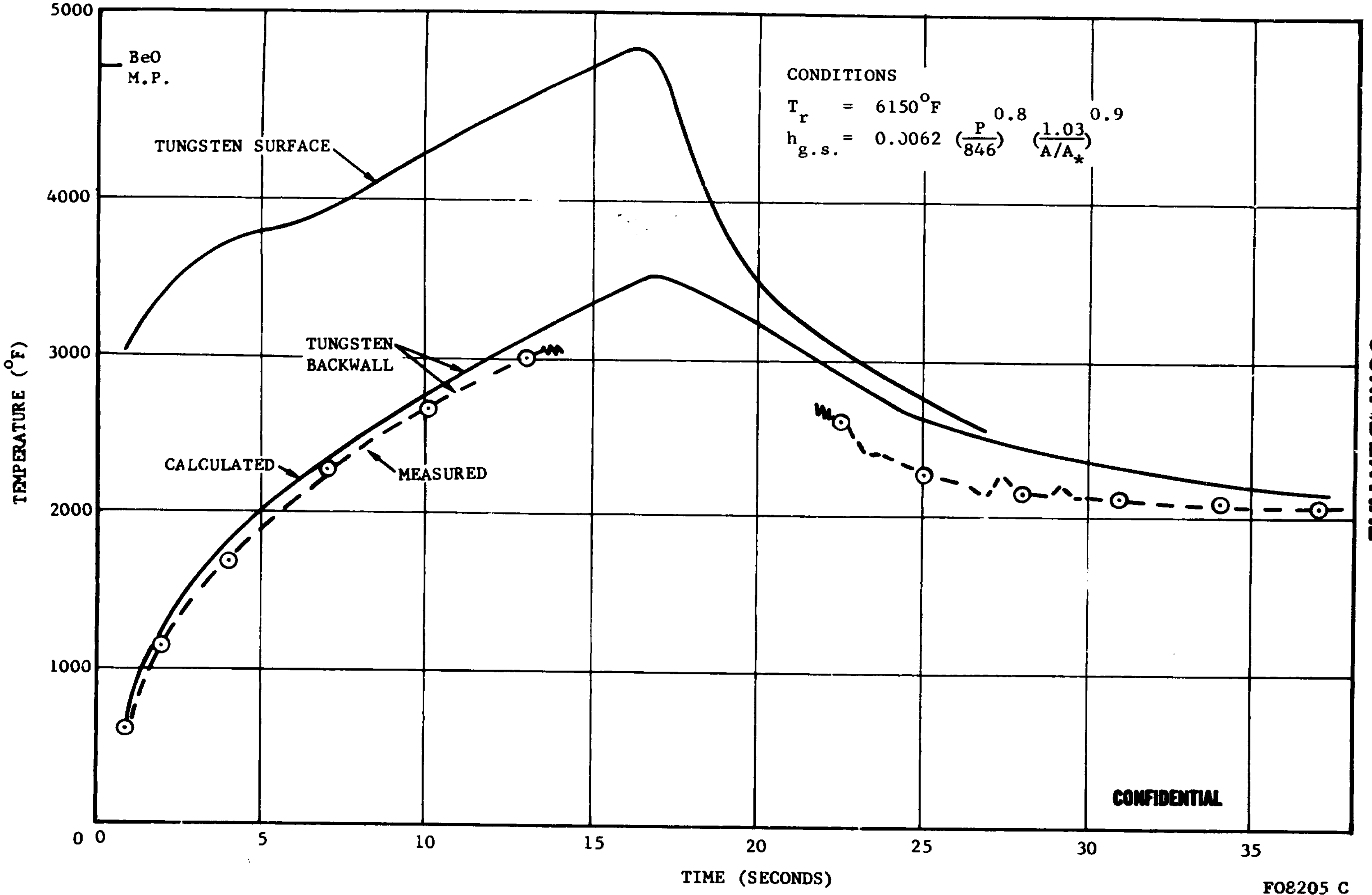

FIGURE 23. TEMPERATURE RESPONSE WITH DEPOSITION AT UPSTREAM AREA RATIO OF 1.03, TEST T-16

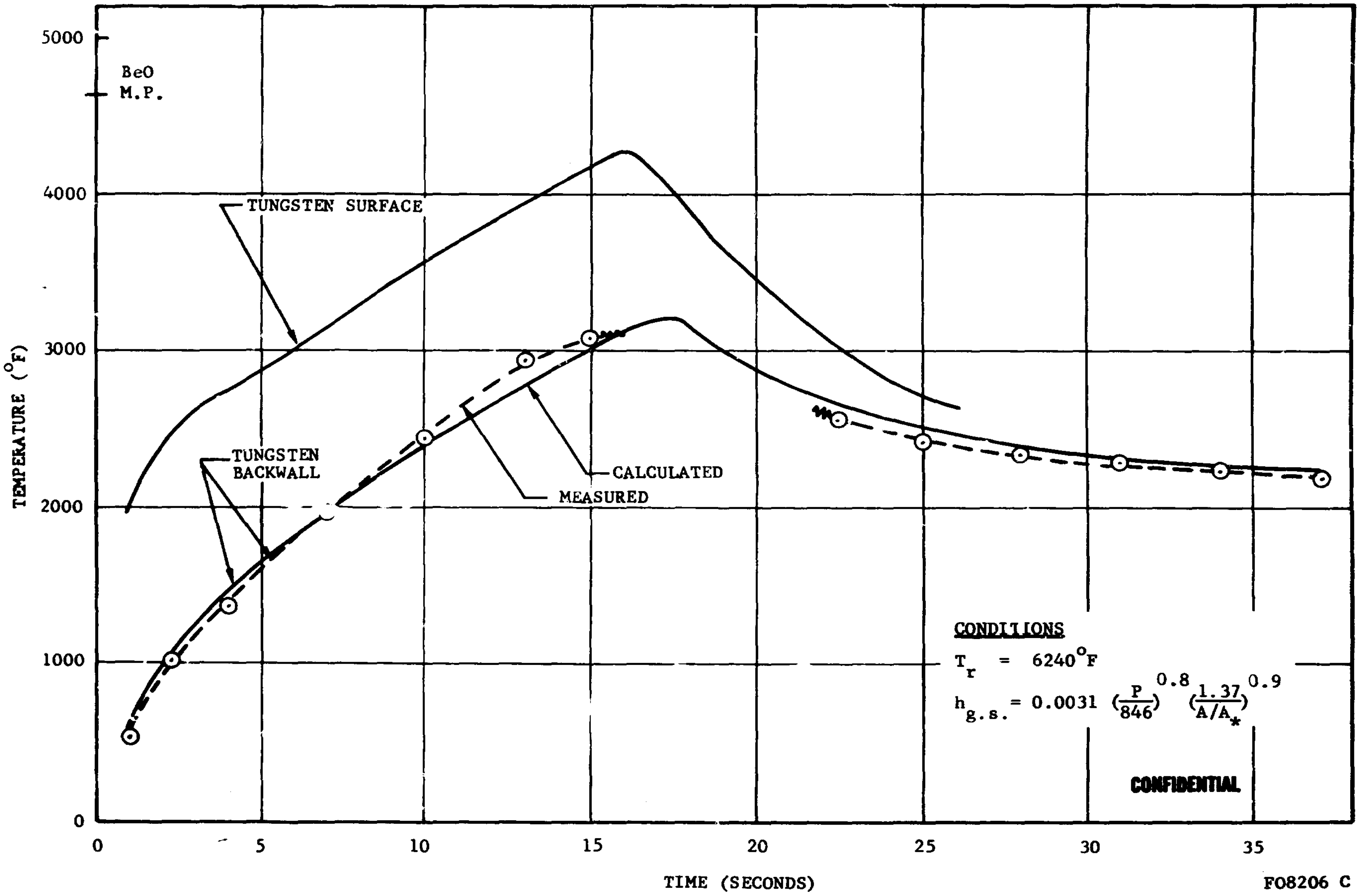

FIGURE 24. TEMPERATURE RESPONSE WITH DEPOSITION AT UPSTREAM AREA RATIO OF 1.37, TEST Γ-16

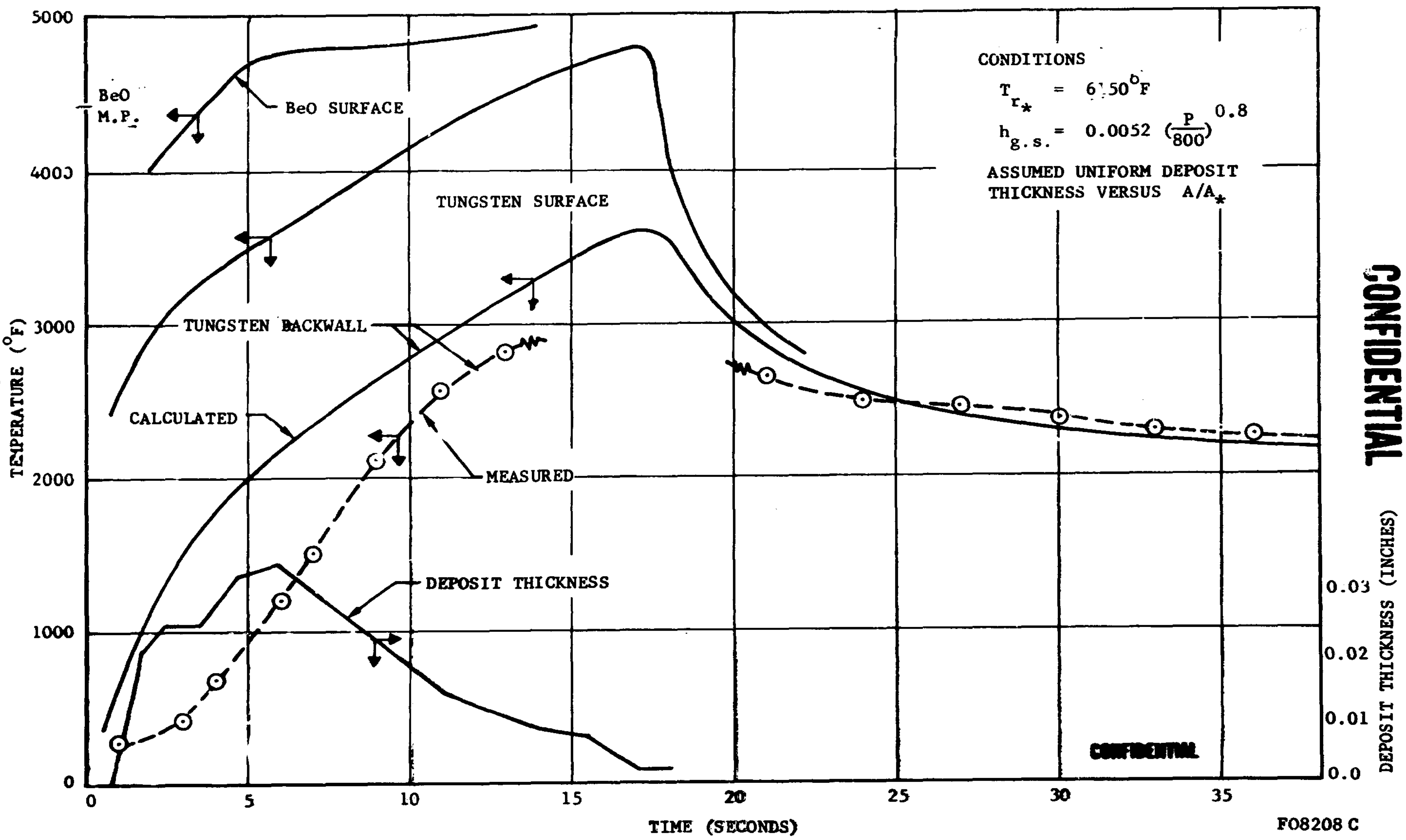

FIGURE 25. THROAT TEMPERATURE RESPONSE WITH DEPOSITION, TEST T-17

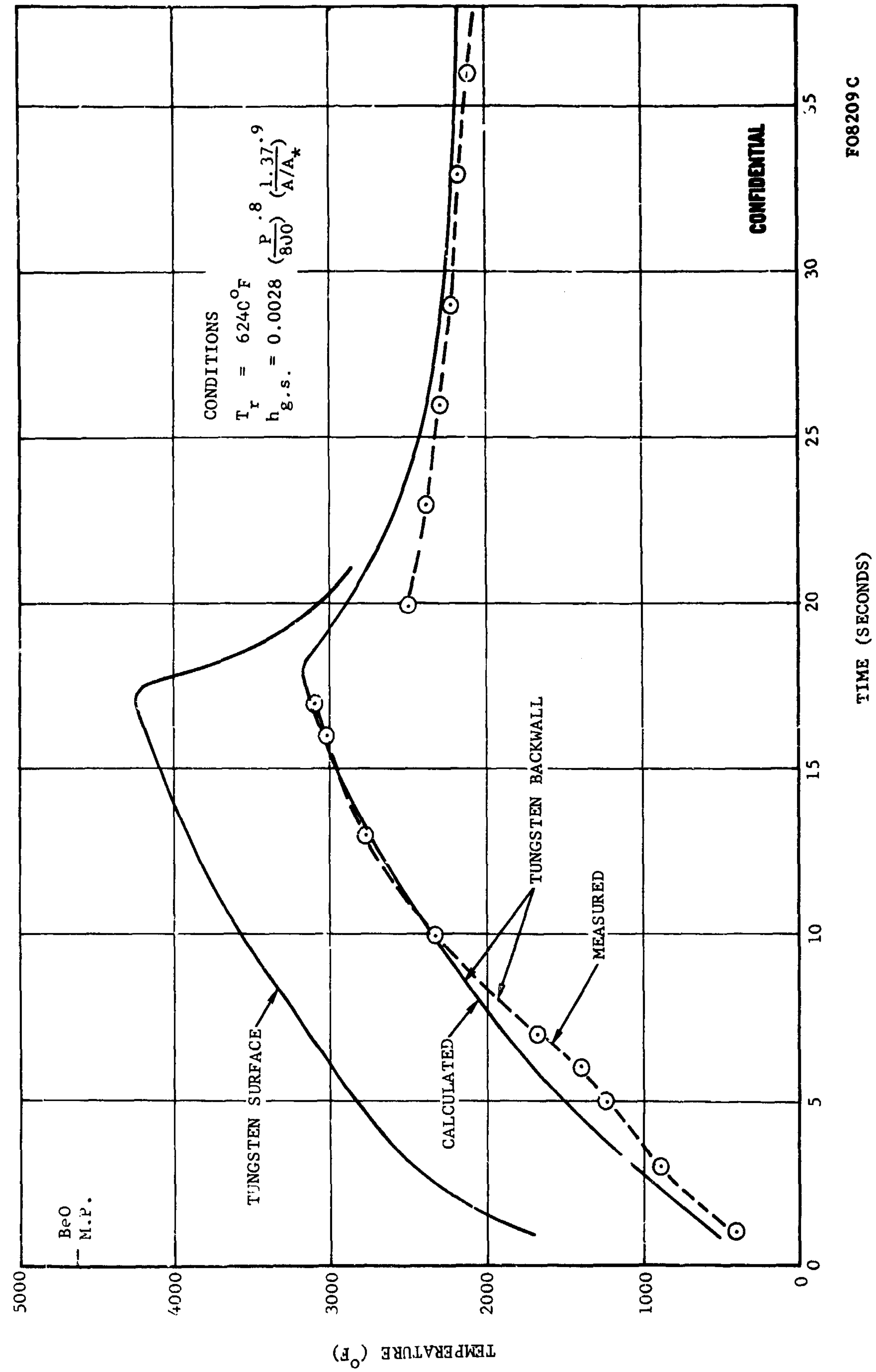

FIGURE 26. TEMPERATURE RESPONSE WITH DEPOSITION AT UPSTREAM AREA RATIO OF 1.37, TEST T-17

CONFIDENTIAL

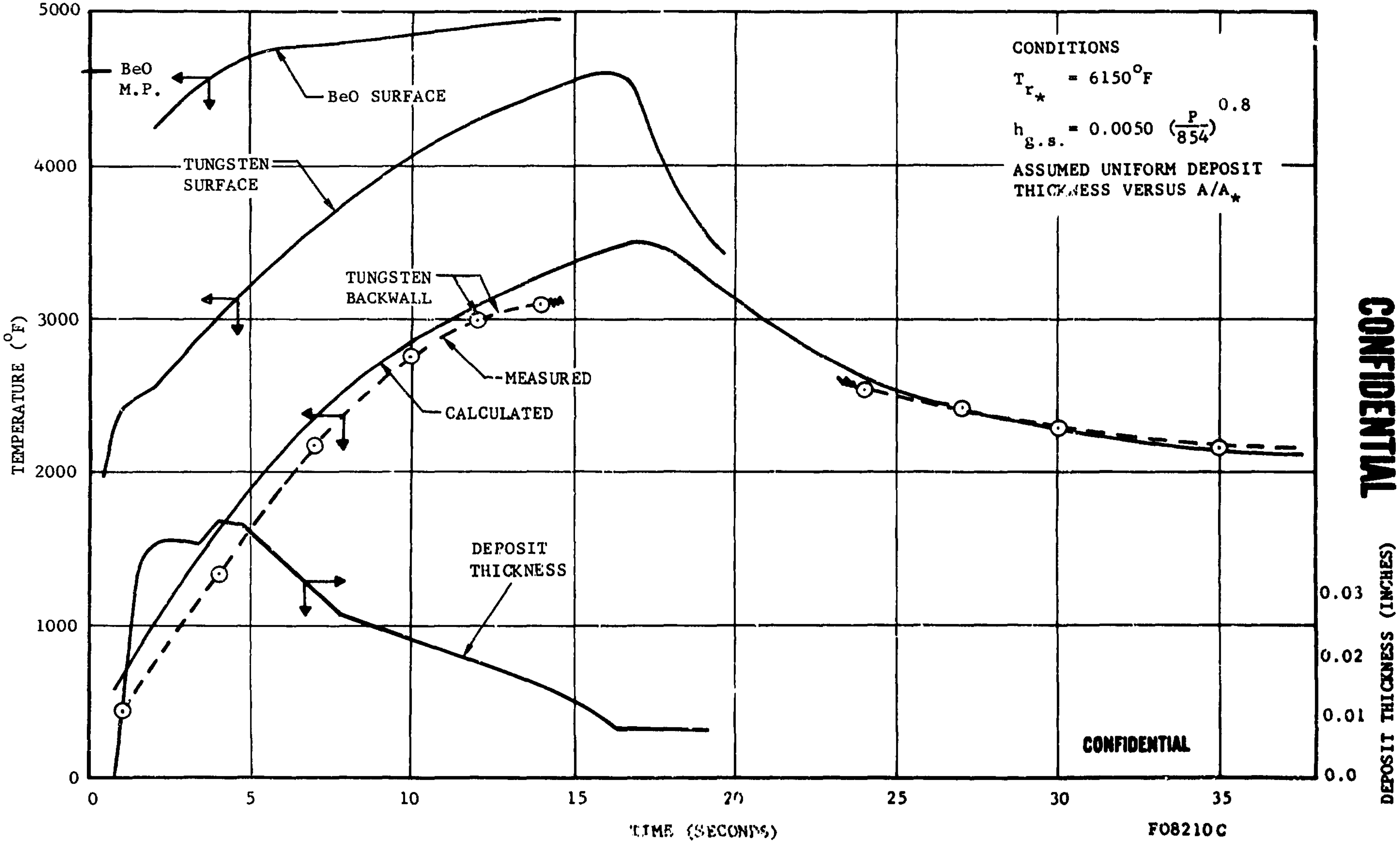

CONFIDENTIAL

FIGURE 27. THROAT TEMPERATURE RESPONSE WITH DEPOSITION, TEST T-18

CONFIDENTIAL

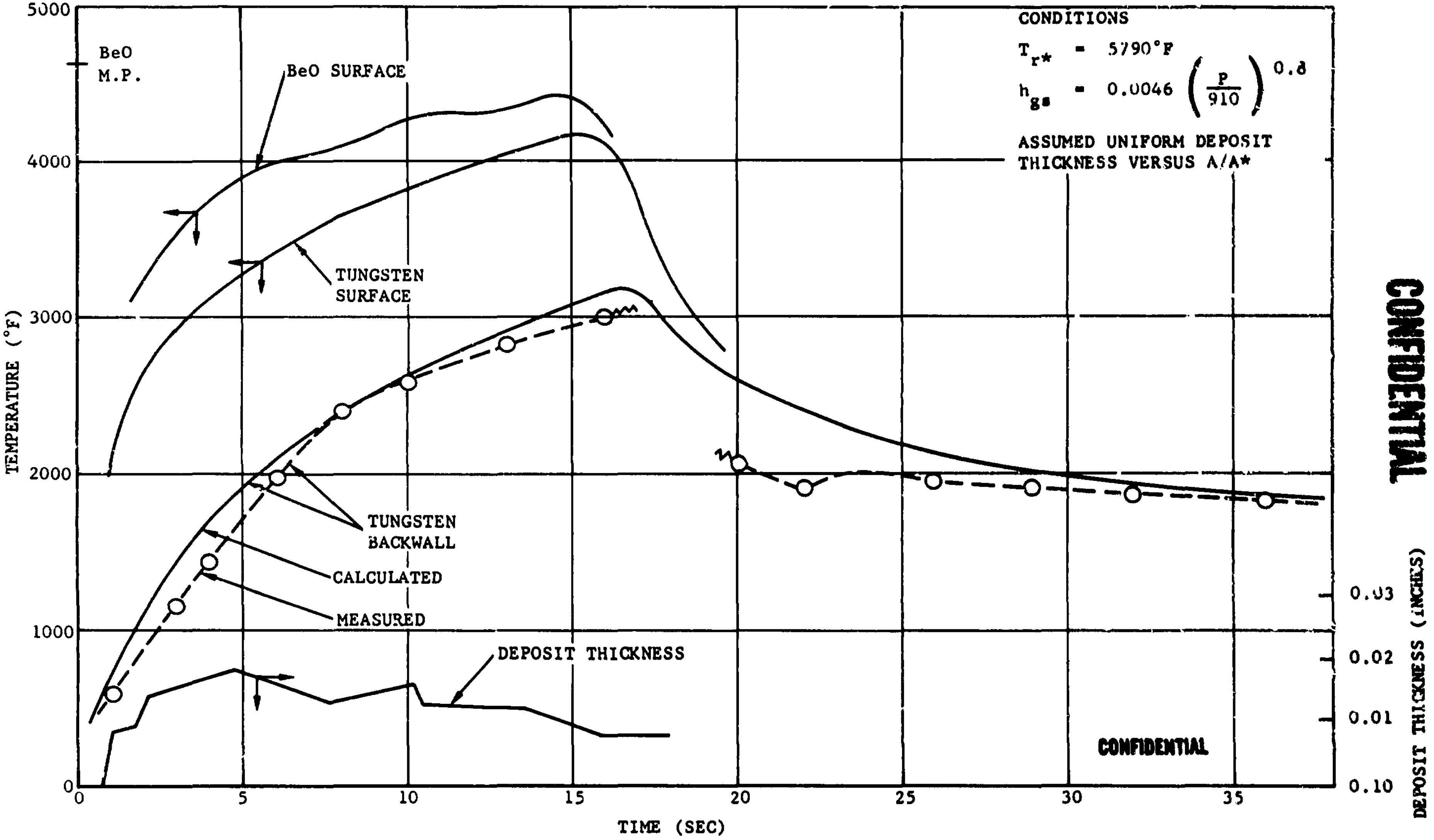

FIGURE 28. THROAT TEMPERATURE RESPONSE WITH DEPOSITION, TEST T-19

F08211 C

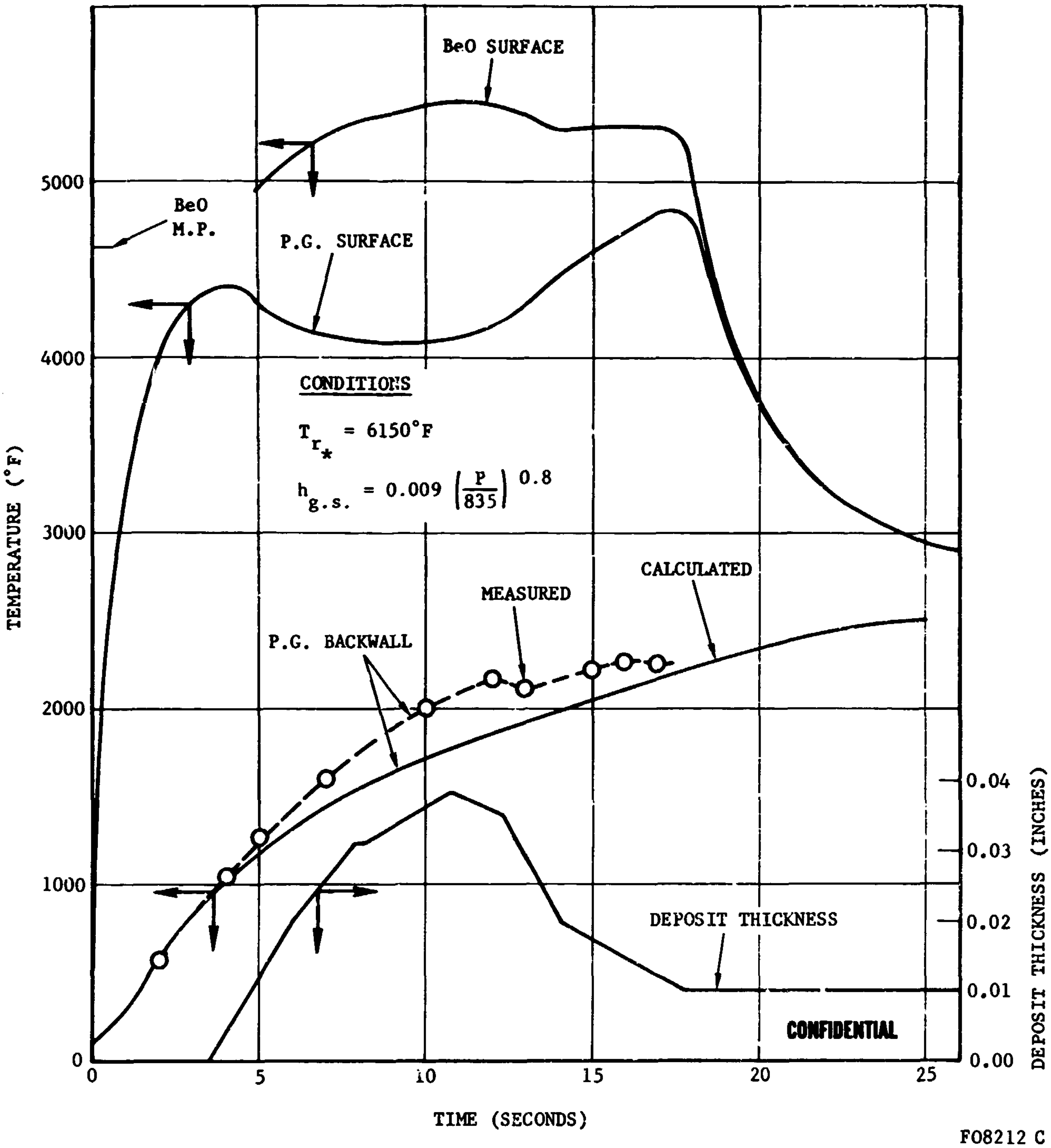

FIGURE 29. THROAT TEMPERATURE RESPONSE WITH DEPOSITION - TEST T-20

CONDITIONS

$T_{r_*} = 6150°F$

$h_{g.s.} = 0.004 \left(\frac{P}{946} \right)^{0.8}$

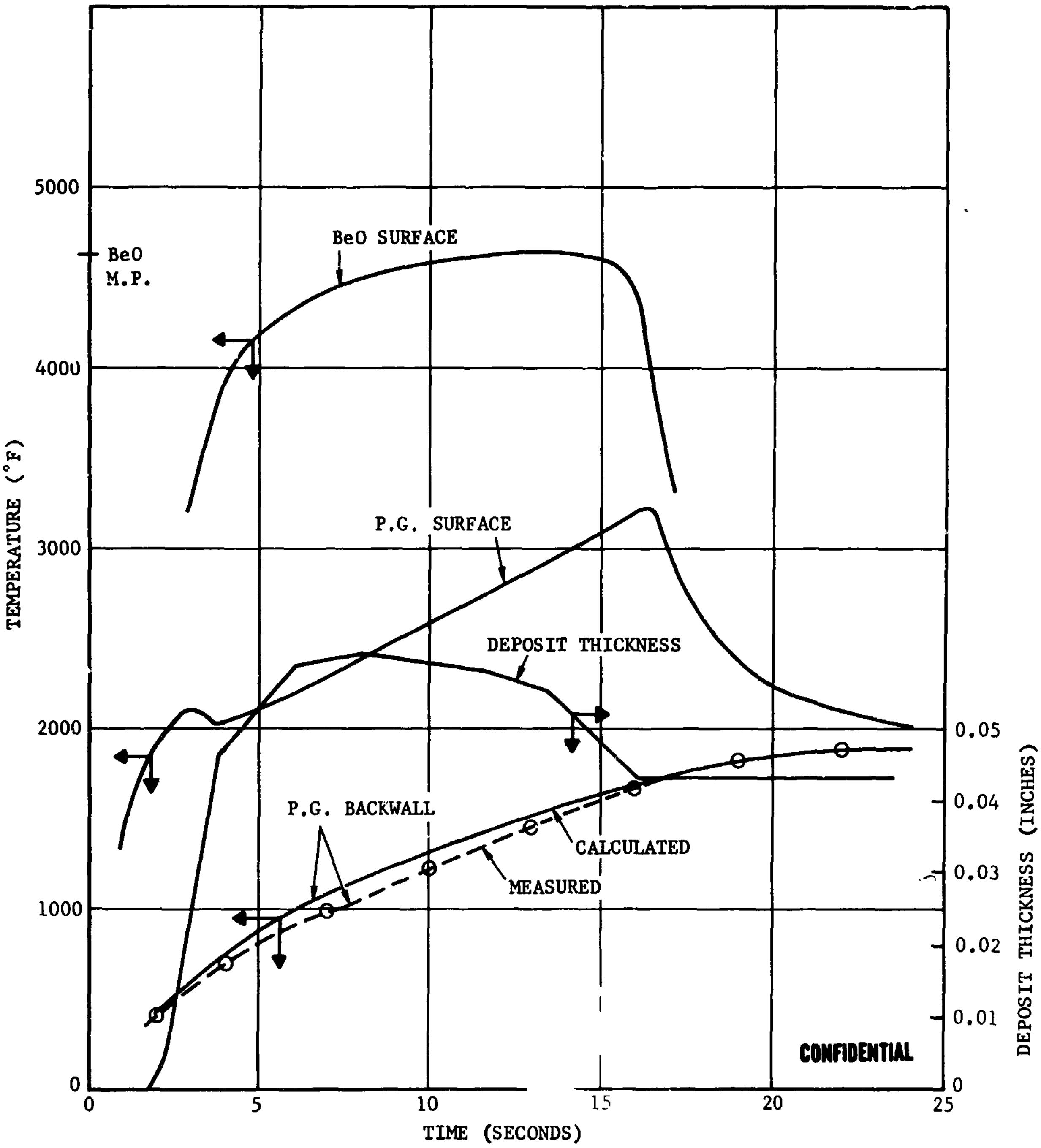

F08213 C

FIGURE 30. THROAT TEMPERATURE RESPONSE WIT' 'POSITION - TEST T-21

CONDITIONS

$T_{r_*} = 5590°F$

$h_{g.s.} = 0.0062 \left(\frac{P}{865}\right)^{0.8}$

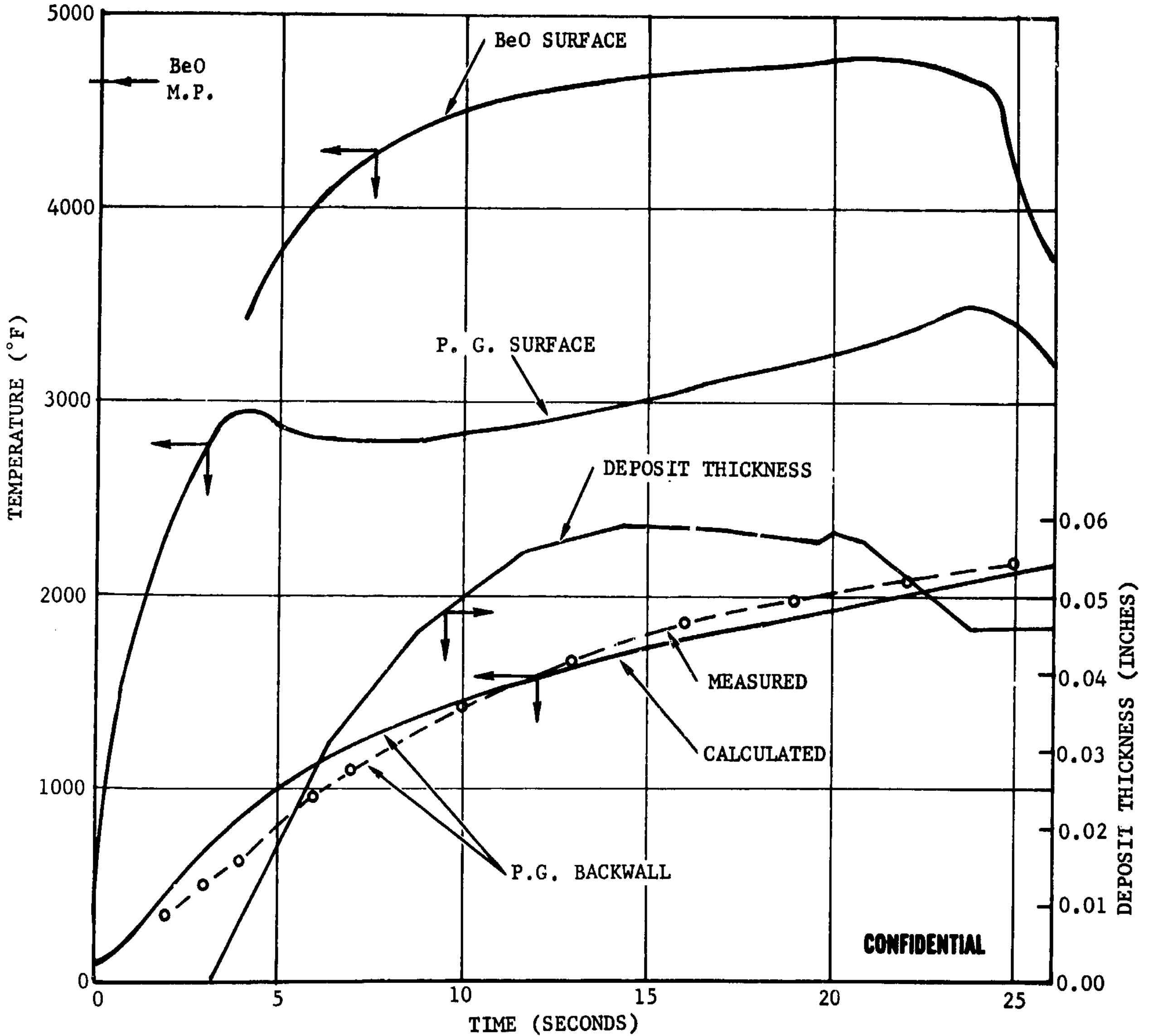

F08214 C

FIGURE 31. THROAT TEMPERATURE RESPONSE WITH DEPOSITION - TEST T-22

CONDITIONS

$T_{r_*} = 6150°F$

$h_{g.s.} = 0.0060 \left(\frac{P}{850}\right)^{0.8}$

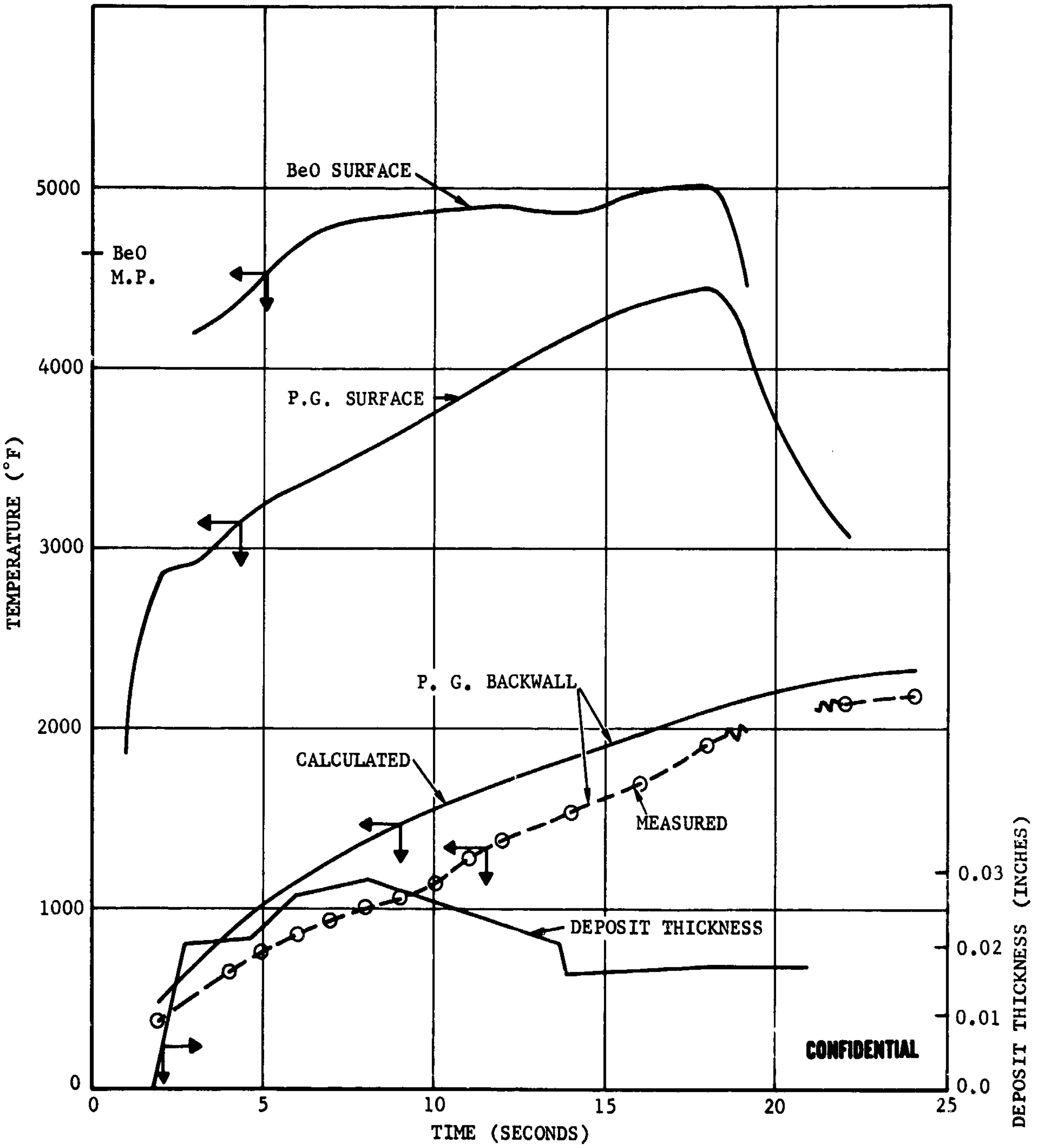

F08180 C

FIGURE 32. THROAT TEMPERATURE RESPONSE WITH DEPOSITION - TEST T-23

CONDITIONS

$T_{r_*} = 6150°F$

$h_{g.s.} = 0.0072 \left(\frac{P}{830}\right)^{0.8}$

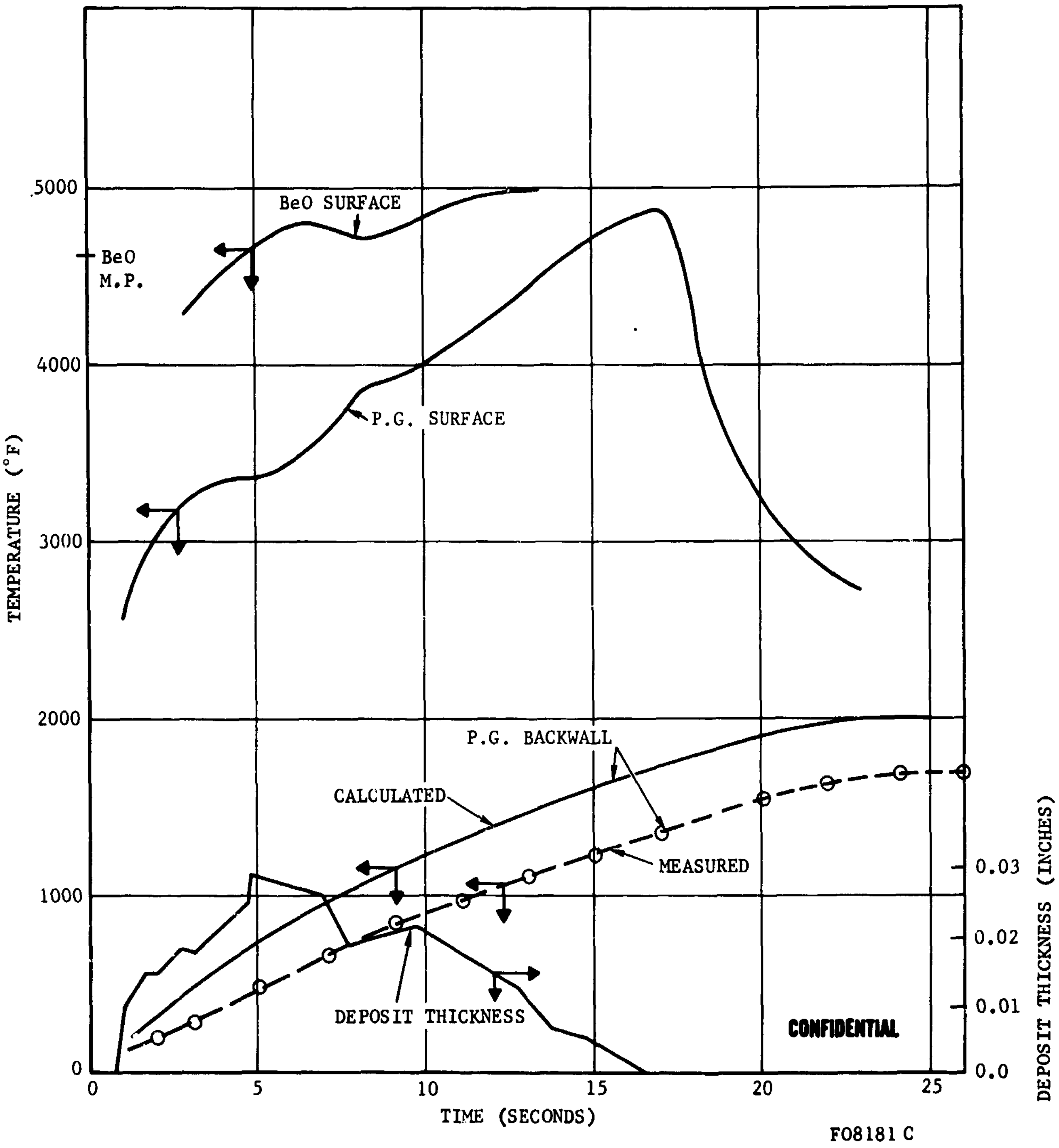

FIGURE 33. THROAT TEMPERATURE RESPONSE WITH DEPOSITION - TEST T-25

CONFIDENTIAL

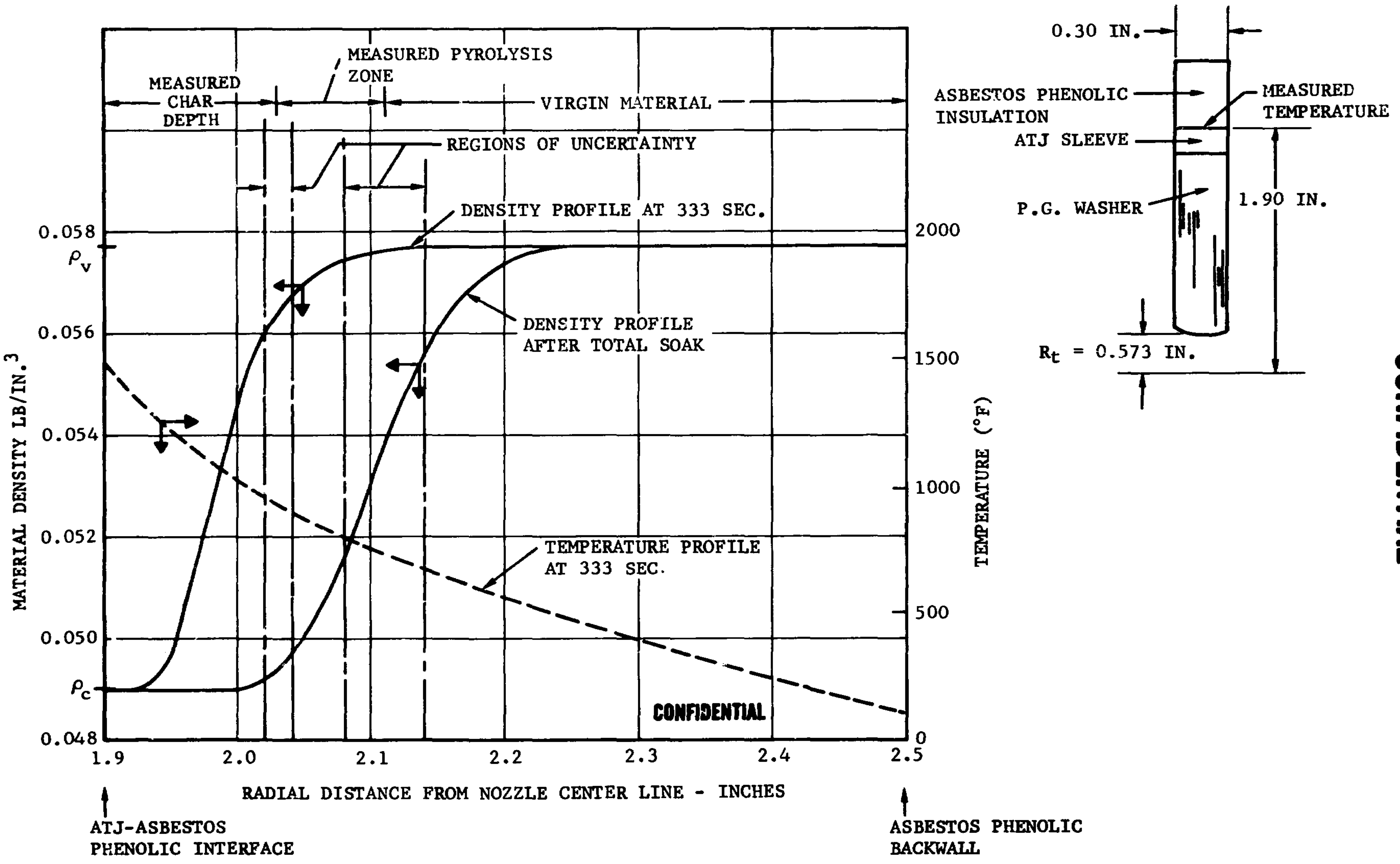

FIGURE 34. NOZZLE THROAT INSULATION DENSITY AND TEMPERATURE PROFILES

F08182C

CONFIDENTIAL

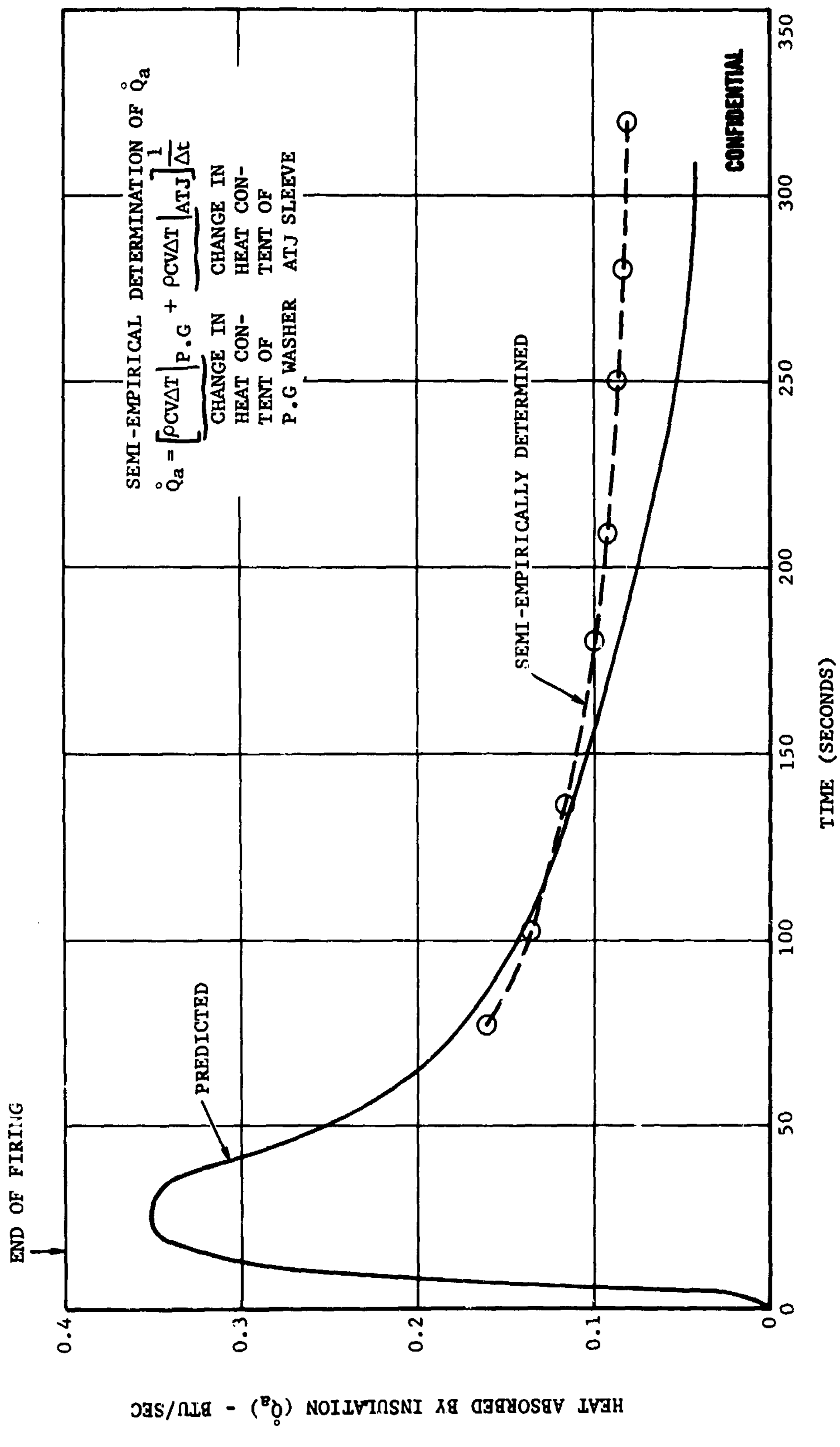

F08215 C

FIGURE 35. NOZZLE THROAT INSULATION HEAT ABSORPTION

Test T-10: As discussed in Section 2.4, the Type II slotted grain design of Test T-10 induced unsymmetrical heating and corrosion of the aft closure, entrance, and throat insert. Since the equilibration temperature of the throat P.G. washer is employed in establishing the total heat absorbed during firing, the calculated heat absorbed and corresponding heat transfer coefficient will represent the circumferential average. Also, the techniques employed in determining the throat deposit thickness produce a circumferential average. Therefore, the throat thermal response presented in Figure 17 must also be considered to represent the circumferential average. The correlation obtained between measured and calculated P.G. backwall temperature is very good. Also, the times at which the deposit thickness decreases and approaches zero are comparable to the calculated times at which the deposit and P.G. surface temperatures, respectively, approach the BeO melting point.

Test T-11: The throat heat sink thermal response for Test T-11 was calculated using the transient temperature obtained from the thermocouple located just upstream of the geometric throat (entrance area ratio of 1.03). The throat P.G. backwall thermocouple did not record properly and could not be used in the thermal calculations. Therefore, the thermal response and gas side heat transfer coefficient presented in Figure 18 are not precisely comparable to other results. The P.G. surface temperature is shown to be less than the melting point of BeO during the entire firing duration. Also, the calculated transient deposit thickness is shown to be extremely periodic, suggesting that deposit is being removed from the throat in the solid phase. However, this may not necessarily be true because, (1) the thermal response is not for the throat washer, (2) the calculated deposit thickness is the circumferential average, and (3) the deposit melting point is not necessarily equal to that of BeO.

Test T-12: As in Test T-10, the Type II slotted grain was employed in Test T-12. Therefore, the gas side heat transfer coefficient, the corresponding heat sink thermal response (shown in Figure 19) and the deposit thickness represent circumferential averages. Circumferential positions of the two throat thermocouples are presented in Table IX in Section 2.4. The correlation between the two measured and calculated P.G. backwall temperature histories is very good.

Test T-13: Small Motor Test T-13 was not thermally analyzed due to the loss of thermocouple data after the aft closure burn-through at approximately 13 seconds. However, a good qualitative description of the unsymmetrical flow field and surface regression associated with the Type II slotted grain was obtained for Test T-13 (see Section 2.4). The temperature data obtained prior to the burn-through are included in the Appendix.

Test T-14: The throat heat sink thermal response for Test T-14 is shown in Figure 20. The correlation between the calculated and measured P.G. backwall temperature response is very good. Also, the time at which the P.G. surface temperature reaches the melting point of BeO is in agreement with the time the deposit thickness approaches zero.

Test T-15: As in Tests T-8, T-10, T-12 and T-13, Test T-15 employed a slotted grain. However, the initial grain port to throat area ratio was smaller for Test T-15 (3" as compared to 7" diameter port). As in the other slotted grain tests, the throat gas side heat transfer coefficient, the corresponding heat sink thermal response and the transient deposit thickness of Figure 21 represent the circumferential average. The P.G. backwall thermocouple is suspected to have lost thermal contact at 5 seconds in the firing as is evident by the erratic temperature response subsequent to this time. Therefore, the comparison between the measured and calculated P.G. temperature response is relatively poor. However, good agreement does exist between the time the calculated BeO surface reaches the melting point and the time the deposit thickness decreases. Also, the calculated P.G. surface temperature never reaches the BeO melting point, in good agreement with the finding of throat deposits in the post-test inspection of the nozzle.

Test T-16: The calculated thermal response of the tungsten throat insert at three axial positions is presented in Figures 22, 23 and 24. The thermal analysis employed in these calculations assumed a nearly isothermal deposit surface temperature in the axial direction. The local heat transfer coefficient at all positions was dependent on the instaneous chamber pressure and area ratio. The axial variation of the heat transfer coefficient was based on the Bartz correlation and the magnitude was established when the calculated and measured tungsten equilibration temperatures were in agreement. The resulting calculated tungsten backwall temperature histories at the three axial positions are in good agreement with the measured results. Also, the time at which the BeO surface temperature approaches the BeO melting point and the time the deposit thickness is shown to decrease are in agreement. The maximum temperature of the tungsten insert is calculated to be 4960°F and occurs just before shutdown.

Test T-17: The thermal response of the tungsten throat insert at two axial positions is shown in Figures 25 and 26. The thermal analyses employed in T-17 assumed a uniform deposit thickness at all axial positions on the throat insert. This assumption will result in a lower throat heat transfer coefficient than would be calculated from the isothermal deposit surface temperature assumption employed in T-16. The magnitude variation of the heat transfer coefficient with area ratio was determined in the same manner as for Test T-16. The calculated transient tungsten backwall temperature is in good agreement with the measured at an entrance area ratio of 1.37. However, at the throat, the calculated and measured temperatures are in disagreement. The thermocouple post-test analysis (see Section 4.3), together with the temperature correlation at equilibration, indicate that poor thermal contact probably existed between the tungsten backwall and the throat thermocouple. The time at which the BeO surface temperature approaches the BeO melting point, and the time the deposit thickness is shown to decrease are in agreement.

Test T-18: The same analytical techniques employed in T-17 were used in determining the tungsten thermal response of T-18. The throat thermal response for T-18 is presented in Figure 27. The agreement, between the measured and predicted transient tungsten backwall temperatures, is good. Again, the time at which the BeO surface temperature approaches the BeO melting point, and the time the deposit thickness is shown to decrease are in agreement.

Test T-19: The tungsten thermal response for T-19, presented in Figure 28, was calculated using the analytical techniques described for Test T-17. The resulting agreement, between the calculated and measured transient tungsten backwall temperatures, is good. However, the BeO deposit never reached its melting point. The deposit thickness for T-18 was found to increase and decrease in a very random manner, possibly reflecting unsteady heat transfer, surface roughness or deposit impurity effects.

Test T-20: The nozzle for Test T-20 was unique in that carbon cloth phenolic was employed as the nozzle entrance cone material. The entrance section surface regression could not be precisely determined (see Section 3.4). The regression was great enough to create a step discontinuity in the contour. Boundary layer reattachment on the first washer would promote particle impingement and boundary layer redevelopment. This would cause the throat deposit thickness and heat transfer to increase relative to comparable firings (T-9 and T-25). However, these effects will be opposed by the carbon cloth pyrolysis gas mass addition (film cooling effect). Qualitatively, it is expected that these effects will be most important during the early portion of the firing and after all of the oxide deposits have melted. The calculated throat heat sink thermal response is presented in Figure 29. As in the case of Test T-9, the calculated and measured P.G. backwall temperature of Test T-20 are in agreement during the initial portion of the firing and diverge at the later times. As suggested before, an error in the thermal conductivity of liquid BeO is suspected. Another possible explanation derives from approximations employed in estimating the transient chamber pressure and, subsequently, the deposit thickness. The chamber pressure was not measured for the test, thus introducing an unknown error into the thermal analyses.

Tests T-21 and T-22: The calculated thermal response shown in Figures 30 and 31 are in good agreement with the measured P.G. backwall temperatures. The times at which the deposit thickness actually decreased agree with the times the deposits are calculated to have reached the BeO melting point. The calculated P.G. surface temperatures never reaches the BeO melting point, in good agreement with the laboratory post-test examinations (see Section 3.4).

Test T-23: The calculated and measured transient P.G. backwall temperatures, Figure 32, are in poor agreement, even though the 'measured' total heat absorbed during the firing was employed in establishing the gas side heat transfer coefficient. Based upon the correlations obtained for all the other P.G. inserts, it is suspected that the thermocouple was in poor thermal contact with the P.G. backwall. Good accuracy of the calculated gas side heat transfer coefficient is suggested by the agreement between the calculated time the deposit surface melts, and the observed time the deposit thickness undergoes a decrease. Further, the calculated P.G. surface temperature never reaches the BeO melting point, in agreement with the laboratory post-test analysis (see Section 3.4).

Test T-24: The thermal analyses have not been applied to Test T-24. No temperature data was obtained as a result of a malfunction of the data recording system.

Test T-25: In analyzing the thermal response of Test T-25, the conduction computer program applied to the other P.G. inserts tests was revised to include the 0.50 increase in P.G. washer outside diameter. The gas side heat transfer coefficient employed in the analysis to establish the throat washer thermal response was not based upon the equilibration temperature of the P.G. thermocouple, as was done in all of the other P.G. firings. Instead, the coefficient that resulted in agreement between the times at which the P.G. surface temperature reaches the BeO melting point and when the deposit thickness reaches zero, was employed. When the equilibration temperature was employed in the determination of the gas side heat transfer coefficient, the maximum BeO surface temperature was found to be 3800°F, contradicting the observed deposit thickness decrease and depletion calculated for the firing. These results suggest: (1) a thermal analysis error was introduced when the P.G. heat sink thickness was changed, (2) poor thermal contact was experienced for all P.G. thermocouples, or (3) the data for Test T-25 was reduced improperly. The data reduction is the most logical source, since this was the only test on which an oscillograph was employed in recording thermocouple output. The method employed in reducing the data and thermocouple hookup for T-25 will be reexamined during the final reporting period. At the present time, the calculated thermal response shown in Figure 33 must be considered to be only approximate.

(b) (C) Discussion of Results

The primary objective of the thermal effort for this quarter of the contract has been to characterize the gas side boundary condition and heat sink thermal response of the small rocket motors. The objective has been accomplished by semi-empirical techniques, discussed elsewhere in this report. There are specific analytical assumptions and qualitative interpretations of physical phenomena that may erroneously influence the correlation of the results. These assumptions and phenomena include:

(1) The P.G., ATJ and tungsten thermal properties employed in the analyses are assumed to be correct. Thermal property errors, especially in thermal conductivity, could bias the

correlation of pyrolytic graphite and tungsten throat insert thermal response.

(2) The thermal properties of the liquid and solid phases of the surface deposit (BeO and Al_2O_3) are assumed to be equal and independent of temperature. The validity of these assumptions and the accuracy of the properties employed in the analyses will influence the comparison of results when (a) the metal additive changes, (b) a significant amount of impurities are in the wall deposit, and (c) variation in the fraction of the deposit in the liquid phase occurs during the firing time.

(3) The geometrical throat for the entire firing period is assumed to be located at its original axial position. Also, the throat thermocouple for all firings is assumed to be located at the geometrical throat. Errors will result in the characterization of the gas side boundary condition if the surface deposit influences the axial position of the throat and/or the insert thermal expansion changes the thermocouple-backwall position relative to the throat. The variation of heat transfer with area ratio is significant in the throat region of the nozzle, hence the convective heat transfer correlations will be affected if either of these assumptions are unrealistic.

(4) The throat recovery temperatures in the analyses are determined from the ideal thermochemical characterization of the exhaust. Any combustion inefficiencies (reduction of the recovery temperature) will therefore cause the gas side heat transfer coefficient to be underestimated.

(5) The heat transfer associated with wall deposit phase change, particle impingement, and the downstream progression of the liquid portion of the deposit is assumed to be negligible at the throat compared to that of convection. Also, the heat transferred through the deposit to the nozzle surface is assumed to occur only by conduction.

(6) The throat gas side heat transfer coefficient, transient deposit thickness, and the corresponding heat sink thermal response, represent the circumferential average. Any unsymmetrical heating

and/or deposit flow will, therefore, influence the comparison of results.

The influence of the heat sink thermal properties, assumption (1) above, will be absorbed in the gas side heat transfer coefficient. Therefore, the gas side coefficient may possibly be dependent on the heat sink material. However, the wall deposit thermal properties, assumption (2), may cause the gas side convective coefficient to be dependent on the individual firing. The validity of assuming equal solid and liquid deposit thermal properties may quantitatively be deduced by comparing the measured and calculated P.G. backwall temperatures, of Figures 10 through 21 and 29 through 33. In all of those tests that are considered to have produced reliable thermocouple data, the calculated P.G. backwall temperature is greater than or equal to the measured value during the time the deposit is in the solid state. At times, when the deposit is partially liquid, the calculated P.G. backwall temperature is less than the measured. This suggests that the constant deposit thermal conductivity, employed in the analyses, is greater than that of the solid, and less than that of the liquid phase. This may actually be true if the liquid bulk density is greater than that of the solid (direct relationship between thermal conductivity and bulk density if inter-pore radiation is neglected). Considering that the wall deposit consists of the metal oxide, absorbed gases, and impurities from the surface materials, the absorbed gases will be partially released on solidification causing a porous, solid deposit. However, the net bulk density change may not necessarily be positive in going from pure solid to pure liquid as the 'actual' density change of a material is usually negative. The apparent increase in energy transport when the deposit partially liquifies may also be partially attributed to (1) the energy transported by higher temperature surface liquid as it flows downstream and (2) the importance of convective transport of energy through the liquid as compared to conductive.

The throat heat transfer coefficients, presented in Table XI, were calculated using the total measured heat absorbed during firing and the theoretical recovery temperature. If the actual recovery temperature for the firing is different than the theoretical, caused possibly by incomplete combustion and/or boundary layer mass addition, the calculated heat transfer coefficient will be affected, assumption (4). For example, if the actual recovery temperature is less than theoretical, the calculated heat transfer coefficient will be lower than the actual.

In the discussions that follow, the throat heat transfer coefficients given in Table XI have been adjusted to a common reference pressure. Using the simplified Bartz equation and a reference chamber pressure of 800 psia, the average convective coefficients become,

$$\bar{h}_{800} = \bar{h}\left(\frac{800}{P}\right)^{0.8}$$

where; $\bar{h}_{800}$ is the average throat heat transfer coefficient based upon an average chamber pressure of 800 psia; $\bar{h}$ and $\bar{P}$ are, respectively, the measured average throat heat transfer coefficient and chamber pressure presented in Table XI.

The influence of grain geometry on the nozzle flow field and deposition phenomenon has been discussed in Sections 2.4 and 4.2, respectively. The dependence of heat transfer on grain geometry can be determined by comparing the adjusted throat heat transfer coefficients, keeping in mind the errors (discussed earlier) inherent in the calculations. Table XIV organizes the heat transfer results as a function of propellant and grain design.

From a theoretical standpoint, grain geometry will, in part, define the nozzle flow field and combustion products stay-time. These will, in turn, influence the nozzle boundary layer starting point, local free stream velocity, recovery temperature, and free stream turbulence level. The importance of the grain design in influencing these heat and mass transfer parameters can be deduced, at least qualitatively, as follows.

For the grain designs yielding a symmetrical flow field (end burner and Type I), the Type I grains, for both the 191F and 319 propellants, exhibit higher heat transfer than the end burning grains. The inverse observation for the 54F propellant may be attributed to the fact that, in analyzing Test T-11, the temperature data for the washer upstream of the throat was employed. For the Type I grains, the boundary layer development length to the throat is less than for either the remote or close end burners. This will tend to increase the convective heat transfer at the throat, since turbulent heat transfer and boundary layer mass injection effects are inversely proportional to development length.

The Type II slotted grain produced the highest throat heat transfer for the 191F propellant. This is attributed to unsymmetrical flow effects (see Section 2.4). However, for the 319 propellant (Type III grain), just the opposite was observed. From Section 2.4, it is noted that the unsymmetrical flow effects should not be as important for the Type III grain, compared to the Type II. Also, the stay time for the 319 slotted grain is considerably less than those associated with the other designs. Comparing the 191F and 54F end burning grains (the stay time for the remote end burner is much greater than for the close end burner), the same stay time dependence on heat transfer is noted. Apparently, these comparisons indicate that incomplete combustion occurred on Tests T-15, T-21, T-22 and possibly on T-24.

The influence of nozzle geometry on throat heat transfer can be seen by referring to Table XV.

For both the Type II slotted and close end burner grains, the submerged nozzle throat heat transfer coefficient is greater than that of the

TABLE XIV. INFLUENCE OF GRAIN GEOMETRY ON THROAT HEAT TRANSFER (C)

Test	Propellant	Grain-Nozzle Geometry	$\bar{h}_{800}$ Btu/in^{2}sec°F	$\frac{\bar{h}_{800}}{\bar{C}_p}$
T-1	191F	Remote end burner 25° conventional nozzle	0.0070	0.0070
T-9	191F	7" port - Type I 18° conventional nozzle	0.0092	0.0092
T-10	191F	7" port - Type II (slotted) 18° conventional nozzle	0.010	0.010
T-21	191F	Close end burner 55° steep inlet nozzle	0.0035	0.0039
T-3	319BRF	Remote end burner 25° conventional nozzle	0.0066	0.0083
T-14	319BRF	7" port - Type I 18° conventional nozzle	0.0073	0.0092
T-15	319BRF	3" port - Type III (slotted) 18° conventional nozzle	0.0045	0.0059
T-24	319BRF	Close end burner 55° steep inlet nozzle	No data	-
T-4	54F	Remote end burner 25° conventional nozzle	0.0065	0.0069
T-11	54F	7" port - Type I 18° conventional nozzle	0.0061	0.0070
T-22	54F	Close end burner 55° steep inlet nozzle	0.0059	0.0064
T-7	389	Remote end burner 25° conventional nozzle	0.0070	0.0119
T-8	389	7" port - Type II (slotted) 18° conventional nozzle	No data	

conventional nozzle. This may be attributed to the shorter boundary layer development length and adverse flow field induced by the submerged nozzle geometry. However, as may be seen in Table XV, the increased throat heating associated with the submerged nozzle is not evident in the correlation between Test T-16 and T-18. Both of these tests employed tungsten as a throat insert. The method used in calculating the throat heat transfer coefficient involved the isothermal deposit surface and uniform deposit thickness assumptions for Tests 16 and 18, respectively. The isothermal deposit surface assumption will lead to in a higher heat transfer coefficient than the uniform thickness assumption; therefore, the T-16 and T-18 correlation is not regarded as representative.

TABLE XV. INFLUENCE OF NOZZLE GEOMETRY ON THROAT HEAT TRANSFER

Test	Propellant	Grain-Nozzle Geometry	$\bar{h}_{800}$ Btu/in^{2}sec°F	$\frac{\bar{h}_{800}}{\bar{C}_p}$
T-10	191F	7" port - Type II (slotted) 18° conventional nozzle	0.010	0.010
T-12	191F	7" port - Type II (slotted) submerged nozzle	0.013	0.0118
T-13	191F	7" port - Type II (slotted) 55° steep inlet nozzle	No data	-
T-21	191F	Close end burner 55° steep inlet nozzle	0.0035	0.0039
T-23	191F	Close end burner submerged nozzle	0.0057	0.0060
T-16	191F	7" port - Type I 18° conventional nozzle, W throat	0.0059	0.0059
T-18	191F	7" port - Type I submerged nozzle, W throat	0.0048	0.0051

The influence of propellant formulation on throat heat transfer can be directly associated with boundary layer average specific heat, degree of combustion, Prandtl number, viscosity, and ratio of specific heats. Since the stay time will influence these boundary layer parameters, Table XVI compares the various propellant formulations at relatively constant stay times.

For all grain-nozzle geometries considered in Table XVI, the throat heat transfer coefficient for the 191F propellant is greater than that for the 319BRF. For two of the grain designs, the 191F propellant heat transfer coefficient is greater than that for the 54F (compare Tests T-1, T-4, T-9, and T-11). However, for the close end burner design, (Tests 21 and 22), the 54F produced the higher heat transfer coefficient. The probable errors in the analysis of Test T-11 and poor combustion on Test T-21 are thought to be important here. Based on a comparison of theoretical specific heats, the 54F and 191F propellants should have equal coefficients while the 319BRF should be (and is) significantly lower. The correlations presented in Table XVI between the throat heat transfer coefficients and propellant formulation have not been compared to theoretical predictions. When the theoretical convective analyses development has been completed, the measured and theoretical predictions will be correlated.

The standard materials employed in the entrance cone and throat insert of the small motor tests were ATJ graphite and pyrolytic graphite washers, respectively. However, in two tests, the entrance section material was carbon cloth-phenolic; in four tests, the throat material was tungsten; and in one test, radial thickness of the pyrolytic graphite washers was increased. The results obtained in the motor tests involving these material changes are compared in Table XVII.

Theoretically, when only the pyrolytic graphite throat is replaced with tungsten, and no alteration in the nozzle contour occurs during the firing, the throat heat transfer coefficient should only reflect differences in the gas side surface temperature and roughness. However, the correlations between Tests T-9, T-16, T-14, and T-19 indicate a considerable decrease in heating when tungsten was employed. As previously discussed, the thermal analyses applied to the tungsten insert are approximate due to the significance of axial conduction and the missing axial deposit thickness variation. Tungsten apparently traps more oxide deposit upstream of the throat than the pyrolytic graphite does. Differences in both radial heat capacity and oxide wetting mechanics are likely to be involved.

When carbon cloth-phenolic was employed in the entrance section, Table XVII (comparing Tests T-9, T-20, T-16, and T-17) indicates a decrease in throat heat transfer. No conclusions have been reached in this case, since the results of Test T-20 is in doubt and the results for Tests T-16 and T-17 are not necessarily comparable (see discussion of errors).

Another heat transfer parameter, obtained by dividing the convective coefficient by the average equilibrium boundary layer specific heat, has been given for each test in Tables XIV through XVII. The $\overline{C}_p$ values were obtained from data presented in Section 2.2, Reference 2, at the estimated average nozzle surface temperature (usually the oxide deposit surface) for each test. This particular parameter is slightly more sensitive to the combustion efficiency losses since it tends to eliminate the dependence of

TABLE XVI. INFLUENCE OF PROPELLANT FORMULATION ON THROAT HEAT TRANSFER (C)

Test	Grain-Nozzle Geometry	Propellant	$\bar{h}_{800}$ Btu/in^{2}sec°F	$\frac{\bar{h}_{800}}{\bar{C}_p}$
T-1	Remote end burner 25° conventional nozzle	191F	0.0070	0.0070
T-2	Remote end burner 25° conventional nozzle	24F	0.0054	0.0072
T-3	Remote end burner 25° conventional nozzle	319BRF	0.0066	0.0083
T-4	Remote end burner 25° conventional nozzle	54F	0.0065	0.0069
T-5	Remote end burner 25° conventional nozzle	60 (Al)	0.0038	0.0063
T-6	Remote end burner 25° conventional nozzle	390 (Al)	0.0072	0.0131
T-7	Remote end burner 25° conventional nozzle	389 (Al)	0.0070	0.0119
T-9	7" port-Type I 18° conventional nozzle	191F	0.0092	0.0092
T-11	7" port-Type I 18° conventional nozzle	54F	0.0061	0.0070
T-14	7" port-Type I 18° conventional nozzle	319BRF	0.0073	0.0092
T-21	Close end burner 55° steep inlet nozzle	191F	0.0035	0.0039
T-22	Close end burner 55° steep inlet nozzle	54F	0.0059	0.0064
T-24	Close end burner 55° steep inlet nozzle	319BRF	No data	—

TABLE XVI. (Continued)

Test	Grain-Nozzle Geometry	Propellant	$\bar{h}_{800}$ Btu/in^{2}sec°F	$\frac{\bar{h}_{800}}{\bar{C}_p}$
T-8	7" port-Type II (slotted) 18° conventional nozzle	389 (Al)	No data	
T-10	7" port-Type II (slotted) 18° conventional nozzle	191F	0.010	0.010
T-18	7" port-Type I submerged nozzle: W-ATJ throat	191F	0.0048	0.0051
T-19	7" port-Type I submerged nozzle: W-ATJ throat	319BRF	0.0042	0.0056

the heat transfer coefficient on the surface temperature. Note, in Tables XIV and XVI, that Tests T-5, T-15, T-21 and possibly T-22 exhibit unusually low values. In Table XV, Test T-23 has a much higher value than T-21 but much lower than T-9 (or even T-1). These Tests except for T-5 were regarded as the most likely to exhibit incomplete combustion effects. While Tests T-21, T-22 and T-23 had the lowest C* efficiencies for the 191F and 54F propellants, Test T-15 had the highest recorded for the 319BRF propellant and the value for T-5 was quite reasonable. The high sensitivity of the experimentally determined heat transfer coefficients to the metal combustion efficiency of low flame temperature propellants was discussed in Section 2.3.d. The combination of low heat transfer coefficients and relatively low C* efficiency for the tungsten nozzles appears to warrant further study. These questions will be considered further during the final reporting period of the program. However, it is clear that nonideal metal combustion efficiency has occurred on some, if not all, tests. The effect on the measured values of the throat heat transfer coefficient is evidently very great.

TABLE XVII. INFLUENCE OF NOZZLE MATERIAL ON THROAT HEAT TRANSFER (C)

Test	Propellant	Grain-Nozzle Geometry	Material	Btu/in2sec°F	$\frac{\bar{h}_{800}}{\bar{C}_p}$
9	191F	7" port-Type I 18° conventional nozzle	Throat: P.G. Entrance: ATJ	0.0092	0.0092
16	191F	7" port-Type I 18° conventional nozzle	Throat: W-ATJ Entrance: ATJ	0.0059	0.0059
17	191F	7" port-Type I 18° conventional nozzle	Throat: W-ATJ Entrance: Carbon Phenolic	0.0052	0.0055
20	191F	7" port-Type I 18° conventional nozzle	Throat: P.G. Entrance: Carbon Phenolic	0.0087	0.0087
14	319BRF	7" port-Type I 18° conventional nozzle	Throat: P.G. Entrance: ATJ	0.0073	0.0092
19	319BRF	7" port-Type I 18° conventional nozzle	Throat: W-ATJ Entrance: ATJ	0.0042	0.0056

2.6 (C) CONCLUSIONS, RECOMMENDATIONS, AND FUTURE WORK

a. (C) Conclusions

A number of relatively general conclusions have been reached concerning the mechanisms of nozzle corrosion by beryllium propellants. These are enumerated below. No attempt is made to repeat the many detailed conclusions discussed in the text of Section II:

(1) The combustion of the beryllium metal additive is a transient process which occurs primarily in the exhaust gas stream as the metal particles or agglomerates are carried along by the gas-particle drag forces. The major factors which will determine the time required to ignite and completely burn the particle are: (a) the particle or agglomerate size when it leaves the grain surface, (b) the gas phase temperature and composition along the particle's flow path, (c) the heat absorbed by the particle prior to release from the grain surface, (d) the convective heating of the particle along its actual flow path, and (e) the interference by the metal oxide which forms at or near the particle-gas interface.

(2) The principal design parameters which will have a strong influence on the degree of metal combustion at any particular spatial position in the rocket motor are concluded to be: (a) the original size distribution of metal particles, (b) the propellant flame temperature and composition without metal combustion, (c) the ideal flame temperature and composition, (d) the propellant burn rate and gas phase velocity gradient in the immediate proximity of the grain surface, (e) grain design, (f) aft closure and nozzle contour, (g) metal loading, and (h) chamber pressure.

(3) The primary characteristics of the particular metal additive which have a direct influence on the particle combustion process are concluded to be: (a) the metal melting point (strong influence on agglomeration), (b) metal oxide melting point (probable influence on agglomeration, particle ignition temperature and burning rate), (c) relative stability of metal suboxides, hydroxides and

possibly chlorides, nitrides and carbides (possible influence on ignition delay, critical ignition temperature and combustion interference by condensed phases), and (d) metal vapor pressure-temperature dependence (determines burning rate and transition from surface to vapor diffusion reaction modes).

(4) The primary differences in ballistic performance and motor materials erosion-corrosion (that cannot be derived using the complete combustion and uniform flow assumptions) are directly related to differences in the details and degree of metal combustion and condensed phase deposition.

(5) Burning metal particles will always be larger than the condensed oxide reaction product particles. The slower the metal combustion process, the greater the degree of burning and burned particle stratification and impaction on the motor contour. Stratification of burning particles will tend to decrease the local oxygen availability per particle, slowing combustion and increasing drag losses. Where burning particle concentrations are lowered (via stratification), the combustion process will be accelerated but there will be an apparent excess of available oxygen. If the distribution of metal particles in the flow field should actually be uniform, the apparent excess of oxygen (for continuing metal combustion) will depend entirely on the degree of metal combustion and the original propellant formula excess with respect to carbon and metal. The materials, which form the motor contour, may, therefore, see an exhaust gas phase that has more or less oxygen available for corrosion (H_2O, CO_2, etc.) relative to the ideal combustion case. It is estimated that the oxygen availability can range from zero to about 50 times the ideal value. Material corrosion rates will vary accordingly.

(6) The nonideal availability of oxygen is a necessary but not sufficient condition for the observation of extreme and erratic materials behavior with state-of-the-art beryllium propellants. Two additional phenomena must be considered. Thus, when nonideal metal combustion occurs, ideal exhaust enthalpy levels are not attained and the convective heat flux will be lowered. This reduction will be most

pronounced for propellants with low flame temperatures. The primary change will be in the enthalpy (or temperature) driving potential rather than in the convective heat transfer coefficient. The second phenomenon, associated with nonideal metal combustion, is condensed phase deposition (see below).

(7) The deposition of condensed material on the motor contour will occur when the exhaust flow is turned by the contour and the particle slip direction is toward the wall. Provided that the impact energy is not enough to cause pitting of the surface or rejection of the particle, a deposit will build up. Since the oxides have low thermal conductivities, the deposit surface will eventually melt and material will begin to flow downstream. The deposit will normally initiate well upstream of the nozzle throat and a significant time will lapse before the throat becomes coated. As long as the metal oxide coating persists, corrosion of the underlying wall by the exhaust gases will not occur. Similarly, thermal insulation of the wall will have a major effect on temperature history and thermal stress. In general, the amount of material deposited will be greater and its removal rate less rapid when poor metal combustion occurs. Variation of motor-nozzle contour and grain design will increase or decrease the deposition insofar as such changes influence the metal particle combustion process and the centrifuging of particles to the motor contour. Apparently, it is possible to virtually eliminate deposition simply by proper configuration design, regardless of the degree of metal combustion. It is also possible to encourage deposition in order to take advantage of the corrosion protection and thermal insulation effects.

(8) It has been concluded that the deposition of unburned beryllium on tungsten would be extremely serious. The formation of low melting (2300 to 3000°F) beryllium-tungsten alloys very early in a motor firing could be catastrophic. Subsequent formation of low melting tungsten-carbon alloys would tend to obscure the beryllium effect and would accelerate failure. Tungsten insert failure may also be precipitated solely via the carbide formation route. The formation of axial grooves

(via beryllium and/or carbon attack) in tungsten will permit buckling and extrusion of the insert before simple axial extrusion would occur. Oxidation of tungsten is not regarded as an important failure mechanism and will not produce extreme surface regression. Plastic deformation of tungsten and oxide deposition will tend to cause significant throat shrinkage, obscuring the radial corrosion.

(9) The exposure of graphite materials to unburned beryllium is not expected to be serious. Protective carbide should be formed, preventing further reaction, at surface temperatures below about 5000°F. The carbide is thermally unstable above this temperature and no further reaction would be expected. The potential availability of excess oxygen when the metal has not burned is regarded as the primary cause of abnormally high graphite corrosion.

(10) The thermal instrumentation and data analysis techniques have been highly successful. The thermal insulation effects of the oxide deposits have been removed so that true gas side convective heat transfer coefficients have been obtained. Because the oxide surface temperatures are near the oxide melting point, the heat transfer coefficients are thought to be the best available for very high wall temperatures. The fact that the heat transfer coefficients, for high metal combustion efficiency, are as much as 100 percent higher than those frequently used in design, suggests that nozzle materials failure may often be attributed to inadequate thermal design. Circumferentially nonuniform flow and nozzle submergence will tend to increase the heat transfer even farther. Extreme erosion of pyrolytic graphite and early extrusion of tungsten can often be explained on this basis alone. Preliminary evaluation of theoretical prediction techniques has indicated that the measured heat transfer coefficients can be accurately predicted by the Bartz type correlation equation, but only when correct specific heat, Prandtl number and viscosity properties are employed. Consequently, it is concluded that the basic turbulent boundary layer model is valid. Appropriate techniques for evaluating the boundary layer thermal properties will be given in the Final Report.

(11) Examination of the nozzle corrosion results indicates that the diffusion controlled transport of reactive oxygen containing gases to the graphite surface is the primary cause of corrosion. Above about 5200°F, it appears that hydrogen reactions with graphite become important. However, the production of acetylene may be subject to chemical kinetic reaction rate restrictions even at these temperature levels. It is recommended that pyrolytic graphite surface temperatures be limited to approximately 5500°F, with allowance for axial thermal expansion, to prevent massive surface spallation. The spallation or erosion of the pyrolytic graphite nodules accounts for the occasional observation that polycrystalline graphite will outperform pyrolytic graphite. The combination of isotropic thermal properties and the smaller grain size favor the polycrystalline material with respect to nodule spallation of the pyrolytic graphite. Simplified corrosion prediction techniques will be formalized in the Final Report.

(12) It is concluded that aluminum and beryllium propellant systems are extensively similar with respect to their influence on motor-nozzle materials performance. The combustion of aluminum is less difficult and the oxide deposition protection is usually less important than in the beryllium system. It is clear that the usual materials can be used in either system. However, it is also clear that the effects of poor metal combustion, oxide deposition and high heat transfer must be considered if equivalent materials performance is to be obtained. In general, it is expected that materials performance, with any particular beryllium propellant, could be optimized (or maximized) but mass fraction and ballistic performance penalties will be incurred.

(13) From the designers point of view, the most difficult problems will be to predict or determine the degree of metal combustion and the amount of oxide deposition. For the present, there appears to be no substitute for direct experience with the propellant formulation and motor configuration in question. Appropriate C-star efficiency data can be used to estimate the overall degree of metal combustion. Potential flow field analysis can be used to find condensed phase impaction areas along the motor-nozzle contour. Since particle size distributions

and impact sticking can only be estimated, the total deposition and oxide deposit protection cannot be predicted without making empirical use of motor test data. Extrapolation of results from one motor to another and scale effects still present a problem. However, it is believed that this type of problem would yield to further study.

(14) It is concluded that propellant tailoring efforts should be guided toward the achievement of rapid combustion of the metal additive. In this way, some of the materials performance problems can be eliminated in advance. It is evident that oxide deposition and stratification of burning metal particles contribute heavily to ballistic performance losses. It follows directly that tailoring for rapid combustion would ultimately lead to maximum ballistic performance and propellant mass fraction. Under these conditions, however, the nozzle materials problems will only reduce to the more ordinary ones of controlling thermal response and corrosion-erosion. In general, the nozzle heat transfer will increase in proportion to the ideal ballistic performance (C-star and ISP) of the propellant. The magnitude of the nozzle corrosion problem will be determined primarily by the available oxygen content of the ideal exhaust gases. Evidently, cooled nozzles or a compromise, with respect to the oxide deposition problem, will be required to achieve adequate materials performance for long duration, high pressure firings.

b. (C) Recommendations

The following general recommendations derive from the progress made in the Analytical Studies Task to date.

(1) State-of-the-art and advanced beryllium propellant and materials evaluation motor test data should be examined to establish oxide deposit thickness and erosion histories for the nozzle throat. This information is essential to the understanding of materials performance and, for small throat diameters, to the accurate determination of propellant ballistic performance.

(2) It is recommended that the deposition-erosion histories be published as a matter of routine. In each case, the computation method and raw data (K_n, F, P, etc.) should be available. Reports should also include the basic motor design parameters such as grain configuration, motor-nozzle contour, insulation and heat sink materials and post test condition of the nozzle (residual deposit thickness or net erosion). Empirical correlation of these results should be attempted at two levels: (a) for individual propellant formulations or types (by the manufacturer for his own use) and (b) for classes of propellants such as composites, beryllium, beryllium hydride, oxidizer (AP, RDX, HMX, NG, KP, NP, NF, etc.), flame temperatures, oxidation ratio, etc., (by the Air Force for general use).

(3) It is recommended that motor ballistic performance analyses (computer programs), which only consider linear average erosion, be upgraded to account for the detailed transient variation in nozzle throat area due to both deposition and erosion. It is also recommended that a serious attempt be made to develop a completely analytical technique for predicting deposition, deposit flow along the motor contour and thermal response of the contour forming materials.

(4) It is recommended that a study be conducted to establish the thermal and gas absorption properties of liquid beryllia. It would also be of interest to determine the sensitivity of these properties to impurities such as beryllium, carbon, silica, magnesia, etc.

(5) It is recommended that all empirically determined heat transfer and materials corrosion data for metallized propellants be interpreted with due consideration given to the oxide deposition and metal combustion phenomena. Semiempirical convective heat transfer equations, correlated with unmetallized or low flame temperature propellant test data, should not be used in nozzle design unless underestimation of the throat convective coefficients by 100 percent or more can be tolerated.

(6) The post test analyses of nozzle materials should include the determination of the circumferential variations in the nozzle and motor insulation surface regression. These variations should be related to the potential flow field and condensed phase behavior.

(7) It is recommended that the results of this program be extended to and considered in materials performance evaluation and hardware design efforts for other metallized propellant systems. Specifically, low burn rate, high burn rate, hybrid, fuel rich and slurried propellants (containing beryllium, aluminum, boron, zirconium, etc.) are likely to precipitate extreme and/or erratic materials corrosion-erosion as a result of poor metal combustion, deposition and underestimation of convective heat transfer.

e. (U) Future Work

During the remainder of the program, it will be necessary to confine the analytical effort primarily to the analysis and interpretation of the results of the 500 lb. grain motor firings. Heat transfer, deposition, ballistic performance and corrosion analyses will be performed for each of the four tests. In addition, the program results will be reviewed and reorganized for presentation in the Final Report. Recommended analytical techniques for calculating deposition, ballistic performance, heat transfer, corrosion and erosion will also be presented in the Final Report.

Best Available Copy

SECTION III (C)

LABORATORY STUDIES

3. (U) OBJECTIVES, SCOPE AND SUMMARY

a. Objectives

The objectives of the Laboratory Studies were described in detail in Section 3.1 of the First Quarterly Progress Report, Reference 1. No major changes have occurred during the succeeding reporting periods. The primary objective during the third period has been to complete the laboratory post-test analysis of the small motor test hardware. Secondary objectives included: (1) continuation of the effort to relate the results of the cold flow modeling study to those of the internal burning grain tests, (2) initiation of carbon-tungsten interaction study of fired inserts using the microprobe analysis technique, (3) post-test examination of hardware obtained from other programs using beryllium propellants, and (4) measurement of the size distribution of beryllia collected from the exhausts of the small motor tests.

b. Scope

The scope of the laboratory studies phase of the program has been described in Sections 3.1 of References 1 and 2. Small motor tests, designated T-8 to T-25 were conducted during the reporting period. The scope of the laboratory post-test analysis task is described in Section 3.4.c, page 171 of Reference 2. Nozzles tested in the Aerojet General Corporation ADOBE program, Reference 11, have been received for inspection and analysis. Efforts are continuing to obtain similar hardware from other programs. In order to maintain a balanced effort, any detailed analysis of such hardware has been postponed. The results of analyses of hardware from other programs will be presented in the Final Report. The scope of the tungsten insert post-test analysis effort has been modified slightly as a consequence of the use of inserts which were cracked prior to test. Electron microprobe analysis of the flame side and the crack surfaces will be conducted to determine the extent of carbon diffusion. This work has been segregated from the nozzle post-test analysis task and will continue into the final period of the program.

c. Summary of Progress

The objectives of the laboratory studies during the third reporting period have been attained. The following elements of work have been completed or initiated as indicated below:

(1) The post-test analysis of the hardware and condensed phase deposits has been completed for small motor tests T-8 through T-25.

(2) Electron microprobe analysis of tungsten inserts (tests T-16 through T-19) to determine carbon penetration has been initiated.

(3) Silver infiltrated tungsten and graphite nozzles tested in the Aerojet ADOBE program have been received and inspected. Sections of a tungsten insert tested by Atlantic Research Corporation on the PALLAS program were received and analyzed.

(4) Condensed phase material collected from the exhaust plumes (small motor tests) have been analyzed using a Coulter counter (to determine particle size distributions) in addition to the determination of their composition and shape.

3.2 (U) CONDENSED PHASE REACTION STUDIES

a. (U) Interaction of Beryllium Compounds with Graphite and Tungsten

A cursory study of the reactions of BeO and Be_3N_2 with graphite and tungsten was conducted during the first quarter (Section 3.2, Reference 1). Within the experimental temperature range (to 4800°F) beryllium nitride was found to be stable with each material. Post-test analysis of hardware tested during the reporting period has given no indication that the condensed nitride was present. However, it is doubtful that attack by the nitride could be distinguished from that by the other reactive species.

The reactions of BeO with graphite and asbestos phenolic char were studied during the first quarter (Reference 1). Reaction was observed with both solid and liquid beryllia. However, solid deposits on graphite would not be expected to react at rocket pressures. It had also been concluded that a protective intermediate layer of beryllium carbide would form as beryllia flowed from coated to uncoated surfaces. The thermal stability of such a layer would strongly depend on the graphite surface temperature and the local static pressure. Thus, it was speculated that, during the motor pressure decay, the deposit could be expelled from graphite surfaces at temperatures above about 4200°F. The loss of deposits via the decomposition of the carbide would presumably remove any evidence of the existence of the carbide interlayer.

Examination of nozzle deposits indicates that they can be removed with relative ease. X-ray diffraction analysis of the deposit samples showed that relatively large amounts of Be_2C were present in the deposit samples from most (not all) nozzles. While the carbide was always found in the chamber residue and no carbide was found in the exhaust plume samples, further generalization is difficult. Thus, deposits on the graphite exit cones could have solidified before the surface reached the minimum beryllia-carbon reaction temperature of about 3700°F (at 1 atmosphere). Furthermore, these deposits could insulate the exit cone surface enough to preclude melting of the deposit. Note here that, while the deposit is solid, interface reactions could not proceed very rapidly because solid state diffusion is a slow process. Then, when samples are removed for analysis, the carbide might be left behind or exist in undetectable quantities. A second problem arises when there are no deposit samples found on the pyrolytic graphite surfaces after the test. In such cases, the motion pictures of the firing show that large amounts of deposit material are ejected during the early stages of the pressure decay. It should also be noted that the deposition of carbon, via pyrolysis gas cracking during motor cooldown, may lead to the formation some beryllium carbide.

The predicted inertness of BeO deposits with respect to graphite and tungsten has been adequately demonstrated. The observed expulsion of deposits during motor depressurization, the presence of beryllium carbide in the remaining deposits and the low degree of deposit adherence, all tend to confirm the postulated interlayer mechanism of beryllia deposit sticking on graphite. The expected wetting of tungsten by beryllia has also been confirmed. There were only two tests, T-12 and T-18, where definite indications of beryllia attack of graphite was observed. In these submerged nozzle tests, the ATJ graphite entrance cone (including part of the nose cap) developed numerous narrow axial grooves. This is almost always observed in aluminum propellant firings on the polycrystalline graphite entrance cones and nose caps. It is believed that these sections reach surface temperatures above the oxide melting points. The flow of the liquid tends to thin the deposit layer until surface tension forces cause a transition from sheet to stream or bead flow. Then, if the gaseous reaction products (Al_2O_3 or BeO plus carbon products) can escape more readily or if the carbide decomposition temperature is reached, the streams or beads of oxide would form a narrow axial groove as they travel downstream. Submerged nozzles would be particularly prone to this action since stagnation flow induced deposition will continue throughout the entire firing and higher entrance cone heating rates will be experienced.

It has been predicted that beryllia will attack graphite at temperatures above about 4800°F when a continuous deposit coating exists and pressures are in the range of 500 to 1000 psi. For stream or bead flow, reactions could start at the melting point of beryllia, about 4600°F. A continuous deposit of alumina should not react with graphite at temperatures below about 5200°F in the same pressure range. The threshhold temperature for reaction of alumina (with carbon) in stream or bead flow is not known. However, the stability of the aluminum oxycarbides may prevent a serious depression of the reaction threshhold temperature from 5200°F. The oxide stream grooving has not been observed to occur in the nozzle throat (pyrolytic graphite and tungsten) or exit cone (ATJ graphite) sections. The asbestos phenolic and carbon cloth phenolic insulation materials did not appear to have been pitted or grooved in any systematic manner.

It is speculated that the beryllia-graphite reactions at temperatures above about 4800°F may be an important contributor to the higher erosion (compared to aluminum propellants) experienced in a number of other beryllium programs. However, such reactions are not regarded as the logical primary causal factor in erosion. The high temperature hydrogen-graphite reactions and the potentially higher availability of water as a result of incomplete beryllium combustion continue to provide the basic explanation of high erosion. For tungsten, the water and carbon reactions are the most dangerous. It is clear that additional study of the tungsten-carbon and tungsten-beryllium problem is required. With that exception (see Paragraph b, following), the condensed phase reaction studies are regarded as complete for the purposes of the present program.

b. (U) Microprobe Analysis of Tungsten Inserts

Motor tests T-16 through T-19 were materials comparison tests which utilized tungsten as the throat insert material. There were 2 different nozzle configurations, but in each case the tungsten insert was backed by polycrystalline graphite and a pyrolytic graphite washer was installed at the upstream edge. The reaction between carbon and tungsten is well defined and represents a definite failure mechanism for tungsten throat inserts. A eutectic between tungsten and carbon is formed with a liquidius temperature of 2710°C. It is logical to assume that the materials which would be used for the construction of nozzles would not be as pure and the end use conditions as ideal as the laboratory testing to determine the minimum liquidius point. Thus, the temperatures where a liquid is formed could be even lower. The temperature where a liquid is formed is probably the maximum temperature to which the back side of a tungsten insert should be designed. Carbide formation and flow on the flame side surface should promote both uniform and irregular erosion. Irregular carbide erosion could lead to insert buckling and obtrusion.

The tungsten which was used for the manufacture of the throat inserts was arc cast, rolled and extruded. The density was 19.3 gm/cm^3 or 100% of theoretical. During the machining of the inserts, some cracks developed. It was decided to test the inserts with particular attention to be focused on the relation between the cracks and insert performance. Normally, the cracks would be considered detrimental because they could provide a preferred path for gas flow or carbon diffusion. Any gases in the area of the backside of the insert would be expected to be rich in hydrocarbons. Pyrolysis gases could also deliver carbon to the flame side surface. Recent advances in electron microprobe techniques have made it possible to examine elements with atomic numbers as low as 5 (boron). It was decided to examine the tungsten inserts with the electron microprobe with particular emphasis on determining the extent of tungsten carbide formation.

In general, the tungsten inserts were in very good condition and the anticipated problem areas around the cracks did not arise. X-ray diffraction analysis of the back surface of the inserts showed a tungsten carbide phase, but this was relatively thin (0.001"). However, samples of the tungsten inserts were examined with the electron microprobe.

The insert from T-17 was the first one examined and the most extensive work was done on it while evolving the microprobe techniques. The carbon proved to be quite hard to detect. The two tungsten-carbon compounds are W_2C and WC. WC has 6.13 weight per cent carbon while W_2C has only 3.16 weight per cent carbon. Where the reaction zones are thick enough they can be easily detected by optical techniques. However, the low weight per cent of carbon in the compounds, along with the high x-ray absorption of tungsten, made detection more difficult.

A cross section of the insert was examined and the area near the back side showed a definite dual layered tungsten-carbon compound. The outer layer (the side against the graphite) had 6 weight per cent carbon and the inner layer was a compound with about half or 3 weight per cent carbon. This corresponded very closely with the expected results. The thickness of each layer was 20-30 microns. A cross section of an area with a crack was also examined. There were no detectable carbon compounds found except at the back side surface. One sample from each of the inserts from T-16, T-18 and T-19 were examined in an area which contained a crack. In each case the only carbon compounds found were at the back side surface. The thickness of the tungsten-carbon compounds at the back surface was approximately 50 microns in each case. This probably was formed during the cooling of the insert after the test.

The results showed that carbon compounds can be detected in dense tungsten and that the electron microprobe may be a valuable tool in the post-test examination of dense tungsten nozzle inserts. Those tests were designed so the maximum back side temperature was not high enough for appreciable carbide formation to occur. There did not appear to be any gas flow behind the insert or through the crack. The microprobe analysis work will be continued with emphasis being given to the flame side surfaces of the inserts. The grooved area of the insert from test T-17 will also be examine since the groove is associated with the origional axial crack in that insert.

3.3 (U) CONDENSED PHASE IMPACTION AND DEPOSITION

a. (U) Arc Plasma Studies

The arc plasma studies were completed during the second reporting period and the results were presented in Section 3.3, Reference 2. No additional work has been undertaken during the third reporting period. The results of the arc plasma studies were incomplete in that relations between particle impingement parameters and oxide sticking could not be established at low pressures. It is believed that a study, in which particle momentum, impact angle, pressure and surface temperature are systematically varied, would be of considerable general interest. Such an effort could provide oxide sticking threshhold temperatures for the wall materials which would commonly be used in impingement areas. It might then become practical to encourage or prevent oxide deposition. (Deposition may not be desirable in very small or plug nozzles.) However, it is not expected that arc plasma tests could contribute much information towards exposing the dynamic characteristics of oxide deposit flow. No further arc plasma work is contemplated in this program.

b. (U) Cold Flow Modeling

Cold flow modeling studies were conducted during the first quarter of the program and the results were presented in Section 3.3 of Reference 1. The study produced particle impingement data (quantity impinged along the model contour) for several of the aft closure-nozzle contours tested in the small motor test series. An initial attempt to use this impingement data was reported in Section 3.3 of Reference 2. The results showed that the total amount of material deposited was a strong function of the number of particles in the upper end of the size range. While this is not a new result, it led to an estimate of the actual beryllia particle size in the end burning grain tests, T-1 through T-4. The quality of the result could only be as good as the input from the cold flow modeling study and the estimate of the total amount of oxide deposition in any given test.

During the present reporting period, an analytical model has been formulated to describe the flow of deposits along the motor-nozzle contour. This model is currently being checked out (see also Section 2.5e). The cold flow deposition data can be used as the basic input (along with the gas side heat transfer coefficient) to the model. A primary output would be a deposit thickness history along the nozzle contour. If this calculated history closely approximates the actual thickness history (derived through ballistic performance analysis) at the nozzle throat, then the cold flow technique offers real potential as a design aid. The procedure can be worked in reverse (by trial and error) to find a suitable impingement profile, given the deposit thickness history at the throat. If either procedure were carried out a number of times, it might eventually be possible to indirectly obtain beryllia particle size estimates.

Particle impingement profile data was generated for several combinations of grain and nozzle shapes. It is planned to use this data in the deposition flow model in an attempt to reproduce the throat deposit histories for representative end burning and center perforated grain tests. The end burning grain tests (T-1 through T-7, T-21 through T-24) used three nozzle contours (conventional, steep inlet and submerged). These will be examined first, since the cold flow modeling is probably most realistic for the uniform axial flow case. An attempt will be made to check the quality of the impingement profile data for the simple cylindrically perforated grain (Type I). However, the modeling data does not provide for mass addition (grain burning) along the core. It will also be necessary to average out the effects of the grain recession with time.

The slotted grain designs (Types II and III) which were tested (T-8, T-10, T-12, T-13 and T-15) do not have corresponding cold flow impingement profiles. Considering the complexity of the flow field and the results of the NASA cold flow modeling study (Section 3.3, Reference 2), it is not obvious that the circumferential variations in impingement could be treated in the near future. Consideration of the non-uniform flow field case would be the next step, if the deposition flow model (with cold flow impingement profile input) can be worked out for the simpler cases. Any results obtained using the cold flow data and the deposit flow analytical model will be presented in the final report.

3.4 (C) POST TEST ANALYSIS

a. (C) Analysis of Motor Hardware

(1) (C) Current Program Hardware

The results of the post test analysis of the hardware from the first seven small motor tests, designated T-1 through T-7, was presented in Section 3.4 of Reference 2. This section presents the results of the laboratory post-test analysis of the remaining small motor tests, designated T-8 through T-25. The results are given separately for each of the 18 tests in Paragraphs (a) through (r) following. The general procedure followed in the post-test examination is described in Section 3.4c, Reference 2. Descriptions of the motor, grain and nozzle hardware designs may be found in Section 5 of References 1 and 2. The results of the ballistic performance analyses for each test were given in Section 2.3. Similarly, the results of the thermal and corrosion post-test analyses were presented in Sections 2.5 and 2.2, respectively.

(a) (C) Motor Test T-8

Motor Test T-8 featured a slotted grain (Type II), the Arcocel 389 aluminum analog propellant and the conventional pyrolytic graphite heat sink nozzle. The aft closure is shown in Figure 36 and the nozzle is shown in Figures 37, 38 and 39 in the as-received condition. Most of the grain inhibitor was retained on the aft closure. A cross section of the throat insert and exit cone is shown in Figure 40 .

A series of deposit samples were taken from the hardware and analyzed by x-ray diffraction. The results are summarized in Table XVIII. The deposit analysis did not reveal any unexpected results. There were large amounts of aluminum metal found in the chamber residue and aft closure deposits. There was some aluminum oxycarbide found in the same areas. This is formed by the reaction of alumina and carbon. There was also gamma alumina found. The retention of these phases would contribute to lower motor performance. The Al_2SiO_5 which was found in the deposits upstream of the pyrolytic graphite is a product of the reaction between alumina and asbestos.

The hardware was in very good condition. There was some delamination of the pyrolytic graphite throat washers. Although it is difficult to detect in the hardware photographs, there are two shallow grooves in the aft closure insulator and ATJ graphite entrance cone. The grooves are located at the 0° (top) position. A more extensive discussion of the grooving phenomenon observed with the slotted grains (T-8, T-10, T-12, T-13 and T-15) may be found in Section 2.4.

(b) (C) Motor Test T-9

Motor Test T-9 was the first test of a beryllized propellant in an internal burning, cylindrically perforated grain configuration. The nozzle and the aft closure are shown in Figures 41 and 42. All of the hardware was in very good condition and nothing unusual was found in the post-test analysis. The graphite inlet cone was cracked in four places (broken during disassembly) and is shown in Figure 43. There was some loss of material from the asbestos phenolic aft closure. A cross section of the insulator is shown in Figure 44 with the original profile drawn in. The char recession was approximately 0.18 inch. A cross section of the nozzle throat and exit cone is shown in Figure 45.

A series of deposits were taken from the hardware and analyzed by X-ray diffraction. The results are summarized in Table XIX.

The deposits did not show anything unexpected. Most of the aft closure face was protected by the grain end inhibitor and the Cab-o-Sil bond. The bottom quadrant of the closure appeared to have more deposit, mostly BeO, than the remaining area exposed to the flame. The Mg_2SiO_4 and MgO are products of the decomposition of the asbestos used as reinforcement in the

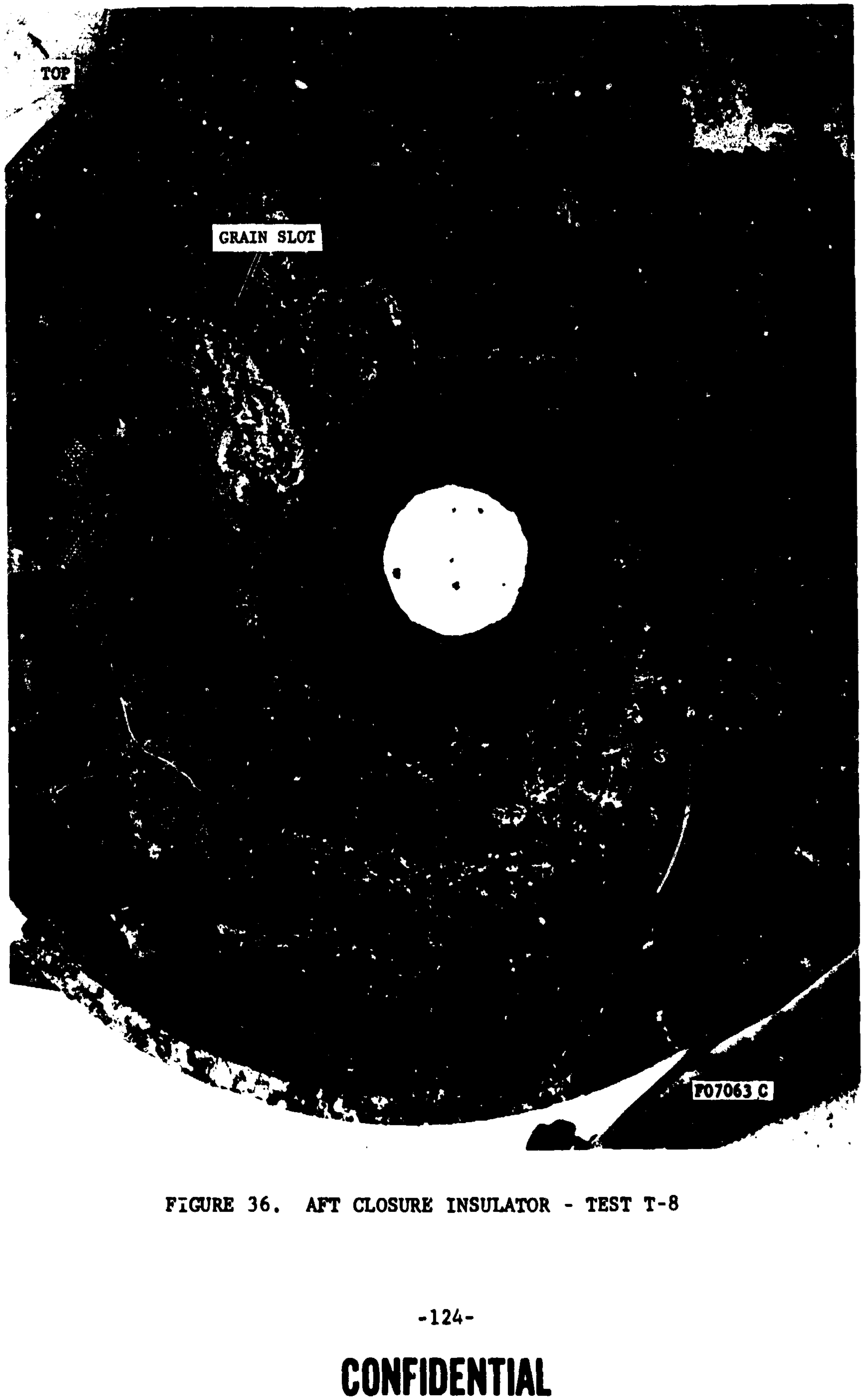
TOP
GRAIN SLOT
F07063 C

FIGURE 36. AFT CLOSURE INSULATOR - TEST T-8

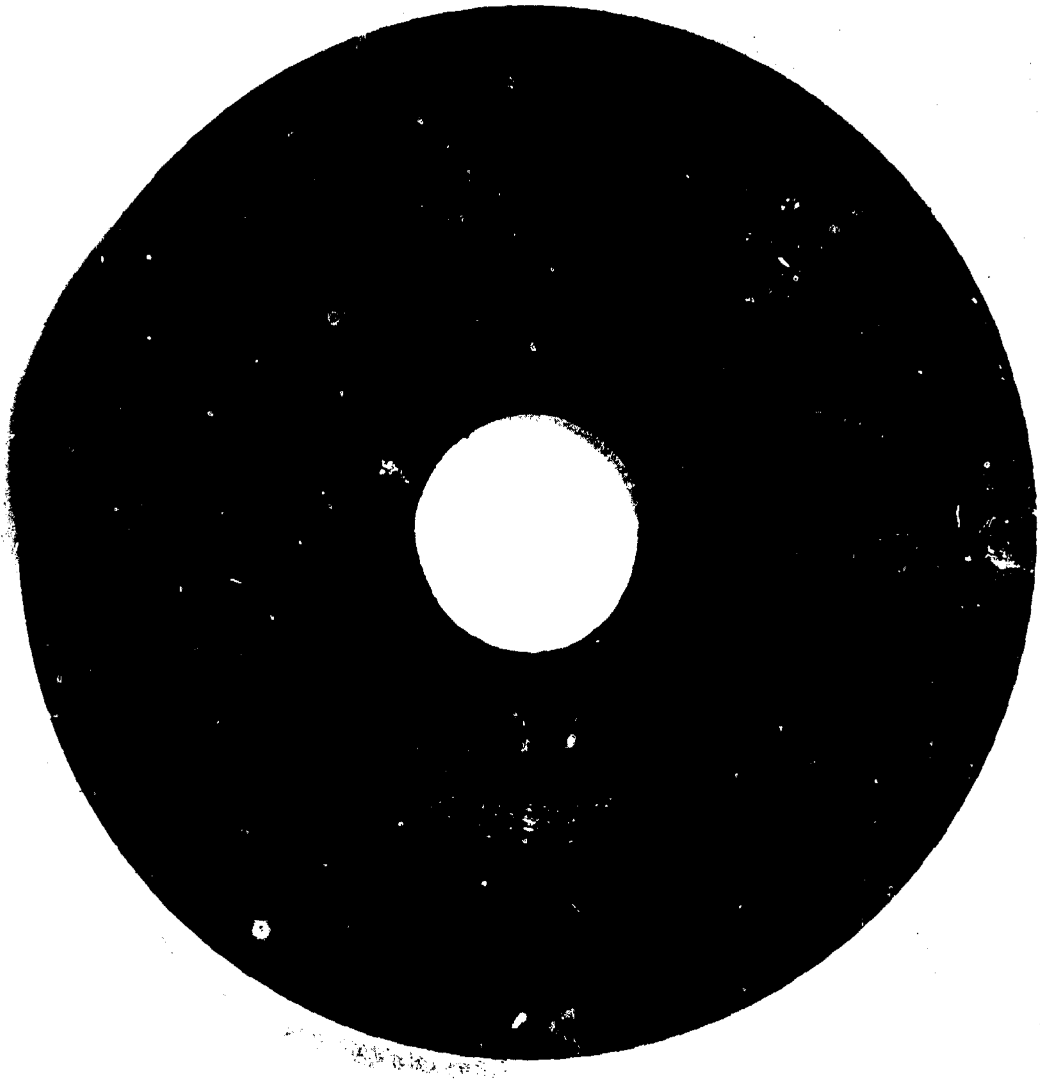

CONFIDENTIAL
F07064 C

FIGURE 37. ATJ GRAPHITE ENTRANCE CONE - TEST T-8

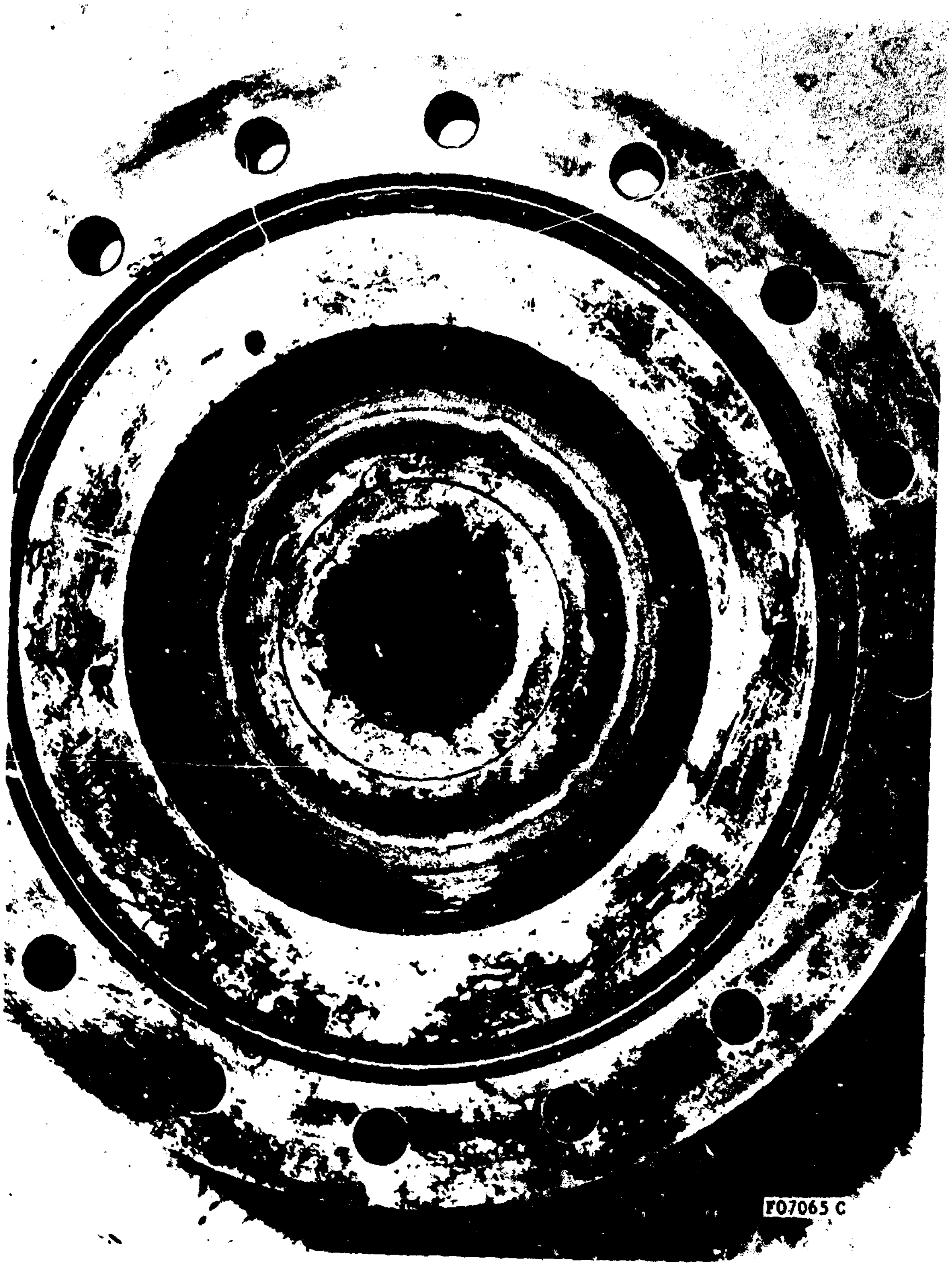

FIGURE 38. NOZZLE FROM TEST T-8 - THROAT APPROACH VIEW

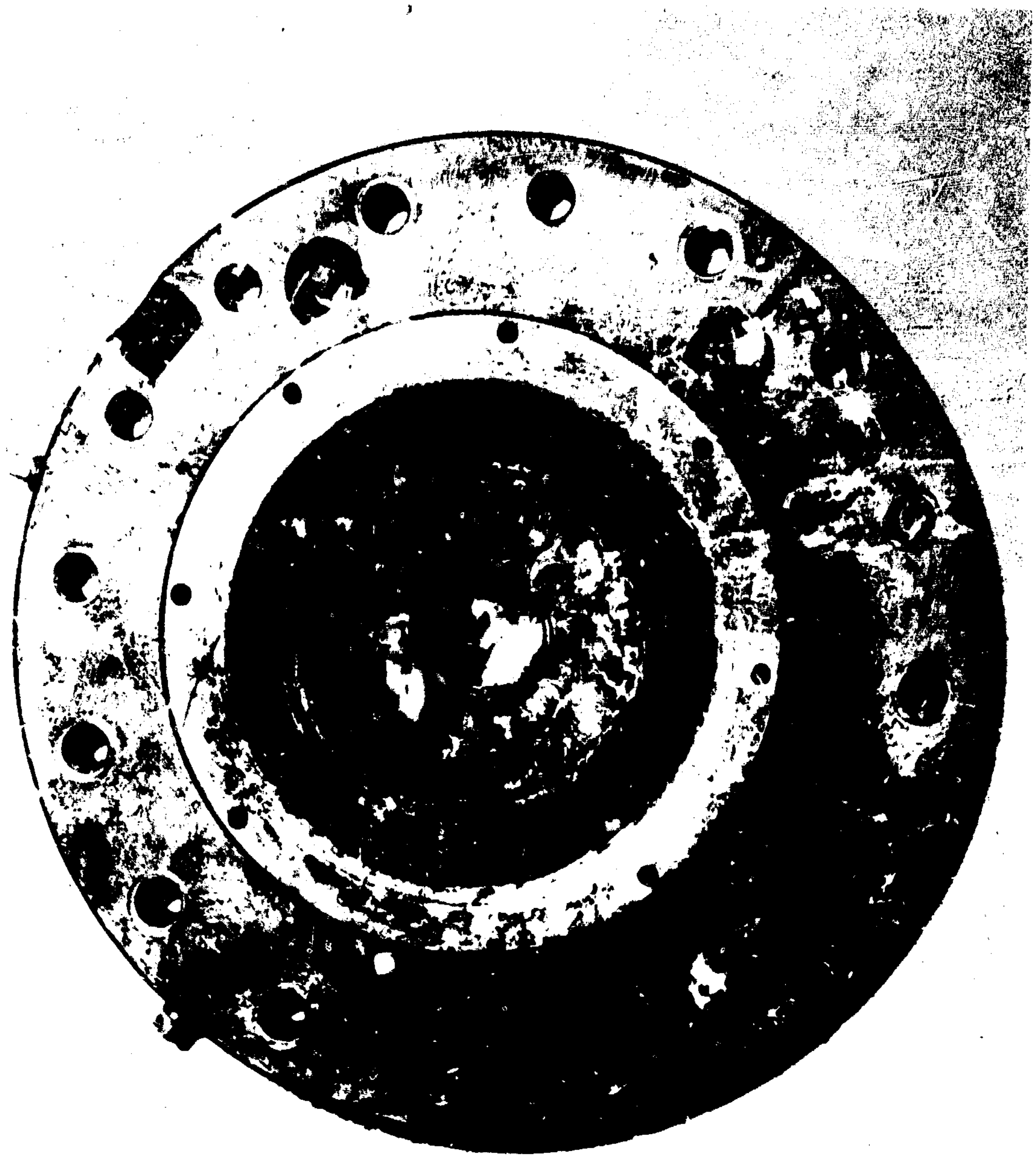

CONFIDENTIAL
F07066 C

FIGURE 39. NOZZLE FROM TEST T-8 · EXIT CONE VIEW

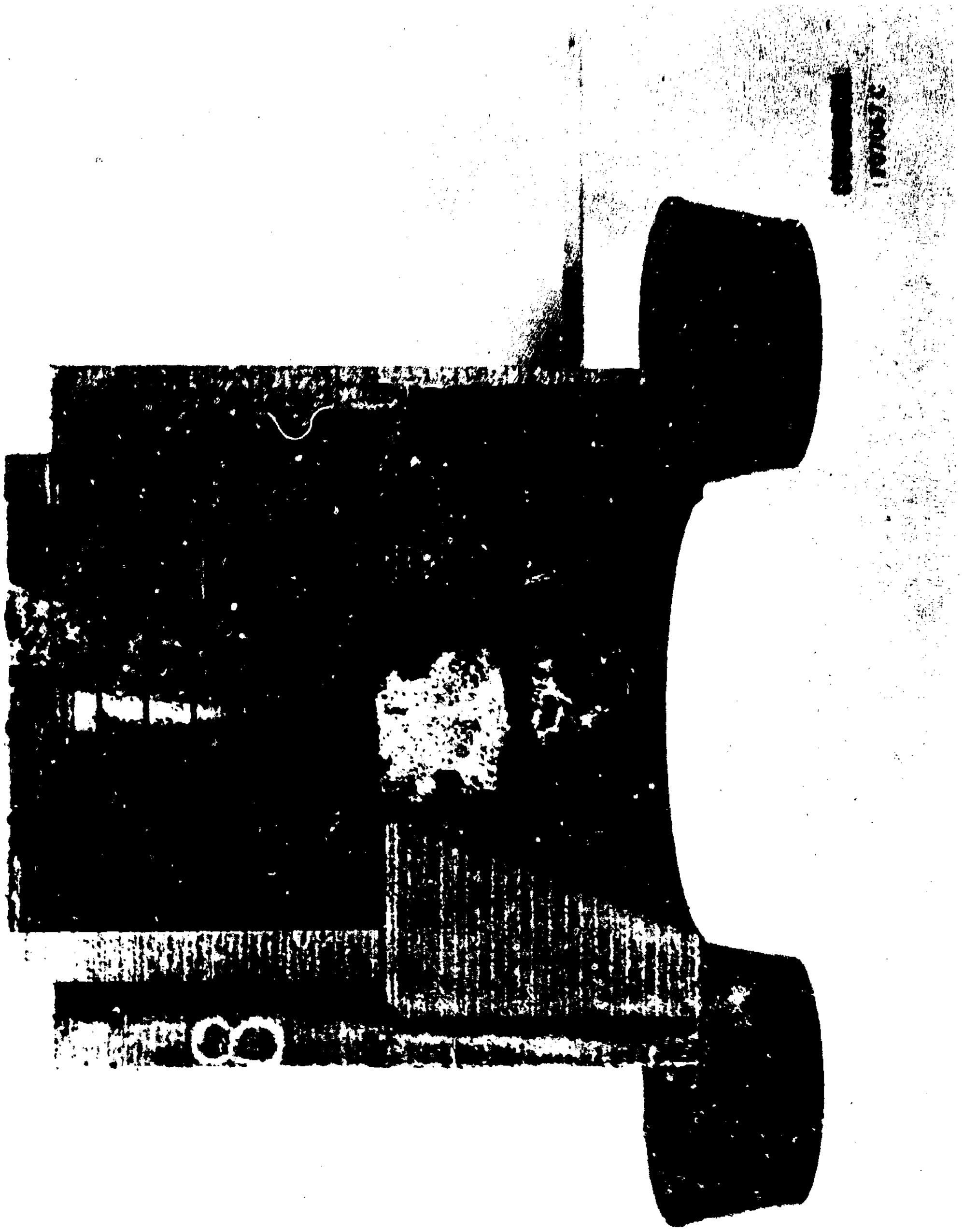

FIGURE 40. NOZZLE FROM TEST T-8 - CROSS SECTION

TABLE XVIII. MOTOR TEST T-8 DEPOSIT ANALYSIS (C)

Sample Number	Sample Location	Composition	
T-8-1	Chamber residue	Al	80-90%
		Al_2OC	5-10
		Al_2SiO_5	2-5
T-8-2	Aft closure, center of slot.	Al	60-70
		Al_2OC	15-20
		α Al_2O_3	10-15
		γ Al_2O_3	2-5
		Al_2SiO_5	2-5
		Unknown	2-5
T-8-3	Pressure port, opposite slot, back side of insulator.	Al	70-80
		Al_2OC	5-10
		α Al_2O_3	5-10
		γ Al_2O_3	5-10
		Mg_2SiO_4	5-10
		Al_2SiO_5	2-5
T-8-4	Pressure port, in slot, back side of insulator.	Al	80-90
		Al_2OC	2-5
		α Al_2O_3	2-4
		γ Al_2O_3	2-4
		Al_2SiO_5	2-5
T-8-5	Aft closure, surface deposit and char layer.	Al	trace
		α Al_2O_3	5-10
		γ Al_2O_3	75-85
		Mg_2SiO_4	10-15
T-8-6	Graphite entrance cone	Al	45-55
		α Al_2OC	15-20
		γ Al_2O_3	5-10
		Al_2O_3	5-10
		Mg_2SiO_4	2-5
		Al_2SiO_5	2-5
		Graphite	5-10
T-8-7	Convergent face of pyrolytic graphite throat insert. Thin (0.010") loose deposit.	Al	70-80
		Al_2OC	5-10
		α Al_2O_3	5-10
		γ Al_2O_3	2-5
		Mg_2SiO_4	2-5
T-8-8	Graphite exit cone, thick surface deposit.	Al	2-5
		Al_2OC	20-30
		α Al_2O_3	50-60
		γ Al_2O_3	5-10

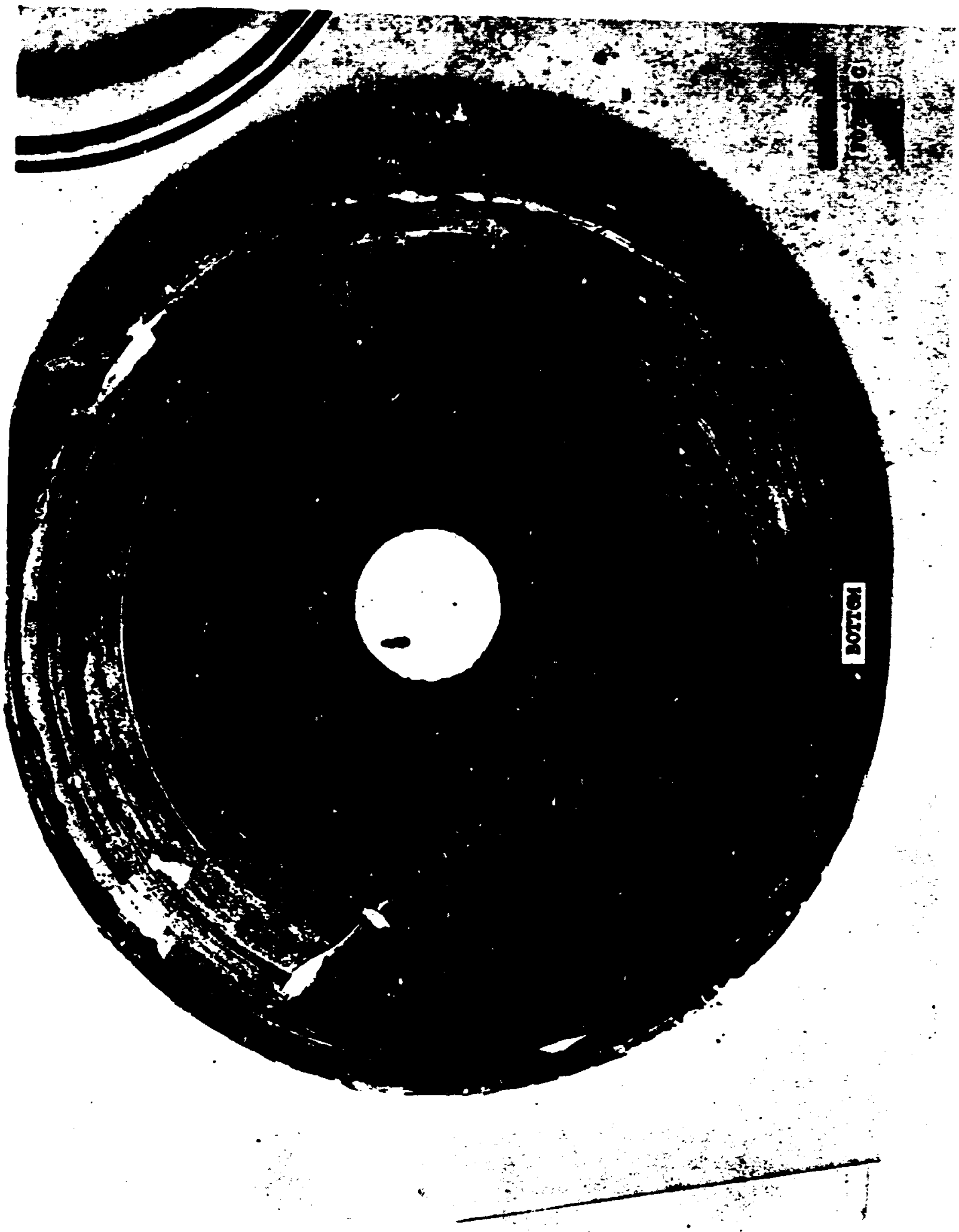

FIGURE 41. AFT CLOSURE INSULATOR - TEST T-9

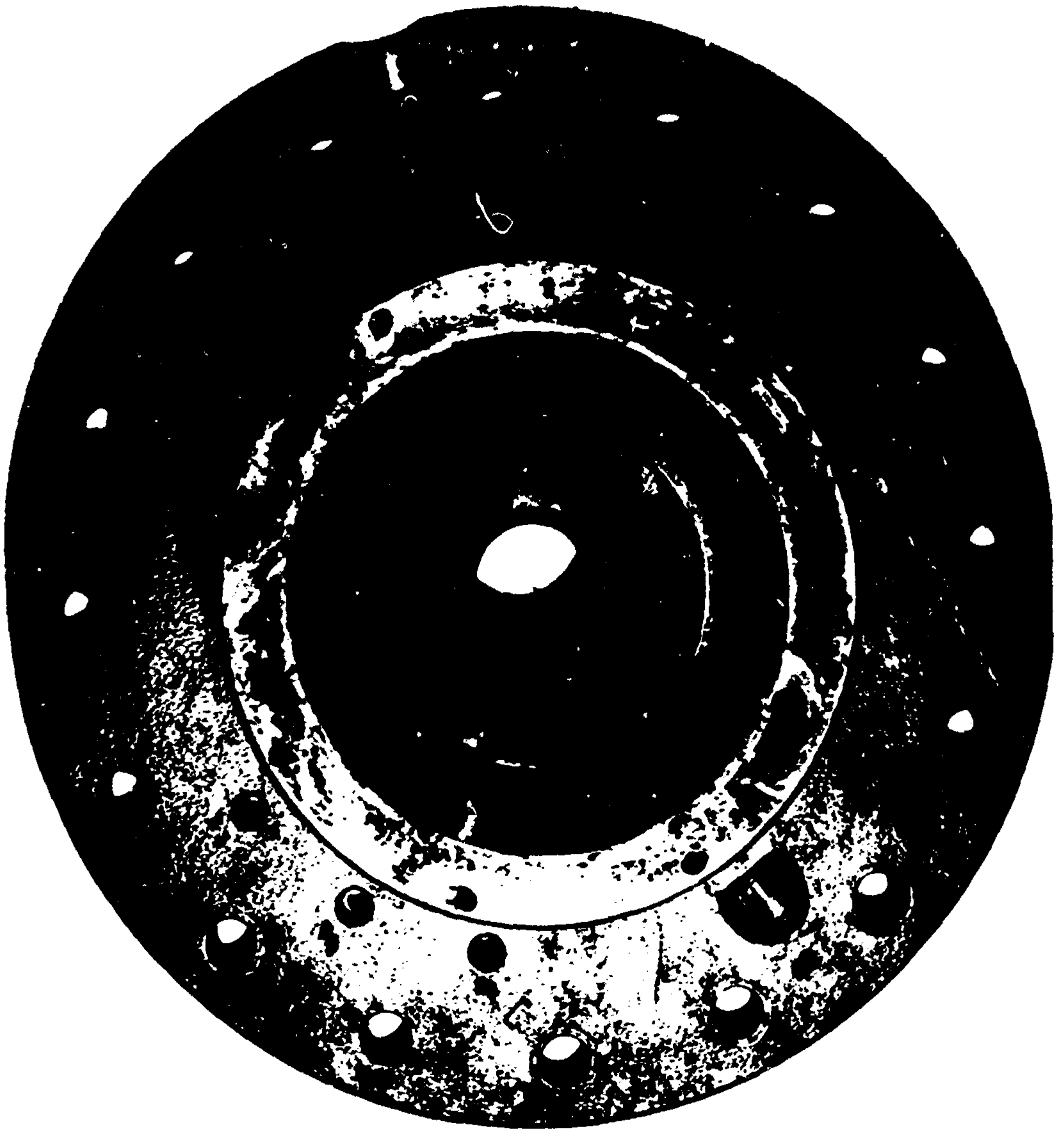

CONFIDENTIAL
F07069 C

FIGURE 42. NOZZLE FROM TEST T-9 - EXIT CONE VIEW

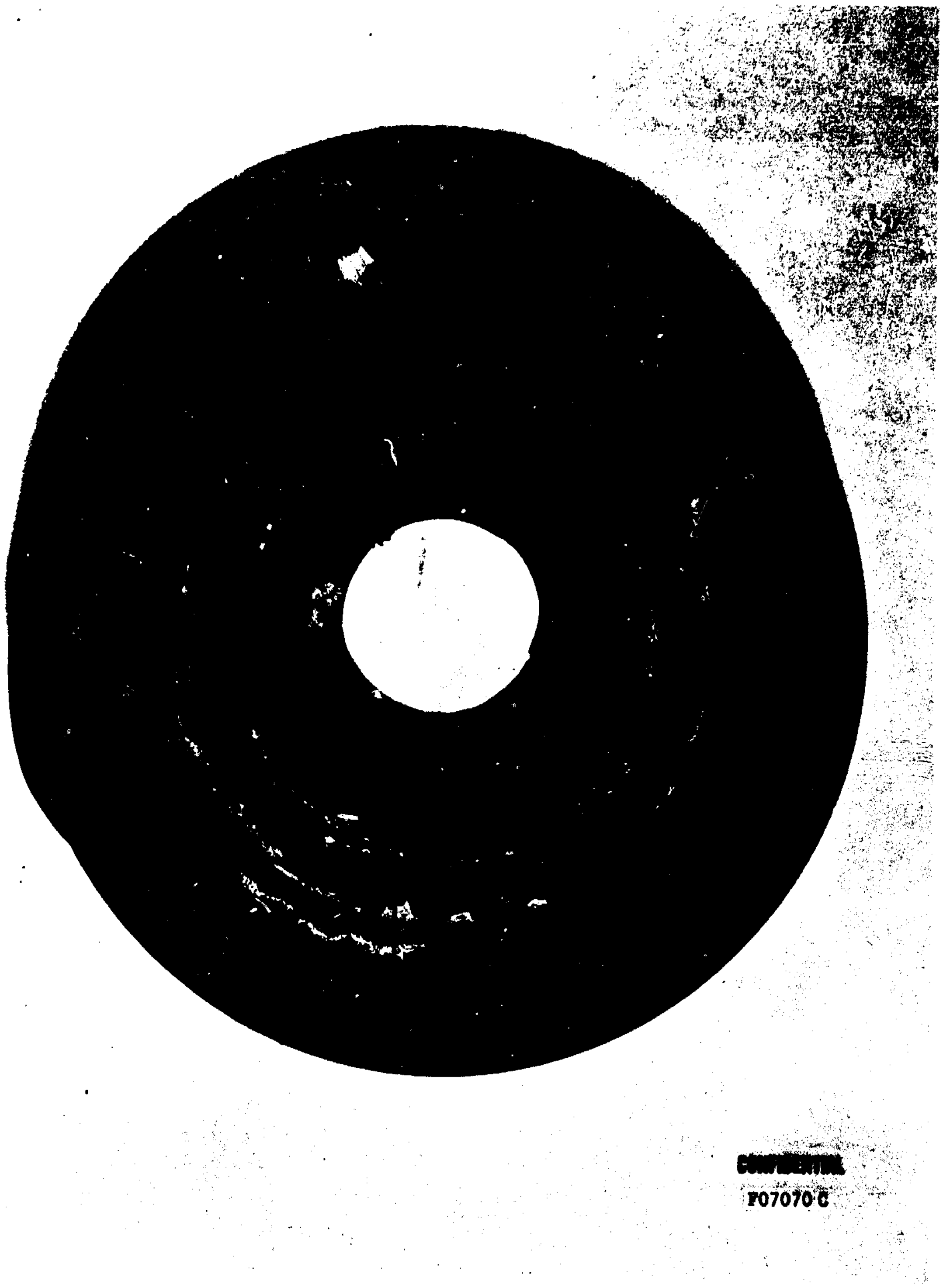
CONFIDENTIAL
F07070 C

FIGURE 43. ATJ GRAPHITE ENTRANCE CONE - TEST T-9

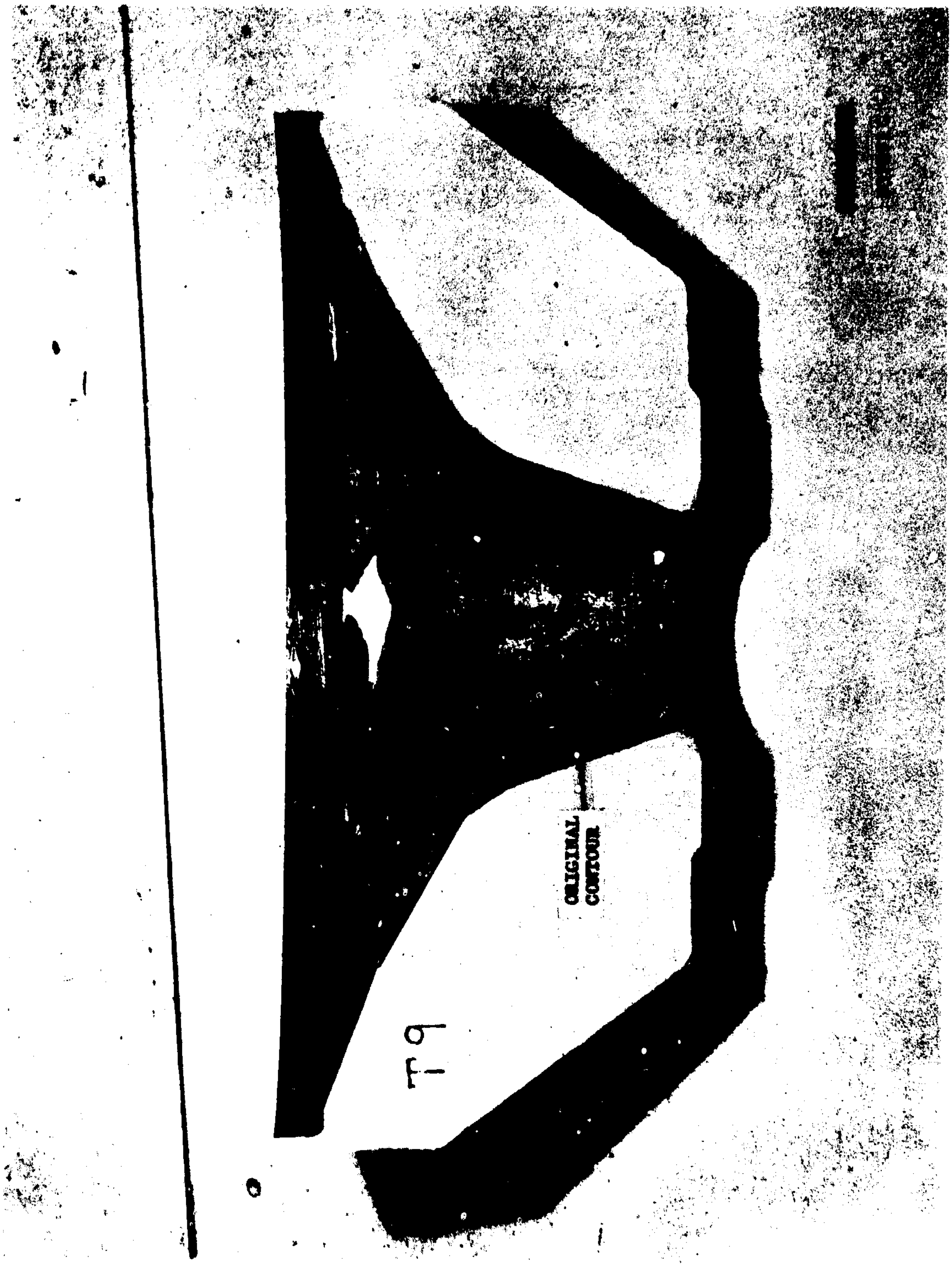
ORIGINAL CONTOUR
T-9

FIGURE 44. AFT CLOSURE INSULATOR CROSS SECTION - TEST T-9

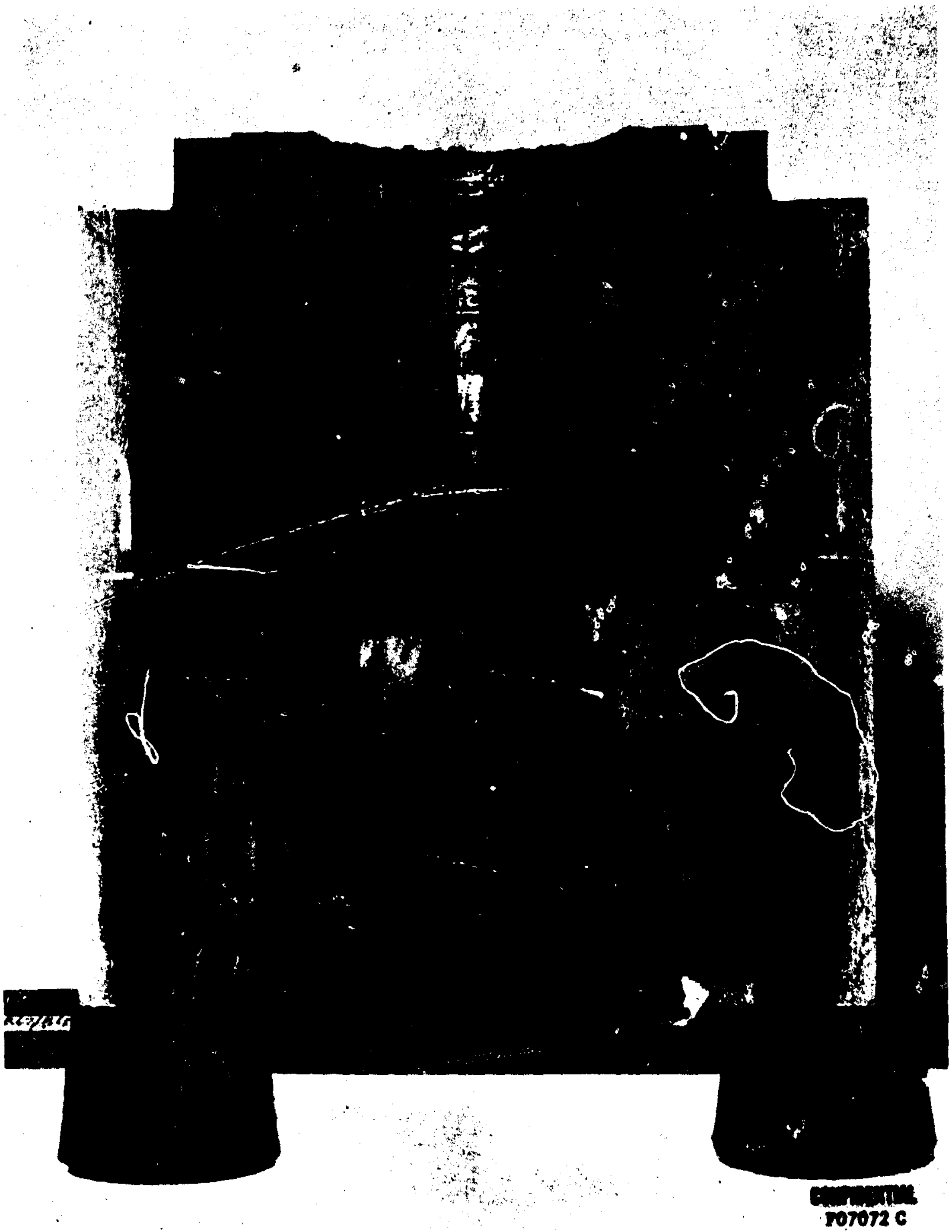
CONFIDENTIAL
F07072 C

FIGURE 45. NOZZLE FROM TEST T-9 - CROSS SECTION

TABLE XIX. MOTOR TEST T-9 DEPOSIT ANALYSIS (C)

Sample Number	Sample Location	Composition	
T-9-1	Chamber slag	BeO	90-95%
		BeO	trace
		Amorphous Carbon	5-10
T-9-2	Aft closure - bubbled material from bottom quadrant	BeO	55-65
		Be_2C	20-30
		Mg_2SiO_4	5-10
		Graphite	5-10
T-9-3	Aft closure - bottom quadrant area near entrance cone, entire char thickness	BeO	50-60
		Be_2C	15-20
		Mg_2SiO_4	10-15
		MgO	5-10
		Graphite	5-10
T-9-4	Graphite entrance cone	BeO	30-40
		Be_2O	5-10
		Mg_2SiO_4	5-10
		MgO	10-15
		Graphite	30-40
T-9-5	Thermal expansion gap, (RTV 102 char)	Amorphous Carbon	100
T-9-6	Convergent face of pyrolytic graphite throat washers	BeO	30-40
		Be_2C	5-10
		MgO	5-10
		Amorphous Carbon	30-40
		Graphite	5-10
T-9-7	Graphite exit cone	BeO	85-95
		Be_2C	2-5
		Mg_2SiO_4	2-5
		MgO	2-5
		Graphite	2-5

aft closure. The graphite entrance cone had a continuous, relatively thick coating (0.050"), a mixture of aft closure material and combustion products. This was probably the result of asbestos flow from the aft closure char. This mixture of oxides was also found on the pyrolytic graphite throat insert and the graphite exit cone. The pyrolytic graphite washers were in very good condition with no washers being broken, cracked, or delaminated. There did not appear to be any gas flow behind the washers. The graphite exit cone was coated with a very thin layer consisting primarily of BeO.

(c) (C) Motor Test T-10

Motor Test T-10 used a slotted, internal burning, beryllium propellant grain. The aft closure and nozzle are shown in the as-received condition in Figures 46 and 47. The graphite entrance cone was cracked in three places and is shown in Figure 48. A cross section of the aft closure is shown in Figure 49 with the original contour drawn in. The char recession was similar to that in Test T-9 except for the groove opposite the grain slot. Cross sections of the nozzle and graphite exit cone are shown in Figures 50 and 51.

A series of deposits were taken from various areas on the hardware and analyzed by X-ray diffraction. The results are summarized in Table XX and compare favorably with those from Test T-1 (Table XI Reference 2) which also used the Arcocel 191F propellant.

The location of the slot in the propellant and non-uniform erosion of the aft closure can be seen in Figure 46. A distinct axial groove was formed 180° from the grain slot or top position. The groove extended along the aft closure and graphite entrance cone and slightly beyond the pyrolytic graphite washer at the original geometric throat. The groove depth and width gradually diminish as the throat is approached. The first and second pyrolytic graphite washers were fractured in the groove area and were badly delaminated (see Figure 51). The graphite entrance cone was coated with exhaust products and aft closure insulating material. The pyrolytic graphite washers in the throat insert had a 0.020 to 0.030 inch thick coating of similar material. The graphite exit cone was covered with a relatively thick (0.050-0.100 inch) coating of BeO and Mg_2SiO_4 (decomposition product of asbestos).

(d) (C) Motor Test T-11

Motor Test T-11 used the Arcane 54F propellant in a C.P. (Type I) grain. The aft closure is shown in the as-received condition in Figure 52. The condition of the aft closure suggests that the grain inhibitor bond may have failed in the area indicated in Figure52 . A shallow, axial groove can be seen extending downstream from the affected section of the aft closure insulator. The graphite entrance cone was cracked in three places and is shown in Figure 53 (the axial groove can also be seen here). A cross

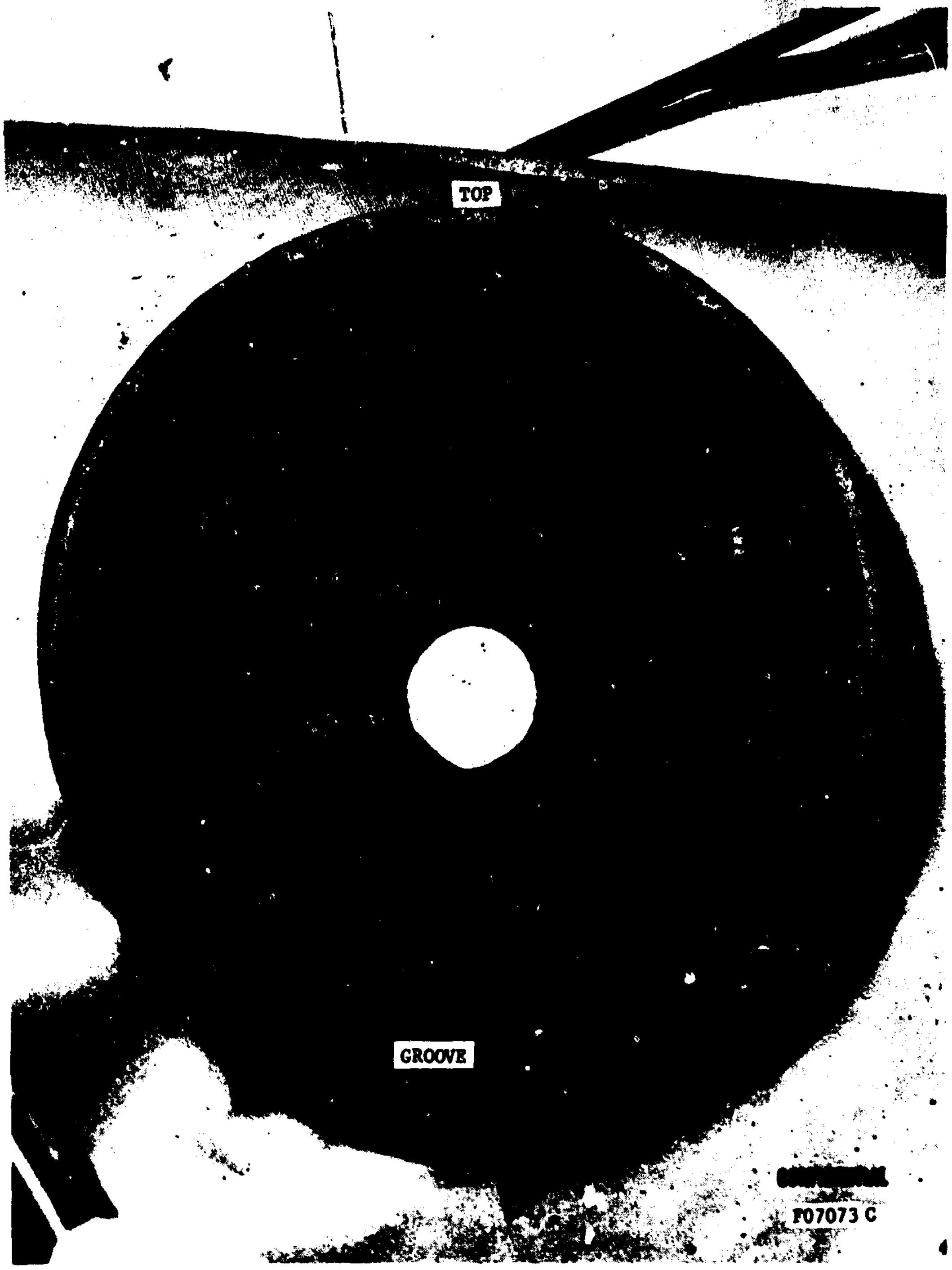
TOP
GROOVE
F07073 C

FIGURE 46. AFT CLOSURE INSULATOR - TEST T-10

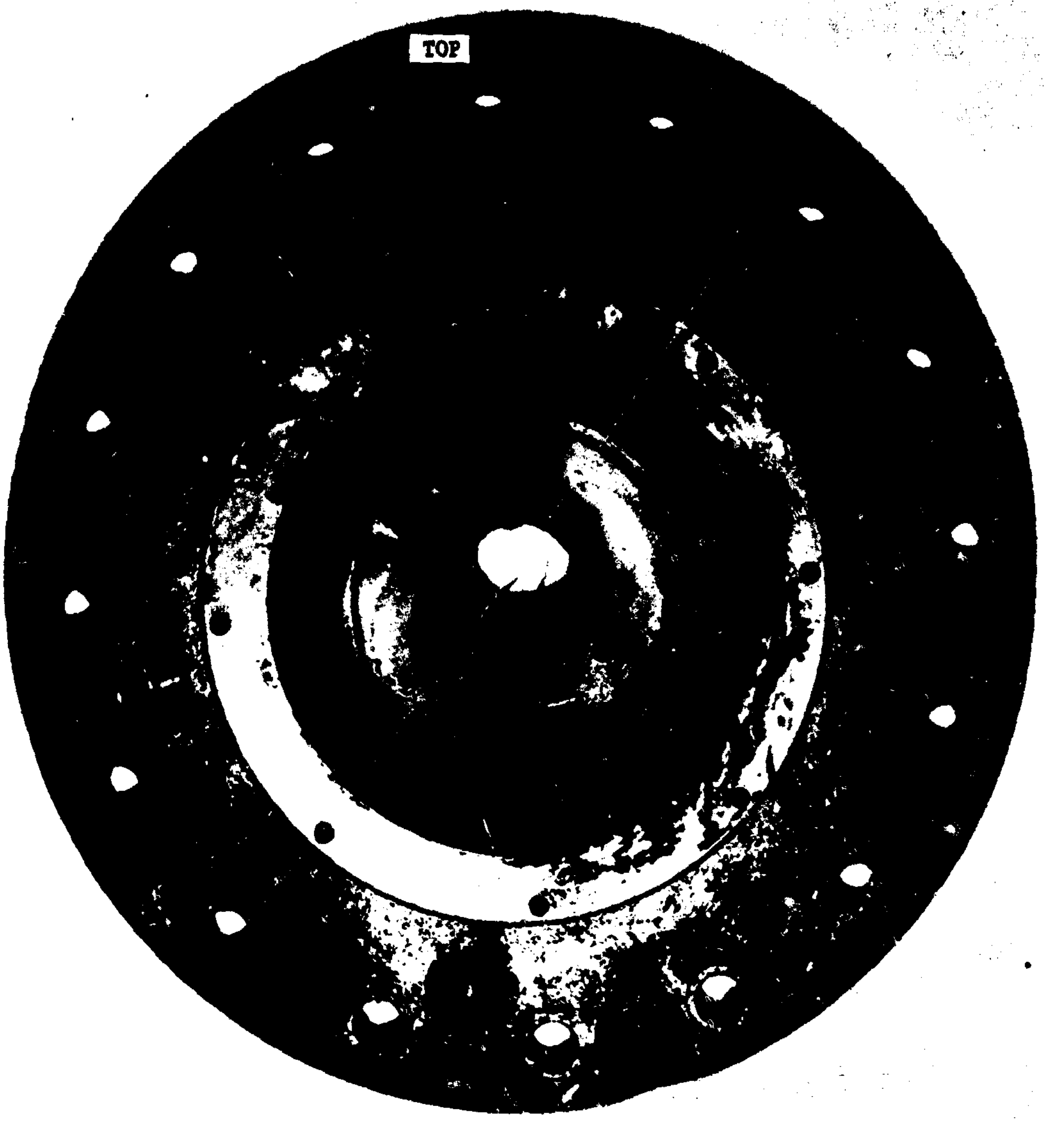

CONFIDENTIAL
F07074 C

FIGURE 47. NOZZLE FROM TEST T-10 - EXIT CONE VIEW

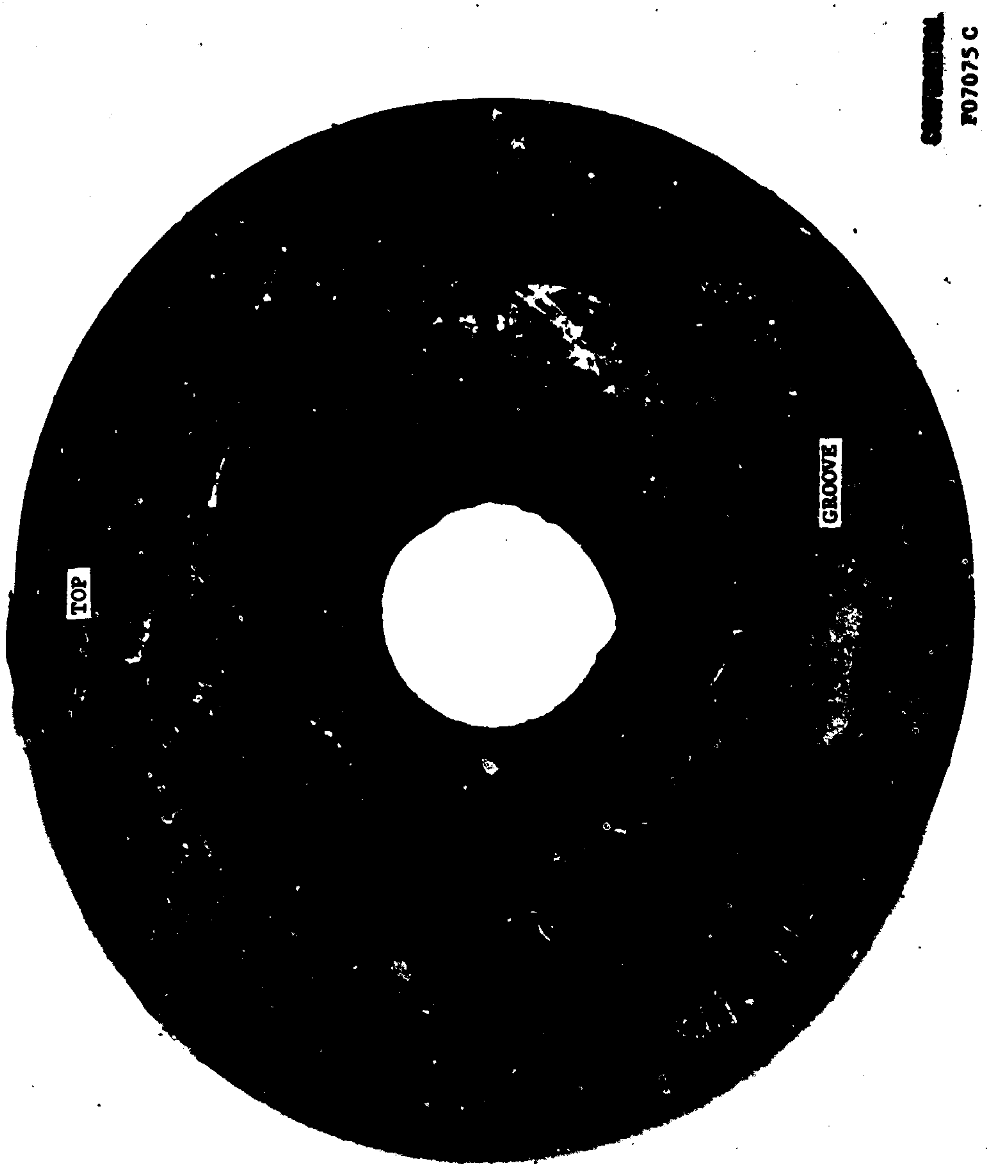
TOP
GROOVE
F07075 C

FIGURE 48. ATJ GRAPHITE ENTRANCE CONE - TEST T-10

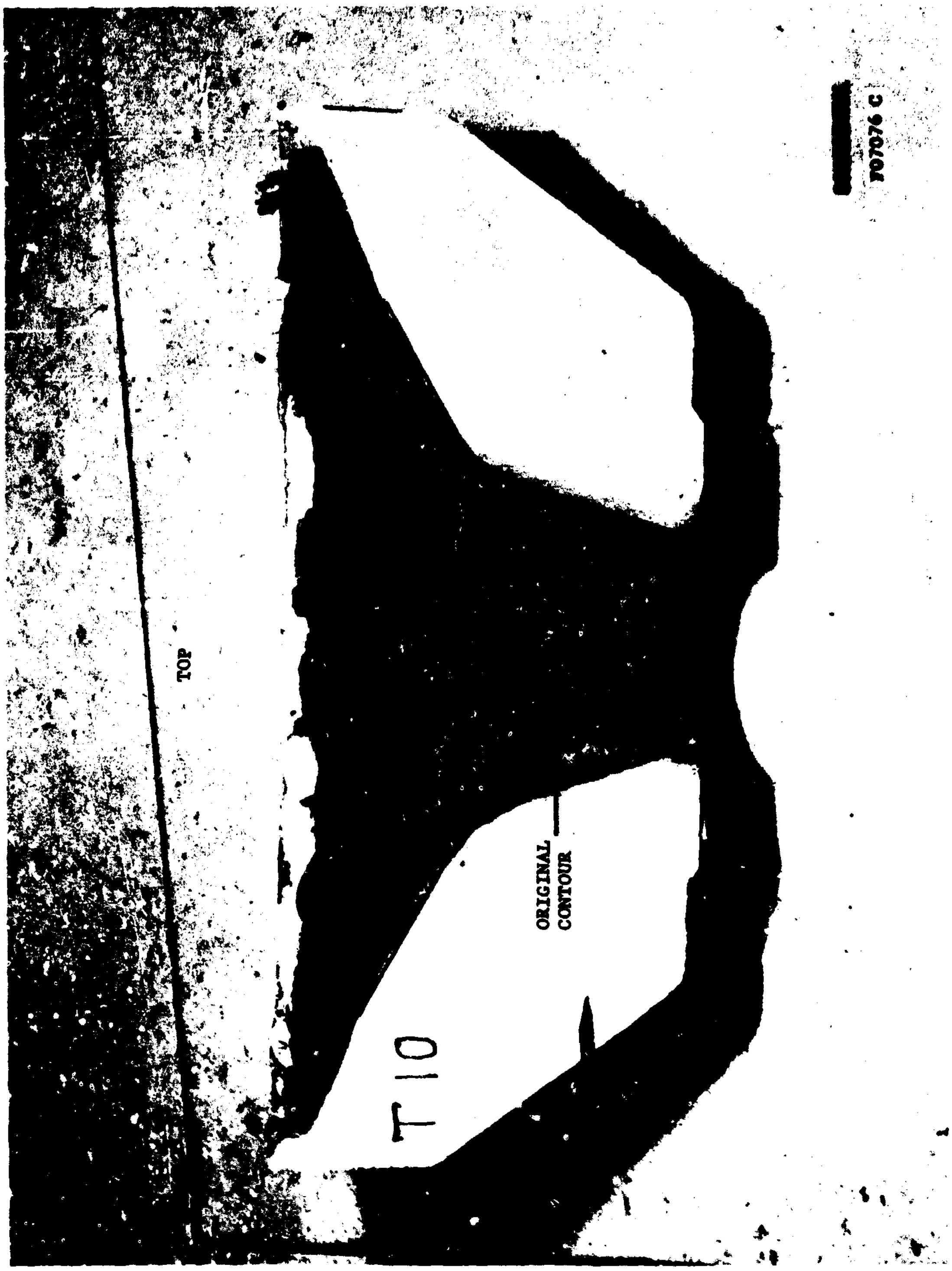
TOP
ORIGINAL CONTOUR
T10
F07076 C

FIGURE 49. AFT CLOSURE INSULATOR CROSS SECTION - TEST T-10

FIGURE 50. NOZZLE FROM TEST T-10 - CROSS SECTION (TOP HALF)

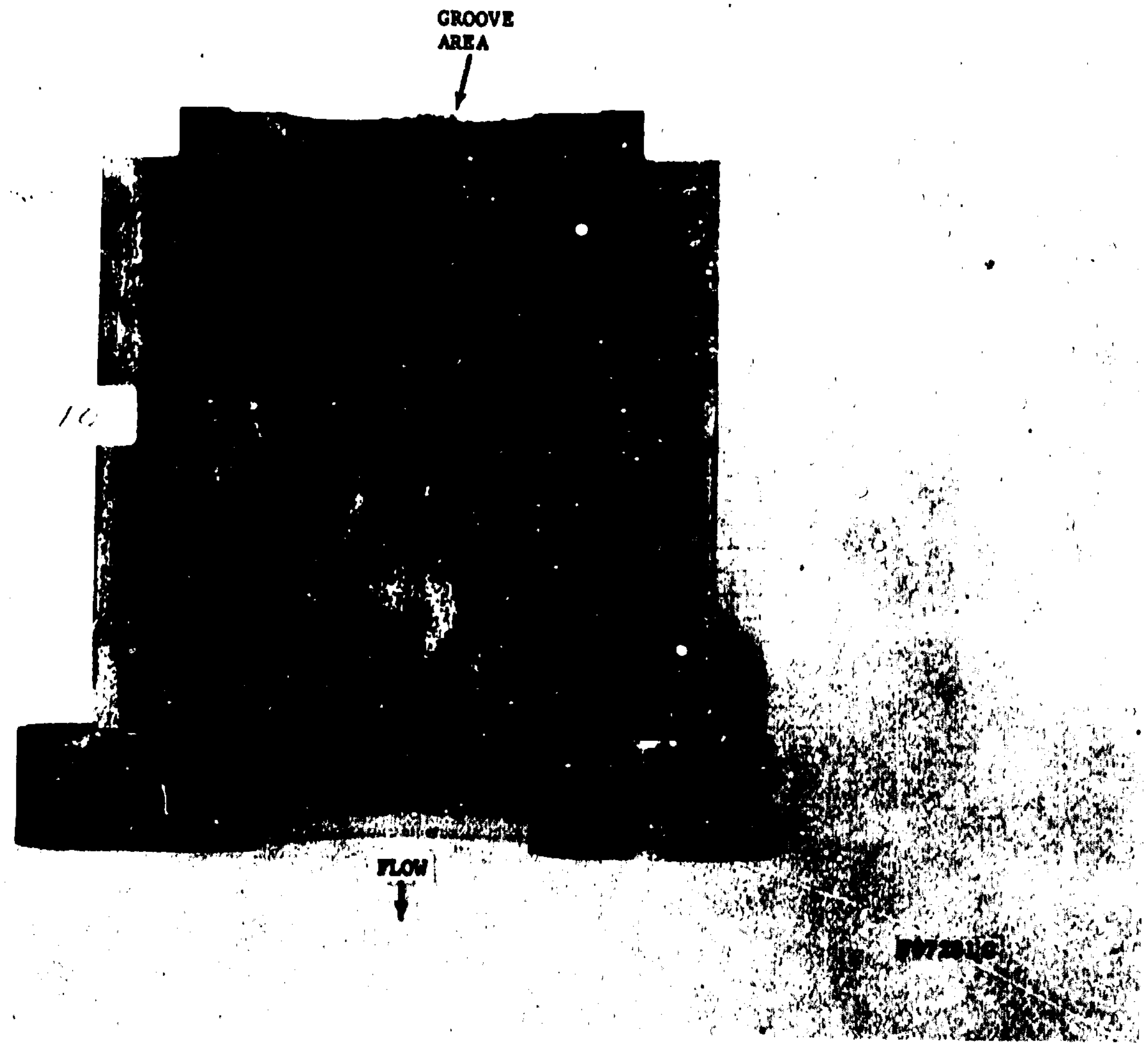
GROOVE AREA
FLOW

FIGURE 51. NOZZLE FROM TEST T-10 - CROSS SECTION (BOTTOM HALF)

TABLE XX. MOTOR TEST T-10 DEPOSIT ANALYSIS (C)

Sample Number	Sample Location	Composition	
T-10-1	Chamber residue	BeO	60-70%
		Be_2C	20-30
		Amorphous Carbon	10-20
T-10-2	Aft closure - surface material from slot area	BeO	50-60
		Be_2C	10-15
		Mg_2SiO_4	20-30
		MgO	5-10
		Graphite	2-5
T-10-3	Aft closure - entire char opposite slot area	BeO	5-10
		Be_2C	15-20
		Mg_2SiO_4	50-60
		MgO	10-15
		Graphite	5-10
T-10-4	Graphite entrance cone near aft closure	BeO	75-85
		Be_2C	5-10
		Graphite	5-10
T-10-5	Graphite entrance cone near pyrolytic graphite throat insert	BeO	80-90
		Be_2C	2-5
		MgO	2-5
		Graphite	5-10
T-10-6	Spacer area	Mg_2SiO_4	50
		SiO_2	50
		Amorphous Carbon	present
T-10-7	Surface coating on convergent face of pyrolytic graphite washers	BeO	80-90
		Be_2C	5-10
		Mg_2SiO_4	2-5
		Graphite	2-5
T-10-8	Graphite exit cone, thick white coating which appeared to have flowed over surface	BeO	85-95
		Mg_2SiO_4	5-10
		Amorphous Carbon	trace
		Graphite	trace
T-10-9	Graphite exit cone, at trailing edge, gray coating	BeO	85-95
		Be_2C	2-5
		Mg_2SiO_4	5-10
		Amorphous Carbon	trace
		Graphite	trace

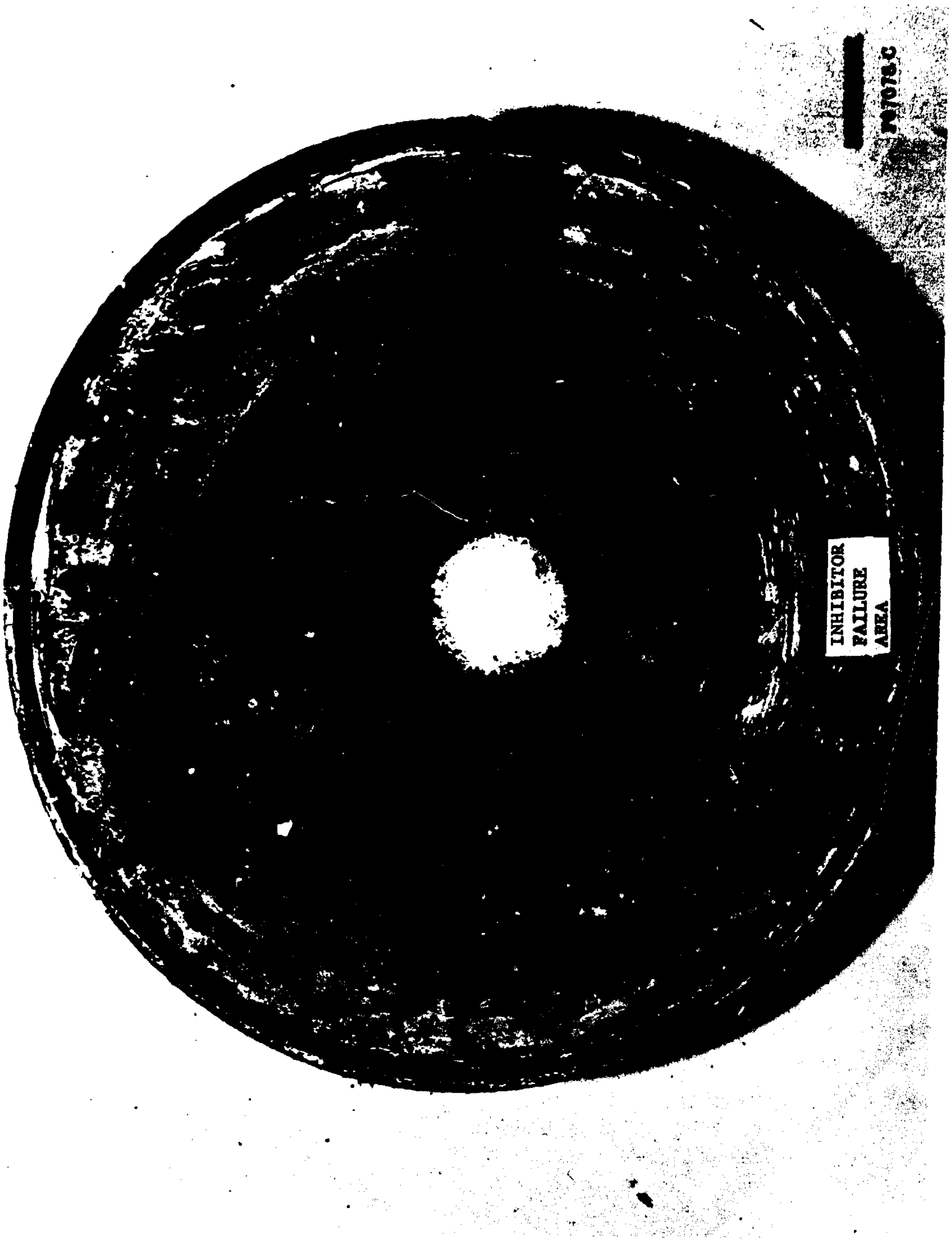
P67078-C
INHIBITOR
FAILURE
AREA

FIGURE 52. AFT CLOSURE INSULATOR - TEST T-11

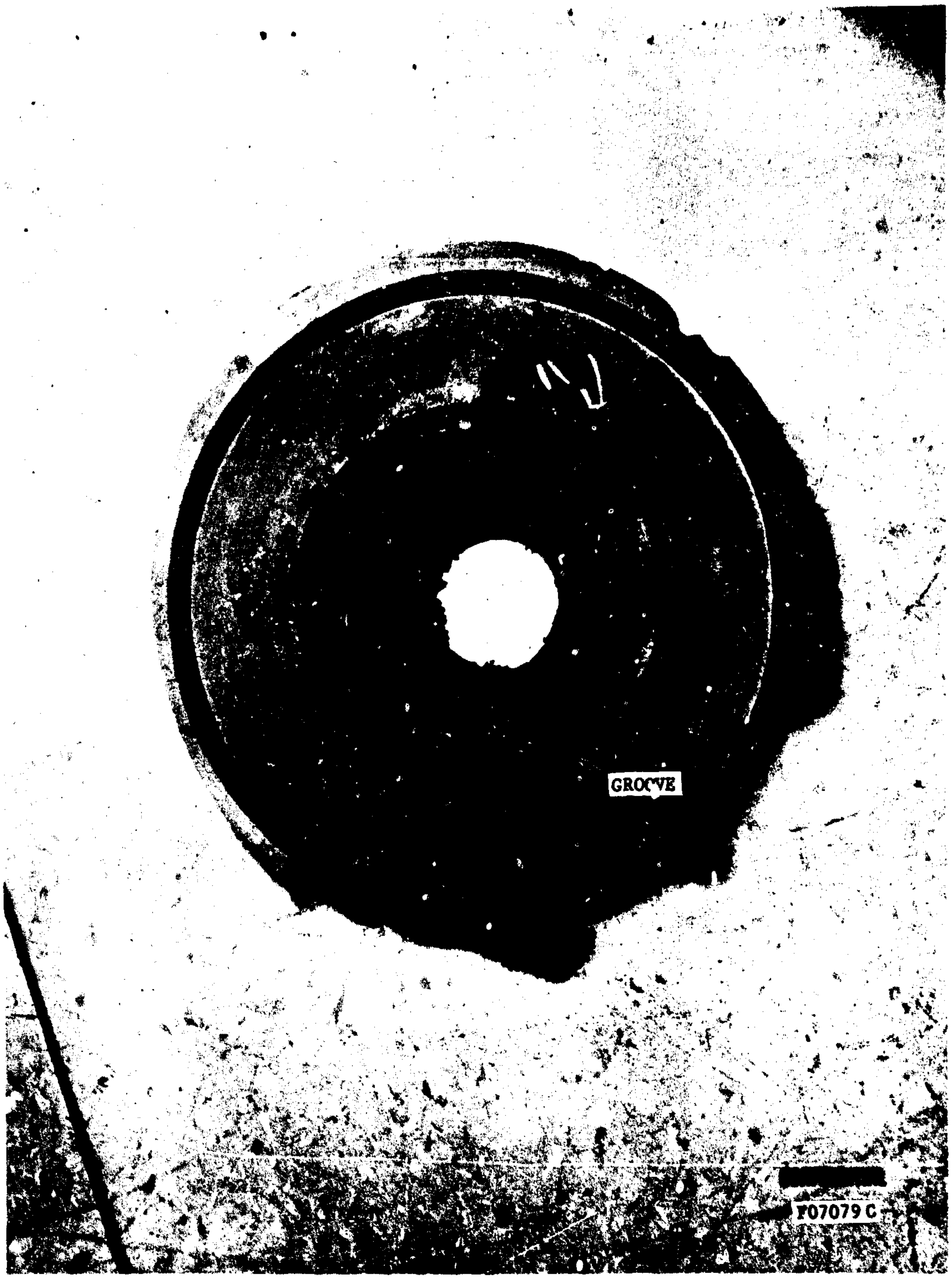
GROOVE
F07079 C

FIGURE 53. ATJ GRAPHITE ENTRANCE CONE - TEST T-11

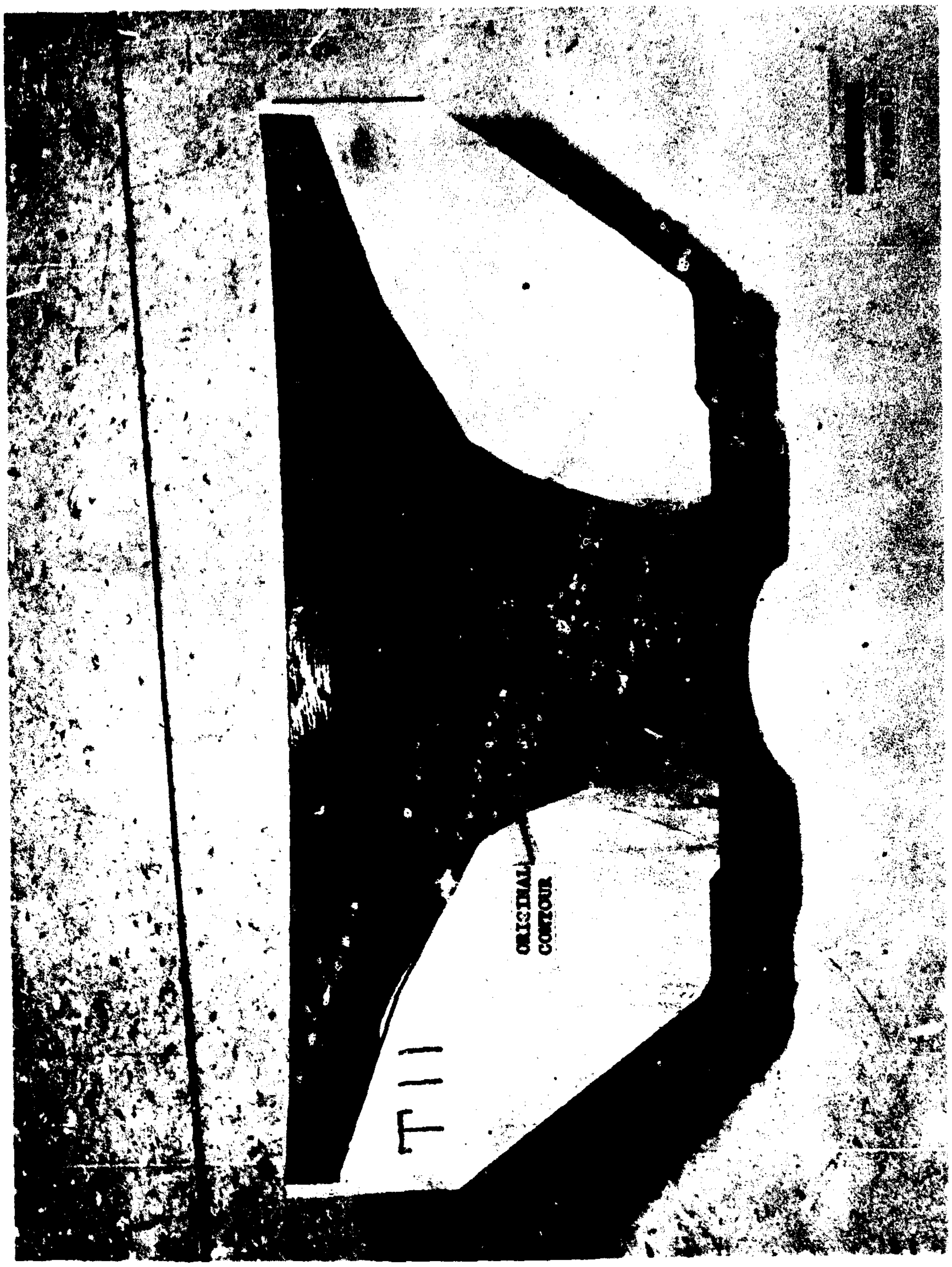
ORIGINAL
CONTOUR

FIGURE 54. AFT CLOSURE INSULATOR CROSS SECTION - TEST T-11

section of the aft closure insulator is shown in Figure 54 with the original contour drawn in. A cross section of the throat insert and graphite exit cone is shown in Figure 55. The nozzle throat entrance and exit cone views are not shown as they show nothing unusual.

A series of deposits were taken from various areas on the hardware and analyzed by X-ray diffraction. The results are summarized in Table XXI. No unusual results were obtained.

In general, the hardware from this test was in very good condition. All deposits analyzed included both the condensed exhaust products (BeO) and decomposition products of the asbestos (MgO and Mg_2SiO_4). The graphite entrance cone was covered with a thin (0.020 inch) layer as were the pyrolytic graphite throat insert and the graphite exit cone. There was come BeO found at the back edge of the spacer area indicating that some liquid beryllia had been forced into that area. There was no evidence of gas flow behind the pyrolytic graphite washers. The slight grooving in the ATJ graphite entrance cone did not extend into the pyrolytic graphite throat section.

(e) (C) Motor Test T-12

Motor Test T-12 used a slotted, internal burning, beryllium propellant grain and a submerged nozzle. The nozzle and aft closure are shown in Figures 56 and 57 in the as-received condition. The entrance cap was carbon cloth-phenolic. The black deposit shown in these figures is amorphous carbon, a product of the decomposition of pyrolysis gas from the resin binder. The entrance cap and throat shape is more clearly shown in Figure 58 where the amorphous carbon has been removed. The nozzle is shown after removal from the aft closure in Figure 59. The ATJ graphite entrance section, with deposits removed, is shown in Figure 60. A close-up of the pyrolytic graphite throat insert is shown in Figure 61 and a cross section in Figure 62.

A series of deposits were taken from various areas on the hardware and analyzed by X-ray diffraction. The results are summarized in Table XXII.

The hardware from this test was in very good condition. The aft closure was only charred in the area of the slot in the propellant grain. There was some relatively minor erosion and change of contour of the carbon cloth-phenolic entrance cap. The carbon cloth-phenolic was thoroughly charred but much of this occurred after the test terminated. The graphite entrance cone had two axial grooves, in line with and opposite the grain slot. Only the groove opposite the slot extended into the pyrolytic graphite washer stack. Some of the washer surfaces were covered with unusual appearing deposits but all were found to be either combustion products (BeO), insulator residue (Mg_2SiO_4, MgO, carbon) or products of the reaction between the two (Be_2C). The area at the junction of the carbon

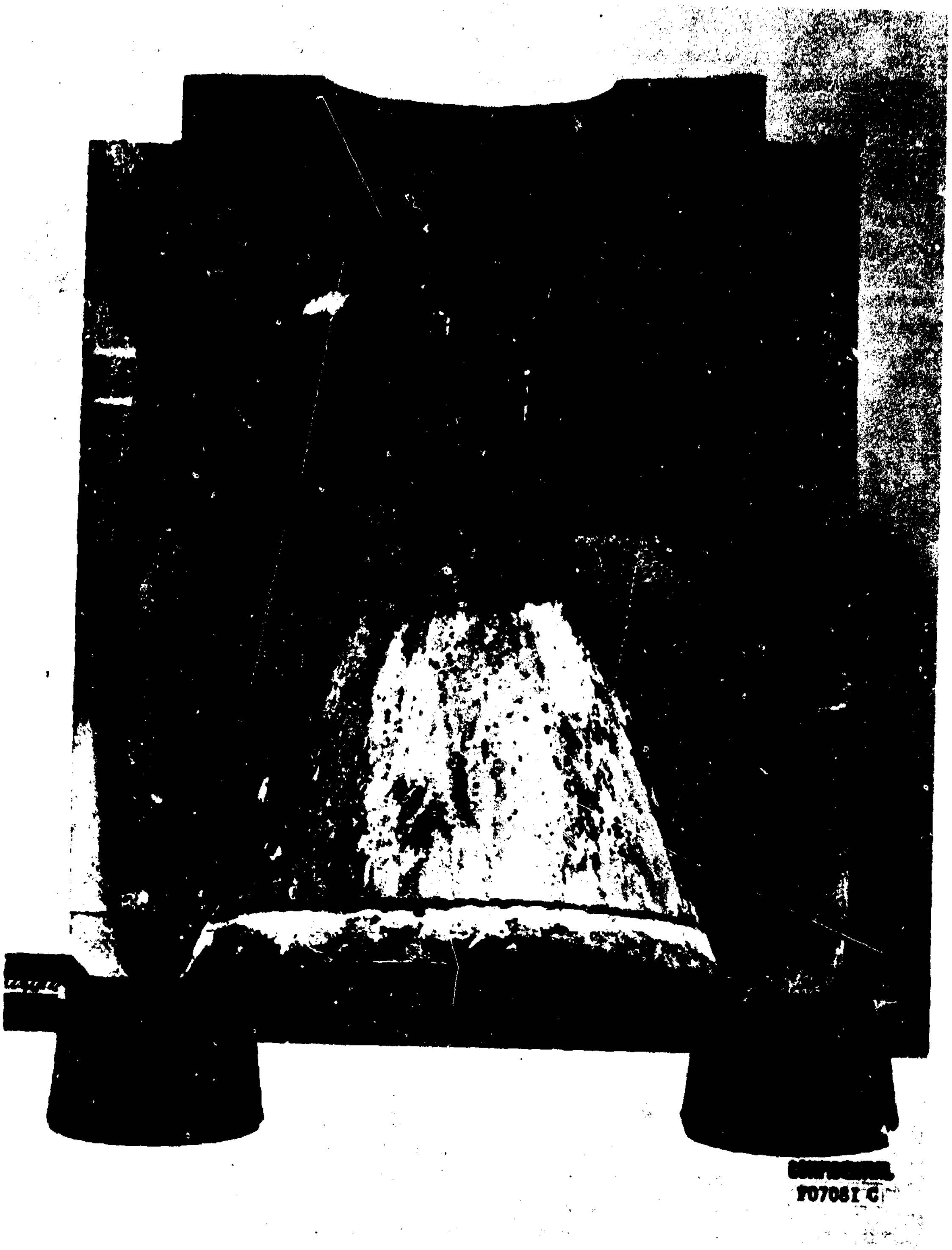

FIGURE 55. NOZZLE FROM TEST T-11 - CROSS SECTION

TABLE XXI. MOTOR TEST T-11 DEPOSIT ANALYSIS (C)

Sample Number	Sample Location	Composition	
T-11-1	Chamber residue	BeO	70-80%
		Be_2C	10-15
		Mg_2SiO_4	5-10
		MgO	2-5
		Graphite	5-10
T-11-2	Aft closure (slot area)	BeO	35-45
		Be_2C	40-45
		Mg_2SiO_4	10-15
		MgO	trace
		Graphite	5-10
T-11-3	Aft closure, charred inhibitor (opposite slot)	BeO	50-60
		Be_2C	40-45
		Mg_2SiO_4	2-5
		Graphite	10-15
T-11-4	Graphite entrance cone, thick bubbled area near aft closure	BeO	80-90
		Be_2C	5-10
		Mg_2SiO_4	2-5
		Amorphous carbon	trace
		Graphite	2-5
T-11-5	Graphite entrance cone, thin layer	BeO	50-60
		Be_2C	30-35
		Mg_2SiO_4	2-5
		MgO	5-10
		Graphite	10-15
T-11-6	Divergent face, pyrolytic graphite washers	BeO	80-90
		Be_2C	trace
		Mg_2SiO_4	5-10
		Amorphous carbon	trace
		Graphite	low
T-11-7	Graphite exit cone, white deposit	BeO	70-80
		Be_2C	5-10
		Mg_2SiO_4	5-10
		MgO	5-10
		Graphite	10-15
T-11-8	Spacer area at back edge of pyrolytic graphite washer	BeO	5-10
		Mg_2SiO_4	trace
		Graphite	90-95

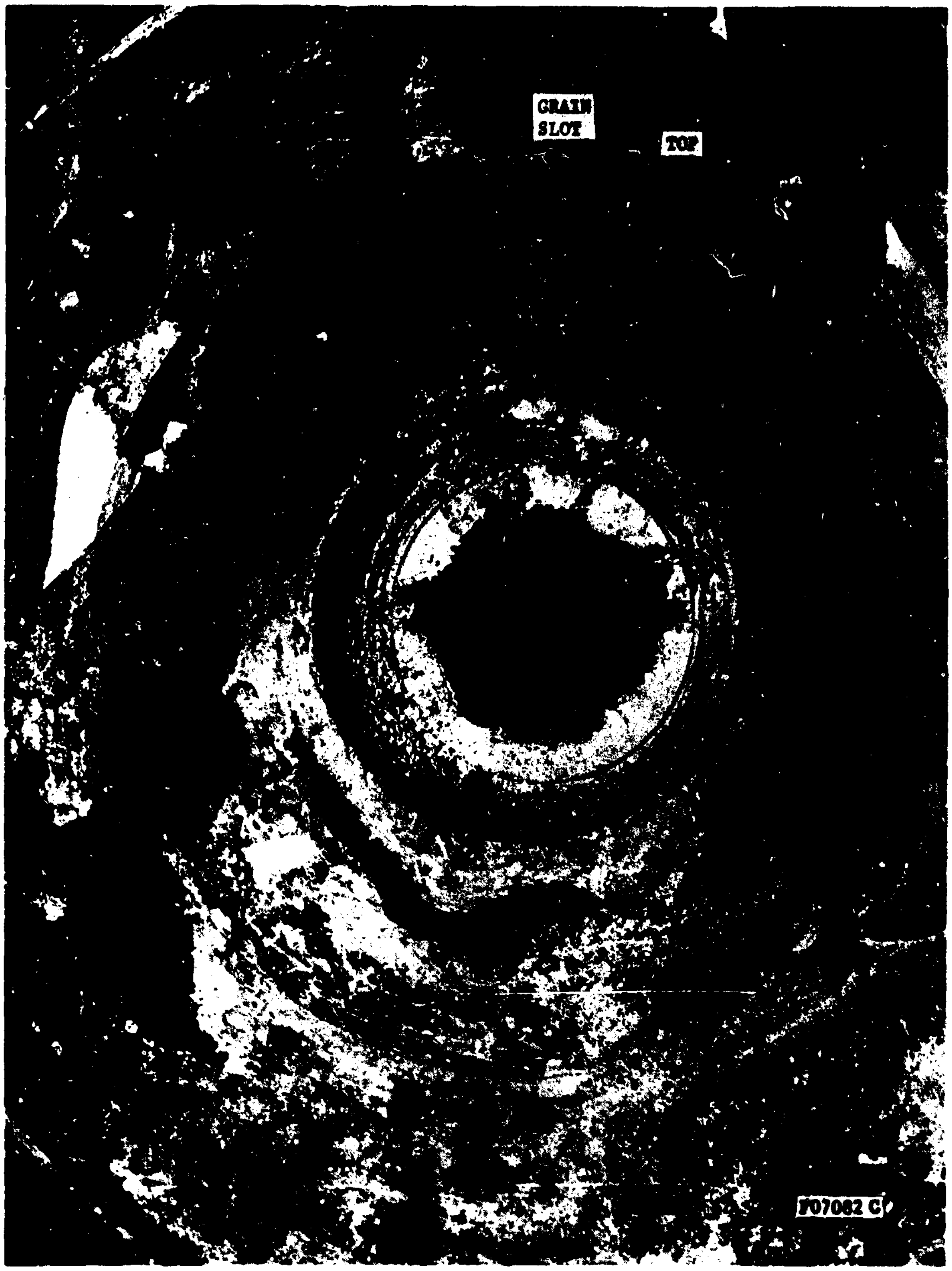
GRAIN
SLOT
TOP
F07082 C

FIGURE 56. AFT CLOSURE INSULATOR AND NOZZLE - TEST T-12 (AS RECEIVED)

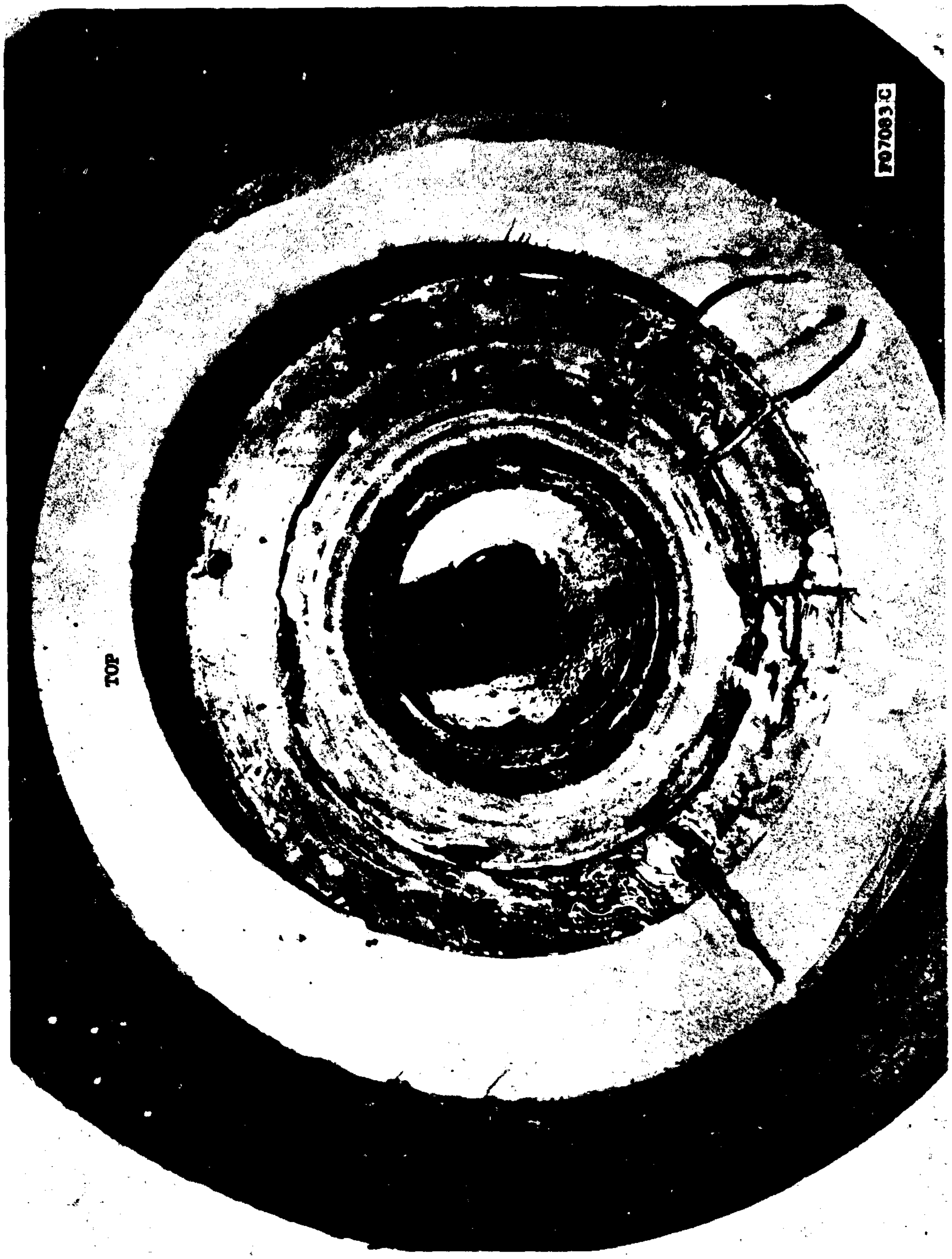
F07083C
TOP

FIGURE 57. NOZZLE FROM TEST T-12 - EXIT CONE VIEW

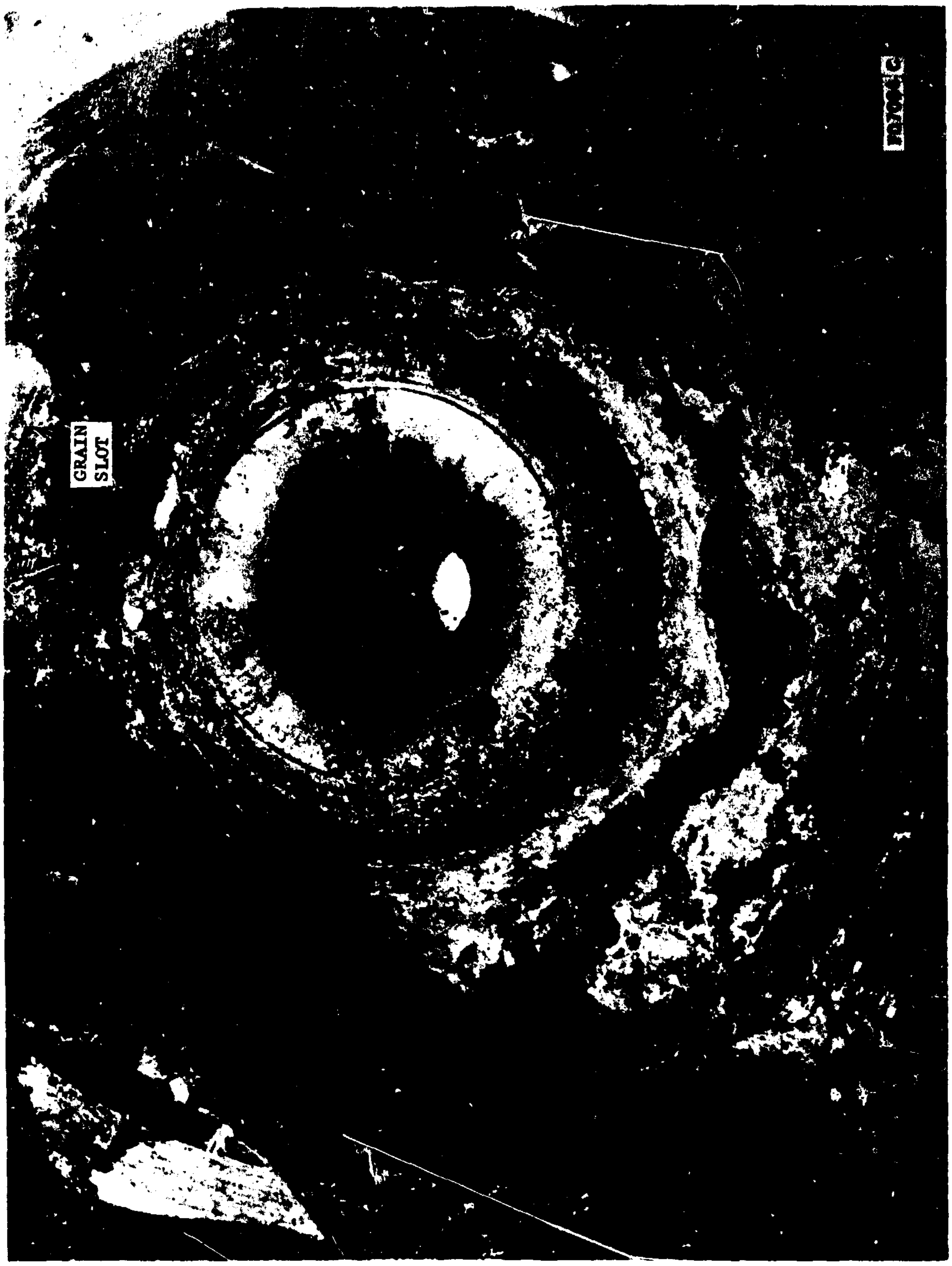

FIGURE 58. AFT CLOSURE INSULATOR AND NOZZLE - TEST T-12 (SOOT REMOVED)

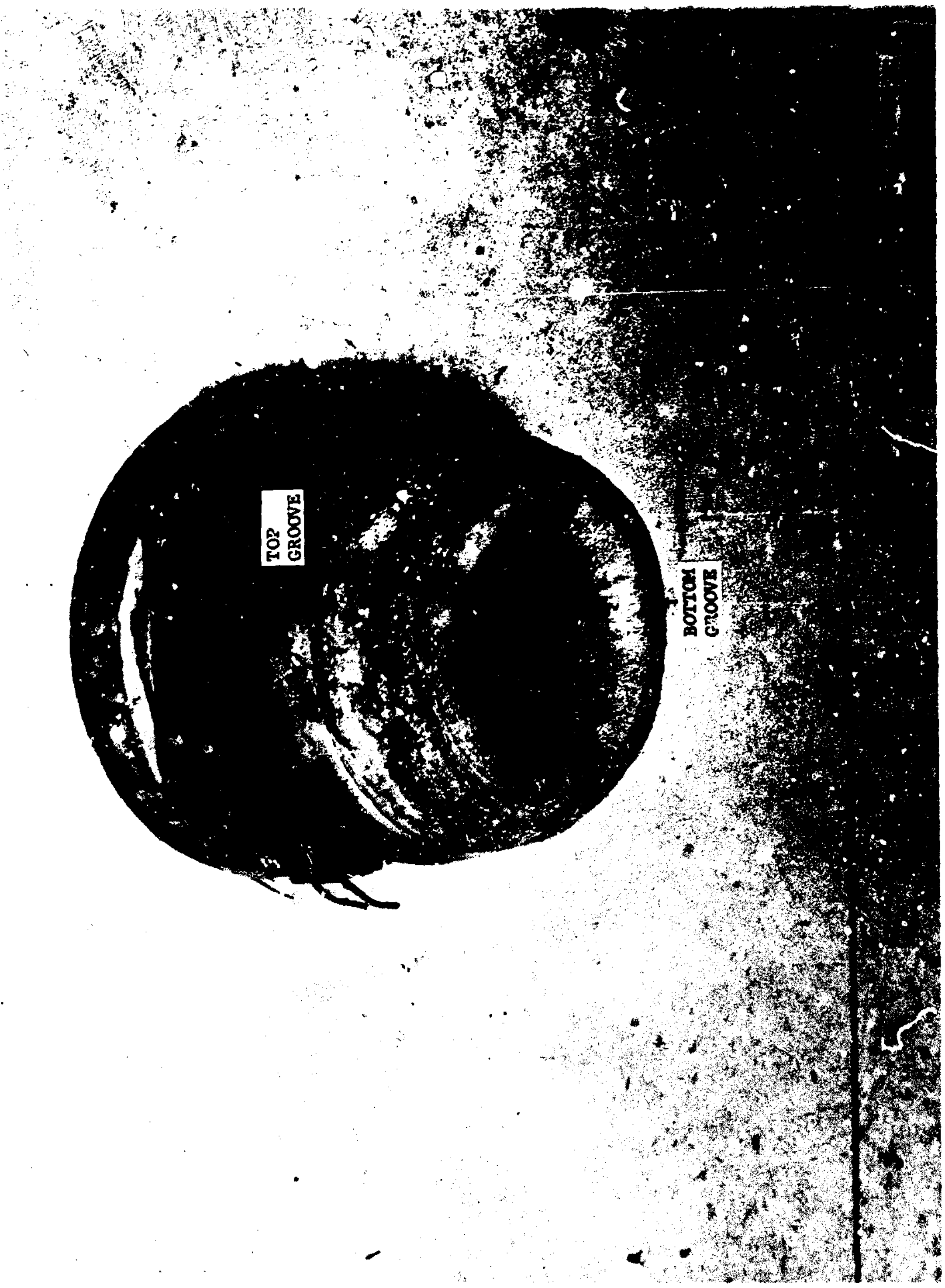
TOP GROOVE
BOTTOM GROOVE

FIGURE 59. SUBMERGED NOZZLE FROM TEST T-12 (SOOT REMOVED)

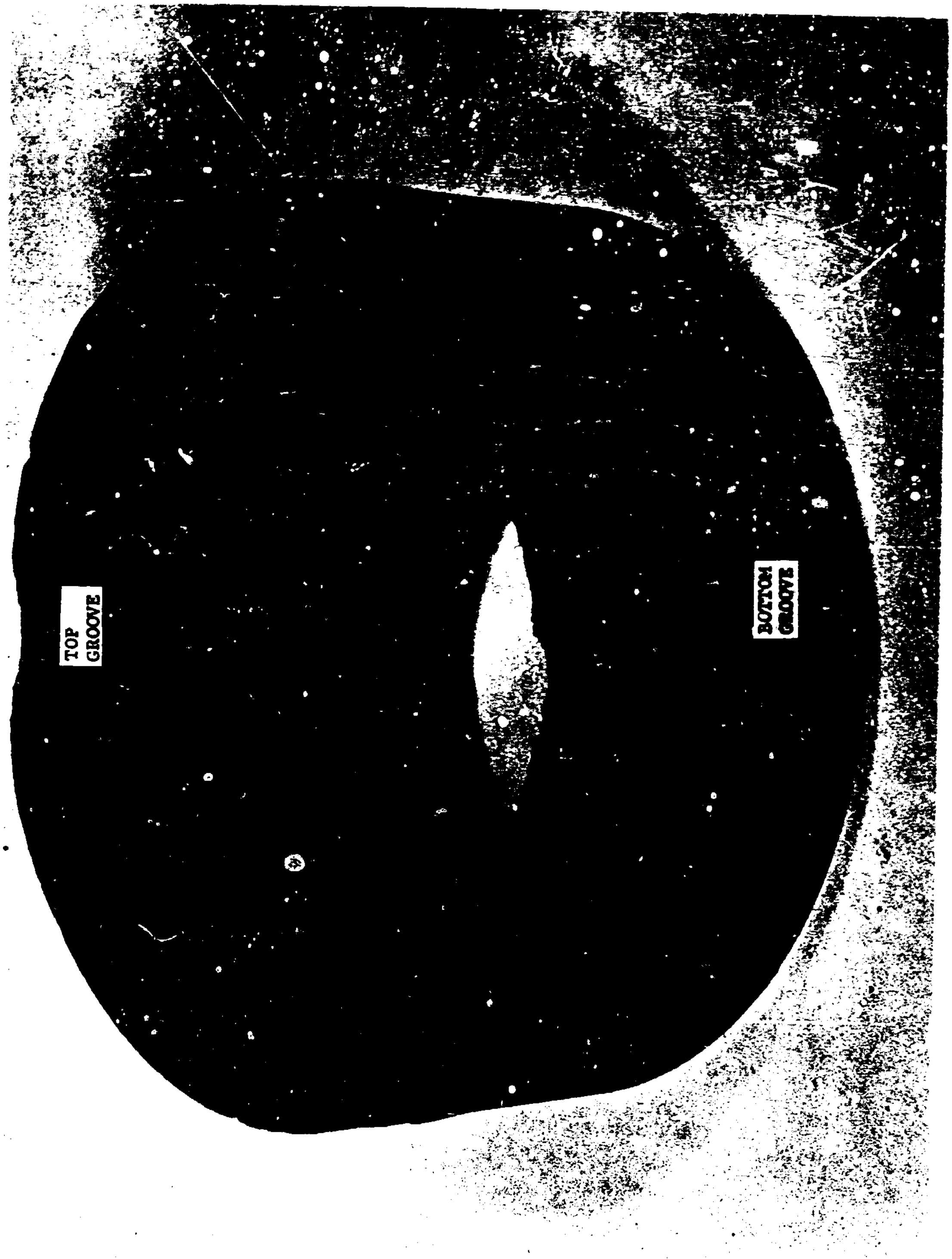
TOP GROOVE
BOTTOM GROOVE

FIGURE 60. ATJ GRAPHITE ENTRANCE CONE - TEST T-12

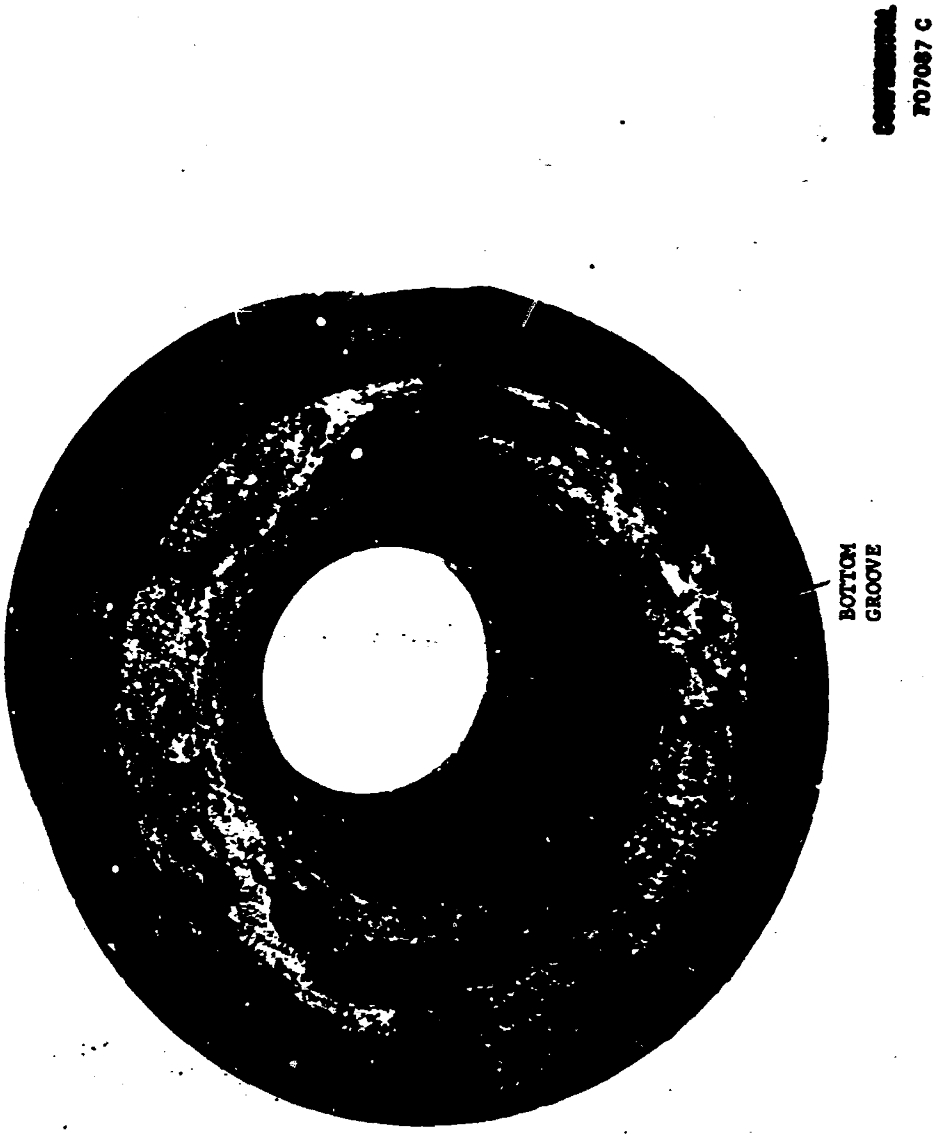
F07087 C
BOTTOM GROOVE

FIGURE 61. NOZZLE THROAT SECTION - TEST T-12 (THROAT APPROACH VIEW)

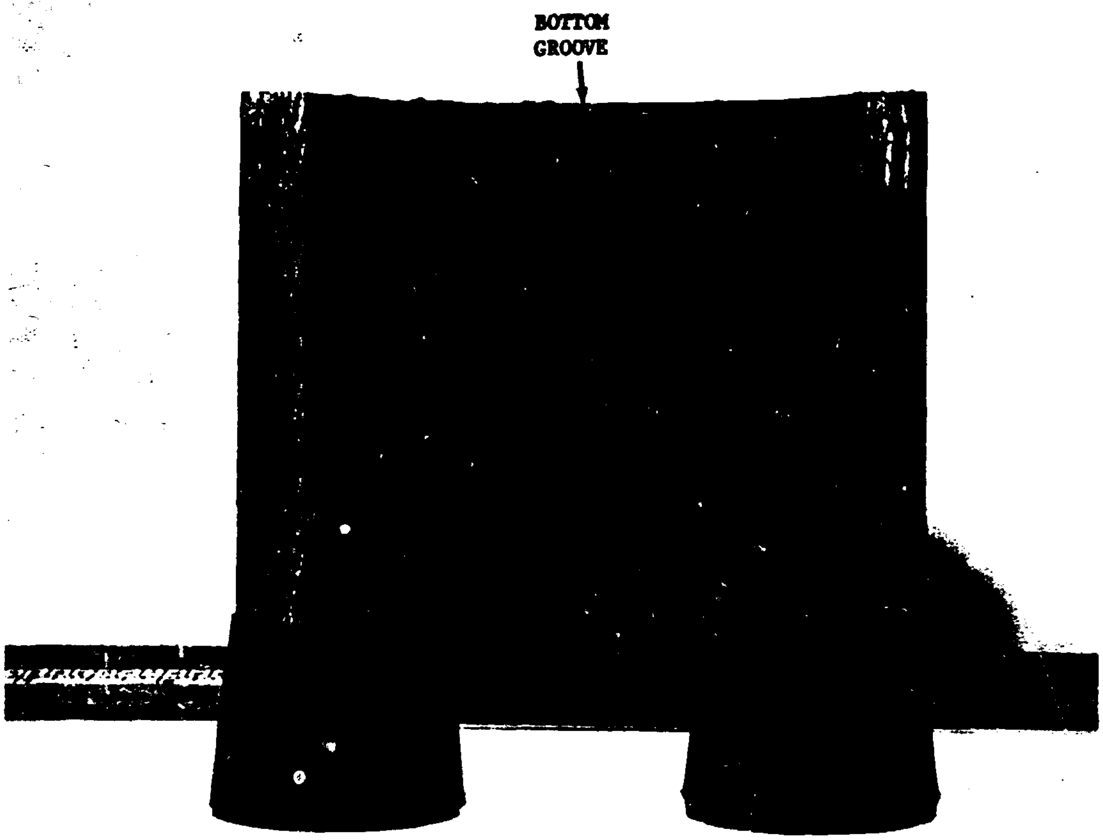
BOTTOM
GROOVE
CONFIDENTIAL
F07088 C

FIGURE 62. NOZZLE THROAT CROSS SECTION - TEST T-12

TABLE XXII. MOTOR TEST T-12 DEPOSIT ANALYSIS (C)

Sample Number	Sample Location	Composition	
T-12-1	Chamber residue	BeO	60-70%
		β BeO	trace
		Be_2C	15-20
		Amorphous carbon	5-10
		Graphite	5-10
T-12-2	Loose residue on aft closure	BeO	70-80
		Be_2C	10-15
		Mg_2SiO_4	trace
		Amorphous carbon	trace
		Graphite	10-15
T-12-3	Soot from face of graphite entrance cone	Amorphous carbon	100
T-12-4	Aft closure, slot area near carbon cloth-phenolic entrance cap, entire char layer	BeO	20-30
		Be_2C	5-10
		Mg_2SiO_4	trace
		MgO	trace
		Amorphous carbon	trace
		Graphite	5-10
T-12-5	Large bubble on carbon cloth-phenolic near slot	BeO	80-90
		Be_2O	5-10
		Mg_2SiO_4	trace
		Graphite	5-10
T-12-6	Graphite entrance cone near carbon cloth-phenolic entrance cap. Deposit had metallic appearance.	BeO	75-85
		Be_2C	15-20
		Mg_2SiO_4	2-5
		Amorphous carbon	trace
		Graphite	
T-12-7	Throat area	BeO	85-95
		Mg_2SiO_4	trace
		Graphite	trace
T-12-8	Graphite exit cone, white deposit	BeO	95+
		Be_2C	trace
		Mg_2SiO_4	trace
		Amorphous carbon	trace

cloth-phenolic entrance cap and the asbestos phenolic aft closure was closely examined for unusual compounds. This is an area of potentially low gas velocity where something unexpected might have been, but was not, found. The pyrolytic graphite throat washers were coated with a layer (mostly BeO) approximately 0.040 inch thick. The graphite exit cone was coated with a relatively thick, irregular layer which was mostly BeO.

(f) (C) Motor Test T-13

Motor Test T-13 used a slotted, internal burning, beryllium grain and a steep inlet nozzle. A burn through of the nozzle holder and the steel aft closure occurred during the test. The entire nozzle assembly, steel aft closure, aft closure insulator and nozzle, is shown in the as-received condition in Figures 63 and 64. The aft closure insulator showing the burn through groove is shown in Figure 65 and the nozzle is shown in Figures 66 and 67. Figures 68 and 69 show the damage to the steel aft closure and to the nozzle retainer ring.

A series of deposits were taken from various areas on the hardware and analyzed by X-ray diffraction. The results are summarized in Table XXIII.

The burn through occurred between the aft closure insulator and the ATJ graphite entrance cone. There was a very small hole between the entrance cone and the aft closure, but on disassembly a deep groove was found in both the aft closure insulation and throat insert insulation (see Figures 63 , 65 and 67). There was beryllia and beryllium carbide found along the entire surface of the groove indicating that propellant gases exhausted through the groove and the gases were hot enough to carry melted beryllia to the exit area. The burn through did not occur in, or opposite, the grain slot area.

The graphite entrance cone was cracked in four places: in line with the slot in the grain, approximately opposite the slot, where the burn through occurred, and approximately opposite the burn through. There was a deep, axial groove in the ATJ graphite starting from the point where the burn through occurred. This groove can be seen in Figure 70 and it extended the entire length of the pyrolytic graphite throat insert. There was another less severe groove opposite the slot in the grain. This groove was broader and extended through the first four pyrolytic graphite washers (i.e. did not extend through the throat washer). A very shallow groove was also found in the ATJ entrance section in line with the grain slot. Aside from the axial grooves, the pyrolytic graphite washers were in very good condition.

(g) (C) Motor Test T-14

Motor Test T-14 used an internal burning, beryllium grain and a conventional nozzle. The aft closure and the nozzle are shown in Figures 71, 72 and 73

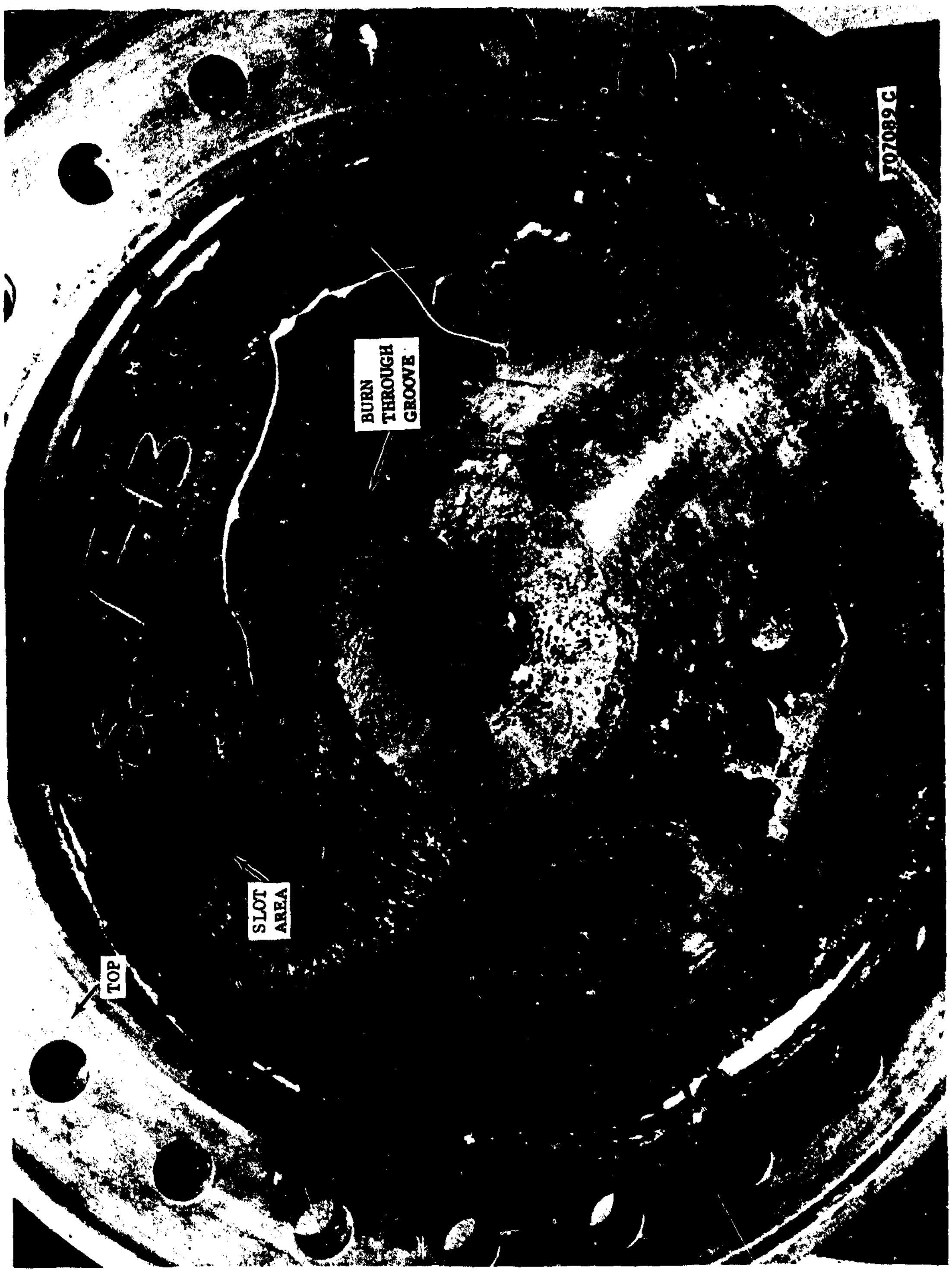
707089 C
BURN THROUGH GROOVE
SLOT AREA
TOP

FIGURE 63. AFT CLOSURE INSULATOR AND NOZZLE ENTRANCE - TEST T-13 (AS RECEIVED)

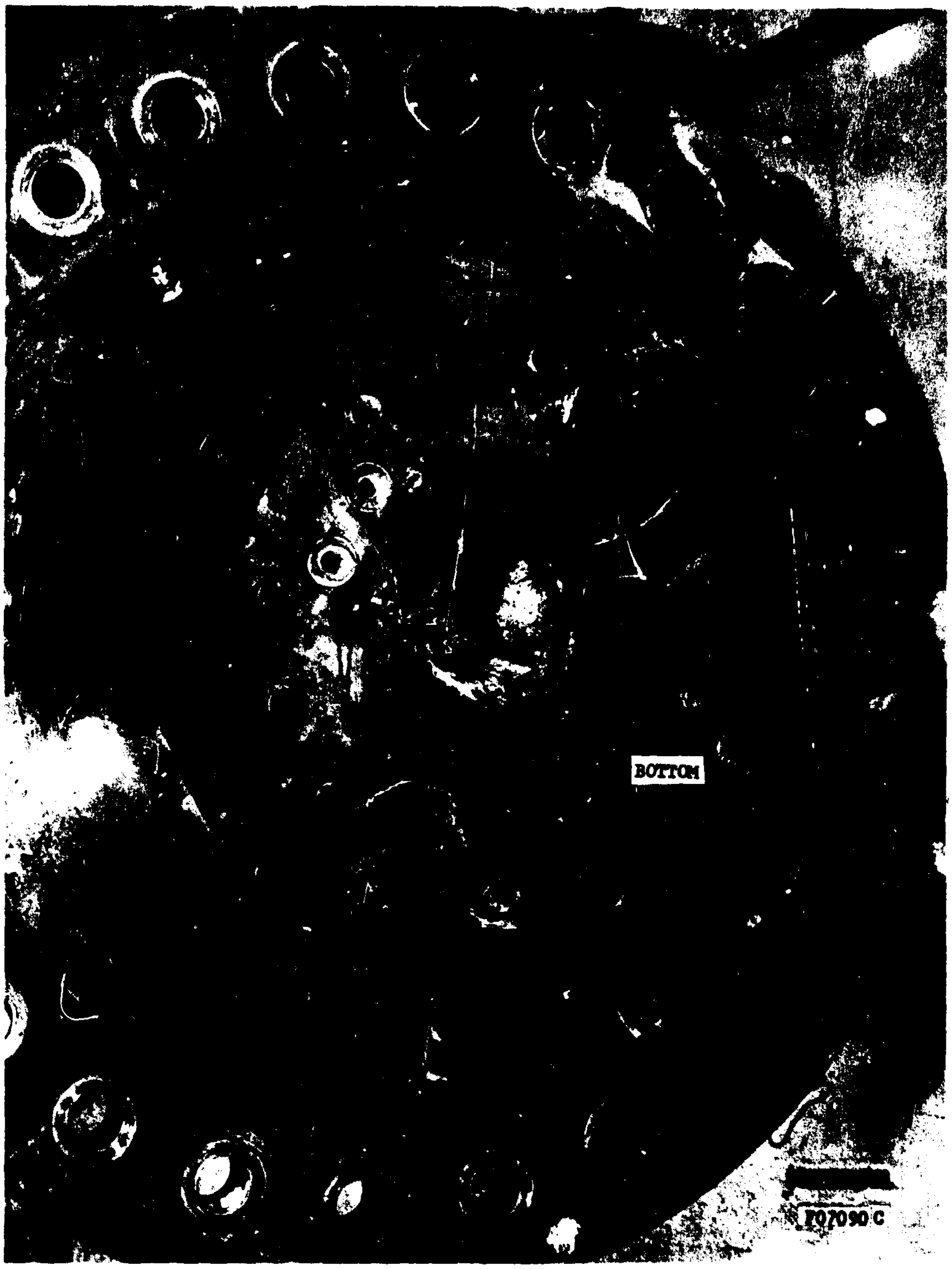
BOTTOM
F07090 C

FIGURE 64. NOZZLE FROM TEST T-13 - EXIT CONE VIEW

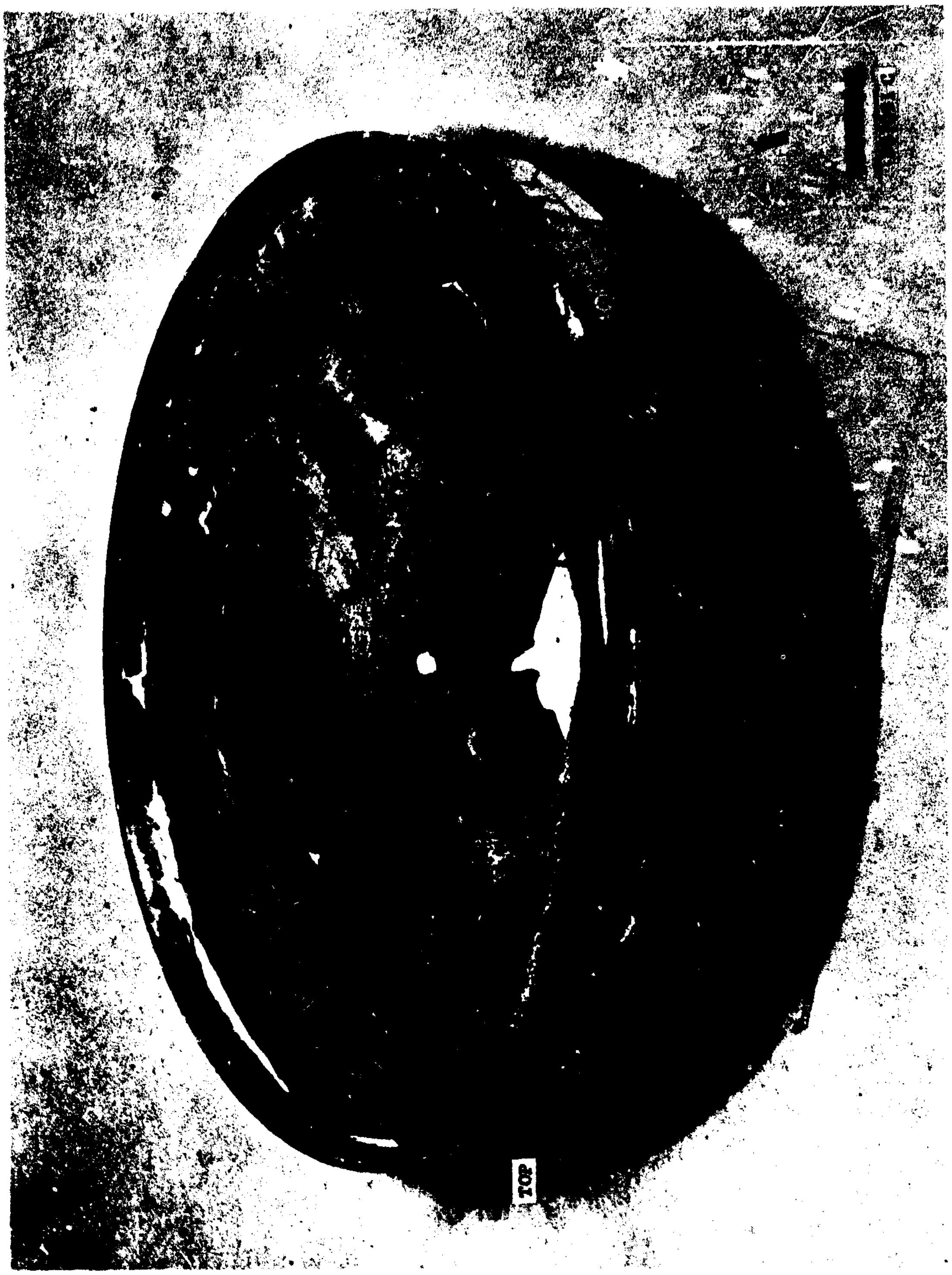

FIGURE 65. AFT CLOSURE INSULATOR DAMAGE - TEST T-13

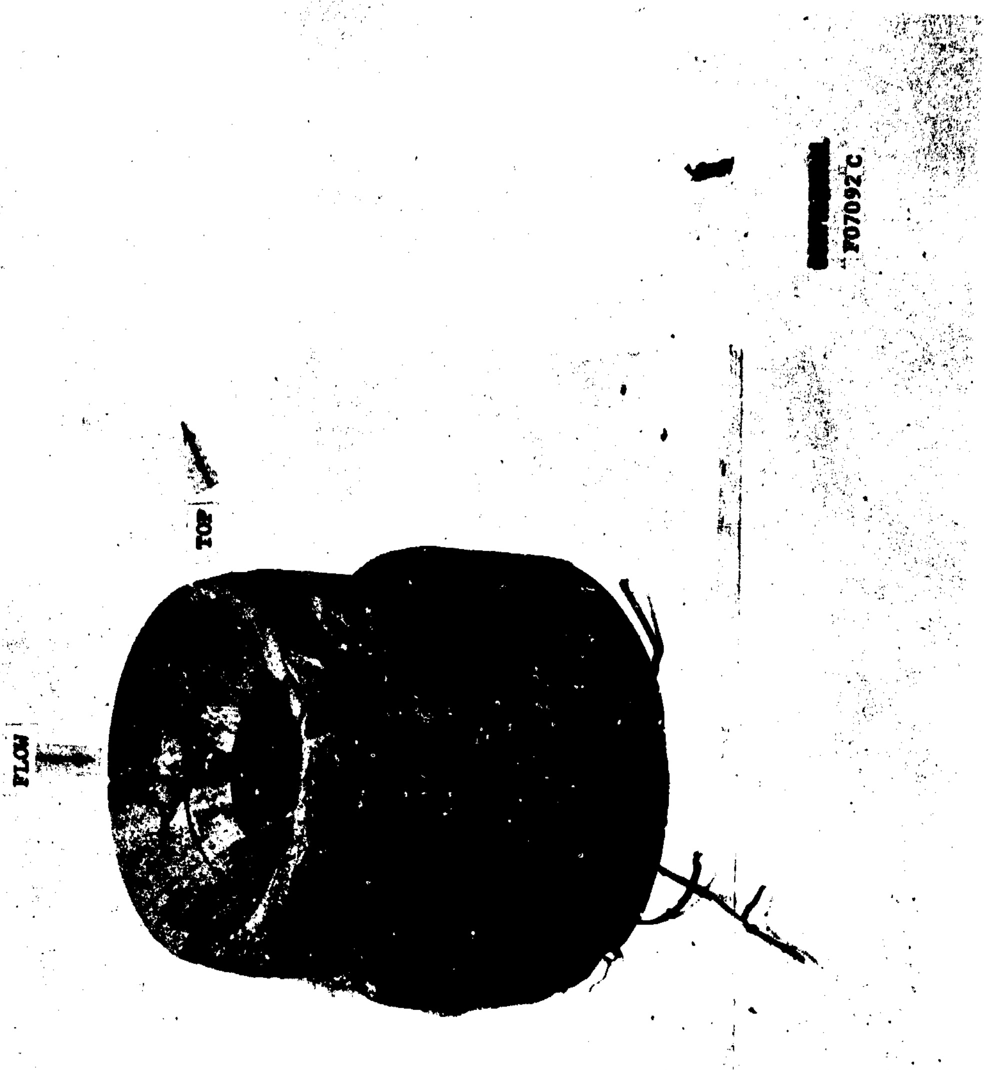
F07092C
TOP
FLOW

FIGURE 66. NOZZLE FROM TEST T-13 - DAMAGED AREA

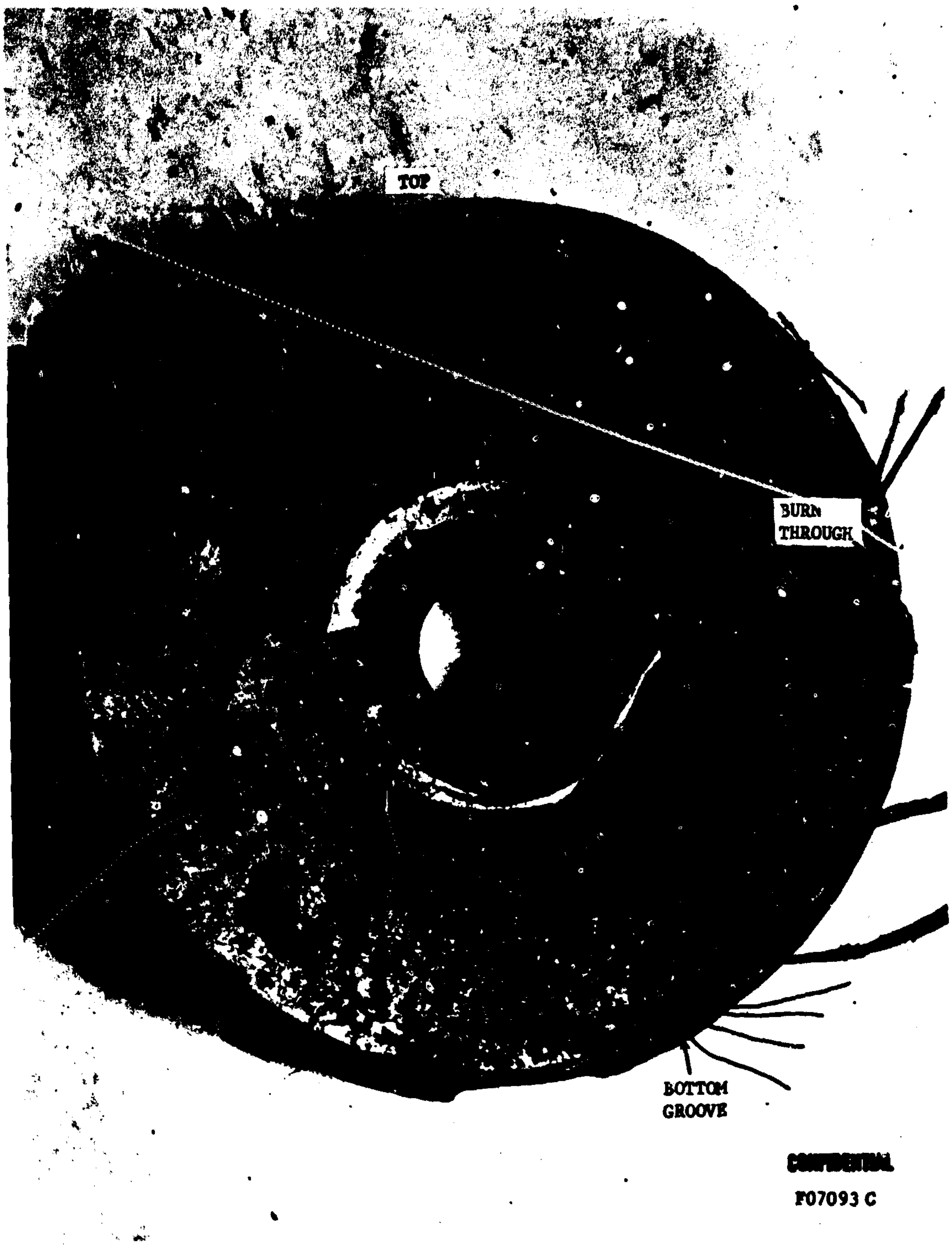
TOP
BURN THROUGH
BOTTOM GROOVE
CONFIDENTIAL
F07093 C

FIGURE 67. NOZZLE FROM TEST T-13 - ENTRANCE CONE VIEW (LOOSE DEPOSITS REMOVED)

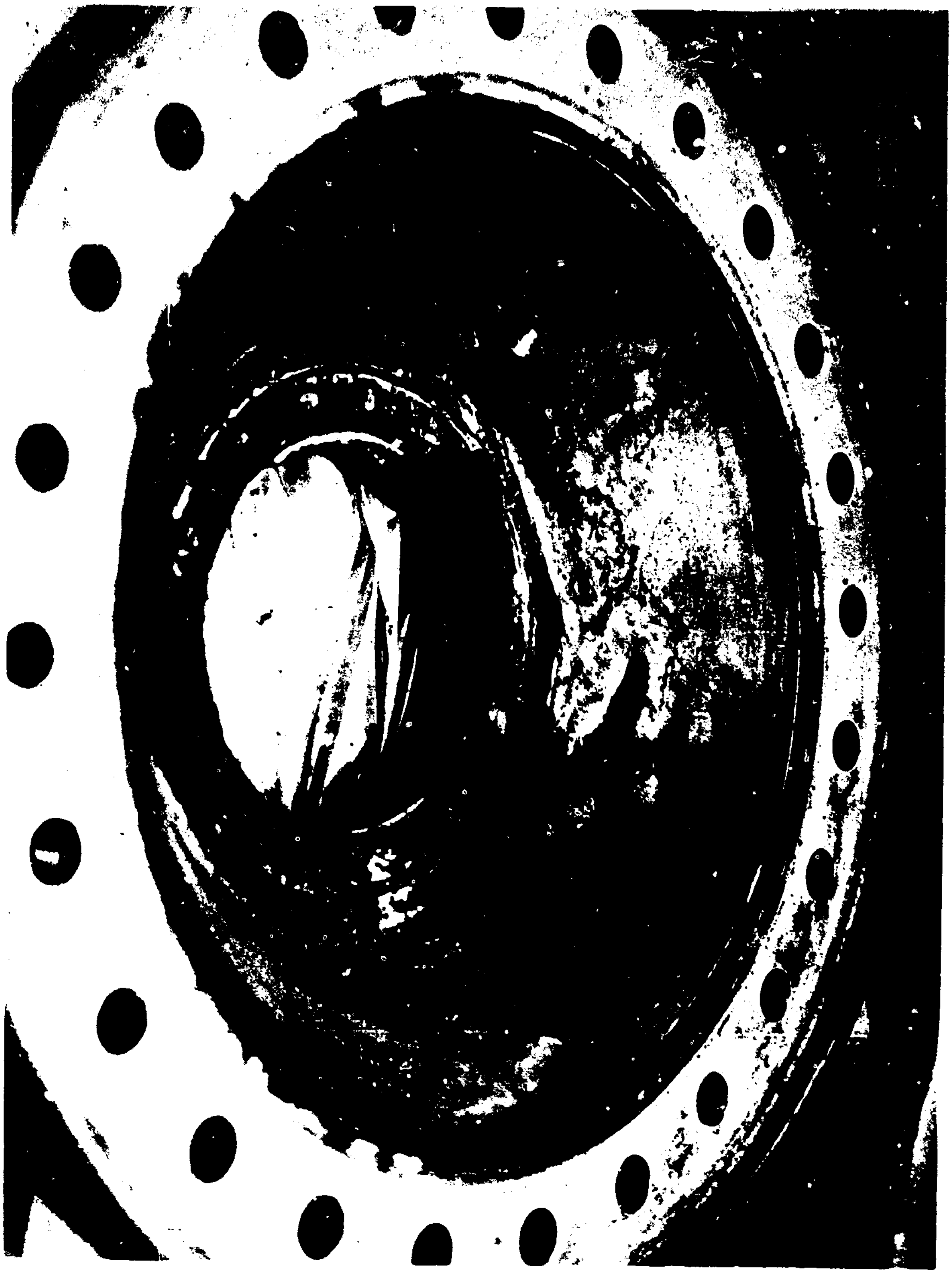

FIGURE 68. STEEL AFT CLOSURE DAMAGE - TEST T-13

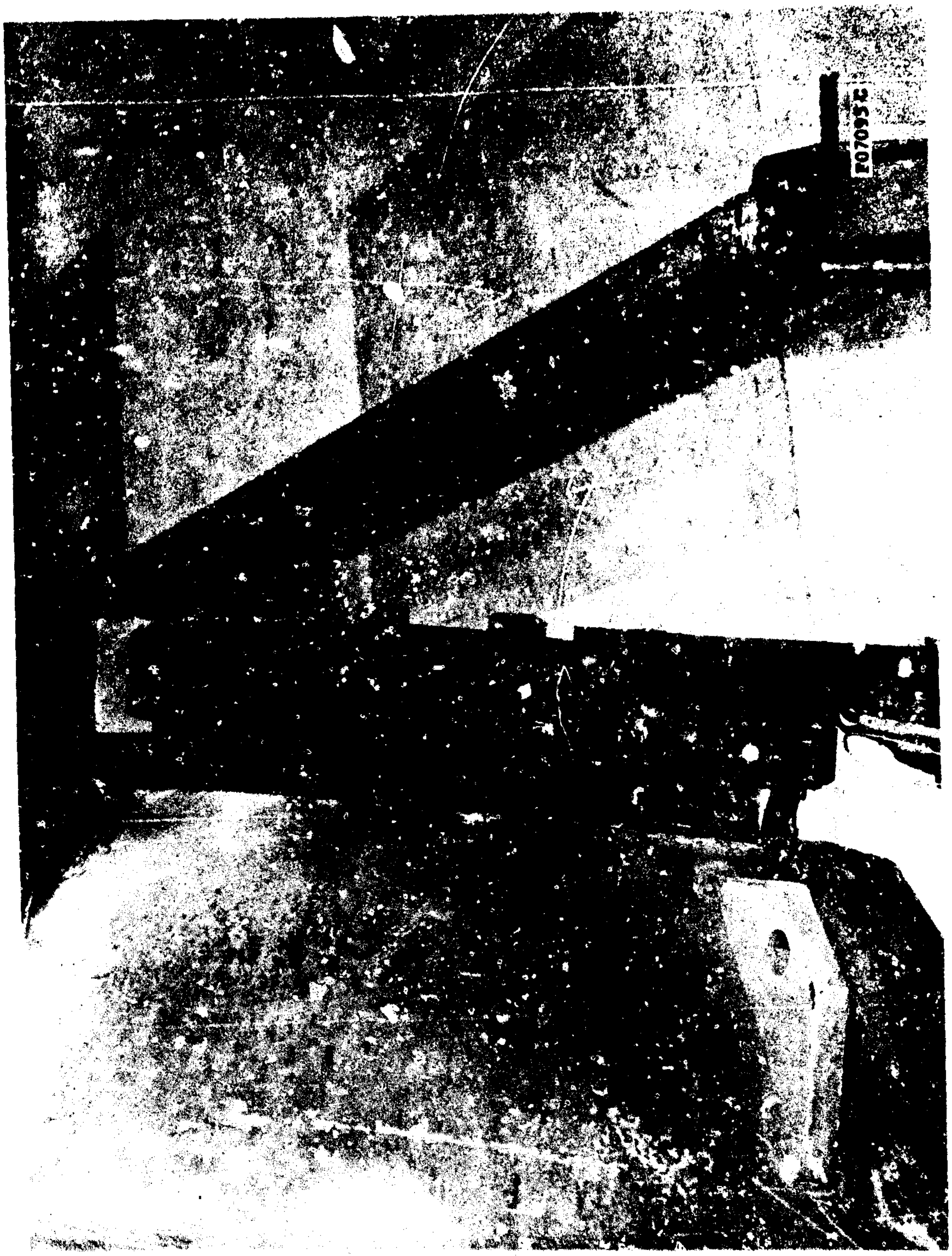

FIGURE 69. NOZZLE END SUPPORT RING DAMAGE - TEST T-13

TABLE XXIII. MOTOR TEST T-13 DEPOSIT ANALYSIS (C)

Sample Number	Sample Location	Composition	
T-13-1	Chamber residue	BeO	60-70%
		β BeO	trace
		Be_2C	15-20
		α Be	2-5
		β Be	2-5
		Graphite	2-5
T-13-2	Residue in pressure port in slot area	BeO	75-85
		Mg_2SiO_4	2-5
		MgO	2-5
		Amorphous carbon	present
		Graphite	2-5
T-13-3	Residue in pressure port opposite slot area and char in the immediate vicinity	BeO	45-50
		Mg_2SiO_4	45-50
		MgO	2-5
		Amorphous carbon	present
		Graphite	2-5
T-13-4	Aft closure, thick deposit and char near nozzle in slot area	BeO	20-25
		Mg_2SiO_4	60-70
		MgO	2-5
T-13-5	Aft closure, black surface residue in groove	BeO	60-70
		Be_2C	20-30
		Amorphous carbon	present
T-13-6	Graphite entrance cone, in groove	BeO	85-90
		Be_2C	2-5
		Mg_2SiO_4	2-5
		Amorphous carbon	present
T-13-7	Graphite entrance cone, brown deposit	BeO	15-20
		Be_2C	15-20
		Graphite	55-65
T-13-8	Throat coating	BeO	90-95
		Graphite	5-10
T-13-9	Spacer area at back, 0.15" thick, left of groove	BeO	75-85
		Be_2C	10-15
		Graphite	5-10

TABLE XXIII. (Continued) (C)

Sample Number	Sample Location	Composition	
T-13-10	Graphite exit cone. Thick (0.15-0.2 inches) white deposit, surface only	BeO	75-85%
		Be_2C	5-10
		Graphite	5-10
T-13-11	Groove in aft closure, approximately opposite throat, black surface deposit	BeO	60-70
		Be_2C	20-30
		Amorphous carbon	present
T-13-12	Groove in outer insulation sleeve of throat insert approximately 1" from trailing edge, black surface deposit	BeO	50-60
		Be_2C	15-20
		Mg_2SiO_4	15-20
		MgO	2-5
		Amorphous carbon	present
		Graphite	10-15

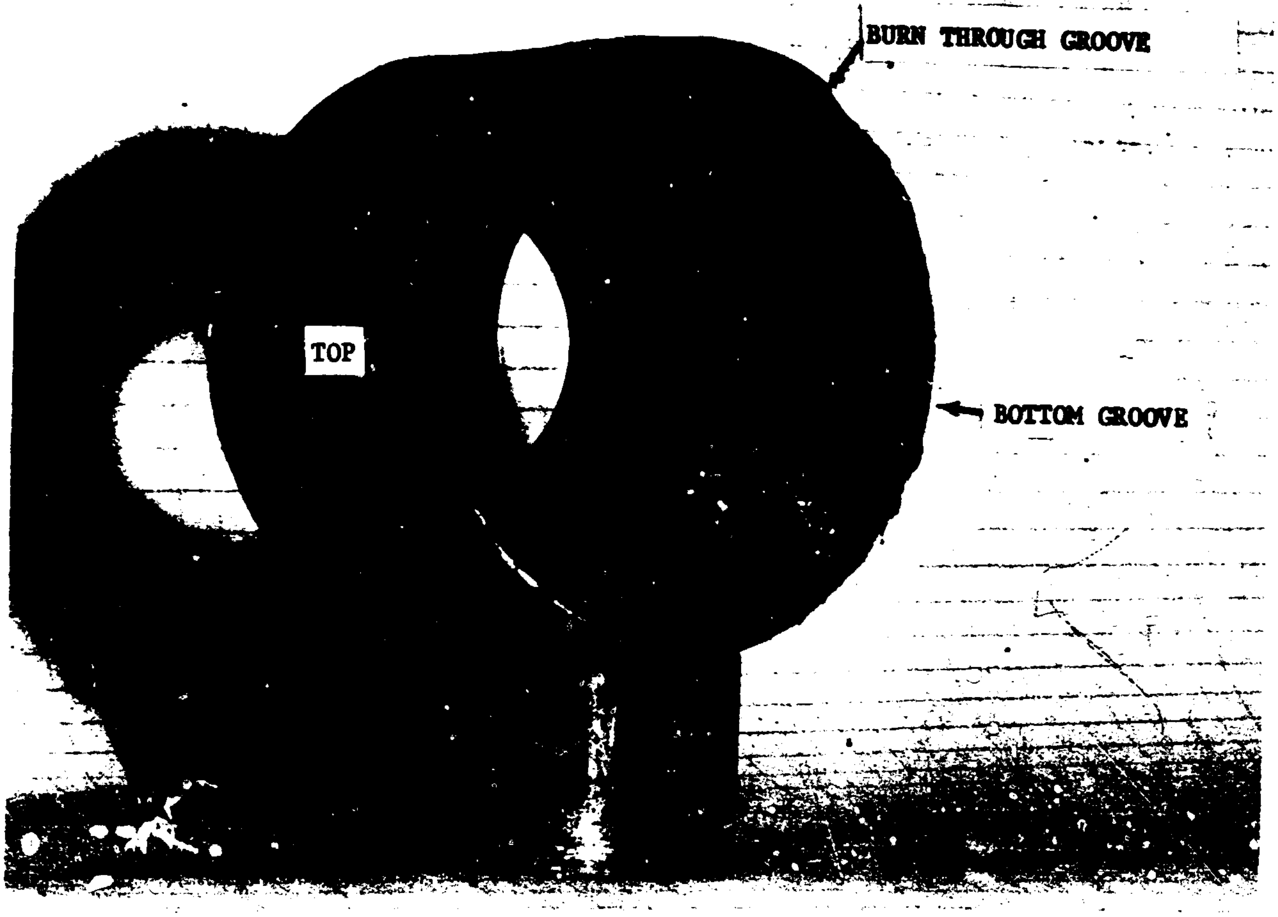
BURN THROUGH GROOVE
TOP
BOTTOM GROOVE

F07280 C

FIGURE 70. PYROLYTIC GRAPHITE THROAT INSERT FROM TEST T-13

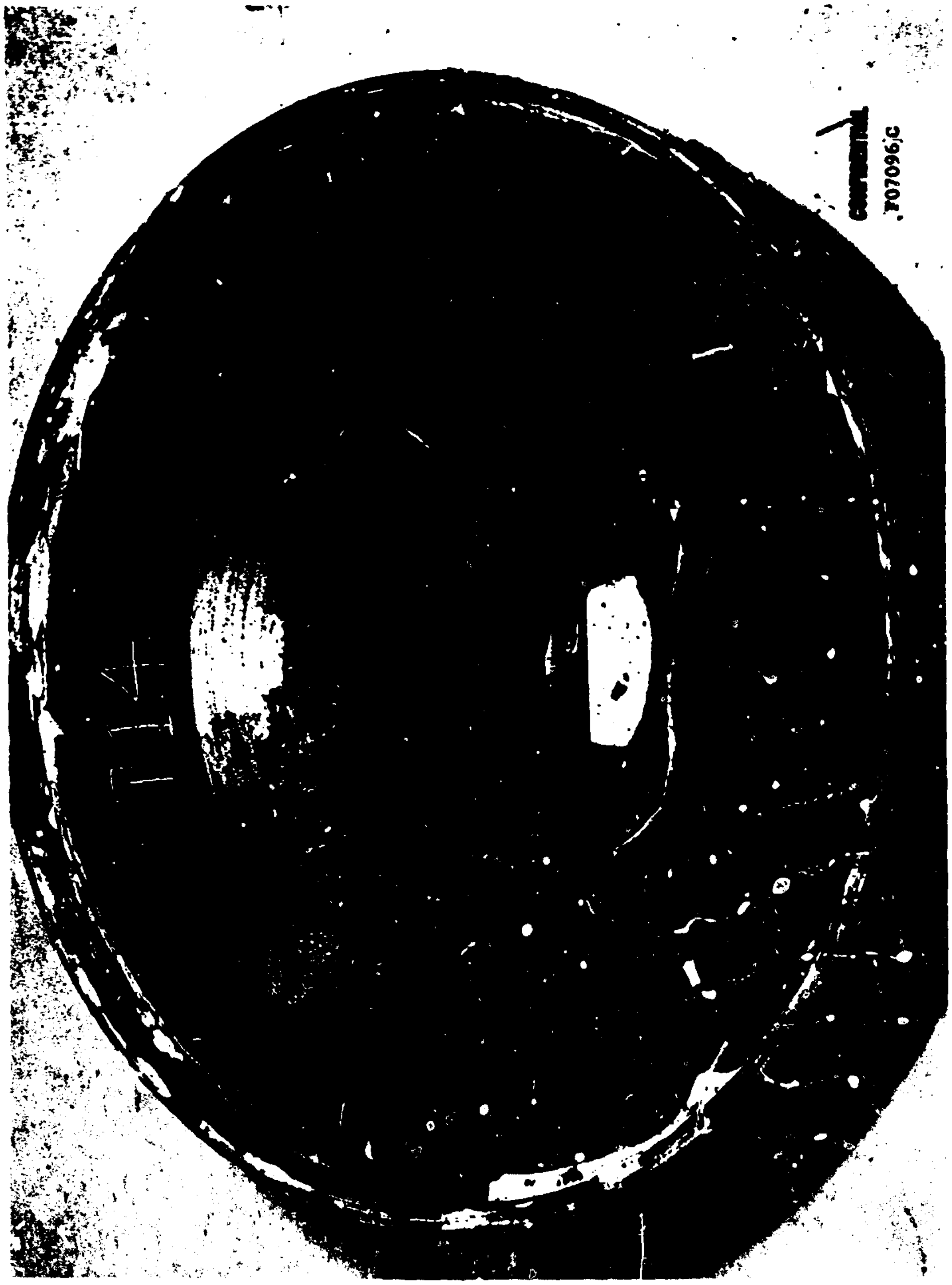

FIGURE 71. AFT CLOSURE INSULATOR FROM TEST T-14 (AS RECEIVED)

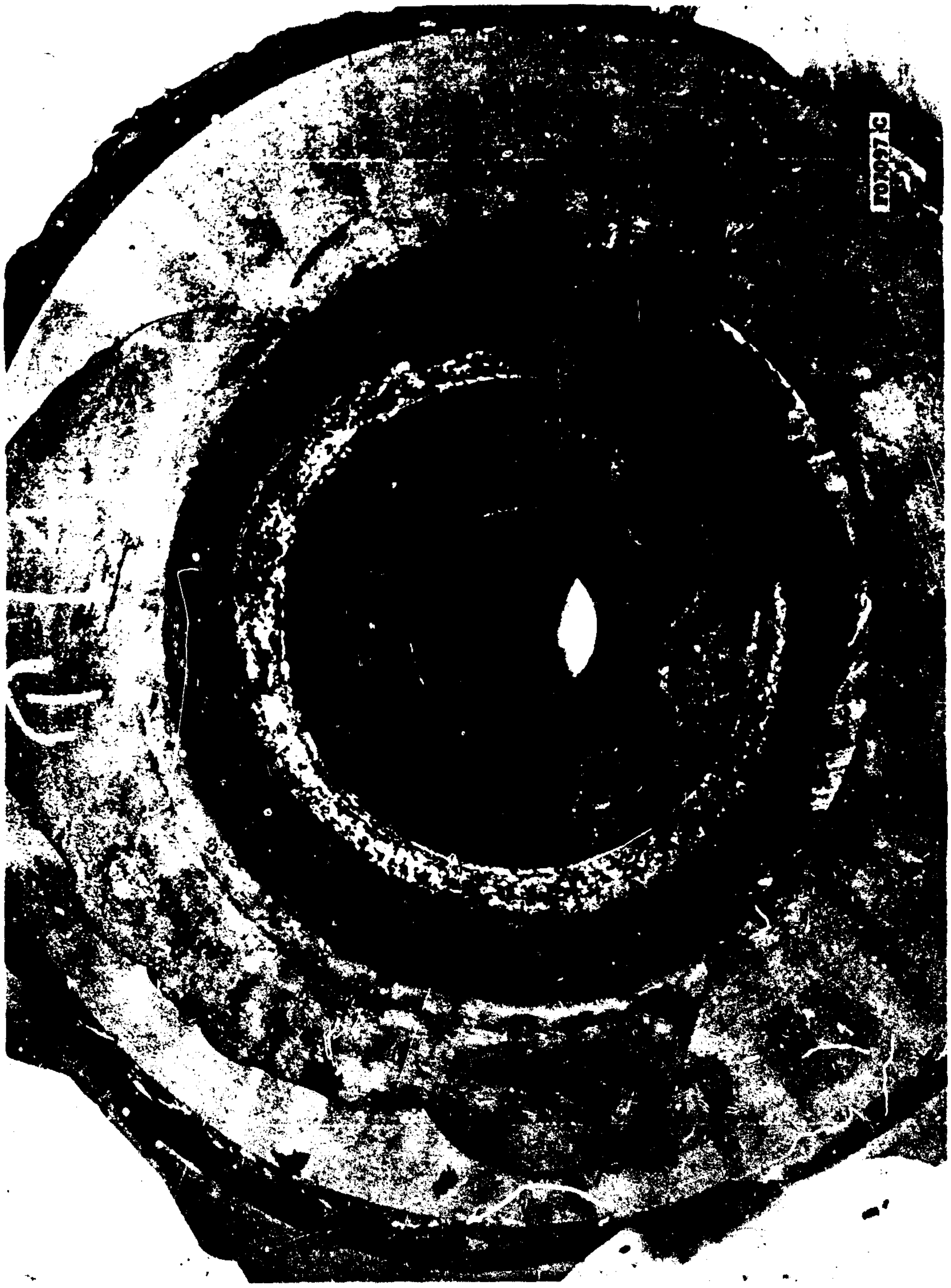

FIGURE 72. NOZZLE FROM TEST T-14 - ENTRANCE CONE VIEW (AS RECEIVED)

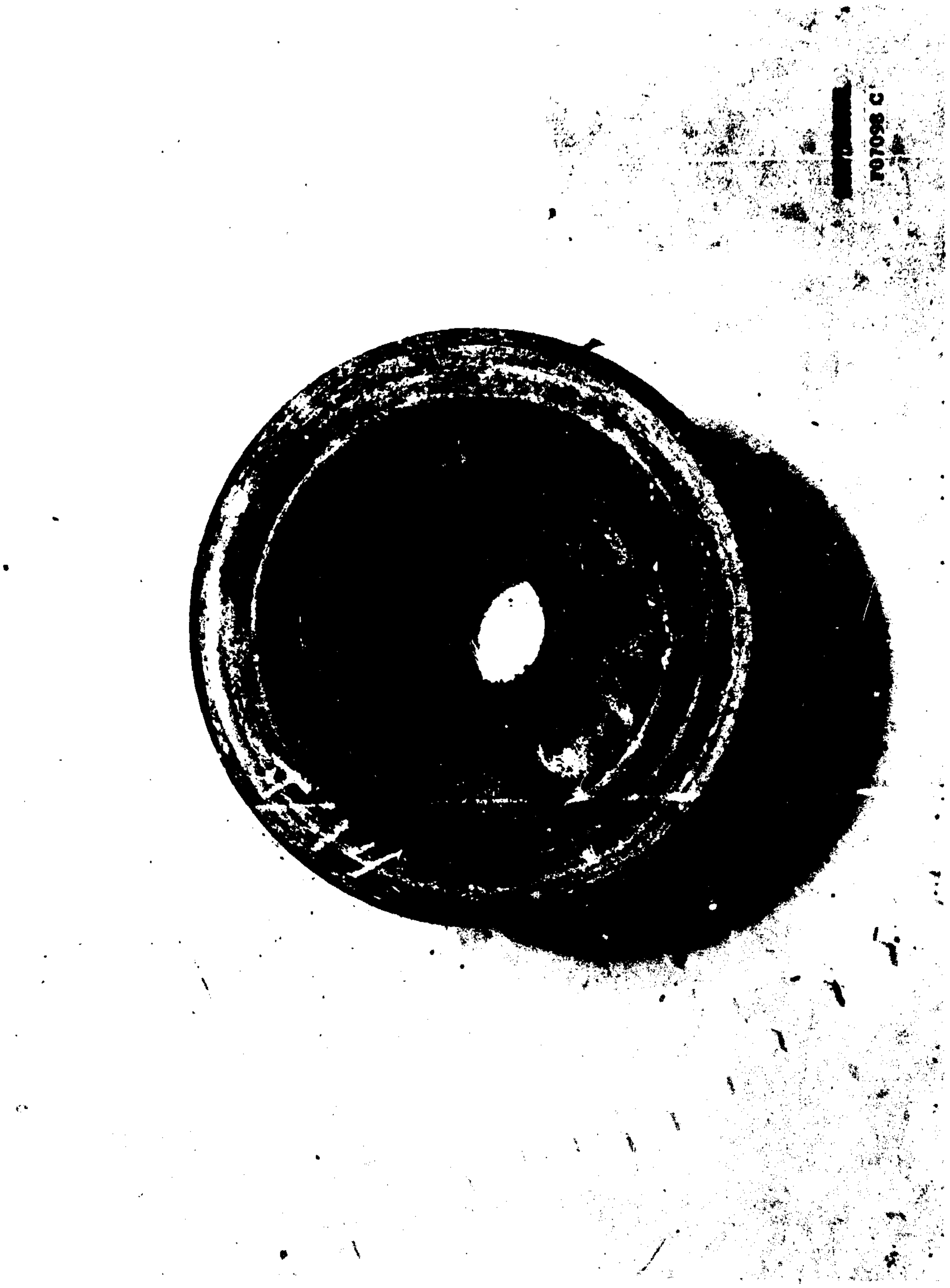

FIGURE 73. NOZZLE FROM TEST T-14 - EXIT CONE VIEW (AS RECEIVED)

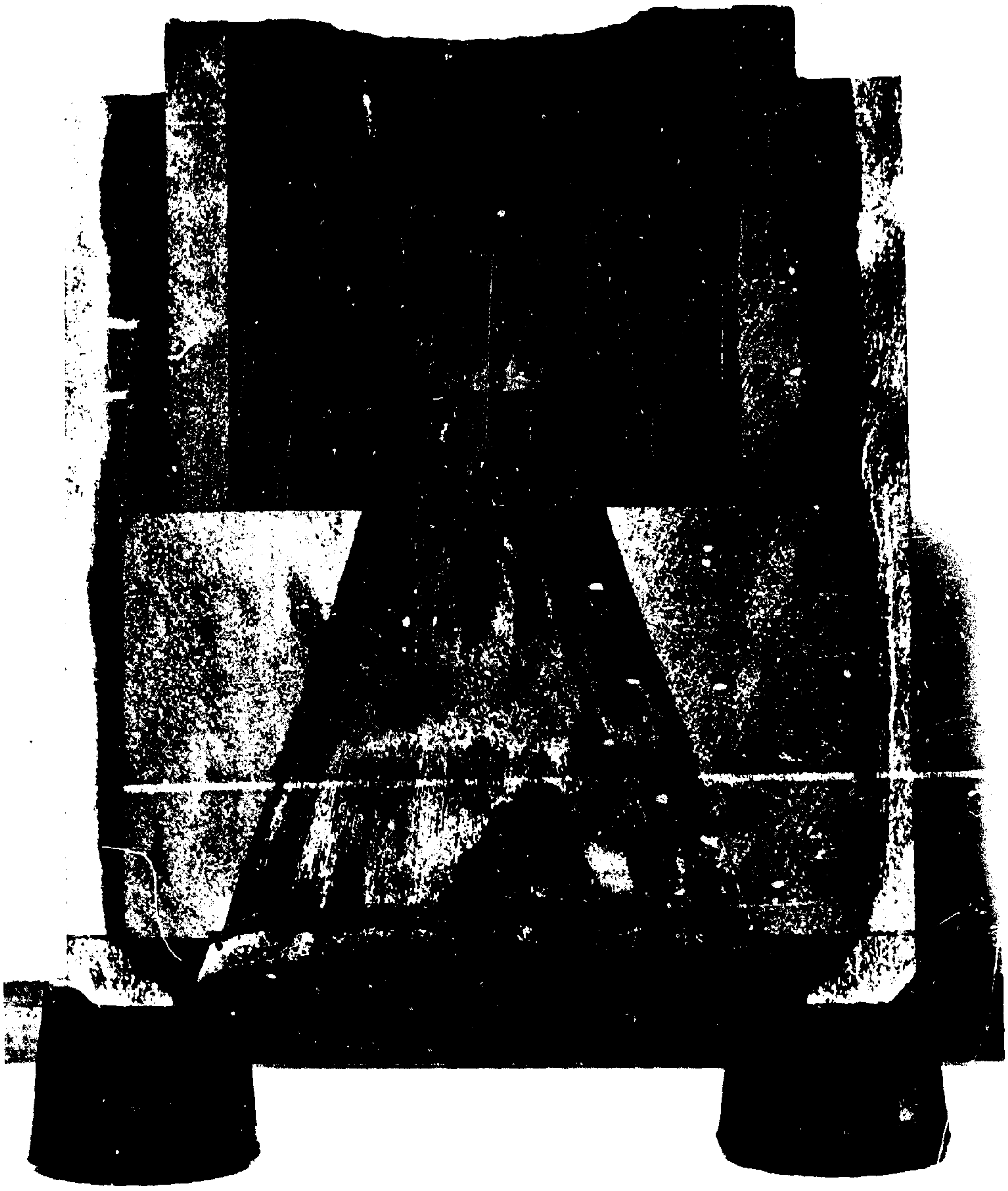
CONFIDENTIAL
F07039 C

FIGURE 74. NOZZLE FROM TEST T-14 - CROSS SECTION

TABLE XXIV. MOTOR TEST T-14 DEPOSIT ANALYSIS (C)

Sample Number	Sample Location	Composition	
T-14-1	Chamber residue	BeO	90-95%
		βBeO	trace
		Graphite	5-10
T-14-2	Aft closure insulator	BeO	50-60
		Be_2C	5-10
		Mg_2SiO_4	25-30
		MgO	5-10
		Amorphous carbon	present
T-14-3	Spacer area, approximately 0.06 inch thick, at flame front	BeO	60-70
		Mg_2SiO_4	2-5
		MgO	trace
		Amorphous carbon	20-25
T-14-4	Graphite entrance cone	BeO	90-95
		Amorphous carbon	5-10
T-14-5	Pyrolytic graphite throat insert washers #1 and #2, thin surface coating	BeO	85-95
		Amorphous carbon	5-10
T-14-6	Deposit at joint between pyrolytic graphite washer and graphite exit cone	BeO	25-30
		Mg_2SiO_4	5-10
		Amorphous carbon	50-60
		Graphite	5-10
T-14-7	Trailing edge of graphite exit cone	BeO	30-40
		Mg_2SiO_4	15-20
		Amorphous carbon	40-50

in the as-received condition. A cross section of the nozzle assembly is shown in Figure 74.

A series of deposits were taken from various areas on the hardware and analyzed by X-ray diffraction. The results are summarized in Table XXIV.

The hardware was in very good condition. There was some loss of material from the flame front surface of the asbestos-phenolic aft closure insulator, but this was very uniform and not serious. All surfaces exposed to the flame had a nearly continuous coating of beryllia or beryllia-melted asbestos. However, in all cases, this coating was very thin and adhered to the substrate. The pyrolytic graphite washer upstream from the throat washer was delaminated, but there was no foreign material found in the crack. There was Mg_2SiO_4 (the residue from melting of asbestos) found on the graphite exit cone indicating that material must have flowed over the throat. There was no evidence of any excessive gouging or loss of material from any of the nozzle surfaces.

(h) (C) Motor Test T-15

Motor Test T-15 used a slotted, internal burning, beryllium propellant grain (Type III). The aft closure is shown in Figure 75 and the nozzle is shown in Figures 76 and 77 in the as-received condition. The entrance cone is shown in Figure 78. A cross section of the nozzle is shown in Figure 79.

A series of deposits were taken from various areas on the hardware and analyzed by X-ray diffraction. The results are summarized in Table XXV.

In general, the hardware was in very good condition. There was some loss of material from the aft closure where it was exposed to the flame, but it was not excessive. The deposits on the aft closure were found to contain beryllium carbide which indicates the beryllia was in contact with the charred insulator for a relatively long period of time. The molded asbestos-phenolic insert, which was upstream from the graphite entrance cone, was completely eroded through in the slot area. The graphite entrance cone was cracked in 2 places, in line with and opposite the grain slot. The graphite entrance cone was also grooved in the slot area. The graphite entrance cone, pyrolytic graphite throat insert and the graphite exit cone all had a fairly continuous coat of beryllia. There was a groove in the pyrolytic graphite throat insert which was in line with the slot in the grain. This groove extended to the graphite exit cone. There was also a groove opposite the grain slot which extended through the first two pyrolytic graphite washers. Four of the pyrolytic graphite washers were delaminated, with the 3 upstream washers being badly delaminated. There did not appear to be any detrimental effects from the delaminations, however. The graphite exit cone was in excellent condition.

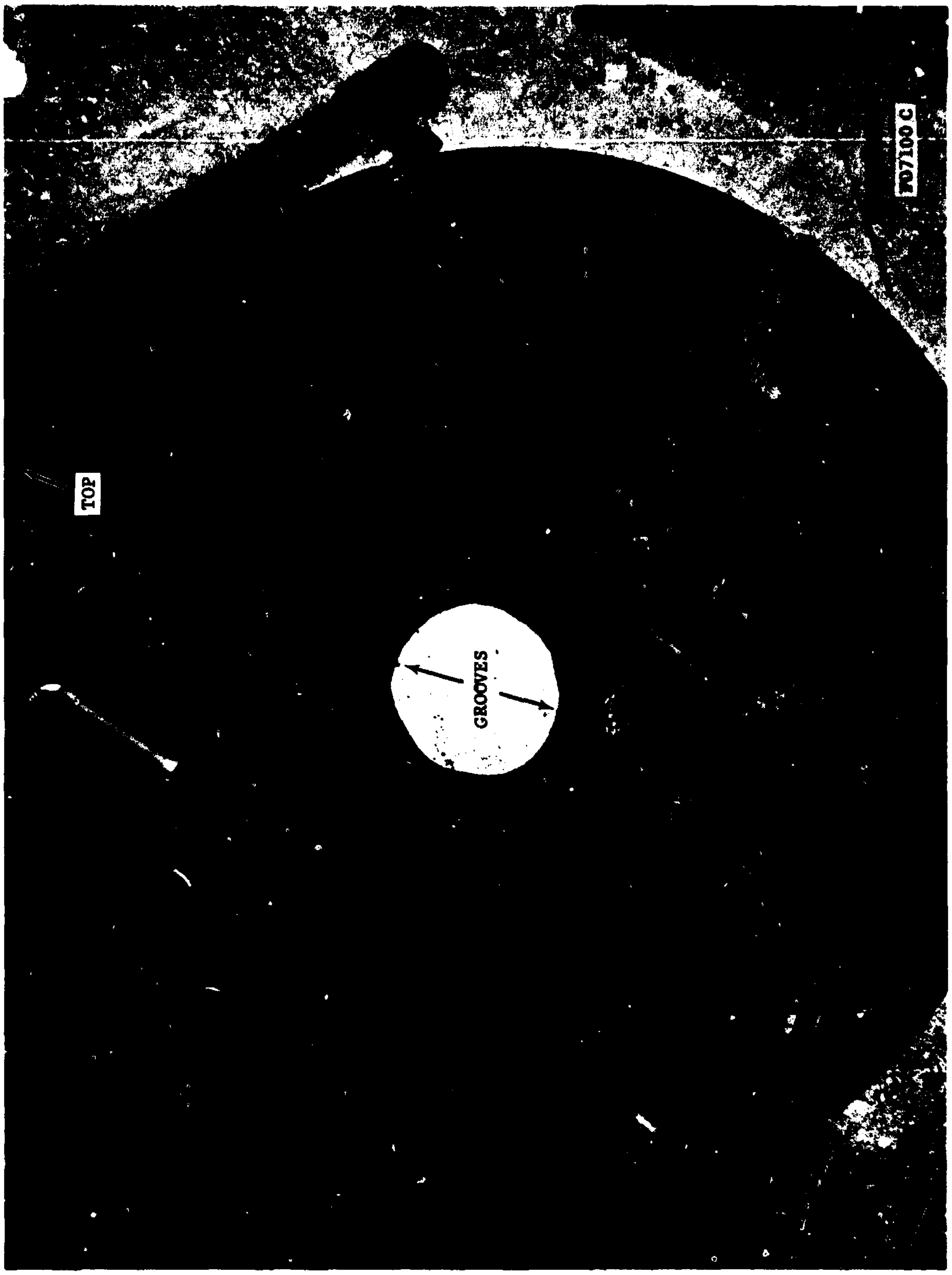
F07100 C
TOP
GROOVES

FIGURE 75. AFT CLOSURE INSULATOR - TEST T-15

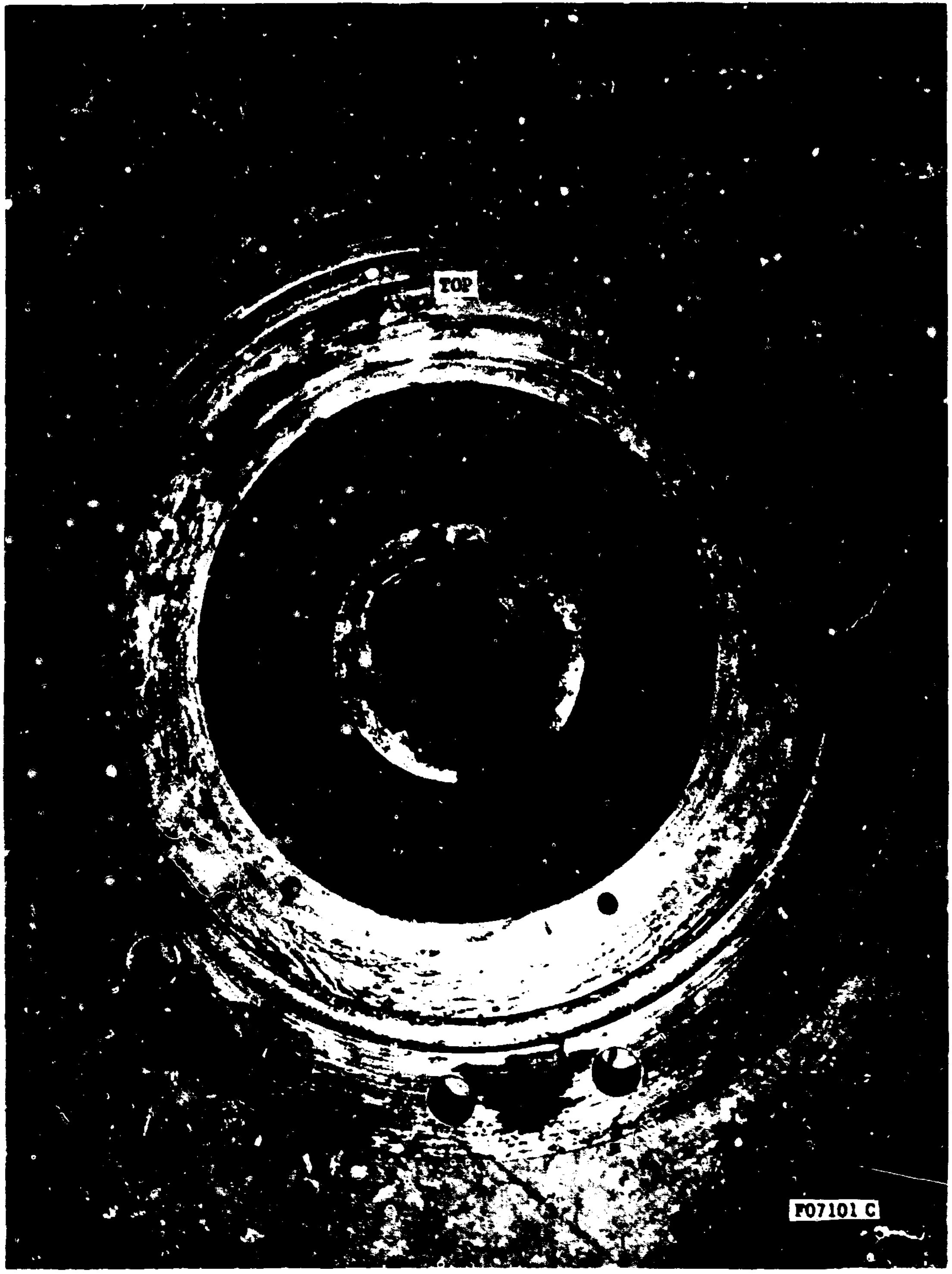
TOP
F07101 C

FIGURE 76. NOZZLE FROM TEST T-15 - THROAT APPROACH VIEW

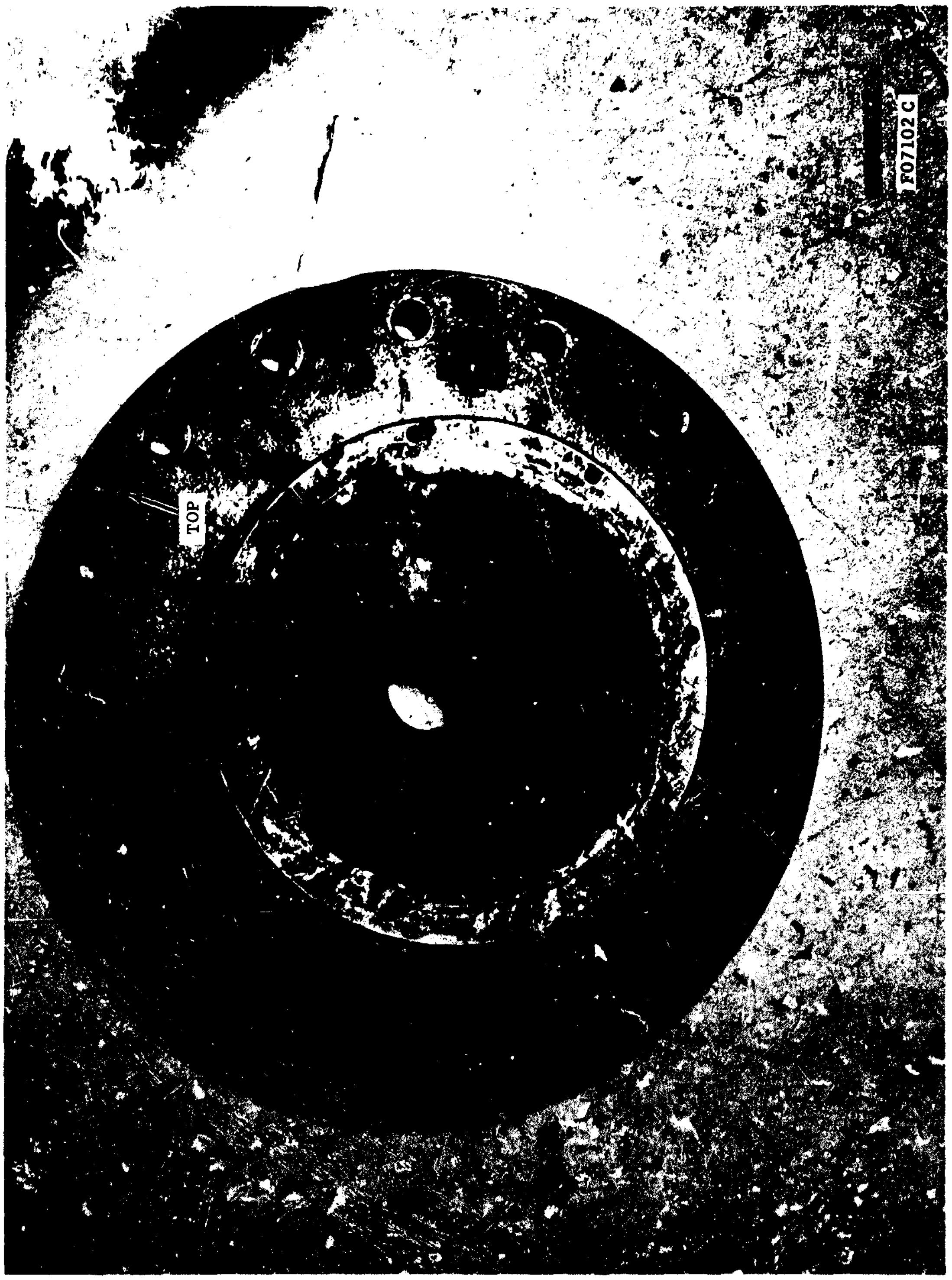
F07102 C
TOP

FIGURE 77. NOZZLE FROM TEST T-15 - EXIT CONE VIEW

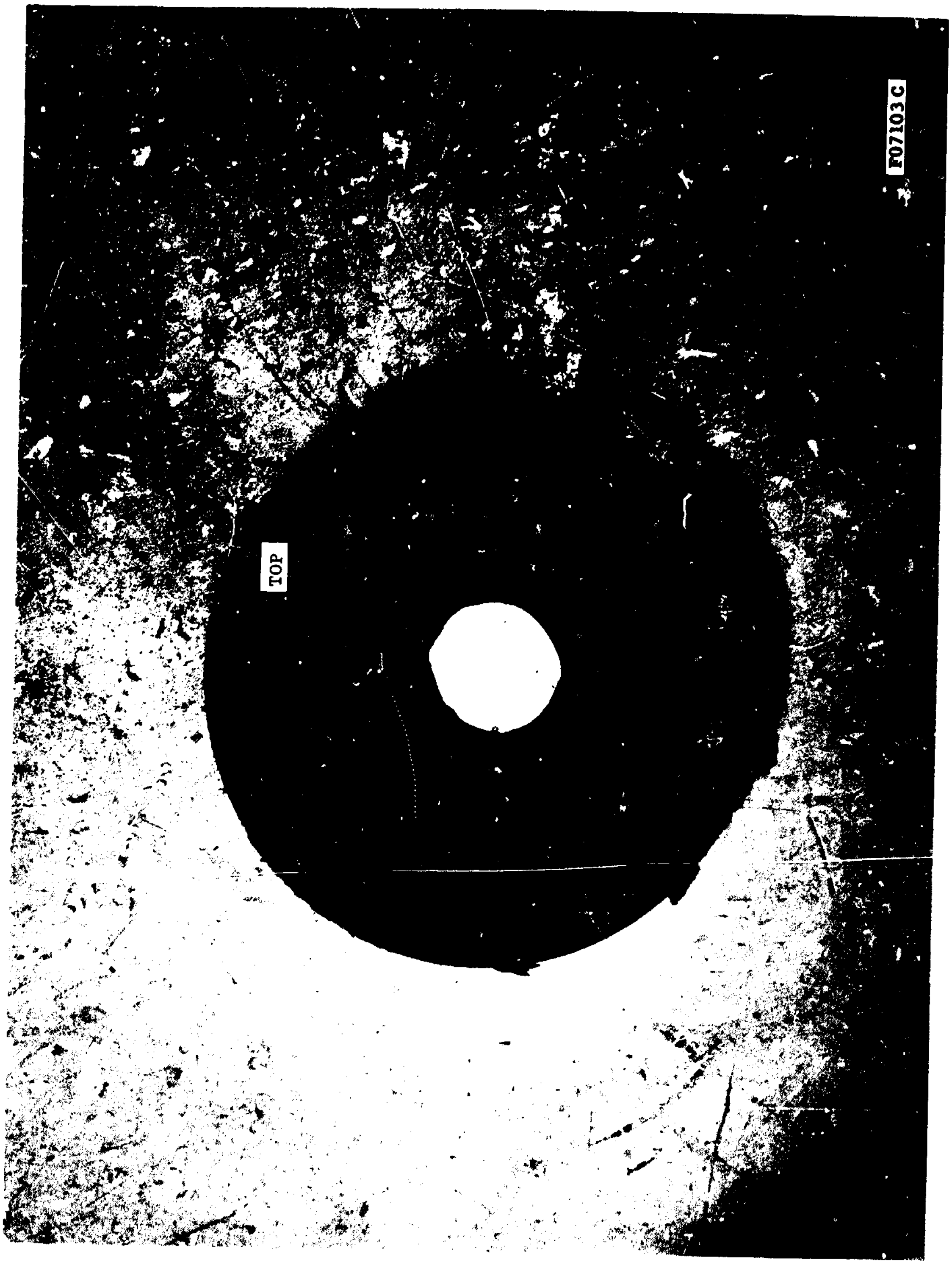
F07103 C
TOP

FIGURE 78. ATJ GRAPHITE ENTRANCE CONE - TEST T-15

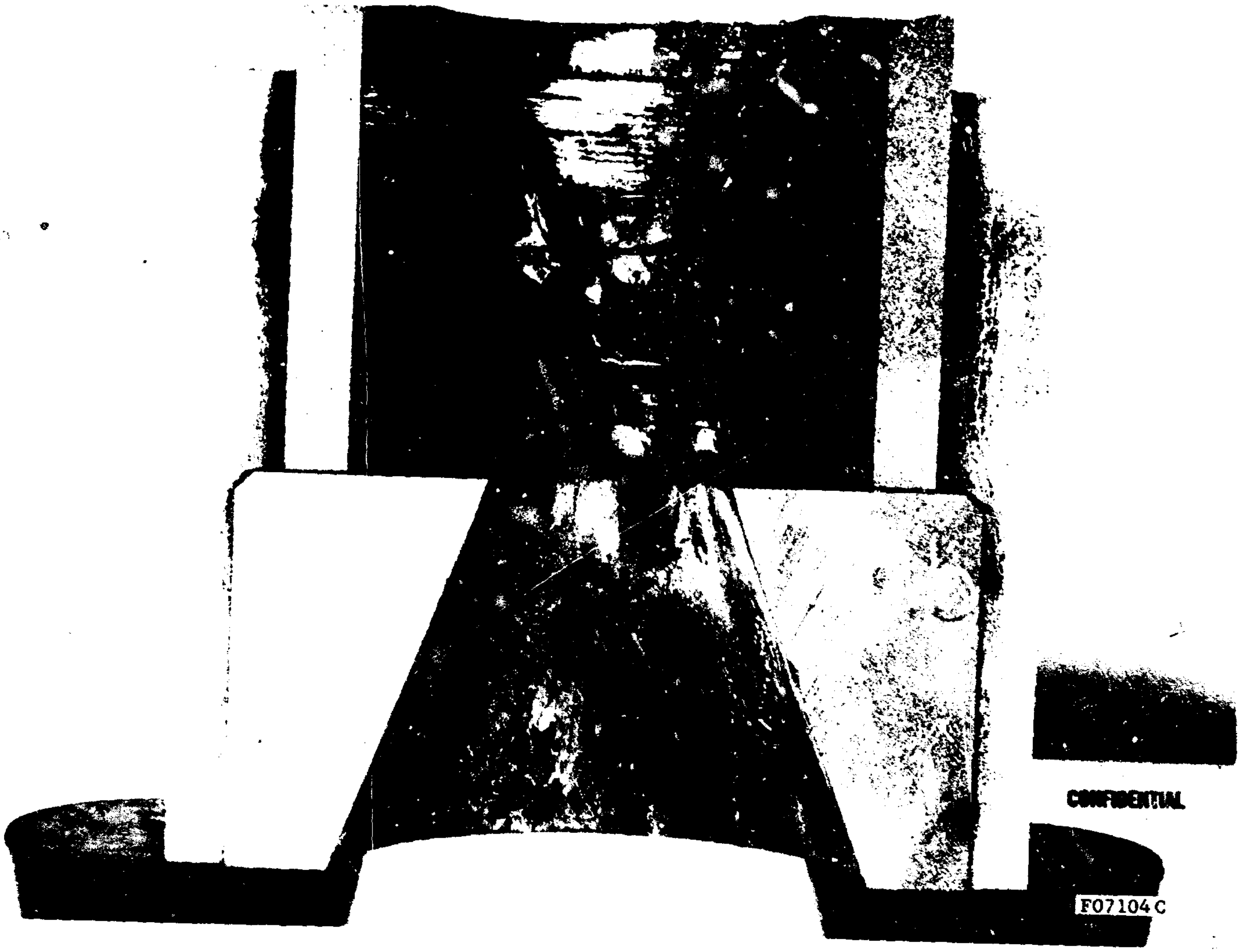
CONFIDENTIAL
F07104C

FIGURE 79. NOZZLE FROM TEST T-15 - CROSS SECTION

TABLE XXV. MOTOR TEST T-15 DEPOSIT ANALYSIS (C)

Sample Number	Sample Location	Composition	
T-15-1	Chamber residue	BeO Amorphous carbon Graphite	95+% present trace
T-15-2	Aft closure, slot area, near grain surface deposit only	BeO Be_2C Mg_2SiO_4 MgO Graphite	80-90 2-5 2-5 trace 2-5
T-15-3	Aft closure, slot area near nozzle, surface deposit and char	BeO Be_2C Mg_2SiO_4 Graphite	80-90 5-10 2-5 2-5
T-15-4	Aft closure, edge near grain, metallic appearing deposit	Be_2C Amorphous carbon	50 50
T-15-5	Graphite entrance cone, near slot area	BeO Be_2C Mg_2SiO_4 Amorphous carbon Graphite	50 trace trace trace 2-4
T-15-6	Convergent face of pyrolytic graphite washers, white surface deposit	BeO Amorphous carbon	80-90 present
T-15-7	Graphite exit cone	BeO	95+

(i) (C) Motor Test T-16

Motor Test T-16 was the first test of a tungsten throat insert. This test was designed specifically to compare the performance of tungsten with pyrolytic graphite in the throat area under identical conditions of propellant type, configuration, throat size and firing conditions (see Test T-9). The tungsten used was arc cast, rolled and extruded into a bar and machined to shape. During the machining, the tungsten insert developed an axial crack. However, it was decided to proceed with the test and observe any detrimental effects which could be related to the crack. Except for the tungsten insert itself, there was no significant difference in the appearance of the aft closure insulator and nozzle from this test relative to Test T-9. Consequently, photographs are not presented. Figure 80 shows one half of the tungsten insert after sectioning. Additional work with the tungsten was discussed in Section 3.2.

A series of deposits were taken from various areas on the hardware and analyzed by X-ray diffraction. The results are summarized in Table XXVI.

The condition of the hardware suggested that the test conditions between T-9 and T-16 were very similar. The aft closure insulator was in the same condition; the char regression was approximately 0.2 inch for the area actually exposed to the flame. The polycrystalline graphite parts were coated with beryllia and asbestos residue.

The tungsten throat insert was in good condition. There were no obvious detrimental effects from using a cracked insert. The original axial crack ran the full length of the back surface but did not extend to the flame surface except at the trailing edge. There was no evidence of any gas flow through the crack. A 360°, circumferential crack developed during the test. This crack was approximately at the throat section and did not extend to the flame front. The flame side contour was covered with beryllia. Tungsten carbide was found on the surface of the insert. There was also tungsten carbide found on the graphite exit cone. There was no grooving or irregular loss of material from the tungsten. It was visually apparent that some flow of the flame side surface had occurred. The effected areas started at the upstream edge, had a stream pattern, and few extended to or beyond the geometric throat. These surface patterns are presumed to be the result of surface carburization with minimum flow.

(j) (C) Motor Test T-17

Motor Test T-17 was designed to be identical to Test T-16 except for the substitution of carbon cloth-phenolic for the ATJ graphite as the entrance cone material. This test was designed to show the relative performance characteristics of these two entrance materials and their influence on the tungsten throat insert performance under similar test conditions. Test T-20 also used a carbon cloth entrance section and otherwise differed from

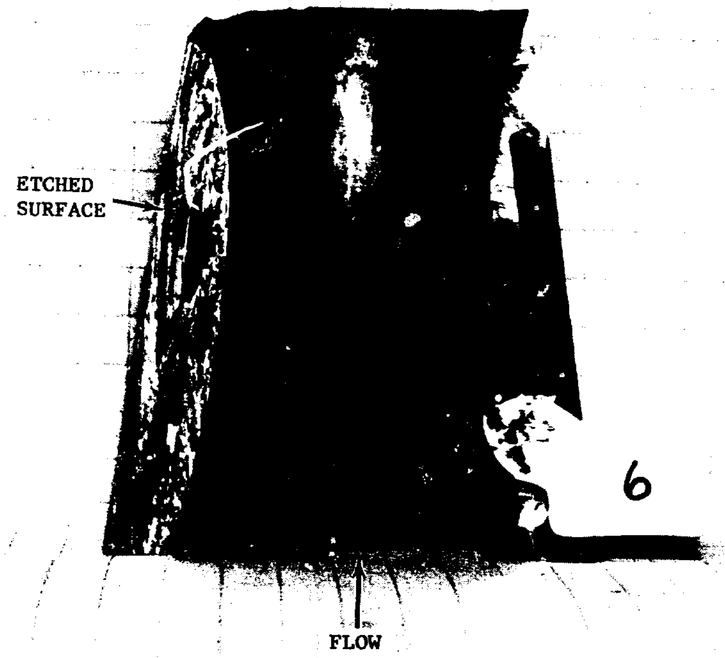
ETCHED SURFACE
6
FLOW

CONFIDENTIAL
F07110 C

FIGURE 80. TUNGSTEN INSERT - TEST T-16

TABLE XXVI. MOTOR TEST T-16 DEPOSIT ANALYSIS (C)

Sample Number	Sample Location	Composition	
T-16-1	Chamber residue	BeO	80-85%
		Be_2C	10-15
		Mg_2SiO_4	2-5
		Carbon	2-5
T-16-2	Aft closure, surface deposit and char	BeO	25-35
		Be_2C	10-15
		MgO	2-5
		Mg_2SiO_4	40-50
		Carbon	10-15
T-16-3	Residue in pressure port and surrounding char	BeO	60-70
		Be_2C	10-15
		MgO	2-5
		Mg_2SiO_4	5-10
		Carbon	5-10
T-16-4	Graphite entrance cone, hard surface deposit	BeO	65-75
		Be_2C	15-20
		MgO	2-5
		Carbon	5-10
T-16-5	Back edge of spacer area, hard black deposit, 0.020-0.022 inches thick	$2(Fe_{0.94}Mg_{0.06})OSiO_2$	
T-16-6	Surface, deposit on pyrolytic graphite washer	BeO	60-70
		Be_2C	10-15
		Pyrolytic graphite	15-20
T-16-7	Surface deposit, trailing edge of tungsten insert	BeO	60-70
		W	2-5
		WC	20-25
		W_2C	10-15
T-16-8	Graphite exit cone	BeO	20-30
		W	5-10
		WC	50-60
		W_2C	10-15
		MgO	2-5
		Carbon	5-10

Test T-17 only in the throat heat sink material. The tungsten used for the throat insert was from the same billet as used for Test T-16, and the insert was also cracked during machining. The insert is shown in Figure 81 before the test and the crack can be seen at the trailing edge. The insert is shown in Figures 82 and 83 after the test where the same crack can be seen. The nozzle inlet section is shown in Figure 84 in the as-received condition. A cross section of the tungsten insert is shown in Figure 85, with essentially all the deposits in place as received. Figure 86 shows a cross section of the tungsten insert after the deposit had been cleaned off. A cross section of the carbon cloth inlet section is shown in Figure 87.

A series of deposits were taken from various areas on the hardware and analyzed by X-ray diffraction. The results are summarized in Table XXVII.

This test also showed that there were no harmful side effects from using a cracked tungsten insert. There was no evidence of excessive gas flow in the cracked area. There was a second crack which developed during the test. This was a circumferential crack in the back surface at approximately the throat section which extended half way through the wall thickness. There was a beryllia deposit on about 25% of the flame side contour. There was a wide, shallow groove in the convergent face of the insert that extended nearly to the throat. The surface of the insert surrounding the groove was tungsten carbide. In the grooved area, the material had a definite appearance of melting. The melted material was tungsten carbide and beryllia. There was also tungsten carbide found on the polycrystalline graphite exit cone.

The grooved area appeared to be at a more advanced stage of carbide formation and flow than that observed on the insert from Test T-16. It is believed that this is due to the carbon cloth-phenolic entrance section used on Test T-17. The carbon cloth pyrolysis gases are thought to be the primary source of the carbon reaching the tungsten surface. The entrance cone was fairly clean with only occasional beryllia deposits. During cool-down, the carbon cloth moved into the thermal expansion gap, exposing the face of the pyrolytic graphite washer. This movement has prevented the accurate determination of the carbon cloth erosion.

(k) (C) Motor Test T-18

Motor Test T-18 used a submerged nozzle with a tungsten throat insert. This test was designed to provide a materials performance comparison with Test T-12, which was similar except that a slotted grain and pyrolytic graphite throat section were used. The throat insert was machined from the same tungsten billet as Test T-16 and T-17. This insert did not develop cracks during machining. Almost none of the aft closure insulator was exposed to the flame during the test and is not shown. The nozzle nose cap and entrance section are shown in Figure 88 after removal of the carbon soot. The sectioned tungsten insert is shown in Figure 89 with the

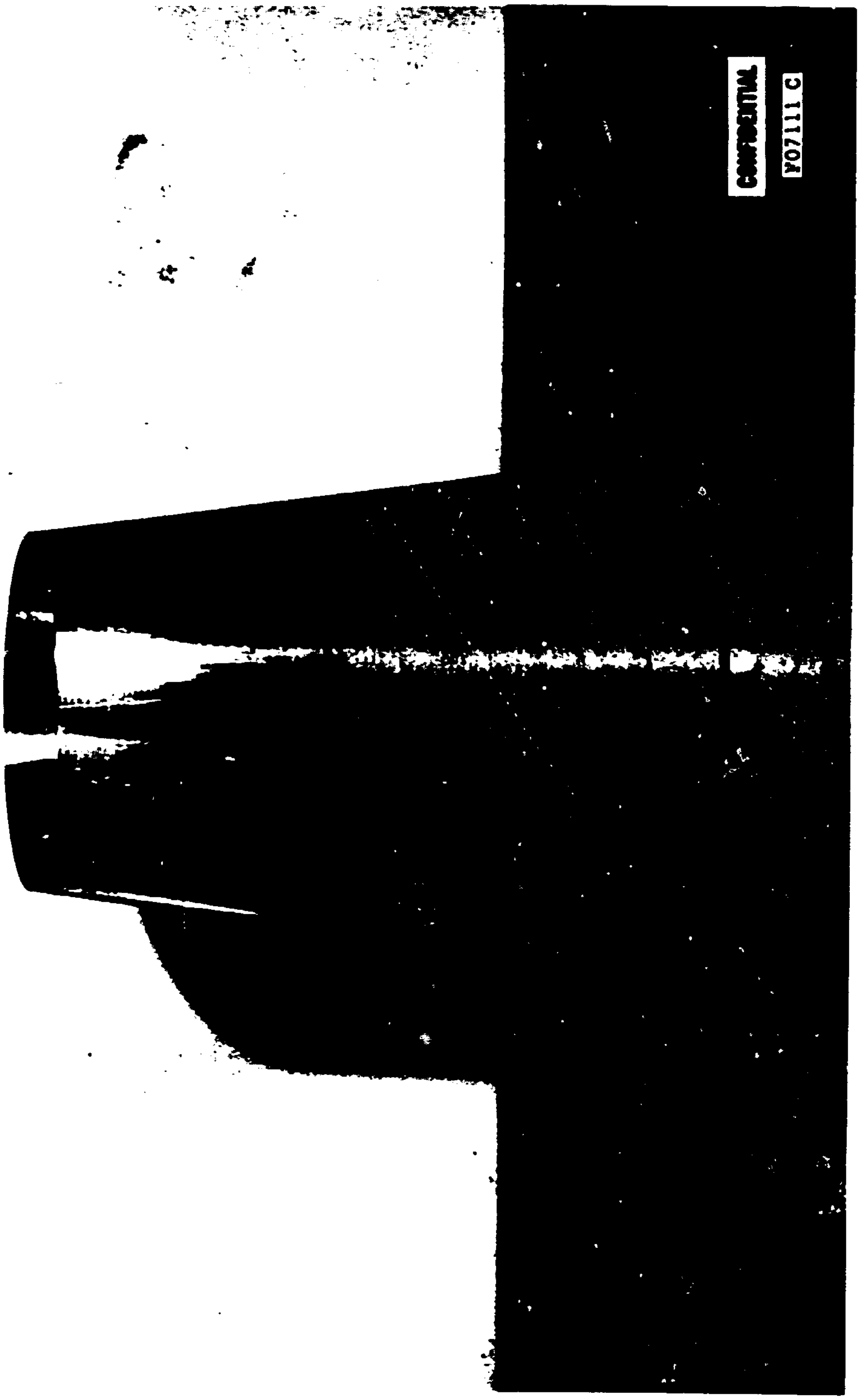
CONFIDENTIAL
F07111 C

FIGURE 81. TUNGSTEN INSERT FOR TEST T-17 - BEFORE TEST

FIGURE 82. TUNGSTEN INSERT FROM TEST T-17 - AFTER TEST (TRAILING EDGE)

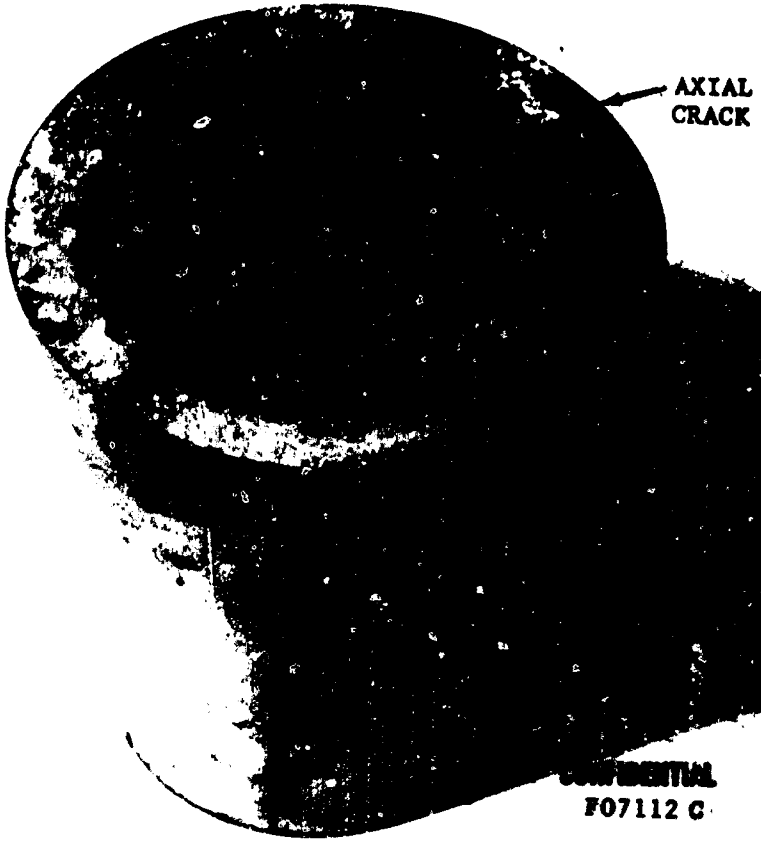
AXIAL CRACK
CONFIDENTIAL
F07112 C

FIGURE 83. TUNGSTEN INSERT FROM TEST T-17 - AFTER TEST (LEADING EDGE)

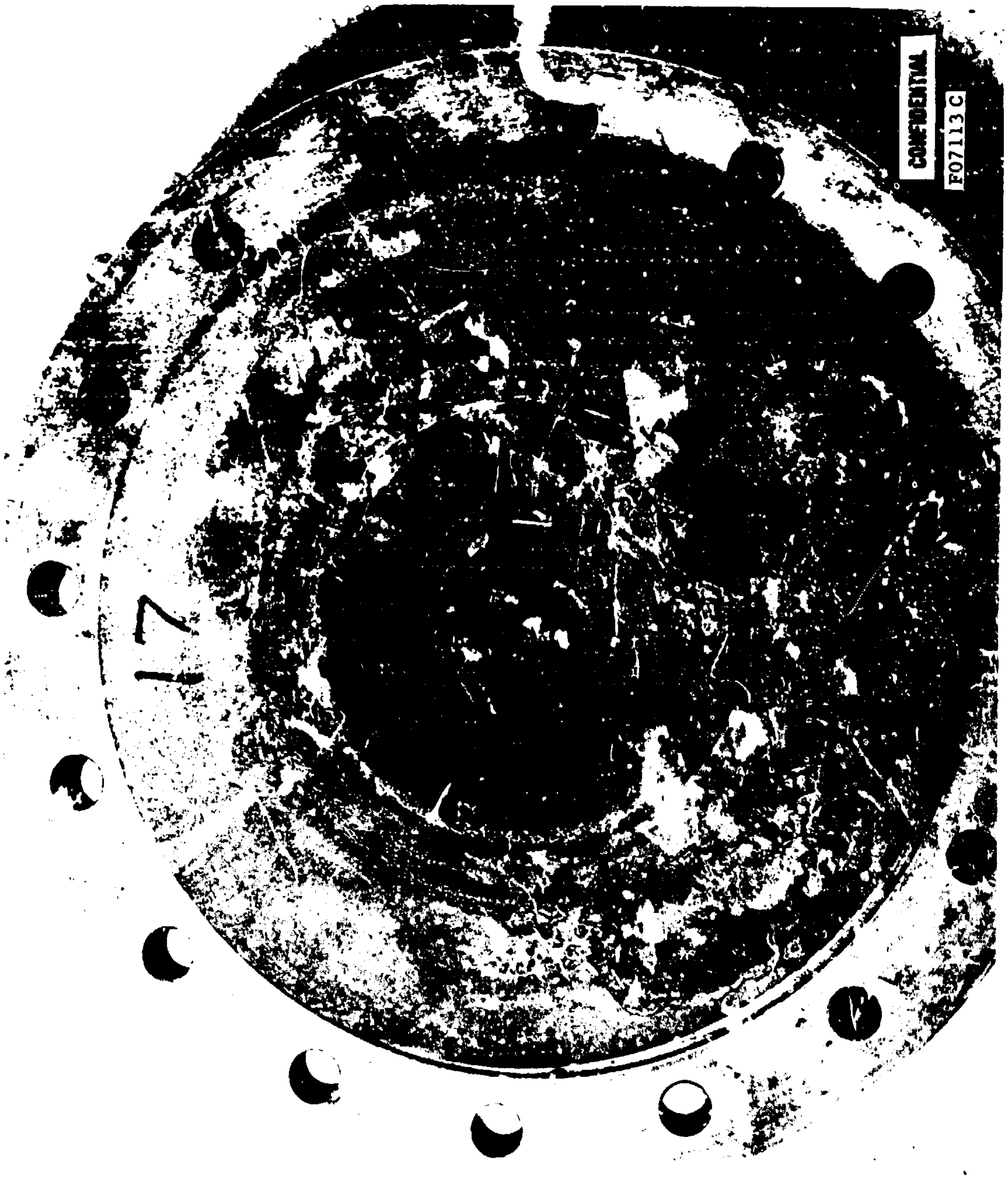
CONFIDENTIAL
F07113 C
17

FIGURE 84. NOZZLE FROM TEST T-17 - ENTRANCE VIEW

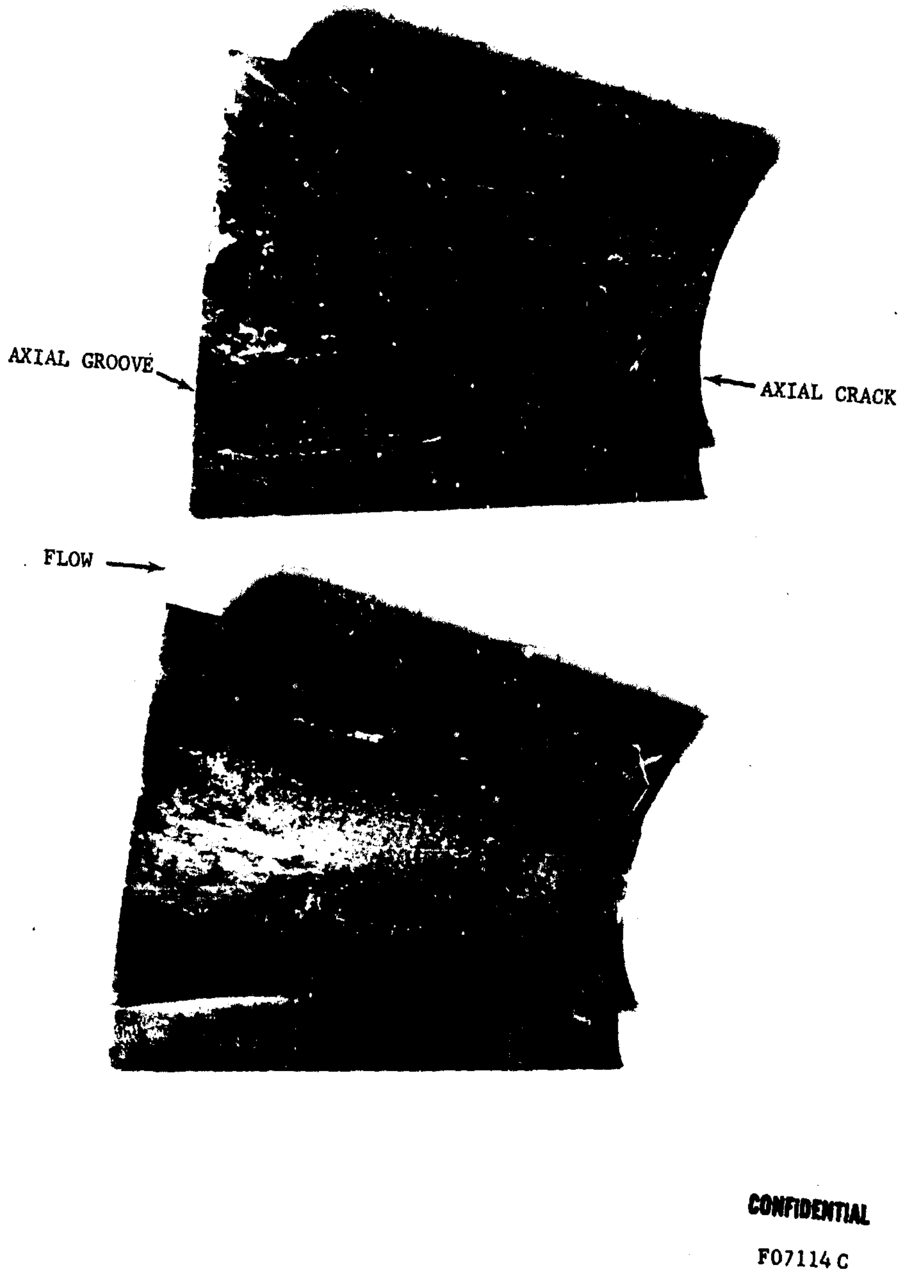
AXIAL GROOVE
AXIAL CRACK
FLOW
CONFIDENTIAL
F07114 C

FIGURE 85. TUNGSTEN INSERT FROM TEST T-17 (BEFORE DEPOSIT REMOVAL)

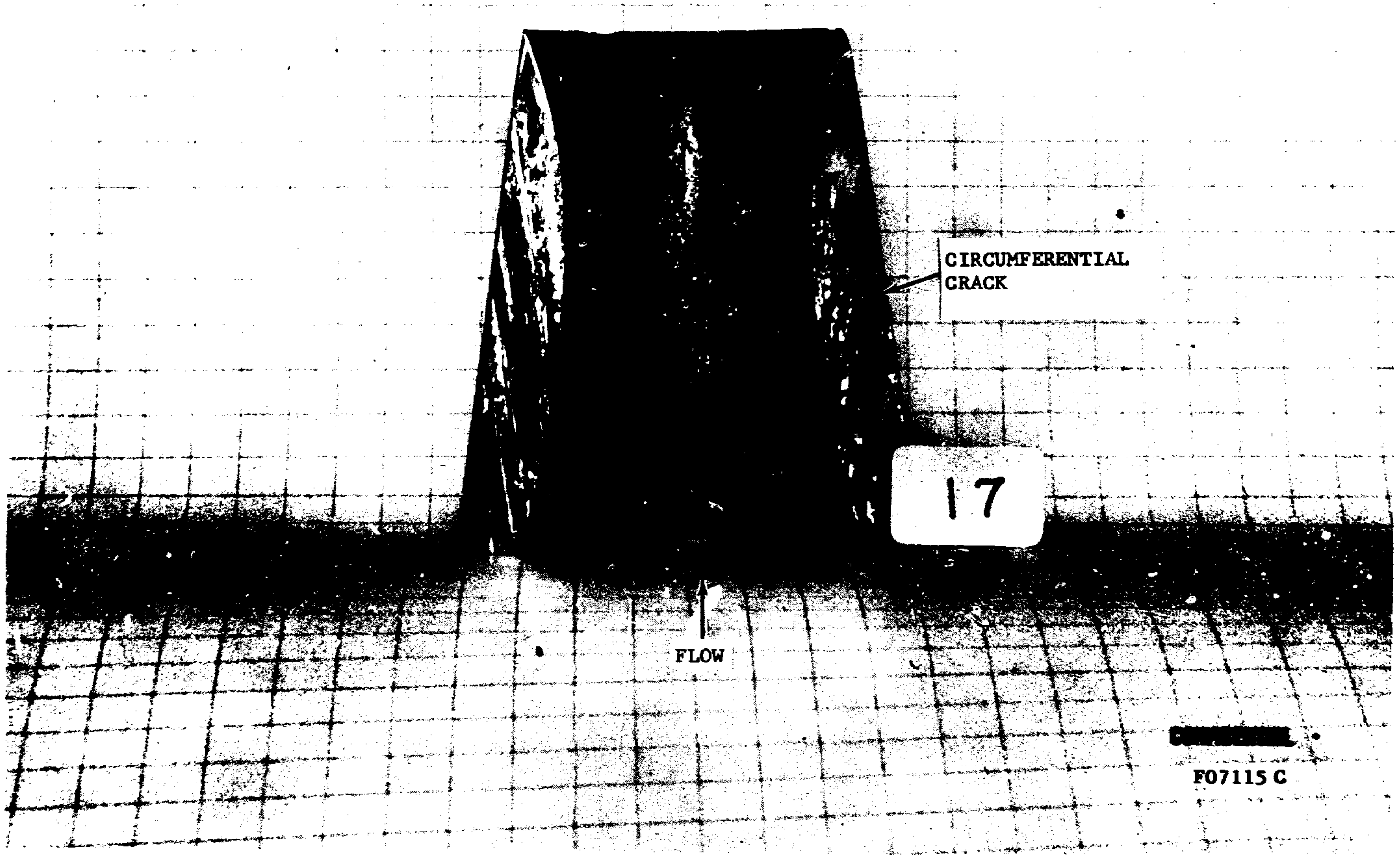
CIRCUMFERENTIAL CRACK
17
FLOW
[redacted]
F07115 C

FIGURE 86. TUNGSTEN INSERT FROM TEST T-17 (DEPOSITS REMOVED, ETCHED)

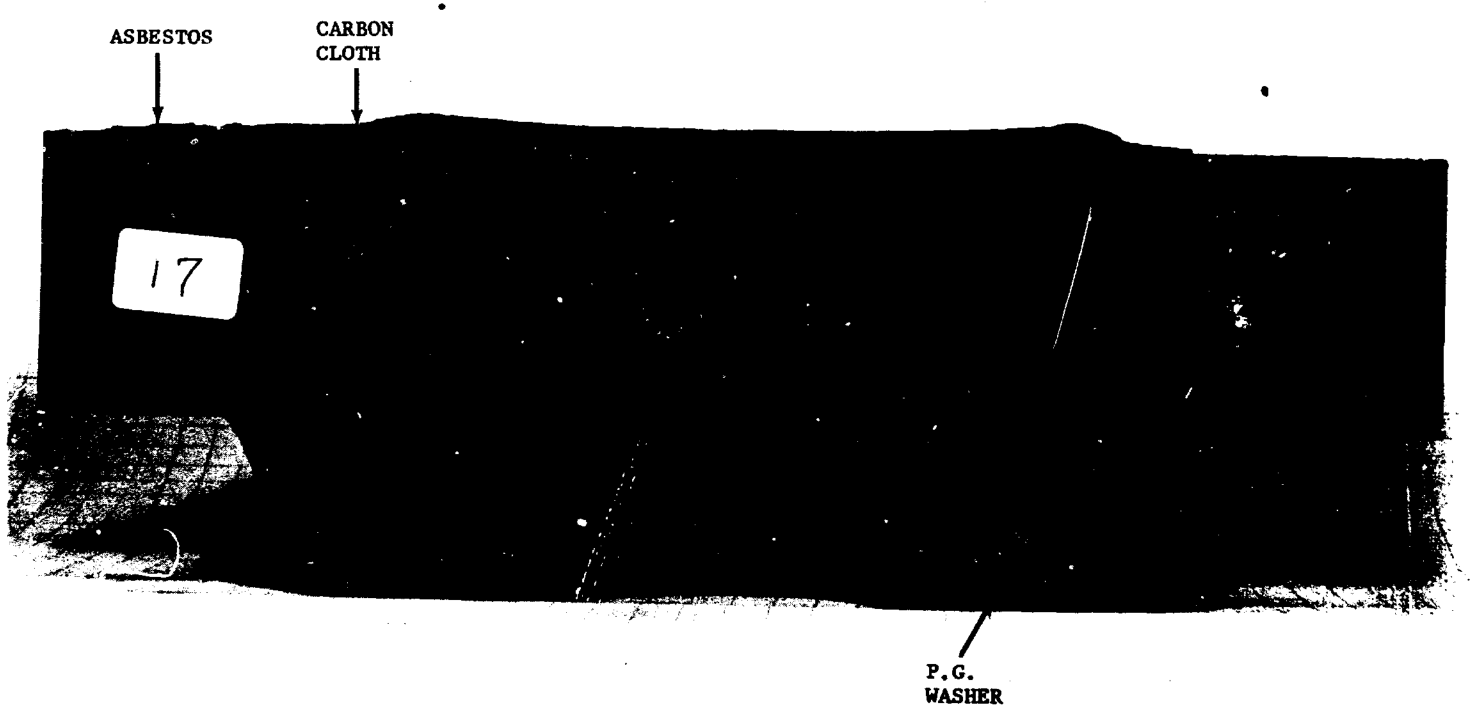
ASBESTOS
CARBON CLOTH
17
P.G. WASHER

CONFIDENTIAL
F07116 C

FIGURE 87. CARBON CLOTH PHENOLIC ENTRANCE CONE - CROSS SECTION

TABLE XXVII. MOTOR TEST T-17 DEPOSIT ANALYSIS (C)

Sample Number	Sample Location	Composition	
T-17-1	Chamber slag	BeO	60-70%
		Be_2C	10-15
		Mg_2SiO_4	2-5
		Unknown	10-15
T-17-2	Graphite exit cone, thick (0.1 inch) slag on center of bottom	BeO	2-5
		W	2-5
		WC	2-5
		W_2C	80-90
		Unknown	2-5
T-17-3	Deposit on steel housing, downstream of exit cone insulator	BeO	75-85
		MgO	2-5
		Mg_2SiO_4	15-25
T-17-4	Tungsten insert, black powder on convergent face	BeO	25-35
		Mg_2SiO_4	10-15
		Carbon	45-55
T-17-5	Tungsten insert, metallic deposit from groove at upstream edge	BeO	55-65
		Be_2C	15-20
		W	5-10
		WC	5-10
		W_2C	5-10
		MgO	2-5
		Carbon	2-5
T-17-6	Tungsten insert, surface deposit on downstream edge	BeO	25-30
		WC	25-30
		W_2C	15-20
		MgO	2-5
		Carbon	trace

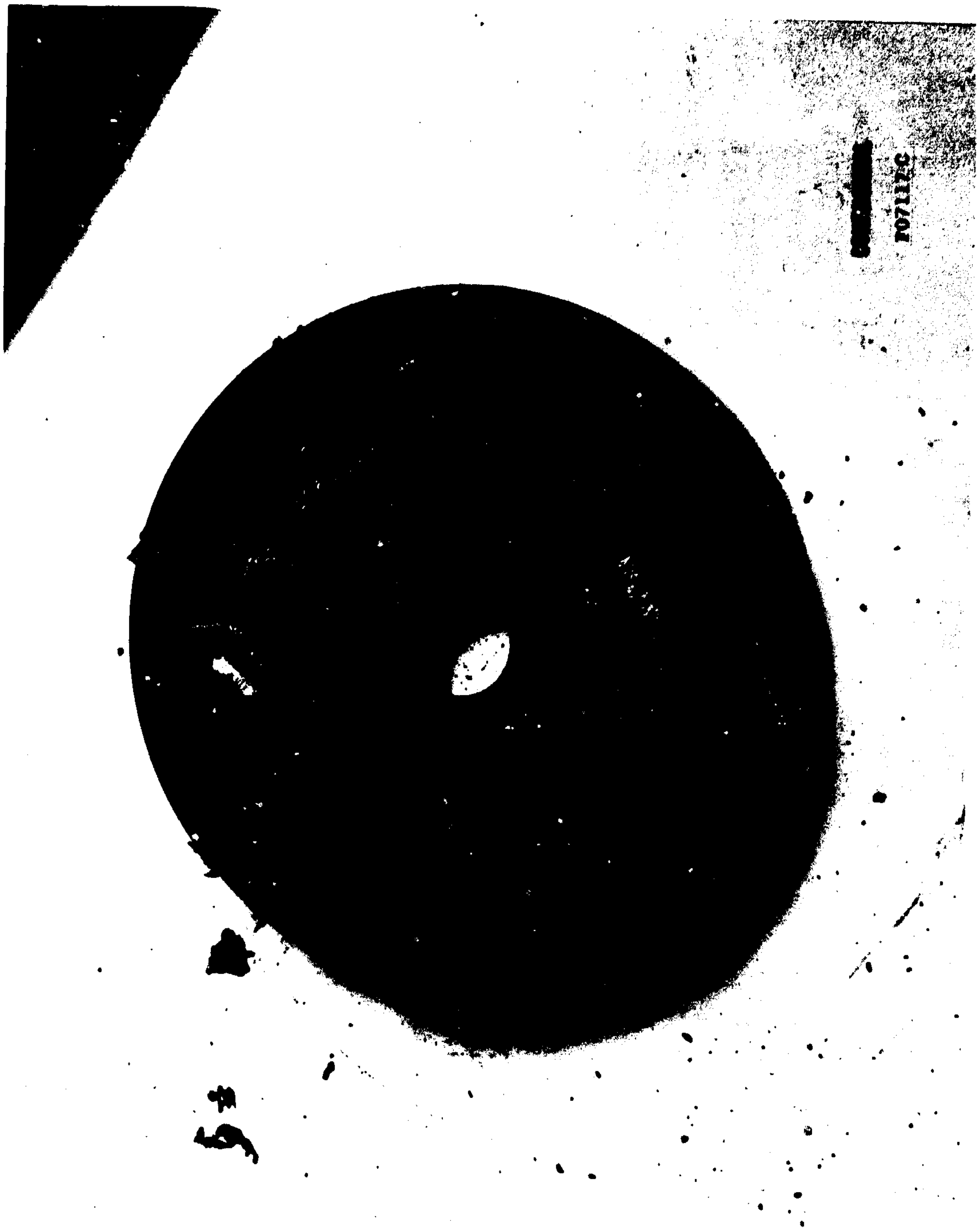

FIGURE 88. NOZZLE FROM TEST T-18 - NOSE CAP VIEW (LOOSE DEPOSITS REMOVED)

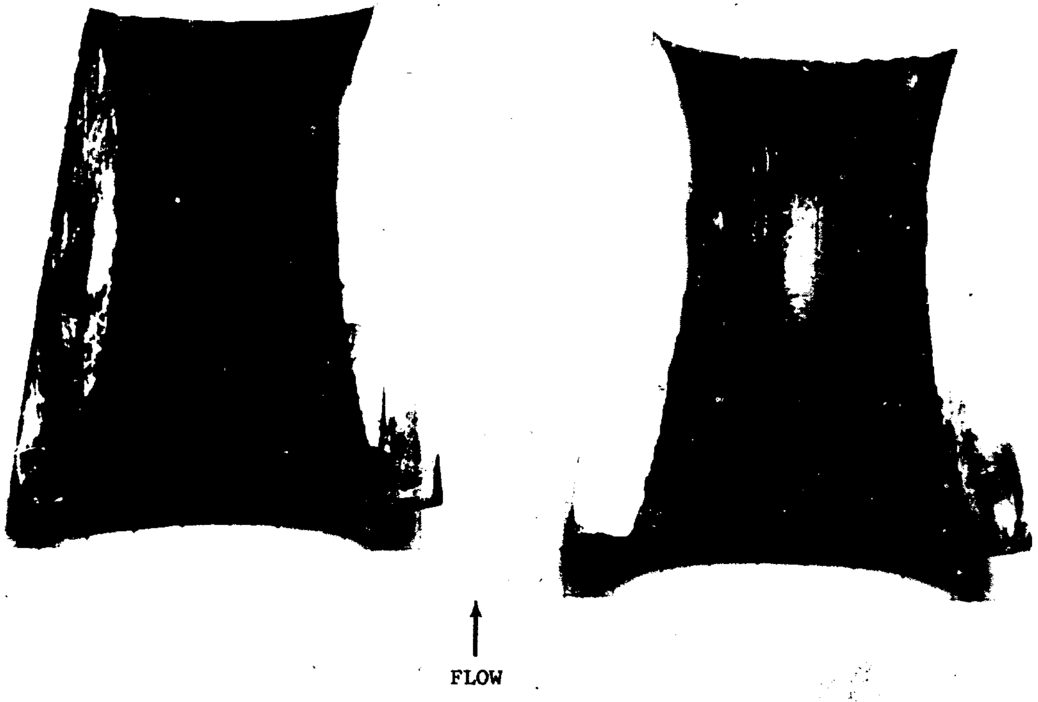

CONFIDENTIAL
F07118 C

FIGURE 89. TUNGSTEN INSERT FROM TEST T-18 (BEFORE DEPOSIT REMOVAL)

deposits essentially intact. Figure 90 shows a section of the insert after removal of loose deposits.

A series of deposits were taken from various areas on the hardware and analyzed by X-ray diffraction. The results are summarized in Table XXVIII.

TABLE XXVIII. MOTOR TEST T-18 DEPOSIT ANALYSIS (C)

Sample Number	Sample Location	Composition	
T-18-1	Top of carbon cloth-phenolic entrance cap	BeO	5-10%
		Carbon	90+
T-18-2	Top of graphite entrance cone, thin adherent coating	BeO	2-5
		Carbon	90+
T-18-3	Deposit on flame surface of pyrolytic graphite washer	BeO	60-70
		Be_2C	5-10
		Carbon	10-20
		Pyrolytic graphite	10-15
T-18-4	Graphite exit cone, thin surface deposit	BeO	90+
		W	5-10

The hardware was in very good condition. The graphite entrance cone had an unusual appearance. There were a large number of small grooves in the top surface on the entire circumference. These grooves were approximately 0.05 inch deep and 3/4 to 1-1/2 inches long. The carbon cloth-phenolic entrance cap was in very good condition. There was essentially no deposit found on the surface of the carbon cloth. The contour did not change significantly.

The tungsten insert was also in very good condition. There was a continuous coating of beryllia over the entire surface. There was no carbide found on the flame side surface of the tungsten insert. There was no circumferential crack in the tungsten insert. This was the only test where a circumferential crack did not occur.

(1) (C) Motor Test T-19

Motor Test T-19 used a nozzle identical to that in Test T-18 (i.e. submerged with tungsten throat insert). The major change was the substitution of the Arcocel 319BRF for the Arcocel 191F propellant used in Test T-18. The aft closure insulator was not exposed to the flame and is not shown. The nozzle is shown in Figures 91 and 92 in the as-received condition. A cross

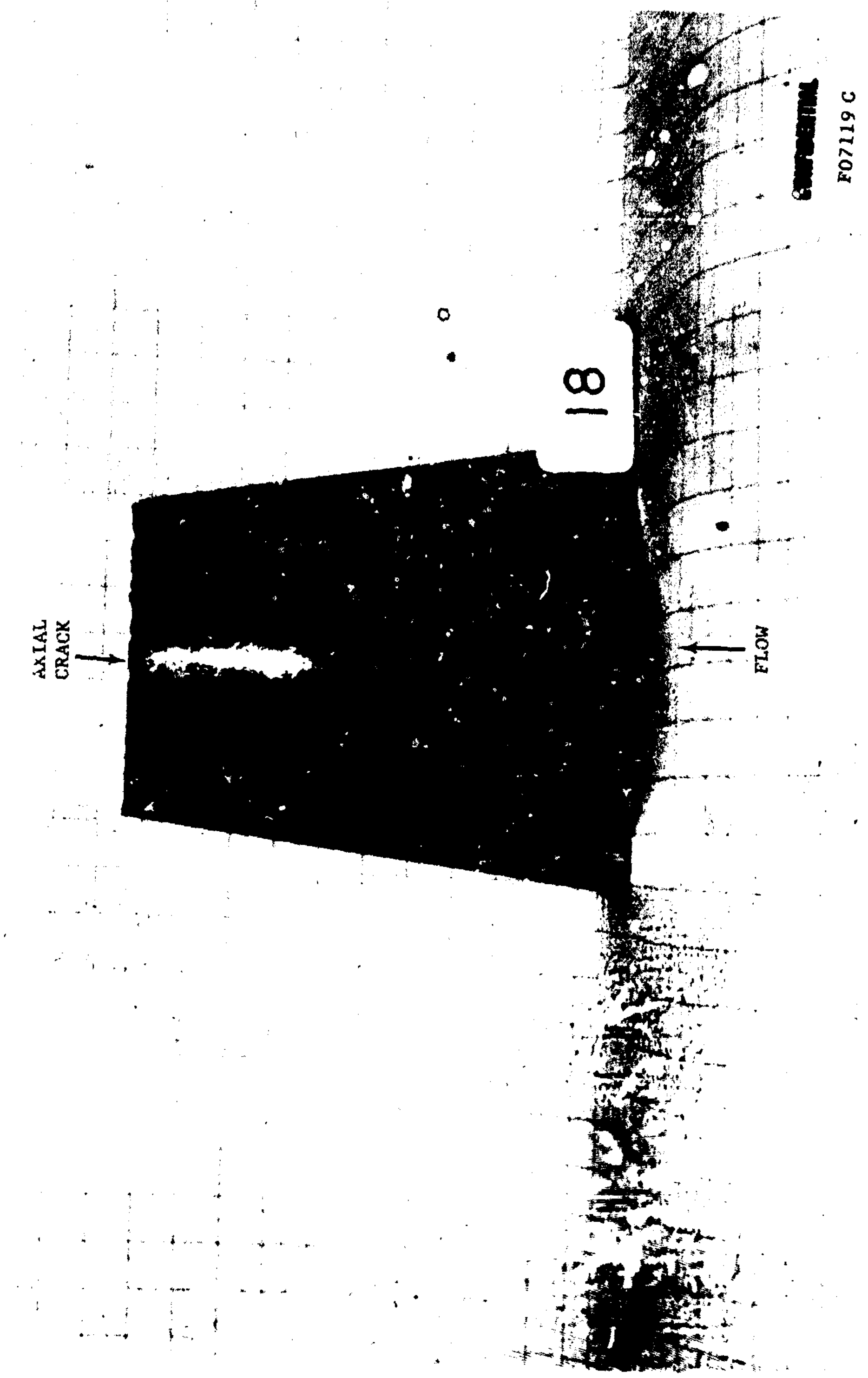
CONFIDENTIAL
F07119 C
18
AXIAL CRACK
FLOW

FIGURE 90. TUNGSTEN INSERT FROM TEST T-18 (LOOSE DEPOSITS REMOVED)

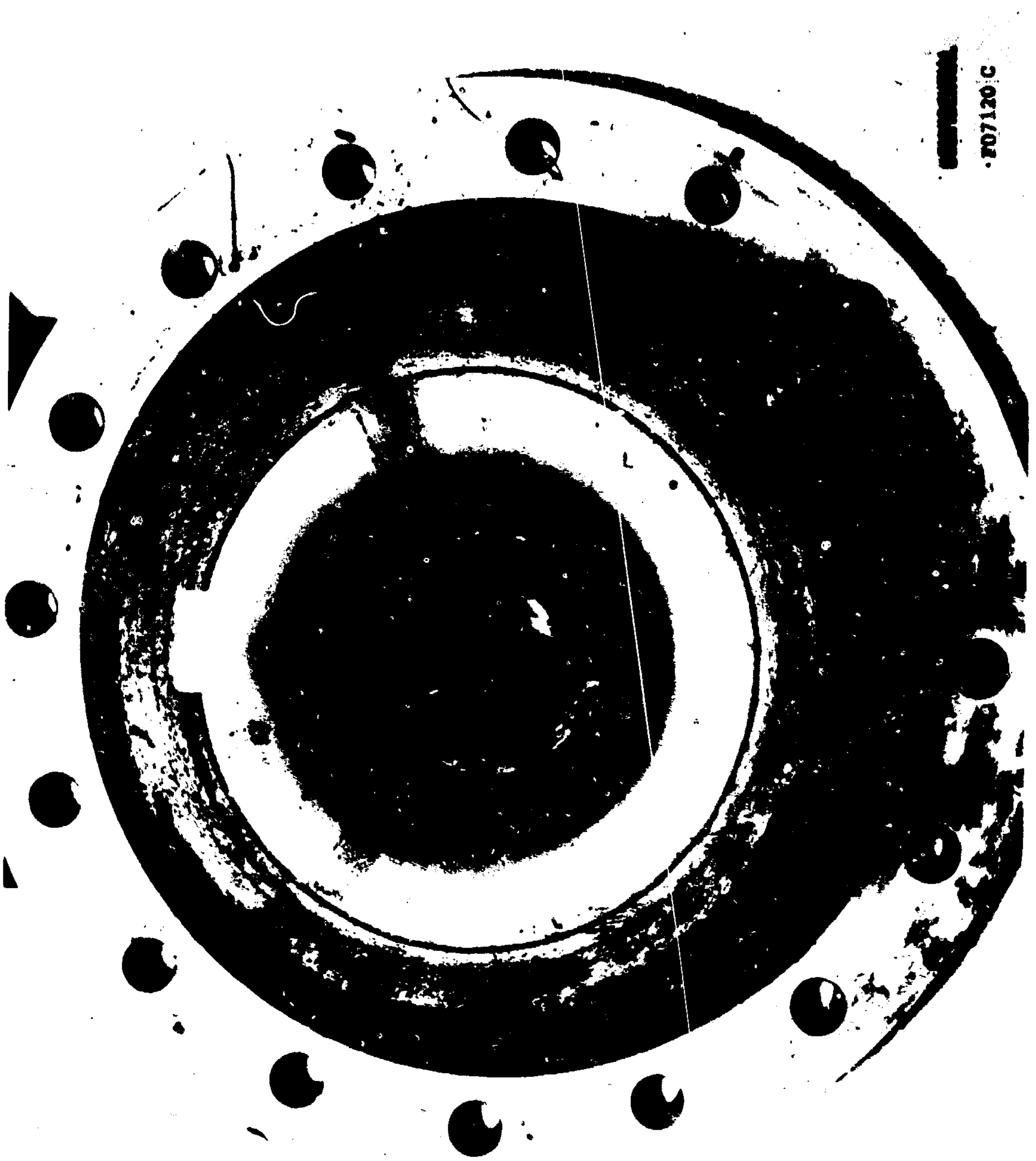

FIGURE 91. NOZZLE FROM TEST T-19 - NOSE CAP VIEW

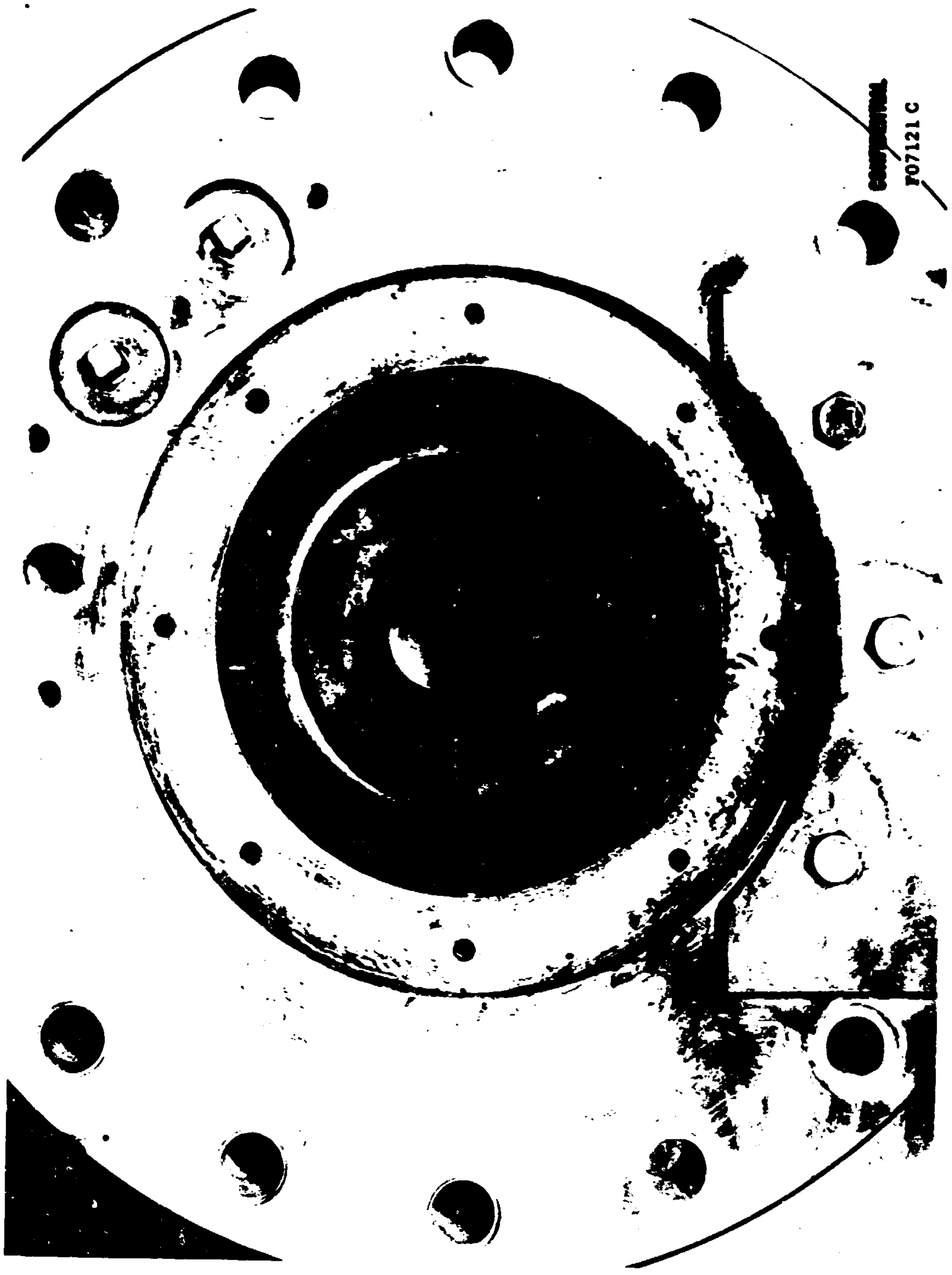
CONFIDENTIAL
F07121 C

FIGURE 92. NOZZLE FROM TEST T-19 - EXIT CONE VIEW

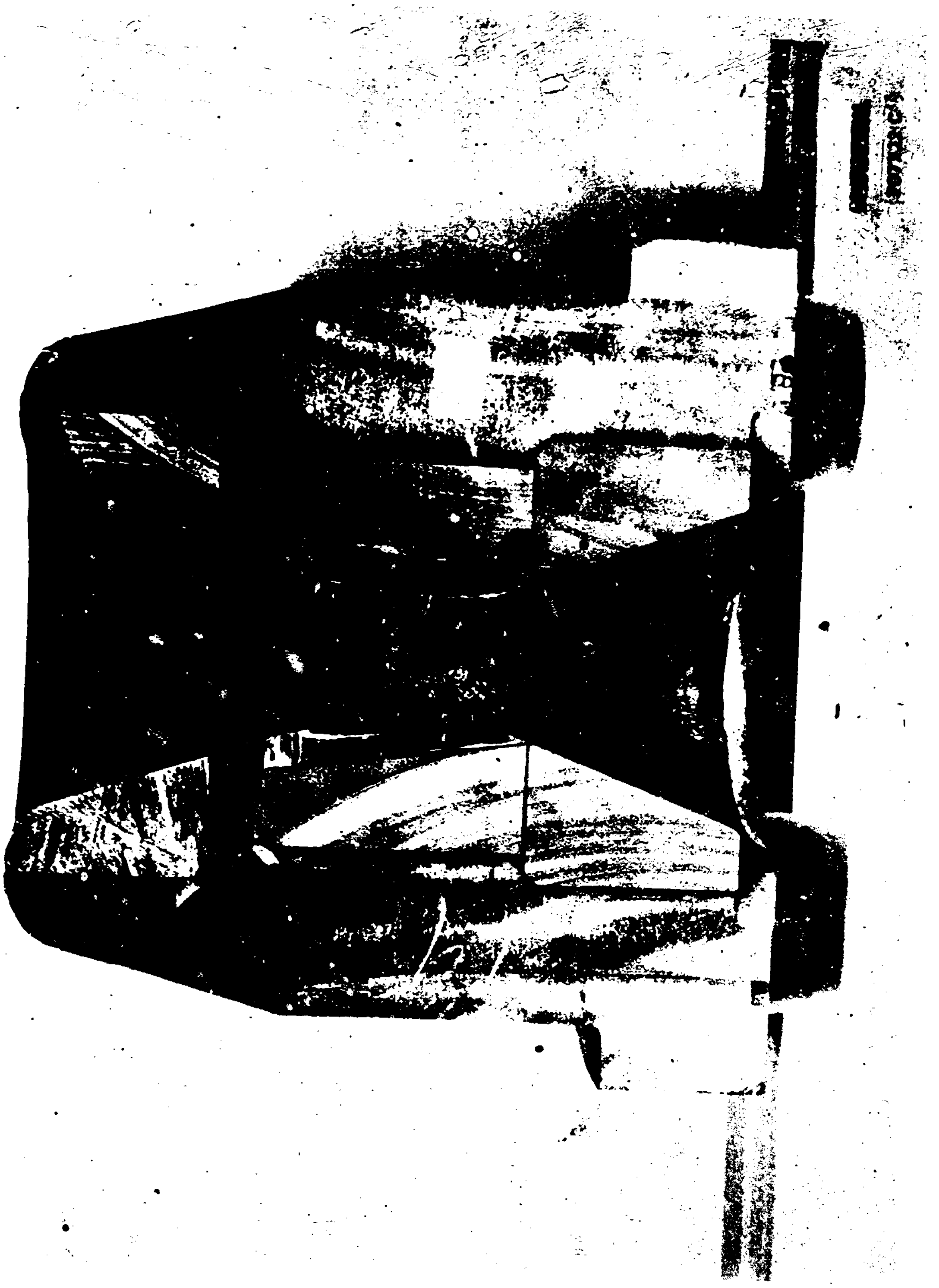

FIGURE 93. NOZZLE FROM TEST T-19 - CROSS SECTION

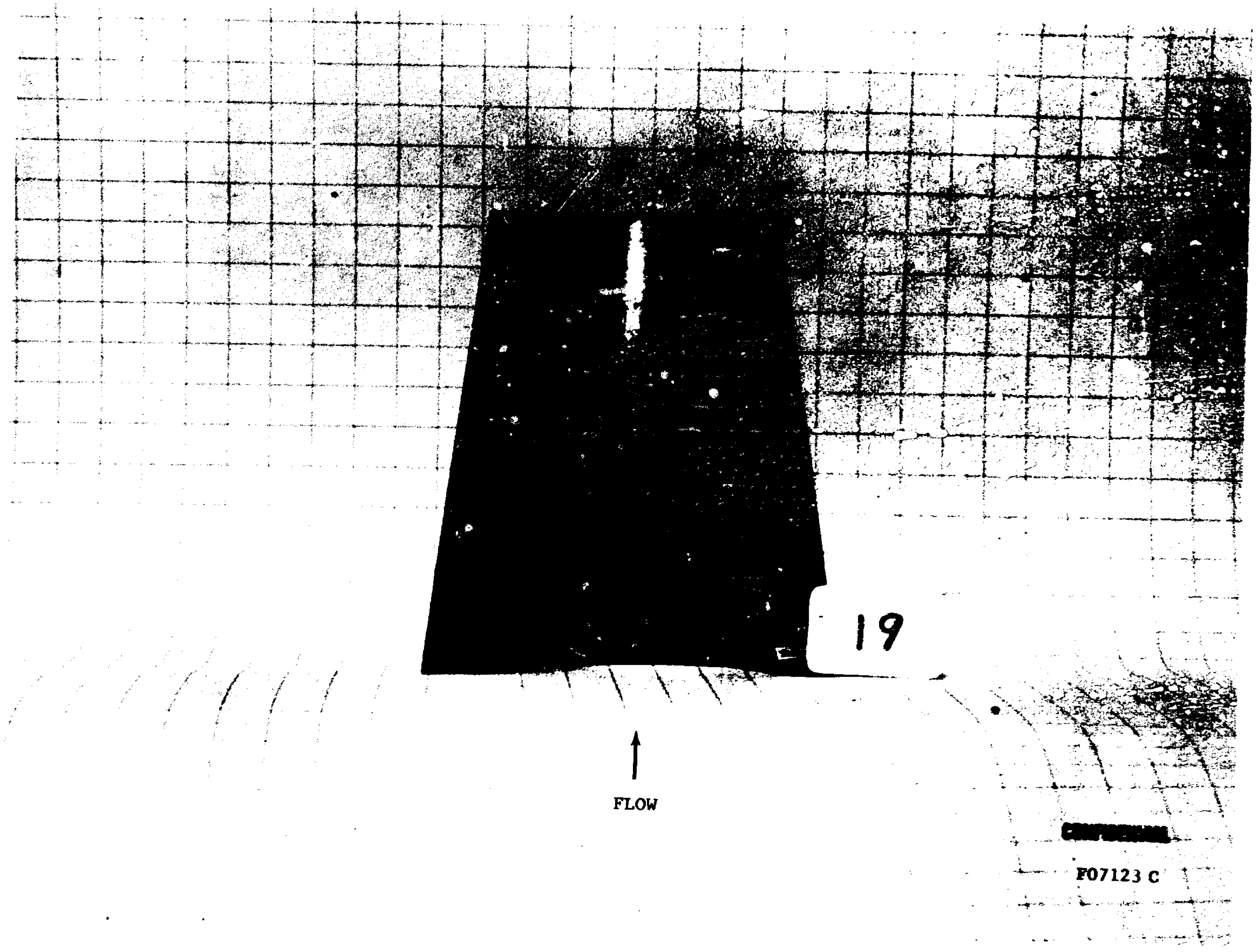
19
FLOW
F07123 C

FIGURE 94. TUNGSTEN INSERT FROM TEST T-19 (LOOSE DEPOSITS REMOVED)

section of the nozzle is shown in Figure 93 and a close-up of a cross section of the tungsten insert is shown in Figure 94 . This insert had three short axial cracks in the trailing edge after machining.

A series of deposits were taken from various areas on the hardware and analyzed by X-ray diffraction. The results are summarized in Table XXIX.

TABLE XXIX. MOTOR TEST T-19 DEPOSIT ANALYSIS (C)

Sample Number	Sample Location	Composition	
T-19-1	Aft closure	BeO	65-75%
		Be_2C	10-15
		Mg_2SiO_4	5-10
		MgO	5-10
		Graphite	4-6
		Amorphous carbon	4-6
T-19-2	Graphite entrance cone, thin (0.010 inch) continuous coating	BeO	85-90
		Graphite	10-15
T-19-3	Convergent face of tungsten insert, thin (0.010 inch) continuous coating	BeO	80-90
		Amorphous carbon	10-20
T-19-4	Trailing edge of tungsten insert, thick (0.030 inch) coating	BeO	80-85
		Graphite	2-4
		Unknown	10-15
T-19-5	Graphite exit cone, thin (0.005 inch) adherent coating	BeO	45-55
		Graphite	45-55

The hardware from this test was in as good condition as the hardware from Test T-18. The tungsten throat insert had a continuous coating of beryllia. There was no evidence of grooving, irregular loss of material or contour change. There was a circumferential crack formed, at approximately the throat section, which extended about halfway through the insert wall. The carbon cloth-phenolic entrance cap was in very good condition with essentially no lost material. There was very little beryllia deposit on the carbon cloth surface. The polycrystalline graphite entrance cone was in very good condition and was the only section of the nozzle which differed in appearance with respect to the hardware from Test T-18. The top surface of the entrance cone was very smooth and clean. However, there was a BeO coating on the convergent face of the graphite entrance cone. The graphite exit cone was coated with beryllia which readily flaked off. The original axial cracks in the tungsten did not propagate.

(m) (C) Motor Test T-20

Motor Test T-20 used an internal burning beryllium grain and a conventional nozzle. This test used a carbon cloth-pehnolic entrance cone but was otherwise identical to Test T-9. The nozzle inlet is shown in Figure 95 in the as-received condition. A cross section of the entire nozzle is shown in Figure 96.

A series of deposits were taken from various areas on the hardware and analyzed by X-ray diffraction. The results are summarized in Table XXX.

The hardware appearance from this test was very similar to that of the hardware from other tests. The carbon cloth entrance cone surface had very little deposit on it. There was very little deposit on the pyrolytic graphite or graphite exit cone, but there was no evidence of any damage to either area. The carbon cloth-phenolic entrance cone was badly delaminated and some material was lost in the area directly adjacent to the pyrolytic graphite throat insert.

(n) (C) Motor Test T-21

Motor Test T-21 used an end burning beryllium grain and a pyrolytic graphite throat insert. The aft closure is shown in Figure 97 and the nozzle entrance section is shown in Figure 98 and 99 in the as-received condition. A cross section of the nozzle is shown in Figure 100.

This test was conducted with the propellant grain very close to the aft closure insulator so that the combustion gases had a short residence time relative to Tests T-1 through T-7. In an effort to obtain more information about the combustion process, a series of holes were drilled in the aft closure insulator. These holes were lined with metal foil which acted as cups. The layout of the holes is shown in Figure 101. The metal used to make the cups was pure nickel for the 0.250 inch diameter holes and pure tantalum for the 0.125 inch diameter holes. It was thought that there was a possibility that at the ignition of the grain the beryllium metal would require a sufficient length of time to burn that some of these particles could be trapped in the cups and be extinguished. As the grain continued to burn, subsequent deposition of material on the top of the initial particles would not cause a phase change. Also, the top layer of particles would protect the underlying particles during cool-down. Post-test examination of the metal cups would be done by optical microscopy and X-ray diffraction. The particular phases which were looked for were beryllium metal, beryllium nitride, beryllium chlorides and beryllium alloys of the cup material.

T-20
CONFIDENTIAL
F07124 C

FIGURE 95. NOZZLE FROM TEST T-19 - ENTRANCE CONE VIEW

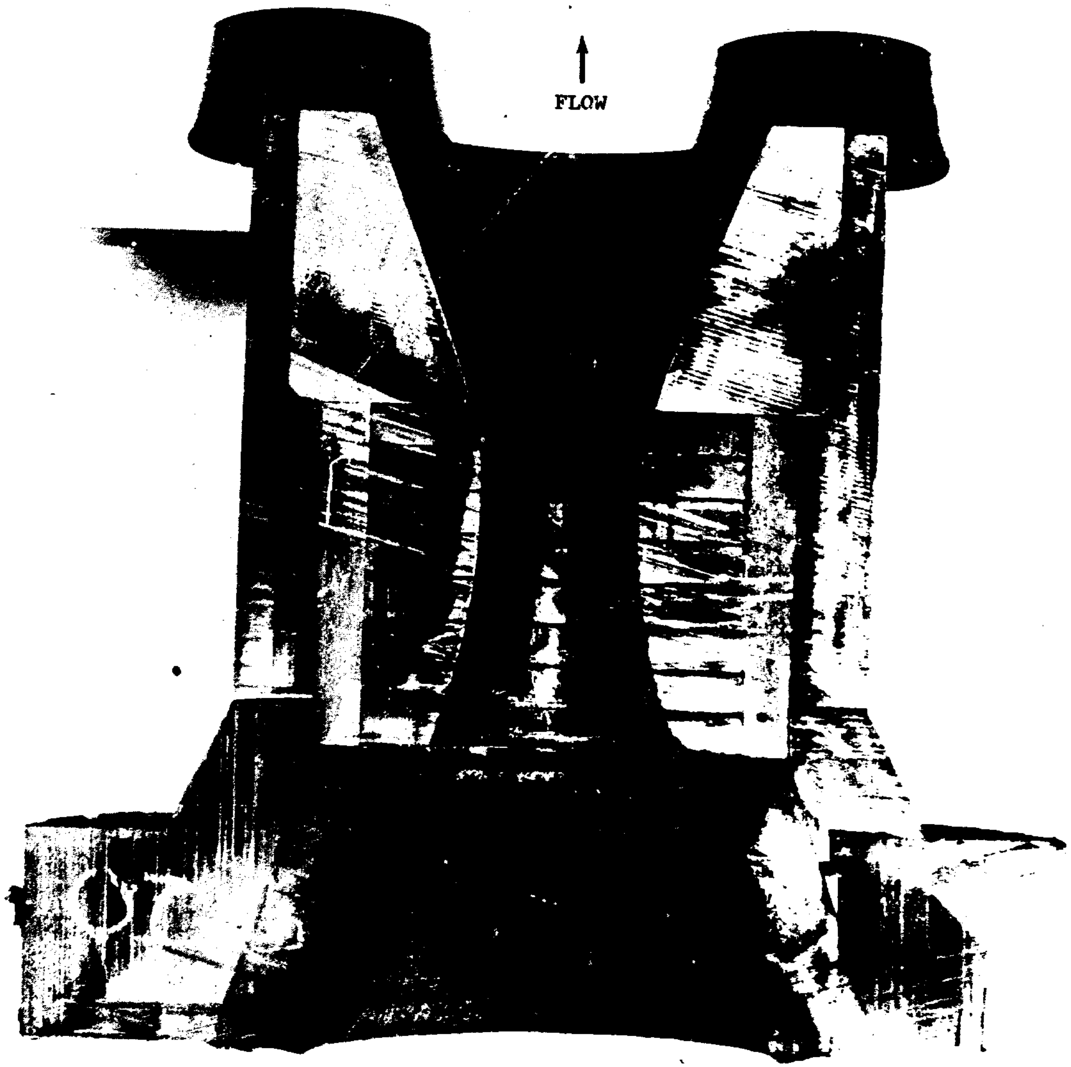

CONFIDENTIAL
F07125 C

FIGURE 96. NOZZLE FROM TEST T-20 - CROSS SECTION

TABLE XXX. MOTOR TEST T-20 DEPOSIT ANALYSIS (C)

Sample Number	Sample Location	Composition	
T-20-1	Chamber residue, loose powder	BeO	30-40%
		Be_2C	10-15
		Mg_2SiO_4	5-10
		Carbon	40-50
T-20-2	Chamber residue, metallic appearing slag	BeO	80-85
		Be_2C	5-10
		Mg_2SiO_4	2-5
		Carbon	2-5
		Unknown	5-10
T-20-3	Aft closure, surface deposit, top of bottom quadrant	BeO	55-65
		Be_2C	25-30
		Mg_2SiO_4	2-5
		Carbon	5-10
T-20-4	Aft closure, bubbled deposit with metallic appearance	BeO	80-90
		Be_2C	5-10
		Mg_2SiO_4	5-10
		Carbon	2-5
T-20-5	Carbon cloth-phenolic entrance cone, surface and char material	BeO	trace
		Carbon	95+
T-20-6	Pyrolytic graphite throat insert, thin deposit on first washer	BeO	5-10
		Pyrolytic graphite	80-90
T-20-7	Graphite exit cone, near throat insert, material appeared to have flowed	BeO	55-65
		Be_2C	2-5
		MgO	trace
		Carbon	35-45
T-20-8	Asbestos-phenolic exit cone insulator	BeO	80-90
		Mg_2SiO_4	5-10
		Carbon	2-5

FIGURE 97. AFT CLOSURE INSULATOR FROM TEST T-21 (AS RECEIVED)

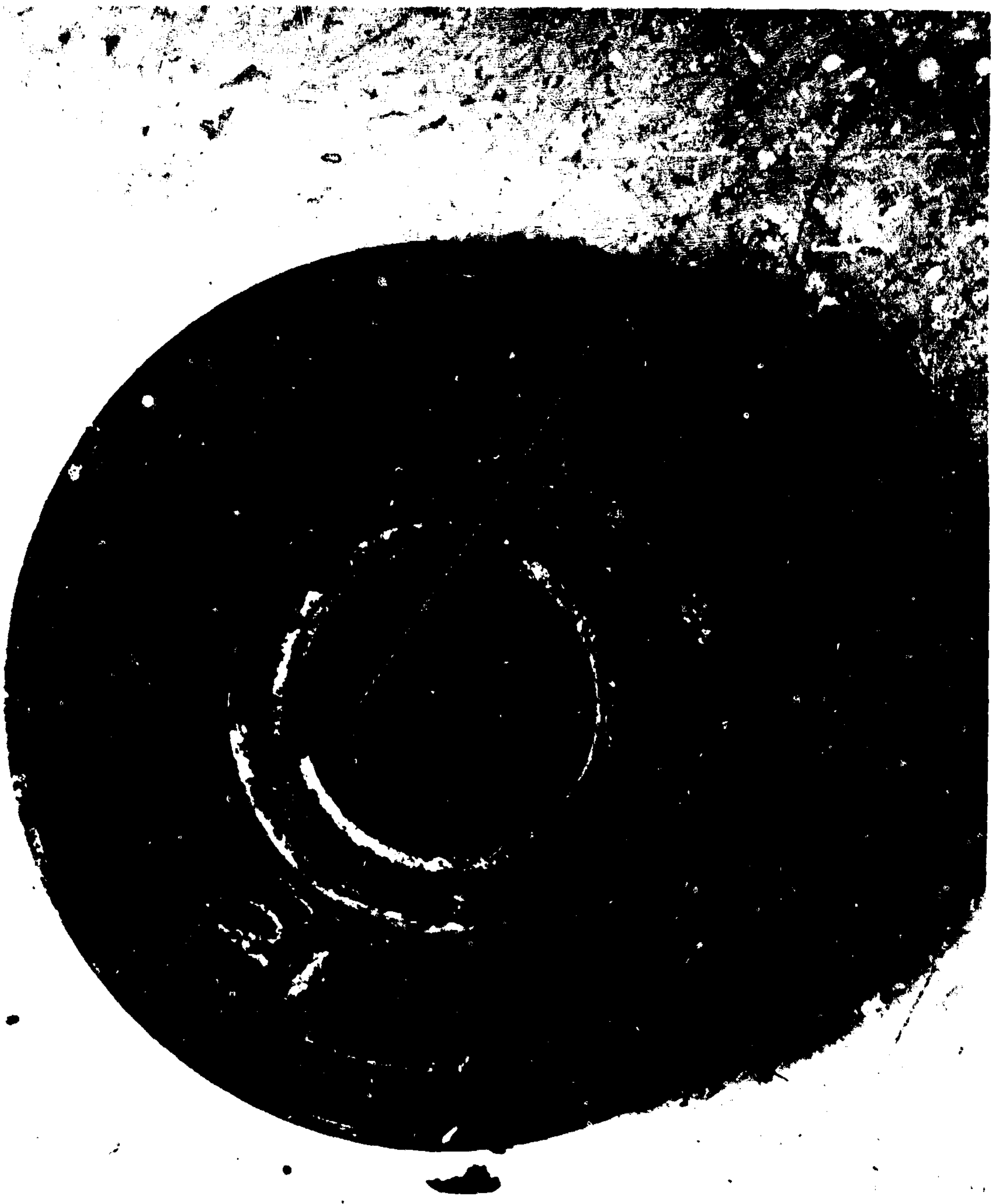

CONFIDENTIAL
F07127 C

FIGURE 98. NOZZLE FROM TEST T-21 - THROAT APPROACH VIEW

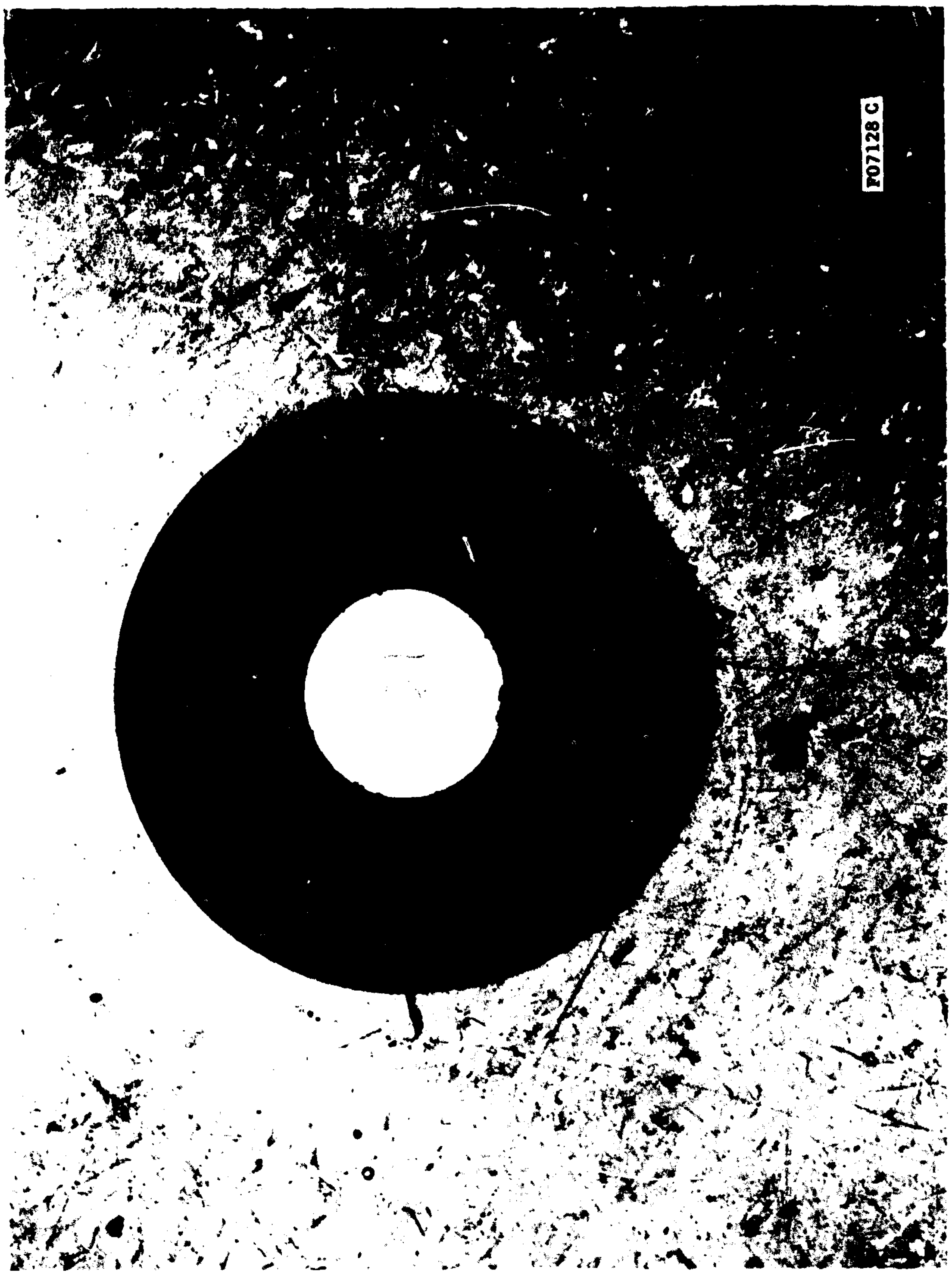

FIGURE 99. ATJ GRAPHITE ENTRANCE RINGS - TEST T-21

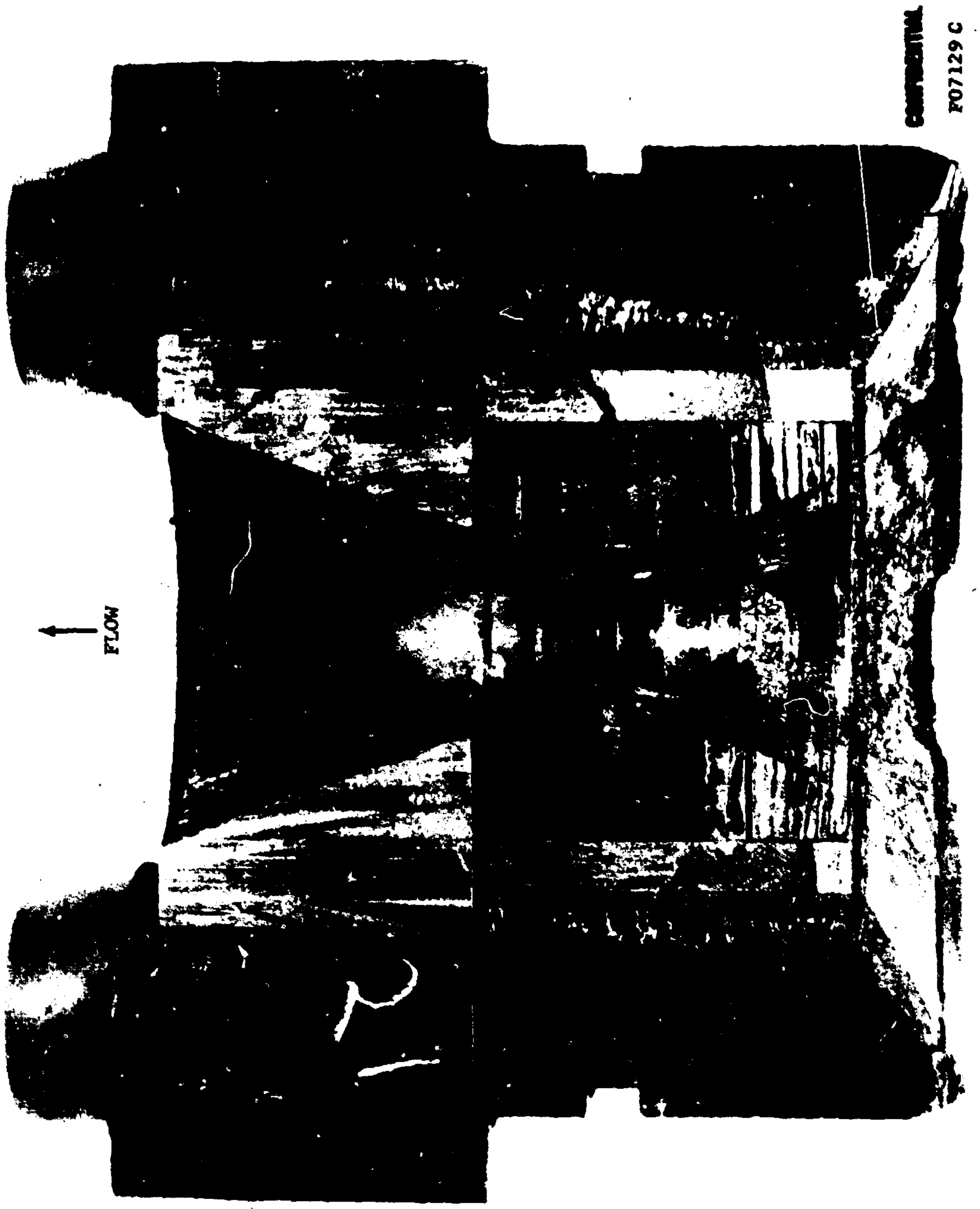
FLOW
CONFIDENTIAL
F07129 C
21

FIGURE 100. NOZZLE FROM TEST T-21 - CROSS SECTION

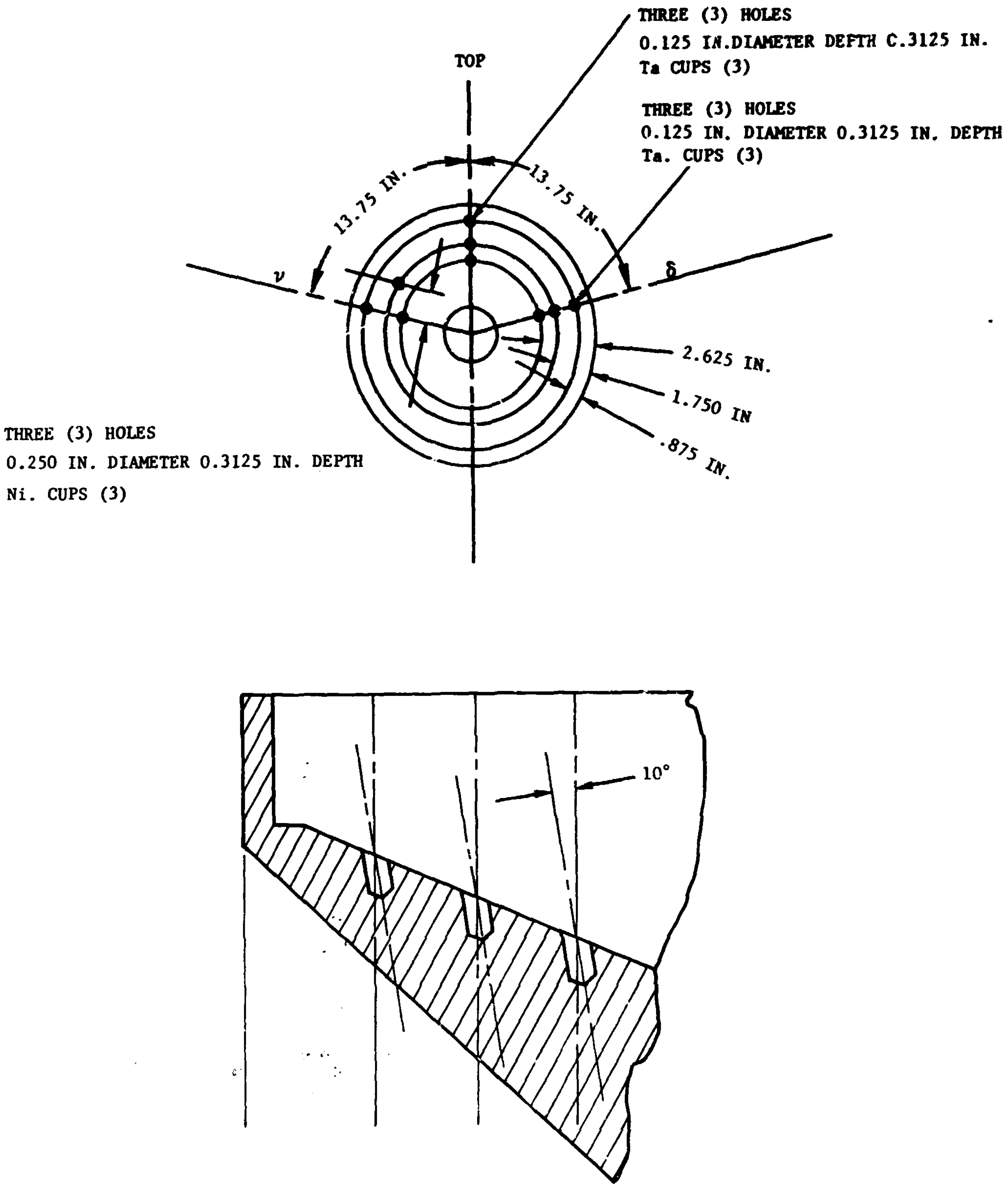
THREE (3) HOLES
0.125 IN.DIAMETER DEFTH C.3125 IN.
Ta CUPS (3)
TOP
THREE (3) HOLES
0.125 IN. DIAMETER 0.3125 IN. DEPTH
Ta. CUPS (3)
13.75 IN.
13.75 IN.
ν
δ
2.625 IN.
1.750 IN
.875 IN.
THREE (3) HOLES
0.250 IN. DIAMETER 0.3125 IN. DEPTH
Ni. CUPS (3)
10°

FIGURE 101. LAYOUT OF HOLES IN AFT CLOSURE FOR TEST T-21

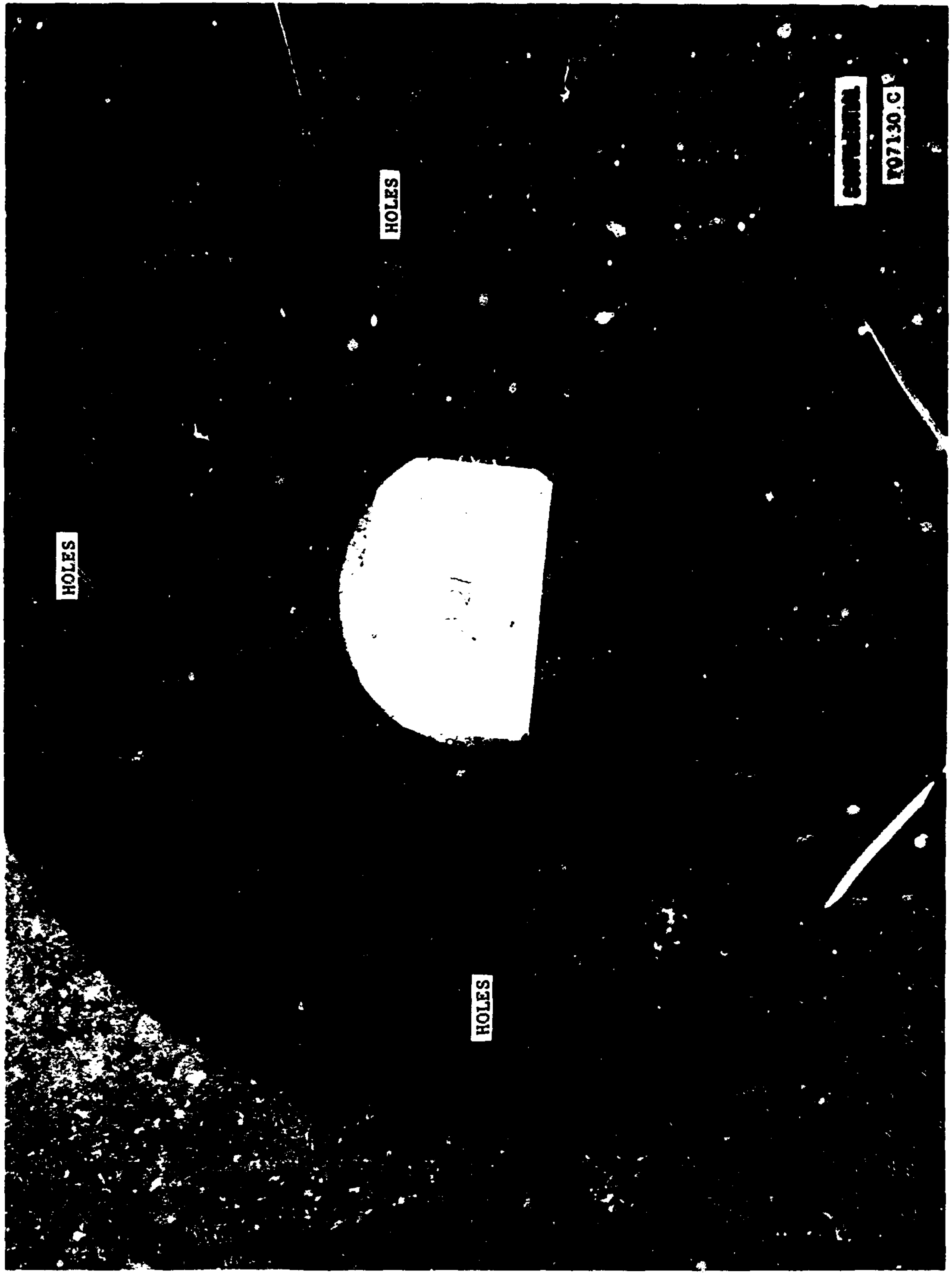
HOLES
HOLES
HOLES
CONFIDENTIAL
F07130.C

FIGURE 102. AFT CLOSURE INSULATOR FROM TEST T-21 (LOOSE DEPOSITS REMOVED)

The aft closure is shown in Figure 102 in the post-test condition with the surface layer of beryllia removed. All nine of the holes can be seen and there was very little excessive charring or material loss of the asbestos-phenolic insulator in the immediate proximity of the hole. Examination of the metal cups showed that the nickel cups were nearly all melted and the outer edge of the tantalum cups were melted. The nickel cups apparently melted before any exhaust products entered the cups. There were no beryllium compounds found on examination of the melted nickel. The tantalum cups contained some molten material which was identified as a magnesium silicate of the forsterite type. This material results from the melting of asbestos. The bottom of the tantalum cup was carefully examined for any beryllium compounds, but none could be identified.

The overall condition of the hardware was excellent. The pyrolytic graphite was in very good condition with very little deposit of any kind. The graphite entrance and exit cones were coated with typical beryllium oxide deposits, but there was no detrimental effects on the substrate.

(o) (C) Motor Test T-22

Motor Test T-22 was essentially identical to Test T-21, the only difference being the type of beryllium propellant. The Arcane 54F composite propellant was used in this test (see also Test T-24). The aft closure insulator was modified with metal cups to examine the condensed exhaust products as was done in Test T-21. The layout for the metal cans was the same as shown in Figure 101. The aft closure insulator is shown in Figure 103 and the nozzle throat approach section is shown in Figure 104, in the as-received condition. Figure 105 shows the graphite entrance rings. A cross section of the nozzle is shown in Figure 106. Large amounts of deposit material were on the ATJ graphite exit cone.

The results of this test were very similar to the results from Test T-21. The hardware was in very good condition with no apparent effects from non-equilibrium combustion. The aft closure was not charred excessively. The polycrystalline graphite parts exposed to the exhaust were coated with beryllia. The pyrolytic graphite throat insert was relatively clean of any deposit, although there was considerable amorphous carbon from the post-test pyrolysis gases built up on the flame front face. It was impossible to get any useful data from the metal cans inserted in the aft closure. The cans were either melted closed or full of melted material from the aft closure. There were no discernible compounds which could be directly attributed to a non-equilibrium combustion or partially combusted beryllium metal.

(p) (C) Motor Test T-23

Motor Test T-23 was identical to Test T-21 except for the use of a submerged nozzle. The nozzle nose cap and entrance section are shown in

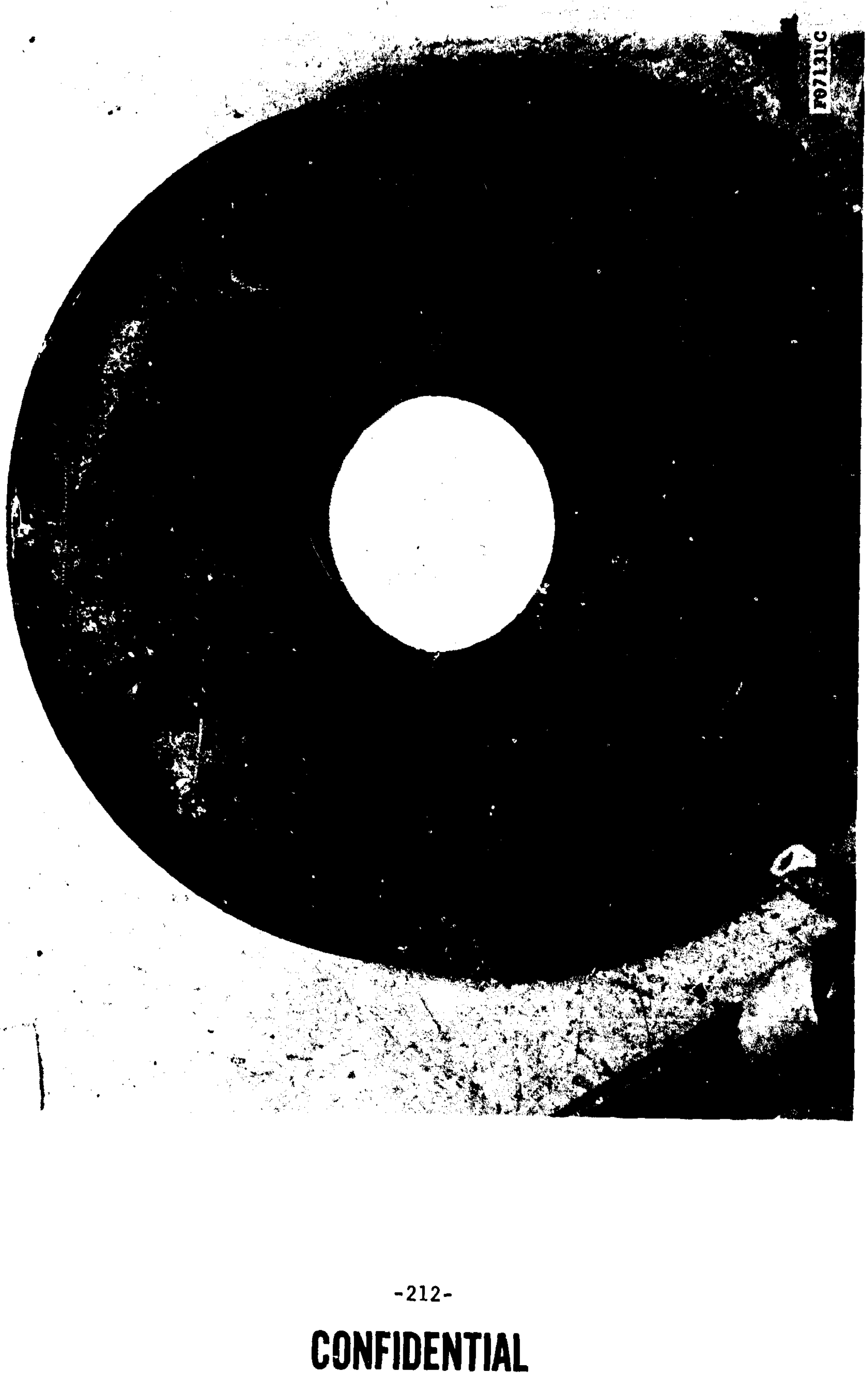

FIGURE 103. AFT CLOSURE INSULATOR FROM TEST T-22 (AS RECEIVED)

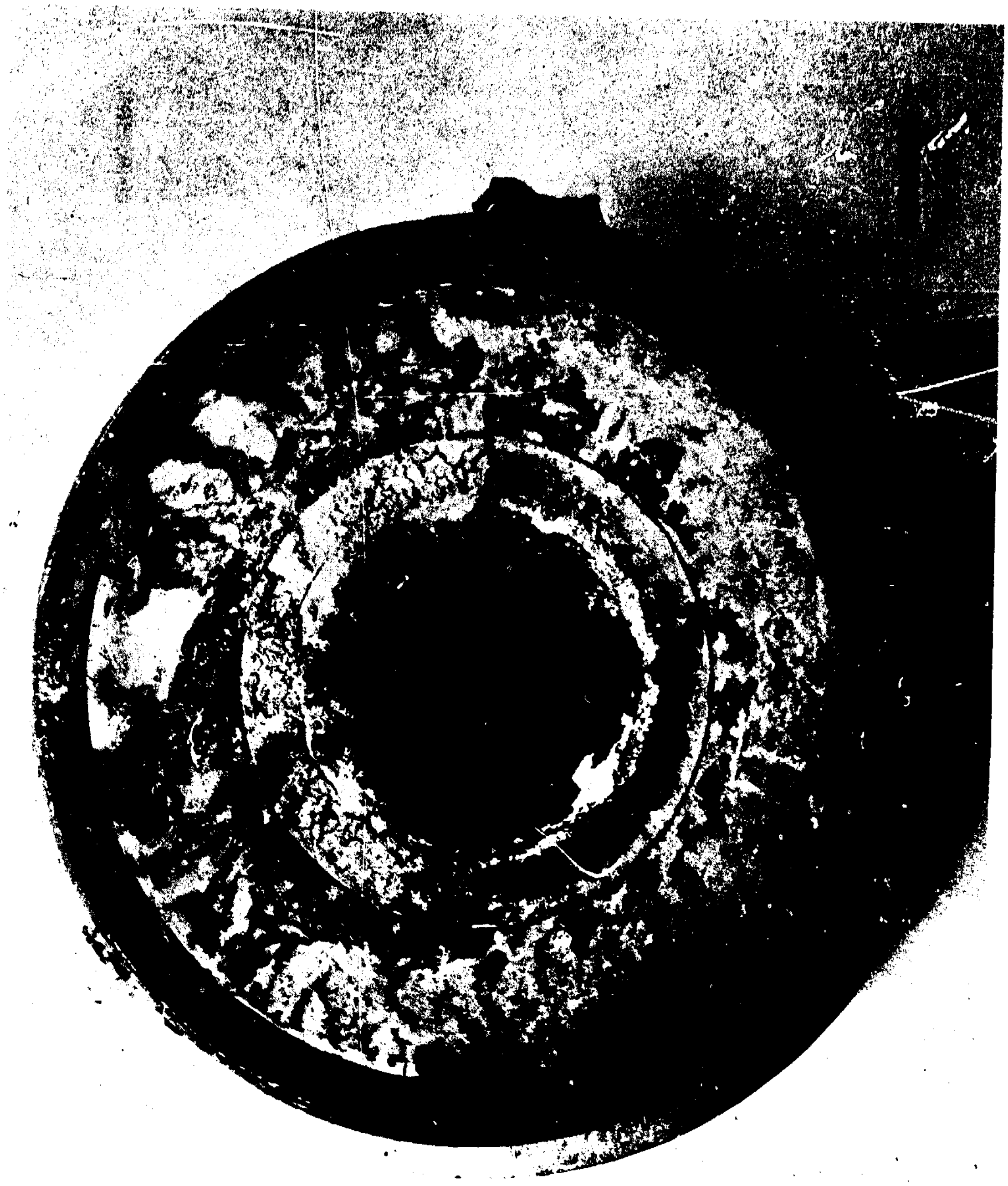

FIGURE 104. NOZZLE FROM TEST T-22 - ENTRANCE VIEW (AS RECEIVED)

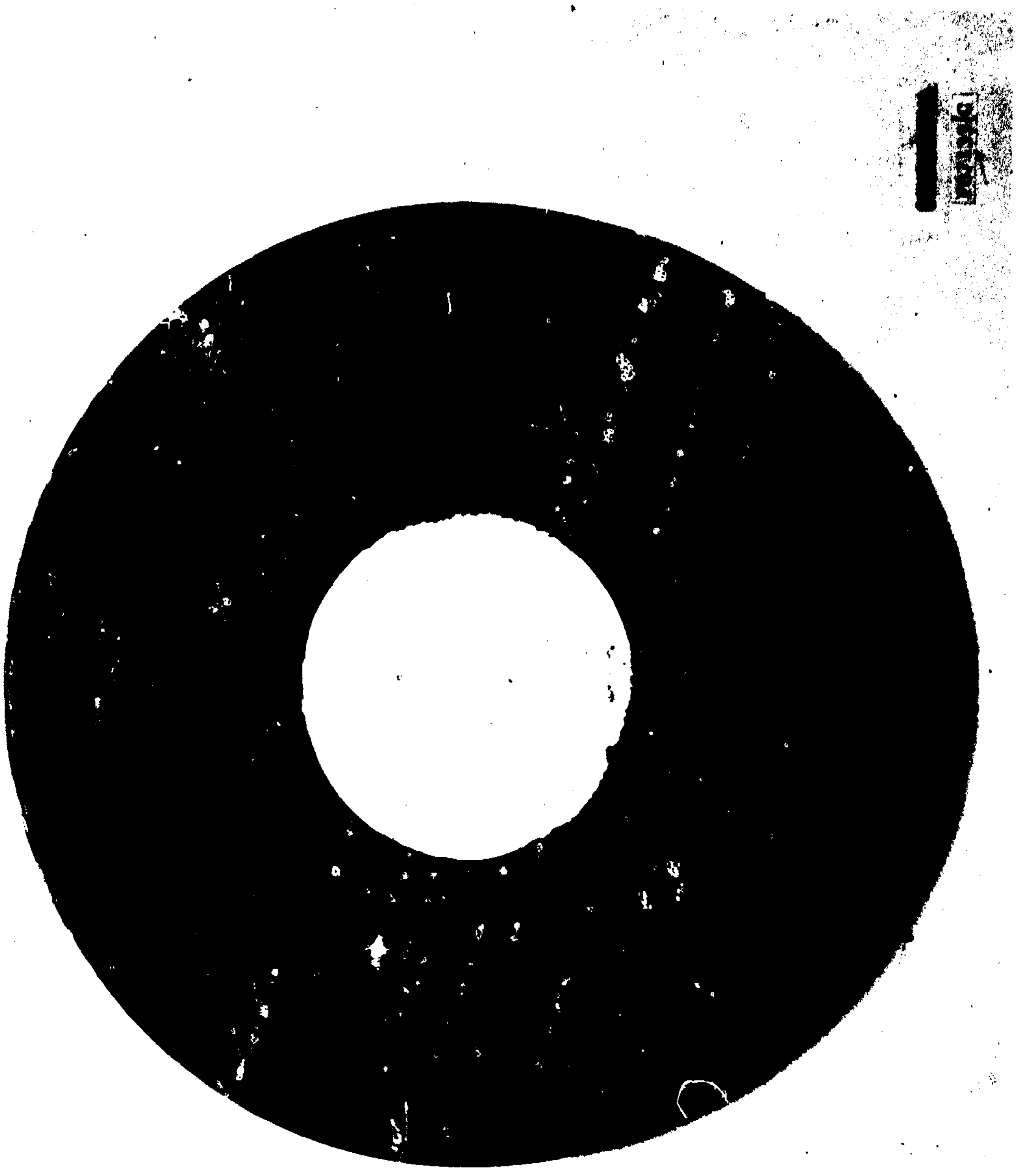

FIGURE 105. ATJ GRAPHITE ENTRANCE RINGS - TEST T-22 (LOOSE DEPOSITS REMOVED)

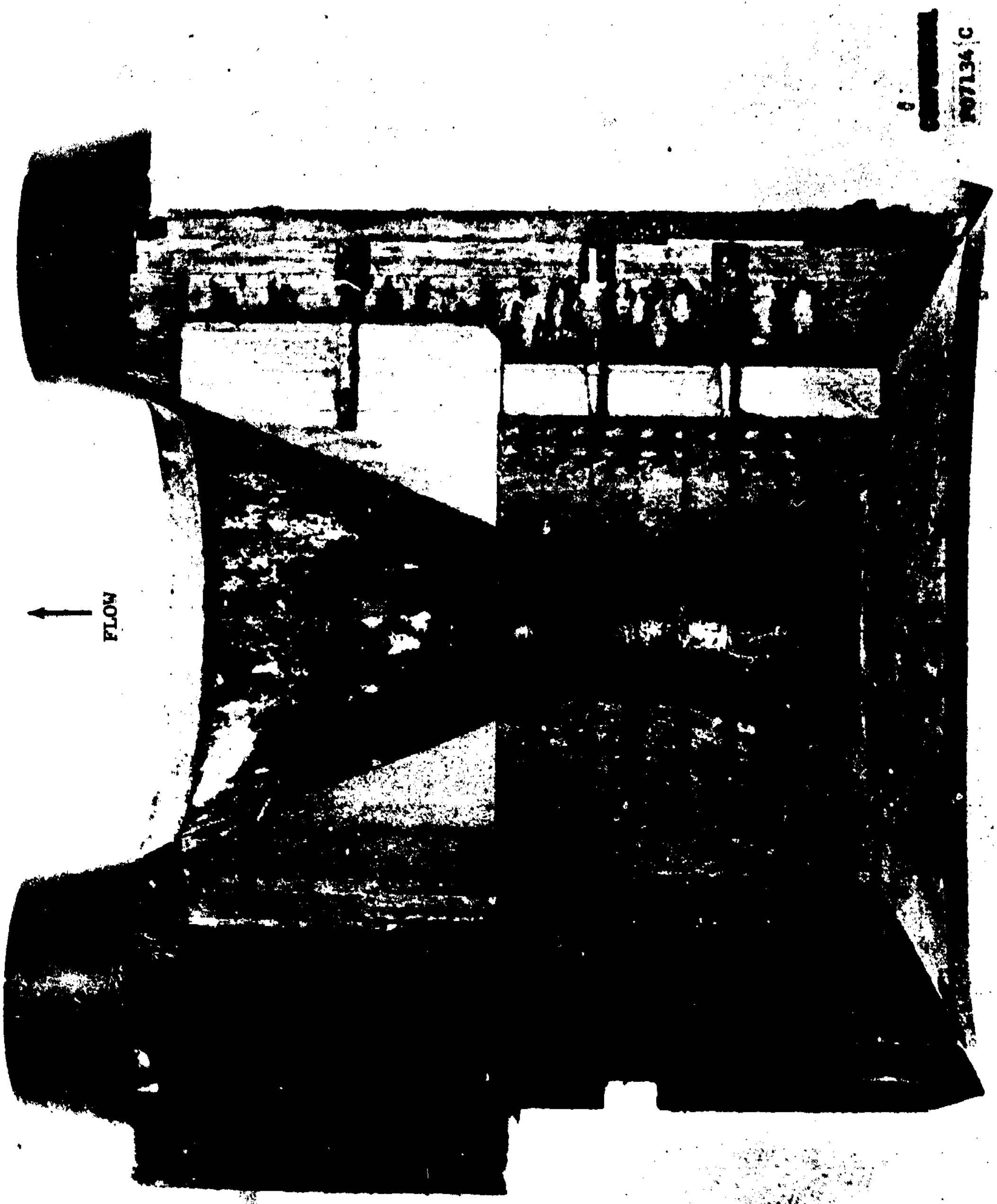
FLOW
P07134 C

FIGURE 106. NOZZLE FROM TEST T-22 - CROSS SECTION

Figure 107 in the as-received condition. A cross section of the nozzle is shown in Figure 108. The appearance of the aft closure insulator and exit cone was not unusual.

A series of deposits were taken from the hardware and analyzed by X-ray diffraction. The results are summarized in Table XXXI.

TABLE XXXI. MOTOR TEST T-23 DEPOSIT ANALYSIS (C)

Sample Number	Sample Location	Composition	
T-23-1	Graphite entrance cone, loose bubbled deposit	BeO	65-75%
		Be_2C	5-10
		MgO	5-10
		Graphite	5-10
		Amorphous carbon	5-10
T-23-2	Pyrolytic graphite throat coating, (0.012 inch) thick	BeO	85-95
		Be_2C	2-5
		Graphite	2-5
		Pyrolytic graphite	2-5
T-23-3	Graphite exit cone, thick white deposit which appeared to have flowed	BeO	70-75
		Be_2C	5-10
		Mg_2SiO_4	2-5
		MgO	2-5
		Graphite	2-5
		Amorphous carbon	2-5

There were some very thick (~0.2 inch) deposits found on the graphite entrance and exit cones which were mostly beryllia. The graphite entrance cone had a very heavy deposit of amorphous carbon but this is normal (from the decomposition of pyrolysis gases). The carbon cloth-phenolic entrance cap was charred to a depth of 0.15 to 0.25 inch but the surface was free of any deposits. There was a slight delamination of the carbon-cloth at the very top, but there was no beryllia found in the crack. The pyrolytic graphite throat insert was relatively clean with only a thin (0.012 inch) coating of beryllia.

(q) (C) Motor Test T-24

Motor Test T-24 used an end burning Arcocel 319BRF propellant, and was otherwise identical to Tests T-21 and T-22. The aft closure and nozzle are shown in Figure 109 in the as-received condition. A cross section of

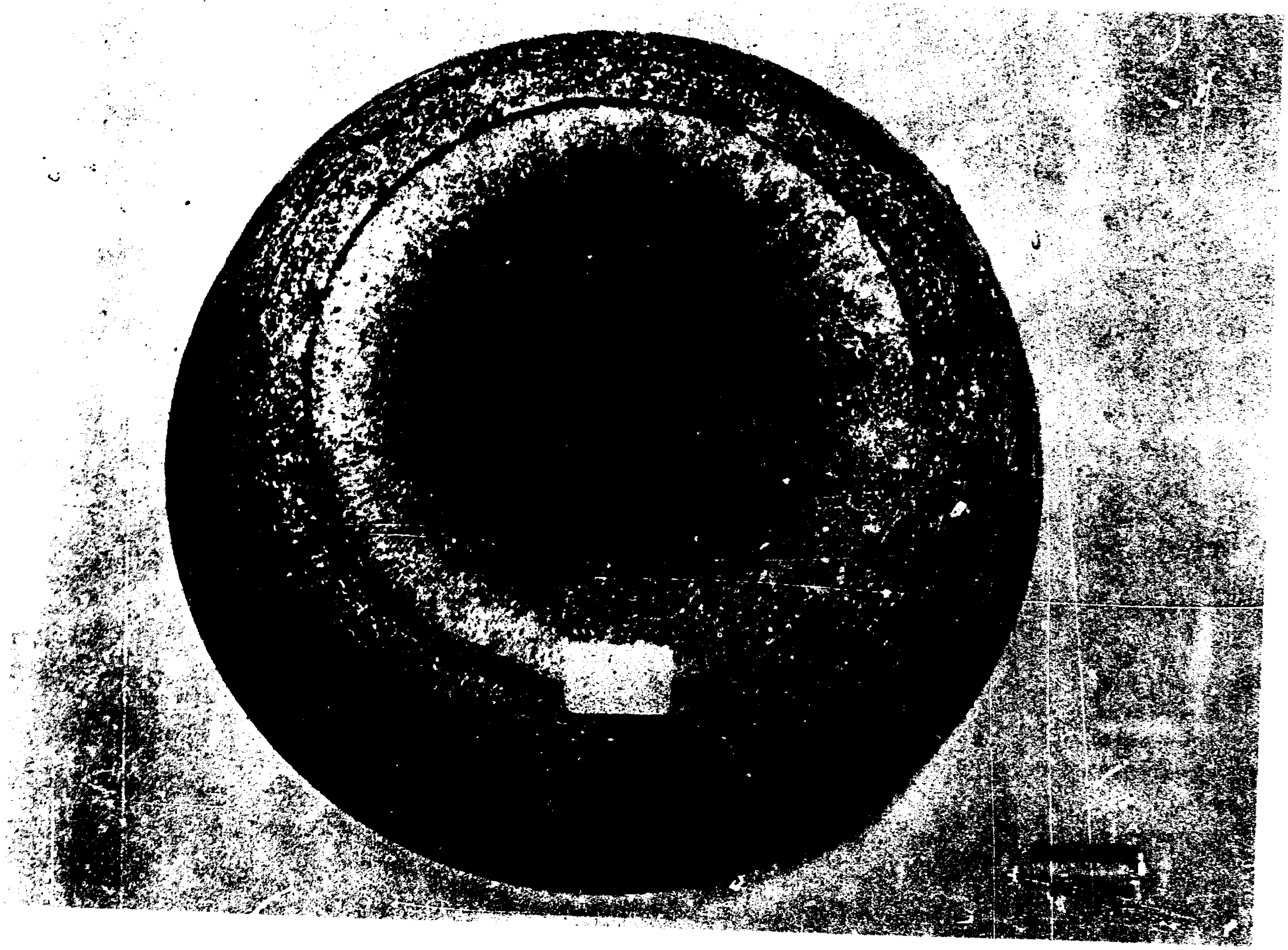

FIGURE 107. SUBMERGED NOZZLE FROM TEST T-23 - ENTRANCE VIEW

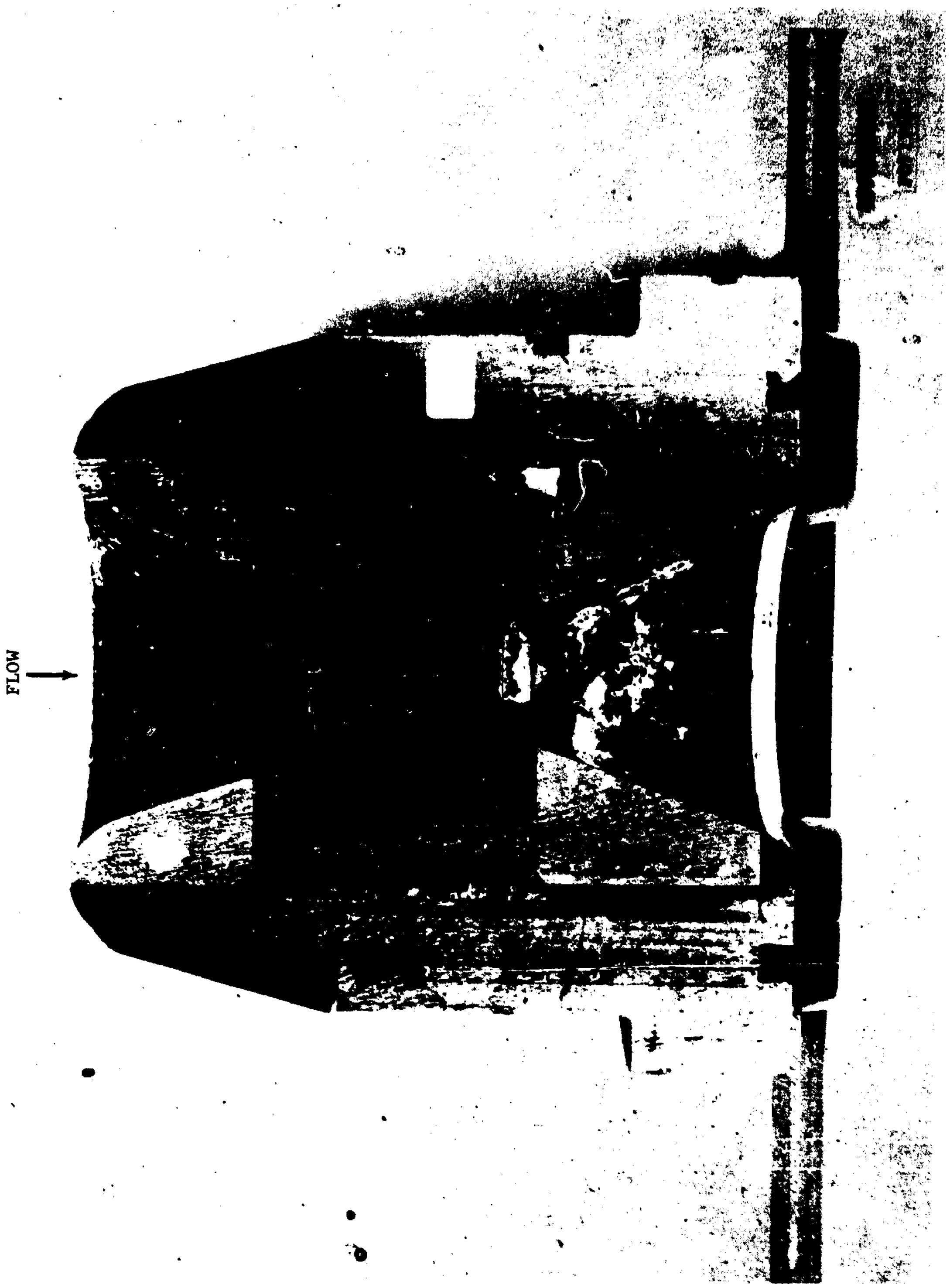

FIGURE 108. SUBMERGED NOZZLE FROM TEST T-23 - CROSS SECTION

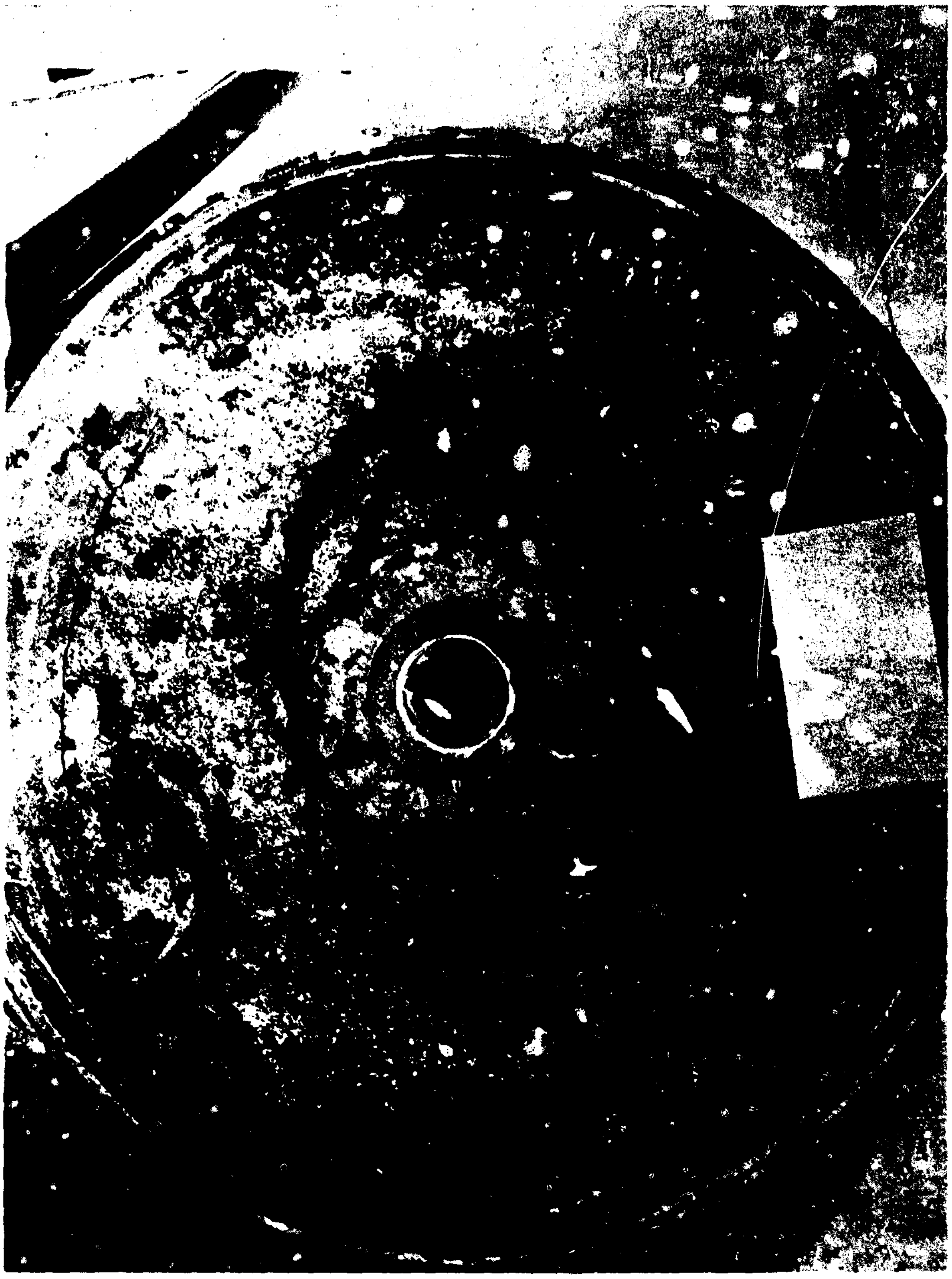

FIGURE 109. AFT CLOSURE INSULATOR AND NOZZLE FROM TEST T-24

the nozzle is shown in Figure 110. This firing was unusual in that a very long hang-fire occurred.

The test hardware was in good condition. The aft closure had a fairly uniform coating of beryllia on the flame front. The ATJ graphite entrance and exit cones had a thin, adherent coating. The pyrolytic graphite throat insert had a non-continuous, thin coating and there was some delamination of the washers.

(r) (C) Motor Test T-25

Motor Test T-25 was identical to Test T-9 except that a thicker pyrolytic graphite heat sink was used. The nozzle is shown in Figures 111 and 112 in the as-received condition. A cross section of the nozzle is shown in Figure 113. Nothing unusual was noted in the appearance of the aft closure insulator (not shown).

A series of deposits were taken from various areas on the hardware and analyzed by X-ray diffraction. The results are summarized in Table XXXII.

TABLE XXXII. MOTOR TEST T-25 DEPOSIT ANALYSIS (C)

Sample Number	Sample Location	Composition	
T-25-1	Graphite entrance cone, surface deposit	BeO	25-30%
		Be_2C	25-30
		Mg_2SiO_4	5-10
		Graphite	5-10
		Amorphous carbon	30-40
T-25-2	Deposit in crack in graphite entrance cone	BeO	20-30
		Be_2C	2-5
		Graphite	50-60
		Amorphous carbon	5-10
T-25-3	Pyrolytic graphite throat insert	BeO	75-85
		Be_2C	5-10
		MgO	2-5
		Graphite	5-10
		Pyrolytic graphite	2-5
T-25-4	Exit cone insulator	BeO	90-95
		Amorphous carbon	5-10

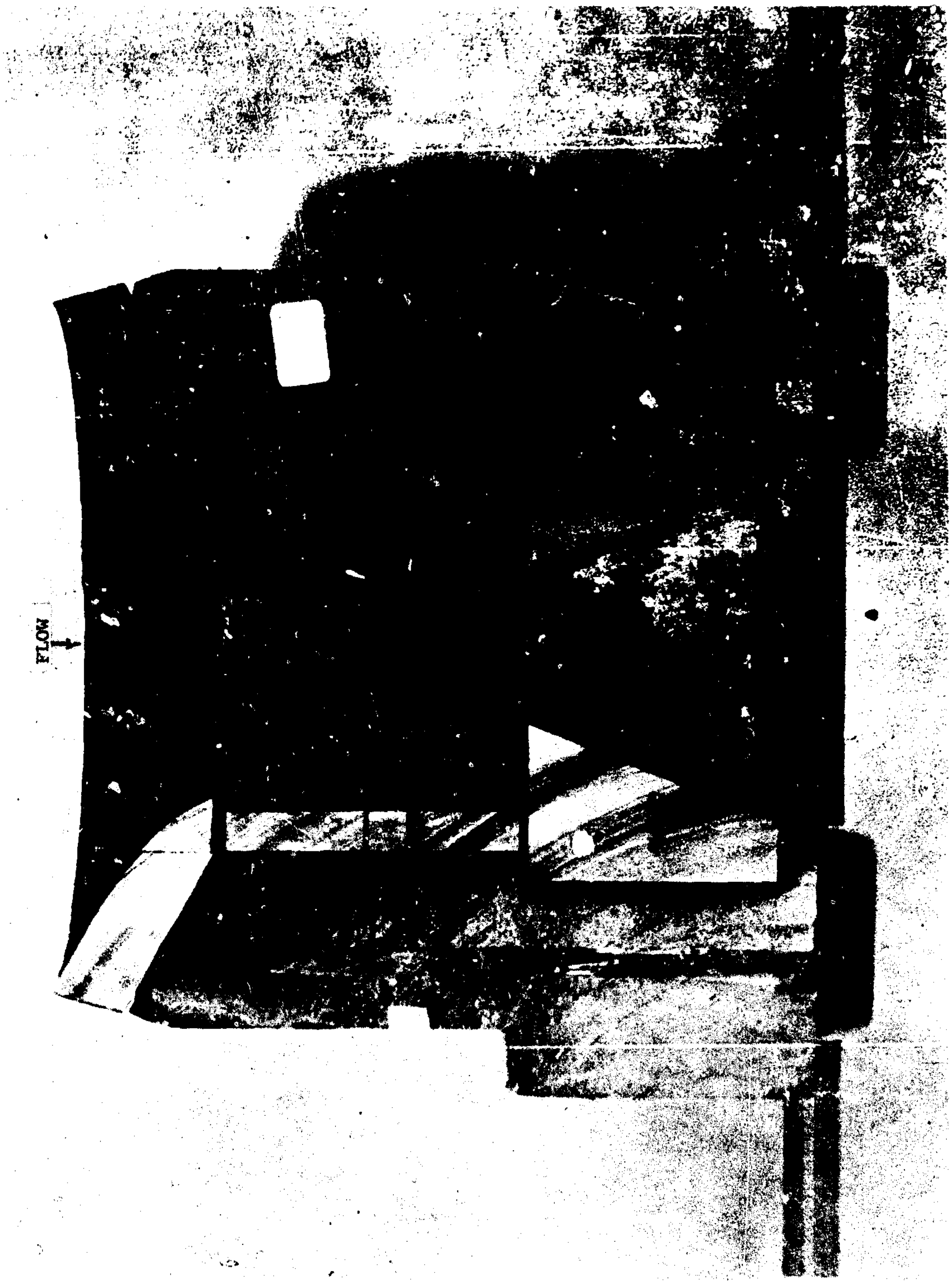

FIGURE 110. NOZZLE FROM TEST T-24 - CROSS SECTION

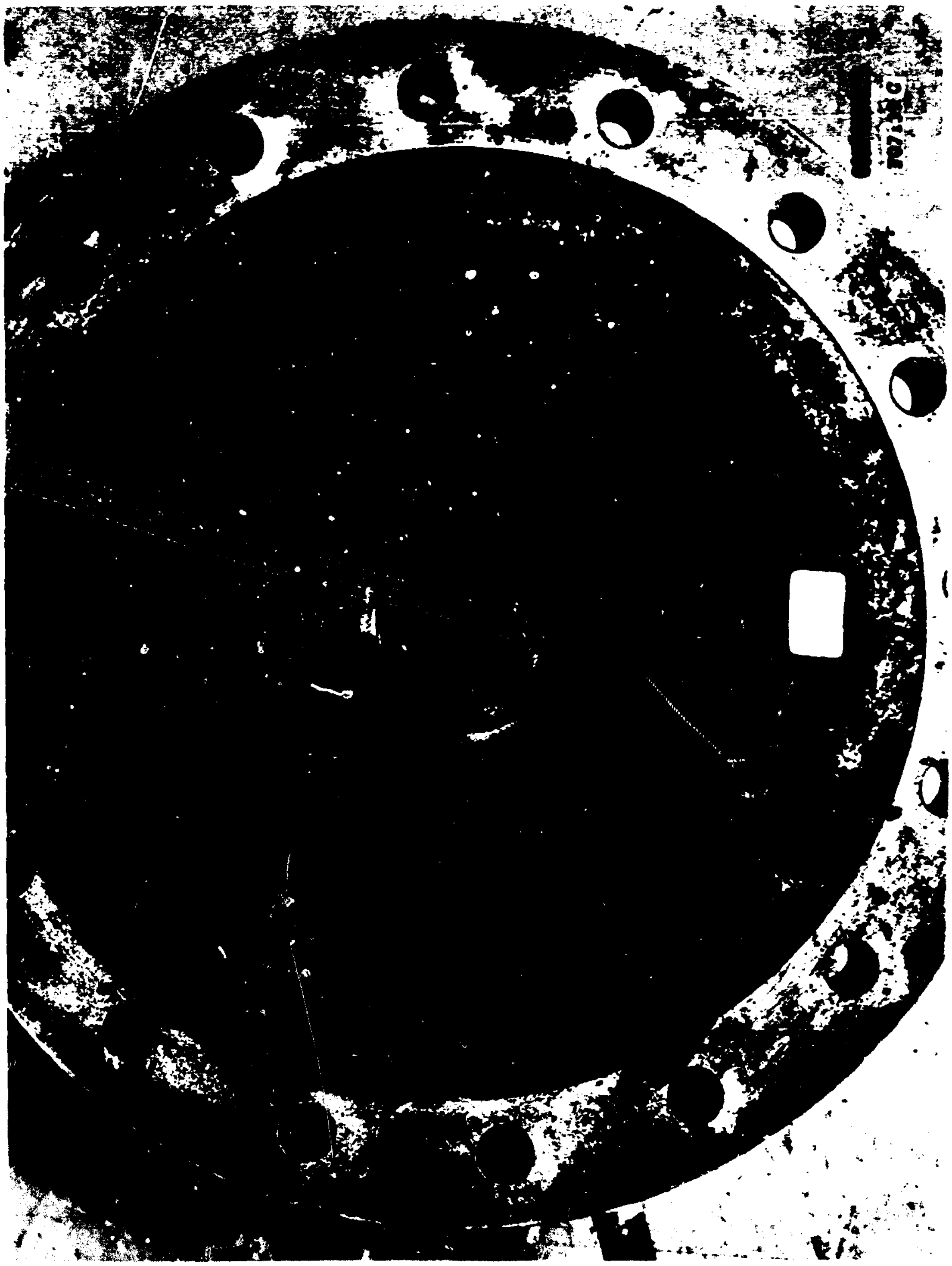

FIGURE 111. NOZZLE FROM TEST T-25 - ENTRANCE CONE VIEW

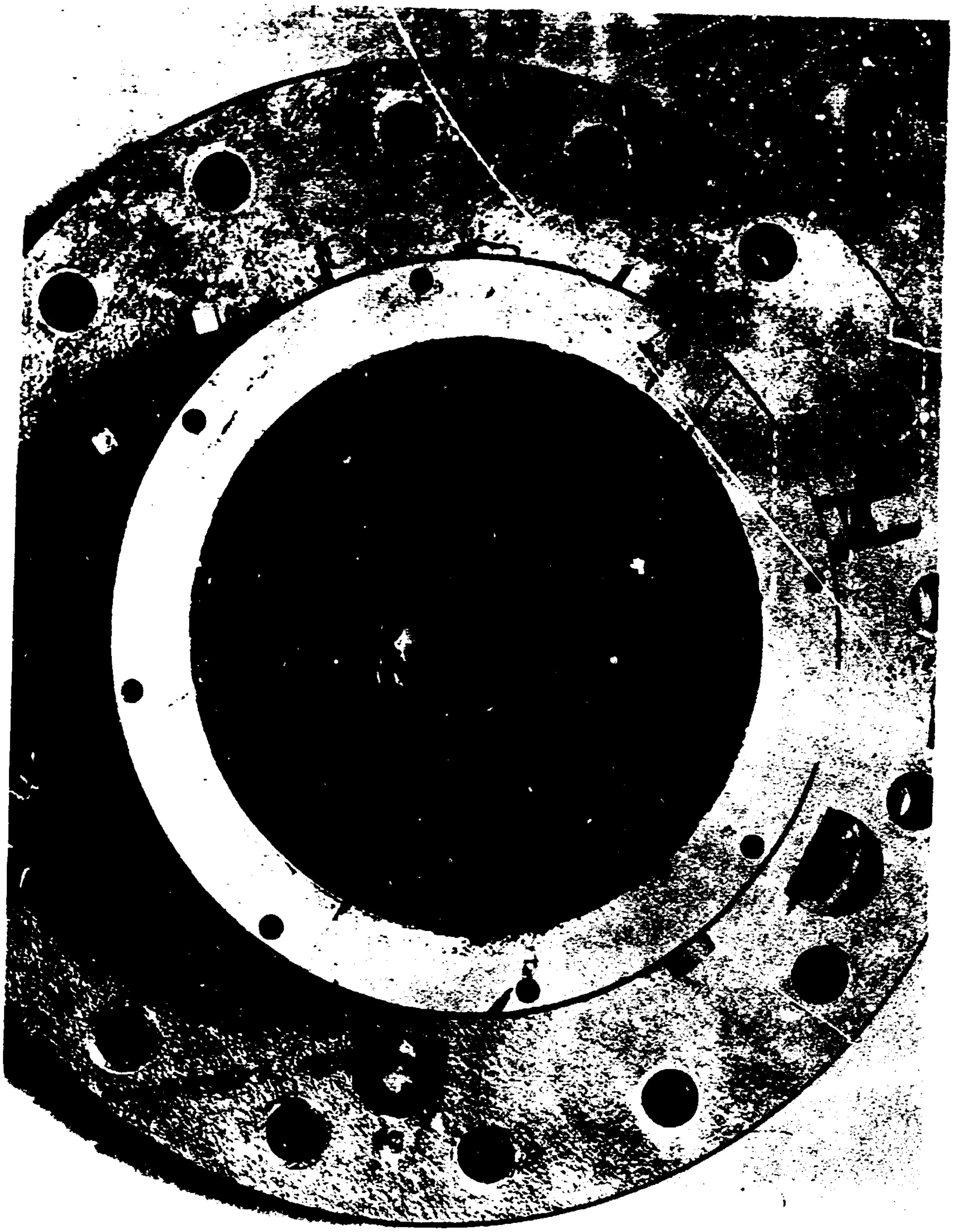

FIGURE 112. NOZZLE FROM TEST T-25 - EXIT CONE VIEW

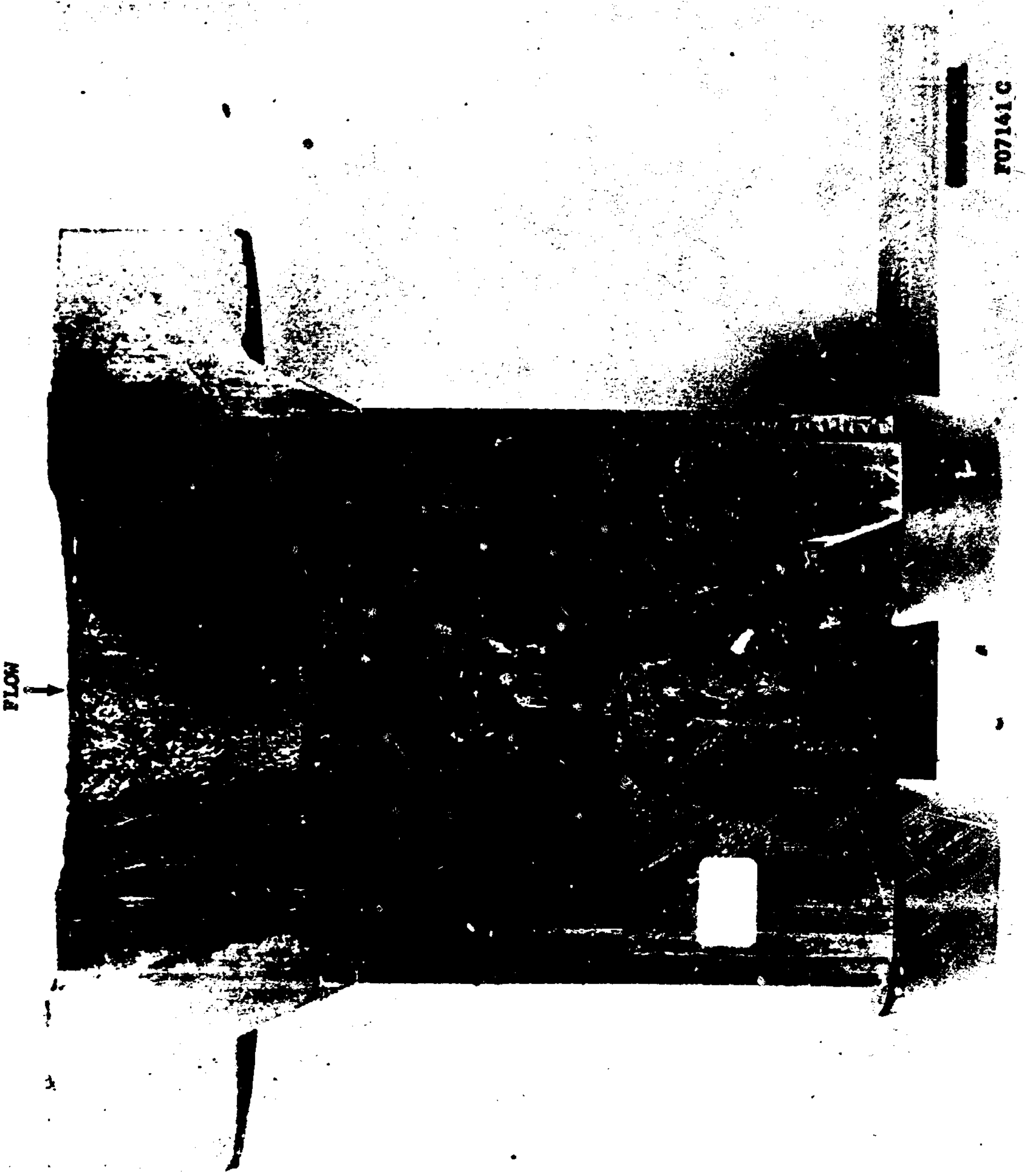
FLOW
F07141 C

FIGURE 113. NOZZLE FROM TEST T-25 - CROSS SECTION

There was nothing unusual or unexpected found during the examination of the hardware and in the deposit analysis. There was some delamination of the pyrolytic graphite washers, but this did not result in any grooving, non-uniform loss of material or gas leakage. The graphite entrance cone and exit cone were coated with a thick (0.05 inch) beryllia deposit and the pyrolytic graphite throat insert had a thin (0.01 inch) continuous coating of beryllia. There was approximately 0.15 inch of material lost from the flame front of the asbestos phenolic aft closure.

(2) (C) Hardware From Other Programs

A series of silver-infiltrated tungsten and graphite nozzles tested in the Aerojet ADOBE program (Reference11)have been received and inspected. The exact definition of the work to be done on these nozzles has not been determined.

Four pieces of a tungsten insert tested by Atlantic Research Corporation on the PALLAS program were received and analyzed. The four pieces are shown in Figure 114. The four pieces were from a ring upstream of the throat. The appearance of the fractured surfaces was clean, suggesting post-test fracturing. There was evidence of severe melting on the flame side surfaces. Samples of material taken from this face showed that there was considerable tungsten carbide formed in the melted areas. There were no tungsten-beryllium alloys found. The density was measured as 16.5 gm/an^3 or 85%. There was some silver found on the back side.

The limited amount of information immediately available about the test conditions made complete analysis difficult. The insert apparently was 85% dense tungsten infiltrated with silver. The duration of the test was long enough to completely delete the silver infiltrant. The density of the tungsten was not high enough to prevent severe physical erosion. The exhaust gases or insulation pyrolysis products must have had a high carbon content. The insert may also have been exposed to the carbon-bearing pyrolysis gases, causing the surface to become further carburized after motor shutdown. Two of the pieces which were adjacent appeared to have lost considerable material by physical erosion as opposed to carbide melting. These two pieces are shown in the top of Figure 114. The other two pieces appeared to have lost considerable material by carbide formation and melting. These are shown in the bottom Figure 114. Some of the carbide formation in this case may have resulted from the interaction of the tungsten with the carbon or graphite support at the leading edge of the insert. The original contour of the upstream edge could only be distinguished in a very small area. The rest of the upstream edge area was gone and the surface had a melted appearance. The most probable mechanism for the loss of material in this area is the formation and melting of tungsten carbide.

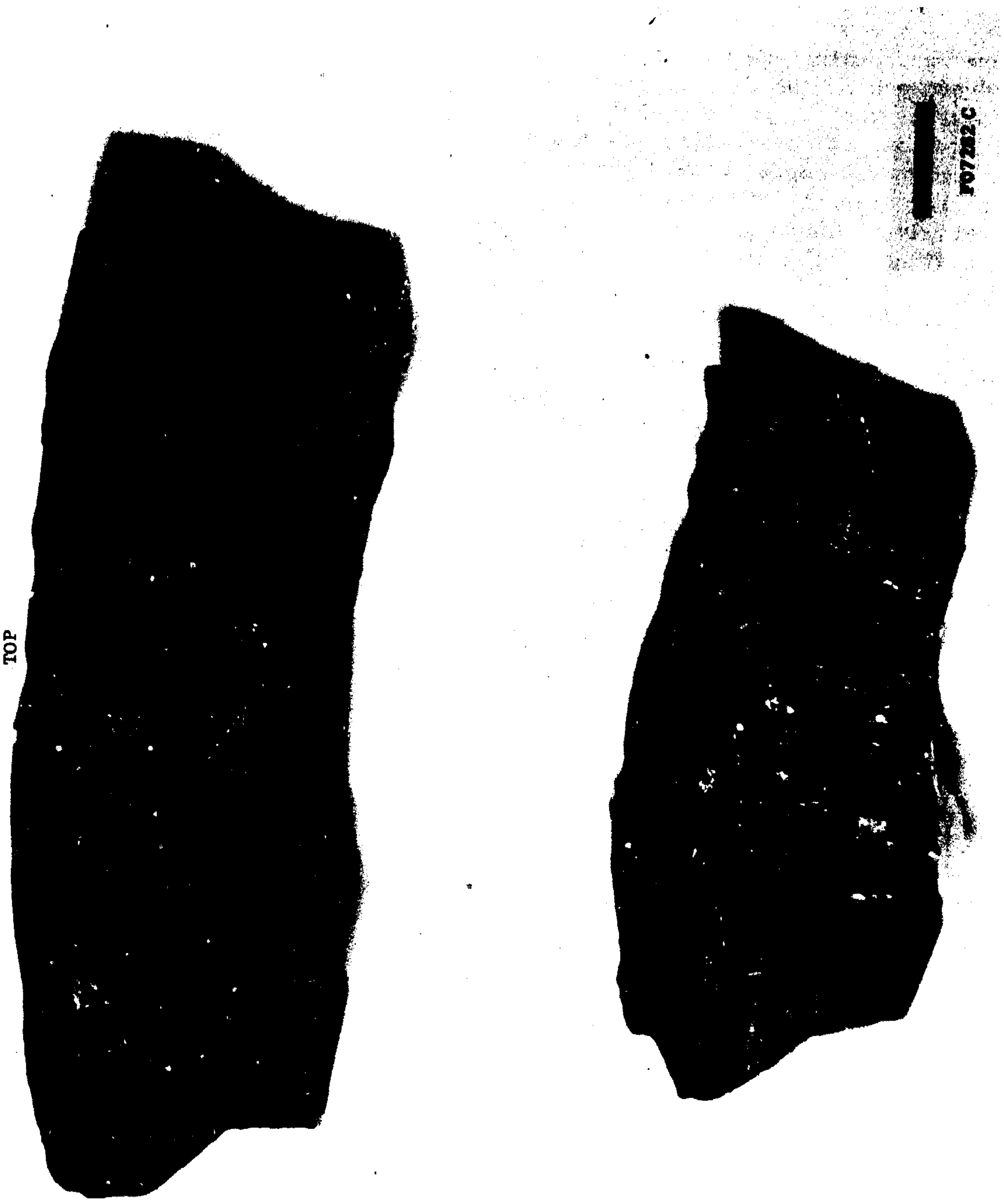
TOP
F07282C

FIGURE 114. TUNGSTEN RING FROM PALLAS SCALE MOTOR

b. (C) Exhaust Particle Sample Analysis

The exhaust plumes of Tests T-8 through T-25 were sampled for the condensed phases present. The sampling technique is discussed in Section 4.3 of Reference 2. The particles were rinsed from the inside of the bottles with benzene. This mixture was then concentrated to prepare samples for examination by electron microscopy.

The examination of the particles was limited to a single sample from each test because of the limited amount of information which was being learned. All particles examined from Tests T-9 through T-25 appeared to be very similar to the particles examined from Tests T-1 through T-4. These particles were all beryllium oxide and in general were very crystalline in habit. There were a very large number of very fine particles (0.01 to 0.2 micron) which were either crystalline or spherical (no obvious crystal habit). The crystalline particles were hexagonal, the crystalline form of normal beryllium oxide. The larger particles (larger than 5 microns) were irregular shapes (amorphous), crystalline (hexagonal) and spherical (no crystal habit). The spherical particles were in the minority relative to the hexagonal rods. The remaining particles were mostly irregular shapes. The number of the hexagonal crystalline particles was an order of magnitude greater than the number of spherical particles. The type of particles which were found are shown in Section 3.4b of Reference 2.

The particles collected from Test T-8 were all spherical, essentially identical to the particles found in Tests T-5, T-6 and T-7. The particles collected in Tests T-5 through T-7 are discussed in Reference 2. The particles collected in Test T-8 were approximately 60% gamma-alumina and 40% alpha-alumina.

A Coulter Counter was used to measure the particle size of the beryllia samples collected from Tests T-9 through T-15. A Coulter Counter measures the size of a particle by flowing a suspension of the particles in an electrically conducting fluid through an aperature and measuring the change in electrical resistivity across the aperature. The method is applicable to sizes ranging from approximately 0.6 to 200 microns. A significant number of the beryllium oxide particles collected were in this size range. Particle size data for the larger beryllia particles would be useful in estimating 2 phase flow losses.

The initial work done using the Coulter Counter to obtain the particle size was unsuccessful. The instrument requires that the particles be suspended in an electrolyte with a dispersant to separate the particles. If the small particles should agglomerate, they will appear as a much larger single particle in the measurement. The particles were observed during the counting process and it was found that there were many agglomerations which did not disperse in the suspending agent. Consequently, the particle size measurement was much higher than the true value. A number of different dispersing agents were tried without success as were a number of different electrolytes. The measurements were also very inconsistent. The calibration of the instrument gives reproducible results in the range of 1 to 2%. However, the measurements on the same beryllium oxide sample gave results ranging from less than 1 micron to as much as 10 microns as the average size.

The method appears to be useful in obtaining the particle size (or mean mass particle diameter) of exhaust products. However, for the beryllium oxide samples collected, the limited amount of effort expended was not sufficient to determine the proper conditions (i.e. proper electrolyte and dispersing agent) to allow good measurements to be made. The large number of very fine particles in the sample were probably the principle reason why there were large agglomerations. These particles were so small that there were appreciable charges on them and were very difficult to disperse.

3.5 (C) CONCLUSIONS, RECOMMENDATIONS, AND FUTURE WORK

a. (C) Discussion of Results and Conclusions

Preliminary conclusions, based on the laboratory studies conducted during the preceding stage of the program, were presented in Sections 3.5 of References 1 and 2. The results of the laboratory post-test analyses of the 18 motor firings conducted during this reporting period have led to the new and revised conclusions discussed below.

The laboratory post-test analysis of the fired hardware did not produce any evidence to contradict conclusions previously reached concerning the reactivity of condensed beryllium phases with wall materials. There is ample evidence that the ATJ graphite (entrance and exit cones), pyrolytic graphite, tungsten, asbestos phenolic and carbon cloth-phenolic have been exposed to beryllia and mixtures of beryllia and magnesium silicate (asbestos decomposition product) over wide ranges of temperature and pressure.

Evidence has been obtained to support the previous conclusion that molten beryllia will attack graphite at sufficiently high temperatures (compare ATJ graphite nose caps from Tests T-18 and T-12 with T-19 which was cooler). Low melting tungsten carbides were formed in Tests T-16, T-17 and T-18. On these tests, tungsten carbide or tungsten metal flowed onto the graphite exit cones. Large amounts of beryllium carbide were found in almost all of the nozzle and insulation deposit samples. Since high temperature liquid oxide attack of graphite and carburization of tungsten are also commonly observed with aluminum systems, it is concluded that these phenomena are not responsible for extreme erosion in beryllium systems.

The finding of rather large quantities of beryllium carbide along the nozzle contour apparently cannot be explained simply. The carbide could be formed during the combustion process and subsequently deposited along with the oxide. However, it is more likely that the carbide is the result of reactions between graphite and liquid beryllia, or possibly between graphite and beryllium. In either case, the carbide product could be transported along the contour with the liquid beryllia. This is apparently how the magnesium silicate reaches the throat and exit cone surfaces. Mixtures of these three materials would presumbably have a melting point below that of beryllia, which could prevent the thermal decomposition of the carbide. The mixture could then solidify on the exit cone surface or be expelled from the motor. By comparing the deposit analysis results, it can be observed that: (1) the exit cone deposits almost always contain asbestos decomposition products when that insulator was exposed to the flame, but do not always contain beryllium carbide; (2) no carbide was found on the exit cones of the first four tests; (3) no carbides were found on, or downstream of, the tungsten inserts; (4) the smallest amounts of the carbide appear when the Arcocel 319BRF propellant or a submerged nozzle were used in the test; and (5) the most carbide appeared on Test T-13, the only test where beryllium metal was found in the chamber residue. When the ballistic performance and deposition results are also taken into account, these observations strongly suggest that the beryllium carbide formation may be a direct result of reactions of unburned beryllium metal with carbonaceous char and nozzle inlet surfaces. It was not originally anticipated that beryllium carbide might serve as an indirect indicator of incomplete metal combustion. Consequently, some additional deposit sampling and correlation work will be performed during the final period of the program in an attempt to clarify the issue.

The examination of exhaust plume particle samples has provided no new results. No carbides, nitrides or beta beryllia were found. It has been concluded that the sampling procedure is biased in three major ways. First, only a very small sample is collected, from about the center of the plume and at a large distance from the motor. Secondly, unburned beryllium particles which might reach the throat should vaporize and burn in the exit cone, while any beryllium carbide formed in the chamber would tend to decompose at the temperatures of the exhaust within the nozzle. The third source of bias is that small amounts of dispersed beryllium nitride or carbide could not be detected. It has also been concluded that the analysis of exhaust condensables may also be biased when the entire exhaust is collected. A small motor, used for that purpose, could have very short residence times and, therefore, incomplete metal combustion. The carbide produced by beryllium reaction with the graphite nozzle could conceivably flow along the wall and be expelled. When such deposits are mixed with the exhaust particles, both beryllium and beryllium carbide would appear. In addition, beryllia reactions with graphite are believed to be the source of the formation of beta beryllia (see page 117, Reference 1). It is currently thought that sampling techniques could be devised to clarify the issue, but no action will be taken during the remainder of this program.

b. (U) Recommendations

It continues to be apparent that the post-test analysis of nozzle and chamber deposits can provide basic information which can be used to improve the understanding of both materials and propellant performance. It is recommended that such post-test analyses be conducted in other programs using beryllium and beryllium hydride propellants. It is also recommended that tungsten inserts tested with either beryllium or aluminum propellants be examined to determine the extent of carbide formation. When possible, all surfaces of the tungsten should be examined if graphite or materials which contain carbon are used to support the tungsten.

c. (U) Future Work

The major task remaining in the laboratory studies phase of the program is the post-test analysis of the hardware, deposits and exhaust plume particle samples from the four development motor tests (T-51 through T-54). Selected analyses will be performed on available hardware from the ADOBE and other programs. The electron microprobe study of carbon diffusion in (available) tungsten inserts will be completed. The comparison of the laboratory study and motor post-test analysis results will be completed and recommendations will be made concerning their use in support of future hardware design efforts.

SECTION IV (C)

CORRELATION STUDIES

4.1 (U) OBJECTIVES, SCOPE AND SUMMARY

a. Objectives

The primary objectives of the correlation studies effort in this program are to obtain and correlate data (from this and other programs) in a manner which can be used to help verify and/or explain the mechanisms of beryllium propellant erosion and corrosion in rocket motors. The correlation studies effort is divided into two basic functions: correlation and instrumentation. The correlation function incorporates three basic divisions of work: data acquisition, data classification, and data correlation. The instrumentation function for this program encompasses the acquisition of data for the correlation function through thermal instrumentation, ballistic instrumentation, and exhaust plume sampling.

The objectives of the correlation function during the third reporting period of this program are outlined below.

(1) Data Acquisition

- (a) Acquire thermal and ballistic data from the motor tests of this program.
- (b) Obtain data from related programs which will aid in establishing correlations.

(2) Data Classification

- (a) Classify and record all pertinent data from the tests of this and related programs (to avoid duplication of effort, the data from this program are presented in Section V of this report).

(3) Data Correlation

(a) Attempt to find correlations with motor test data only. This effort will be restricted to the propellants used in this program.

(b) Attempt correlations to support basic corrosion/erosion theories.

The objectives of the instrumentation functions for the third reporting period of this program are outlined below.

(1) Thermal Instrumentation

(a) Continue to evaluate the instrumentation and data requirements based on performance and the program objectives.

(b) Provide adequate and flexible instrumentation as required.

(c) Obtain or manufacture necessary special instrumentation.

(2) Exhaust Plume Sampling

(a) Obtain exhaust plume particle samples from all tests.

b. Scope

The correlation studies effort has been separated into two basic functions: instrumentation and correlation. The overall scope of the instrumentation function is defined and limited by the requirement that sufficient instrumentation be provided on each motor to characterize the nozzle thermal history and the motor performance. In addition, the instrumentation must be provided in accordance with the test schedule. The scope of the correlation function is more difficult to define even though there are more specific requirements and limitations. The correlation effort will include the collection and organization of appropriate beryllium and aluminum propellant motor design and test data, and the correlation of the results of laboratory tests, motor tests, and analytical studies. This effort will be limited to studying selected types of propellant and nozzle systems and to providing support in the general areas of the analytical efforts.

The effort expended on the correlation studies during this quarter was divided almost equally between the instrumentation and correlation functions. Where it was necessary to set a priority, the instrumentation function was accomplished first. This was necessary to prevent undue delays in the design, fabrication, and test schedules.

The scope of the instrumentation function was defined and limited by the following requirements:

(1) Adequate instrumentation will be supplied according to the fabrication and test schedule.

(2) Exhaust plume particles will be taken from all tests.

(3) Consideration will be given to both the small-scale motor tests and the development motor tests.

(4) All instrumentation will be continually reviewed for quality and quantity of data required.

The overall scope of the data correlation function has been defined and limited by the following general requirements:

(1) State-of-the-art propellants with beryllium metal additives will be investigated.

(2) A minimum number of aluminum propellants and test data, which are comparable to the beryllium propellants and data, will be considered.

(3) Both composite and double base propellants will be considered and compared.

(4) Emphasis will be placed on correlating data accumulated from the small motor tests during this program.

c. Summary of Progress

The following is a brief description of the progress made in the correlation studies effort during the second reporting period:

(1) The performance of the thermal and ballistic instrumentation on all of the small scale motor tests were evaluated.

(2) The thermal instrumentation for the development motors were designed, manufactured, and installed in accordance with data requirements.

(3) Exhaust plume particle samples were acquired from all the remaining small motor tests using Samples #2.

(4) Data from the small motor tests were subjected to comparative analysis. Observations and correlations are reported. Special emphasis was given to a study of the nozzle throat deposition phenomena.

4.2 (C) CORRELATION

a. (U) Data Acquisition

The motor test data obtained during the first quarter of this program were selected with the primary objective of providing a basic background of information on beryllium propellant motor design problems. This type of information was particularly useful in the initial hardware design phase of this program. The data selected for study during the second quarter of this program were chosen with the primary purpose of establishing raw data correlations. Most of the data used were from small motor tests with propellants similar to those being tested on this program. Data obtained during the third reporting period of this program were selected primarily for the purpose of establishing correlations to describe the metal oxide deposition phenomenon. Most of the data acquired for this purpose were taken from the tests performed during this program. Additional data from small motor tests on other programs were acquired for correlations related to the corrosion/erosion pehnomenon. However, this correlation effort was not completed during this reporting period.

The literature survey and data acquisition required for this program are not considered complete. It is anticipated that data from other programs will be continually reviewed, evaluated, and collected for use through the duration of the program.

b. (C) Correlation

(1) (C) Observations on Deposition Data

In the Second Technical Progress Report (Reference 2), it was reported that one of the most important factors in the study of beryllium propellant corrosion and erosion is the behavior of the metal oxide deposition. The alumina and beryllia deposits protect the nozzle from corrosion or erosion and, in some cases, cover over erosion that occurred earlier in the firing. Since deposition can significantly alter the expected chamber pressure, thrust, thrust vector, and performance and, since the phenomenon is particularly dramatic with the beryllium propellants, it is important that appropriate consideration be given to the correlation of deposition data. An attempt will be made in the following paragraphs to: (1) compare deposition curves from the small motor tests, (2) make observation about various apparent phenomena, and (3) to indicate potential generalities and correlations. It is recognized that the data available is quite limited (no duplicate tests to insure consistency), and, consequently, the conclusions drawn from these data may need further verification.

The deposition correlations attempted with the data from this program are keyed to three general design parameters: (1) the propellant composition, (2) the grain design, and (3) the nozzle design. It is emphasized that the small number of tests available for this program prevented empirical examination of the effects of many potentially important design variables or parameters. The results of correlations established here may be obscured or altered by variables or parameters not evaluated on this program.

For simplicity, the observations made with the data are organized and presented in outline form. This method should be helpful, since there are a large number of observations and potential correlations.

OUTLINE OF DEPOSITION OBSERVATIONS (C)

I. Effect of Propellant Composition

A. Direct comparisons are made between the deposition-time curves for the different propellants used on this program in similar grain and nozzle configurations.

(1) Type I grains, conventional P.G. nozzle (see Figure 115):

- Deposition curves have characteristic shape (head and shoulders).

(2) Close end burning grain, steep inlet P.G. nozzles (see Figure 116):

- Deposition curves have characteristic shape.
- 319BRF propellant has least deposition.
- Deposition earliest for 191F, latest for 54F.

(3) Remote end burning grain, conventional P.G. nozzles (see Figure 117):

- Quantity of deposition in descending order: 24F, 54F, 191F and 319BRF.

- Peak deposition in descending order: 24F, 54F, 191F and 319BRF.
- 191F, 54F and 24F have same general deposition curve shapes.
- Order of deposition initiation: 191F, 54F, 24F and 319BRF.

B. Comparison of deposition curves from 191F and 319BRF beryllium and aluminum analog propellants in all similar configurations (Figure 118):

(1) Of beryllium propellants, 319BRF characteristically has lower peak and total deposition than 191F.

(2) Except for the remote end burning grain configuration, the two beryllium propellants have same general shapes of deposition curves.

(3) 389 aluminum analog has less total and peak deposition when compared to the 390 analog.

(4) 389 also has earlier initiation and removal of deposition than the 390.

(5) Except for the remote end burner, deposition appears to start at about the same time for both 319BRF and 191F.

C. Comparison of deposition curves for 191F and 54F beryllium and aluminum analog propellants in all similar configurations (Figure 119):

(1) The most interesting observation here is that, except for the Type I grain comparisons, the 54F propellant and its analog always have more deposition than the 191F and its analog.

(2) In all cases tested, the 191F and its analog always lose the throat deposits first.

(3) The deposition curves of the two beryllium propellants are most similar in the close end burner configuration.

D. Comparison of 319BRF and 54F beryllium and aluminum analog propellants in all similar configurations tested (Figure 120):

(1) In all cases tested, 319BRF and its analog always have less total deposition.

(2) The curves are most similar in the close end burner and Type I grain configurations.

E. Summary and Conclusions (Propellant Composition):

(1) With the exception of Test T-11, the quantity of deposition, regardless of grain type or nozzle configuration, is always ordered as follows: 54F, the most, followed by 191F and 319BRF.

(2) With the exception of Test T-11, the initiation of deposition is always earliest for the 191F propellant.

II. Effect of Grain Design

A. Stay Time:

(1) Consider all propellants with end burning grains only (see Figure 121):

a. Aluminum analogs, when compared to their beryllium counterparts, always had:

- less total deposition,
- lower peak deposition,
- earlier peak deposition,
- earlier deposition removal.

b. Beryllium propellants:

- 319BRF always had less total deposition than the others,
- 319BRF always had lower peak deposition,
- 191F had earlier start and earlier end of deposition,
- descending order of peak deposition was: 24F, 54F, 191F and 319BRF,
- 319BRF in close configuration resembled 191F and 54F in the remote position.

c. Aluminum analogs more nearly resemble counterpart beryllium propellants when the beryllium propellants were in the longest stay time configurations, particularly the 319BRF and the 390 analog.

(2) Compare total range of stay time (Type I with end burning grains) for only the beryllium propellants (191F, 319BRF, 54F) with P.G. nozzles (see Figure 122):

a. If stay time were the overriding parameter, then the above results indicate that the Type I grain would have more deposition than even the close end burner; however, the Type I always had lower total and lower peak deposition than the end burning grains.

b. Deposition started earlier w. n Type I grains for all propellants, earliest for the 54F propellant.

c. 191F demonstrated the least difference in the effects of stay time on the magnitude and shape of the deposition curve; 319BRF shows the most difference.

B. Grain Configuration:

(1) Type I grain deposition curves from all tests except T-20 are plotted in Figure 123:

a. Note that there are at least 3 points of similarity (head and shoulders shape).

b. Location in time of first shoulder is almost identical for all cases shown (3 to 3.5 seconds after start).

c. Location in time of the head was about 4.5 to 6.5 seconds after start.

d. Location in time of second shoulder is 12.5 to 14 seconds after start.

e. None of these tests had corrosion early in run.

f. Start of deposition was in no case later than 1.5 seconds after start of test.

(2) Type II grain deposition curves are shown in Figure 124:

a. There are at least 3 points or similarity:

- initial deposition,
- corrosion in middle of run (the aluminum analog did not have measurable corrosion),
- final deposition.

b. The later the initial deposition, the greater the corrosion.

c. Final deposition appears to be lasting.

(3) Type III grain deposition compared with other 319BRF grains (see Figure 125):

a. The lower stay time of the Type III grain may be causing more deposition than the end burner. Test T-15 had the second highest deposition for the 319BRF next to T-24.

b. Deposition start time and shape are similar to T-24.

C. Summary and Conclusions (Grain Design):

(1) Stay time:

a. With the exception of T-8, the aluminum analogs always have:

- less total deposition,
- lower peak deposition,
- earlier peak deposition,
- earlier deposition removal.

b. Aluminum analogs are more likely to resemble their beryllium counterparts with respect to deposition/corrosion curve shape when the beryllium propellant has a long stay time.

c. Type I grains (which have lower stay time than end burners) show lower total deposition which is contrary to trend shown by end burners.

d. Stay time affects the deposition by different propellants in varying degrees:

- 191 shows least difference in shape and magnitude of deposition curve,
- 319 shows most difference in shape and magnitude of deposition curve.

(2) Grain configuration:

a. All Type I grains have similar features (head and shoulders shape) except for T-20 which has initial corrosion before the first shoulder.

b. All beryllium Type II grains had similar features (initial deposition, followed by corrosion/erosion, followed by deposition).

c. Quantity of deposition adhering to the nozzle throat for beryllium propellants can be generally associated with the grain type in descending order: (1) close end burners, (2) Type III, (3) remote end burners, (4) Type II and (5) Type I. Note: Type II grains produced large amounts of deposition near the end of the run which covered over the erosion that occurred in the middle of the run.

III. Effects of Nozzle Design

A. The effects on deposition of nozzle type for various propellants and grain designs are illustrated in Figure 126:

(1) 191F propellant Type I grain:

a. Deposition curves have similar shapes.

b. Deposition quantity is more for the tungsten than P.G. nozzle of similar configuration.

c. The submerged tungsten nozzle gave more deposition than the conventional tungsten.

d. The order of deposition initiation was: submerged W, conventional W, conventional P.G.

e. The submerged nozzle gave a greater initial pulse of deposition (first shoulder).

(2) 191F propellant with the close end burning grain:

a. The steep inlet gave more deposition than submerged P.G. nozzle.

b. The submerged nozzle gave greater initial pulse of deposition (first shoulder).

(3) 319BRF propellant Type I grain configuration:

a. Submerged tungsten gave more deposition than conventional P.G.

b. The tungsten throat had earlier deposition initiation.

B. Heat Sink Effects (see Figure 127):

(1) Test T-25 has greater heat sink and comparably greater deposition thickness than T-9.

(2) With similar propellants, grain design, and nozzle configurations, the tungsten and thick throat P.G. nozzles give very similar deposition curves.

(3) The basic shapes of the deposition curves were maintained regardless of heat sink thickness with similar nozzle, grain, and propellants.

C. Carbon Cloth Entrance Section (see Figure 128):

(1) There was a similarity in the deposition curve with and without the carbon cloth entrance.

(2) Peak deposition with the carbon cloth entrance section is slightly greater.

D. Summary and Conclusions (Nozzle Design Effects):

(1) Order of amount of deposition:

- steep inlet highest,
- submerged next,
- conventional least.

(2) Tungsten nozzles give greater quantity of, earlier initiation of, and longer lasting deposition than P.G. for a given propellant and grain design.

(3) Submerged nozzles give greater initial pulse of deposition.

(4) Greater throat heat sink gives greater total deposition.

(5) Greater throat heat sink gives greater initial deposition.

(2) (C) Discussion of Results

Discussions of the correlation of corrosion, ballistic performance and convective heat transfer have been included in Section II. The purpose of this paragraph is to analyze the observations (or facts) presented in outline form in Paragraph (1) above.

The program, as a whole, has been based on the assumption that nozzle erosion and deposition can always be explained by means of basic fluid mechanics, chemistry and heat transfer arguments. It is also presumed that the fundamental arguments apply equally well to both aluminum and beryllium propellant systems except in degree. Thus, while alumina deposition and flow has long been recognized, it has commonly been regarded as a nuisance (very small nozzles), a major problem (transpiration cooling) or simply neglected. Consequently, very little effort has been devoted to the development of physical and analytical models to characterize deposition effects. It is particularly interesting, then, to test the deposition data, obtained in the small motor tests, against the hypotheses and assumptions which provided the basis for the original selection of the test design. In most cases, new questions arise and new levels of understanding are reached.

Examination of the deposition curves leaves the impression that there are systematic characteristics. The time gap, between ignition and the appearance of deposits at the throat, is common to all tests except T-8 and T-10. This is in agreement with the program results which predict that impingement occurs well upstream of the throat and that deposits must flow long the contour to reach the throat. The issue is somewhat confused for the Type II slotted grains since the complicated grain flow field could promote deposition near the throat, but not uniformly over the circumference.

The "head and shoulders" deposit curve shape (see Figures 115 and 123) is most distinct for the Type I grain design. The initially exposed section of the asbestos phenolic aft closure insulation erodes at an average rate of about 10 mils per second, producing significant quantities of liquid decomposition products of asbestos. It follows that the first shoulder in the deposition curve may be a reflection of a lower melting deposit mixture of beryllia and asbestos. It can also be expected that the particular combination of the Type I grain design and the associated aft closure insulator-nozzle contour is least conducive to particle deposition. That is, the gas flow field is such that oxide or burning metal particles tend to slip away from the wall rather than toward it (see Section 2.4). A concentration of the particles near the centerline seems likely and this should contribute to the performance loss.

The main deposit pulse (head) probably is the result of the gradual runoff of deposits initially frozen along the contour. The peak deposit thickness would be related to the heat sink capacity of the nozzle inlet materials, the amount of low melting impurity in the deposit and the amount of deposition occurring upstream of the inlet section. The hottest propellant (Arcocel 191F) produces the highest peak deposition. It is tempting to speculate that this is due to higher decomposition of asbestos, but this could also derive from a different beryllia particle size distribution (with respect to the other propellants), higher deposit flow velocities or different beryllia particle size distributions.

The second shoulder occurs when the grain has burned approximately half way through. The changes in the chamber flow field will tend to increase the rate of beryllia deposition. The oxide particles will hit the contour at a point which continuously moves away from the throat. The increase in the deposit flow path length should be offset by higher contour temperatures. Thus, the deposit thickness may vary considerably during the latter part of the firing.

Similar arguments can be applied to the end burning grain tests. Consider the deposit histories compared in Figures 116 and 117. In these tests, the entire asbestos phenolic aft closure insulator was exposed to the flame. Post-test analysis (Section 3.4) showed that very little char erosion had occurred and that large amounts of beryllia were retained on the char at the end of firing. The end burner chamber flow fields should produce more

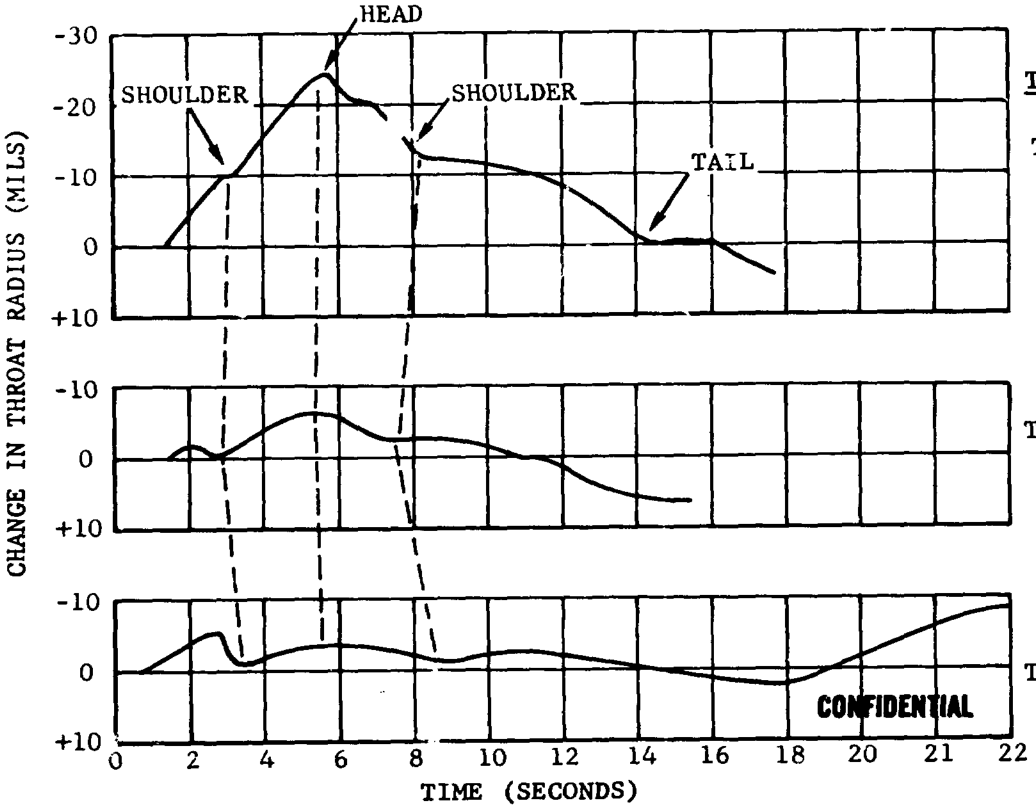

TEST	PROPELLANT	GRAIN TYPE	NOZZLE
T-9	191F	I	CONVENTIONAL P.G.
T-14	319BRF	I	CONVENTIONAL P.G.
T-11	54F	I	CONVENTIONAL P.G.

FO8071C

FIGURE 115. PROPELLANT EFFECTS ON THROAT DEPOSIT HISTORY (I)

NOTE: ALL TESTS HAVE SHOWN ARE CLOSE END-BURNING GRAIN AND STEEP INLET PYROLYTIC GRAPHITE NOZZLES

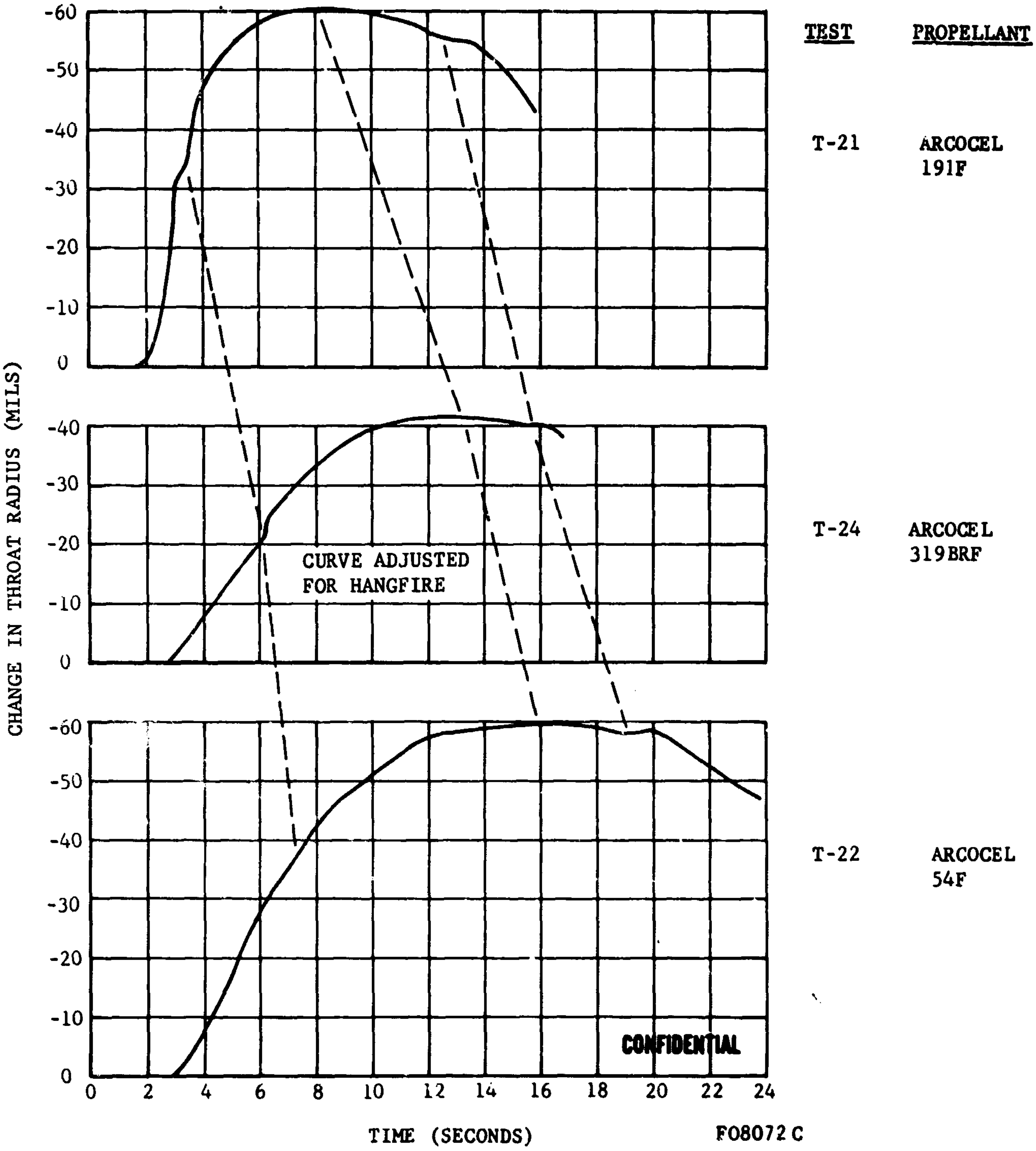

FIGURE 116. PROPELLANT EFFECTS ON THROAT DEPOSIT HISTORY (II)

NOTES:

ALL NOZZLES ARE CONVENTIONAL PYROLYTIC GRAPHITE

TIME SCALE ADJUSTED TO ELIMINATE IGNITER SPIKES

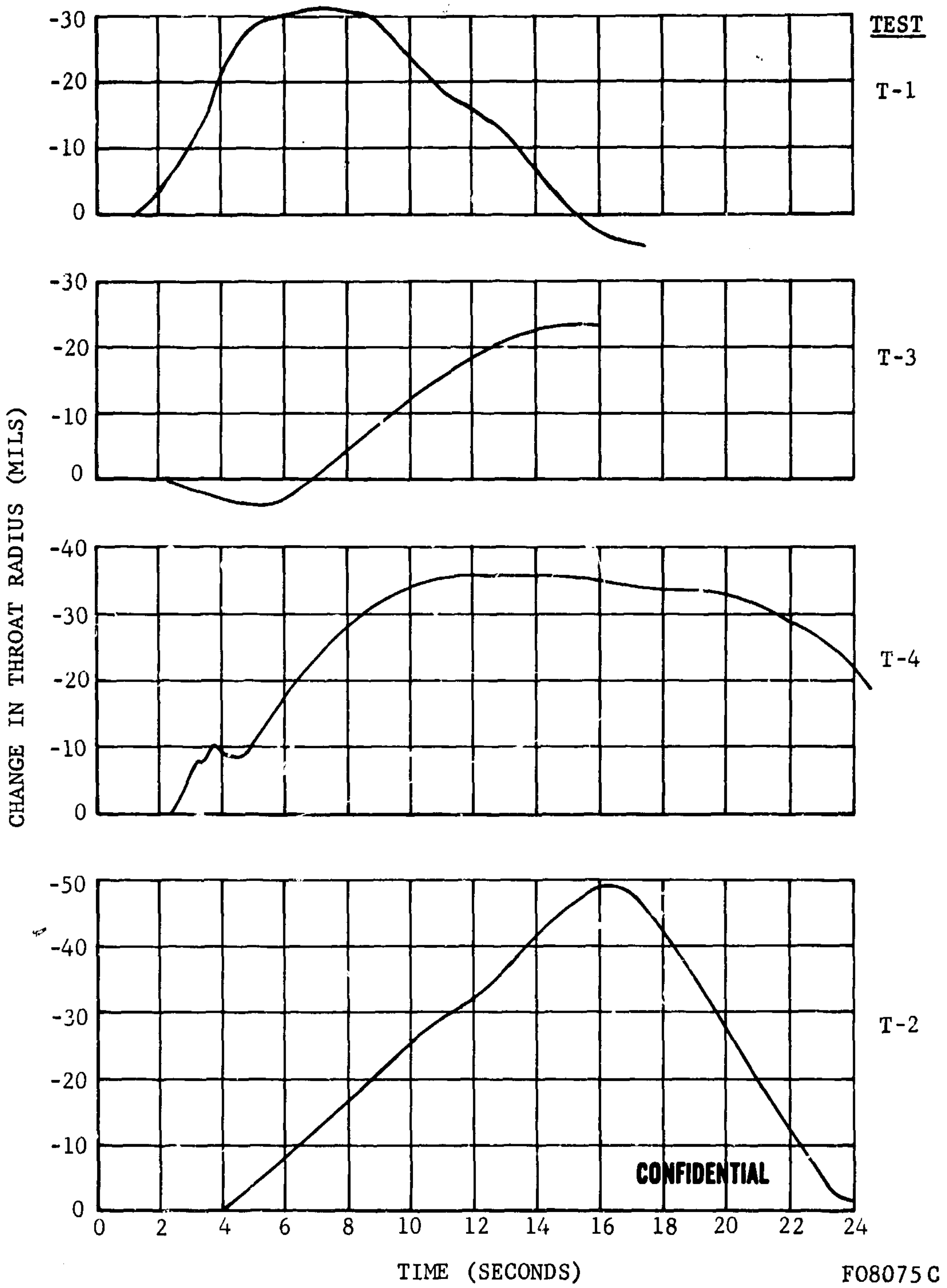

TEST	PROPELLANT	GRAIN
T-1	191F	REMOTE END BURNER
T-3	319BRF	REMOTE END BURNER
T-4	54F	REMOTE END BURNER
T-2	24F	REMOTE END BURNER

FIGURE 117. PROPELLANT EFFECTS ON THROAT DEPOSIT HISTORY (III)

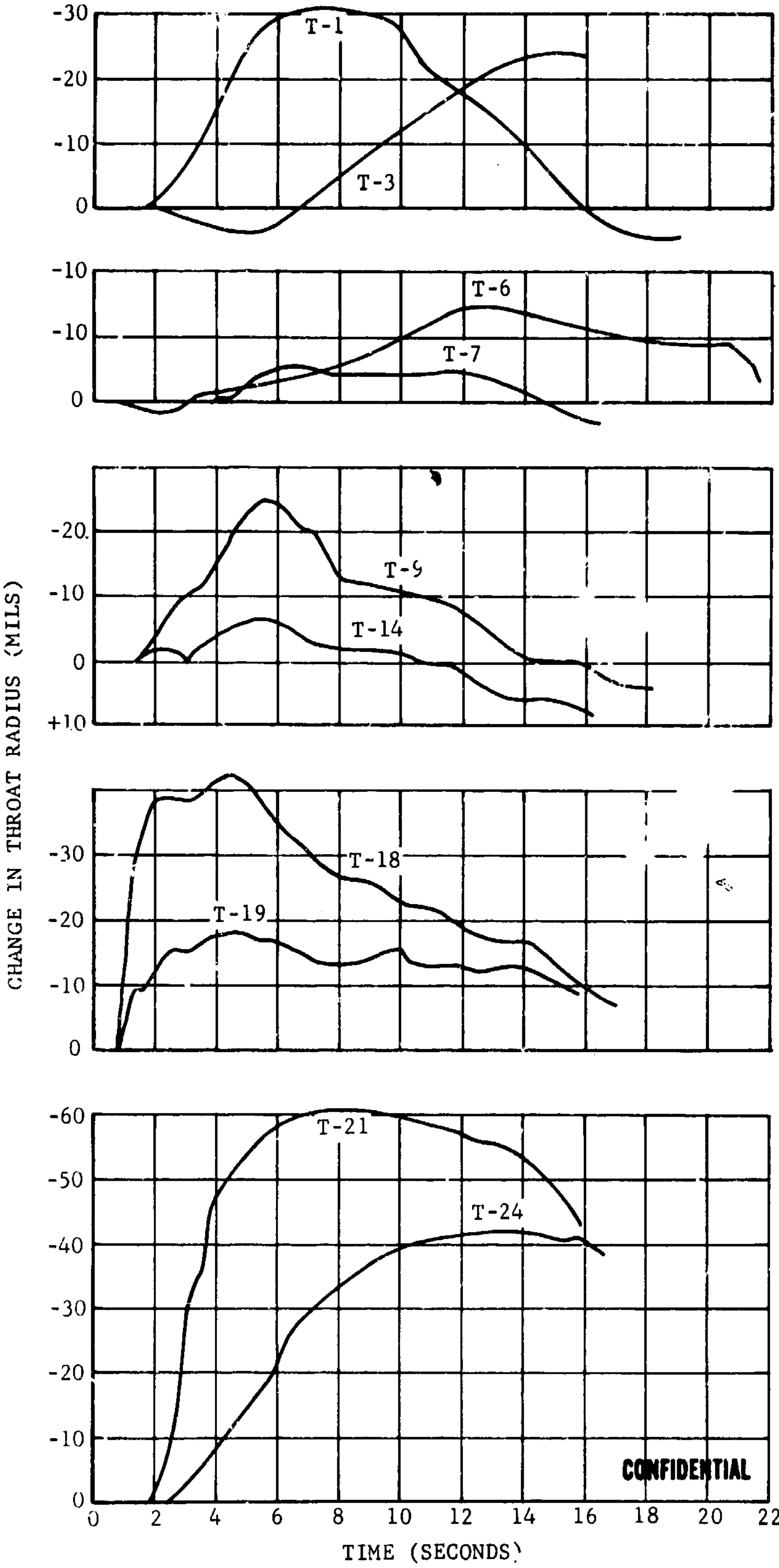

TEST	PROPELLANT	GRAIN	NOZZLE
T-3	319BRF	REMOTE END BURNER	CONVENTIONAL P.G.
T-1	191F	REMOTE END BURNER	CONVENTIONAL P.G.
T-6	390	REMOTE END BURNER	CONVENTIONAL P.G.
T-7	389	REMOTE END BURNER	CONVENTIONAL P.G.
T-9	191F	I	CONVENTIONAL P.G.
T-14	319BRF	I	CONVENTIONAL P.G.
T-18	191F	I	SUBMERGED TUNGSTEN
T-19	319BRF	I	SUBMERGED TUNGSTEN
T-21	191F	CLOSE END BURNER	STEEP INLET P.G.
T-24	319BRF	CLOSE END BURNER	STEEP INLET P.G.

F08108 C

FIGURE 118. PROPELLANT EFFECTS ON THROAT DEPOSIT HISTORY (IV)

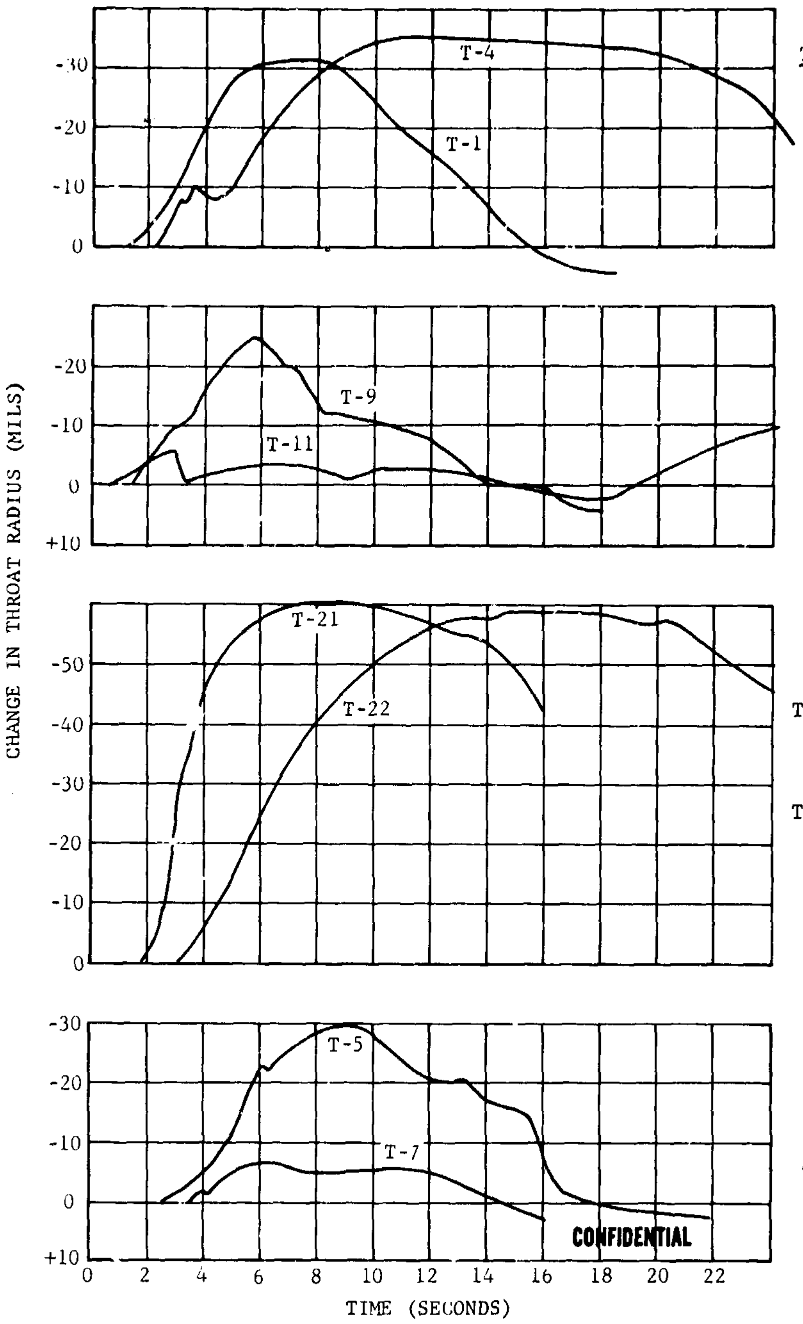

TEST	PROPELLANT	GRAIN	NOZZLE
T-1	191F	REMOTE END BURNER	CONVENTIONAL P.G.
T-4	54F	REMOTE END BURNER	CONVENTIONAL P.G.
T-9	191F	I	CONVENTIONAL P.G.
T-11	54F	I	CONVENTIONAL P.G.
T-21	191F	CLOSE END BURNER	STEEP INLET P.G.
T-22	54F	CLOSE END BURNER	STEEP INLET P.G.
T-7	389	REMOTE END BURNER	CONVENTIONAL P.G.
T-5	60	REMOTE END BURNER	CONVENTIONAL P.G.

F08109C

FIGURE 119. PROPELLANT EFFECTS ON THROAT DEPOSIT HISTORY (V)

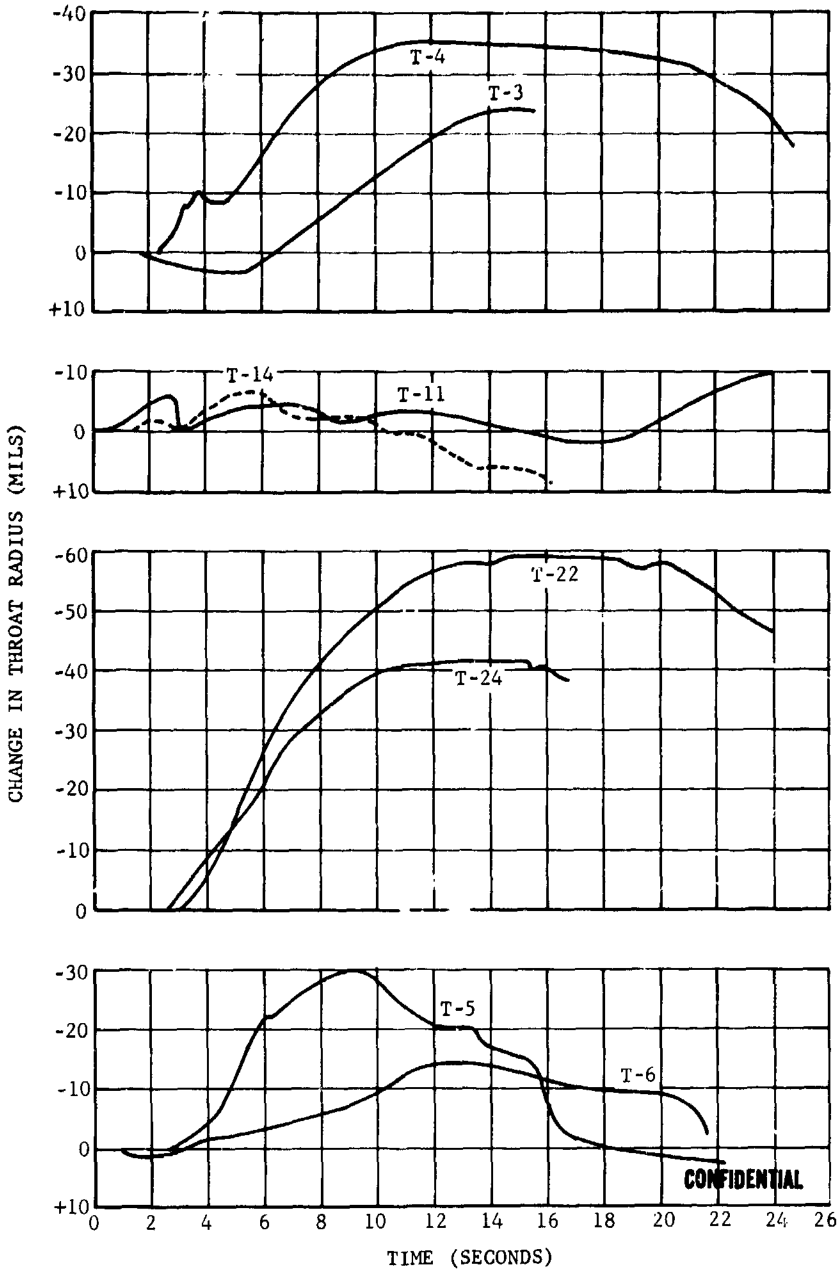

TEST	PROPELLANT	GRAIN	NOZZLE
T-3	319BRF	REMOTE END BURNER	CONVENTIONAL P.G.
T-4	54F	REMOTE END BURNER	CONVENTIONAL P.G.
T-14	319BRF	I	CONVENTIONAL P.G.
T-11	54F	I	CONVENTIONAL P.G.
T-24	319BRF	CLOSE END BURNER	STEEP INLET P.G.
T-22	54F	CLOSE END BURNER	STEEP INLET P.G.
T-6	390	REMOTE END BURNER	CONVENTIONAL P.G.
T-5	60	REMOTE END BURNER	CONVENTIONAL P.G.

F08110 C

FIGURE 120. PROPELLANT EFFECTS ON THROAT DEPOSIT HISTORY (VI)

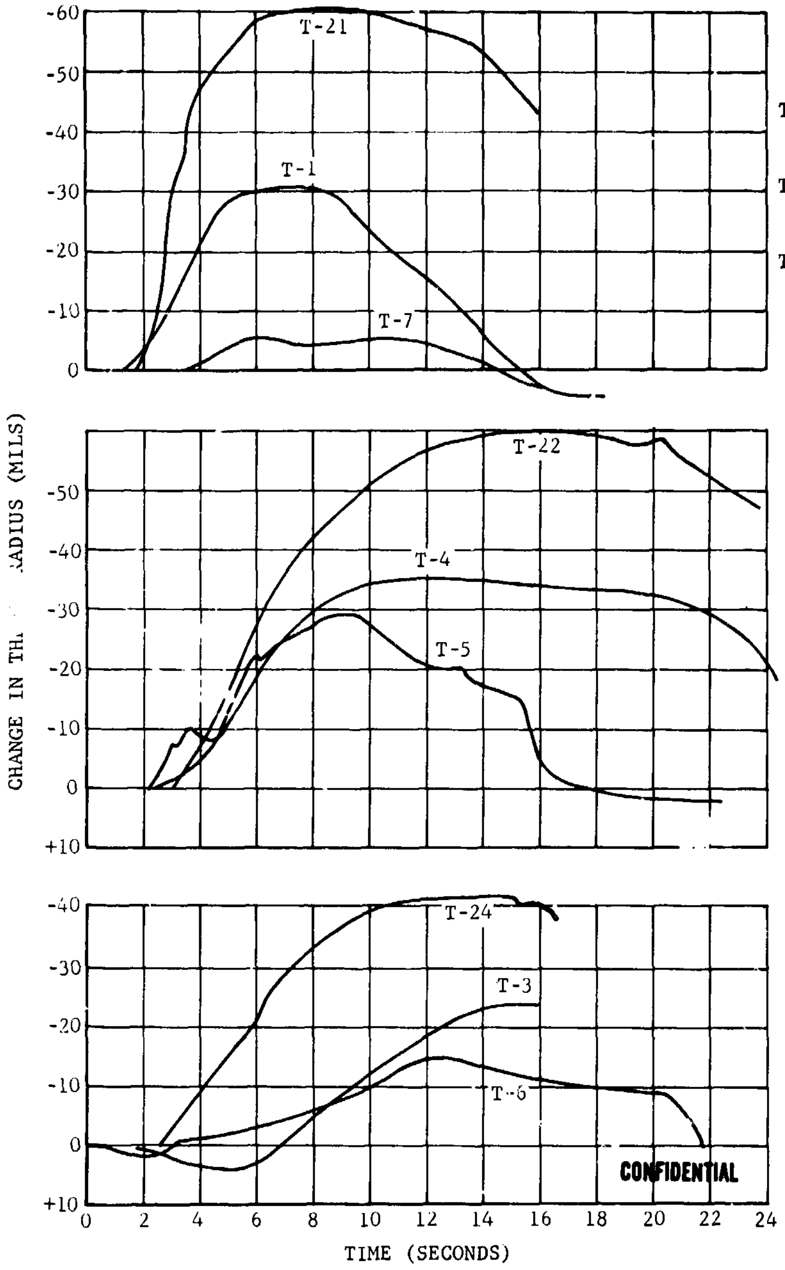

TEST	GRAIN	PROPELLANT	NOZZLE
T-21 (Be)	CLOSE END BURNER	191F	STEEP INLET P.G.
T-1 (Be)	END BURNER	191F	CONVENTIONAL P.G.
T-7 (Al)	END BURNER	389	CONVENTIONAL P.G.
T-22 (Be)	CLOSE END BURNER	54F	STEEP INLET P.G.
T-4 (Be)	END BURNER	54F	CONVENTIONAL P.G.
T-5 (Al)	END BURNER	60	CONVENTIONAL P.G.
T-24 (Be)	CLOSE END BURNER	319BRF	STEEP INLET P.G.
T-3 (Be)	REMOTE END BURNER	319BRF	CONVENTIONAL P.G.
T-6 (Al)	REMOTE END BURNER	390	CONVENTIONAL P.G.

*LARGE AFT CLOSURE INSULATORS

F08112C

FIGURE 121. EFFECT OF STAY TIME ON THROAT DEPOSIT HISTORY (I)

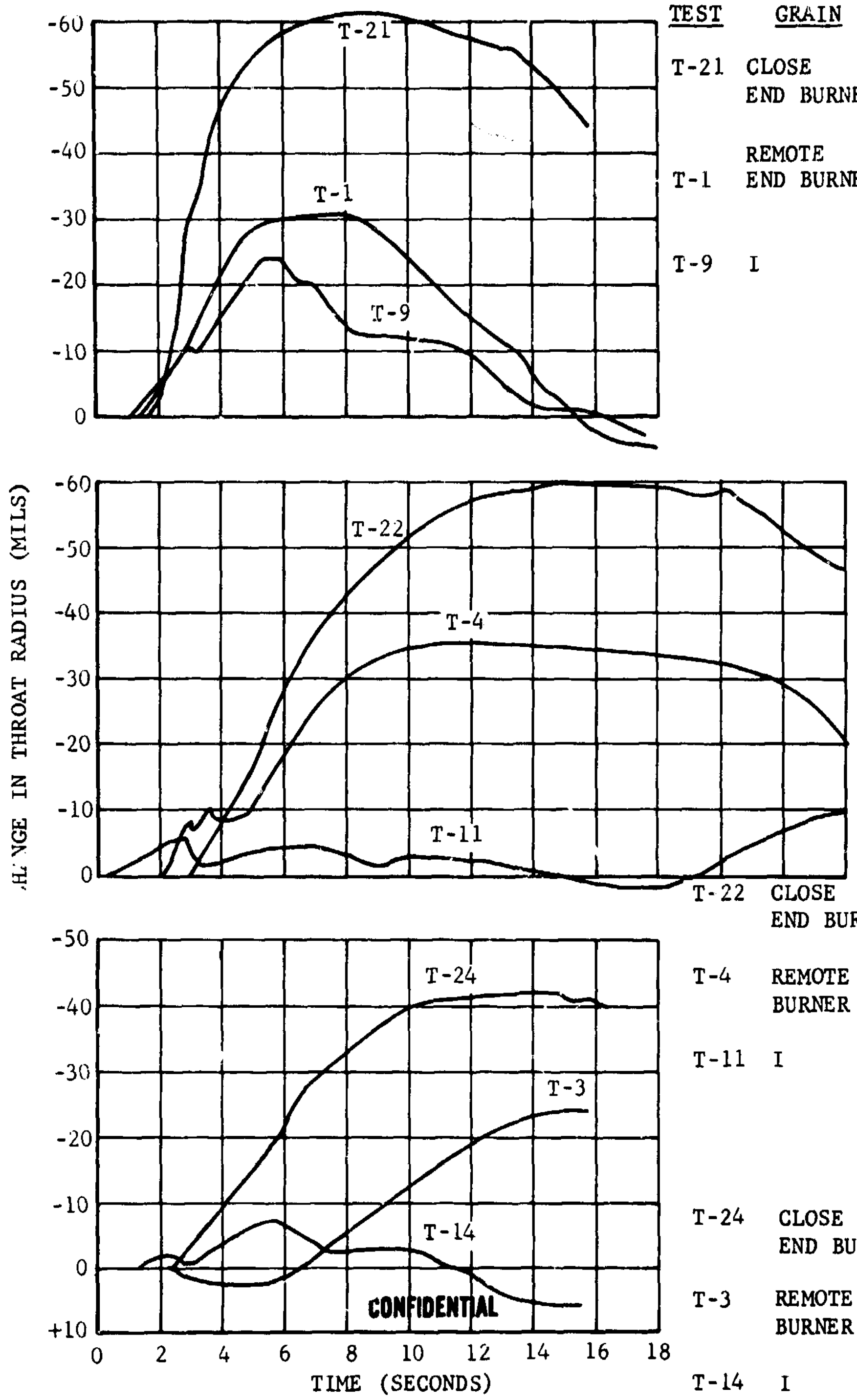

TEST	GRAIN	PROPELLANT	NOZZLE
T-21	CLOSE END BURNER	191F	STEEP INLET P.G.
T-1	REMOTE END BURNER	191F	CONVENTIONAL P.G.
T-9	I	191F	CONVENTIONAL P.G.
T-22	CLOSE END BURNER	54F	STEEP INLET P.G.
T-4	REMOTE END BURNER	54F	CONVENTIONAL P.G.
T-11	I	54F	CONVENTIONAL P.G.
T-24	CLOSE END BURNER	319BRF	STEEP INLET P.G.
T-3	REMOTE END BURNER	319BRF	CONVENTIONAL P.G.
T-14	I	319BRF	CONVENTIONAL P.G.

FIGURE 122. EFFECT OF STAY TIME ON THROAT DEPOSIT HISTORY (II) F08111 C

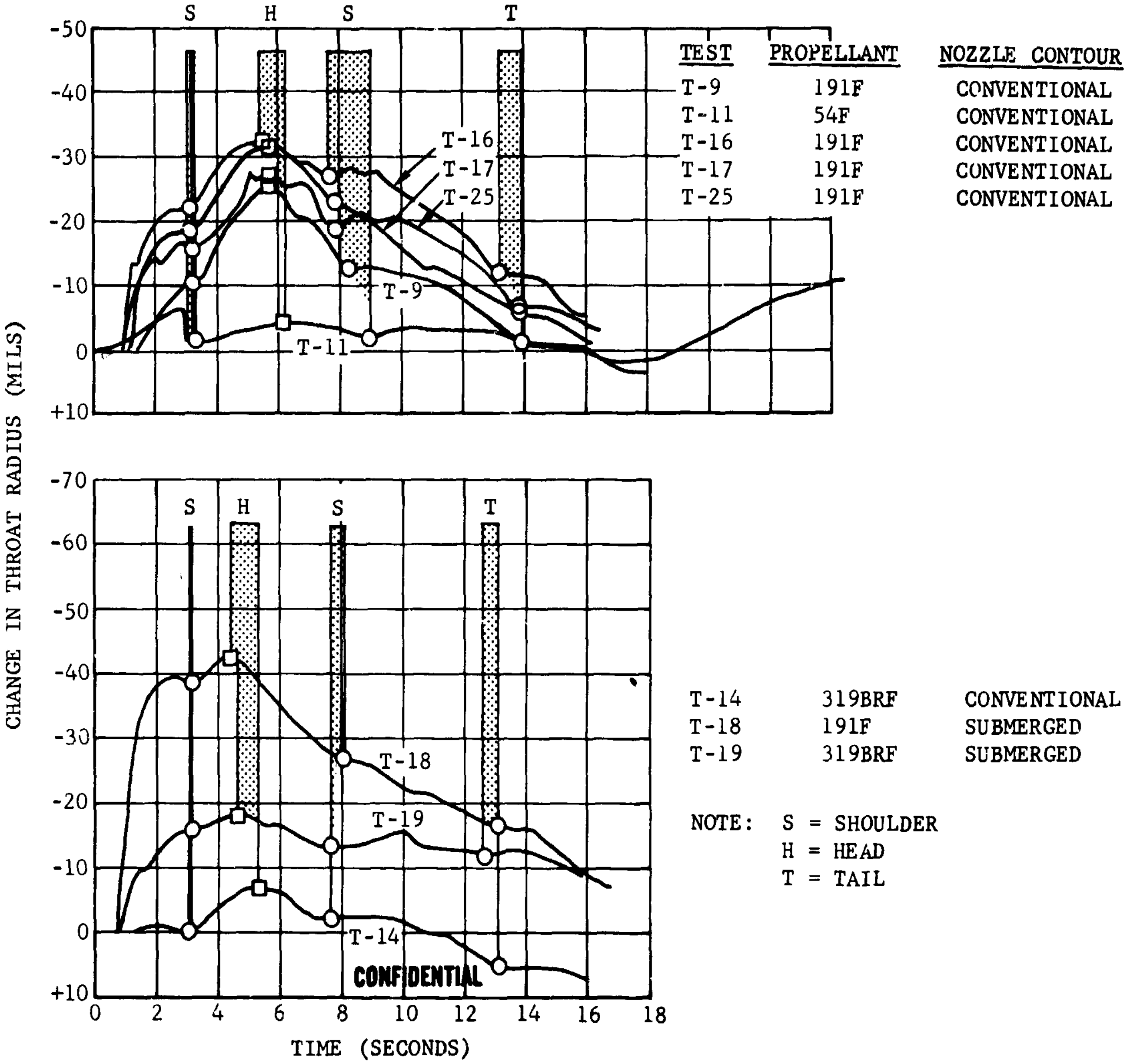

F08113C

FIGURE 123. EFFECT OF GRAIN TYPE ON THROAT DEPOSIT HISTORY (I)

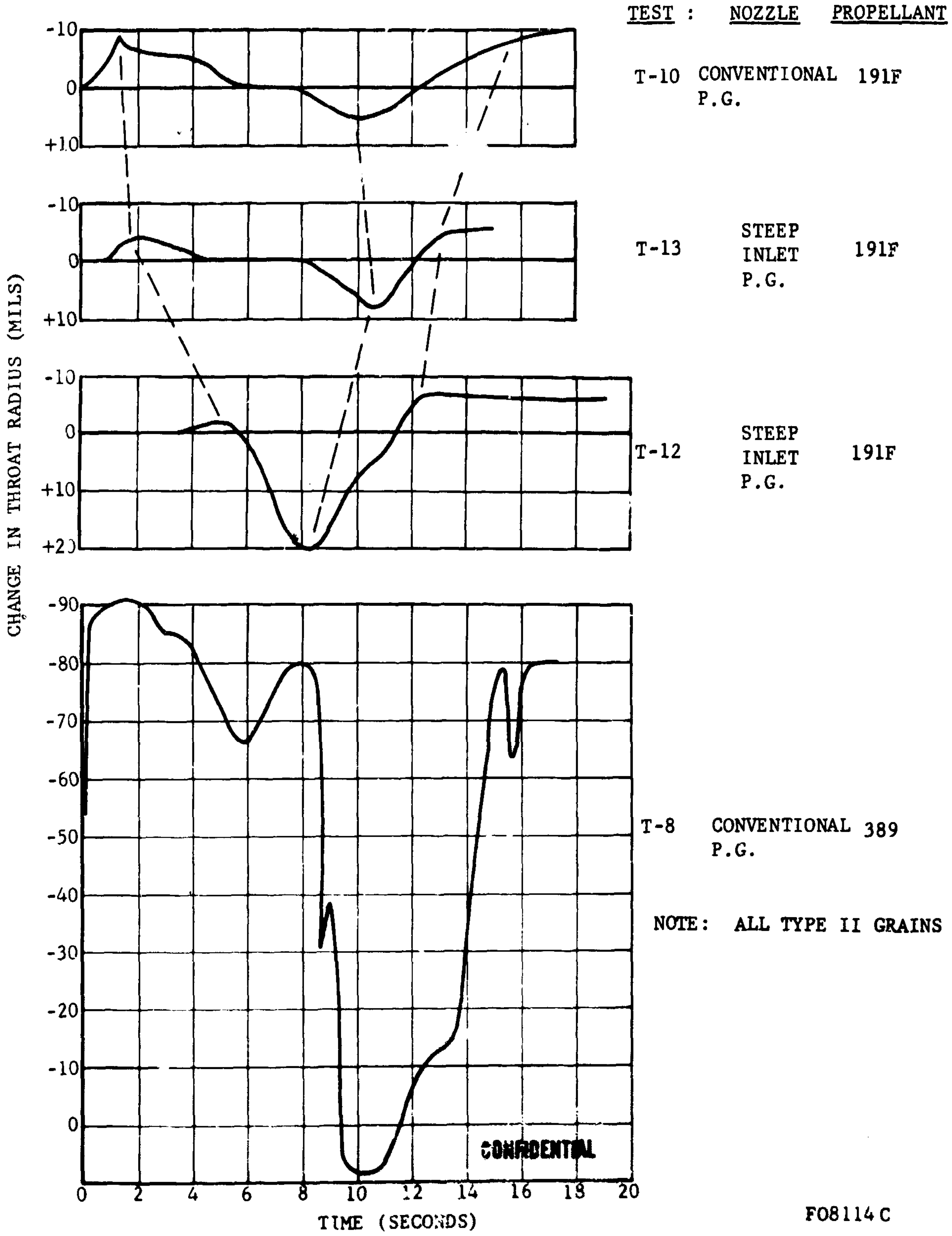

FIGURE 124. EFFECT OF NOZZLE AND GRAIN TYPE ON THROAT DEPOSIT HISTORY

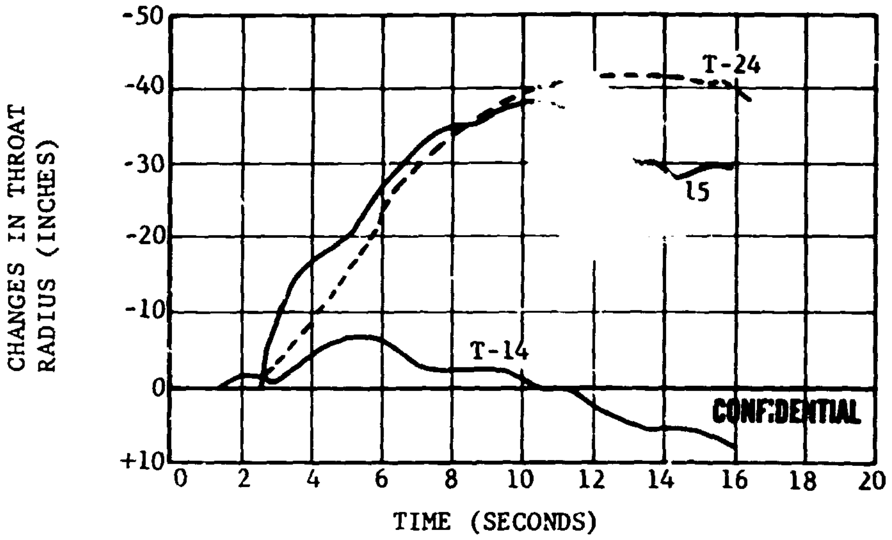

TEST	PROPELLANT	GRAIN	NOZZLE
T-14	319BRF	I	CONVENTIONAL P.G.
T-15	319BRF	III	CONVENTIONAL P.G.
T-24	319BRF	CLOSE END BURNER	STEEP INLET P.G.

F08115

FIGURE 125. EFFECT OF GRAIN TYPE ON THROAT DEPOSIT HISTORY (II)

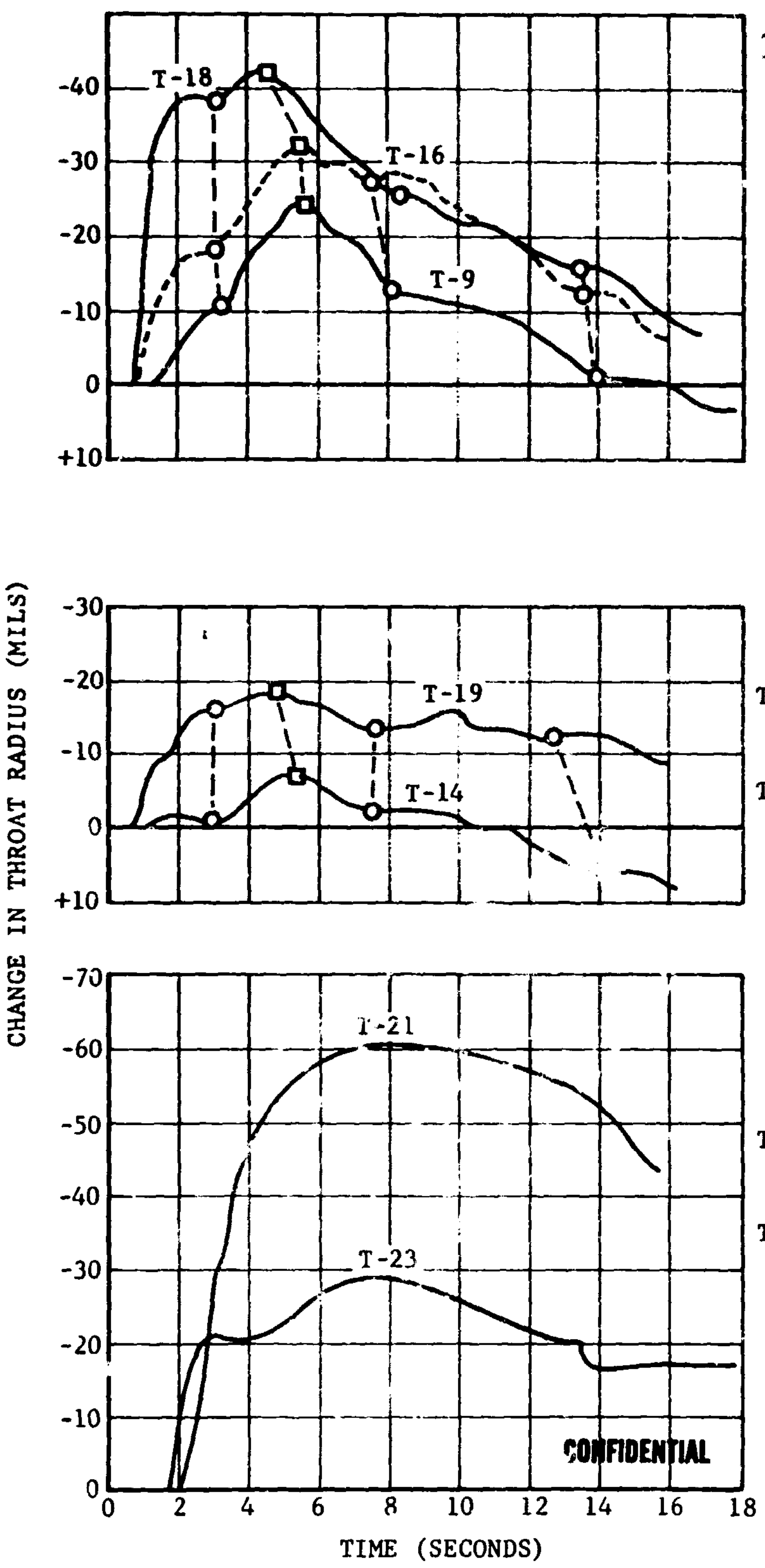

TEST	PROPELLANT	GRAIN	NOZZLE
T-9	191F	I	CONVENTIONAL P.G.
T-16	191F	I	SUBMERGED TUNGSTEN
T-18	191F	I	SUBMERGED TUNGSTEN
T-19	319BRF	I	SUBMERGED TUNGSTEN
T-14	319BRF	I	CONVENTIONAL P.G.
T-21	191F	CLOSE END BURNER	STEEP INLET P.G.
T-23	191F	CLOSE END BURNER	SUBMERGED P.G.

F08116C

FIGURE 126. NOZZLE EFFECTS ON THROAT DEPOSIT HISTORY

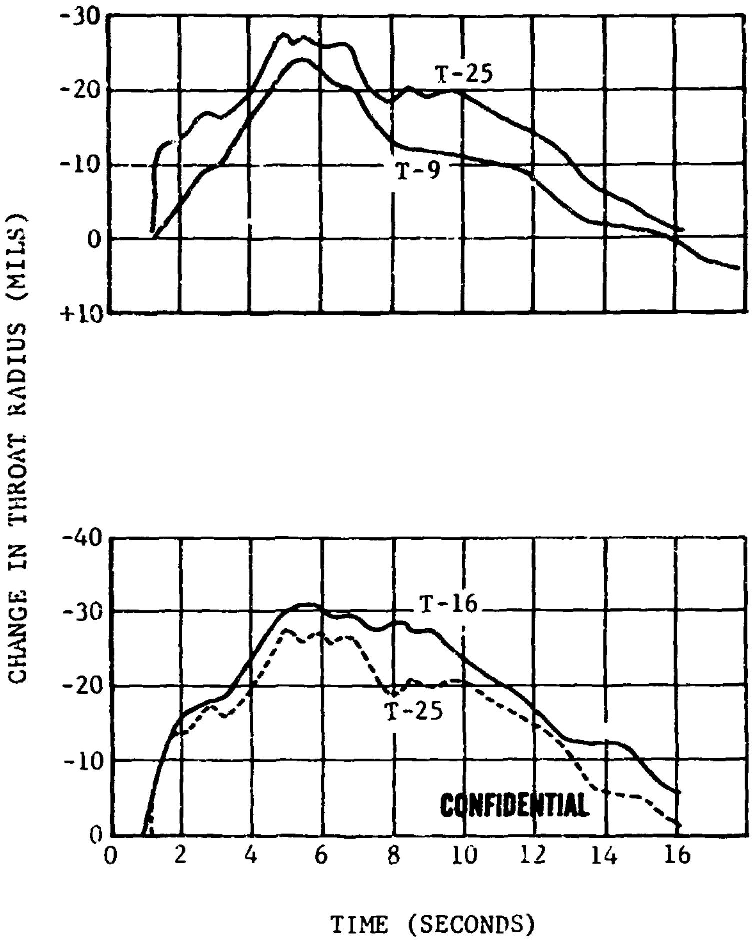

TEST	PROPELLANT	GRAIN	NOZZLE
T-25	191F	I	CONVENTIONAL P.G. (THICK HEAT SINK)
T-9	191F	I	CONVENTIONAL P.G.

T-16	191F	I	CONVENTIONAL TUNGSTEN
T-25	191F	I	CONVENTIONAL P.G. (THICK HEAT SINK)

F08117C

FIGURE 127. EFFECTS OF HEAT SINK ON THROAT DEPOSIT HISTORY

NOTE:

191F PROPELLANT
- T-16, T-17 } GRAIN TYPE I CONVENTIONAL TUNGSTEN NOZZLE
- T-9, T-20 } GRAIN TYPE I CONVENTIONAL P.G. THROAT

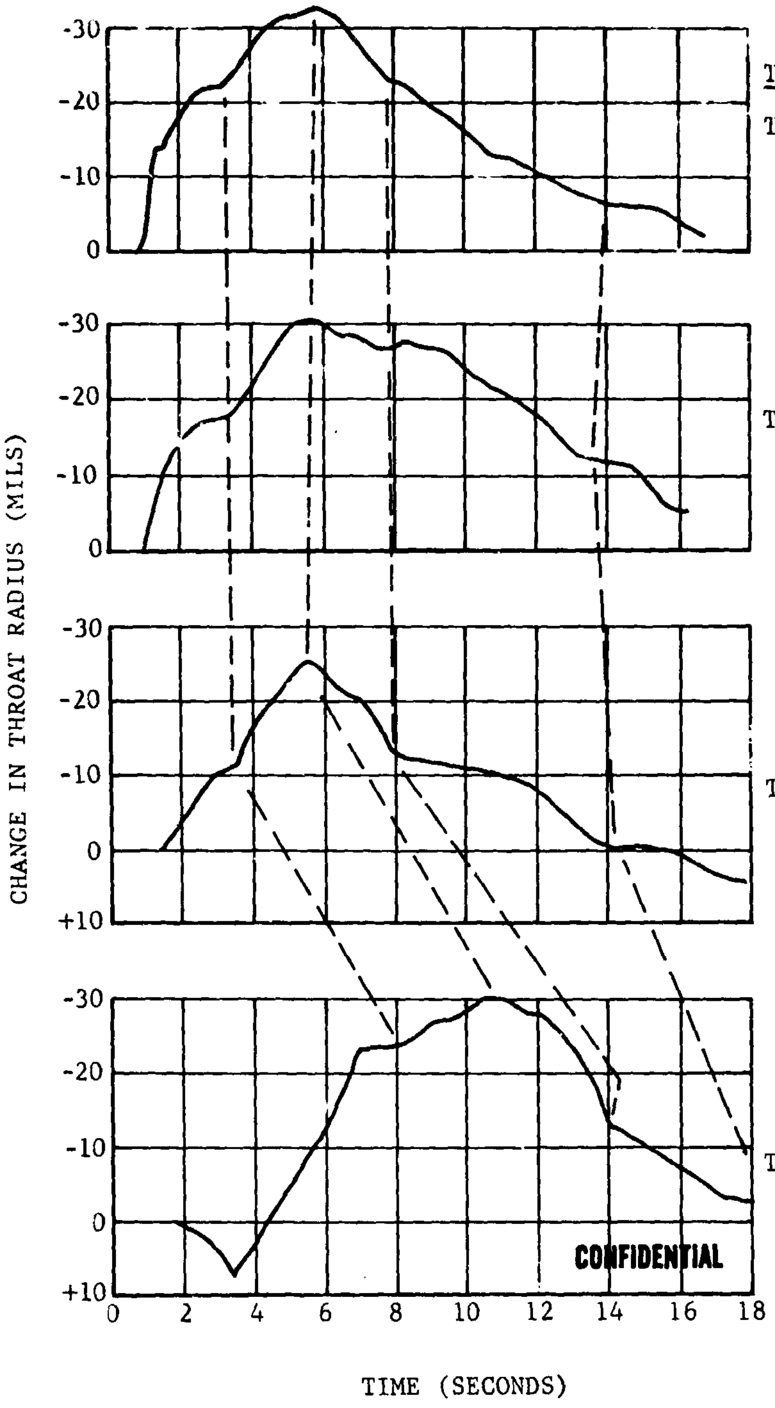

TEST	ENTRANCE	NOZZLE	PROPELLANT
T-17	CARBON CLOTH	CONVENTIONAL TUNGSTEN	191F
T-16	CONVENTIONAL	CONVENTIONAL TUNGSTEN	191F
T-9	CONVENTIONAL	CONVENTIONAL P.G.	191F
T-20	CARBON CLOTH	CONVENTIONAL P.G.	191F

F08118C

FIGURE 128. EFFECT OF CARBON CLOTH ENTRANCE ON THROAT DEPOSIT HISTORY

deposition, at greater distances from the throat, than would occur with the Type I grains. In general, the initial deposition time gap appears to be greater, as expected. Except for Test T-4, there is no major first shoulder. There is also little tendency towards a tail-off for the remote end burning grains (Figure 117). Evidently, the simple deposition histories obtained for the end burners are basically the result of (1) a nearly constant deposition rate, (2) a cold surface mass storage effect and (3) a heating surface mass release effect.

The close end burners (Figure 116) produced throat deposits with twice the peak value and considerably longer residence times. The sharper gas flow field turns are expected to increase the deposition somewhat and the slower heating of the nozzle would slow the deposit removal process (relative to the remote end burners). However, there is another possibility which is compatible with the lower measured ballistic performance (see Section 2.3). That is, deposition of unburned beryllium particles may have occurred. The beryllium particles which are least likely to burn in a very short distance are the largest (20 to 50 microns). These are the most likely to slip to the wall and, while there may only be a few, they represent a significant fraction of the total mass of beryllium. By comparison, the largest beryllia particles may be less than 10 microns in diameter. The resulting deposit may have a lower melting point. The beryllium would tend to vaporize (cooling the deposit) and burn near the wall (heating the deposit) as the mixture flows over the nozzle contour. Except for the possibility of beryllium-carbon reactions (see Sections 3.4 and 3.5) the only evidence of beryllium metal deposition would be lower heat transfer to the nozzle and low delivered c-star and impulse. The low heat transfer and performance would derive from the low exhaust enthalpy attained when all of the metal does not burn. Lower heat transfer and performance were actually experienced in Tests T-21 through T-24. It should be noted that the anticipated increase in nozzle corrosion due to oxygen enrichment of the exhaust gases could not occur while deposits remained along the contour.

At this point, it is worth noting that the Arcocel 319BRF propellant consistently produced less throat deposit than the other beryllium propellants in similar configurations. This would be quite reasonable if the metal combustion efficiency was actually better for the 319 propellant. Other evidence indicates that this is probably true. The lower flame temperatures, with and without metal burning, of the Arcane 54F with respect to the Arcocel 191F may account for the greater throat deposit thicknesses with the composite (see Figures 116 and 120). That is, lower metal combustion efficiency up to the particle impact point could produce greater deposition. On the other hand, the high flame temperature of the Arcocel 191F should always cause the deposits to flow faster, making them appear to be thinner. The least deposition for the Arcocel 54F occurred on Test T-11, which also gave the highest c-star and impulse efficiency obtained for this propellant.

The behavior of the aluminum analog propellants (see Figures 118 and 121) appears to be quite reasonable. The lower melting point of the alumina (3700°F against 4600°F for beryllia) and the greater difference between the melting point and flame temperature would cause higher deposit flow velocities and thinner deposits. The thermal insulation effect is not diminished in proportion to the deposit thickness because alumina has about one third the conductivity of beryllia. However, the alumina flow should transist, from the continuous to stream or bead flow, whenever it becomes too thin. This should occur at lower temperatures than for beryllia. It is suspected that the completely burned aluminum and beryllium have similar oxide particle size distributions within the combustion chamber. No direct proof of this has been found to date, however.

The stay time effect (see Figure 122) apparently leads to the most confusion. It has been suggested that the beryllium metal particles require longer times to burn than aluminum. This is based primarily on the assumption that the more refractory beryllia limits the particle heating rate and vaporization of beryllium (even when water-beryllia reactions are proceeding) to a greater degree. It has also been observed that about 25% of the beryllium metal must burn before the local flame temperature reaches the melting point of the beryllia. This, of course, is not the case for the aluminum propellants. In estimating the stay times for the various grain designs, only the gas phase stay times have been computed. Particle stay times could only be deduced if the initial velocity (ejection from the grain), velocity lag, velocity slip and size distribution effects were considered. Even then, the more fundamental factor is the net heating of the metal particles. If convective heating (velocity lag and slip) dominates, then it is not certain which grain design produces the shortest stay time from the grain surface to the particle impaction point or to the nozzle throat. The unusually low chamber velocities (about 10 feet per second) permit the least particle velocity lag to develop but very long stay times are available. With the internal burning grains, the particles are ejected in a direction normal to the flow and experience considerable velocity slip. Evidently, stay time is a useful parameter only when the gas and particle flow fields are nearly identical. It also follows that either a direct or inverse correlation between throat deposition and stay time could be obtained, depending on whether particle velocity slip is toward or away from the contour.

The Type II grains have produced rather unique deposition histories (see Figure 124). On ignition, a complex flow field is established and should produce an equally complex oxide particle deposition pattern. As the slot in the grain burns (and possibly a second slot is developed in the grain opposite the original slot), the flow and particle impaction areas will change considerably. It is likely that the throat deposit will not be circumferentially uniform. Once again, the asbestos insulation is exposed to the flow and erodes significantly in Tests T-10 and T-13. Test T-12 used a submerged nozzle and asbestos erosion occurred only at the end of the grain slot. The initial deposit pulses appear to agree with asbestos decomposition products argument. The return of the deposits during the latter half of the test has not been explained. The decay of the motor pressure may be the dominant factor. Similar behavior can be seen at the end of Test T-11. If greater particle slip occurs at low pressure, resulting in increased impaction rate and lower impact velocity, then the renewal of deposition could occur. Surfaces upstream of the throat may also release oxide deposits during a pressure decay. No explanation has been devised to explain the extreme deposition in Test T-8. The deposition analysis was most difficult for this test and the result may be greatly in error.

Test T-15 was the only one using the Type III slotted grain design. Again asbestos decomposition products may have a significant effect on the deposition (see Figure 125). The grain burns away from the throat quite rapidly, exposing grain inhibitor, the cab-o-sil bond and some asbestos. The addition of such low melting silica and silicate impurities probably accounts for the appearance of the shoulders in the deposit curves. Notice that no throat erosion appears on the deposit history. As can be seen in Section 3.4, two axial grooves were formed in the throat. Clearly then, the deposit thickness must have been circumferentially non-uniform, at least during the early portion of the firing when the grooves are thought to be formed.

It can be seen that the deposition data for the tungsten inserts is very similar to that for the pyrolytic graphite inserts (Figure 126). This was anticipated but only on the basis that the liquid oxides wet tungsten and should form a good mechanical bond. It is possible that some carburization of the tungsten surface occurs before the deposit arrives and this may have some influence on the results. The thicker deposits on tungsten are believed to be primarily the result of the axial heat conduction effect.

The predicted increase in the amount of deposition for the submerged nozzle, compared to the conventional contour, can be seen in Figure 126 (see also Section 2.4). Unfortunately, the Type I grain design was not tested with a submerged pyrolytic graphite nozzle. In comparing the results of Tests T-16 and T-18, note that the submerged design does not expose any significant amount of asbestos during the early part of the firing. The cab-o-sil bond is exposed in about the same way for either nozzle type as the firing progresses. Comparison of Tests T-14 and T-19 also shows the increase in deposition for the submerged nozzle. The thermal analysis tends to confirm the nearly constant deposit thickness on Test T-19, since the calculated deposit temperatures did not exceed the melting point of beryllia. Visual inspection of the deposit also shows that slight ripples (aligned transversely to the flow direction) were forming on the surface. Similar ripples were observed on Test T-18, except that long, narrow streams of deposit had flowed downstream of the ripple in several places. This behavior is analogous to the case of two phase annular flow (liquid annulus, gas core) which has been studied rather extensively. Thus, surface waves develop, become unstable and crest. The breakdown of a surface wave is normally not circumferentially uniform.

The increase in throat heat sink capacity (see Figure 127) produced the expected results. Considering the preceding discussions, it is probable that increases in the nozzle entrance cone heat capacity and changing aft closure insulation materials could produce even longer periods of deposition protection. The Type I grain design is probably a poor choice, since it tends to produce the least deposit.

The effects (on deposition) of substituting carbon cloth for ATJ graphite in the nozzle entrance cone can be seen in Figure 128. Note that the deposit curve for Test T-20 is somewhat in doubt since pressure data was not obtained. The typical Type I grain head and shoulders behavior is evident. A second major factor is that the carbon cloth regression will produce a discontinuity in the contour, exposing the face of the first pyrolytic graphite washer. The resulting flow interruption could promote particle impaction directly on the washer surfaces. It is not obvious that this does not also occur with the ATJ graphite inlets, since the thermal expansion gap is between the ATJ and the first washer. This gap could cause a similar flow interruption. Since the carbon cloth should not trap as much deposit as the ATJ, it is tempting to conclude that the heat capacity of the throat insert is the dominating factor. It follows that scale-up of the nozzle will automatically result in greater throat deposition.

It has been observed that the steep inlet nozzle contour tends to produce more deposition than the submerged nozzle. Unfortunately, the steep inlet nozzle was primarily used with only the close end burner grain. As previously discussed, the high deposit thicknesses are most probably the result of factors other than the nozzle contour.

4.3 (U) MOTOR TEST INSTRUMENTATION

a. Thermal Instrumentation

(1) Conduction

(a) Small Motor Tests

The primary objective of providing conduction thermal instrumentation on the test hardware is to obtain sufficient temperature response data to experimentally characterize the performance of the nozzle and other critical motor components. In general, the measured temperature transients will be compared with the computer calculated transients. It is expected that, through multiple trials and comparisons, the various combustion and thermodynamic phenomenon may be verified and/or explained. The ultimate goal is that the complete thermal history of a given motor with a given beryllium propellant can be computed directly (or computed indirectly with minor testing to provide only key data points). The following paragraphs are devoted to: (1) describing the type, quantity and location of instrumentation used on the small scale motors, (2) evaluating the quality of the data output from the thermal instrumentation used on the small motor tests, and (3) describing the instrumentation to be used on the development motor nozzles.

The type, quantity, location, and performance of the instrumentation used on the first seven motor tests were presented in detail in the Second Technical Progress Report (Reference 2). A portion of this data is presented again in this report to aid in the over-all evaluation of the performance of the thermal instrumentation on the small motor tests.

The thermocouple locations and numbering system, used on nozzles T-1 through T-22, were shown in cut-away views (Figures 95 through 101) in Reference 2. The nozzle used in Test T-23 had the same instrumentation as nozzles T-21 and T-22 (see Figure 99, Reference 2). The nozzle used in Test T-24 had the same instrumentation as nozzle T-12 (Figure 97, Reference 2). The locations of the thermocouples used on T-25 are illustrated in Figure 129. During this program, special consideration was given to maintaining flexibility in the type and number of thermocouples installed. While the figures mentioned above illustrate the potential thermocouple locations on each nozzle, the actual use of a given thermocouple location (port), and the type of thermocouple used in that location, were determined as late as possible in the fabrication and assembly sequence. This flexibility made it possible to ascertain the need for the instrumentation and the appropriate type of thermocouple based on the test results of previous firings. Table XXXIII presents a list of the thermal instrumentation actually used on all of the small motor tests, with the exception of T-1 through T-7 (previously presented in Reference 2).

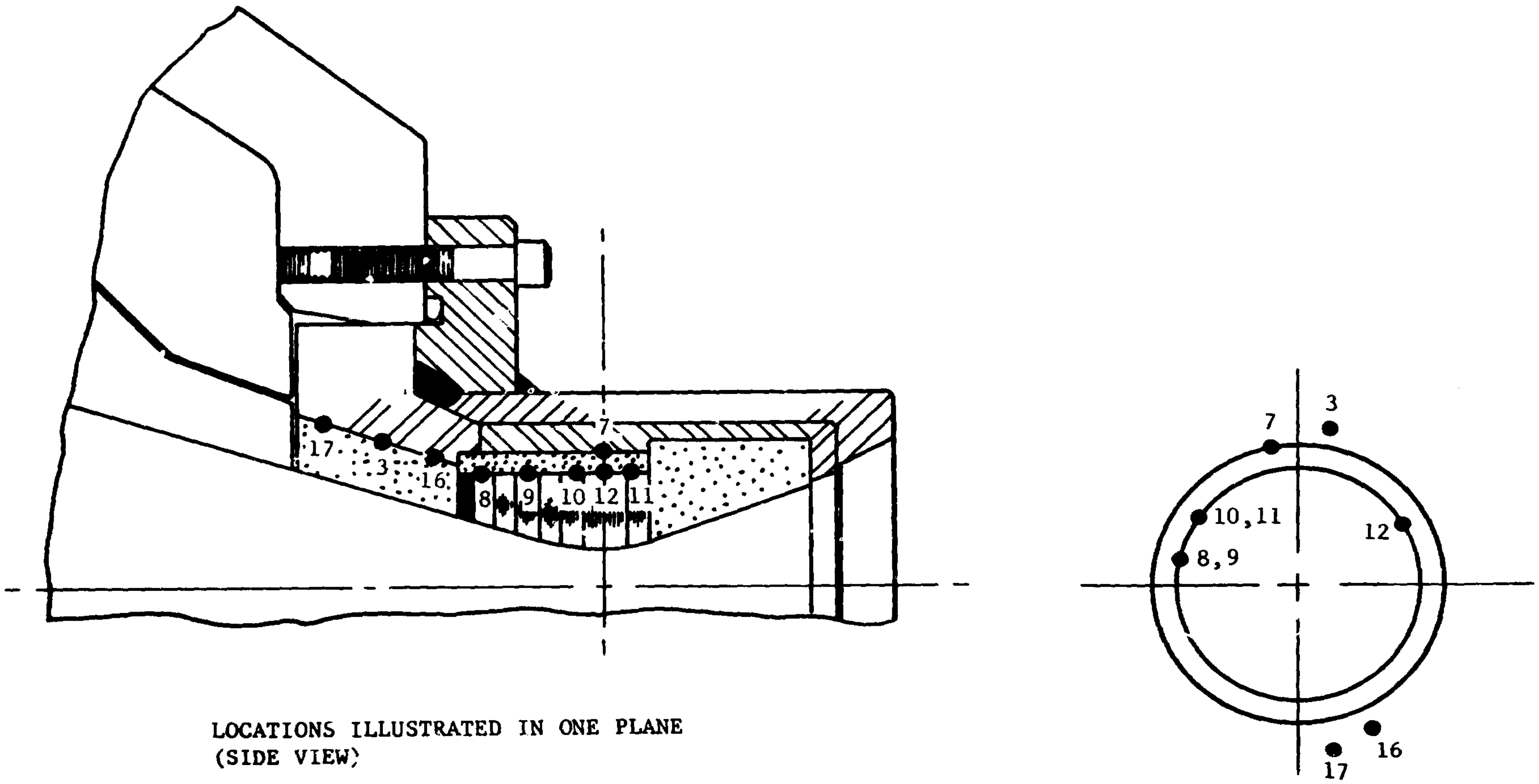
17
3
16
7
8
9
10
12
11
3
7
10,11
12
8,9
16
17

LOCATIONS ILLUSTRATED IN ONE PLANE
(SIDE VIEW)

CIRCUMFERENTIAL LOCATIONS
(END VIEW)

F08184U

FIGURE 129. THERMOCOUPLE LOCATIONS FOR NOZZLE T-25

TABLE XXXIII. THERMAL INSTRUMENTATION LIST

Test	Instrumentation Port Numbers*																										
Number	1	2	3	5	7	8	9	10	11	12	13	14	15	16	17	18	19	20	21	23	24	25	121	122	123	101	102	103
T-8	S		K		K		K	K	K	K				K	K	K												
T-9			K		K		S	S	K	S				S	K													
T-10	S		K		K		S	S	K	S				S	K	K												
T-11			K				S	S	K	S				S	K													
T-12					SI		SI	SI		SI									SI									
T-13					SI		SI	SI		SI							SL	SL	SI									
T-14			K		K		S	S	K	S				S	K													
T-15	S		K		K		S	S	K	S				S	K	S												
T-16		K	K		K	S	S	S		S				S	K													
T-17		K			KL	S	S			S																		
T-18					KI	SI				SI									SI									
T-19					KI	SI				SI									SI									
T-20					K		S	S	K	S																		
T-21					KI			SI		SI							SL			KI								
T-22					KI		SI	SI		SI							SL	SL		KI	SI	SI						
T-23					KI		SI	SI		SI										KI	SI	SI						
T-24					KI		SI	SI		SI							SL	SL		KI	SI	SI						
T-25			K		K	S	K	S	K	S				S	K													
T-51		KI			KI																		SI	SI	SI	SI	SI	SI
T-52		KI			KI																		SI	SI	SI	SI	SI	SI
T-53		KI			KI																		SI	SI	SI	SI	SI	SI
T-54		KI			KI																		SI	SI	SI	SI	SI	SI

*Location of thermocouple ports for Tests T-1 through T-22 are given in Sections 4.3, References 1 and 2. Location of thermocouple ports for Tests T-23 through T-54 are given in Section 4.3 of this report.

Symbols:

Symbol	Meaning	Symbol	Meaning	Symbol	Meaning
S	Springloaded type S bayonet thermocouple	SI	Special springloaded type S thermocouple	SL or KL	Same as S or K except has extra long bayonet
K	Springloaded type K bayonet thermocouple	KI	Special springloaded type K thermocouple		

Post-test examinations were performed on all of the bayonet type thermocouples used on the small scale motor tests. Table XXXIV presents the results of these examinations in coded form. The first letter (S, K, R) describes the type of thermocouple ("S" is platinum/platinum-rhodium; "K" is chromel/alumel; "R" is the radiometer, which uses a chromel/alumel thermocouple). The remaining letters describe the post-test condition of the thermocouple (i.e., "A" means the thermocouple was not damaged; "B" means the sensor tip was bent; "F" means the ceramic portion of the sensor tip was broken; "H" means the damage to the thermocouple occurred during or before the firing; etc.). In addition, an attempt was made to evaluate the quality of the thermocouple installation by estimating the amount of spring loading that was used. It was requested that the spring loaded tips be depressed about one fourth inch, in order to insure good thermal contact. Of course, it is not possible to evaluate the tip depression from post-test examinations in all cases; consequently, many of the thermocouples in Table XXXIV do not have symbols indicating installation accuracy. The letter "P" is used to signify proper tip depression, and the letter "Q" indicates that the sensor tip was not properly depressed. The letter "T" has been added to the coding system during this reporting period. This letter indicates that the thermocouple used was different from that called for in the instrumentation list.

It should be noted that post-test examinations were not made on the special submerged thermocouples. These thermocouples cannot be removed without being damaged. For this reason, tests which used the special thermocouples exclusively (Tests T-12, T-18, T-19, T-21, T-23 and T-24) were not included in Table XXXIV.

A review of the quality of the thermocouple data acquired from the small motor tests is presented in Table XXXV. The data from each thermocouple location (or port) were judged: good, fair, poor or unusable. The classification of the data quality was based on the following requirements: (1) the soak-back temperature, or maximum temperature at a given location, was clearly obtained and recorded; (2) the initial temperature rise transient was obtained; (3) the soak-down temperature decline was obtained; and (4) the curves were smooth, indicating good thermal contact and a low noise level in the recording system. Data classified as "good" had all four of the above qualities. Data classified as "fair" had qualities (1), (2) and (3), but the curves are not required to be smooth. Data classified as "poor" had qualities (1) and/or (2). A data classification of good or fair adequately satisfied the data requirements of this program. Temperature versus time plots for the thermocouples used on Tests T-8 through T-25 are presented in the Appendix.

A total of 198 thermocouples were installed on the small motor nozzles. Of this total, the data from 134 were considered good or fair, 32 were considered poor, 23 were considered unusable, and 9 are not available for evaluation (these are from Test T-24).

TABLE XXXIV. POST TEST THERMOCOUPLE EXAMINATION COMMENTS

Test Number	Thermocouple Port Number 1	2	3	4	5	6	7	8	9	10	11	12	13	14	15	16	17	18	19	20
T-1		KAG	SAG	KA	SAG	KA	KA	SFMH	SFIJ	SA	SA	SA	KJN	KJN	KJN					
T-2	SFJH		SJD		SFCHG			SFCH	SFIC	SFIJ	KEJ	SAG	KEJN	KJN	KJN					
T-3	SA		SA	KA	SA		KA	SF	SA	SA	KA	SA			RA					
T-4	SA		SA	KA	SFIG		KA	SF	SA		KEG	SFJ								
T-5	SFH		KA		KB		KA		SFI	SFI	KA	SDFJ								
T-6	SJE		KA		KJE		KA		SCEH	SCI	KA	SJE	RA							
T-7	SFHCI		KA		KDJ		KA		SFH	SFH		SDJE								
T-8	SGJP		KPGD				KEJP		KMPT	KPT	KJP	KPMT				KPMT	KDEQ	KPJD		
T-10	SF		KA				KA		SFJI	SFID	KAE					SFJ	KA	KBD		
T-11			KDBJP						SFIJP	SFHJP	KBDJP	SFJHQ				SFIJP	KBJP			
T-13																			SJNP	SEJNP
T-14			KA				KA		SFHMGP	SFHJDP	KEP	SFJE				SFHJD	KJG			
T-15	SFJPI		KPGJ					KBGJP		SGFIJP	KBJGPI	SJFIP				SFJDHP	KJEP	KBGJP		
T-16		KJPBI	KJP				KJP	SFIPCI	SFIP	SMEP		SFHMP				SPJ	KGJP			
T-17		KJP					KJP	SPM	SFIP			SF								
T-20							KAP		SFJIP	SDPJG	KPC	SPEJ								
T-22																			SMGE	SFG
T-25		Thermocouples not examined																		

Thermocouple Type

R	Radiometer
S	Platinum/platinum-rhodium
K	Chromel/alumel

Symbol

A	All OK	I	Damaged on removal
B	Tip bent	J	Tip OK
C	Douple broken	M	Tip melted
D	Shank bent	N	Plug burnt by exhaust
E	Tip stuck	P	Depressed properly
F	Ceramic broken	Q	Not depressed far enough
G	Gas leaks	T	Not type requested
H	Damaged in place		

TABLE XXXV. QUALITY OF THERMOCOUPLE DATA

Test Number	Thermocouple Port Number																							
	1	2	3	4	5	6	7	8	9	10	11	12	13	14	15	16	17	18	19	20	21	23	24	25
T-1		KG	SG	KF	SG	KG	KG	SF	SG	SG	SG	SG	KU	KU	KU									
T-2	SP		SP		SF			SG	SG	SG	KP	SF	KG	KG	KG									
T-3	SP		SG	KG	SG		KF	SG	SG	SG	KG	SG			RG									
T-4	SG		SG	KU	SF		KU	SU	SG		KG	SG												
T-5	SG		KG		KG		KG		SG	SG	KG	SG												
T-6	SG		KF		KF		KG		SG	SG	KP	SG	RU											
T-7	SG		KG		KG		KG		SG	SG		SG												
T-8	SU		KG				KG		KU	KU	KG	KP				KG	KP	KG						
T-9			KF				KF		SG	SG	KG	SG				SG	KU							
T-10	SG		KP				KG		SU	SF	KF	SG				SU	KG	KF						
T-11			KG						SG	SG	KG	SP				SU	KG							
T-12							SU		SG	SU		SG									SG			
T-13							SU		SP	SP		SU							SU	SP	SP			
T-14			KU				KP		SP	SP	KP	SP				SP	KP							
T-15	SP		KG				KF		SG	SG	KG	SF				SG	KG	KG						
T-16		KG	KG				KG	SG	SG	SP		SP				SG	KG							
T-17		KG					KG	SP	SG			SF												
T-18							KG	SG				SG									SG			
T-19							KU	SG				SG									SG			
T-20							KG		SC	SF	KF	SG												
T-21							KG			SU		SG							SG			KG		
T-22							KG		SG	SG		SG							SP	SF		KG	SG	SG
T-23							KG		SG	SP		SG										KG	SG	SP
T-24							*		*	*		*							*	*		*	*	*
T-25			KU				KP	SU	KP	SP	KP	SG				SP	KF							

Symbols:

R - radiometer
S - platinum/platinum 10% rhodium thermocouple
K - chromel/alumel thermocouple
G - good - 1, 2, 3, 4
F - fair - 1, 2, 3
P - poor - 1 or 2 or 3
U - unusable - none
* - data unavailable

where:

1 - equilibration temperature
2 - startup transient
3 - cooldown transient
4 - smooth curves

There were five tests, which, for various reasons, produced data that were abnormally poor compared to the others. These tests were T-8, T-13, T-14, T-24, and T-25. On Test T-8, chromel/alumel thermocouples were inadvertently installed in ports 9, 10, 12, and 16. Platinum/platinum-rhodium thermocouples were requested for these ports, since the temperatures were expected to exceed the capabilities of the chromel/alumel thermocouples. The data would have been more useful if the chromel/alumel thermocouples were connected to chromel/alumel circuits. Instead, they were connected as though they were platinum/platinum-rhodium thermocouples. As a result, this data was lost after the output of the thermocouples exceeded about 20 millivolts (a 20 millivolt full scale is sufficient to cover the useful temperature range of platinum/platinum-rhodium thermocouples). A bench test was conducted at Aeronutronic to establish the millivolt output as a function of temperature for a chromel/alumel thermocouple in a platinum/platinum-rhodium circuit. The resulting chart was used to reduce the data.

During Test T-13, a leak developed in the nozzle holder which ultimately burned through the aft closure and into the thermocouple plug mounting bracket. The thermocouple lead wires were melted; consequently, the thermal data acquisition was terminated prematurely.

The data recording system was turned off immediately following the motor shutdown on T-14. For this reason, the soak-back and cool-down temperatures were not obtained. The data recording system was not functioning properly during Test T-24. None of the data recorded on the Digital Recording System are available. Ballistic data, however, were recovered since thrust and chamber pressure were also recorded on an oscillograph for redundancy.

During Test T-25, seven thermocouples were either loosened or ejected. Thermocouples in ports 7 and 8 were loosened; thermocouples in ports 3, 9, 10, 16 and 17 were ejected. It is believed that these thermocouples were improperly installed.

A better evaluation of the over-all quality of the thermal data can be obtained if the aforementioned tests (T-8, T-13, T-14, T-24 and T-25) are excluded from consideration. In the remaining small motor tests, it was found that over 80% of the thermal instrumentation adequately fulfilled the data requirements of this program with only about 10% of the data being unusable.

The thermocouples used during this program had either chromel/alumel or platinum/platinum-10% rhodium elements. There were three basic types of thermocouples used: (1) standard spring loaded bayonet, (2) special submerged spring loaded Hi-Cal thermocouples, and (3) special submerged spring loaded ADP thermocouples. Neglecting the 5 above-mentioned tests, the overall quality of data and thermocouple performance for these three basic types of thermocouples are: 79% of the standard spring loaded bayonet type thermocouples gave satisfactory data, 40% of the Hi-Cal thermocouples gave satisfactory data, and 83% of the ADP thermocouples gave satisfactory data.

The 80% figure for demonstrated satisfactory thermocouple performance could be improved significantly. If special care is taken in the selection of the thermocouple location, the selection of the thermocouple type, and the installation of the thermocouple, it is conceivable that thermocouple failures could be virtually eliminated. Of course, a thermocouple may fail where other interrelated motor components fail (i.e., during Test T-13, the thermocouple lead wires were melted when the motor case burned through).

(b) Development Motors

The philosophy for establishing the thermal instrumentation for the development motor tests differed from that for the small motor tests in three basic ways: (1) emphasis was placed on establishing the circumferential variation in temperature as opposed to axial variations, (2) the thermal instrumentation was confined to the throat region only, and (3) redundancy was accomplished by grouping the thermocouples in pairs with a small axial distance (0.5 inch) between them.

During the small motor tests, it was discovered that the metal or metal oxide deposition was much greater than expected. It was also discovered that there were sufficient axial variations in the deposition thickness to cause variations in the relative magnitudes and shapes of the axial temperature distribution profiles. Consequently, the redundancy expected from similar axial temperature profiles was not obtained. For this reason, the redundancy in the development motors was provided by installing pairs of thermocouples at each position (4 circumferential positions on each nozzle).

The locations of the thermal instrumentation for development motors are illustrated in Figures 130, 131 and 132.

The use of thermocouples in rocket motors has been resisted in previous programs for fear that the presence of the thermocouple would in some way weaken the nozzle components and precipitate a failure. It should be pointed out that use of thermocouples on this program has in no way compromised the performance of any of the motors tested.

(2) Radiation

A radiometer for measuring combustion chamber radiation was fabricated and tested during the period covered by the Second Technical Progress Report (Reference 2). No further tests were attempted with the radiometer during this reporting period.

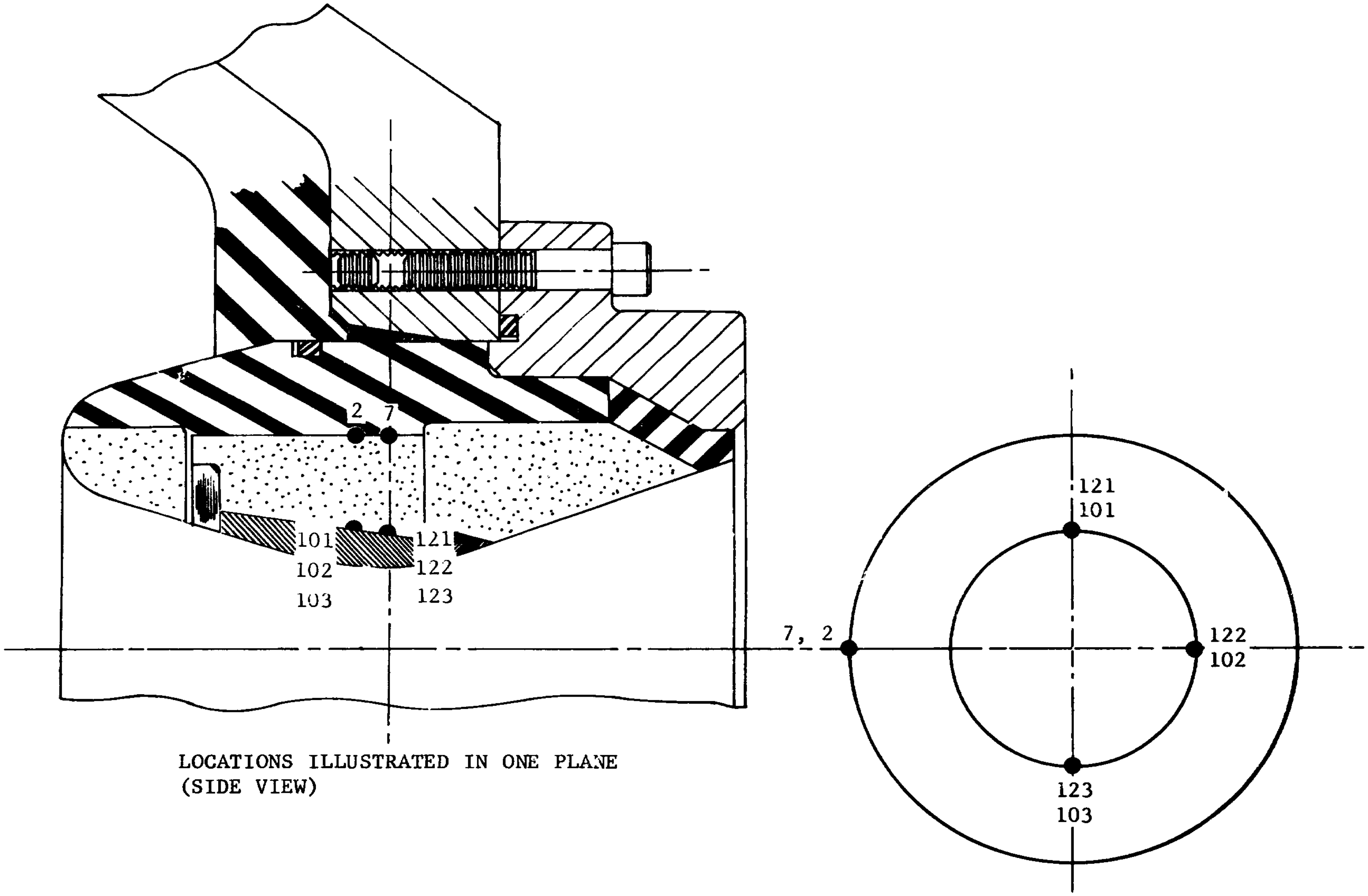
2
7
101
102
103
121
122
123
7, 2
121
101
122
102
123
103

LOCATIONS ILLUSTRATED IN ONE PLANE
(SIDE VIEW)

CIRCUMFERENTIAL LOCATIONS
(END VIEW)

F08073 U

FIGURE 130. THERMOCOUPLE LOCATIONS FOR NOZZLE T-54

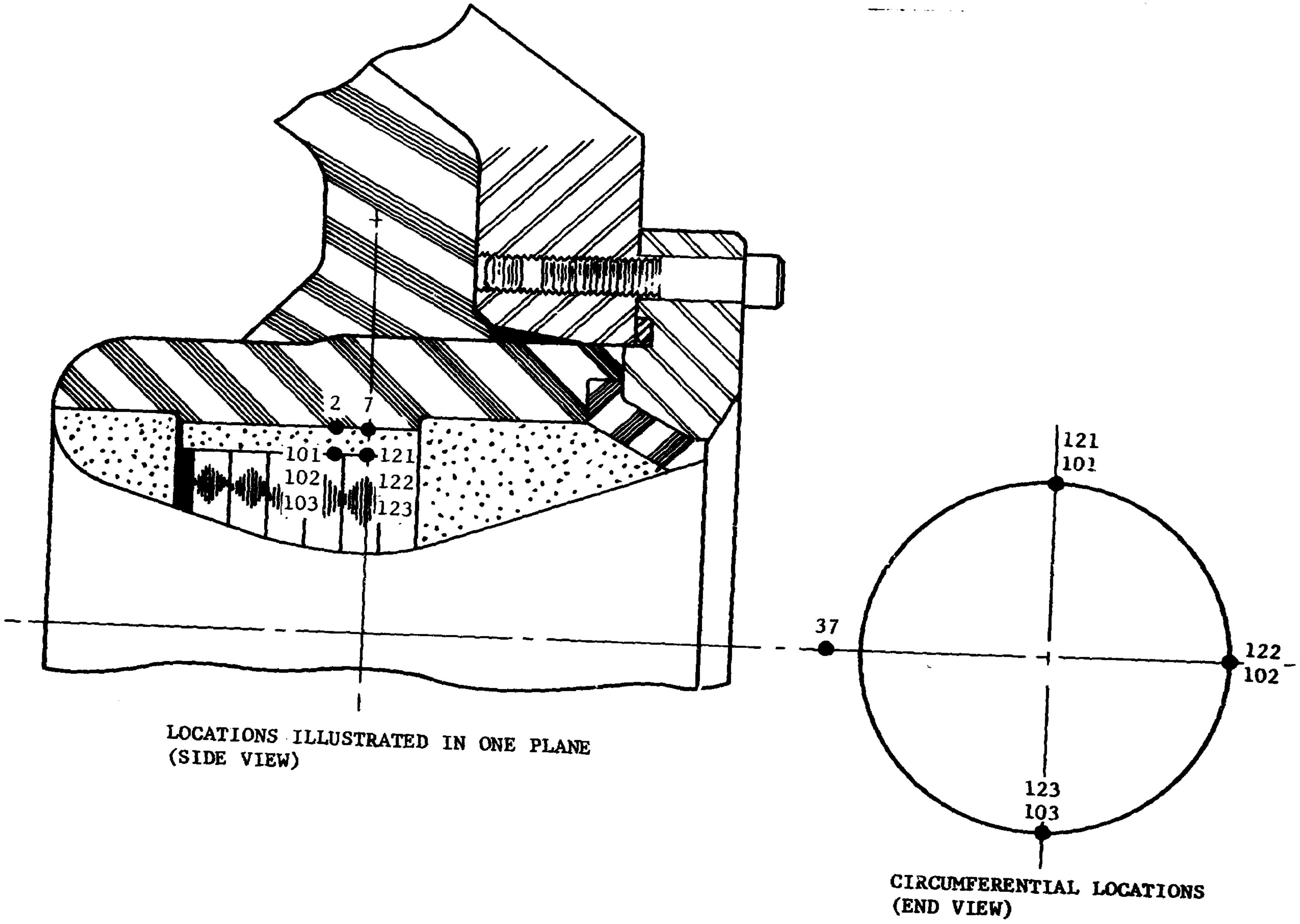
2
7
101
102
103
121
122
123
37
121
101
122
102
123
103

LOCATIONS ILLUSTRATED IN ONE PLANE
(SIDE VIEW)

CIRCUMFERENTIAL LOCATIONS
(END VIEW)

F08074U

FIGURE 131. THERMOCOUPLE LOCATIONS FOR NOZZLE T-53

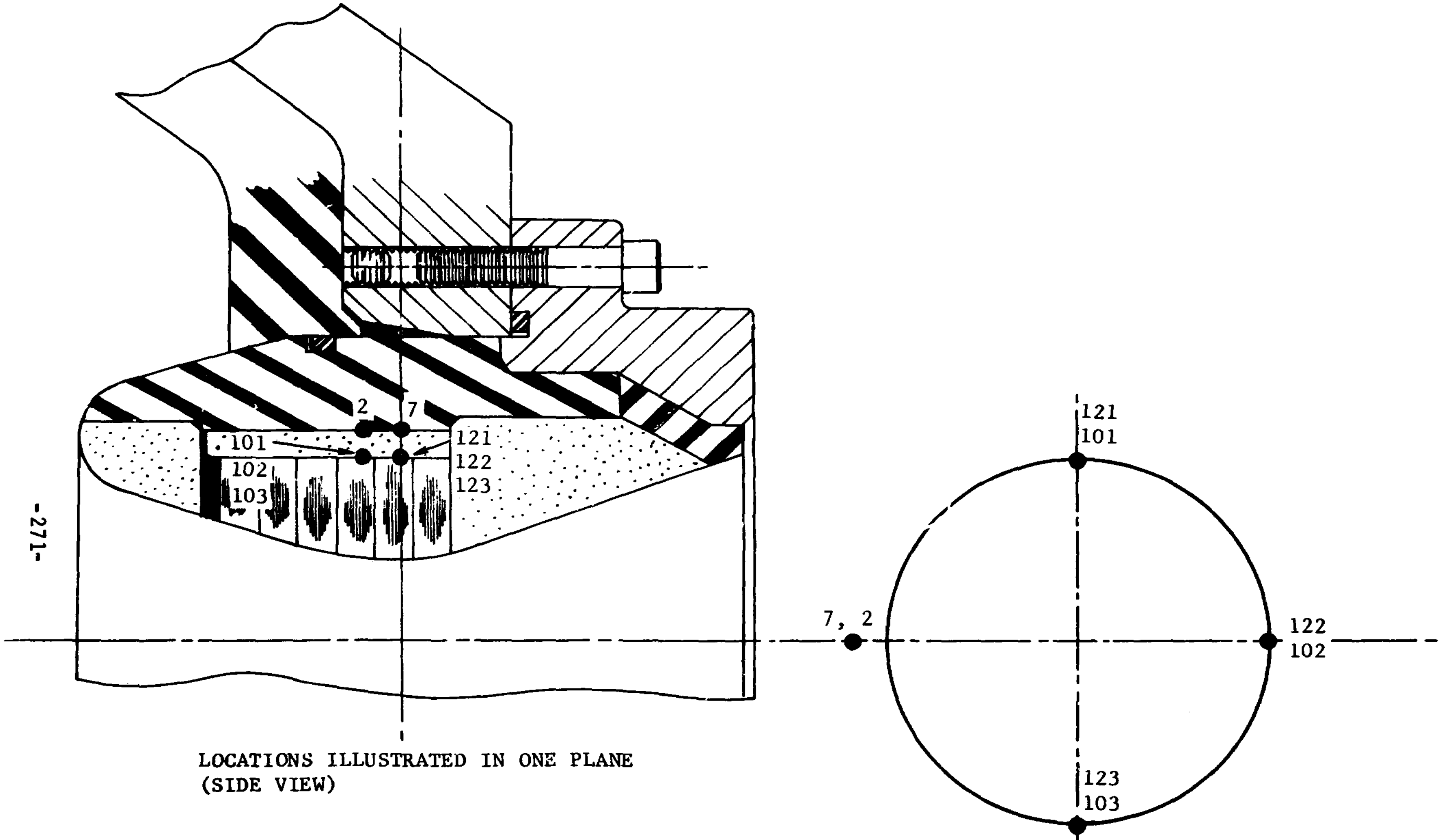
2
7
101
102
103
121
122
123
7, 2
121
101
122
102
123
103

LOCATIONS ILLUSTRATED IN ONE PLANE
(SIDE VIEW)

CIRCUMFERENTIAL LOCATIONS
(END VIEW)

F08216 U

FIGURE 132. THERMOCOUPLE LOCATIONS FOR NOZZLES T-51 and T-52

b. Ballistic Instrumentation

(1) Small Motor Tests

Ballistic data, including chamber pressure, axial thrust and ambient pressure, were recorded for each of the small motor tests. Two dual bridge strain gage axial thrust mounts (0-2000 pound range) were used to measure thrust. Two pressure transducers with ranges 0-1000 psig and 0-2000 psig were used to measure the chamber pressure. The data were recorded on the RPL Digital Recording System at about 3.5 millisecond intervals during each run. An oscillograph was also used to record the thrust and chamber pressure; this system was used only for redundancy.

The pressure data was not obtained for T-20 since the pressure ports were not cleaned after the motor was assembled. However, with the use of the data from Tests T-9 and T-25, the pressure and deposition curves for Test T-20 were derived analytically. The propellant, grains, and motor configurations were identical for Tests T-9, T-20 and T-25. Since the relationships between thrust and pressure for Test T-9 and T-25 were nearly the same initially (when there was no deposition or erosion), and since these two grains burned with constant area, the chamber pressure and the deposition/erosion curves could be established for T-20 with relatively minor assumptions. The stand burner tests indicated that the grain used on Test T-20 should produce a thrust and pressure relationship that lies between that produced for Tests T-9 and T-25. The K_n curve for T-20 was established using the strand burner data and the measured thrust curve. The thrust curve indicates that, if the burning surface area were constant, then the 7.5 mils of measured erosion must have occurred early in the run. It was assumed that the nozzle was free from deposition and erosion for the first 1.9 seconds, and that throat erosion started at 1.9 seconds. Thus, combining the thrust and pressure relationship and the K_n curve, it was possible to establish a compatible chamber pressure and throat deposition/regression curve for Test 20.

A malfunction of the digital system on Test T-24 produced a data tape which remains unusable in its present condition. Data may be recovered from the tape if it is decided that the additional effort can be undertaken at Aeronutronic. The reclamation effort will include writing a computer program and making modifications to the Philco 1000 computer, which ultimately will correct and rewrite the data tape. The ballistic data from Test T-24 were also recorded on the oscillograph. Thus, thrust and pressure data were readily available for examination.

The thrust and pressure data were recorded only on the oscillograph for Test T-25. This was done since the Digital Recording System was not functioning at the time of the firing.

(2) Development Motor Tests

The development motors to be tested during this program will operate at about the same chamber pressure as the small scale motors; however, the thrust is anticipated to be about five times greater. It was decided that the pressure instrumentation presently in use is adequate. However, the thrust mount will be changed to provide a range up to 10,000 pounds.

(3) Additional Data Requirements

Only axial thrust has been measured during this program. It should be pointed out that the motion picture coverage indicates that there may be a significant amount of side thrust attributable to large unsymmetrical build-ups of deposition on the nozzle. The ISP may be enhanced if these side forces could be accounted for in the thrust-time integral.

A significant amount of metal oxide slag and other propellant debris have been found to remain in the motor chambers after the firings. The amount of debris, of course, varies from test to test. The presence of the debris may be attributed to the fact that the motors are being test fired in a horizontal position. In a real application, it is more likely that the G-loading on the motors will be such that any residue or slag formed will be forced to the aft end of the motor where it is likely to be expelled through the nozzle. From the ballistic point of view, this unexpelled portion of the propellant should be accounted for in C* and ISP calculations. However, it is difficult to establish from the debris, slag, etc., which portions are unburned grain and which are liner, etc. No attempt was made to adjust the C* or ISP calculations from this program to account for this phenomenon.

c. Exhaust Plume Sampling

Exhaust plume particle samples were taken on all of the small scale motor tests. Exhaust plume particle sampler No. 1 (see page 212 of Reference 2) was incorporated in the first 5 tests. Particle sampler No. 2 (see page 214 of Reference 2) was used on the remainder of the small scale tests. The quantity of material collected continues to be adequate for analysis. The analysis of the samples may be found in Section 3.4. Particle sampler No. 2 will continue to be used on the development motor tests.

4.4 (C) CONCLUSIONS, RECOMMENDATIONS AND FUTURE WORK

a. (C) Conclusions

It is necessary, in attempting to understand nozzle corrosion, that material temperature and oxide deposit histories be accurately determined throughout the firing period. It is concluded that, with proper selection and installation, thermocouples can be expected to produce useful data in better than

90% of the cases, without compromising the performance of the nozzle or its subcomponents. Approximately 80% of the thermocouples used in this program provided acceptable data return. Ultimately, such temperature data provides the basis for the development or confirmation of the analytical convective and radiative heat transfer techniques which are used in nozzle design. Utilization of such a feedback loop offers the greatest promise of avoiding the inherent dangers of extrapolation from one propellant system or type to another (e.g., aluminum to beryllium).

The program results have clearly demonstrated that it is not sufficient to measure nozzle material temperatures and erosion. Oxide deposits on the nozzle contour obviously provide thermal insulation and protection against corrosion. Analysis of the program motor firing data has produced nozzle throat deposit histories. It is concluded that these deposit histories systematically reflect the influence of the effects of the motor design parameters studied. It is apparent that condensed phase deposition occurs well upstream of the nozzle throat and subsequently flows downstream as nozzle surface temperatures rise to the deposit melting point. It has been concluded that the interaction of the grain flow field with the motor contour is the primary cause or source of deposition. The dependence of throat deposition on insulation materials and nozzle heat sink capacity has also been identified. It is concluded that the character of the throat deposit history can be selectively altered (minimized or maximized) by means of the proper selection of propellant, grain, motor contour, flame side materials and nozzle thermal design.

As a result of attempts to qualitatively correlate the nozzle throat deposition data, it is concluded that it will eventually be possible to predict deposition, at least approximately, in advance of actual testing. Deposition of unburned beryllium particles and addition of low melting silica materials require more study. It is concluded that the correlation of nozzle heat transfer, delivered ballistic performance and nozzle throat deposition data can be expected to clarify the unburned beryllium deposition question.

It is concluded that the retention and expulsion of beryllia deposits will have a significant effect on motor performance. Side thrusts are developed as a result of unsymmetrical deposit expulsion and the deflection of the plume by thick exit cone deposits. These effects may be most important for the horizontally fired motors and are significantly less important for aluminum propellants. Any errors in the thrust measurements will influence the propellant performance and throat deposition (F/P method) calculations.

b. (C) Recommendations

The following recommendations are based on the results of the Correlation Studies to date:

(1) Nozzles tested with beryllium propellants should be instrumented with thermocouples whenever possible to at least obtain throat thermal response data.

(2) Beryllium propellant firing data should be analyzed to determine the nozzle throat size variation (deposition and erosion) as a function of time.

(3) Beryllium motor test instrumentation plans and motor firing orientation should be established with due consideration given to the potential effects of oxide deposit retention and expulsion. It would be most logical to fire all motors, particularly those using plug nozzles, vertically down. Partial plugging of an annular throat would produce particularly confusing ballistic results.

(4) It is recommended that additional studies be conducted to further clarify the influence of aft closure insulation materials (carbon cloth, silica and rubber), grain design (stay time), and motor orientation effects on the nozzle deposition phenomenon.

c. (U) Future Work

During the remainder of the program, the correlation studies task will be concerned primarily with the following:

(1) Analysis of the performance of the special thermocouples used on the development motor tests.

(2) Evaluation of the throat deposit data obtained on the development motor tests.

(3) Completion of the acquisition and correlation of erosion data obtained from other programs.

SECTION V (C)

MOTOR DESIGN FABRICATION AND TEST

5.1 (U) OBJECTIVES, SCOPE AND SUMMARY

a. Objectives

The overall objectives of the motor design, fabrication and test task of the program were described in Section 5.1, Reference 1. The specific objectives for the third reporting period were:

(1) Complete the Small Motor Testing Phase of the program.

(2) Complete post-test ballistic analysis of the data obtained from the small motor tests.

(3) Complete the designs for the Development Motor Testing Phase of the program.

(4) Fabricate and deliver all development motor test hardware to AFRPL for test.

b. Scope

The original scope of this program task was described in Section 5.1 of Reference 1. A number of modifications to the scope of the test plan were described in Section 5.1 of Reference 2. As a result of recommendations made to the Air Force during the third reporting period, the test plan was modified further. Three small motor tests were added and one development motor test was deleted. The additional small motor tests (designated T-23 to T-25) and the development motor tests (designated T-51 to T-54) are described in Table XXXVI. This table supplements Table XXV in Reference 2 which presented similar design data for small motor tests T-1 through T-22.

TABLE XXXVI. MOTOR DESIGN SUMMARY*

Test Number	Propellant	Grain Design	Nozzle Contour	Flame Side Materials: Insulator	Flame Side Materials: Entrance Cone	Flame Side Materials: Throat	Type of Test
T-23	Arcocel 191F	Close End Burner (100#)	Submerged	Carbon Cloth	ATJ Graphite	Pyrolytic Graphite Washers	Non-Equilibrium Combustion Effects
T-24	Arcocel 319BRF	Close End Burner (100#)	Steep Inlet	Asbestos Phenolic	ATJ Graphite	Pyrolytic Graphite Washers	
T-25	Arcocel 191F	Type I (100#)	Conventional 18° Inlet	Asbestos Phenolic	ATJ Graphite	Pyrolytic Graphite Washers (Thick)	Heat Sink Size Effect
T-51	Arcocel 191F	Single Slot (500#)	Submerged	Asbestos Phenolic	ATJ Graphite	Pyrolytic Graphite Washers	
T-52	Arcocel 319BRF	Single Slot (500#)	Submerged	Asbestos Phenolic	ATJ Graphite	Pyrolytic Graphite Washers	
T-53	Arcocel 191F	Single Slot (500#)	Deep Submerged	Asbestos Phenolic	ATJ Graphite	Pyrolytic Graphite Washers	
T-54	Arcocel 191F	Single Slot (500#)	Submerged	Asbestos Phenolic	ATJ Graphite	Tungsten	

*See Table XXV, Reference 2, for summary of Tests T-1 through T-22.

c. Summary of Progress

During the reporting period, the following progress was made toward the achievement of the task objectives:

(1) The designs for all of the program motor tests were completed.

(2) The fabrication of all motor insulation and test nozzles was completed.

(3) The propellant grains for all program motor tests have been fabricated and accepted by Aeronutronic.

(4) All test motor hardware and solid propellant grains have been delivered to the Rocket Propulsion Laboratory for firing.

(5) Small motor tests T-8 and T-12 through T-25 have been conducted.

(6) All available small motor test data and hardware has been returned to Aeronutronic for post-test analysis.

(7) Required fabrication and modifications of ADOBE motor hardware to be used in the Development Motor Testing Phase of the program have been completed.

(8) At the close of the reporting period, one development motor test (500 pound grain) was successfully conducted.

5.2 (C) SMALL MOTOR TESTS

a. (U) Small Motor Design

(1) (U) Propellant Grain Design

All grain designs for the small motor tests were completed during the first reporting period of this program, and are illustrated in Figures 47, 48, 49 and 50 of Reference 1.

(2) (U) Motor Case Design

The motor case designs for all the small motor tests were completed during the second reporting period of this program with the exception of the design utilized for Tests T-21 through T-24. Those designed during the second reporting period are illustrated by Figures 107, 108, 109 and 110 in Reference 2. The motor case designed for Tests T-21 through T-24 is depicted in Figure 133. This design simply involved a single modification of the one shown in Figure 107 of Reference 2. An additional wood filler block was added to shift the position of the end burning grain aft, to eliminate the major portion of the free chamber volume.

(3) (U) Nozzle Design

All nozzle designs for the small motor tests (as originally planned) were accomplished during the first and second reporting period. These designs are shown in Figures 53, 54 and 55 of Reference 1, and in Figures 111 through 115 of Reference 2.

During this reporting period, however, the scope of the original test plan was changed by the addition of three small motor tests designated T-23 through T-25. The nozzle designed for Test T-23 is identical to the one shown in Figure 55 of Reference 1. The grain for this test, however, was a close end burner. Therefore, the nozzle design for Test T-23 is included, Figure 134, to show the grain position relative to the nozzle. The nozzle utilized in Test T-24 is identical to the one employed for Tests T-21 and T-22 (Figure 115, Reference 2), and is not shown here. The nozzle design for Test T-25 is similar to the design used in Tests T-9 through T-11, T-14 and T-15 (Figure 53, Reference 1). The major difference in the design of T-25 is an increased heat sink thickness of the pyrolytic graphite throat washers. This was accomplished by reducing the asbestos phenolic insulation sleeve thickness. Figure 135 depicts the nozzle designed for Test T-25.

b. (C) Test Results

The small motor testing phase (25 tests) was completed during the third reporting period. The results of 18 small motor tests not reported previously are presented here. Presentation of the data and associated empirical analysis of these tests is treated categorically in the manner outlined and discussed in Section 5.2b, Reference 2.

(1) (C) Ballistic Data

The ballistic performance was computed for the remaining small motor tests in the manner discussed in Section 5.2b (1) of Reference 2. Table XXXVII is a compilation of this data. A direct comparison of this ballistic data with data for Tests T-1 through T-7 can be made by referring to Table XXVI, Reference 2. Chamber pressure versus time histories for all small motor

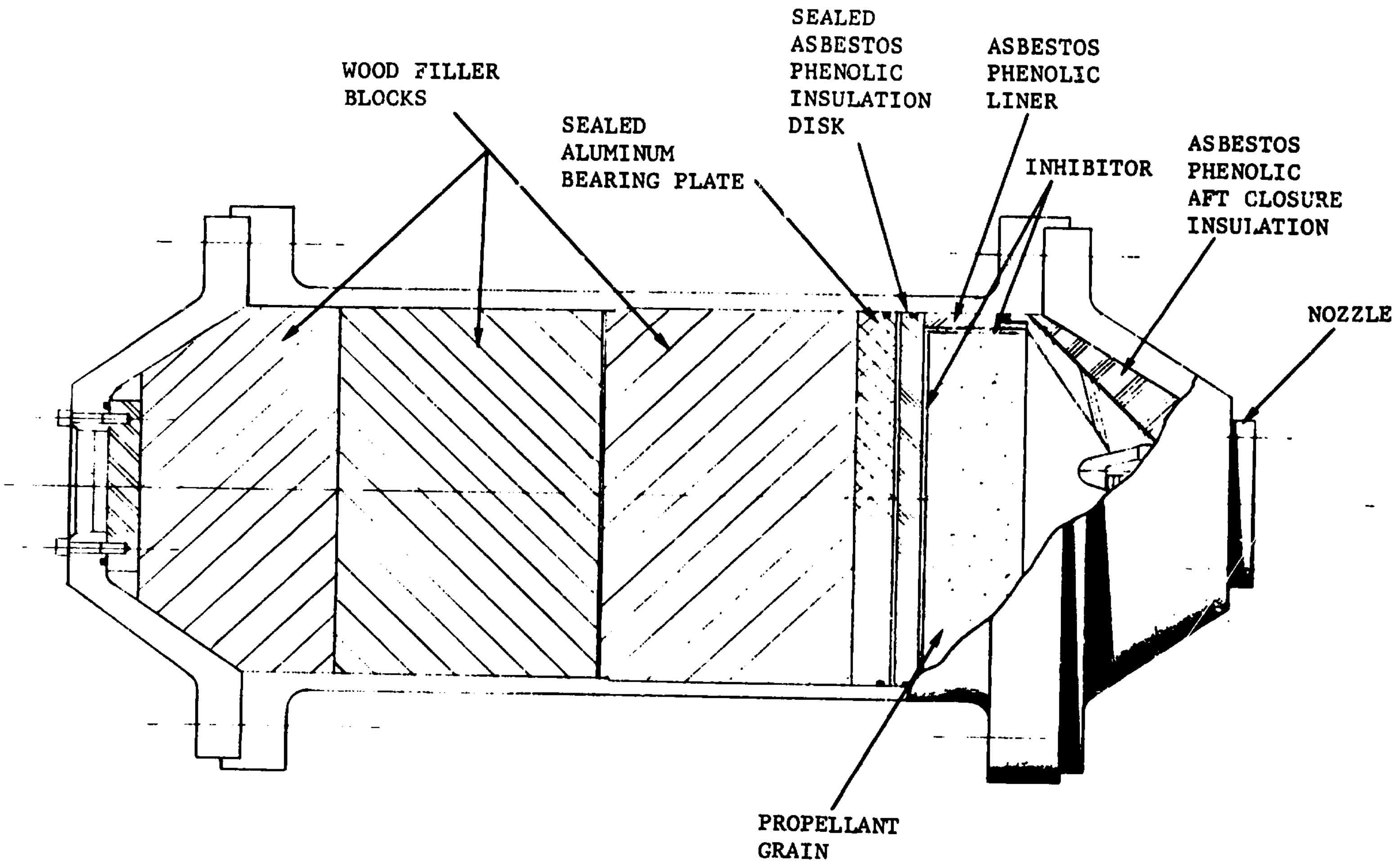
WOOD FILLER BLOCKS
SEALED ALUMINUM BEARING PLATE
SEALED ASBESTOS PHENOLIC INSULATION DISK
ASBESTOS PHENOLIC LINER
INHIBITOR
ASBESTOS PHENOLIC AFT CLOSURE INSULATION
NOZZLE
PROPELLANT GRAIN

F08060 U

FIGURE 133. MOTOR CASE DESIGN - CLOSE END BURNING GRAINS

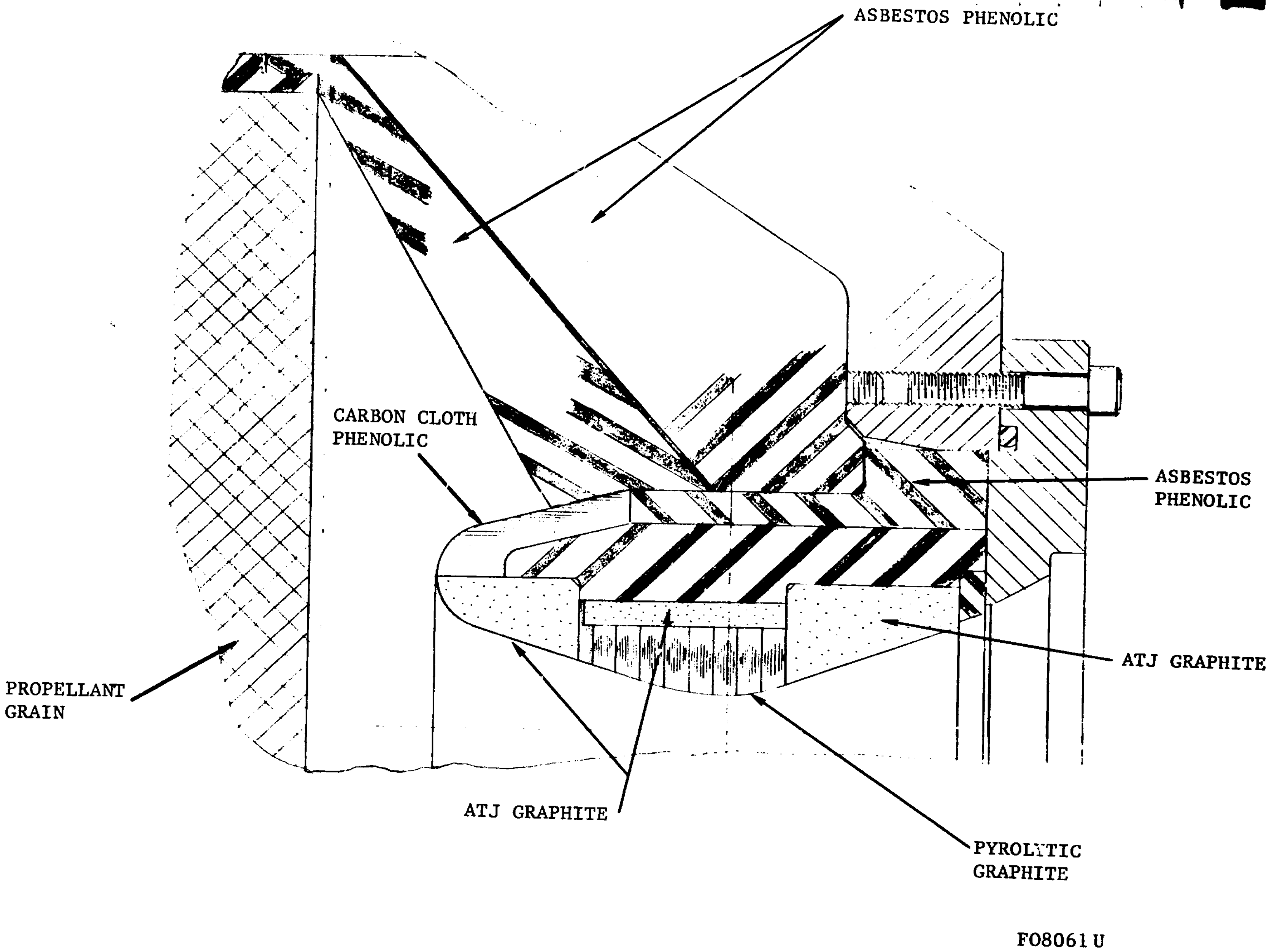
ASBESTOS PHENOLIC
CARBON CLOTH PHENOLIC
ASBESTOS PHENOLIC
ATJ GRAPHITE
PROPELLANT GRAIN
ATJ GRAPHITE
PYROLYTIC GRAPHITE
F08061U

FIGURE 134. NOZZLE DESIGN FOR TEST T-23

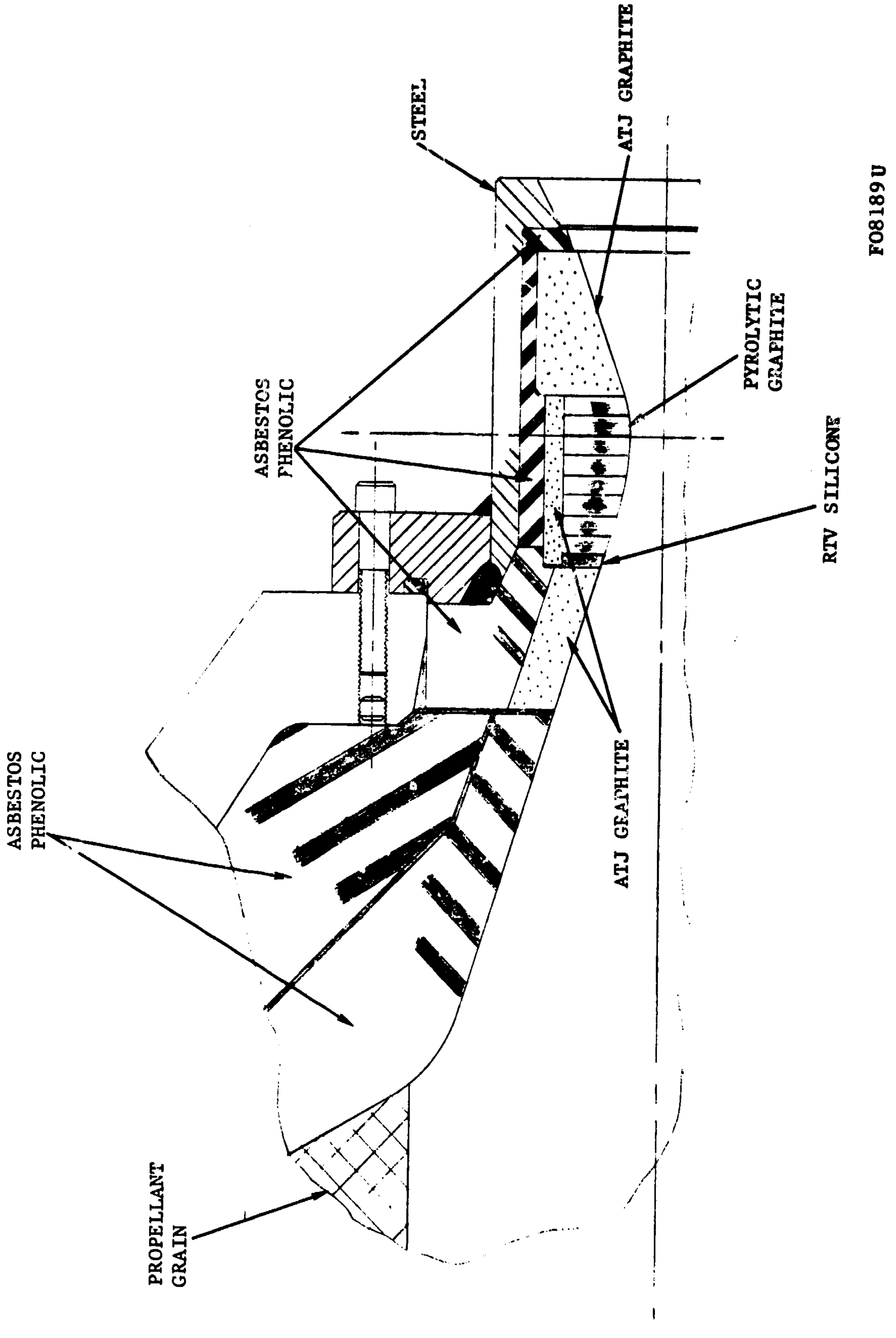
ATJ GRAPHITE
STEEL
F08189U
ASBESTOS PHENOLIC
PYROLYTIC GRAPHITE
RTV SILICONE
ATJ GRAPHITE
ASBESTOS PHENOLIC
PROPELLANT GRAIN

FIGURE 135. NOZZLE DESIGN FOR TEST T-25

TABLE XXXVII. BALLISTIC DATA, TESTS T-8 THROUGH T-25 (C)

Test Number	Propellant	Action Time, t_a (seconds)	Propellant Weight (lb)	Chamber Pressure psig		Thrust (lb)		C* fps			ISP (seconds)	
				Pc_{max}	$\bar{P}c$	F_{max}	$\bar{F}$	C^*_{eq} (800 psia)	C^*_{TSI}	C^*_{ADP}	ISP_{TSI}	ISP_{ADP}
T-8	Arcocel 389	16.95	114.31	1170	799.17	2300	1603	5197	5182	5168		238
T-9	Arcocel 191F	18.74	106.05	895	774.60	1550	1332	5448	5182	5168		235
T-10	Arcocel 191F	18.00	107.93	1390	822.56	2670	1513	5448	5402	5317		252
T-11	Arcane 54F	24.40	107.53	875	775.16	1190	1120	5420	5269	5233	236 to 241	254
T-12	Arcocel 1191F	19.2	108.95	1170	729.90	2200	1346	5448	5270	5065	238	237
T-13	Arcocel 1191F	19.0	107.80	106.0	726.84	1890	1272	5448		5026		224
T-14	Arcocel 319BRF	17.2	102.70	880	812.67	1620	1500	5510	5250	5204	249 to 252	254
T-15	Arcocel 319BRF	16.4	95.55	1180	986.22	1740	1453	5510	6038	5583	241 to 248	249
T-16	Arcocel 191F	17.4	104.42	935	835.98	1600	1412	5448	5170 to 5215	5083	236	235
T-17	Arcocel 191F	18.3	104.45	935	798.36	1540	1295	5448	5199 to 5244	5040	226	227
T-18	Arcocel 191F	17.5	104.44	970	841.03	1620	1390	5448	5180 to 5235	4920	232	233
T-19	Arcocel 319BRF	16.40	102.18	985	895.85	1620	1483	5510	5290 to 5309	5222	237	238
T-20	Arcocel 191F	18.15	105.22	955	826.78	1560	1413	5448		5163		244
T-21	Arcocel 191F	16.90	99.23	1090	933.37	1610	1386	5448	5527 to 5539	4669	236 to 237	236
T-22	Arcane 54F	25.40	103.42	980	857.13	1060	954	5420	5741 to 5758	5017	235	234
T-23	Arcocel 191F	20.10	103.92	1000	811.19	1420	1197	5448		4784		232
T-24	Arcocel 319BRF	23.20	100.99	975	636.12	1490	994	5510		5267		228
T-25	Arcocel 191F	17.80	104.81	950	828.20	1630	1397	5448		5167		237

tests not previously presented are given in Figures 136 through 153. For convenience, thrust versus time for each of these motor tests is also plotted in these figures. The zero time selected for use in the thermal analyses, described in paragraph 2.5, is indicated on the time scale in each figure.

(2) (C) Nozzle Performance

(a) (U) General Data

Measurements of nozzle throat diameters were made before and after Tests T-8 through T-25. These values are listed in Table XXXVIII with generalized values of erosion rates. A comparison of these data with those of Tests T-1 through T-7 may be made by referring to Table XXVII, Reference 2.

(b) (C) Nozzle Throat Radius Change History

A detailed development of the analysis for estimating throat radius change as a function of motor firing time, utilizing two complimentary techniques, was presented in Reference 2. These techniques (the K_n and F/p methods) were used to estimate throat radius changes for Tests T-8 through T-25 that are comparable to those for T-1 through T-7 (Figures 139 through 145, Reference 2). The curves for Tests T-8 through T-25 are shown in Figures 154 through 171.

(3) (C) Discussion of Test Results

The tests reported here can be initially classified as normal or abnormal tests. The word abnormal, in this case, is not intended to imply that any given test was a total failure. It merely indicates some oddity in ballistic behavior or results obtained that sets it apart from those tests which performed according to the nominal design plan. Tests T-9, T-14, T-15, T-16, T-17, T-18, T-19, T-21, T-22, T-23 and T-25 may be classified as normal tests. All of these tests were conducted with either center perforated or end burning grains, with the exception of T-15 which utilized a 3 inch keyed grain. An examination of the pressure-time histories of these tests indicates that essentially neutral burning was achieved, except for pressure excursions caused by throat deposition and/or erosion. Change in throat radius with time was simply and satisfactorily evaluated, utilizing the K_n technique described in Section V, Reference 2. The results of this evaluation were in good agreement with the thermal data for these tests.

Tests T-8, T-10, T-12, T-13, T-20 and T-24 did not behave or were not conducted according to plan. Of these tests, T-8, T-10, T-12 and T-13 may be characterized by a common abnormality. Each of these tests utilized a 7 inch keyed grain. The pressure-time plots exhibited extreme pressure excursions coupled with an inordinate amount of regressive burning during the latter stages of the firing. A definite indication of non-uniform grain burning exists. The resulting variations in burning surface area precluded the use

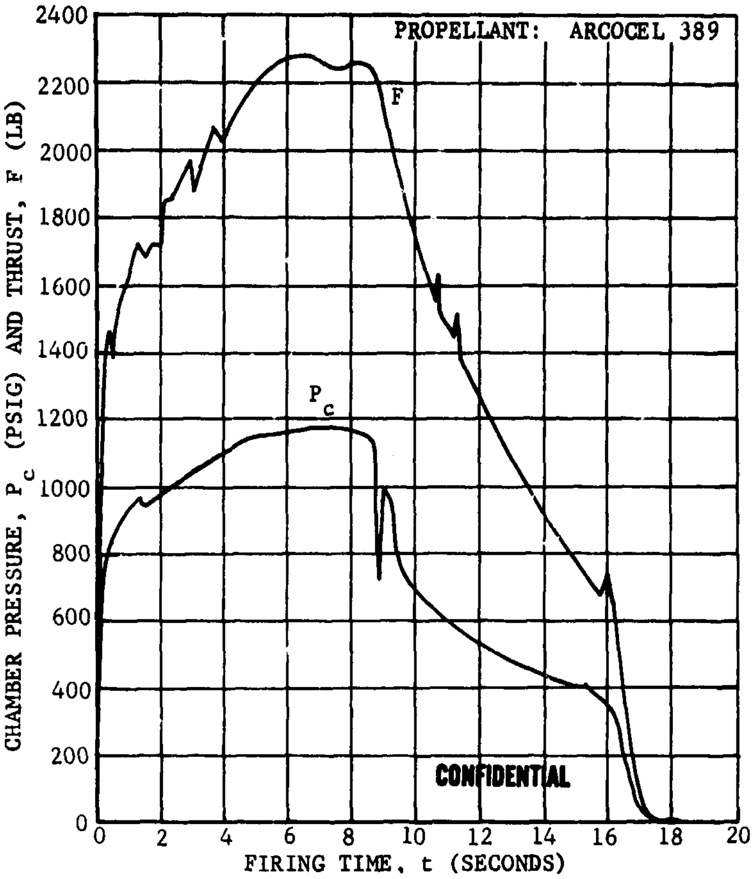

FIGURE 136. CHAMBER PRESSURE AND THRUST VERSUS FIRING TIME TEST T-8

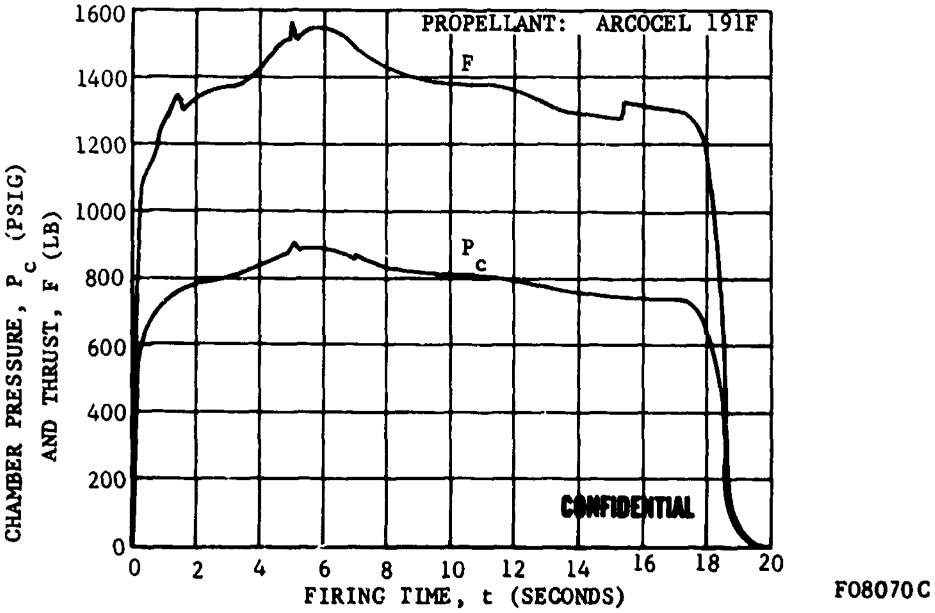

FIGURE 137. CHAMBER PRESSURE AND THRUST VERSUS FIRING TIME TEST T-9

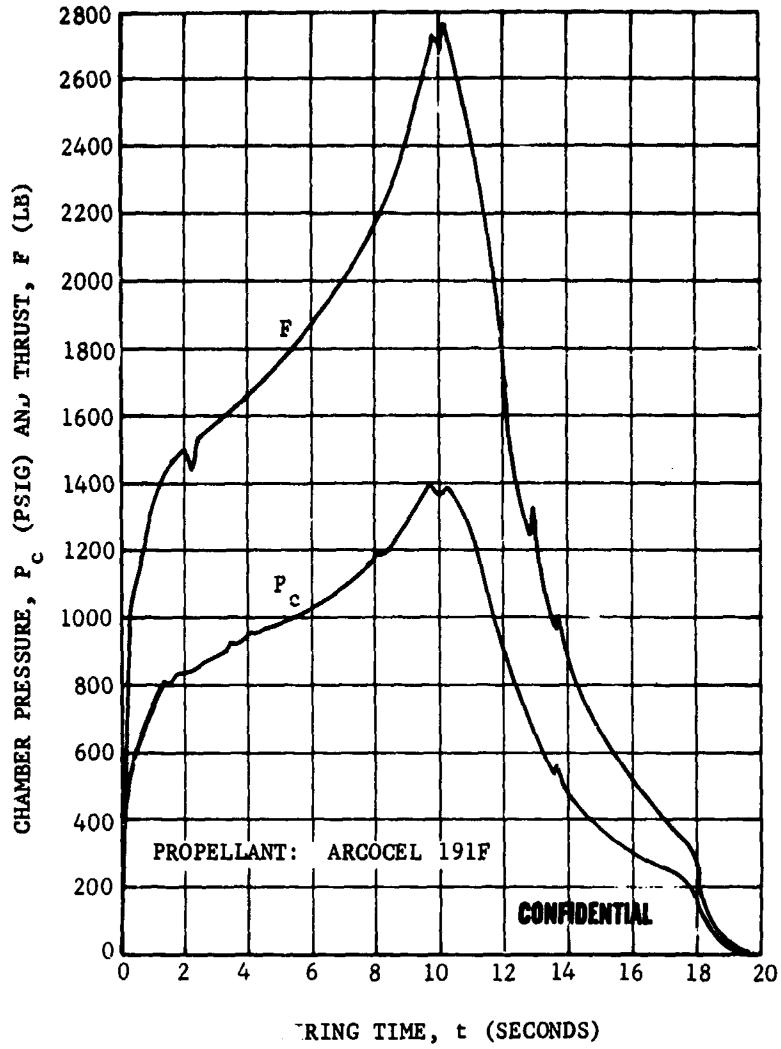

FIGURE 138. CHAMBER PRESSURE AND THRUST VERSUS FIRING TIME TEST T-10

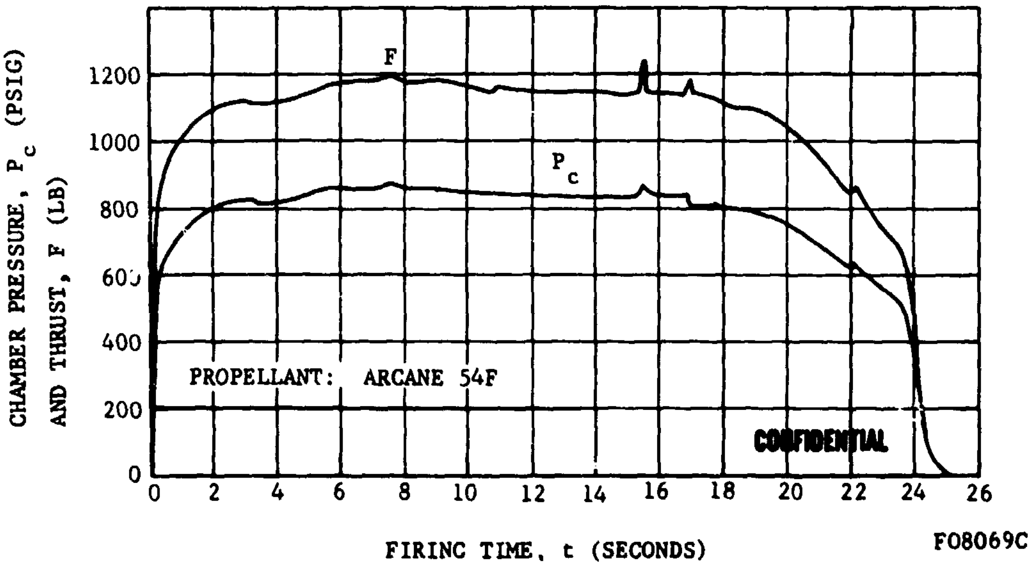

FIGURE 139. CHAMBER PRESSURE AND THRUST VERSUS FIRING TIME TEST T-11

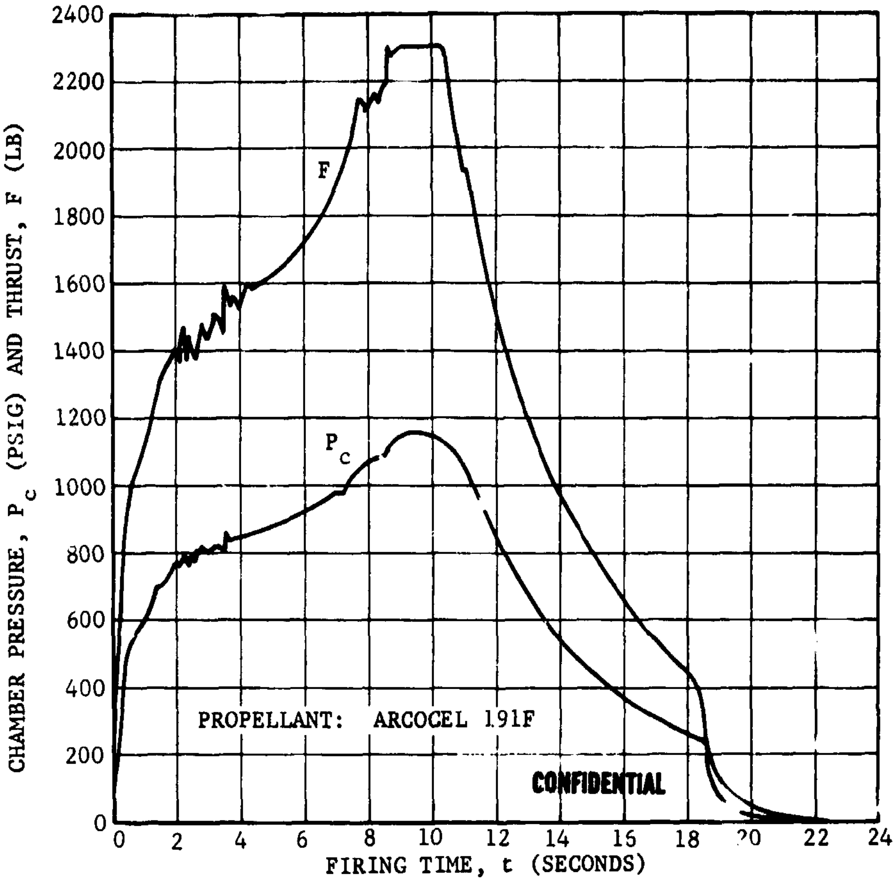

FIGURE 140. CHAMBER PRESSURE AND THRUST VERSUS FIRING TIME TEST T-12

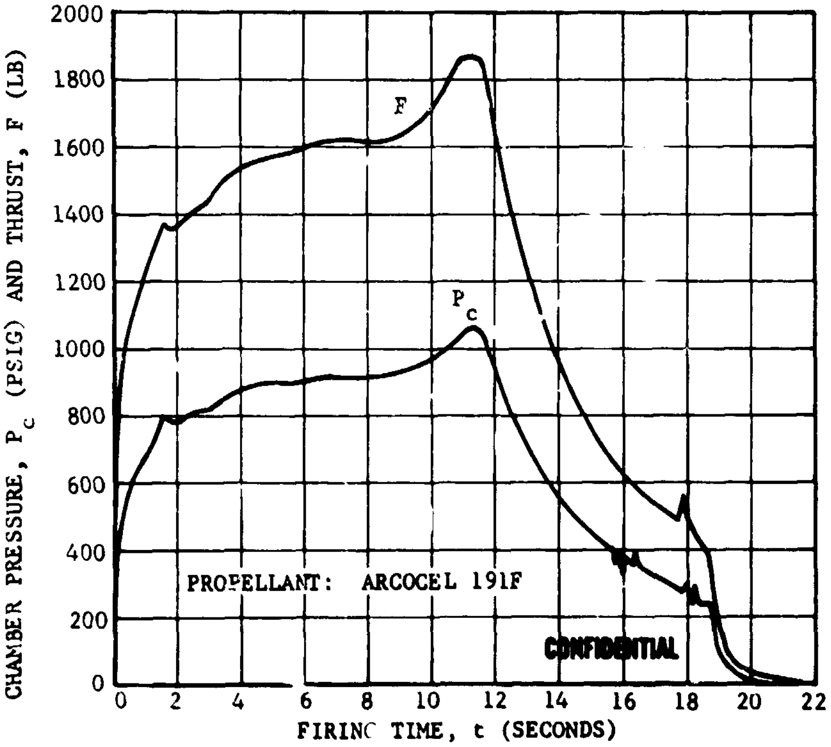

F08068C

FIGURE 141. CHAMBER PRESSURE AND THRUST VERSUS FIRING TIME TEST T-13

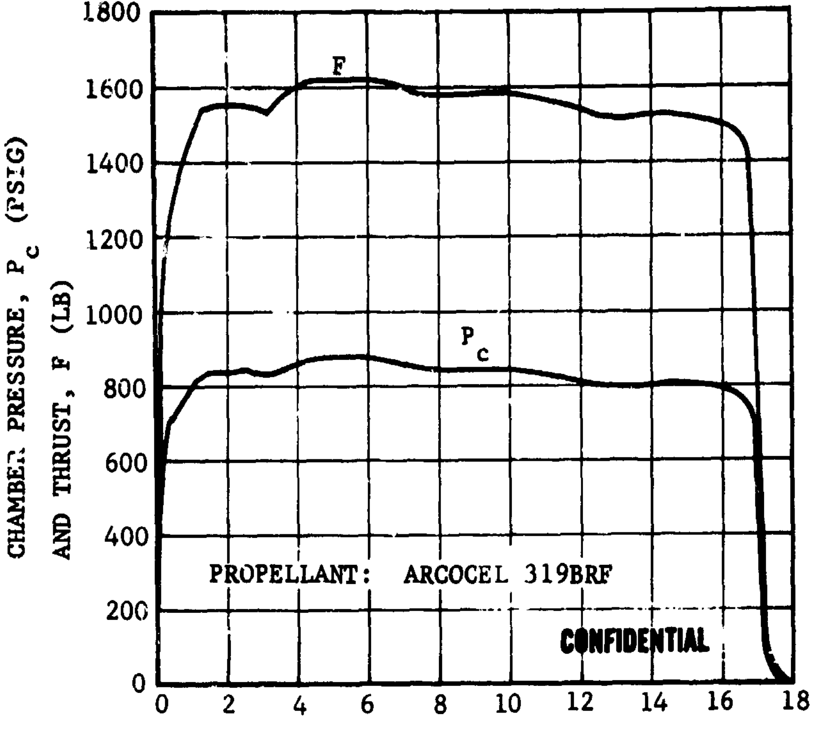

FIRING TIME, t (SECONDS)

FIGURE 142. CHAMBER PRESSURE AND THRUST VERSUS FIRING TIME TEST T-14

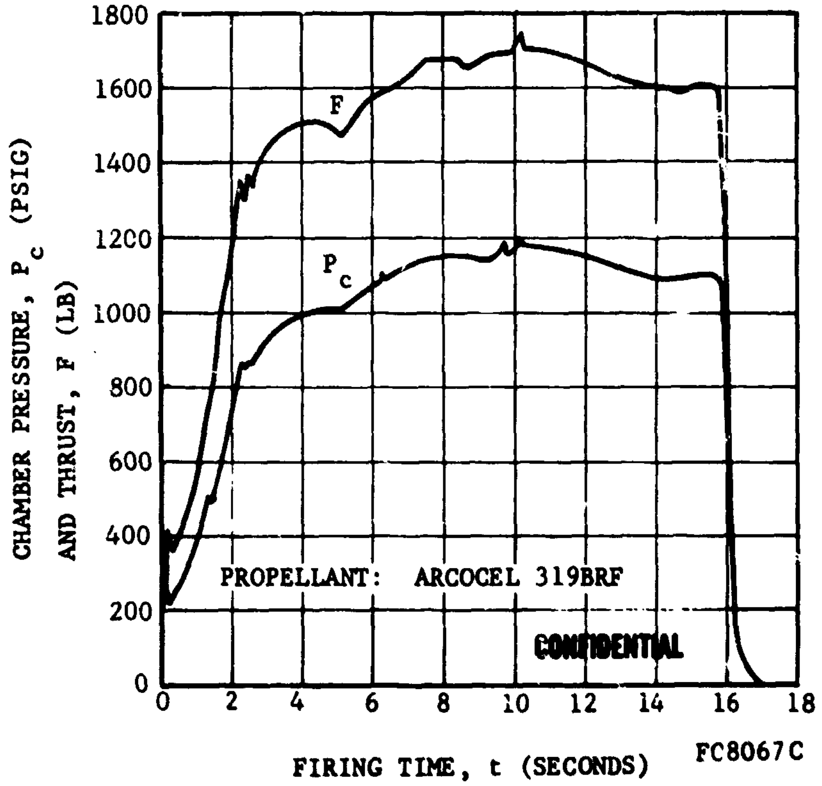

FIRING TIME, t (SECONDS)

FIGURE 143. CHAMBER PRESSURE AND THRUST VERSUS FIRING TIME TEST T-15

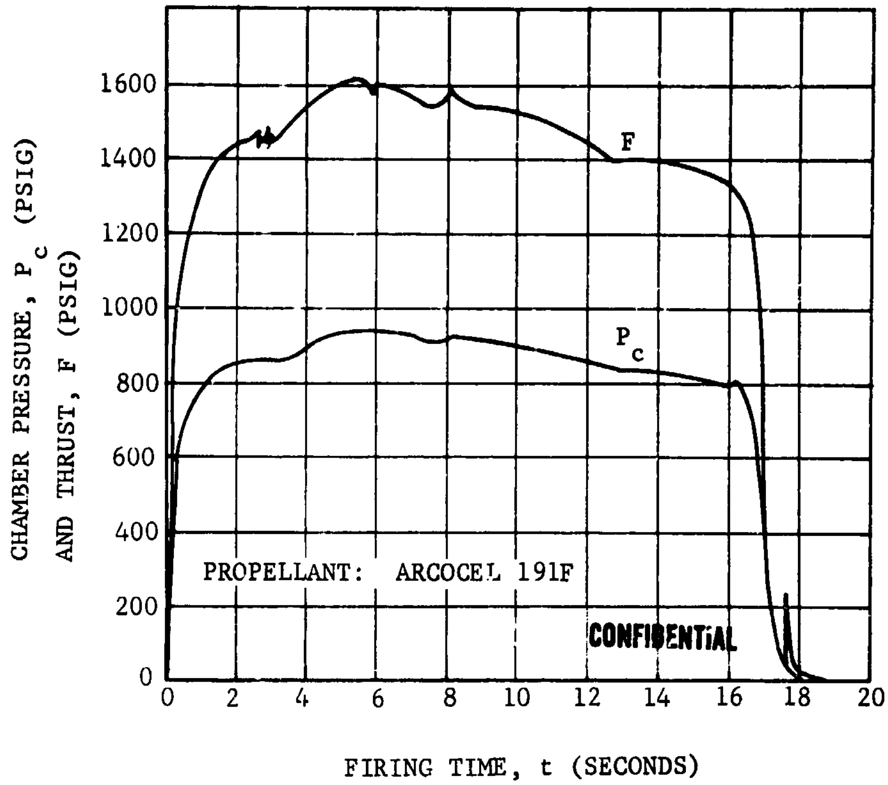

FIGURE 144. CHAMBER PRESSURE AND THRUST VERSUS FIRING TIME TEST T-16

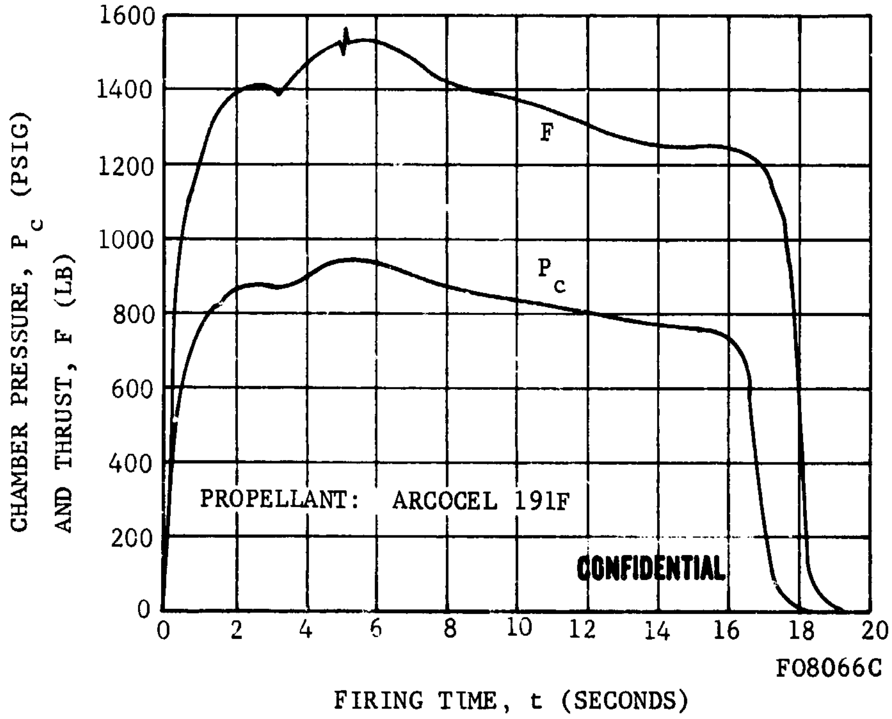

FIGURE 145. CHAMBER PRESSURE AND THRUST VERSUS FIRING TIME TEST T-17

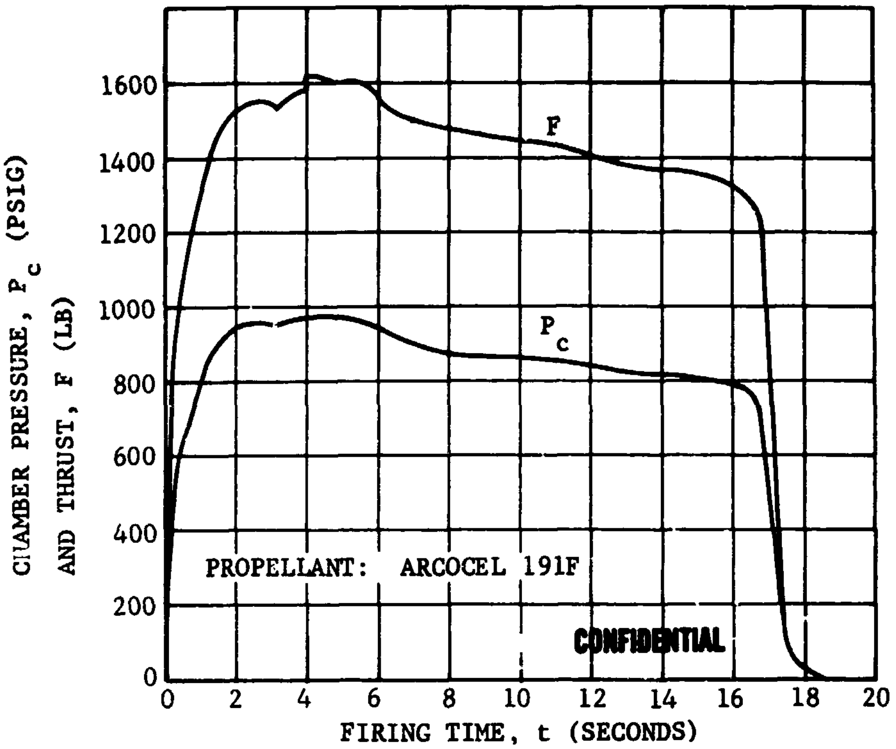

FIGURE 146. CHAMBER PRESSURE AND THRUST VERSUS FIRING TIME TEST T-18

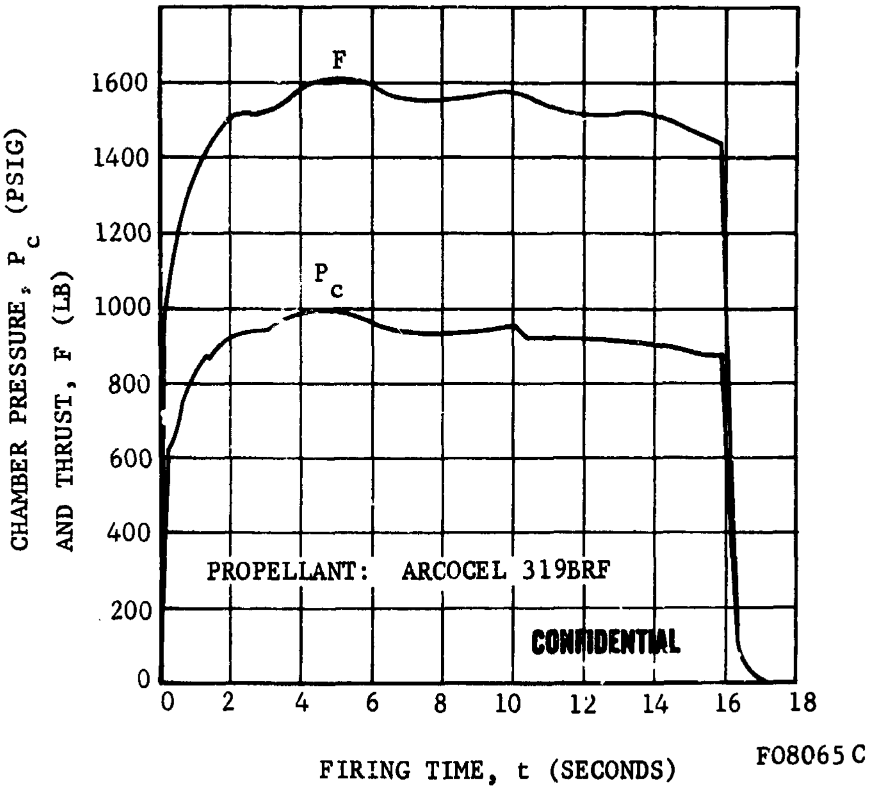

FIGURE 147. CHAMBER PRESSURE AND THRUST VERSUS FIRING TIME TEST T-19

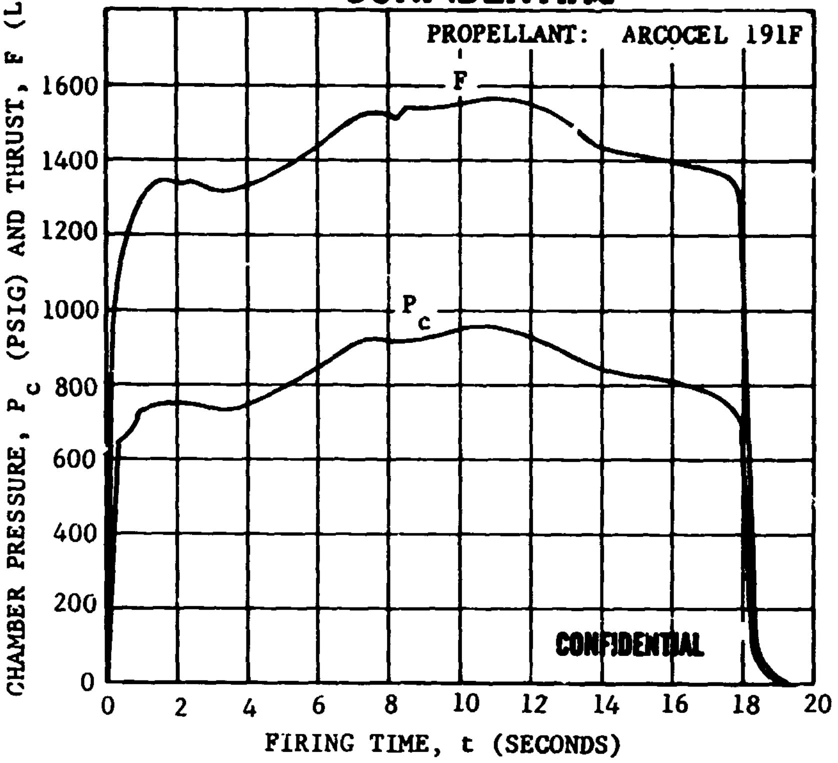

FIGURE 148. CHAMBER PRESSURE AND THRUST VERSUS FIRING TIME TEST T-20

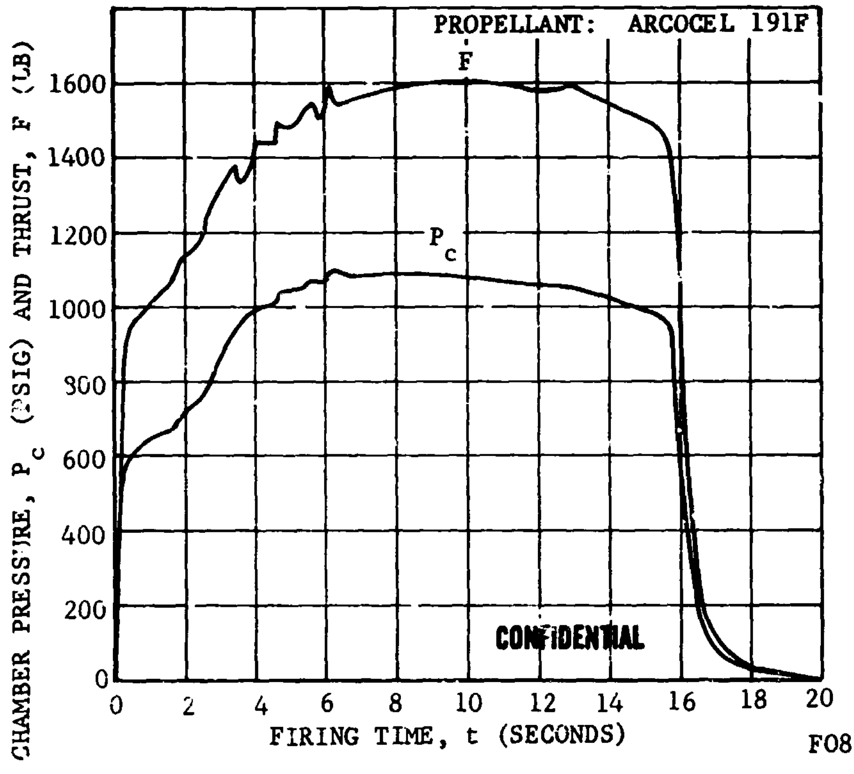

F08064C

FIGURE 149. CHAMBER PRESSURE AND THRUST VERSUS FIRING TIME TEST T-21

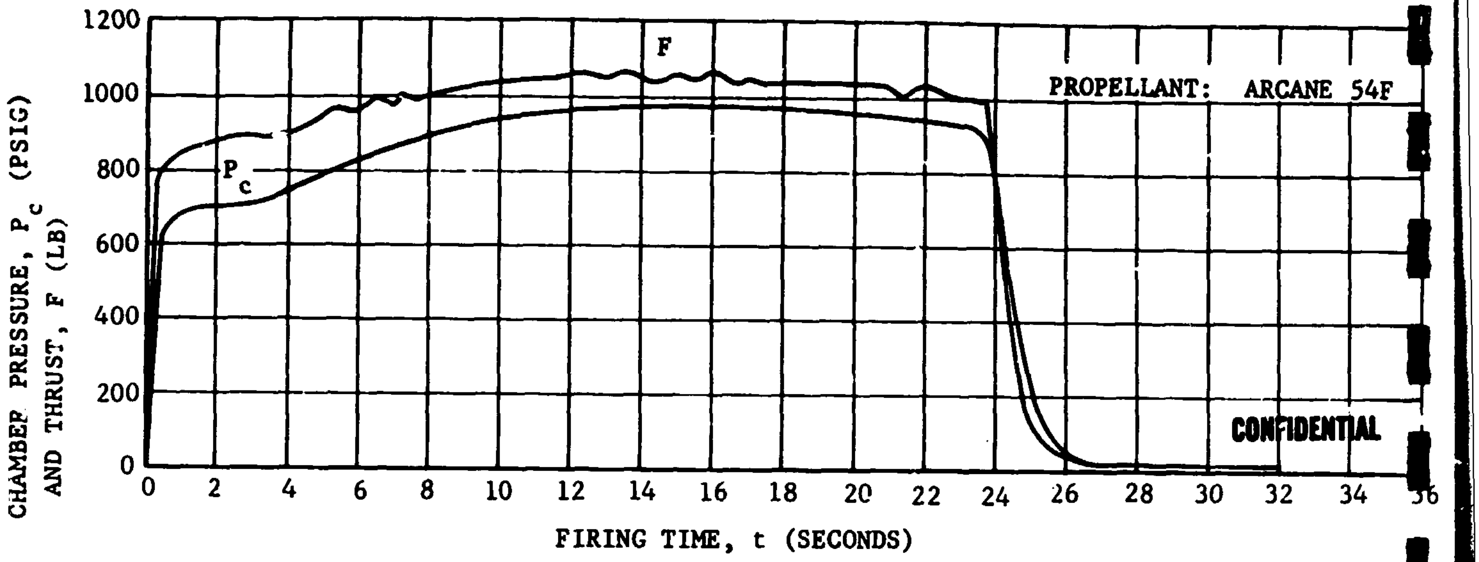

FIGURE 150. CHAMBER PRESSURE AND THRUST VERSUS FIRING TIME TEST T-22

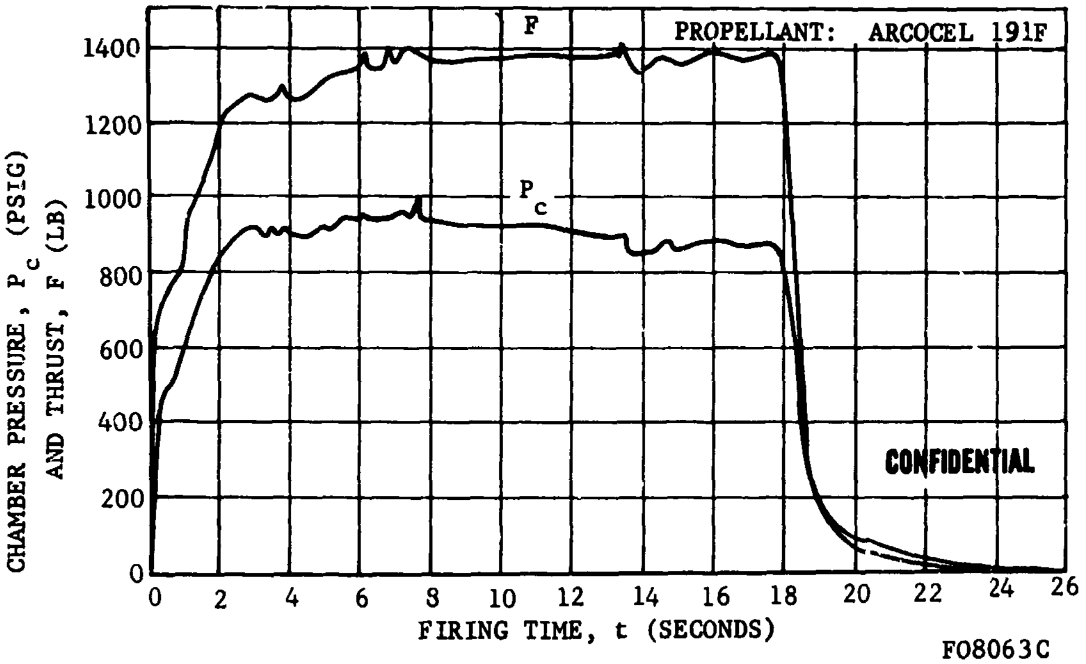

FIGURE 151. CHAMBER PRESSURE AND THRUST VERSUS FIRING TIME TEST T-23

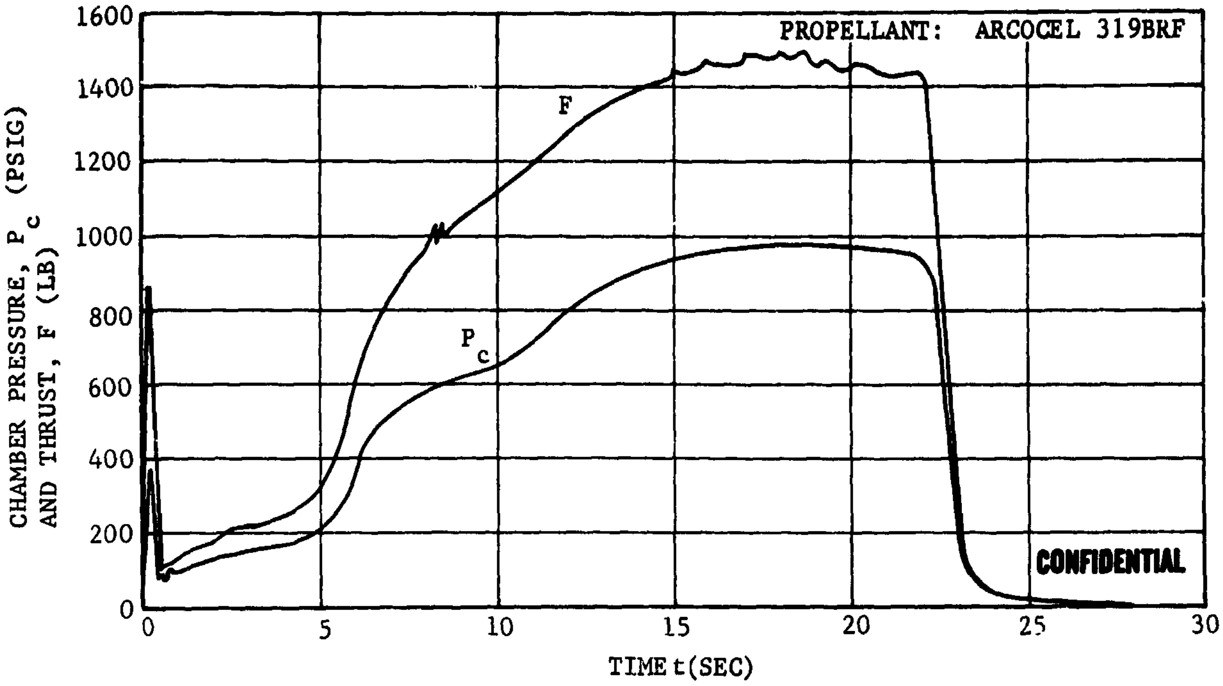

FIGURE 152. CHAMBER PRESSURE AND THRUST VERSUS FIRING TIME TEST T-24

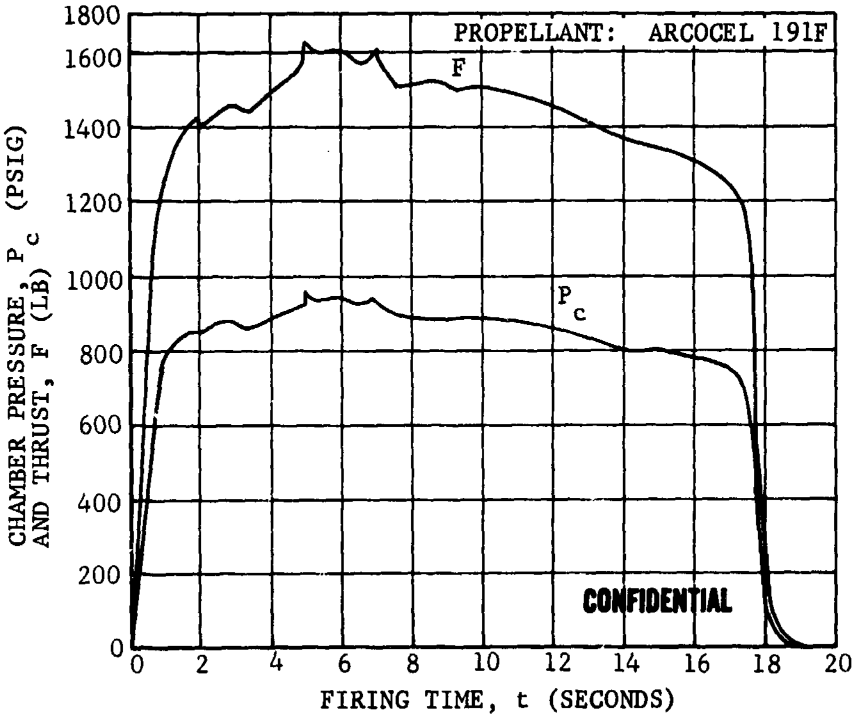

F08062C

FIGURE 153. CHAMBER PRESSURE AND THRUST VERSUS FIRING TIME TEST T-25

TABLE XXXVIII. GENERAL NOZZLE THROAT PERFORMANCE (C)

Test Number	Propellant	Action Time, t_a (seconds)	Throat Diameter $\overline{D}_c$ (inches)		Change in Throat Radius ± δ (inches) + = Erosion - = Shrinkage (deposit, if any, removed)	Estimated Deposition at Throat After Test - δ' (mils) (see Sect 5.2b(2)(b)	Throat Erosion Rate dδ/dt (mils/sec)	
			Before	After (deposit, if any, removed)			Rate	Period of Erosion (seconds)
T-8	Arcocel 389	16.95	1.215	1.2150	0	90	0	
T-9	Arcocel 191F	18.74	1.212	1.2196	+0.0038	0	1.9	15.0 to 17.0
T-10	Arcocel 191F	18.00	1.233	1.2450	+0.0060	16	7.0	7.0 to 10.0
T-11	Arcane 54F	24.4	1.080	1.0815	+0.0008	12	0.32	15.0 to 17.5
T-12	Arcocel 191F	19.2	1.233	1.2724	+0.0197	25	7.6	5.8 to 8.4
T-13	Arcocel 191F	19.0	1.238	1.2573	+0.0097	13	3.2	7.8 to 10.8
T-14	Arcocel 319BRF	17.2	1.218	1.2428	+0.0124	0	2.1	11.2 to 17.2
T-15	Arcocel 319BRF	16.4	1.180	1.1770	-0.0015	29		
T-16	Arcocel 191F	17.4	1.214	1.1967	-0.0087	5		
T-17	Arcocel 191F	18.3	1.214	1.2010	-0.0065	3		
T-18	Arcocel 191F	17.5	1.214	1.1981	-0.0080	8		
T-19	Arcocel 319 BRF	16.4	1.214	1.1860	-0.0140	8		
T-20	Arcocel 191F	18.15	1.214	1.2293	+0.0077	10	4.5	1.8 to 3.5
T-21	Arcocel 191F	16.9	1.165	1.1650		44		
T-22	Arcane 54F	25.4	1.030	1.0240	-0.0030	65		
T-23	Arcocel 191F	20.1	1.179	1.1660	-0.0065	10		
T-24	Arcocel 319BRF	23.2	1.217	1.2123	-0.0024	35		
T-25	Arcocel 191F	17.8	1.222	1.2214	-0.0003	0		

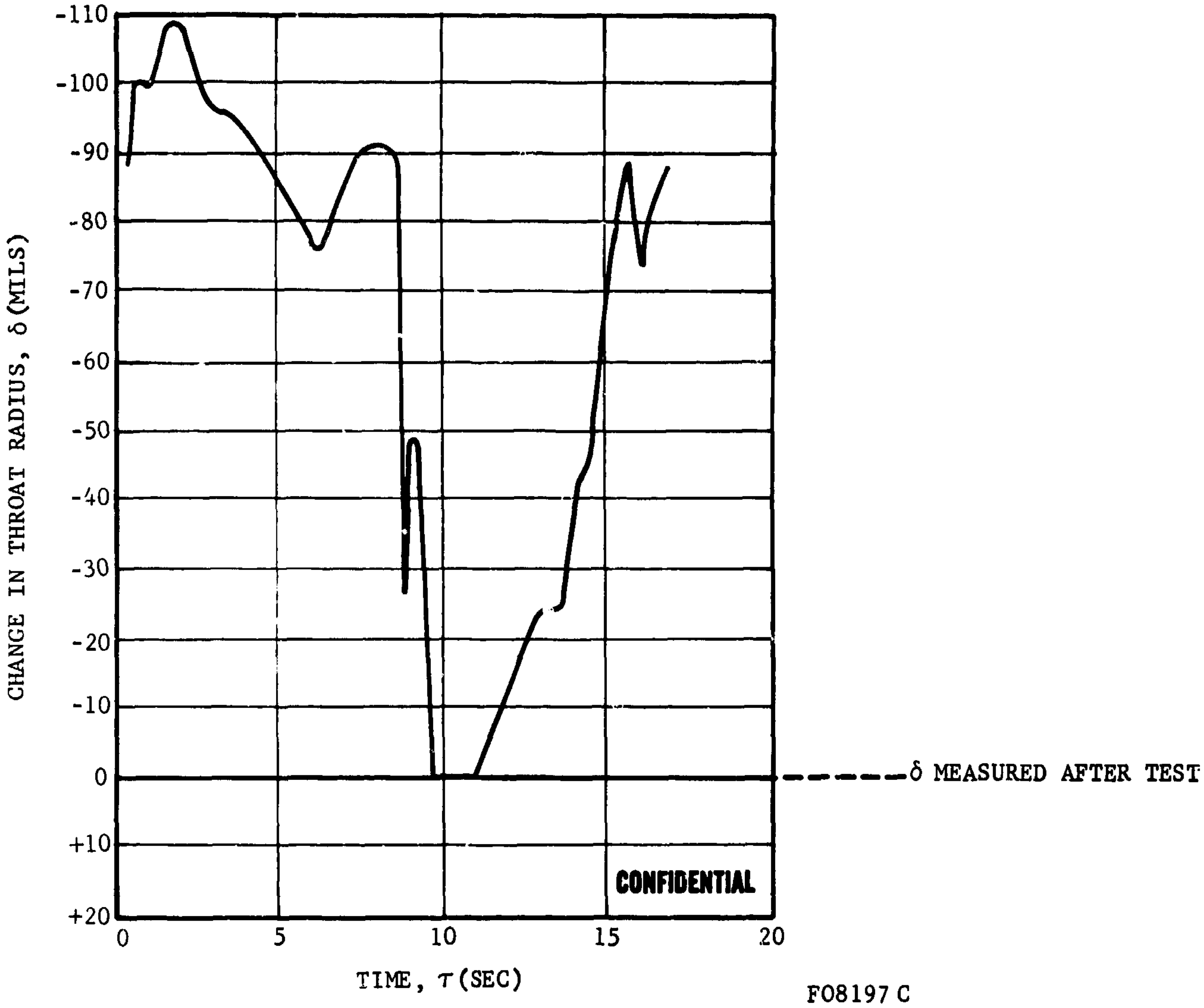

FIGURE 154. CHANGE IN NOZZLE THROAT RADIUS VS FIRING TIME TEST T-8

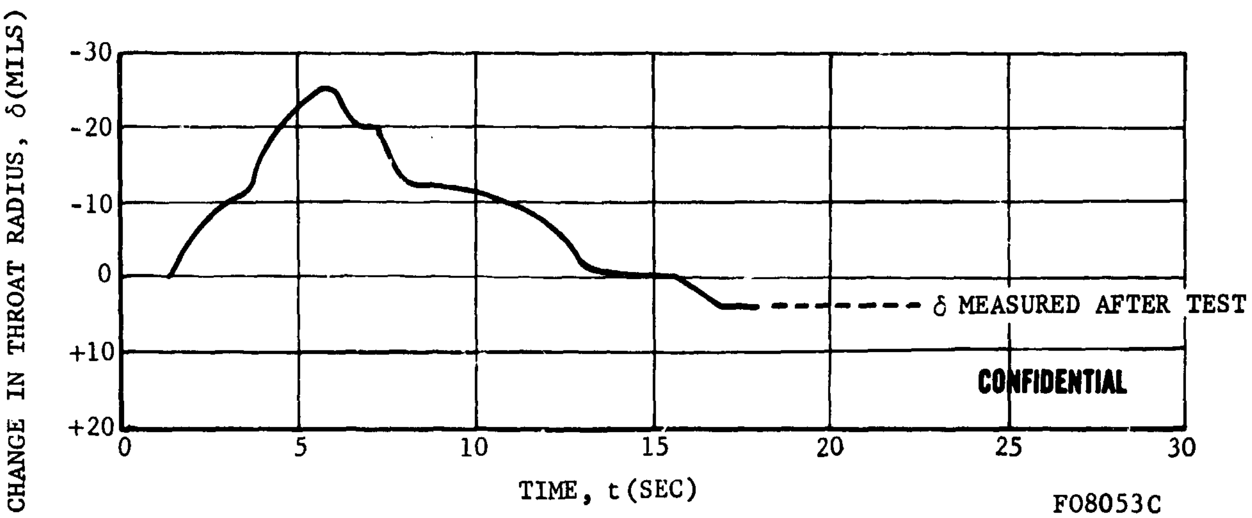

FIGURE 155. CHANGE IN NOZZLE THROAT RADIUS VS FIRING TIME TEST T-9

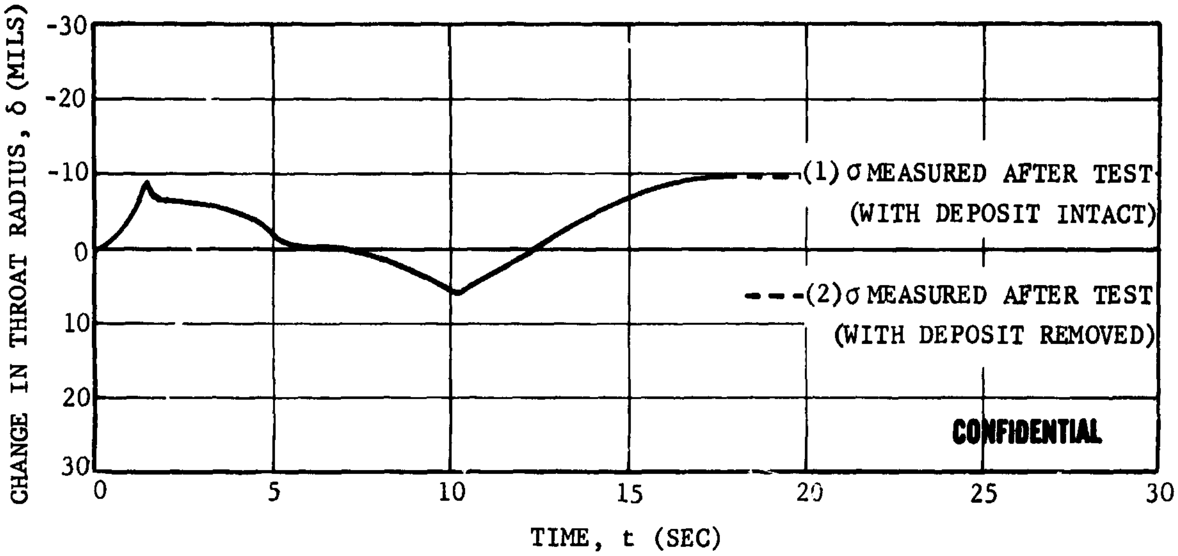

FIGURE 156. CHANGE IN NOZZLE THROAT RADIUS VERSUS FIRING TIME TEST T-10

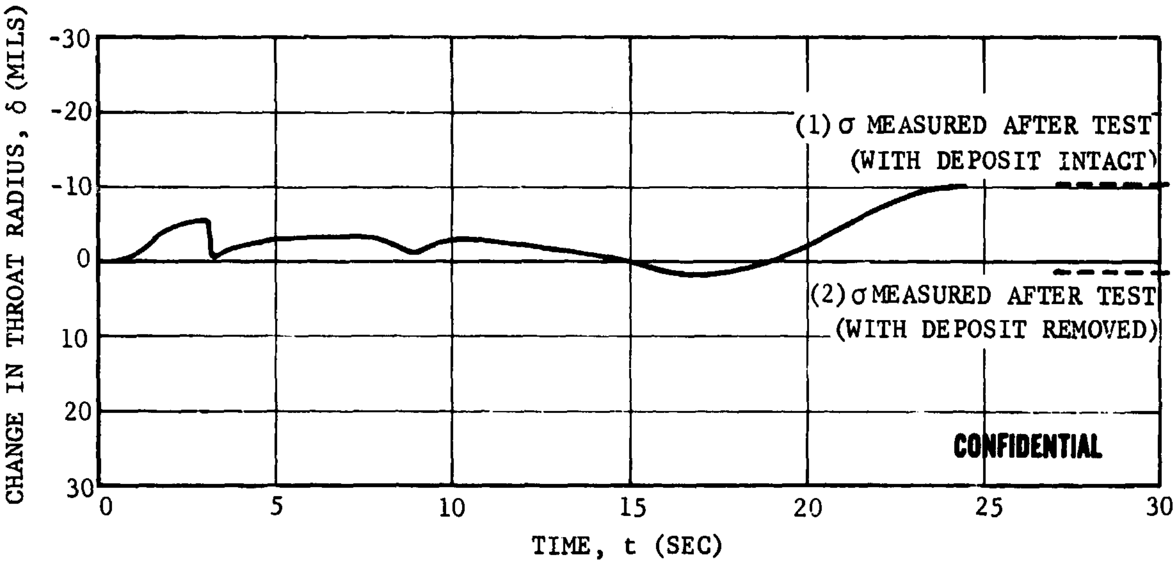

F08052 C

FIGURE 157. CHANGE IN NOZZLE THROAT RADIUS VERSUS FIRING TIME TEST T-11

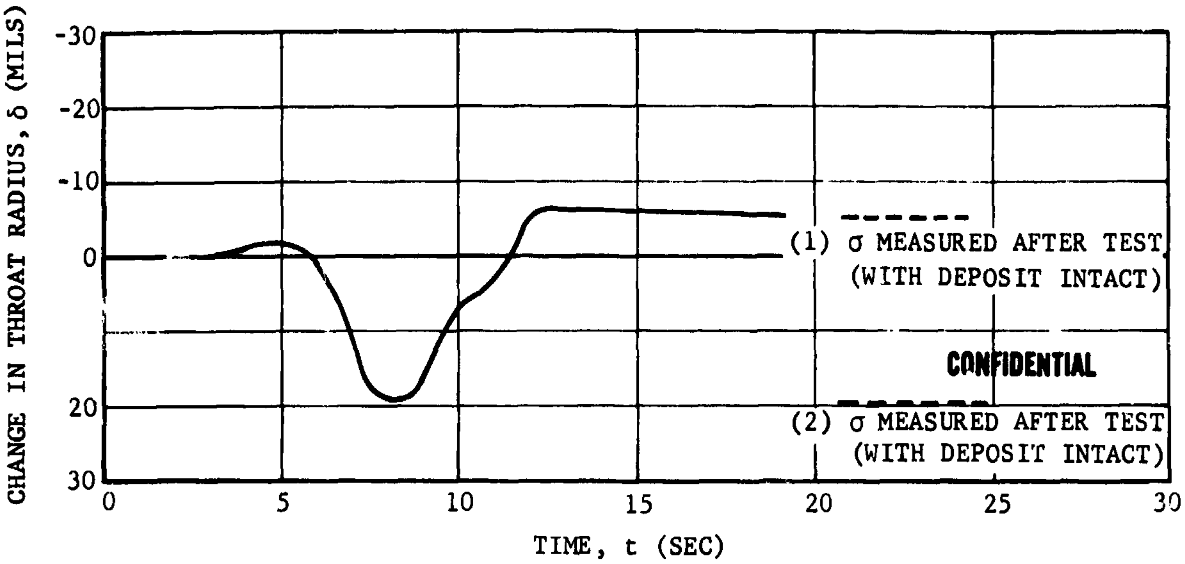

FIGURE 158. CHANGE IN NOZZLE THROAT RADIUS VERSUS FIRING TIME TEST T-12

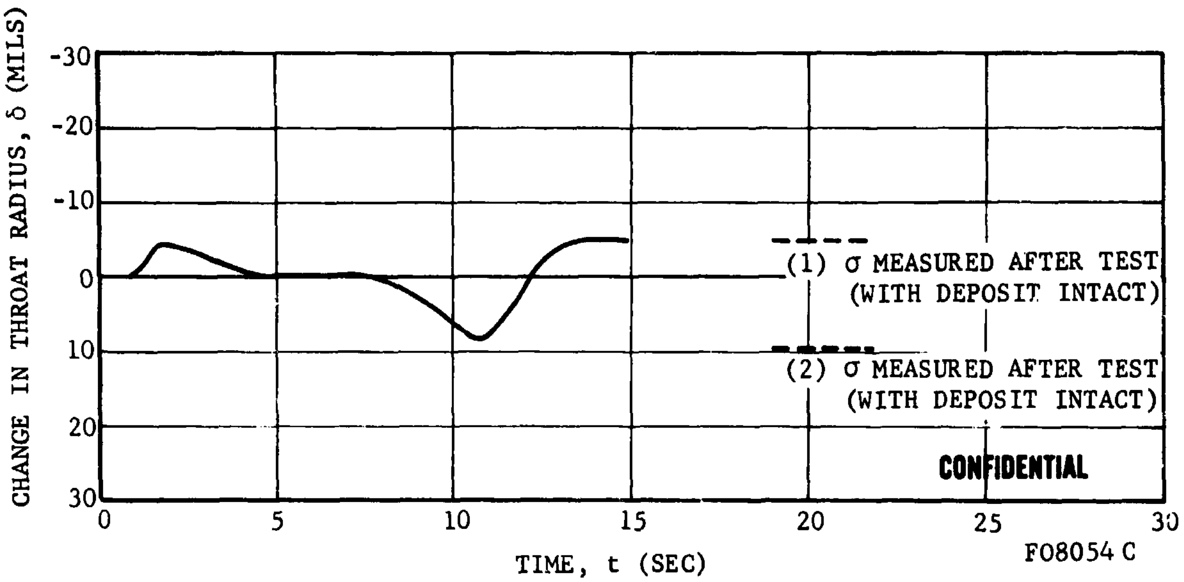

FIGURE 159. CHANGE IN NOZZLE THROAT RADIUS VERSUS FIRING TIME TEST T-13

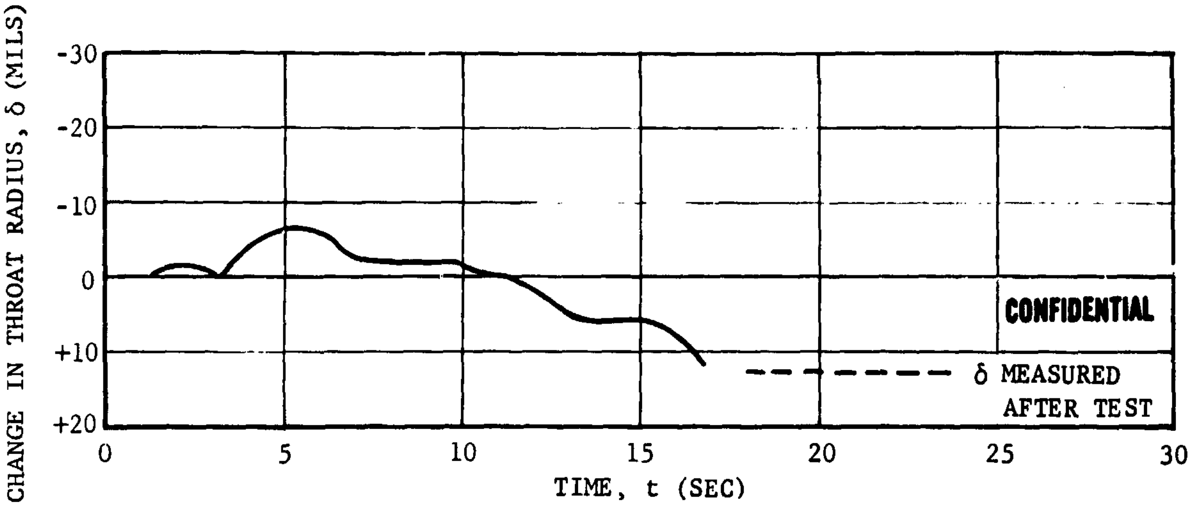

FIGURE 160. CHANGE IN NOZZLE THROAT RADIUS VERSUS FIRING TIME TEST T-14

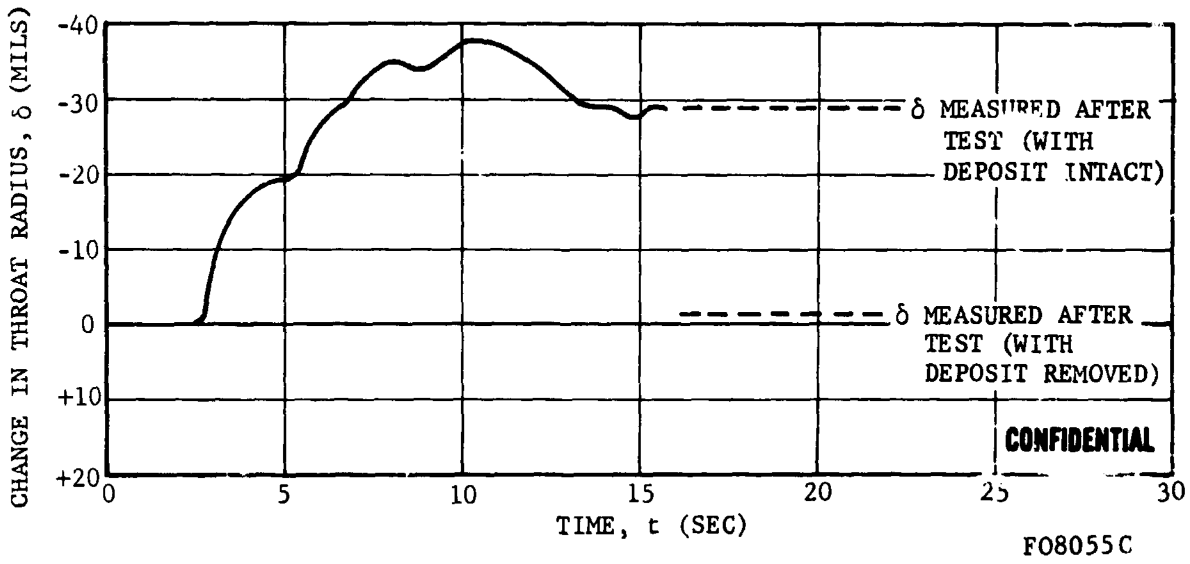

FIGURE 161. CHANGE IN NOZZLE THROAT RADIUS VERSUS FIRING TIME TEST T-15

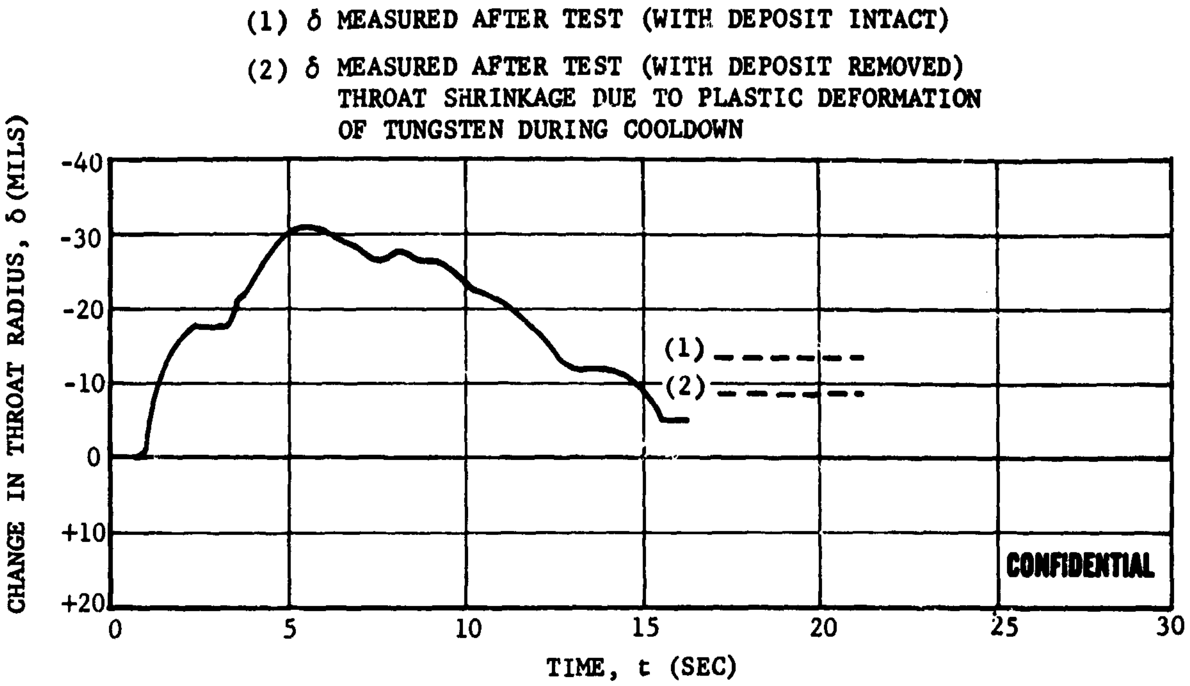

FIGURE 162. CHANGE IN NOZZLE THROAT RADIUS VERSUS FIRING TIME TEST T-16

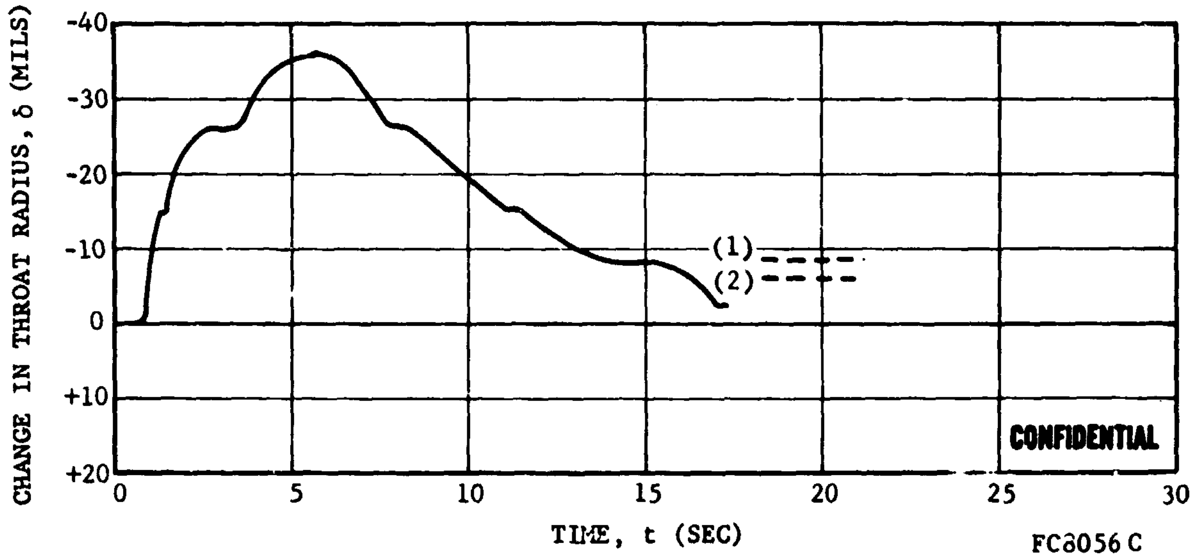

FIGURE 163. CHANGE IN NOZZLE THROAT RADIUS VERSUS FIRING TIME TEST T-17

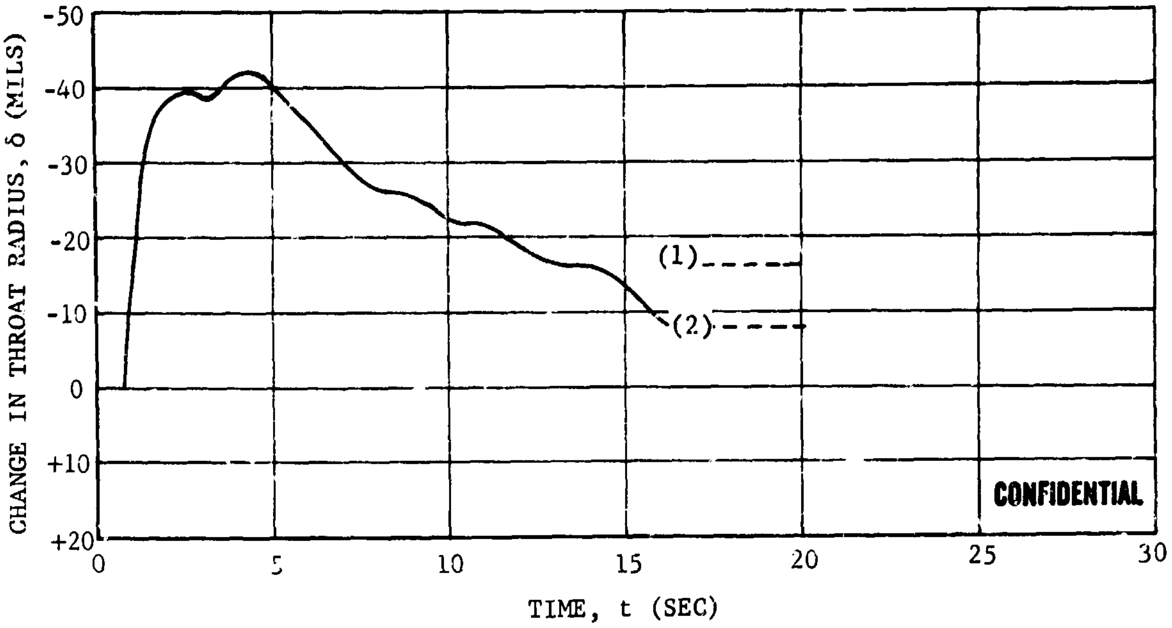

FIGURE 164. CHANGE IN NOZZLE THROAT RADIUS VERSUS FIRING TIME TEST T-18

(1) δ MEASURED AFTER TEST (WITH DEPOSIT INTACT)

(2) δ MEASURED AFTER TEST (WITH DEPOSIT REMOVED) THROAT SHRINKAGE DUE TO PLASTIC DEFORMATION OF TUNGSTEN DURING COOLDOWN

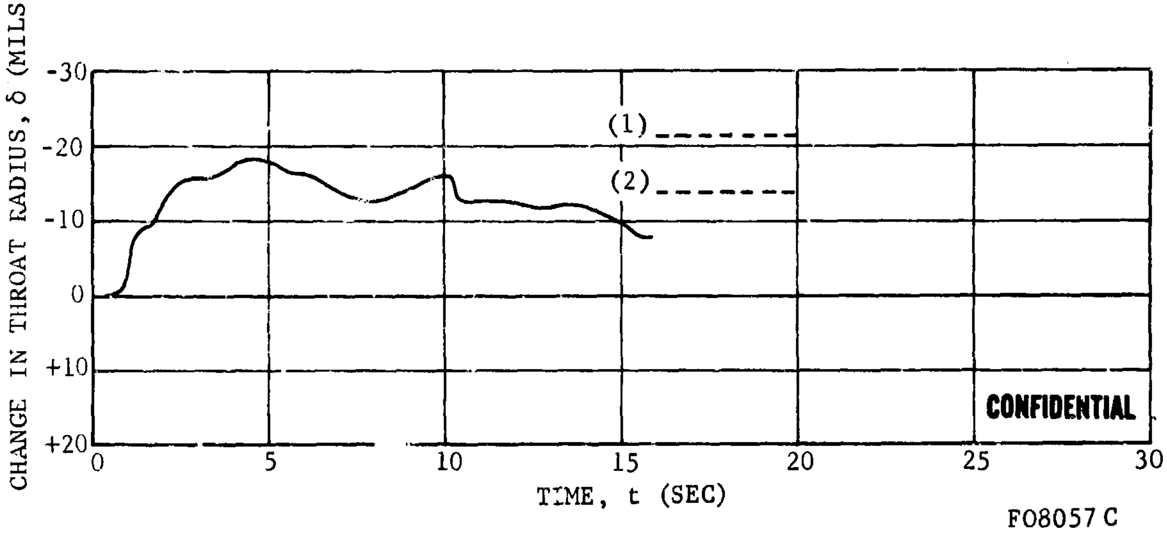

F08057 C

FIGURE 165. CHANGE IN NOZZLE THROAT RADIUS VERSUS FIRING TIME TEST T-19

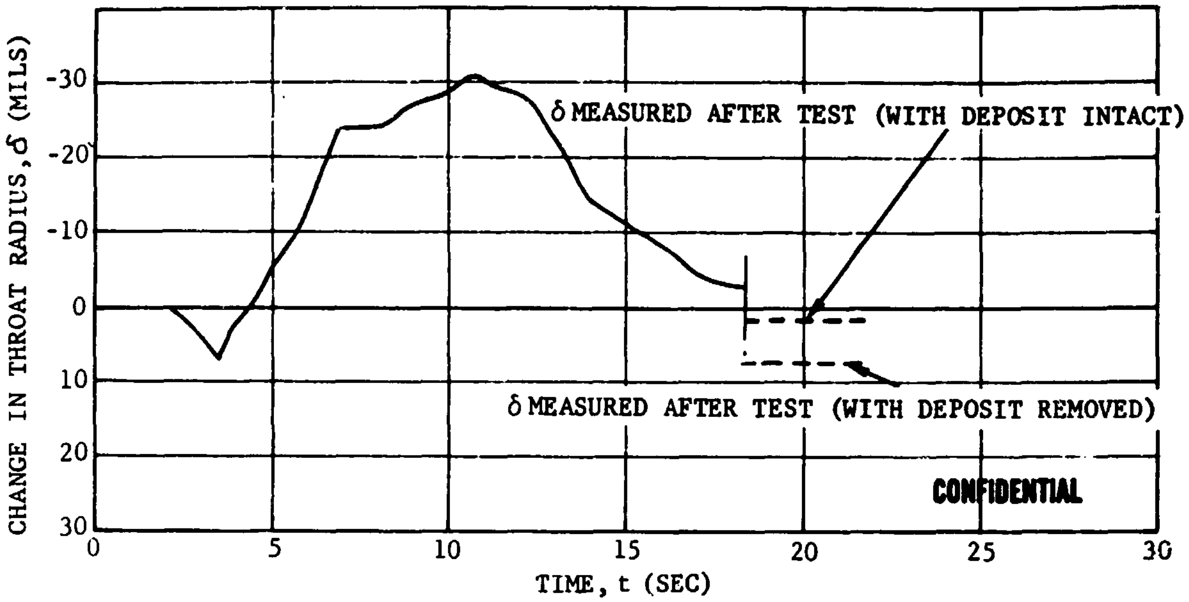

FIGURE 166. CHANGE IN NOZZLE THROAT RADIUS VERSUS FIRING TIME TEST T-20

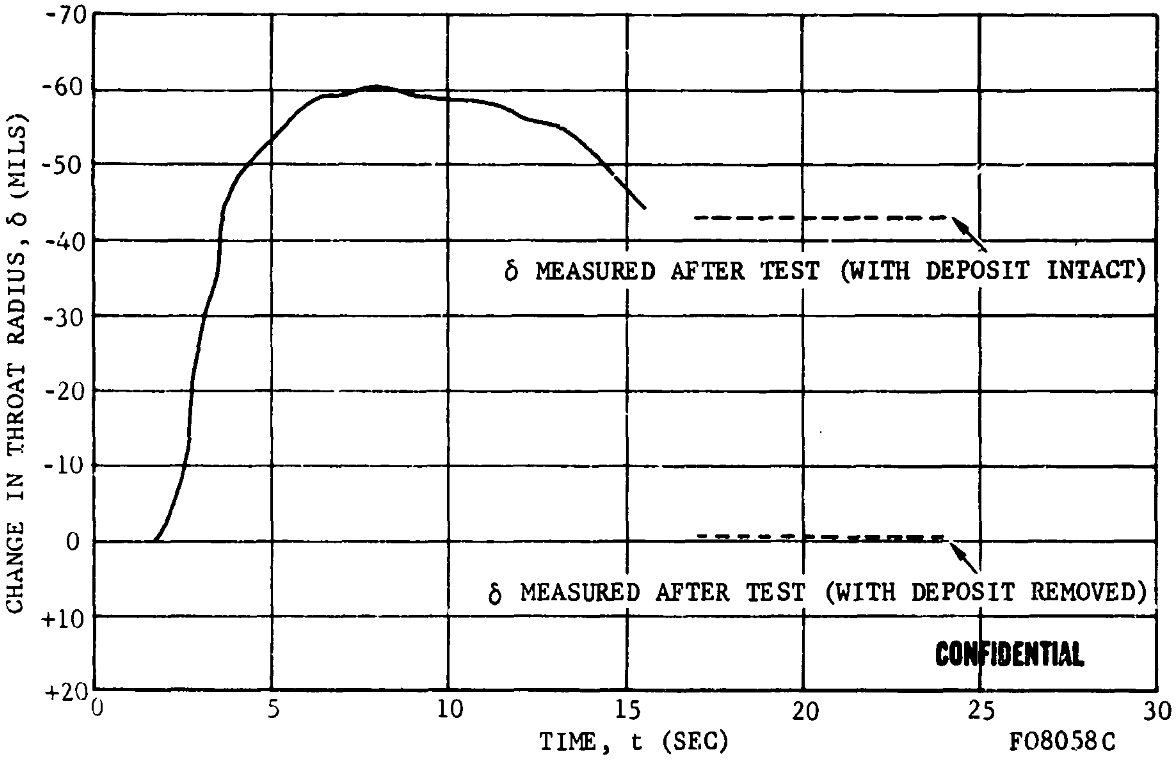

FIGURE 167. CHANGE IN NOZZLE THROAT RADIUS VERSUS FIRING TIME TEST T-21

(1) δ MEASURED AFTER TEST (DEPOSIT INTACT)
(2) δ MEASURED AFTER TEST (DEPOSIT REMOVED)

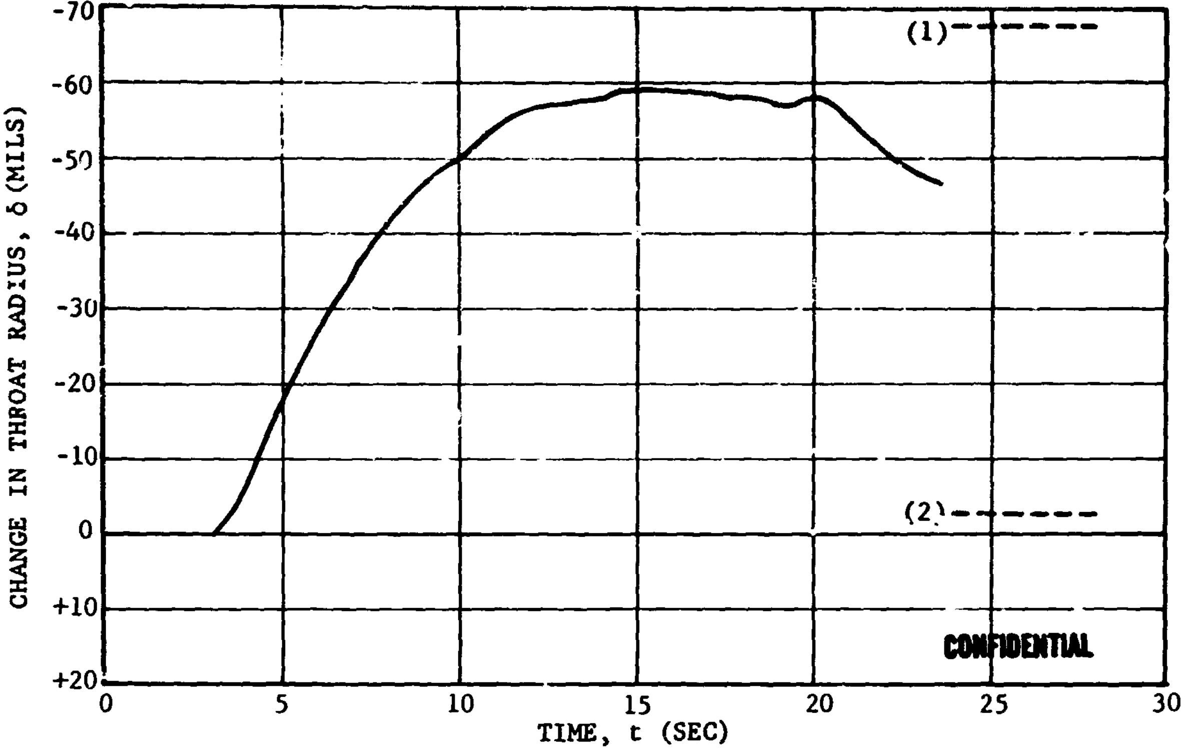

FIGURE 168. CHANGE IN NOZZLE THROAT RADIUS VERSUS FIRING TIME TEST T-22

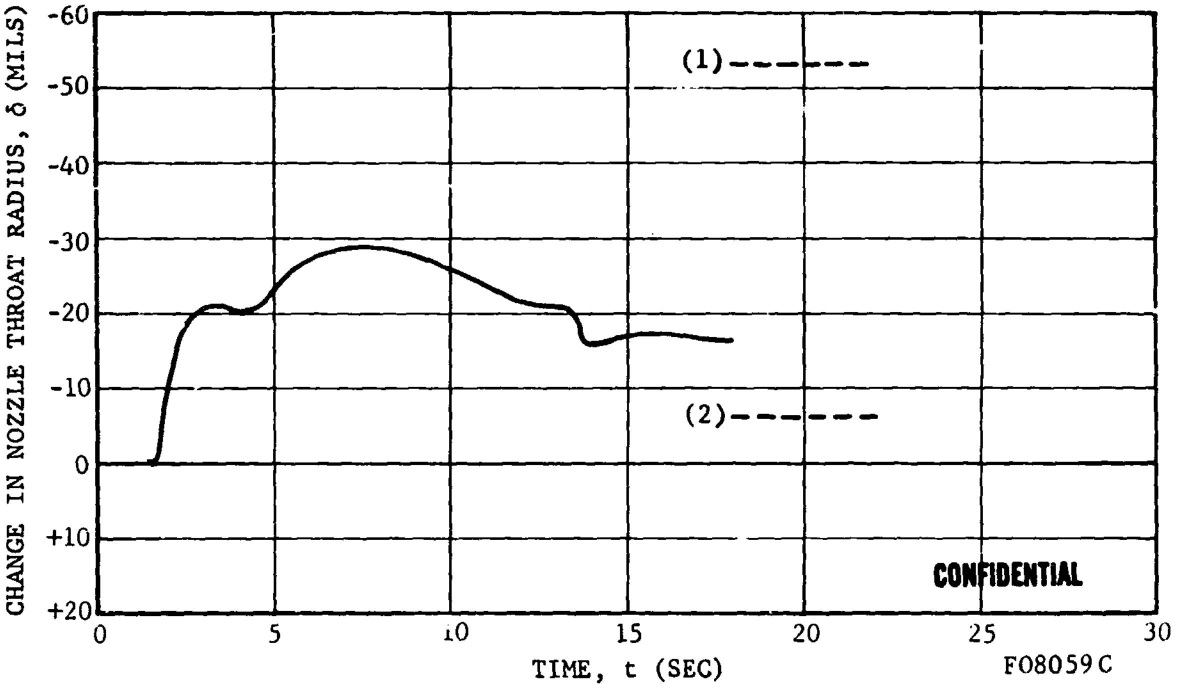

FIGURE 169. CHANGE IN NOZZLE THROAT RADIUS VERSUS FIRING TIME TEST T-23

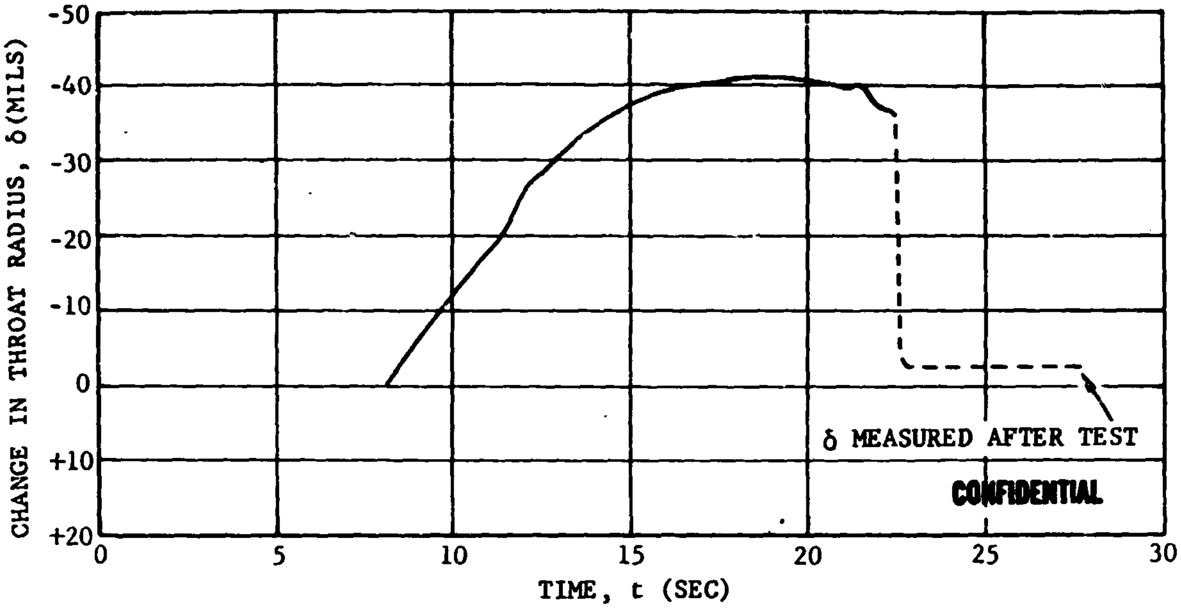

FIGURE 170. CHANGE IN NOZZLE THROAT RADIUS VERSUS FIRING TIME TEST T-24

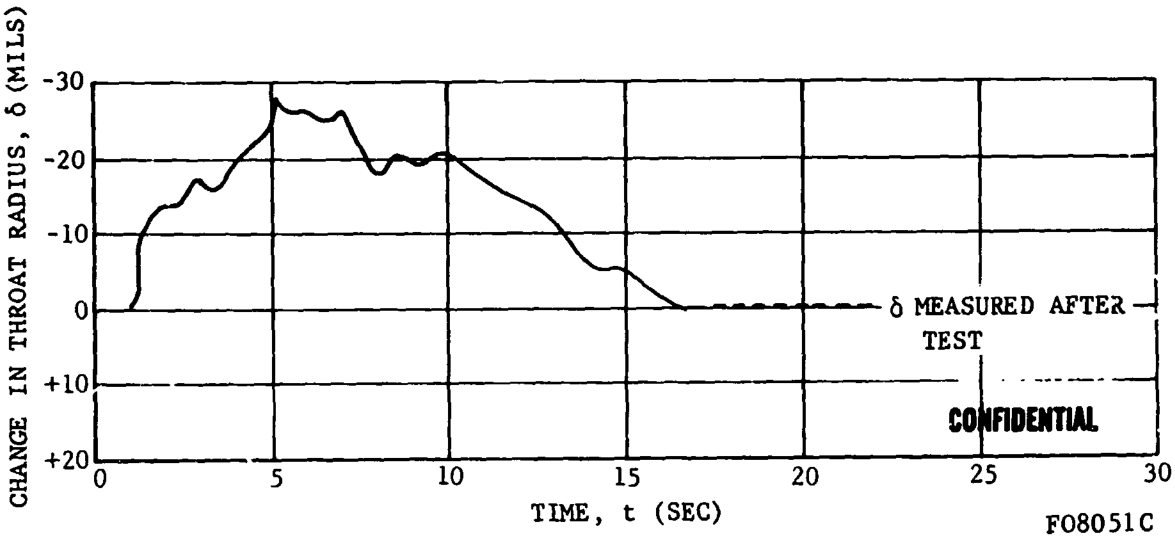

FIGURE 171. CHANGE IN NOZZLE THROAT RADIUS VERSUS FIRING TIME TEST T-25

of the K_n method to evaluate nozzle throat radius as a function of time for these tests. Consequently, the F/P method, discussed in Section V, Reference 2, was utilized for this evaluation. Observations point to an erosive burning situation as the paramount cause of the burning surface variation. This is discussed more fully in Section 2.4 of this Report. Test T-13 was further complicated by a burn-through of the nozzle housing during the final seconds of firing. This burn-through was the result of a gas leak through one of the nozzle holder-aft closure flange bolt holes. This situation was partially a result of a poor RTV-60 seal at the nozzle to aft closure insulation mating surfaces. Subsequent tests with steep inlet and submerged nozzles incorporated positive O-ring and RTV-60 seals at the nozzle-aft closure insulation interface.

Test T-20 was abnormal in that no pressure-time data was generated. During the assembly of this nozzle, the chamber pressure ports were inadvertently plugged with sealing compound. A pressure-time curve was generated from the thrust time curve in the manner discussed in Section IV.

An ignition delay occurred during Test T-24, similar to the one that occurred in Test T-6. There is reason to believe that this delay was caused by either use of an inadequate igniter or poor positioning of the igniter charge. Although the ignition delay adversely affected propellant performance characteristics, it did not hinder calculations of throat radius change versus time. These calculations were made utilizing the K_n technique since the delayed ignition apparently did not result in a major distortion of the grain burning surface.

In the as-received condition, little could be determined about the nature of the deposition and erosion by visual inspection. In returning the hardware from RPL, some of the deposits may have been disturbed or removed. Photographs of the hardware are included in Section III. Throat diameter measurements were obtained prior to removing the throat deposits. These have been converted to the post-test deposit thicknesses given in Table XXXVIII. The accuracy of such measurements cannot be claimed to be high and only averages of approximately six measurements are given. After removal of the deposits, six or more throat diameter measurements were made and averaged. It should be noted that throat grooving occurred in Tests T-10, T-12, T-13 and T-15 (see Section 3.4). It should also be noted that the deposit histories are circumferentially averaged.

5.3 (U) DEVELOPMENT MOTOR TESTS

a. (U) Development Motor Design

(1) (U) Propellant Grain Design

The preliminary internal burning grain design, described in Section 5.3 of Reference 2, was chosen to be used in the 500 pound grain tests, T-51 through

T-54. Figure 172 is a dimensionalized sketch of the grain configuration selected for the four development motor tests. Tests T-51, T-53 and T-54 will utilize Arcocel 191F propellant formulation and T-52 will use the Arcocel 319BRF propellant formulation.

(2) (U) Motor Case Design

Two new motor cases, of the same design as the ADOBE chambers utilized in the small motor tests, were fabricated at AFRPL for the development tests. The partial burn-through of the original ADOBE chambers (see Section 5.2a, Reference 2) preclude their use for the development motor tests which employ longer propellant grains. The various wood filler blocks and bearing plates were eliminated or modified for use in the new cases. The forward block was shortened by approximately 8 inches. The single wood block was inserted into the chamber and butted against the head closure. An asbestos phenolic insulator/seal disk, such as that used for the small motor tests, was then fitted behind the wood filler block. Thin aluminum disks are placed between the wood block and asbestos disk to accommodate the variations in the length of the propellant grain. Each 500 pound grain, in an asbestos phenolic liner, could then be inserted in the new chamber so that the grain was compressed between the insulator disk (at the forward end) and the aft closure insulation (at the aft end). The first grain was oversized on the diameter, due to moisture absorption by the asbestos phenolic grain liner, and did not fit the new chamber. The motor case was then bored out slightly to accommodate the propellant grain.

Figure 173 illustrates the motor case design utilized for the development motor tests. A comparison of Figure 173 with Figure 108, Reference 2, shows how the transformation in chamber configuration from small motor test to development motor tests was effected.

(3) (U) Nozzle Design

The nozzle designs for all development motor tests were completed during this reporting period. Tests T-51 and T-52 will utilize nozzles of identical configuration. Figure 174 illustrates this nozzle design. The throat section consists of a stack of six, c-axis oriented, pyrolytic graphite washers (one half inch thick) in a support ring of ATJ graphite. The entrance and exit sections are ATJ graphite. All flamefront material is backed with an insulator of tape wrapped asbestos phenolic. The asbestos phenolic nozzle insulator also serves as a flamefront material in the transition from the asbestos phenolic aft closure insulation to the ATJ graphite nose cap-entrance part of the nozzle. A small section of the insulator also provides a flamefront at the extreme exit of the nozzle. As in the case of the small motor tests, an RTV-102 filled gap forward of the pyrolytic graphite throat stack is provided to accommodate the thermal expansion of the pyrolytic graphite. The nozzle itself is submerged to a distance of 3.5 inches from the aft end of the grain. RTV-60, coupled

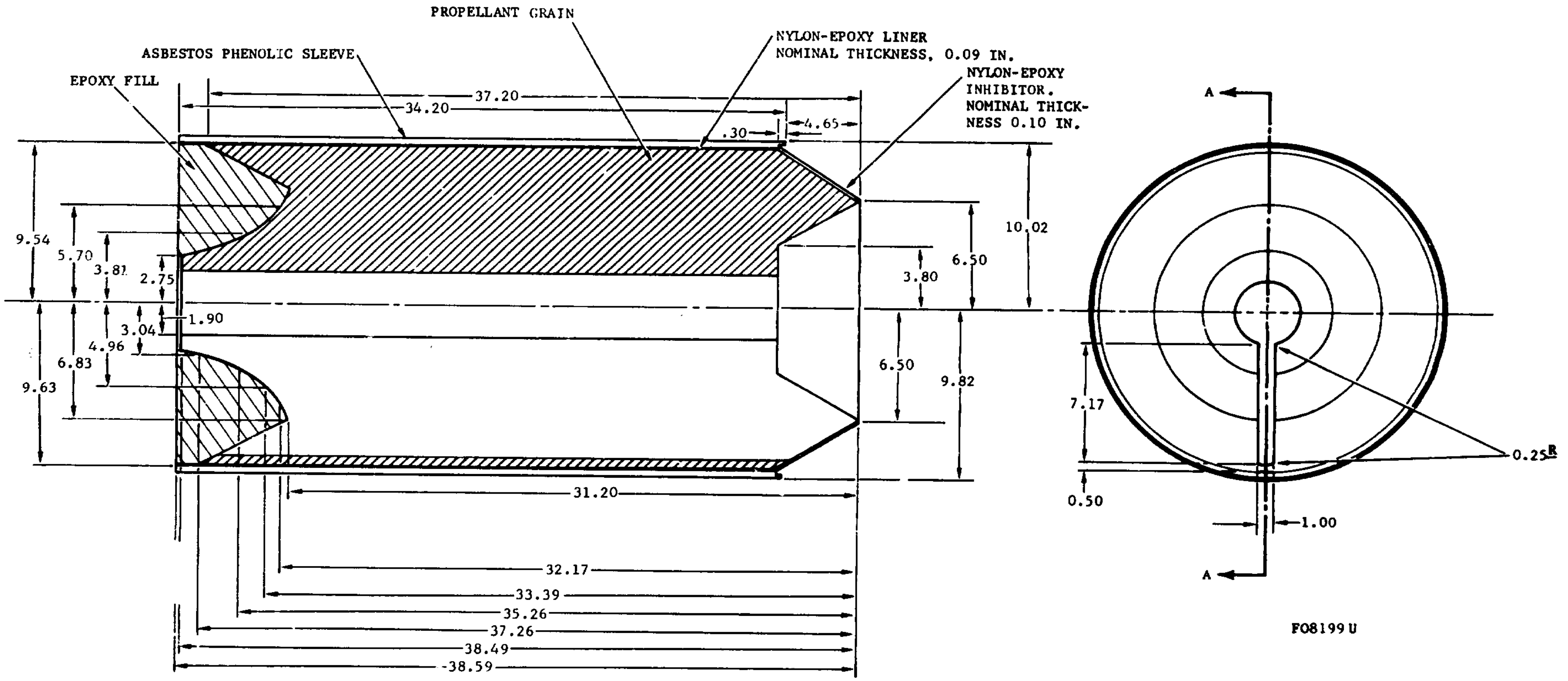
PROPELLANT GRAIN
ASBESTOS PHENOLIC SLEEVE
EPOXY FILL
NYLON-EPOXY LINER
NOMINAL THICKNESS, 0.09 IN.
NYLON-EPOXY
INHIBITOR.
NOMINAL THICK-
NESS 0.10 IN.
37.20
34.20
.30
4.65
9.54
5.70
3.81
2.75
1.90
3.04
4.96
6.83
9.63
10.02
6.50
3.80
6.50
9.82
31.20
32.17
33.39
35.26
37.26
38.49
38.59
A
A
7.17
0.50
1.00
0.25R
F08199U

FIGURE 172. 500 POUND INTERNAL BURNING GRAIN

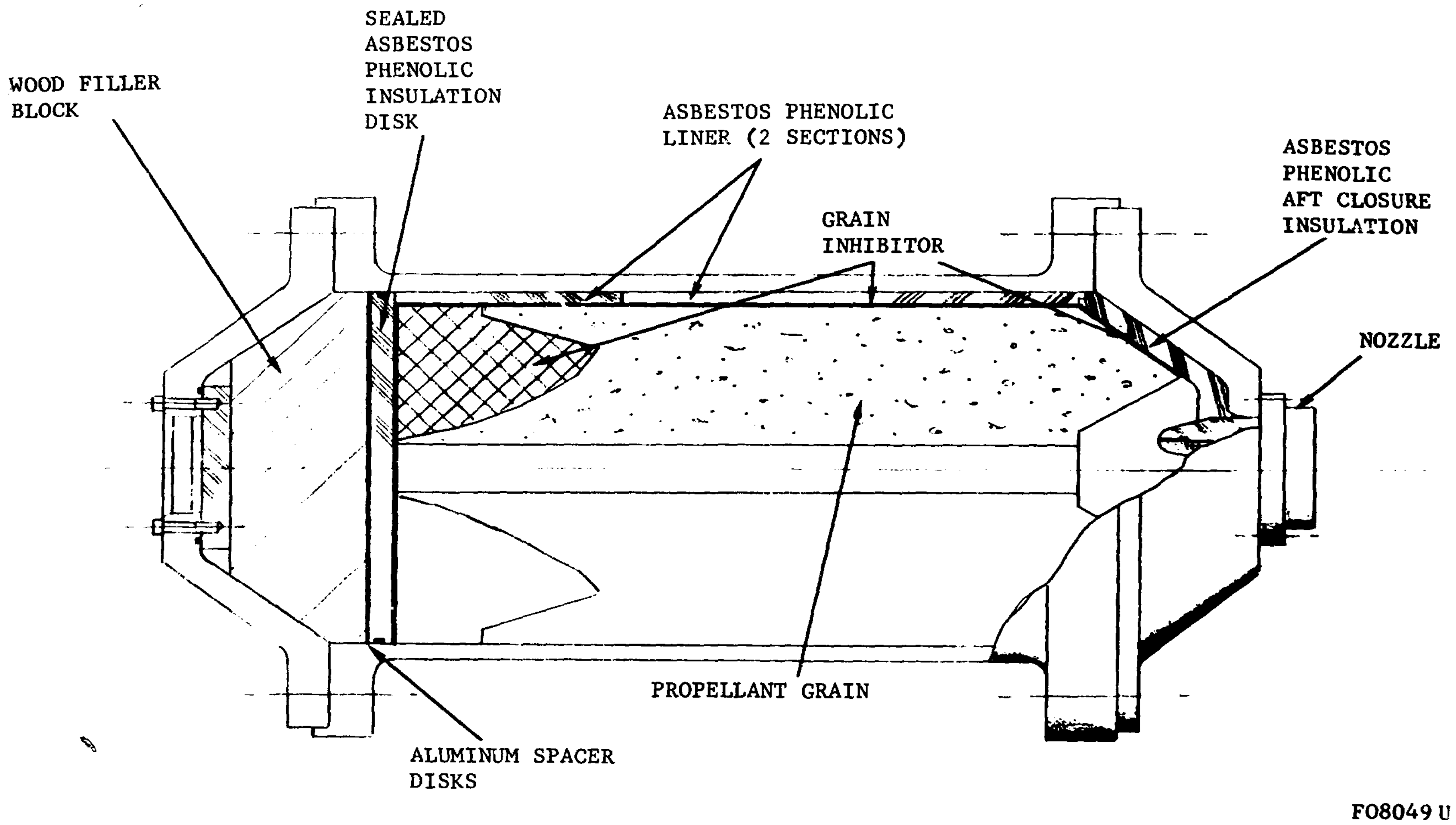
WOOD FILLER BLOCK
SEALED ASBESTOS PHENOLIC INSULATION DISK
ASBESTOS PHENOLIC LINER (2 SECTIONS)
GRAIN INHIBITOR
ASBESTOS PHENOLIC AFT CLOSURE INSULATION
NOZZLE
PROPELLANT GRAIN
ALUMINUM SPACER DISKS
F08049 U

FIGURE 173. MOTOR CASE DESIGN - DEVELOPMENT TESTS

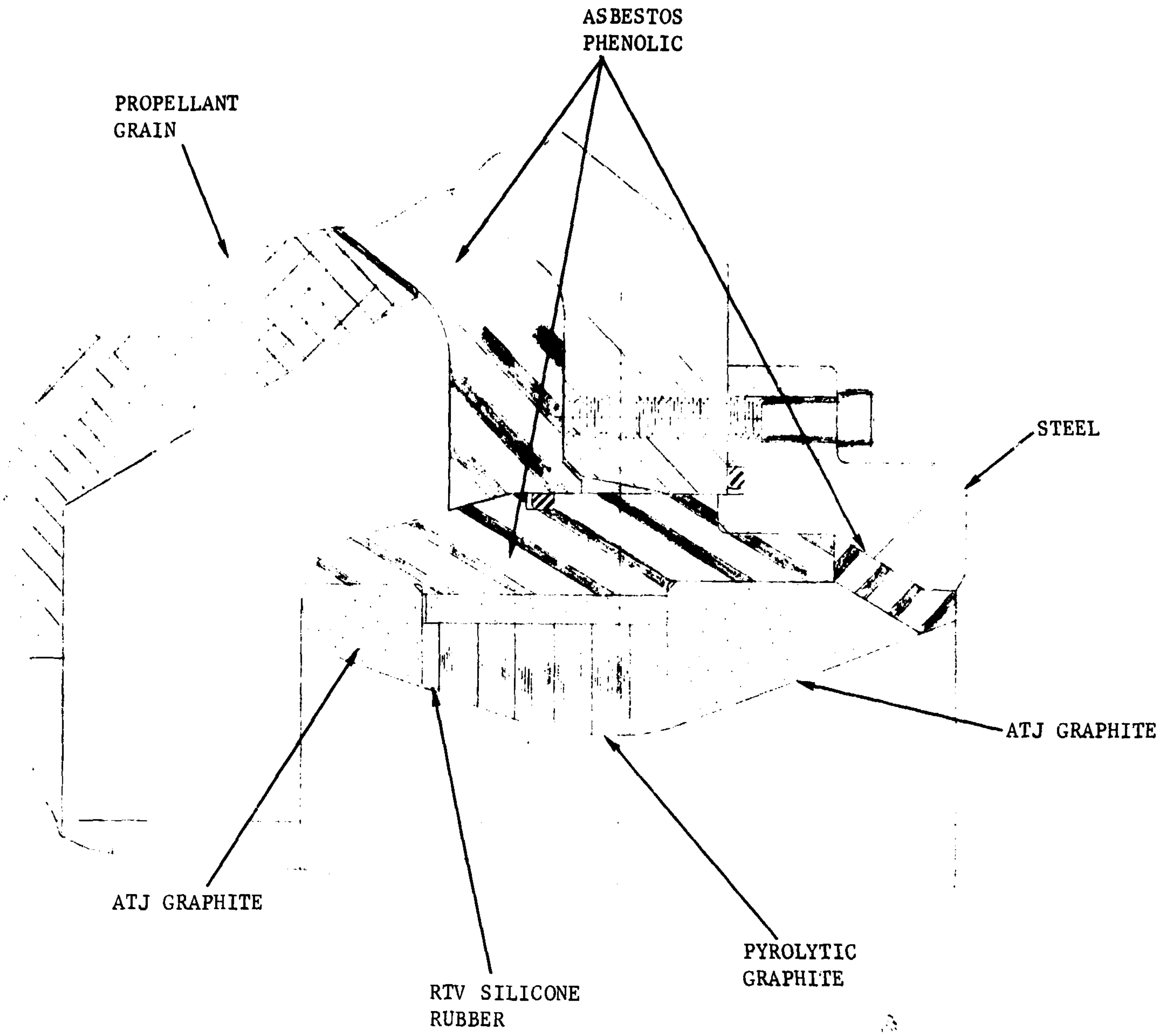
ASBESTOS PHENOLIC
PROPELLANT GRAIN
STEEL
ATJ GRAPHITE
ATJ GRAPHITE
PYROLYTIC GRAPHITE
RTV SILICONE RUBBER

F08050U

FIGURE 174. NOZZLE DESIGN FOR TESTS T-51 AND T-52

with two O-rings provide the seals between the nozzle, aft closure, aft closure insulation and nozzle holder.

The nozzle designed for T-53 is shown in Figure 175. The design is basically the same as the one for T-51 and T-52 shown in Figure 174. The major difference is that the degree of submergence for this nozzle has been increased to translate the nozzle throat and nose cap toward the propellant grain. This "deep submerged" nozzle is positioned 1.5 inches from the aft end of the grain.

Figure 176 illustrates the nozzle design for T-54. This nozzle is essentially the same as T-51 and T-52 except for the throat heat sink section. In the nozzle design for T-54, the pyrolytic graphite throat stack has been replaced by an arc cast, rolled and extruded tungsten throat insert. This conical insert is press fitted into a mating ATJ graphite backup structure. A single pyrolytic graphite washer is fitted just upstream of the tungsten to provide a more erosion resistant material than the ATJ graphite forward of the tungsten. This tends to eliminate the possibility of undercutting the throat insert. A second conical section of the same type tungsten as the throat material has been placed aft of the throat to prevent possible obtrusion of the main insert. During assembly, this second ring was fractured into four segments. Since this would not directly interfere with the intended function of the ring, it was not replaced. In all other respects, the design for T-54 is identical to that of T-51 and T-52.

b. (U) Test Results

Although the first development motor, T-51, was successfully fired during this reporting period, the test results have not been analyzed in detail. The development motor test results will be presented in the Final Report.

5.4 (C) CONCLUSIONS, RECOMMENDATIONS AND FUTURE WORK

a. (C) Conclusions

In general, the performance of the hardware in the reported tests was excellent and the original test objectives were achieved in the majority of the tests. Once again, it is concluded that graphite, tungsten and reenforced plastics can be successfully employed with beryllium propellants. The specific performance of these materials in any given application is clearly dependent on the propellant, grain and nozzle thermal protection design. Apparently, the nozzle design technology developed for aluminum propellant systems must be sensitized to combustion flow field, incomplete metal combustion and oxide deposition effects to achieve acceptable nozzle performance with beryllium propellants. Alternatively, propellant selections and grain designs could be limited to achieve complete combustion and uniform flow fields.

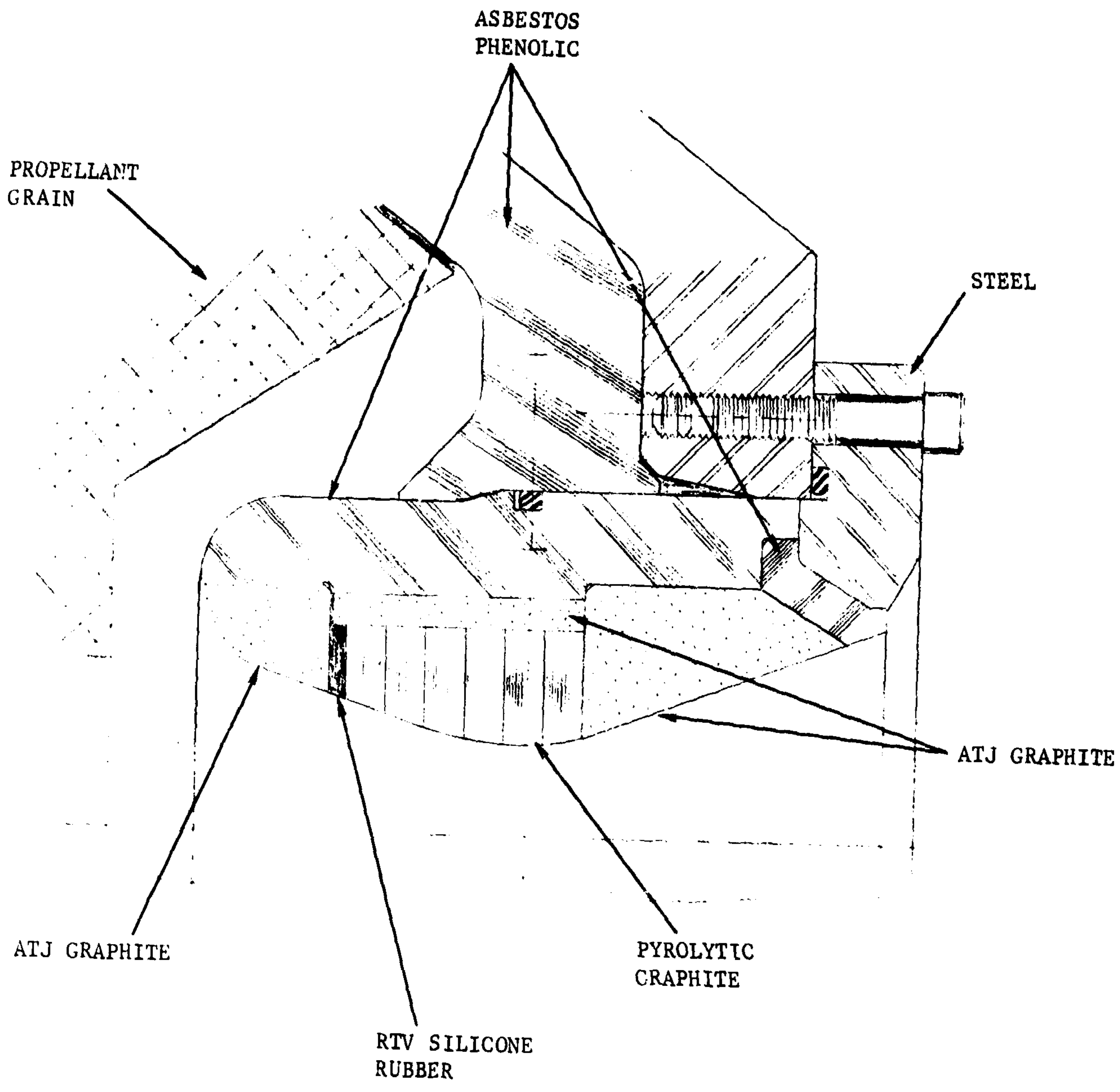
ASBESTOS PHENOLIC
PROPELLANT GRAIN
STEEL
ATJ GRAPHITE
ATJ GRAPHITE
PYROLYTIC CRAPHITE
RTV SILICONE RUBBER

F08200U

FIGURE 175. NOZZLE DESIGN FOR TEST T-53

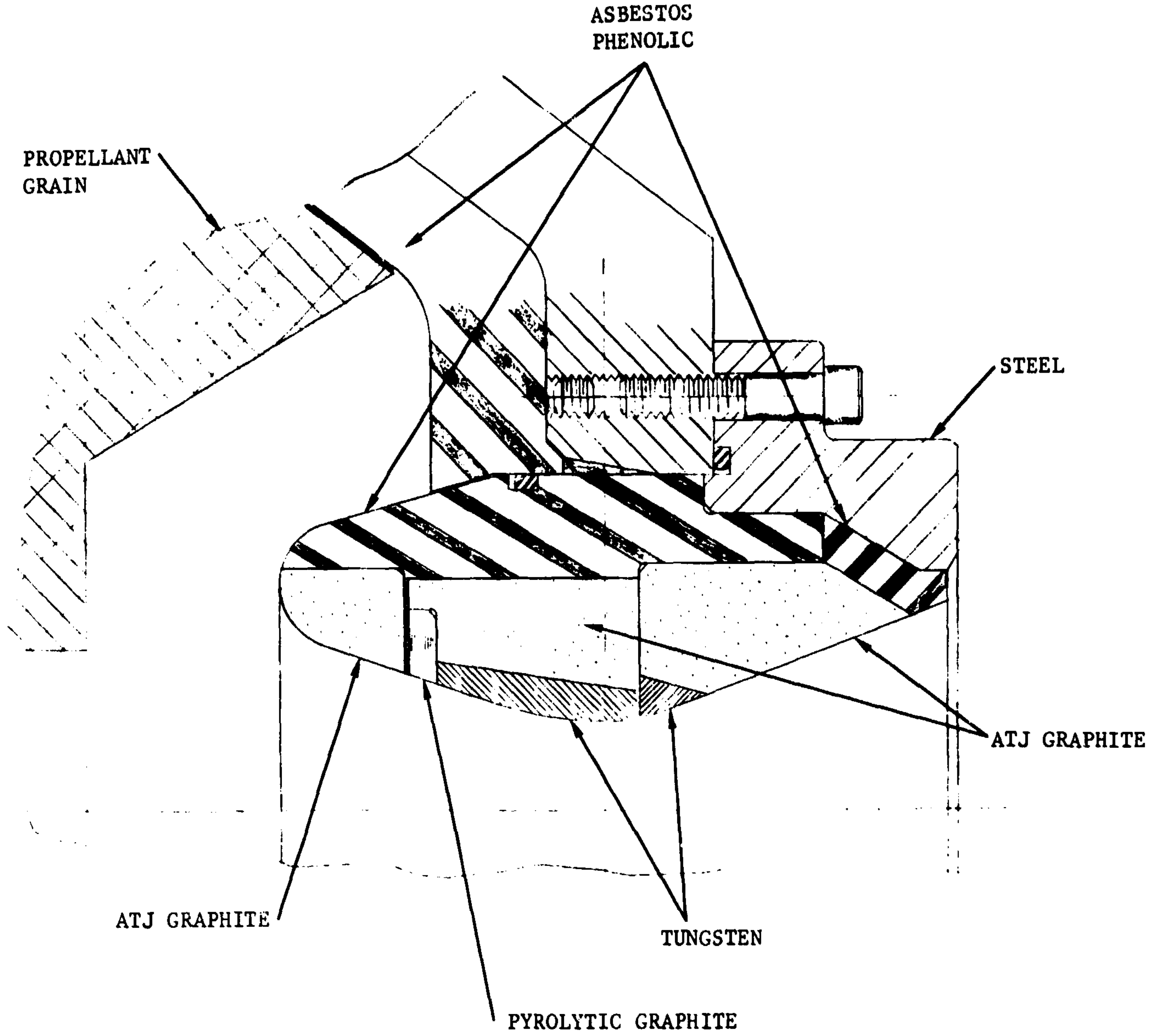
ASBESTOS PHENOLIC
PROPELLANT GRAIN
STEEL
ATJ GRAPHITE
ATJ GRAPHITE
TUNGSTEN
PYROLYTIC GRAPHITE

F08201U

FIGURE 176. NOZZLE DESIGN FOR TEST T-54

The small motor test objectives were partially compromised in a number of individual cases. It has been concluded that, in each instance, the problem could have been avoided. Thus, the leak which developed during Test T-13 could have been avoided by (1) using redundant O-ring seals, (2) eliminating the tight fit between the asbestos aft closure and nozzle insulation sections to permit a better RTV-60 seal, or (3) repotting the set screws in the aft closure-nozzle flange bolt holes. The partial burn-through of the chambers on Tests T-1 and T-2 could have been (and subsequently were) avoided by providing a positive seal at the chamber wall between the two sections of the motor. The loss of pressure data on Test T-20 could have been avoided by relocating the pressure ports in the aft closure insulator to preclude filling during bonding of the grain to the insulator. The problems associated with the thermocouple instrumentation were discussed previously in Section IV. The extreme, non-neutral behavior of the Type II grains, Tests T-8, T-10, T-12 and T-13, appears to be a fluid mechanics induced phenomenon (see Section 2.4). This could probably have been avoided simply by changing the ratio of the slot to core burning surface areas. Of course, the slotted grain tests have provided a great deal of useful information concerning the effects of flow non-uniformities of nozzle erosion. It has also been concluded that the two hang-fires, although associated with the RDX double base propellants, could have been avoided by improving the igniter placement or design.

It has been concluded that the use of the springloaded bayonette or custom-built thermocouples has not had any significant influence on motor or materials performance. In many cases, the bayonette thermocouples fell out or developed significant leaks without affecting nozzle performance. It is reasonably clear that improved installation procedures would prevent such leaks.

The propellant ballistic performance data obtained for the small motor tests is currently viewed with some suspicion. Motion pictures of the firings clearly indicate that large amounts of slag deposits are expelled in a non-symmetrical fashion from the nozzle exit cone surface. Preferential buildup of deposits at the bottom of the exit cone surface (gravity effect on deposit flow) also causes considerable fluctuation of the plume. Consequently, a uniaxial thrust measurement could be unusually low. The measurement of side thrusts in vertical (up and down) and horizontal firings would clarify the issue. Discrepancies between the two sets of pressure data obtained on most firings suggests another source of error in the performance analysis.

Since no exception has been observed to the hypothesis that the oxide deposits are thermally and chemically protective, it is concluded that the oxide deposition phenomenon should be exploited further. It would appear that thicker heat sinks or internally cooled nozzles could be designed to prevent or minimize nozzle erosion. It should be recalled that the nozzles tested were designed to reach surface temperatures above 5000°F during the nominal 20 second firing duration. Clearly, more firing data is required to determine the maximum firing times obtainable for deposit protected heat sinks. Such times are expected to depend on grain design, aft closure insulation materials, etc. Transpiration and film cooled nozzle design concepts are presently viewed as being impractical for use with beryllium propellant systems.

b. (U) Recommendations

A preliminary recommendation is made to repeat some of the small motor tests. This recommendation is based only on the consideration of the quality or normalcy of the particular test. In each case, the original test objective was partially compromised. The question of whether the repetition of these tests is essential to the achievement of the basic program objectives is discussed in Section 7.1.

Test T-8: No heat sink thermal response data was obtained as a result of improper selection of thermocouples. The calculated throat deposit history is extreme and cannot be corroborated through thermal analysis.

Test T-13: No useful thermal data obtained as a result of partial burn-through of the aft closure and thermocouple leads. Throat deposit history cannot be corroborated.

Tests T-6 and T-24: Hang-fires occurred on these end burning grain tests. The throat deposition and heat transfer results could be unduly biased. (No thermal data was obtained for Test T-24).

Test T-20: No pressure data was recorded as a result of sealing of the pressure ports during motor assembly. Throat corrosion and deposition cannot be interpreted.

Tests T-8, T-10, T-12 and T-13: These tests used the Type II slotted grain design. Abnormal grain burning produced unique results. Alteration of the grain design would be more informative than repeating any of these tests.

It is clear that nozzle deposits play a very important role in determining materials behavior with beryllium propellants. It is recommended that throat deposit histories be routinely calculated and the effects of deposition be included in determining propellant ballistic performance. Aluminum propellants should [illegible] be automatically exempted from sim[illegible] consideration.

c. (U) Future Work

All design and fabrication portions of the motor testing phases have been completed. During the final reporting period, the following tasks will be completed:

(1) It is planned to conduct the remaining development motor tests by 30 October 1966.

(2) All development motor test data and motor hardware will be returned to Aeronutronic for post-test analysis.

(3) Ballistic performance and throat deposition analyses will be conducted for the four development motor tests.

SECTION VI (U)

INDUSTRIAL HYGIENE AND SAFETY

In support of the program tasks which involve the handling of, or other exposure to, toxic beryllium compounds, a rigid Industrial Hygiene and Safety Program has been instituted to assure maximum protection of personnel. The program was formulated to Air Force specifications and has been approved by the cognizant Air Force Rocket Propulsion Laboratory Safety Officer. The scope and structure of the Industrial Hygiene and Safety Program was described in detail in Section VI of Reference 1. Cumulative beryllium sampling program results, for the preceding reporting periods, may be found in Tables XX and XVIII of References 1 and 2, respectively. Cumulative sampling results through 1 October 1966 are presented in this section.

During the reporting period, laboratory post test analyses have been performed on motor-nozzle hardware from small motor tests T-8 through T-25. The hardware was packaged by RPL personnel for transfer to Aeronutronic without being cleaned or otherwise decontaminated. Consequently, large amounts of metal oxide slags are associated with each set of hardware. Approximately 100 samples of chamber slag and nozzle deposits were taken for chemical analysis. The nozzles and aft-closure insulation components were sectioned, using the totally enclosed saw located in Control Area #1. During these operations, 25 hours of ambient air sampling, 6 random wipe samples and 6 hours of out-plant sampling were accomplished.

All work has been confined to one laboratory control area and has been conducted in strict accordance with the Industrial Hygiene Program Plan. Evaluation of sampling equipment and quantitative results is continuing in the attempt to determine statistically acceptable [illegible]ations, effectiveness and efficiency. Post program medical examinations have been or are being completed for those personnel having been reassigned to other [illegible]. These examinations have verified the soundness of the environmental health and safety control measures. [illegible] examination results automatically become a permanent part of the employe records maintained by Aeronutronic. No incidents have occurred to date on the program. The confinement of the work to a small area and the stability of the roster of employes have been significant factors in the success of the safety program.

Four additional sets of hardware will be subjected to post test laboratory analysis during the final phase of the contract. Approximately 15 nozzles, from the Aerojet ADOBE Program, have been received. While these nozzles have apparently been decontaminated, they will be treated with the same care as contaminated hardware during any inspection and sectioning operations. With the completion of these tasks, post program cleaning and decontamination will be accomplished in accordance with the Industrial Hygiene Program Plan.

Cumulative results of the Aeronutronic sampling program are presented in Table XXXIX.

TABLE XXXIX. CUMULATIVE BERYLLIUM SAMPLING PROGRAM RESULTS
(To 1 October 1966)

Number Samples Taken	Type and Location	Hours Sampled	Avg. mcg/m^3 Concentration	Max. mcg/m^3 Concentration
18	Personnel - MM Controlled Area #1	[illegible].0	less than 0.096	0.5
*8	Personnel - MSA Controlled Area #1	12.2	less than 0.290	0.71
3	Personnel - MSA & MM Controlled Area #2	4.5	0.34	0.38
9	High Volume Out-Plant Stations	19.3	less than 0.0009	0.003
22	High Volume Controlled Area #1	61.8	0.280	3.4
9	High Volume Controlled Area #2	6.0	0.059	0.24
26	Wipe Samples	N/A	4.98	32.0
2	Sewerage Effluent	N/A	less than 0.001 mg/l	0.001 mg/l

*Data from one analysis not included.

As a major beryllium propellant producer, Atlantic Research Corporation routinely follows Government approved industrial hygiene procedures. The subcontractor has reported that the results of their industrial hygiene sampling program have shown no toxic beryllium concentrations above the allowable limits. In addition, no accidents have been reported during the third reporting period.

SECTION VII (C)

PROGRAM INTEGRATION AND DEMONSTRATION

7.1 (C) PROGRAM INTEGRATION

Within the past decade, beryllium propellants have been under development as analogs of, and potential substitutes for, aluminum propellants. The primary advantage of such a substitution is a gain of approximately 8 percent in the ideal specific impulse. The overall advantage of such a propellant ballistic performance improvement in upper stage and space systems applications should be obvious. In practice, the general substitution of beryllium for aluminum has not been accomplished for three major reasons. These are: (1) low delivered performance in development tests, (2) extreme and erratic nozzle materials erosion compared to aluminum propellants, and (3) toxic beryllium compounds hazards. It might be anticipated that failure to satisfactorily resolve any one of these problems could provide sufficient grounds for abandoning beryllium propellants.

Current investigations of the toxicity problem have been somewhat encouraging. Beryllia formed in the rocket exhaust is apparently significantly less toxic than material formed at low temperatures. This is presumably a consequence of differences in surface activation energies, soluble impurity levels, and crystal habit. The greater problem may involve the hazard associated with the abnormal explosion or burning of the propellant in handling or prior to launch. This problem can probably be resolved in time. The questions concerning atmospheric polution and extraterrestial contamination are apparently of less concern compared to the other issues.

The results of the present program suggest that the observed ballistic performance problems may at least partially be due to inefficient metal combustion and the behavior of the condensed phases in the exhaust. if extensive metal agglomeration occurs at the grain surface and/ metal particle combustion is too slow, condensed phase stratification metal deposition on the motor contour may occur. The degree of condensed phase stratification and deposition will depend on the magnitude of the slip that the metal and oxide particles experience (relative to the gas streamlines). The major performance losses would derive from (1) retention of condensed material within the motor, (2) low velocity expulsion of deposits from the nozzle surface, (3) expulsion of unburned metal along with the nozzle surface deposits, (4) incomplete combustion of metal in the fuel rich portions of a stratified flow, (5) changes in expansion area ratio as a result of nozzle throat deposition, and (6) flow separation and shock losses as a result of irregular deposition on the nozzle expansion cone surface. It is speculated that maximum ballistic performance will be delivered when the propellant, grain design, and motor-nozzle contour ensure the following:

(1) No agglomeration of metal particles occurs at the grain surface. Then, there will be a maximum number of burning particles. The size of the particles will be at a minimum and will be completely determined by the size distribution of the original metal additive. Stratification effects will be minimized.

(2) The ideal flame temperature without any metal combustion should be sufficiently close to or above the metal oxide melting point. This should minimize interference by the oxide in the particle ignition and combustion processes.

(3) The propellant oxidation ratio should be high enough to prevent the formation of significant nonequilibrium quantities of gaseous or condensed species such as $BeCl_2$ or Be_3N_2. The largest metal particles should be the last to burn. During the final stages of their combustion, the local availability of oxygen, HCl and N_2 should dictate which reactions will actually take place in the vapor phase combustion mode. Presumeably, it could take a very long time to eliminate excess quantities of the metal chloride and similar species because of the diffusive mixing requirement and gas-gas reaction kinetics restrictions. Failure to achieve maximum conversion to the metal oxide constitutes an enthalpy loss.

(4) Minimum oxide deposition should be permitted along the motor-nozzle contour. This could be accomplished with grain and motor-nozzle contour designs [illegible] produce circumferentially uniform flow and which

cause the condensed phase particle slip to be directed away from the motor nozzle wall.

(5) The flight time of the slowest burning metal particles must be great enough to complete its combustion before the gas streamline directions change near the contour or motor centerline. That is, it is presumed that the smallest particles and minimum particle slip occur when there is no condensed metal left. It is also presumed that a finite time is required to complete the combustion of any particle. Then, the particle flight time must be great enough to prevent burning particle deposition on the contour and/or stratification of burning particles. The satisfaction of this condition would place constraints on the motor pressure, propellant mass fraction, grain design and/or motor-nozzle contour.

(6) Minimum nozzle throat erosion should be permitted. Changes in nozzle expansion ratio and motor pressure are generally not desireable from the point of view of both ballistic performance and metal combustion/oxide deposition.

The primary objective of this program has been to resolve the extreme nozzle erosion problem with beryllium propellants. It is worth noting that the program procurement cycle started about three years ago. Evidently, the procurement was stimulated by the nozzle problems which occurred some 2 to 5 years ago. Since that time, the number of dramatic nozzle failures has steadily diminished. Including the present program, it appears that the number of cases in which either no nozzle erosion or very high erosion was experienced has increased. Obviously, development testing of more advanced beryllium propellants and motor designs are biasing these observations. It is concluded, then, that the more recent firing experience neither violates the original premise that a problem exists nor contradicts the program results and conclusions to date. However, it is reasonable to assume that, given the desired understanding of the older problem of erosion-corrosion of nozzle materials with beryllium propellants, it would be required to predict the current and future problems with advanced beryllium and possibly other metalized propellants.

The immediate problem, then, is to condense or translate the program results into a practical qualitative and quantitative philosophy for anticipating and/or resolving nozzle materials performance problems with beryllium propellants. Basically it has been concluded that low metal combustion efficiency and underestimation of the convective heat transfer have been the primary causes of unusually poor performance of graphite, tungsten and plastic insulation materials. Beryllia deposit protection, with or without high metal combustion efficiency, is the primary cause of unusually good performance of these materials. In comparable situations, aluminum propellants will exhibit very high metal combustion efficiencies except when agglomeration of the metal at the grain surface occurs to the extent that the degree of aluminum combustion is less than the degree of unagglomerated beryllium particle combustion at appropriate points in the exhaust flow. Underestimation of the convective heat transfer in aluminum systems has complicated the interpretation of both cooled and uncooled nozzle test results and, in some cases, has been a primary cause of failure. Unusually good performance of nozzle materials with aluminum propellants can also be attributed to metal oxide deposition protection.

It has generally been concluded that motor ballistic performance and nozzle materials performance have been and will continue to be closely related. Clearly, low ballistic performance is not desireable, irrespective of whether the nozzle materials also perform poorly or not. At the other extreme, a motor design which satisfies the conditions listed above for achieving maximum ballistic performance may not be acceptable from an overall systems performance point of view (e.g., cooled nozzles would probably be required for small throat diameter, long duration firings). Evidently, then, the problems of the future will fall into the gray area between the extremes where: (1) minor combustion efficienc [illegible] can be tolerated, (2) oxide deposition losses become less signi [illegible] motor size increases and (3) some grain surface agglomeration ca [illegible] rmitted. Under these circumstances, th [illegible] rain design, motor-nozzle [illegible], propellant mass fraction and nozzle materials performance must be optimized.

Without resorting to oxide deposition protection, the nozzle materials performance could hardly be expected to be better than in the case where ballistic performance has been maximized. Because the degree of metal combustion would be higher, the direct substitution of an aluminum propellant would improve the nozzle performance slightly. However, if maximum advantage is taken of the beryllia deposition, protection (thermal and corrosion), then the materials performance can be improved to any degree desired. Thus for short duration tests, the simple uncooled graphite and tungsten nozzles should be adequate without the benefits of oxide deposition protection, provided nozzle surface temperatures do not exceed about 5200 and 5500°F, respectively. Obviously, the low flame temperature propellants (Be composites and BeH$_2$ propellants) would have an advantage in terms of operating time. Apparently, these maximum operating times could be extended significantly if either nozzle cooling or oxide deposit protection are exploited. Long duration firings with high flame temperature propellants should pose the same nozzle performance problems as have been experienced with comparable aluminum propellants. Cooled nozzles, successfully developed for use with aluminum systems, could be used, either with or without oxide deposition protection. The combination of deposition protection and nozzle cooling offers the real possibility of unlimited firing duration without nozzle erosion. In contrast, it is not obvious that deposition can be tolerated in plug nozzles, unless the deposit thickness transients in the annular throat region can be accommodated. The plug nozzle also offers the greatest challenge in preventing deposition.

The results of the present program suggest that the problem of poor metal combustion can be anticipated. Current trends in propellant combustion research indicate that the metal agglomeration characteristics of any particular propellant can be identified. When propellant agglomeration does not occur, the required particle flight time will depend only on the original metal size distribution, flame temperatures and oxygen content of the exhaust. It is currently speculated that the particle flight times will be negligible for high flame temperatures and original metal particle sizes less than about 30 microns. When agglomeration produces a significant number of particles in sizes above 1 or 2 mils, the chamber residence time will have to be increased accordingly to avoid the exposure of motor materials to oxygen rich gases. Basic combustion research and motor testing should be directed to determining the minimum exhaust oxygen content required, to sustain large particle combustion, as a function of pressure, temperature, and exhaust composition. If the exhaust oxygen content falls below the minimum, then the particle will either never burn or the metal chlorides, etc., will form. When sufficient oxygen is available, the required particle flight times can be estimated as a function of particle size either analytically (diffusion flame model) or from appropriate metal particle combustion laboratory experiments.

Once the designer has estimated the magnitude of the metal combustion efficiency problem, he can proceed to develop or modify the grain design and motor-nozzle contour. Calculation or estimation of the exhaust potential flow field will be required. Deposition and stratification of burning metal particles can be avoided by insuring that major streamline turns do not occur until the ciritical particle flight times have been attained. Further adjustment of the grain design and motor-nozzle contour can then be made to encourage or discourage oxide deposition. When deposition is not allowed to occur, the materials selection and thermal-structural design of the nozzle can be accomplished in the usual manner, provided that the convective heat transfer prediction pertains to the complete metal combustion case. The corrosion-erosion of graphite nozzle throat materials can be estimated using appropriate similarity analyses (oxygen and hydrogen reactions). The estimation of tungsten carbide formation and plastic deformation for tungsten inserts will probably have to be based on related testing experience. More work is recommended in this latter area. Once the nozzle throat area changes have been estimated, the ballistic performance implications should be calculated. Significant reduction of the chamber pressure or increase in the action time could be serious from the point of view of the metal combustion efficiency and motor integrity, respectively.

In the event that oxide deposition is to be allowed, the design problem will become more complicated. A proven technique for predicting the deposition and deposit flow is not available. Appropriate experience with similar motor and nozzle designs will provide some guidance. A number of detailed recommendations have been made in Section 2.6 regarding future work in this area. Development and qualification tests, appropriately instrumented, will provide the best source of detailed information on the behavior and effects of deposition.

No attempt will be made here to describe the recommended analytical techniques for predicting heat transfer, corrosion, etc. These analyses are still being developed and checked. A complete description of the recommended analytical design techniques will be included in the Final Report.

It has been recommended in Section 5.4 that several of the small motor tests be repeated. Considering the preceding discussion, it is highly questionable whether the results would justify the cost. On the other hand, there is ample justification for further examination of the metal combustion, oxide deposition, heat transfer, and corrosion phenomena. The introduction of new nozzle materials, insulation materials, grain designs and nozzle contours would be logical, providing only that the resulting motor firings produced data which extended the generality of the program results or challenged their validity. Since it has been argued that the propellant combustion mechanics tends to be a dominating factor in oxide deposition and materials corrosion, it would be most logical to work with propellants which are of current interest to the Air Force. Evidently, the final decision will depend primarily on the degree to which the Air Force believes that the program objectives have been met.

In summary then, unusual nozzle materials problems are a direct result of low metal combustion efficiency and oxide deposition. These phenomena will have a major influence on both ballistic performance and nozzle convective heat transfer. The value of improperly scaled and poorly designed motor test results is highly questionable. The usual motor insulation and nozzle materials can be used with beryllium propellants with the expectation that their performance will be essentially as good as, or better than, in comparable aluminum systems. However, this cannot be accomplished unless the beryllium metal combustion problem is minimized or major ballistic performance losses are acceptable. A qualitative approach to achieving maximum overall motor performance has been described. The specific results of the present program do not and cannot reduce the motor design problem completely to analytical form. Propellant combustion research, development motor testing and technical studies should be directed as much as possible to provide the motor designer with the required metal combustion, deposition data, heat transfer data, and analytical techniques. The designer should become more aware of the progress being made in the propellant combustion, two phase flow, convective heat transfer, and corrosion fields. This kind of interdisciplinary cooperation has frequently been lacking in the past and this, in turn, is partly the cause of the poor ballistic and nozzle performance record of beryllium propellants.

7.2 (C) PROGRAM DEMONSTRATION

The results of this program are to be demonstrated by means of a comparison between predicted and measured performance of a nozzle to be tested with a beryllium propellant under another contract. The motor test selected for this purpose is the Hercules Powder Company's X-259-C-2 to be conducted under Contract AF04(694)-762. It is expected that the performance analysis will be conducted in advance of the motor test. The results of the Program Demonstration Phase will be published separately with limited distribution. The analyses employed in this effort will be fully documented in the Final Report. The Air Force will perform the actual comparison of the predicted and measured results.

The motor test selected for the Program Demonstration Phase is one of two series of tests being performed by Hercules Powder Company and Aerojet General Corporation under the sponsorship of Ballistic Systems Division, Air Force Systems Command, Norton Air Force Base, San Bernardino, California. The X-259-C-2 motor originally featured a submerged nozzle with a pyrolytic graphite throat and Graphitite G-90 nose cap, entrance and exit sections. In addition, thermocouples were to be installed in the throat section of the nozzle, permitting a direct comparison of the predicted and measured thermal response. Subsequently, the nozzle design was changed by eliminating the pyrolytic graphite throat and replacing it with Graphitite G-90. The propellant will be the Hercules VID, which has a flame temperature in excess of 3900°K. The ideal performance of this propellant is approximately 5 seconds above the range studied in the program (280-285 sec). Consequently, it is considered to be an advanced propellant.

The exclusive use of Graphitite G-90 in the demonstration nozzle introduces some problem which have not been completely resolved in the present program. The effects of oxide deposition are expected to be more pronounced because of the axial thermal conductivity effect (G-90 is essentially isotropic compared to pyrolytic graphite). It is planned to use a trial and error technique to establish a reasonable prediction for the nozzle inlet and throat deposit history. Secondly, the polycrystalline graphites used in this program have not experienced significant corrosion-erosion. Several techniques are available and will be used in making predictions of the G-90 erosion. The assumptions, on which the various techniques are based, range from consideration of corrosion alone to adding a physical erosion contribution to the corrosion contribution. The third problem anticipated in the program demonstration analysis derives from the use of an advanced propellant. The qualitative corrosion model suggests that metal combustion problems will not arise with the VID propellant, unless large metal agglomerates form on the grain surface. It is doubtful that the G-90 heat transfer or corrosion-erosion will compare directly with similar data obtained from other motor firings where the metal combustion efficiency was less than ideal. Consequently, the use of empirical correlations of convective heat transfer and corrosion will be minimized.

Evidently then, the nozzle performance predictions will be somewhat experimental and will not necessarily provide a comprehensive demonstration of the program results. It is strongly recommended that a detailed post test evaluation of the nozzle performance predictions be conducted to establish the validity of the pertinent assumptions in the analyses. In this way, logical conclusions can be reached concerning the need for additional investigation of erosion-corrosion mechanics with advanced beryllium propellants.

APPENDIX (C)

The backside surfaces of the polycrystalline graphite entrance section, exit cone and throat insert sleeve together with the pyrolytic graphite or tungsten throat insert were instrumented with thermocouples. The thermocouples were located at various axial positions in the nozzle so that the dependence of the gas side surface boundary condition on area ratio could be characterized. However, as noted in Section 2.5e, the thermal analysis effort was concentrated on the geometrical throat region of the nozzle. Detailed thermal analyses, at locations other than the throat, must be deferred until axial variations in the deposit thickness history can be deduced (see discussion of deposit flow model, Section 2.5.e).

The temperature data acquired from each motor firing are presented in Figures 177 to 193. The start times (t=0) in each figure are identical to those in the pressure and thrust traces of Section 5.2.b. The nozzle positions, corresponding to the thermocouple port numbers indicated in Figures 177 to 193 are shown in Section 4.3. Data for those thermocouples, from which (1) no data was acquired, (2) read ambient temperature during the firing and (3) read negative and positive temperatures in a random nature, are not presented. These thermocouples are denoted, in the figures following, as 'did not record properly'. Also, the plotting of the transient temperature was terminated when an open circuit occurred or the thermocouple output was judged to be unrealistic. The conversion of the thermocouple outputs, from Test T-24, to temperature was not accomplished due to a recording system malfunction. However, a technique has been formulated to eliminate the static type errors in the digital data tape for Test T-24. This data may be presented in the final report, if funds are made available by the Air Force.

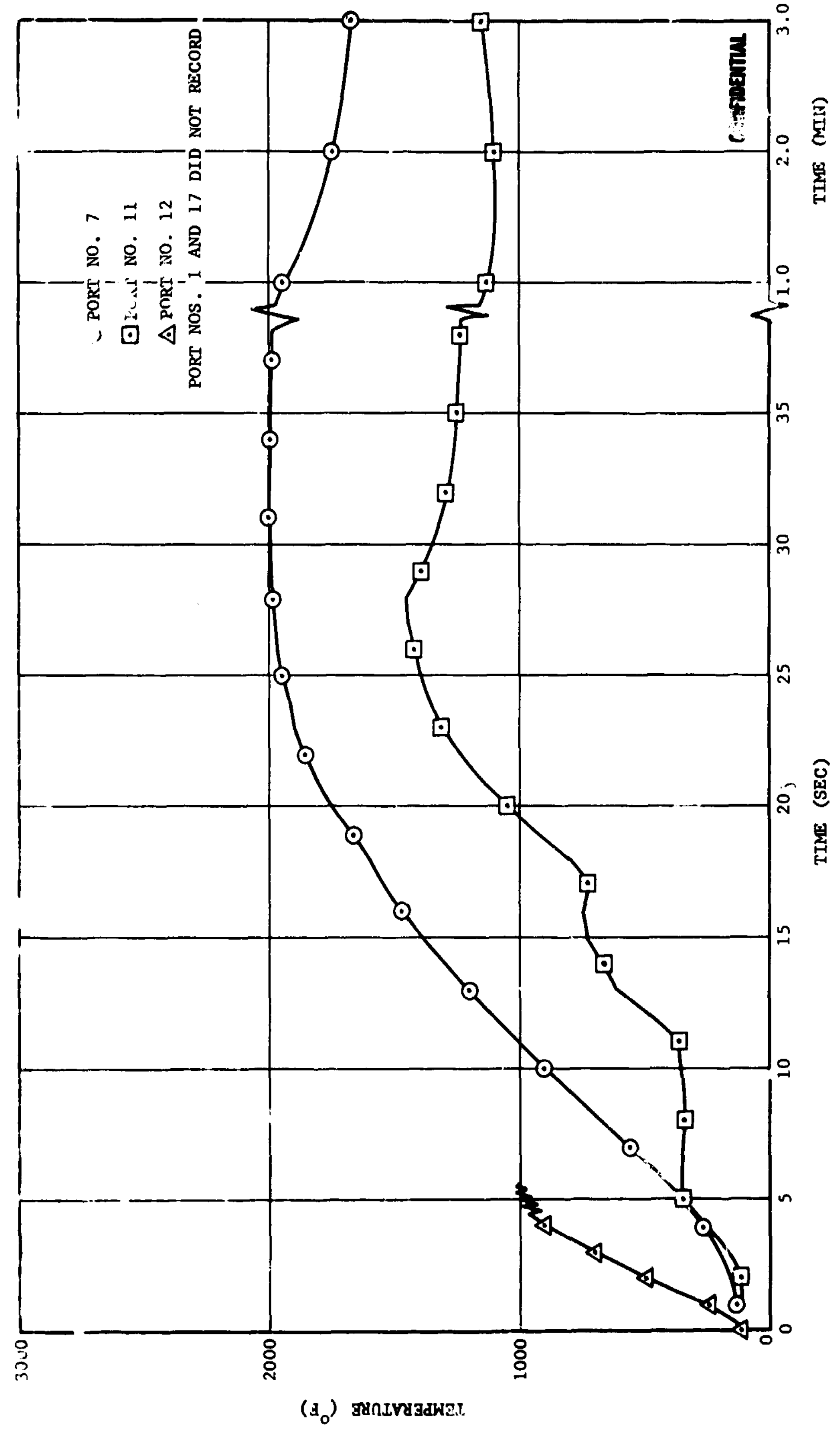

F08120 C

FIGURE 177. MEASURED HEAT SINK TEMPERATURES, TEST T-8

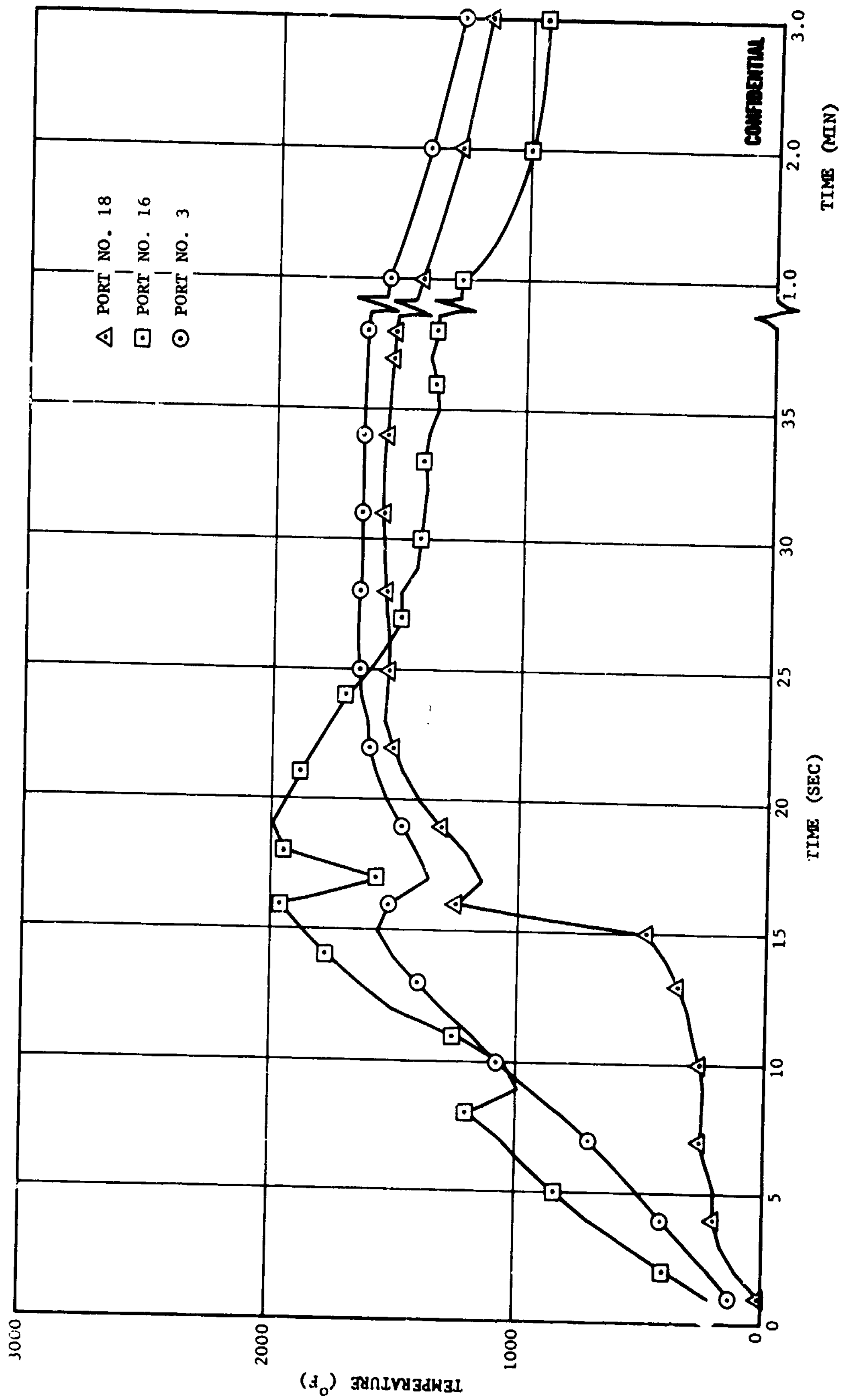

F06119C

FIGURE 177. MEASURED HEAT SINK TEMPERATURES, TEST T-8 (Continued)

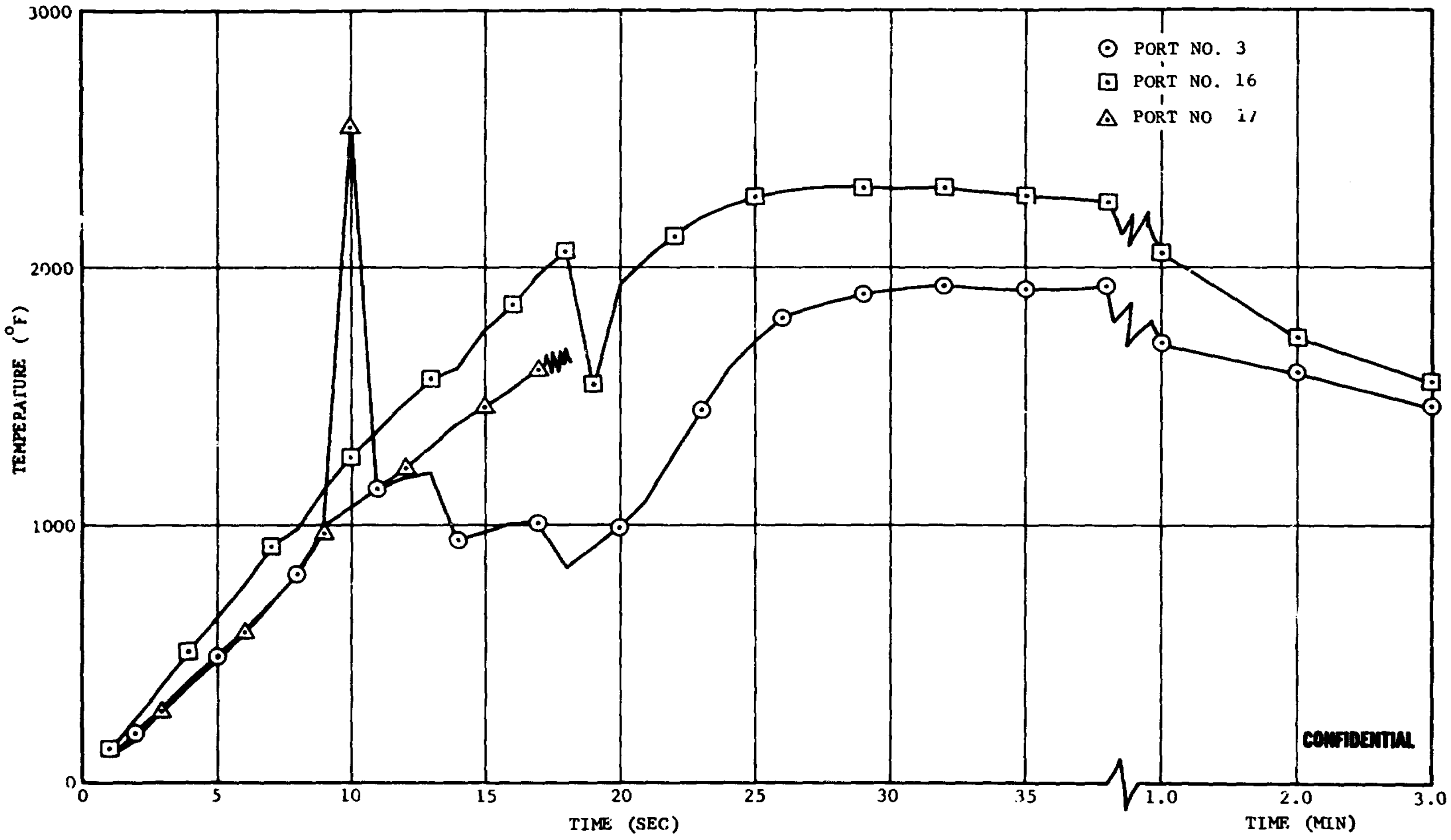

F08121 C

FIGURE 178. MEASURED HEAT SINK TEMPERATURE, TEST T-9

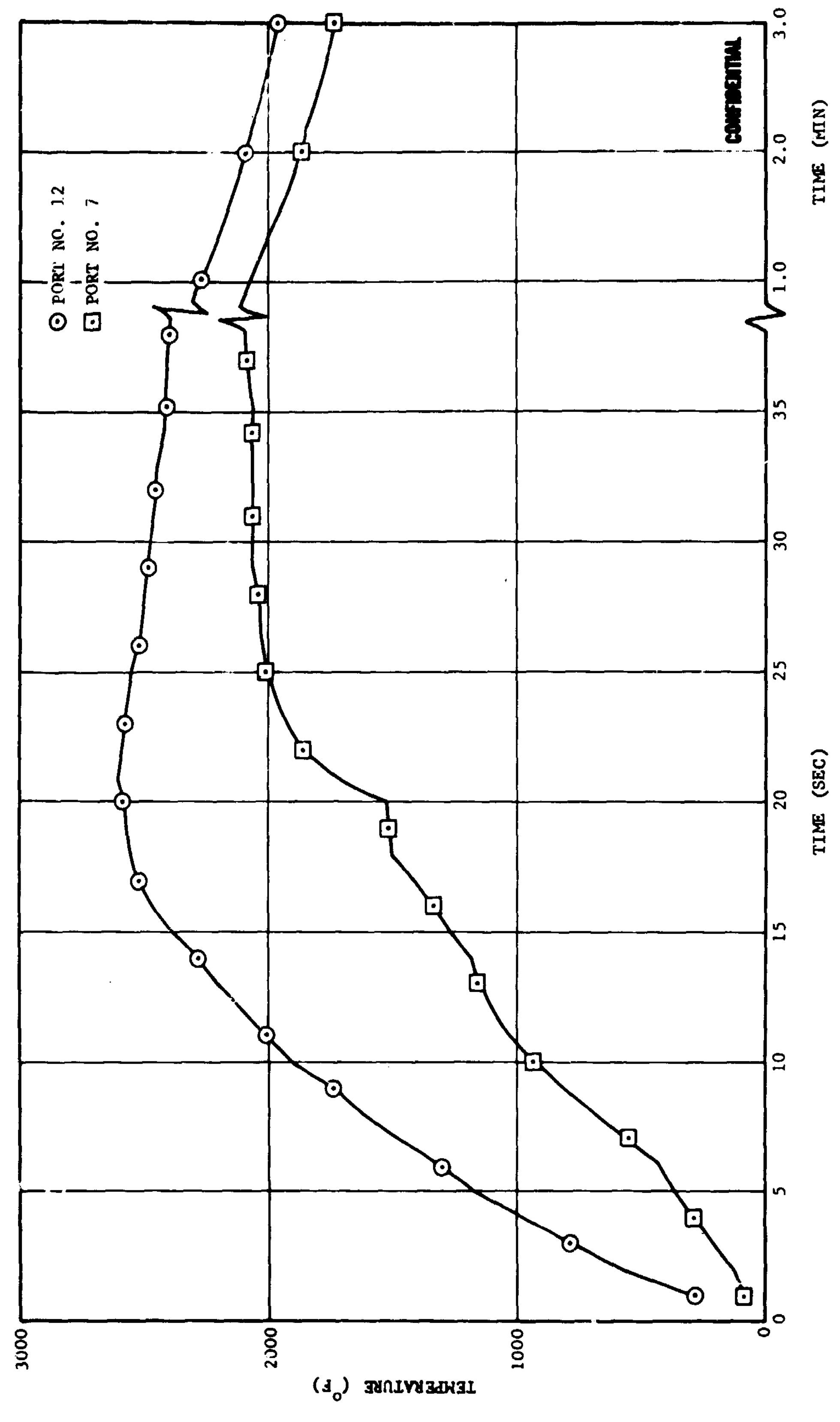

F08122

FIGURE 178. MEASURED HEAT SINK TEMPERATURE, TEST T-9 (Continued)

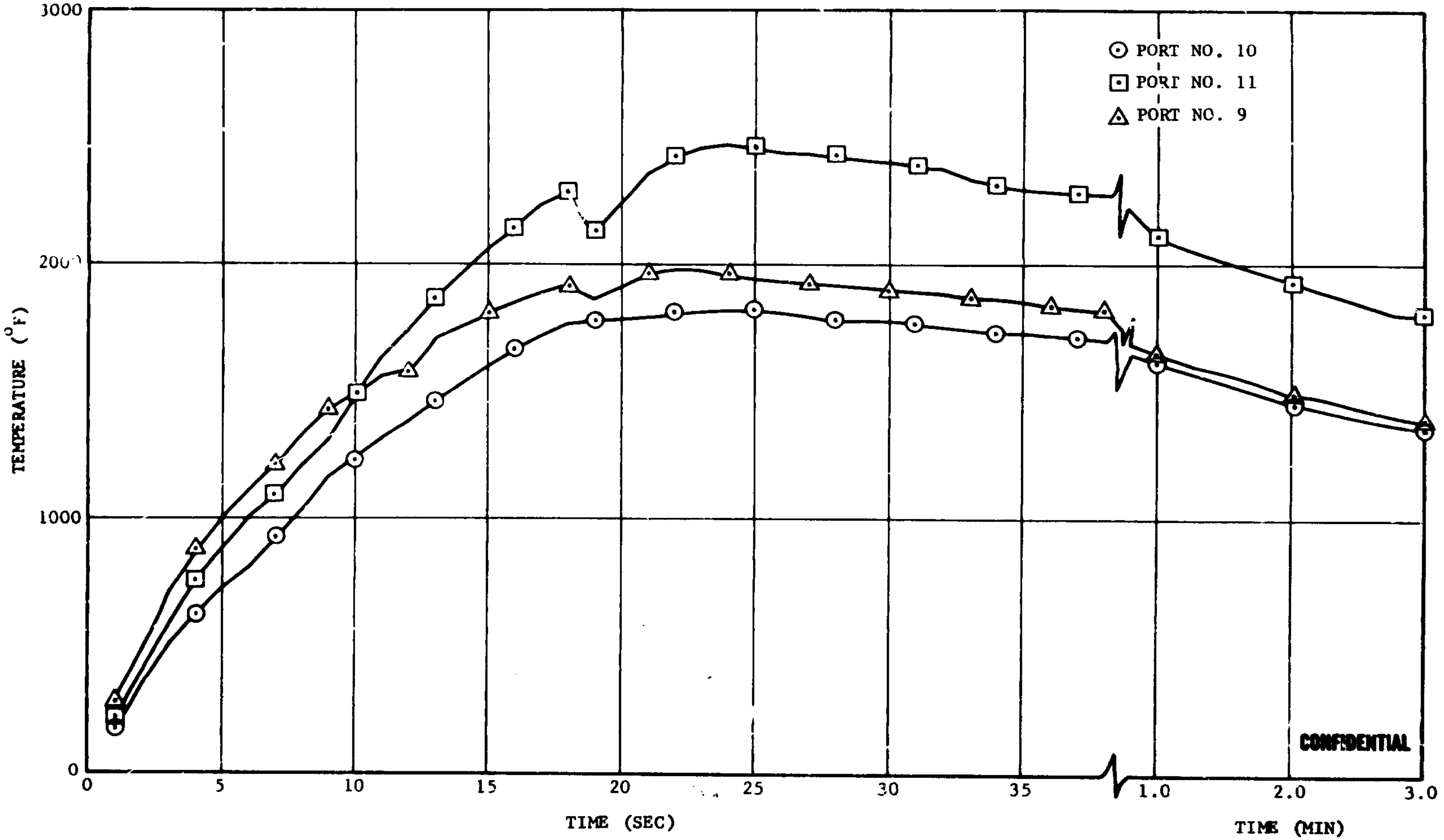

F08123C

FIGURE 178. MEASURED HEAT SINK TEMPERATURE, TEST T-9 (Continued)

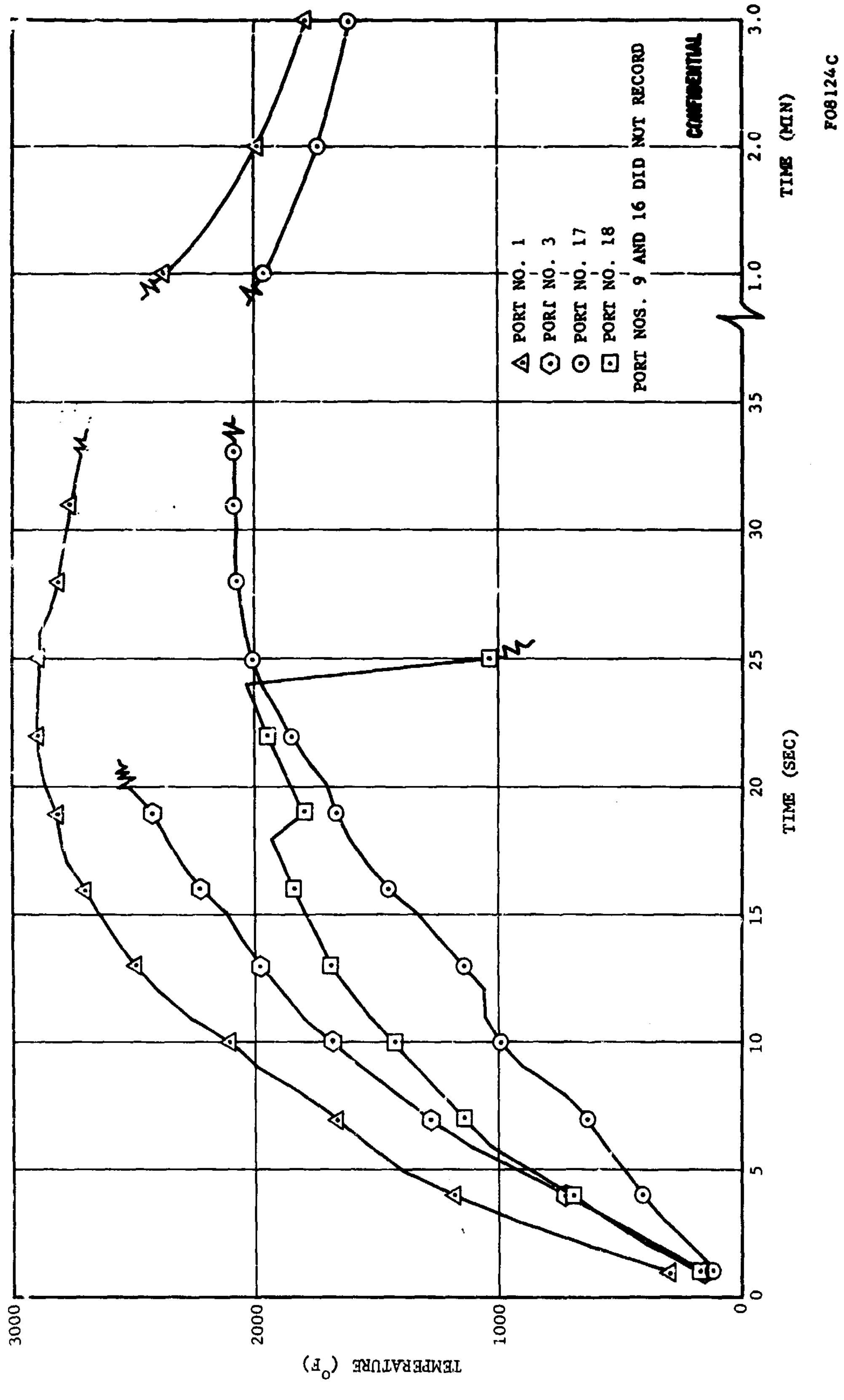

FIGURE 179. MEASURED HEAT SINK TEMPERATURES, TEST T-10

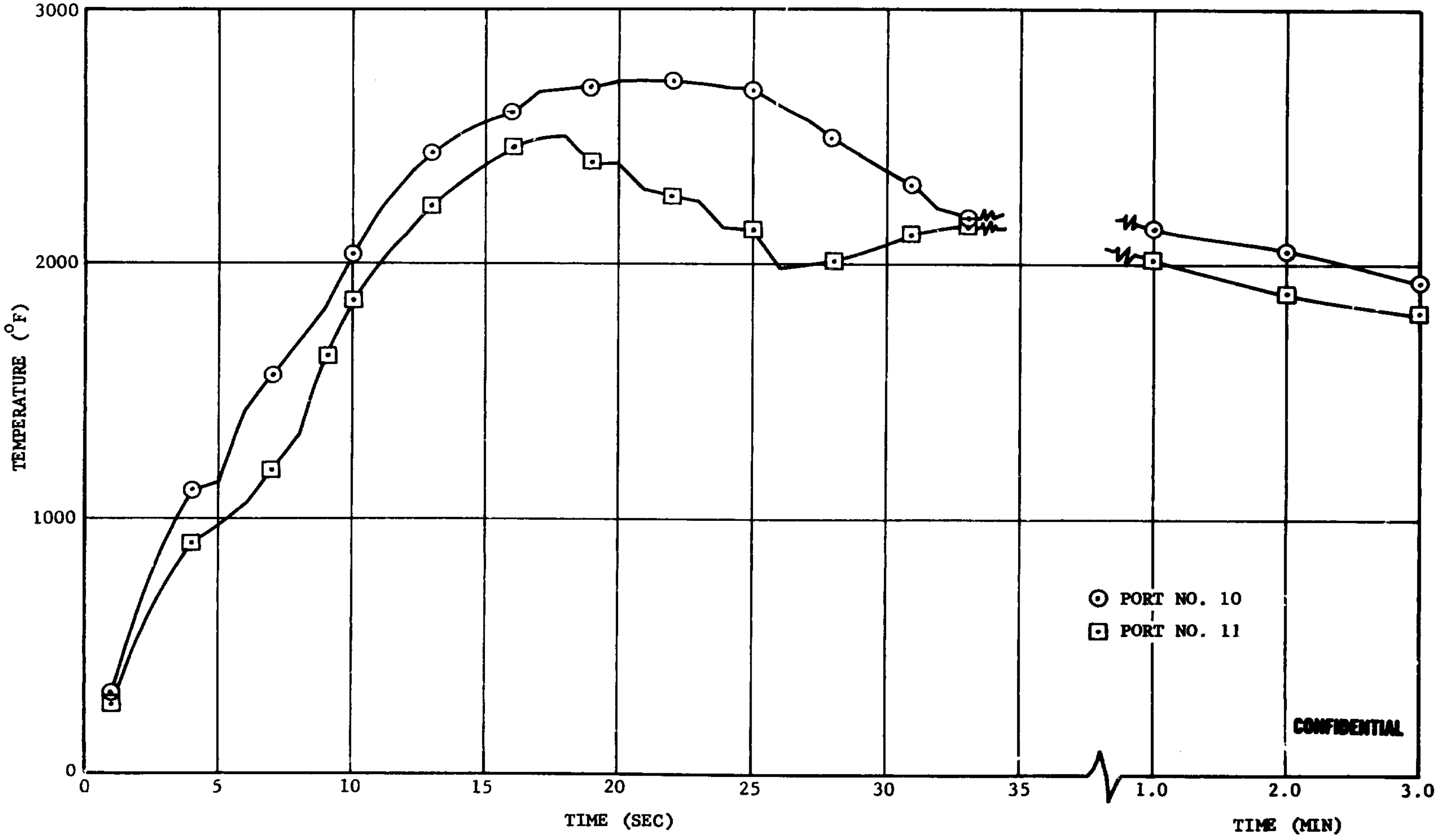

F08125C

FIGURE 179. MEASURED HEAT SINK TEMPERATURES, TEST T-10 (Continued)

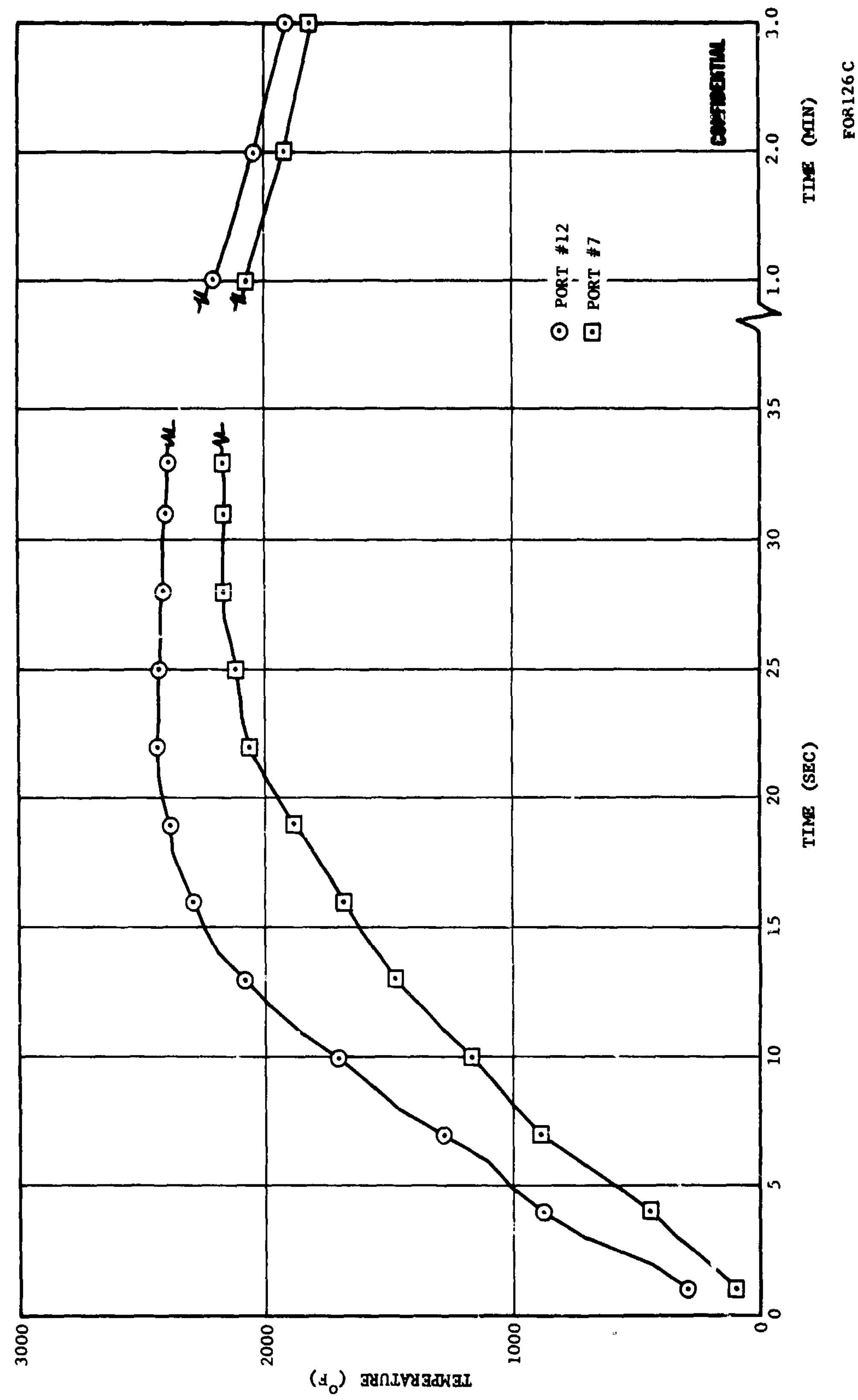

FIGURE 179. MEASURED HEAT SINK TEMPERATURES, TEST T-10 (Continued)

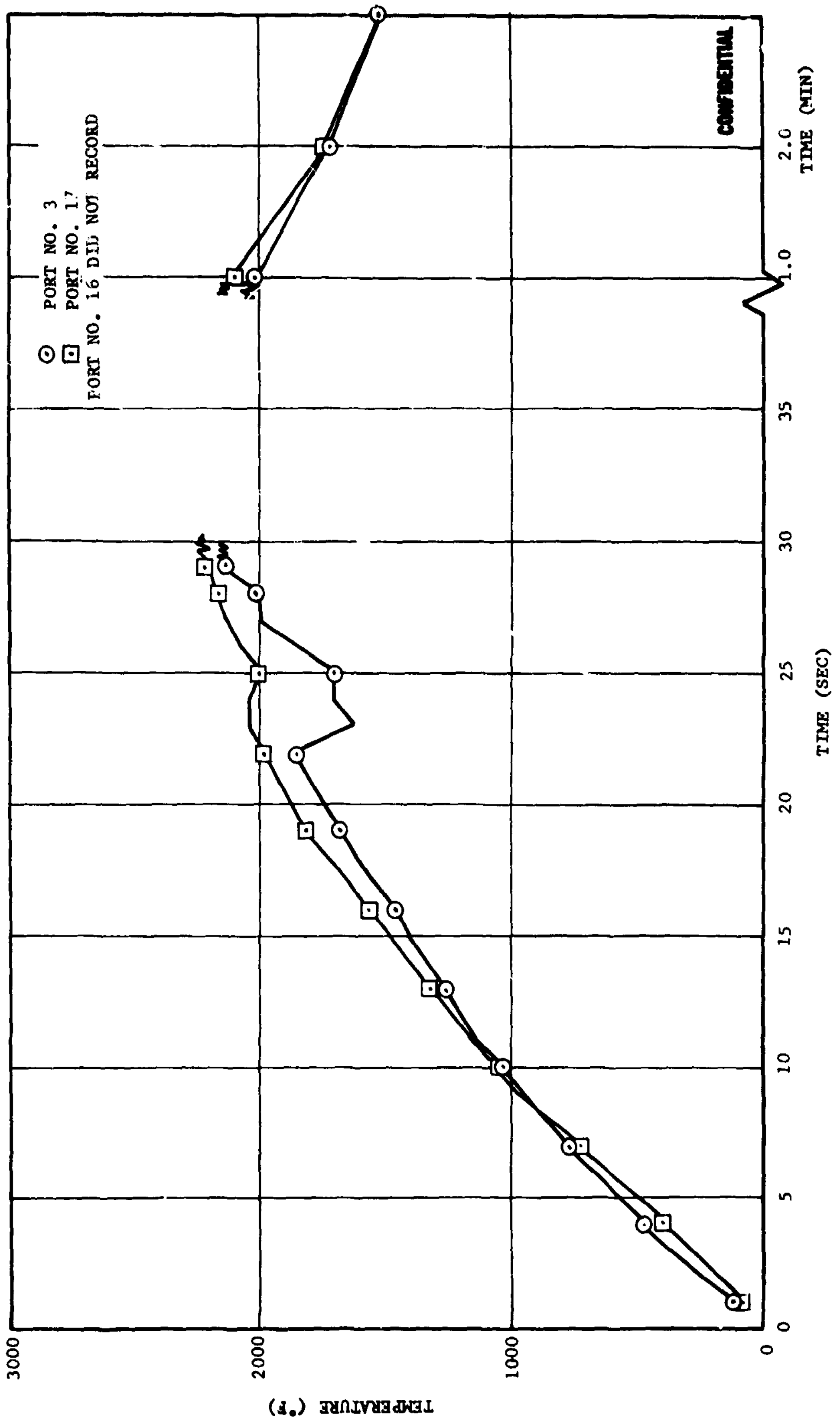

FIGURE 180. MEASURED HEAT SINK TEMPERATURES, TEST T-11

F08127C

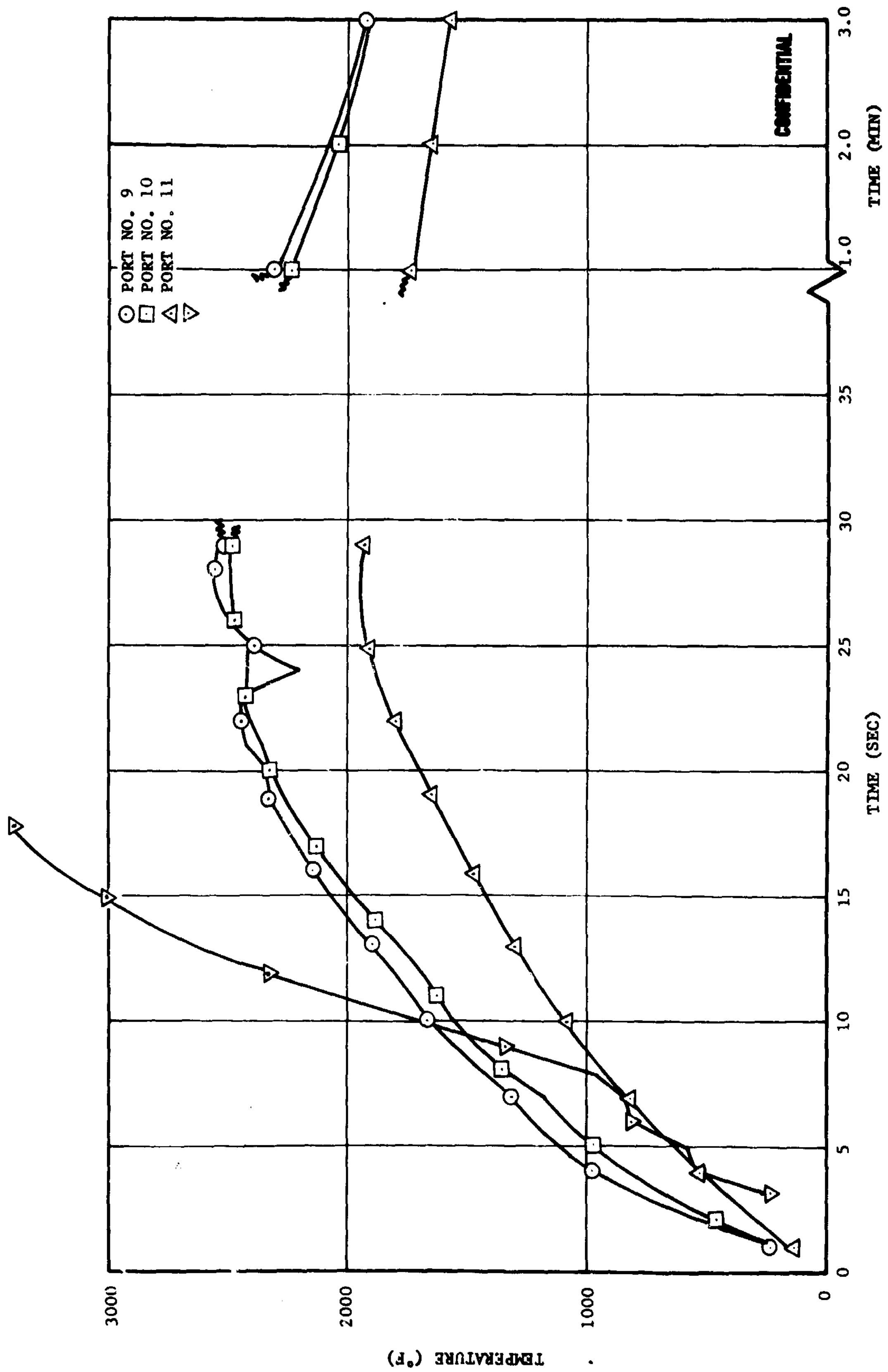

FIGURE 180. MEASURED HEAT SINK TEMPERATURES, TEST T-11 (Continued)

F08128C

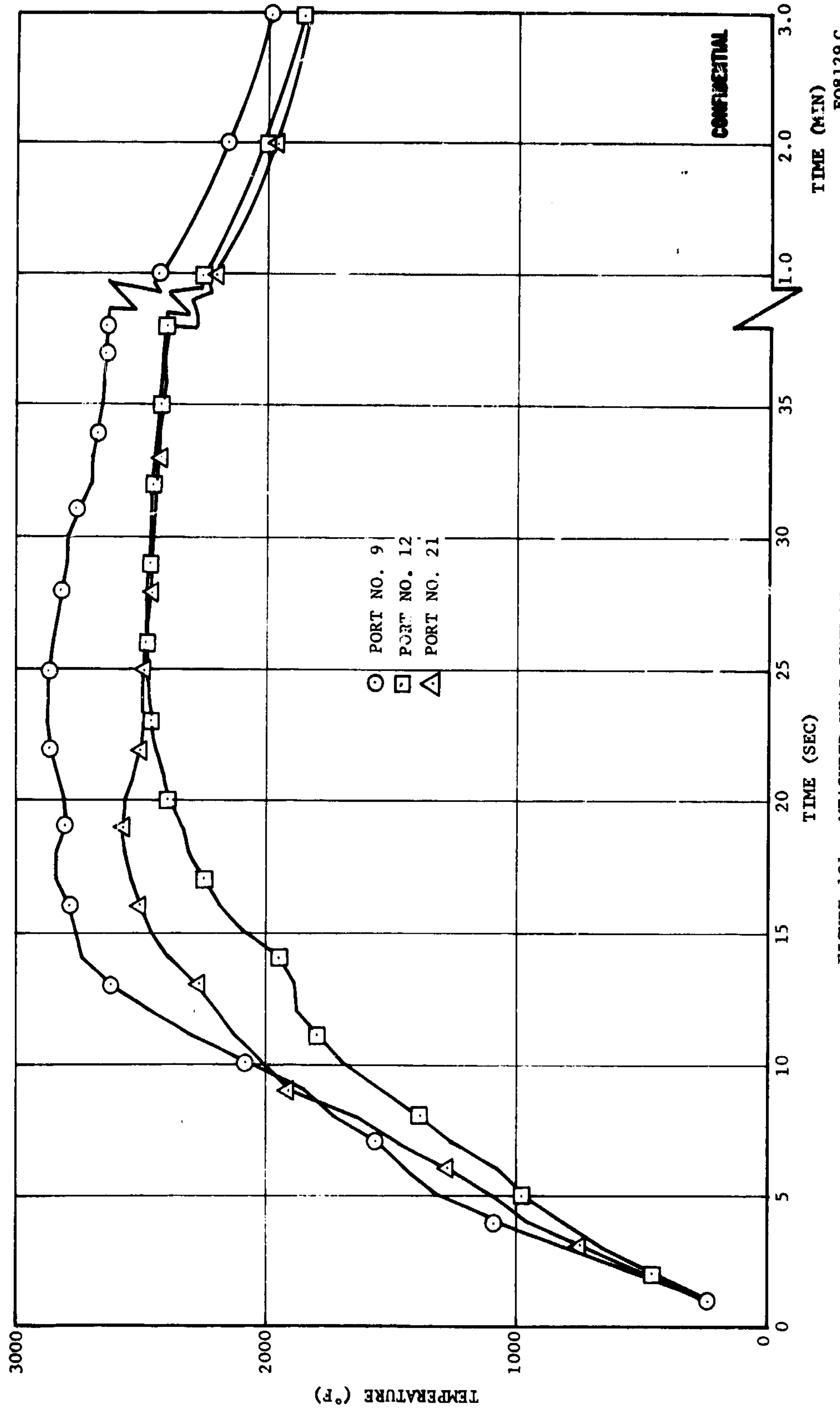

FIGURE 181. MEASURED HEAT SINK TEMPERATURES, TEST T-12

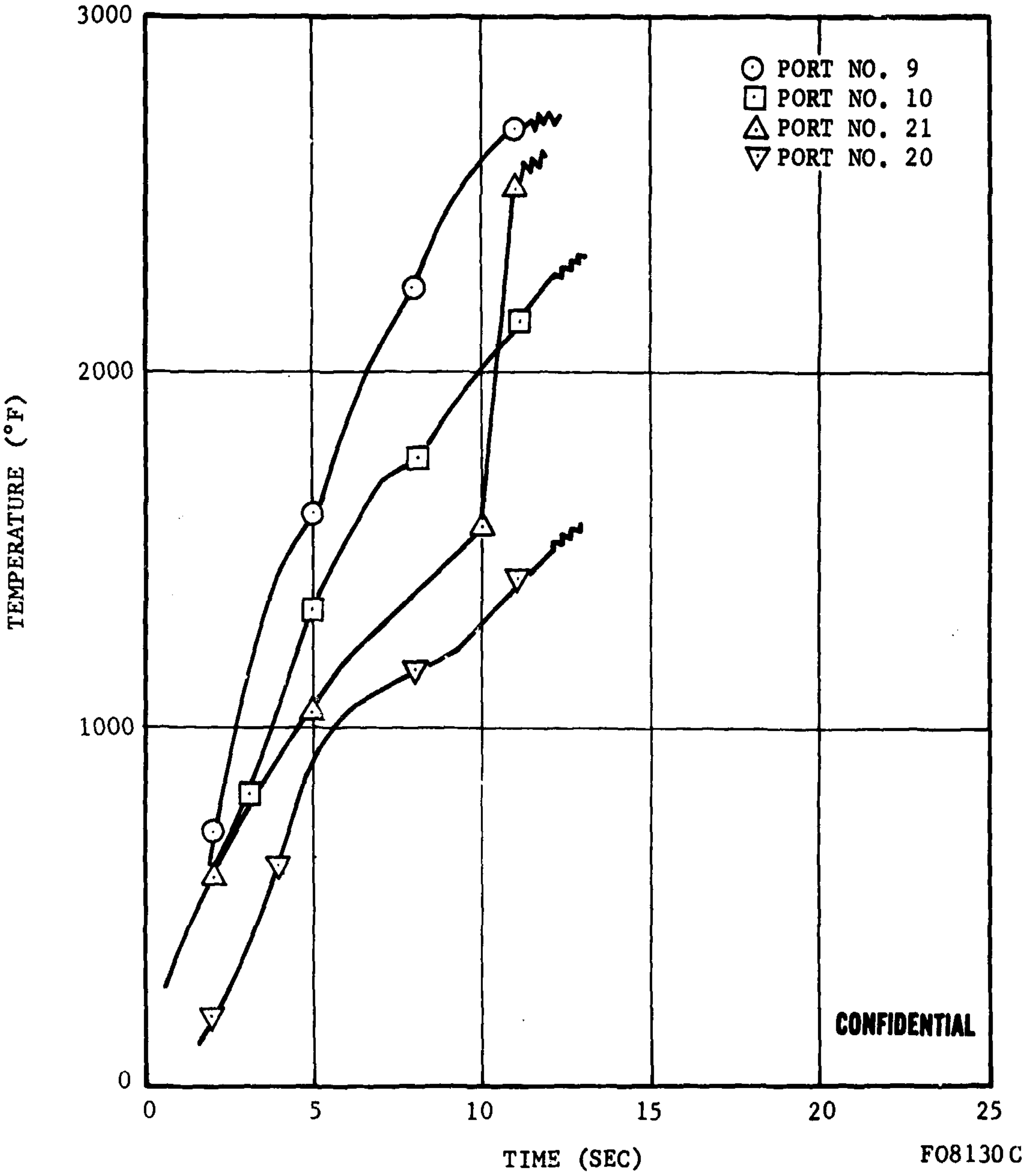

FIGURE 182. MEASURED HEAT SINK TEMPERATURES, TEST T-13

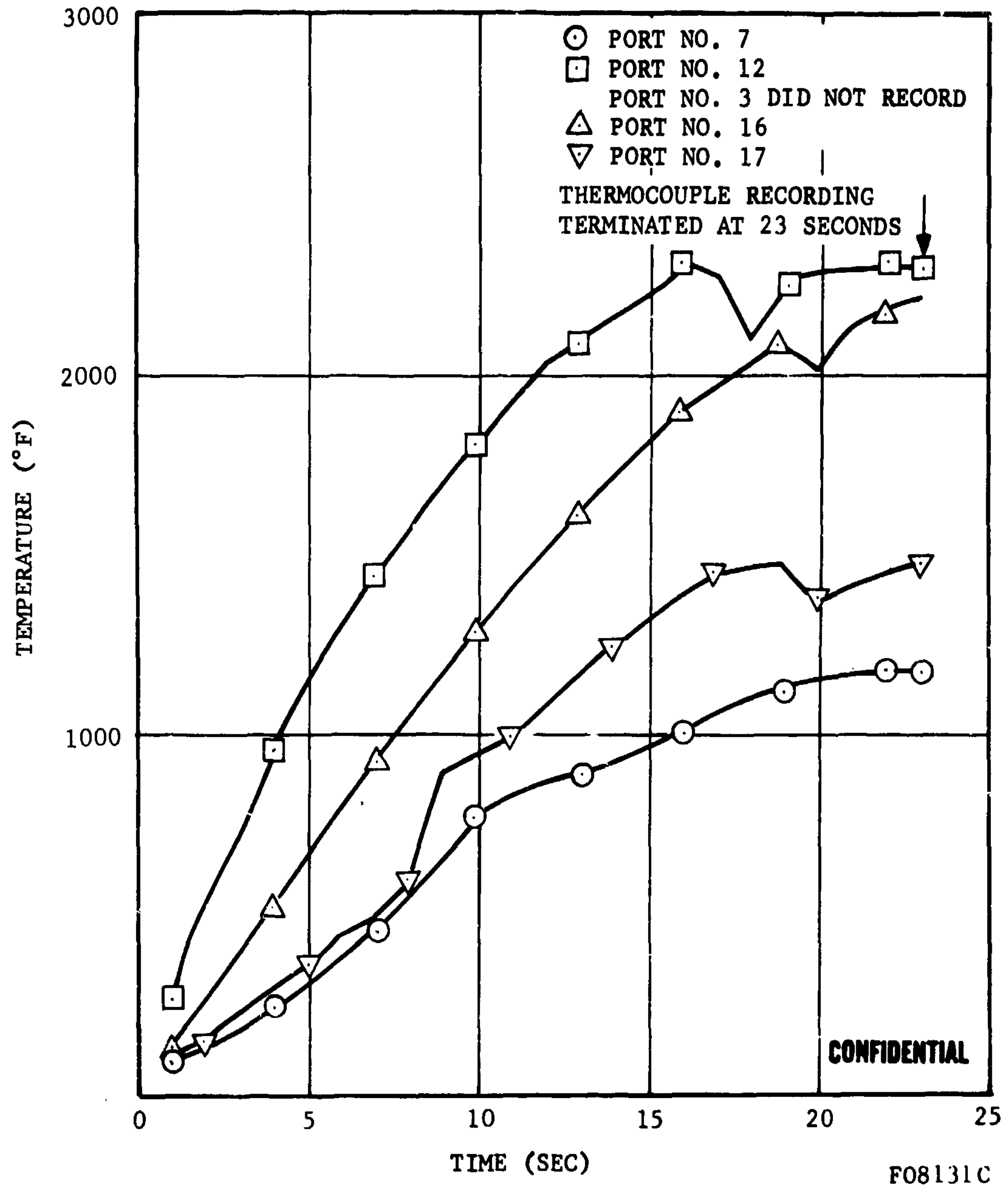

FIGURE 183. MEASURED HEAT SINK TEMPERATURES, TEST T-14

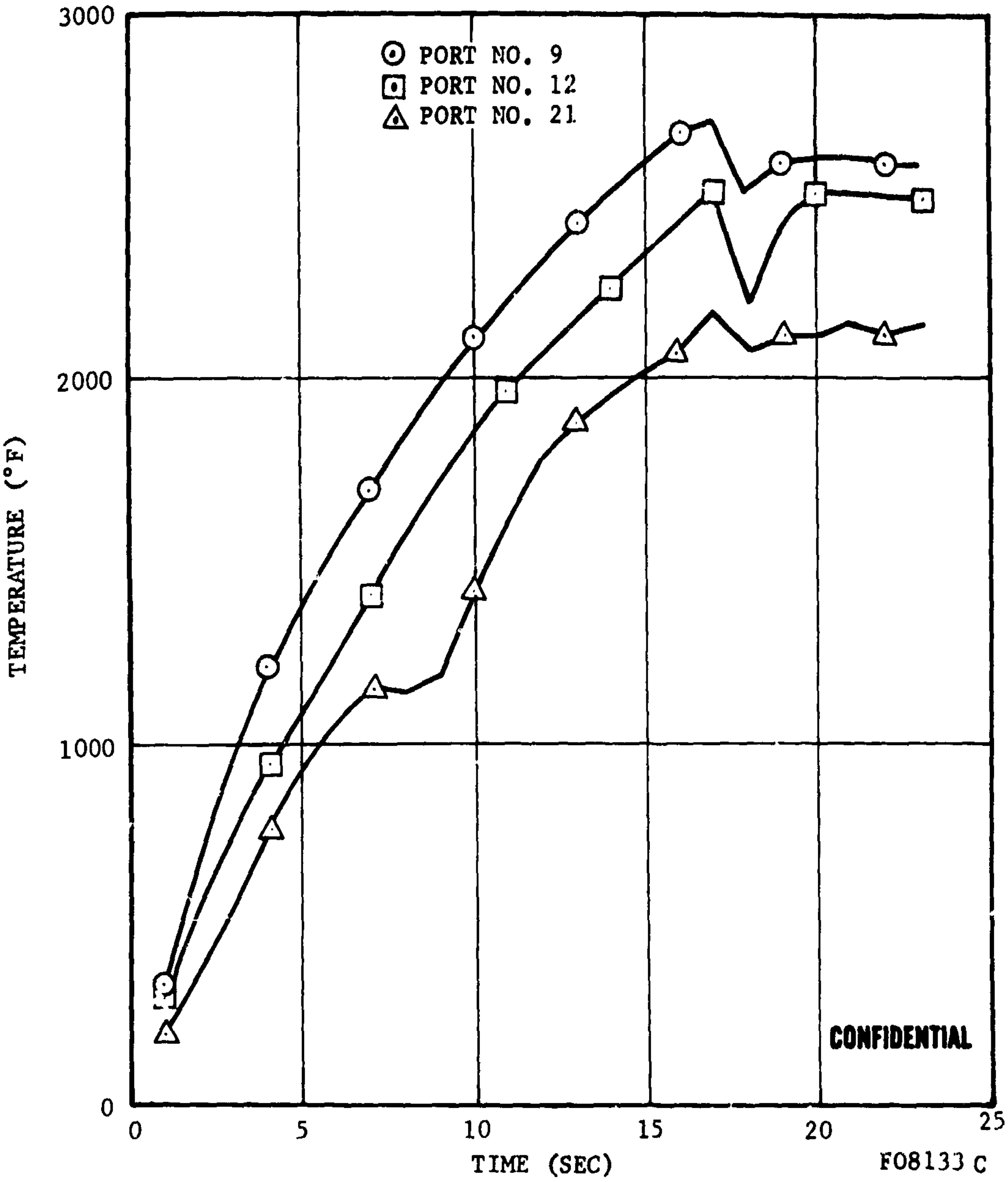

FIGURE 183. MEASURED HEAT SINK TEMPERATURE, TEST T-14 (Continued)

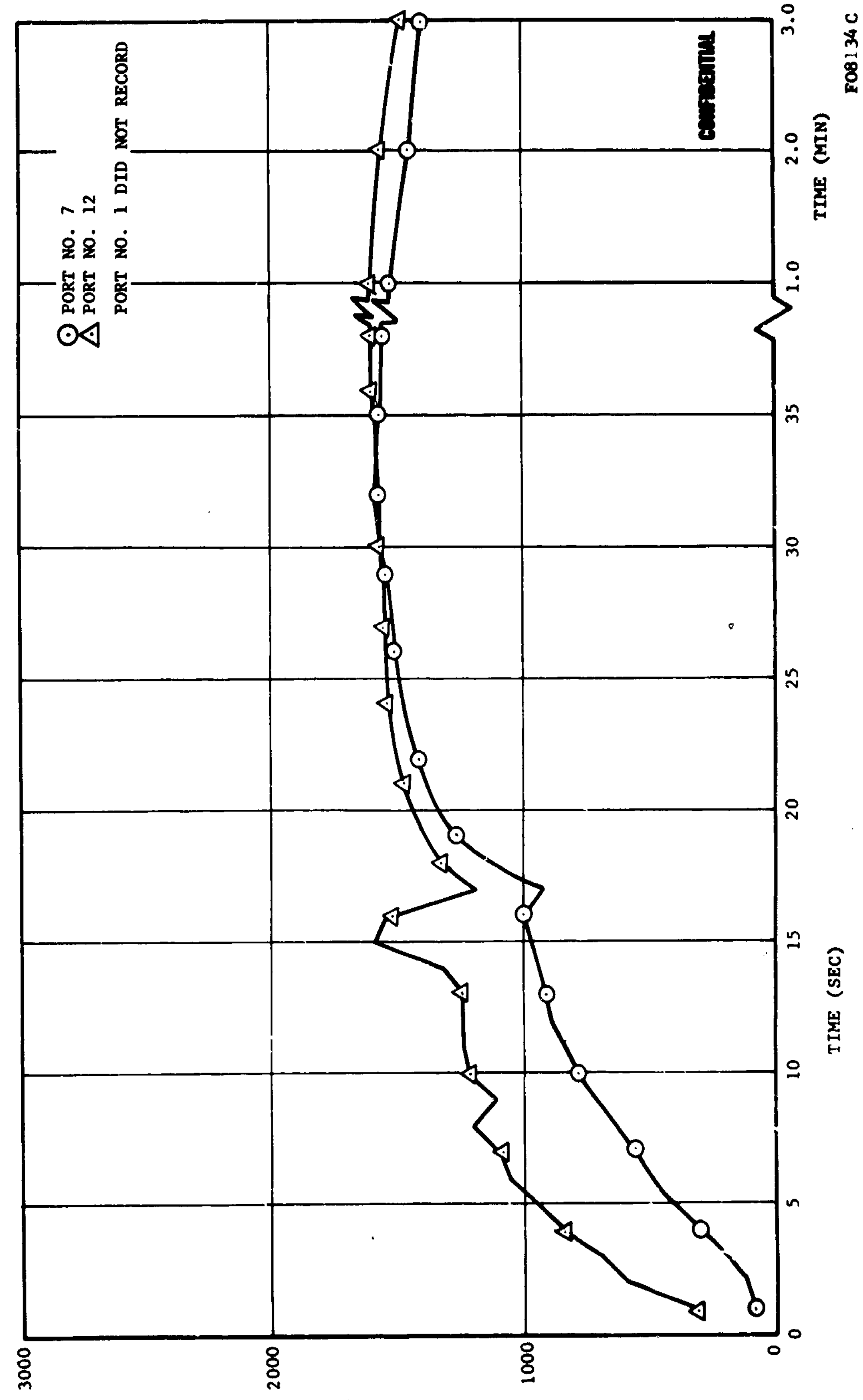

FIGURE 184. MEASURED HEAT SINK TEMPERATURES, TEST T-15

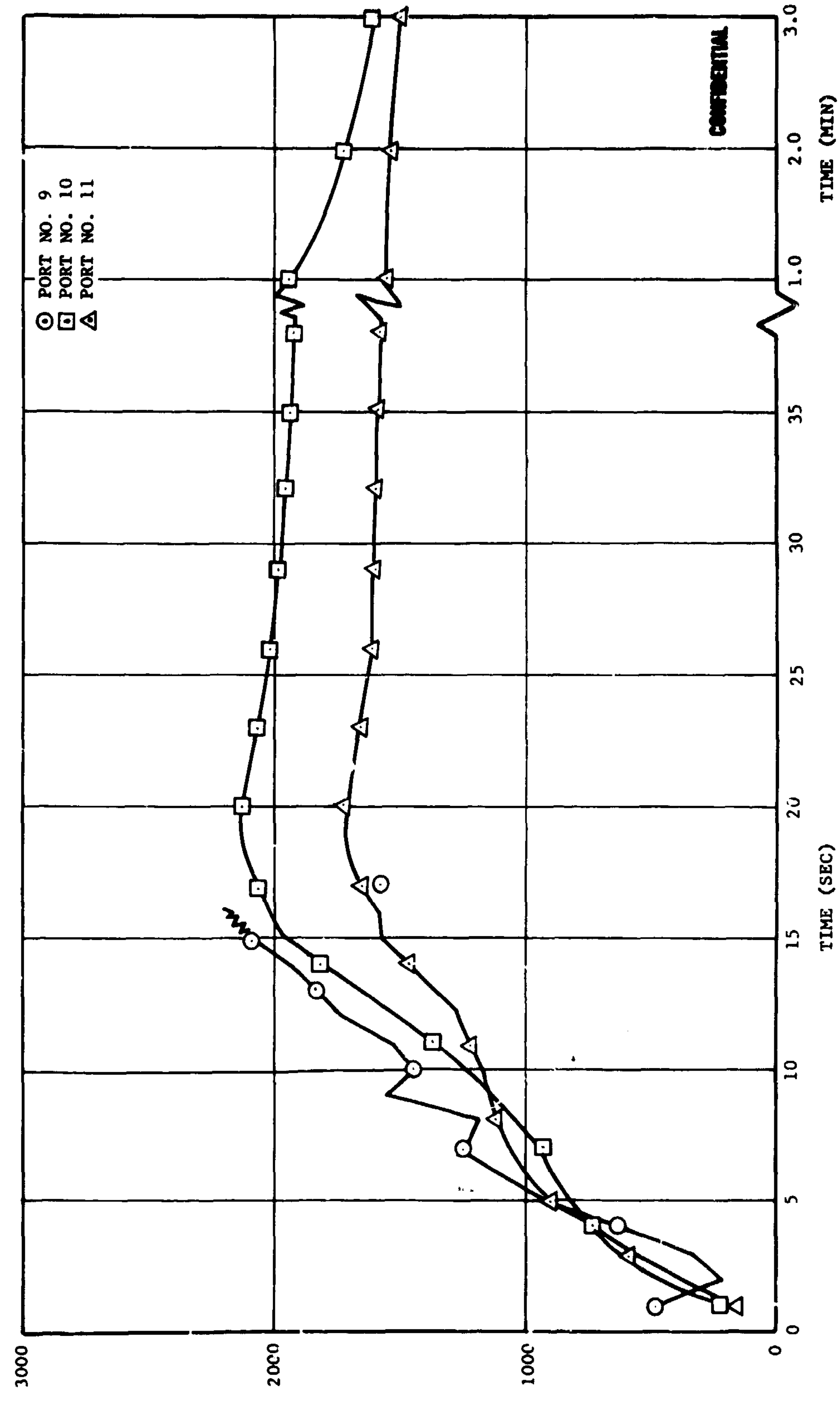

FIGURE 184. MEASURED HEAT SINK TEMPERATURES, TEST T-15 (Continued) F08135C

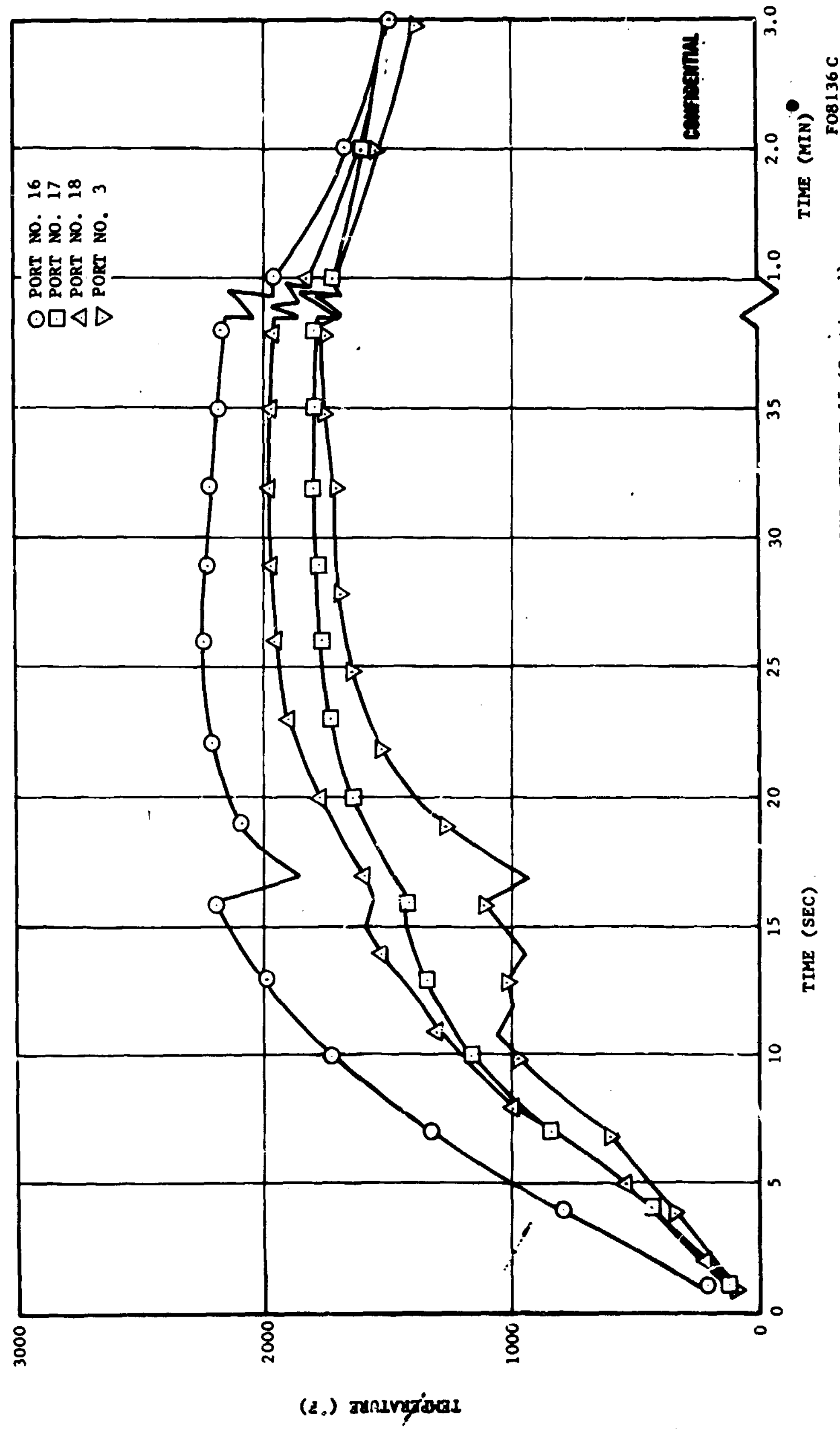

FIGURE 184. MEASURED HEAT SINK TEMPERATURES, TEST T-15 (Continued)

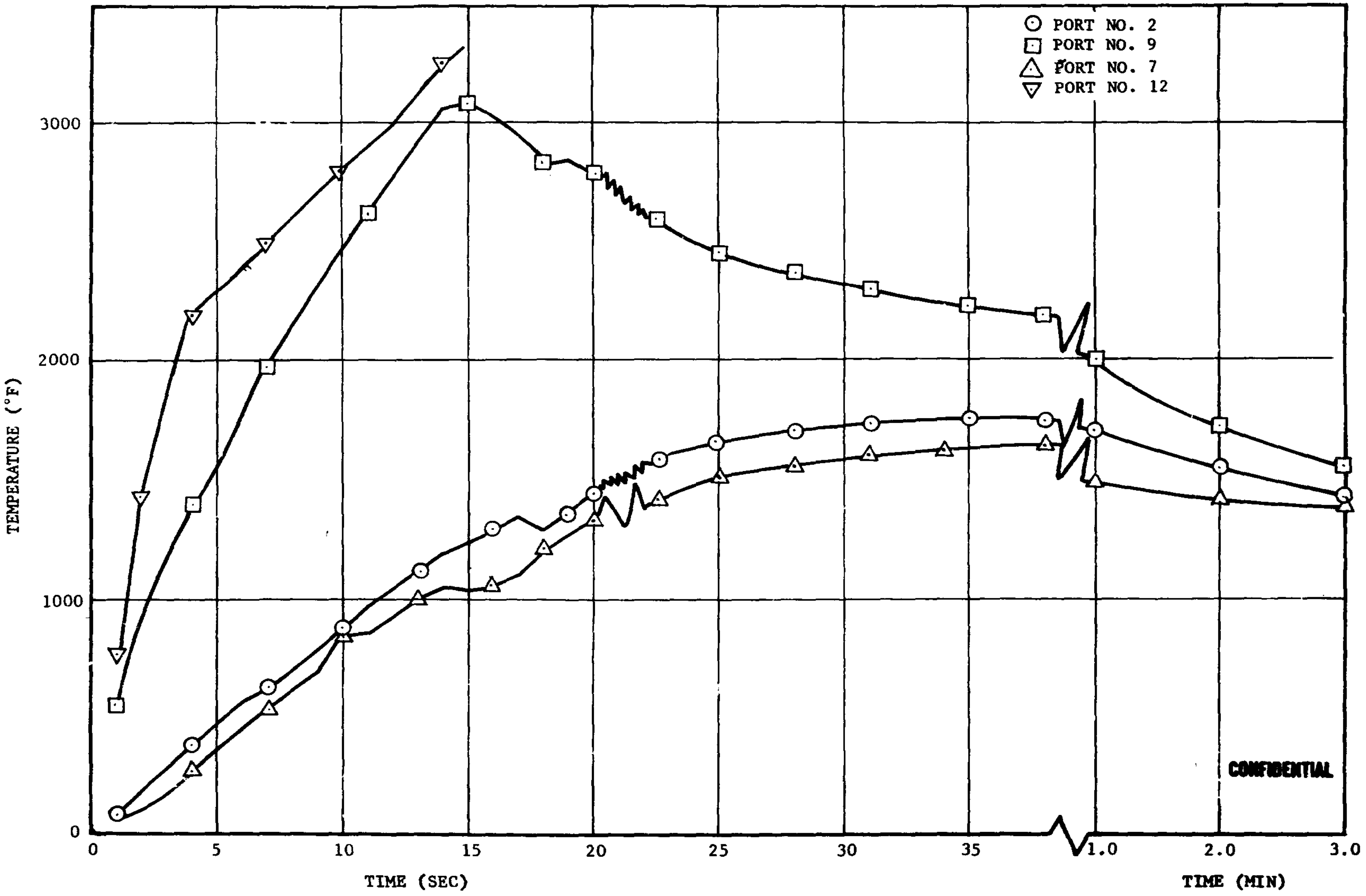

FIGURE 185. MEASURED HEAT SINK TEMPERATURES, TEST T-16

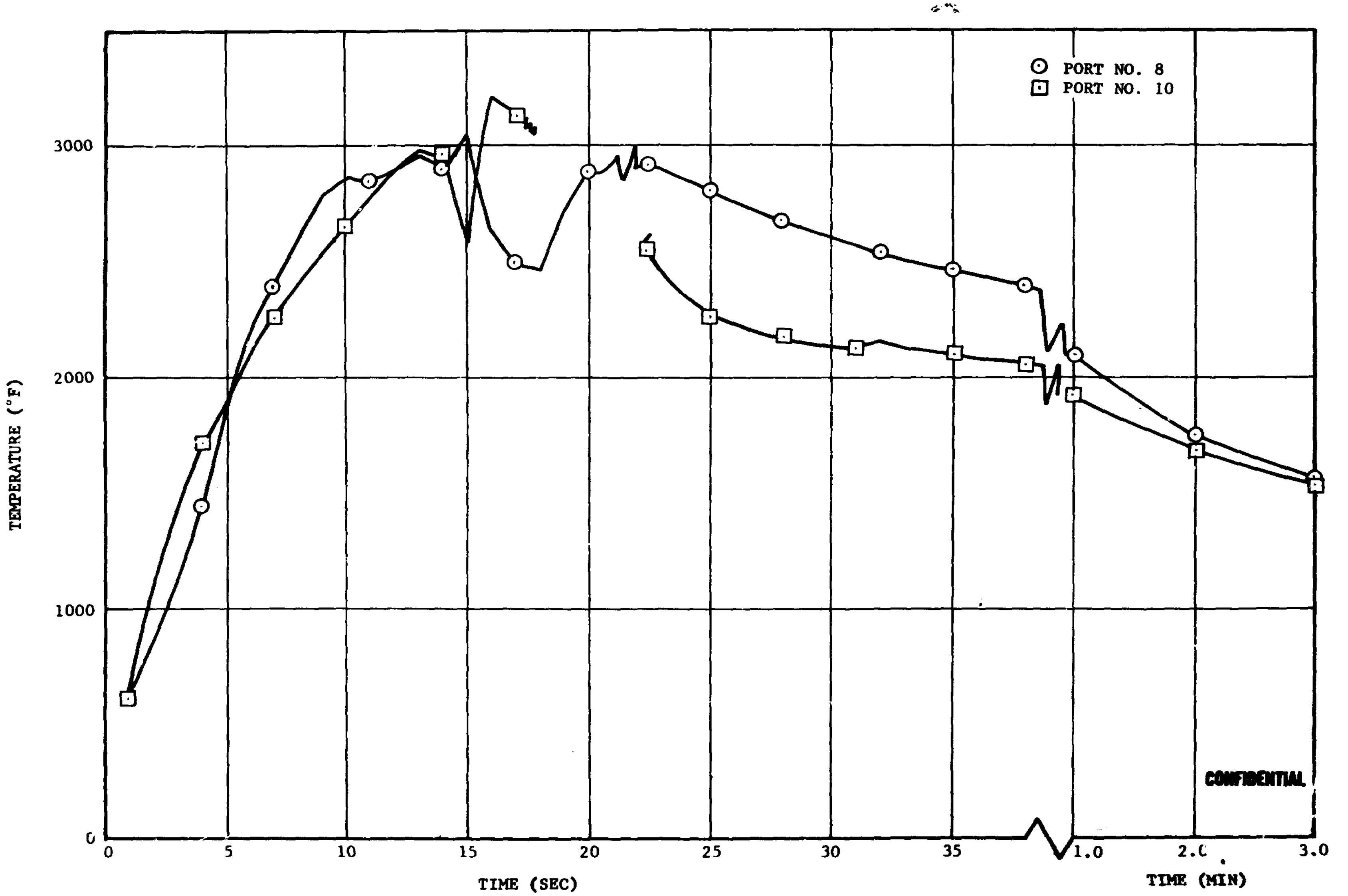

FIGURE 185. MEASURED HEAT SINK TEMPERATURES, TEST T-16 (Continued)

F08138C

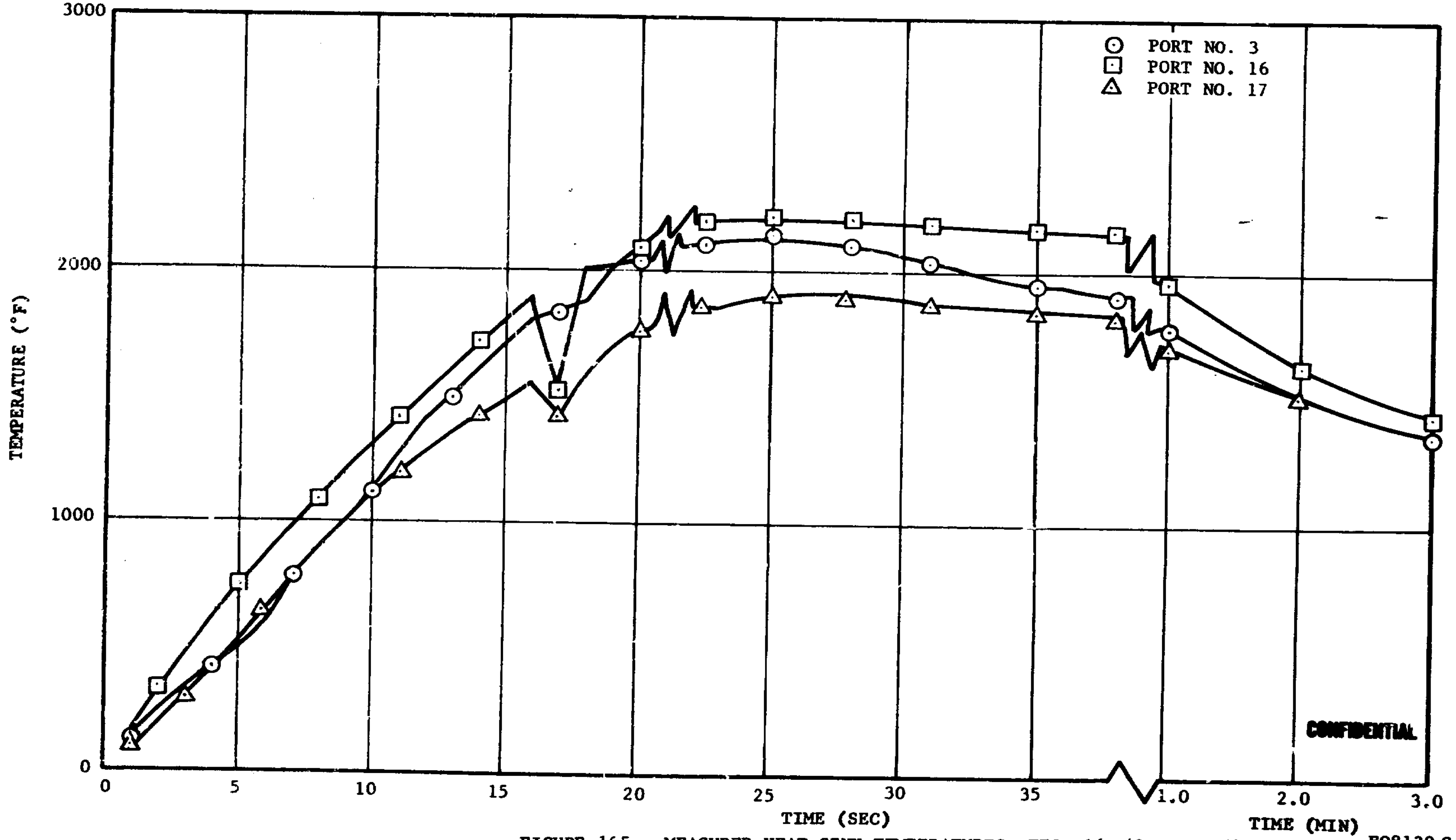

FIGURE 165. MEASURED HEAT SINK TEMPERATURES, TEST 16 (Continued)

F08139 C

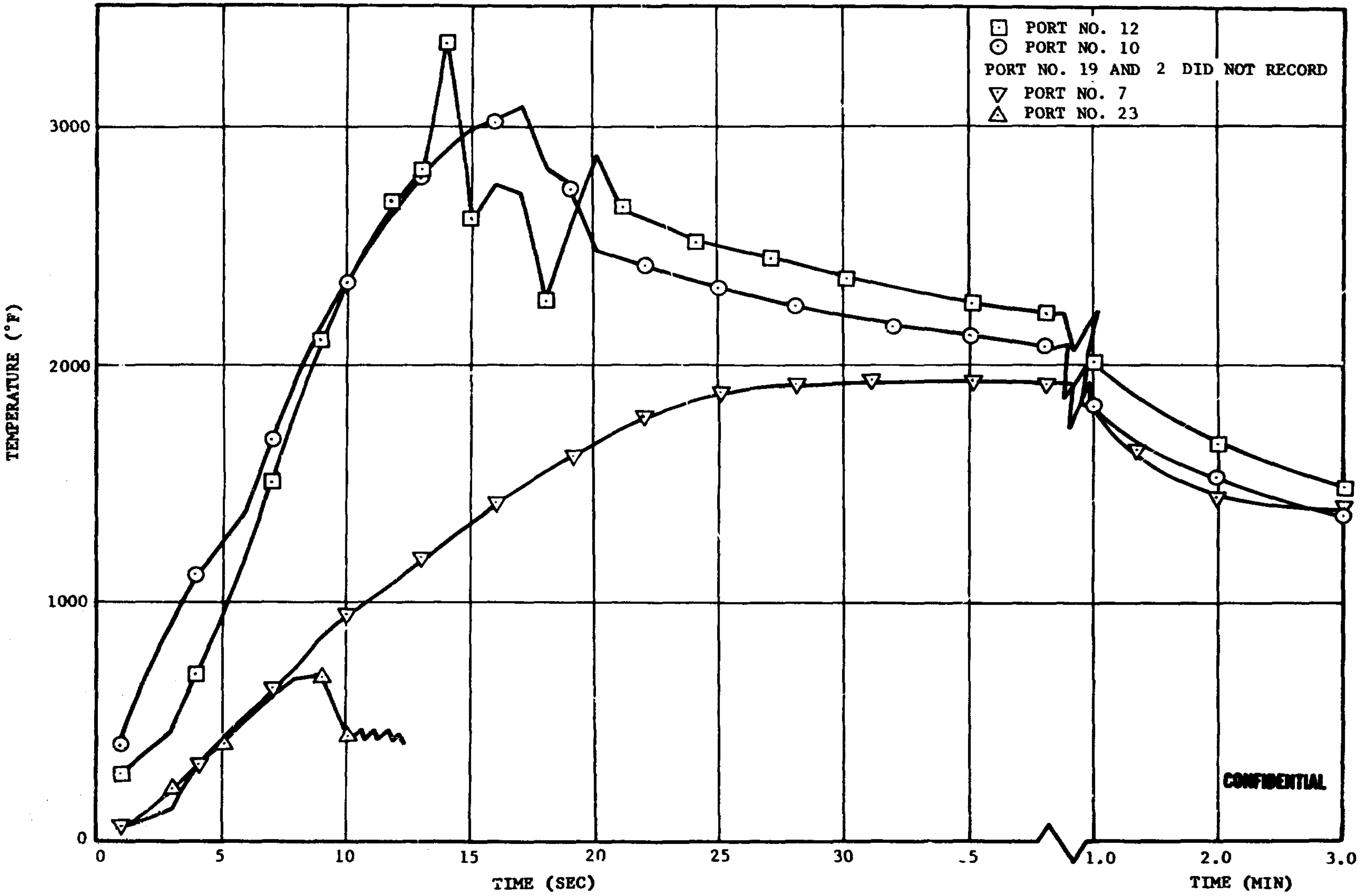

FIGURE 186. MEASURED HEAT SINK TEMPERATURES, TEST T-17

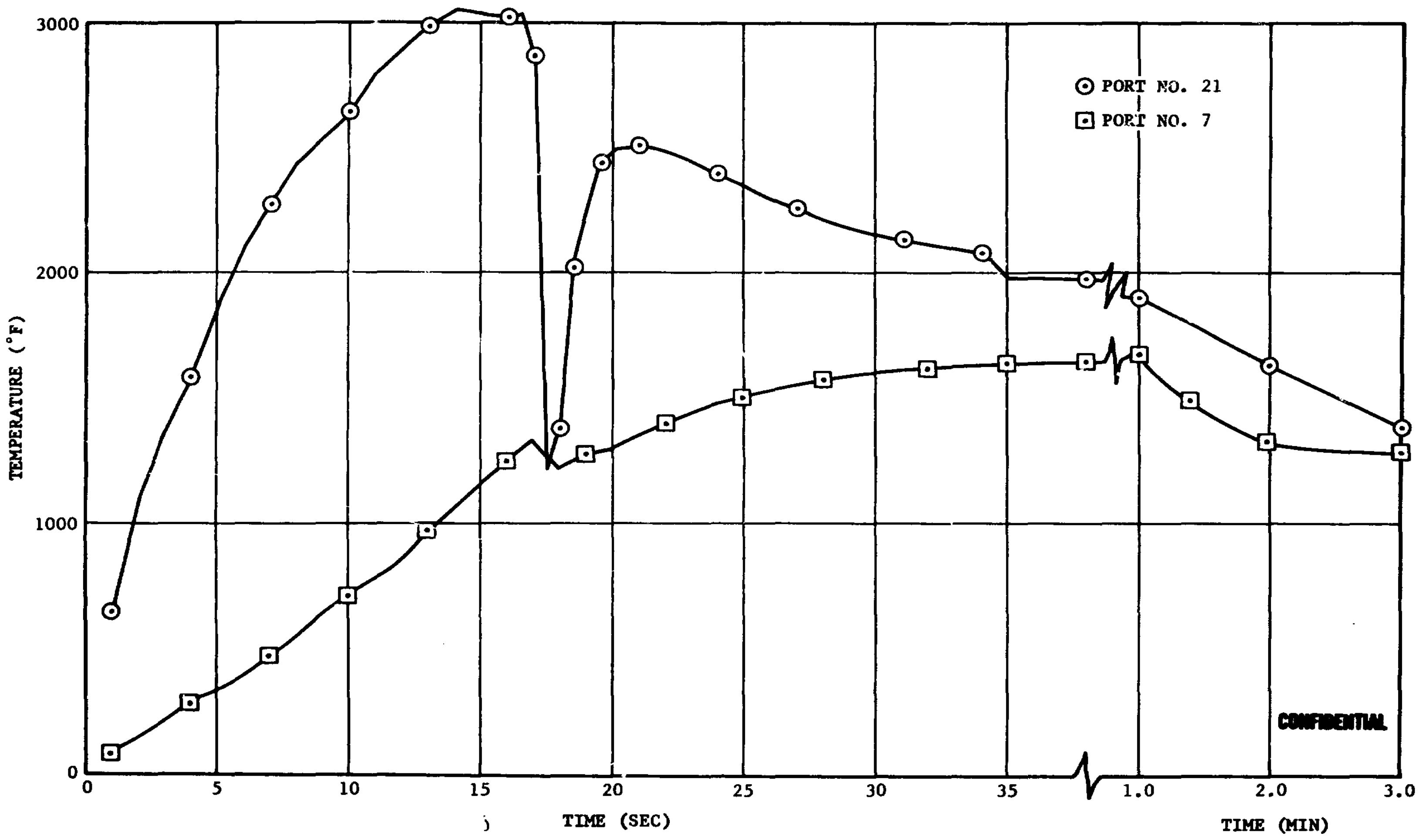

F08141C

FIGURE 187. MEASURED HEAT SINK TEMPERATURES, TEST T-18

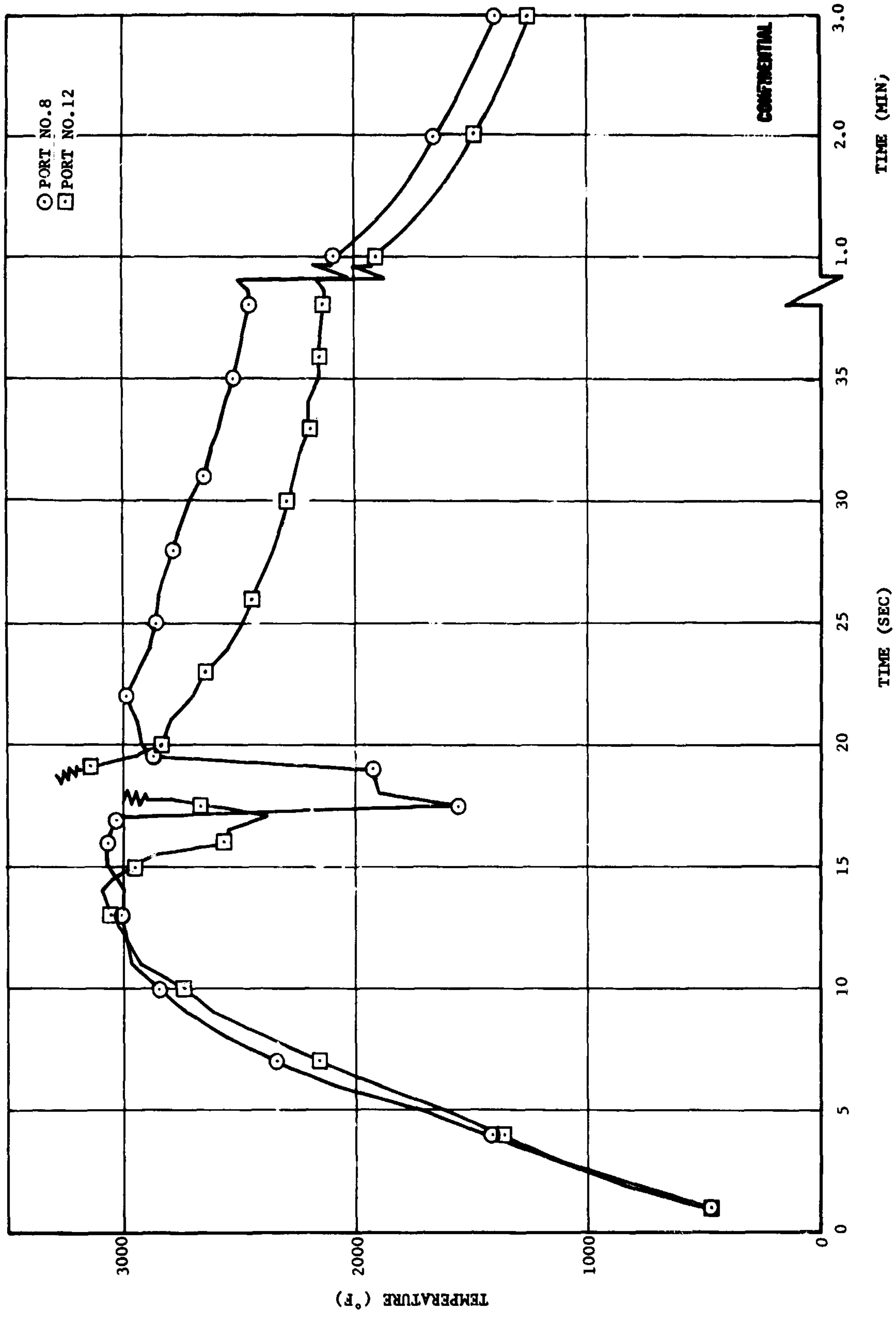

FIGURE 187. MEASURED HEAT SINK TEMPERATURES, TEST T-18 (Continued)

F08142 C

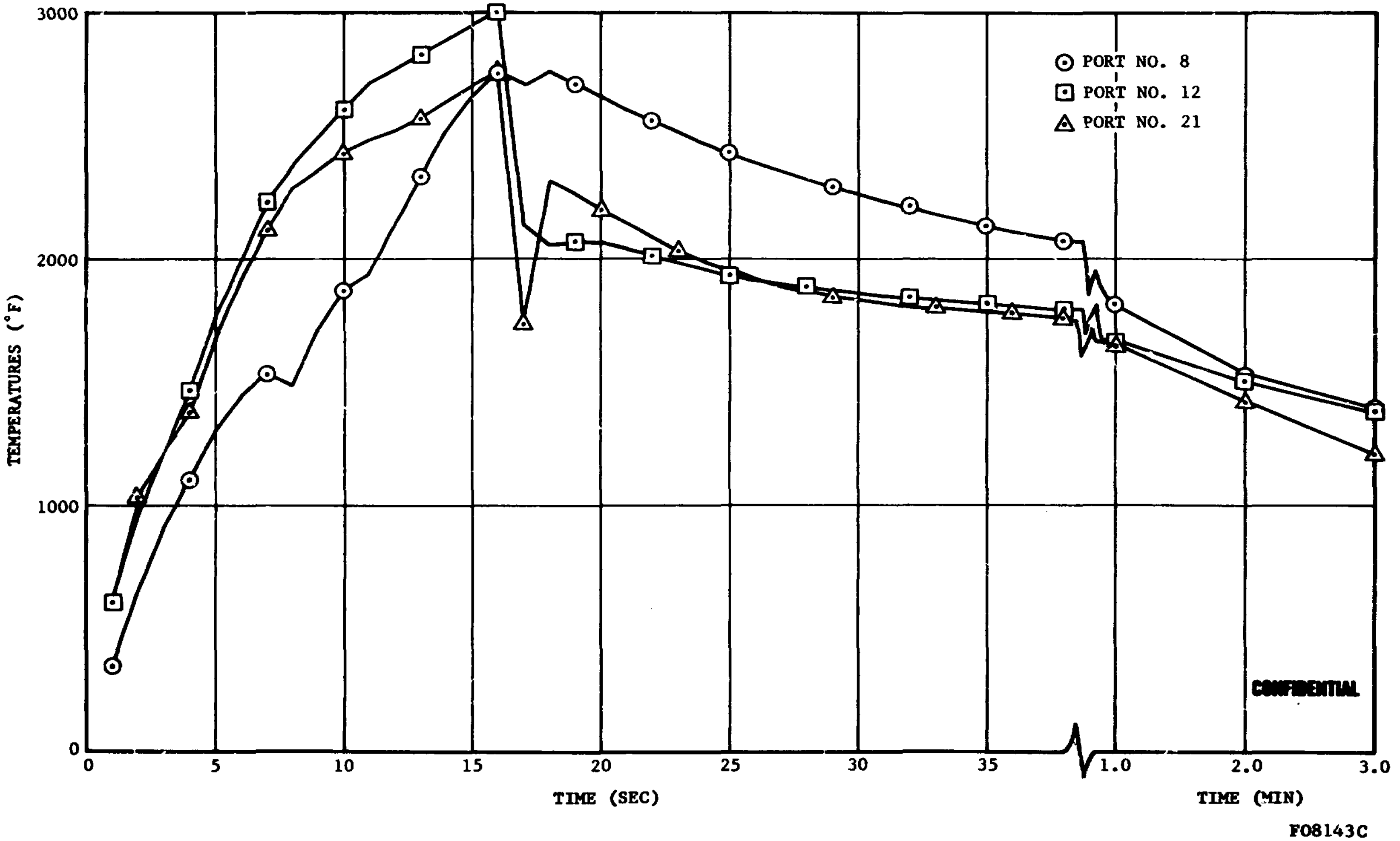

FIGURE 188. MEASURED HEAT SINK TEMPERATURES, TEST T-19

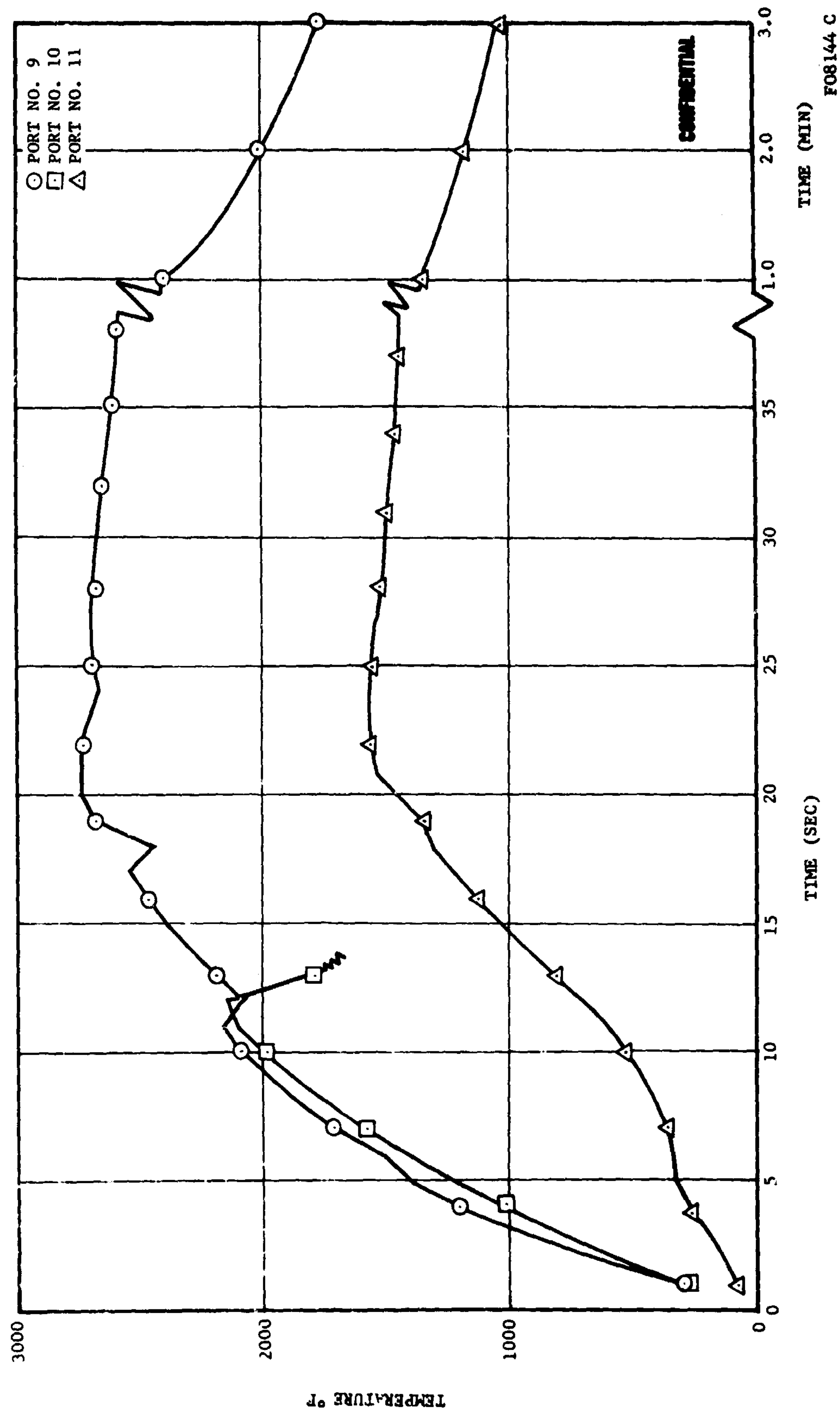

FIGURE 189. MEASURED HEAT SINK TEMPERATURES, TEST T-20

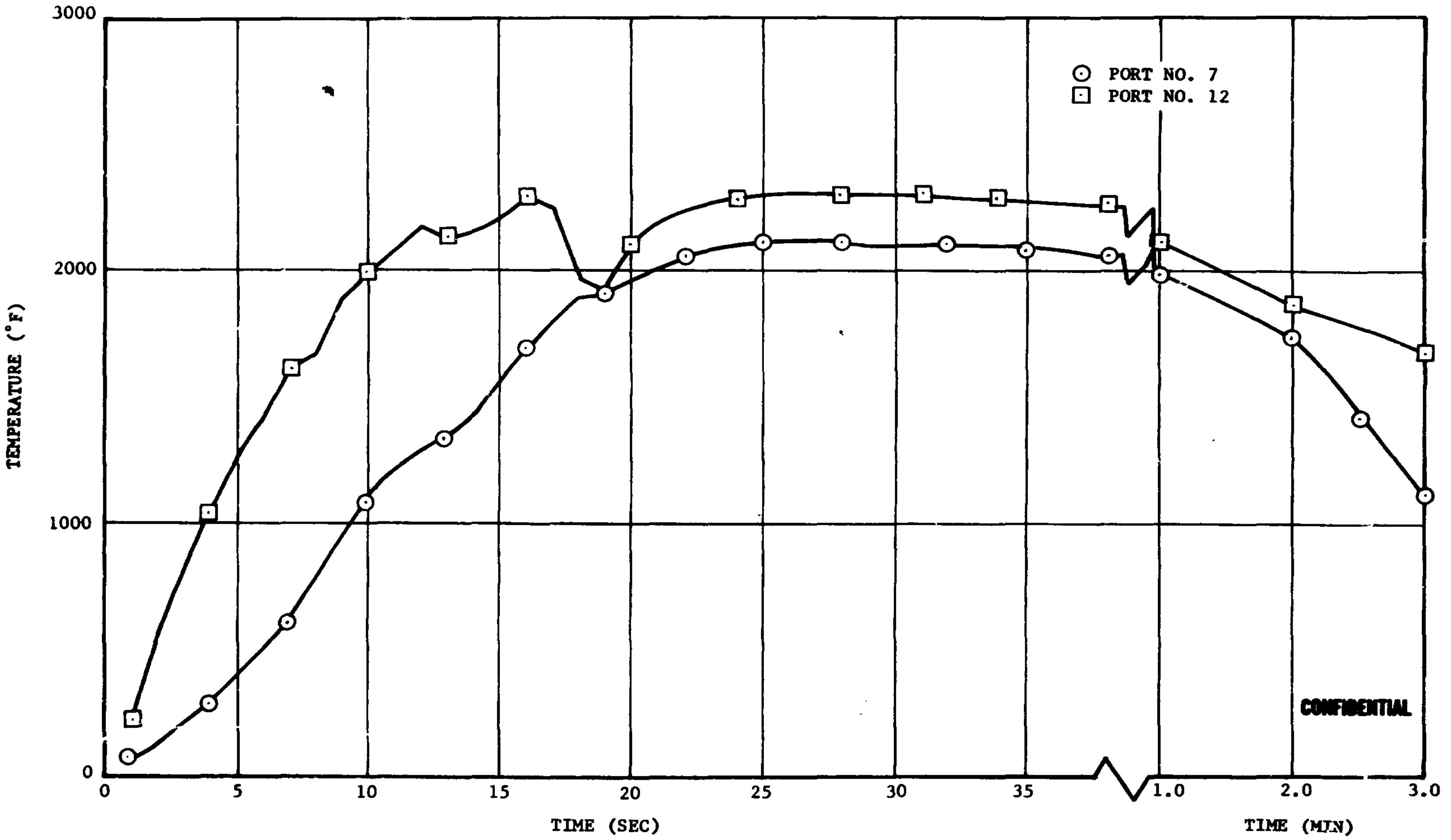

FIGURE 189. MEASURED HEAT SINK TEMPERATURES, TEST T-20 (Continued)

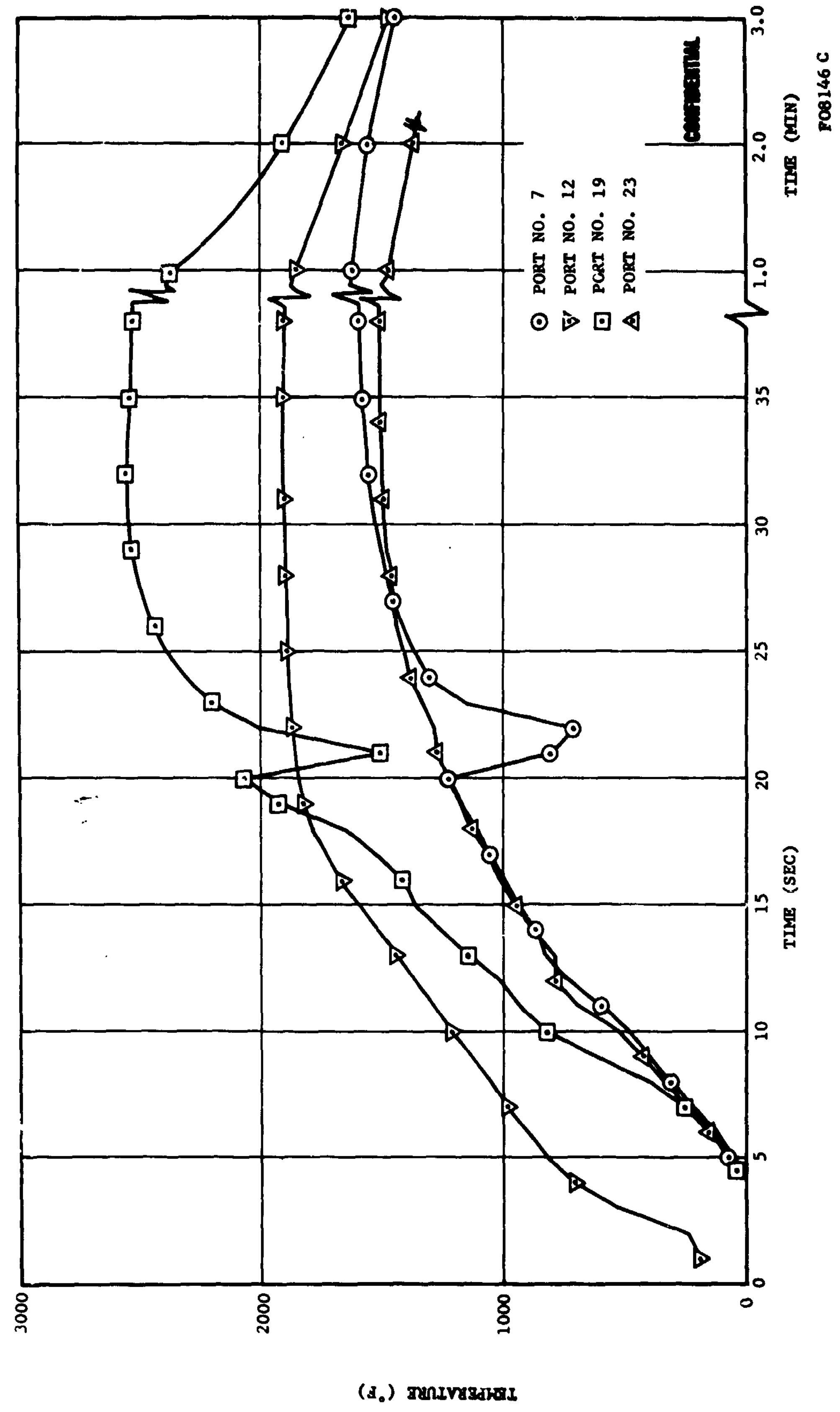

FIGURE 190. MEASURED HEAT SINK TEMPERATURES, TEST T-21

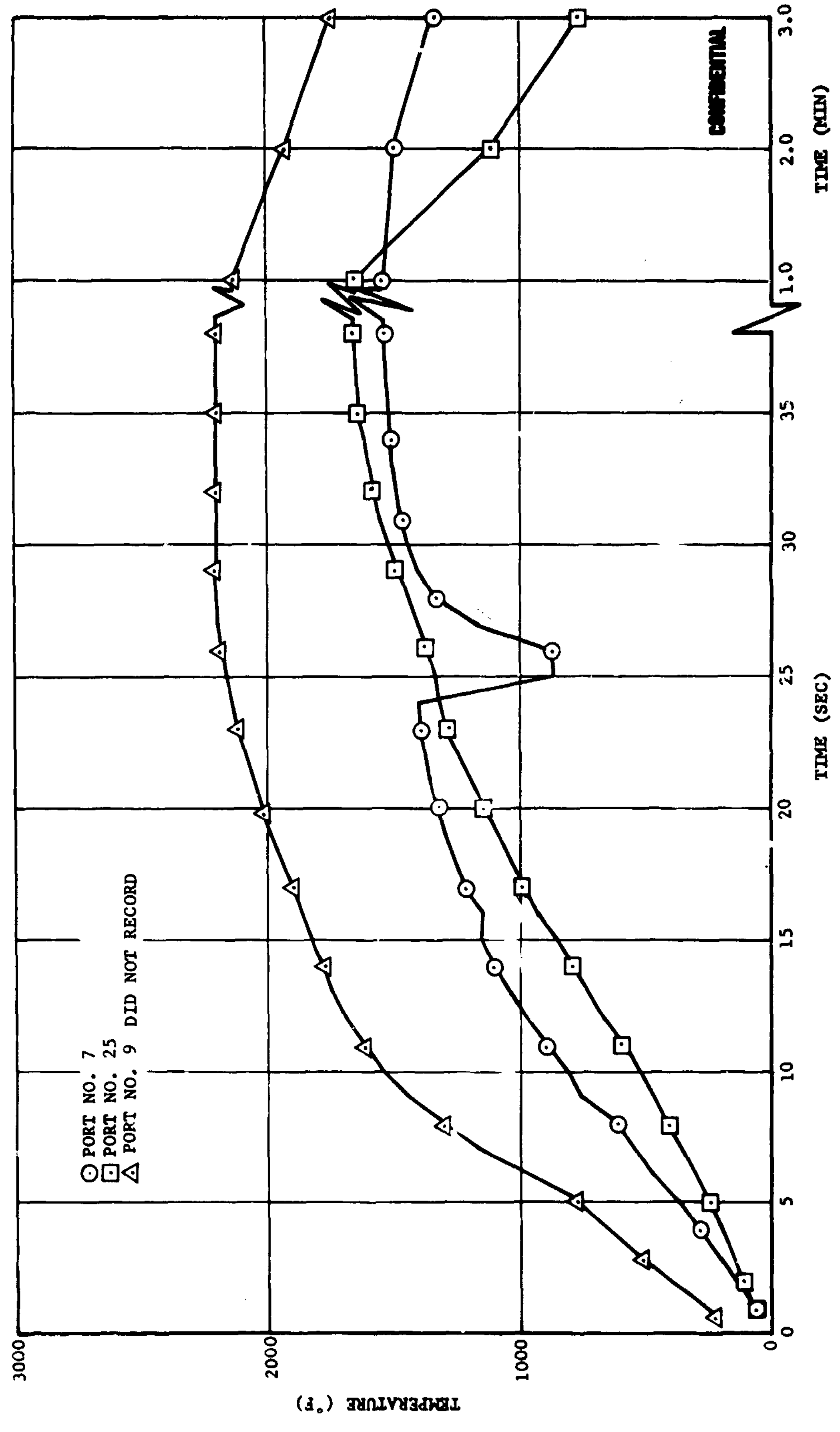

F08147C

FIGURE 191. MEASURED HEAT SINK TEMPERATURES, TEST T-22

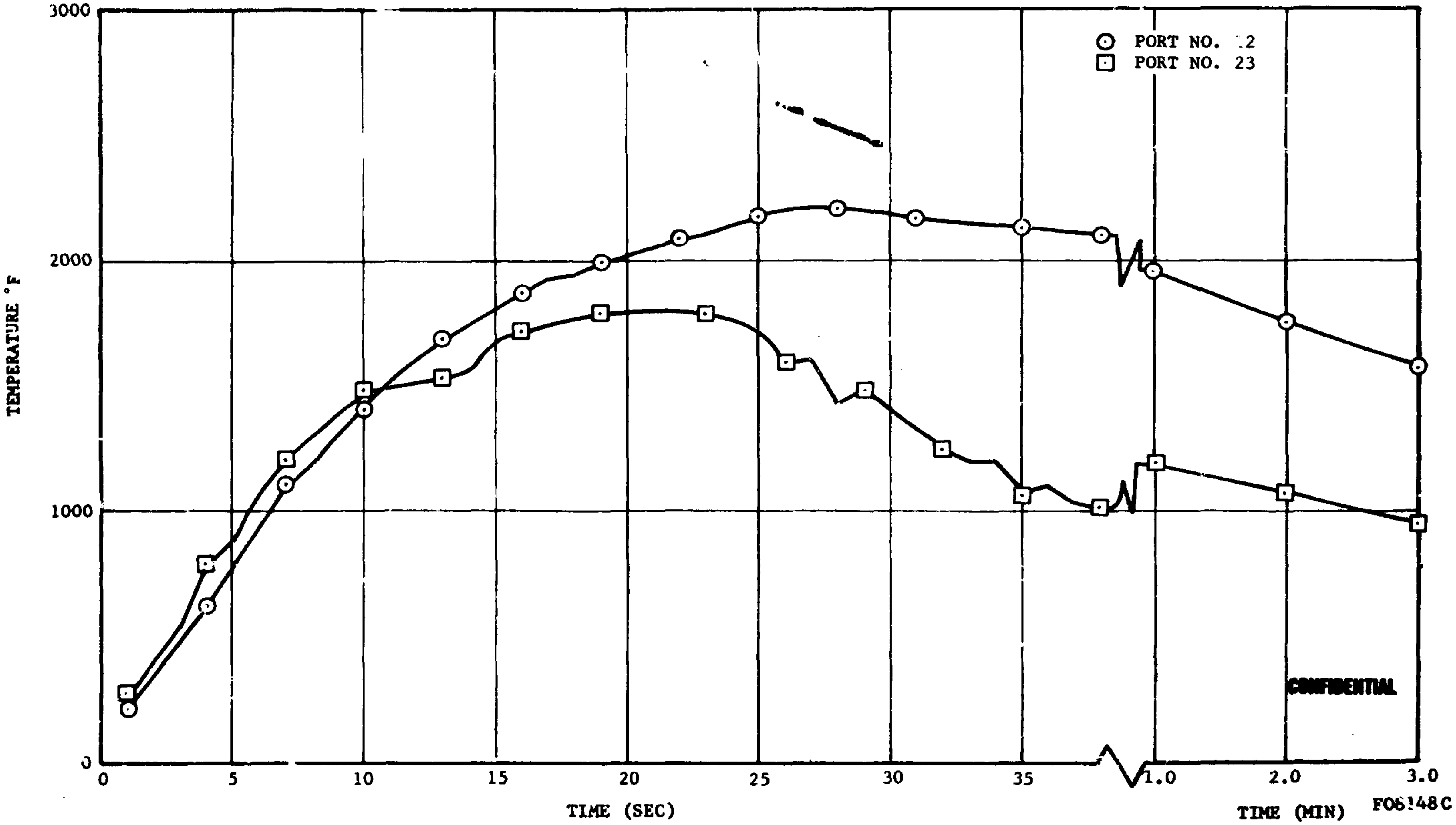

FIGURE 191. MEASURED HEAT SINK TEMPERATURES, TEST T-22 (Continued)

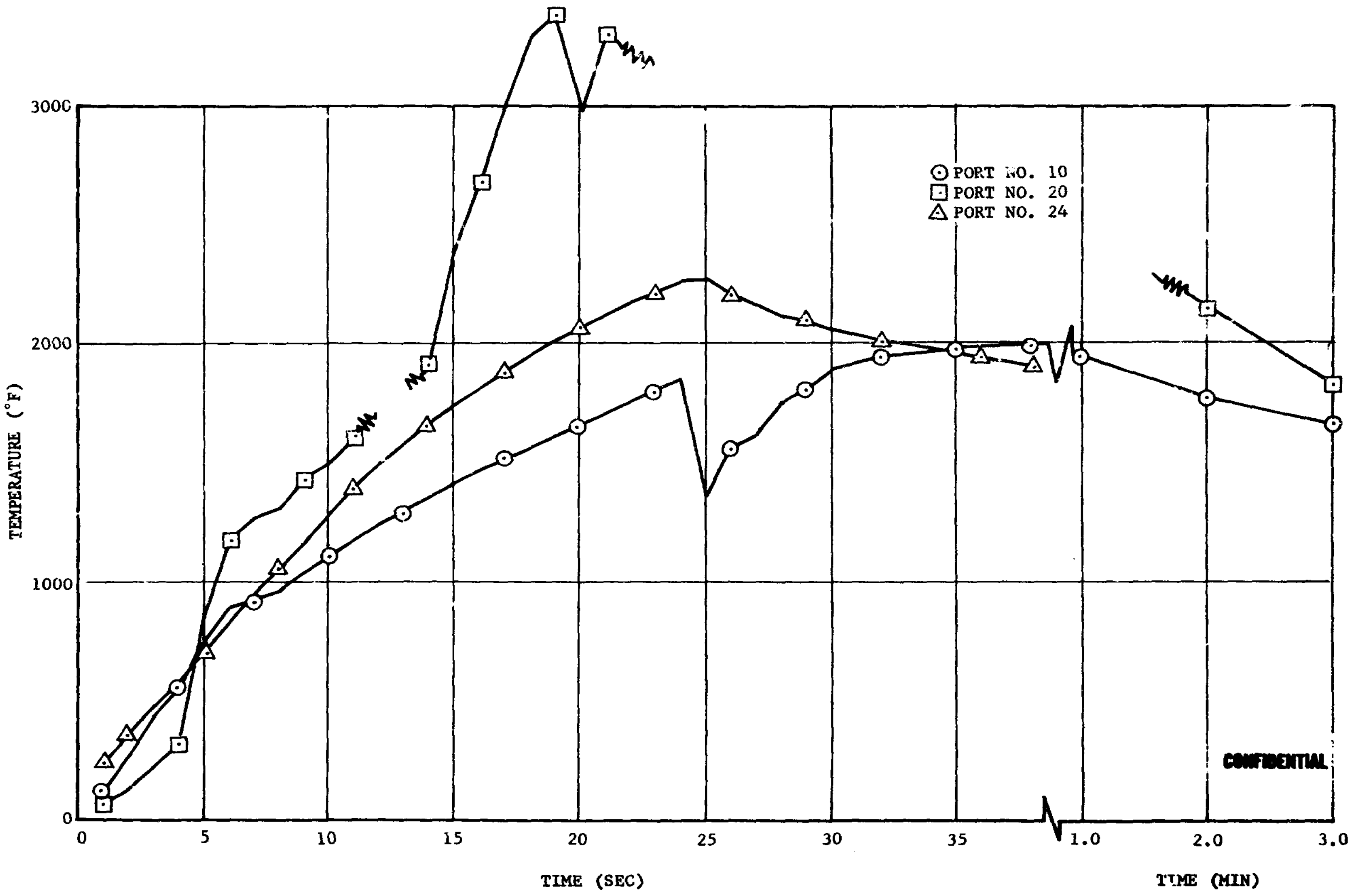

F08149 C

FIGURE 191. MEASURED HEAT SINK TEMPERATURES, TEST T-22 (Continued)

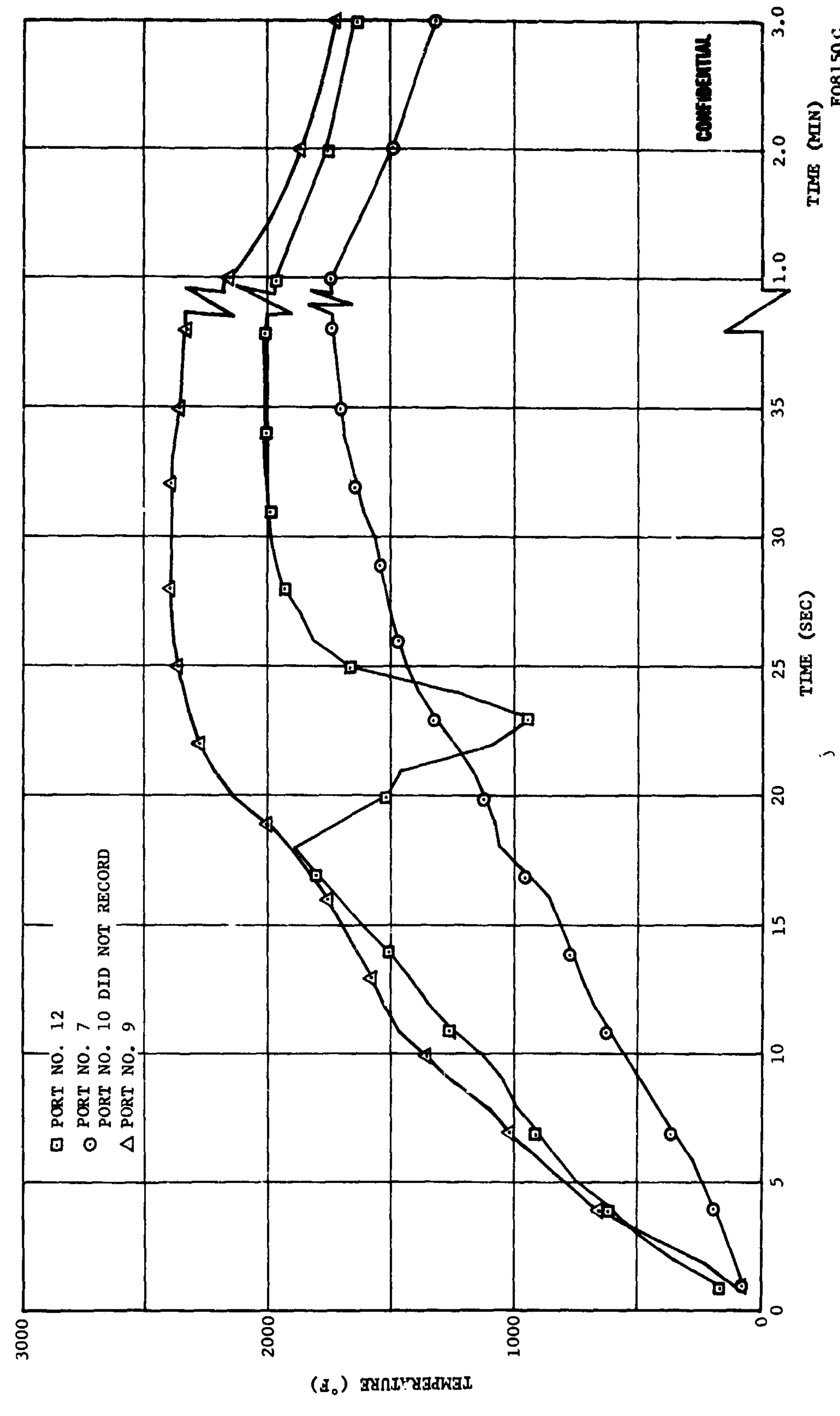

FIGURE 192. MEASURED HEAT SINK TEMPERATURES, TEST T-23

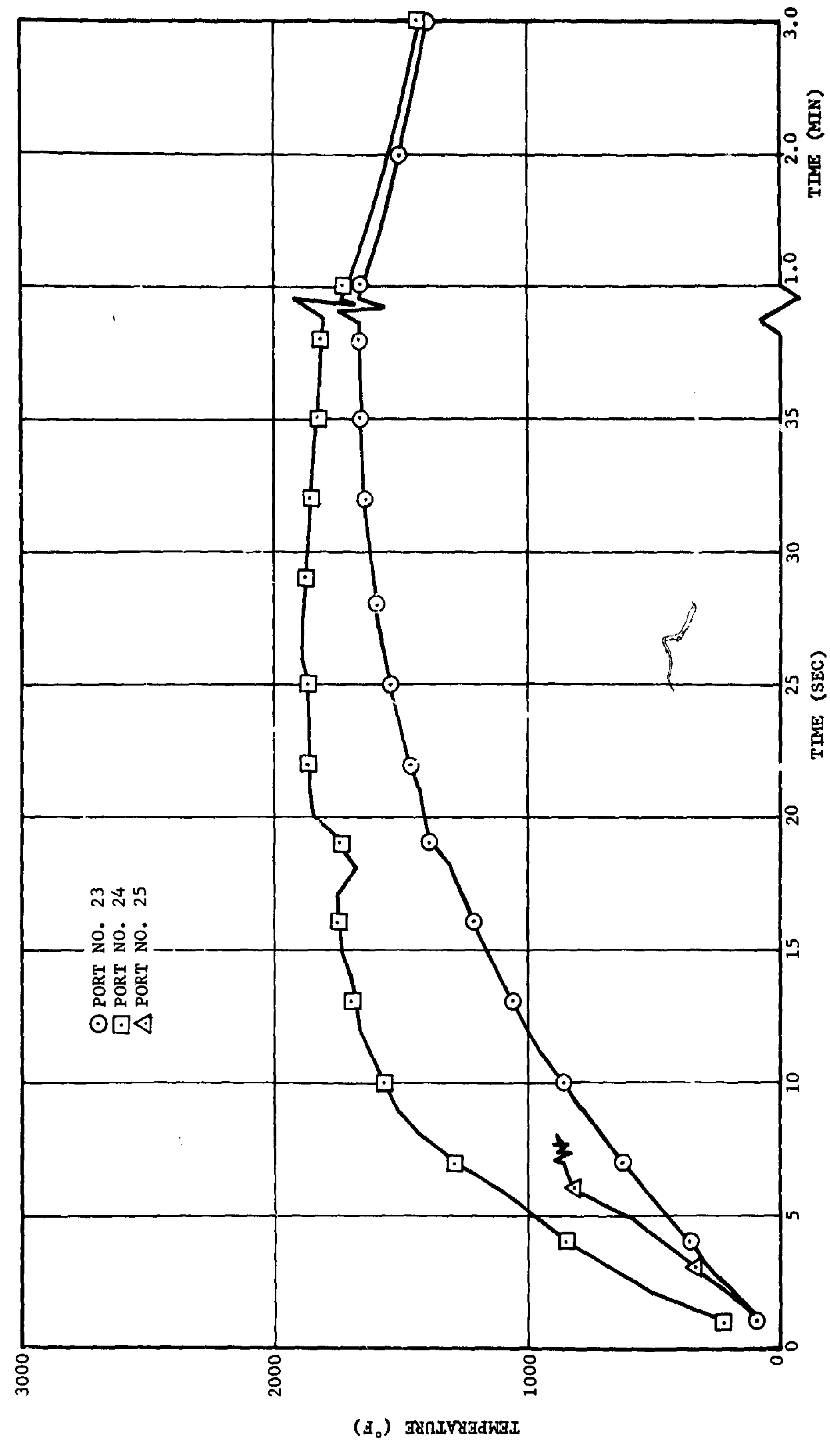

F08151C

FIGURE 192. MEASURED HEAT SINK TEMPERATURES, TEST T-23 (Continued)

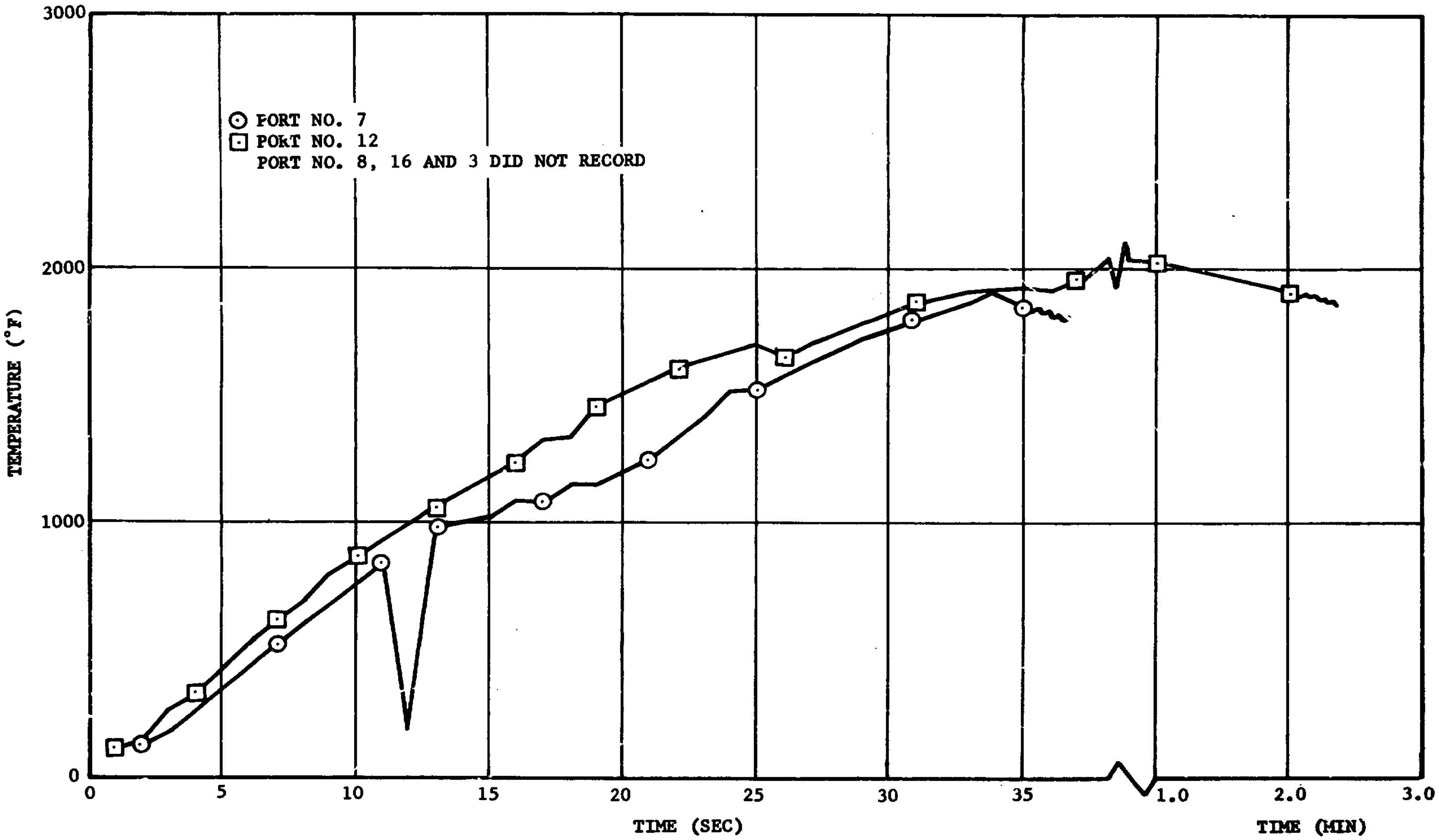

FIGURE 193. MEASURED HEAT SINK TEMPERATURES, TEST T-25

F08152C

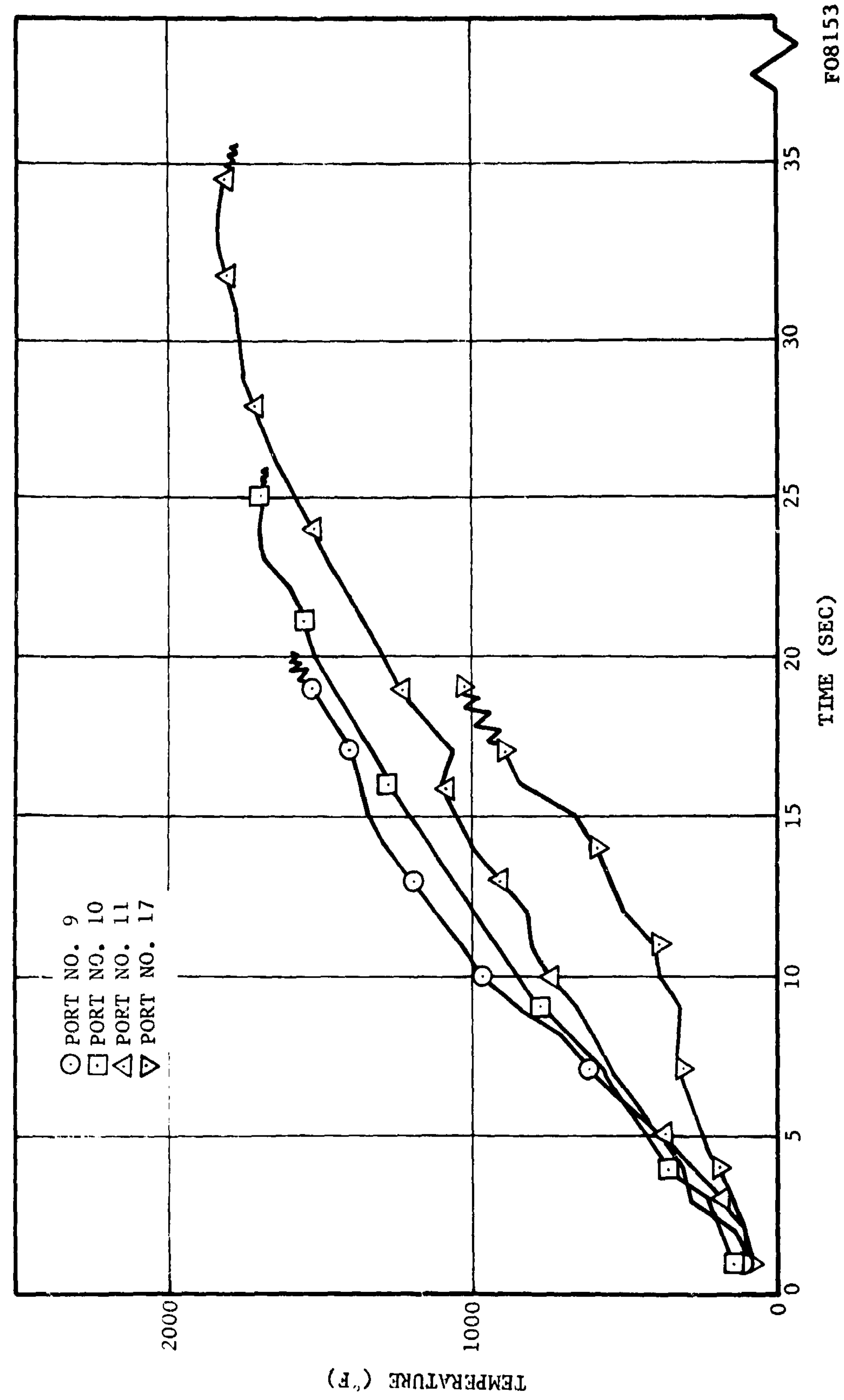

FIGURE 193. MEASURED HEAT SINK TEMPERATURES, TEST T-25 (Continued)

REFERENCES

1. Smallwood, W. L., et al, Beryllium Erosion Corrosion Investigation for Solid Rocket Nozzles (U), First Quarterly Progress Report, Confidential, Contract AF04(611)-10753, AFRPL-TR-65-205, November 1965.

2. Smallwood, W. L., et al, Beryllium Erosion Corrosion Investigation for Solid Rocket Nozzles (U), Second Quarterly Progress Report, Confidential, Contract AF04(611)-10753, AFRPL-TR-66-71, May 1966.

3. "Beryllium Propellants," Chemical Propulsion Newsletter, Vol. 2, No. 8, September 1966.

4. Yount, R. A., "Combustion Studies of LMH_2 Propellants (U)," Proceedings, Second Combustion Conference, Vol. II, Confidential, CPIA Publication No. 105, May 1966, pp 157-165.

5. U. S. Naval Ordnance Test Station, Aluminum Particle Combustion Progress Report, 1 April 1964-30 June 1965, AD 632-606, April 1966.

6. Camp, A. T. and Wilmot, G. B., "Efficient Combustion and Utilization of Beryllium in Propellants (U)," Proceedings, Second Combustion Conference, Vol. II, Confidential, CPIA Publication No. 105, May 1966, pp 151-156.

7. Kuehl, D. K., "Ignition and Combustion of Aluminum and Beryllium," AIAA Journal 3, December 1955, pp 2239-2247.

8. Hove, J. E. and Riley, W. C., Ceramics for Advanced Technology, John Wiley and Sons, 1965.

9. Armour, W. H., et al, An Investigation and Feasibility Demonstration of Nozzle for Restartable Solid Rocket Motors (U), Final Report, Confidential, Contract AF04(611)-9904, AFRPL-TR-66-53, 31 March 1966.

10. Farmer, R. W., Thermogravimetry and Phenol-Formaldehyde Polycondensates, AFML-TR-65-246, January 1966.

UNCLASSIFIED
Security Classification

DOCUMENT CONTROL DATA - R&D

(Security classification of title, body of abstract and indexing annotation must be entered when the overall report is classified)

1. ORIGINATING ACTIVITY (Corporate author) Aeronutronic Division Philco-Ford Corporation Newport Beach, California	2a. REPORT SECURITY CLASSIFICATION Confidential 2b GROUP GP-4

3. REPORT TITLE

Beryllium Erosion Corrosion Investigation for Solid Rocket Nozzles (U)

4. DESCRIPTIVE NOTES *(Type of report and inclusive dates)*

Third Technical Progress Report, 16 March 1966 - 1 October 1966

5. AUTHOR(S) *(Last name, first name, initial)*

Smallwood, William L. et al

6. REPORT DATE November 1966	7a. TOTAL NO. OF PAGES 392	7b. NO. OF REFS 10
8a. CONTRACT OR GRANT NO. AF04(611)-10753 b. PROJECT NO. c. d.	9a. ORIGINATOR'S REPORT NUMBER(S) C-3705 9b. OTHER REPORT NO(S) (Any other numbers that may be assigned this report) AFRPL-TR-66-205	

10. AVAILABILITY/LIMITATION NOTICES

Qualified requestors may obtain copies of this report from DDC.

11. SUPPLEMENTARY NOTES	12. SPONSORING MILITARY ACTIVITY Air Force Rocket Propulsion Laboratory Edwards Air Force Base Edwards, California 93523

13. ABSTRACT This is the third technical progress report for Contract AF04(611)-10753, covering the period 15 March to 10 October 1966. The program is directed toward understanding the basic mechanisms of corrosion and erosion of graphite, tungsten and ablative plastic materials exposed to state-of-the-art beryllium propellant exhausts. The results of 18 solid propellant firings are presented and evaluated. The 100-pound grains were in end burner, center perforated and key configurations. Submerged, steep inlet and conventional nozzle contours were tested. Four of the nozzles used dense tungsten inserts; the others were edge grain pyrolytic graphite. Carbon cloth and asbestos phenolics were used as aft closure, nose cap and entrance cone insulation. Three beryllium formulations and one aluminum analog (one test) were used. Pressure, thrust, and thermocouple data are included. Photographs of the tested hardware, analyses of nozzle deposits and analyses of exhaust plume particle samples are presented. Nozzle throat thermal histories and convective heat transfer coefficients were calculated. Oxide deposition effects provided extensive thermal insulation and corrosion protection of the nozzle contour. Throat corrosion occurred on only 7 tests. The key grains produced two axial grooves in the nozzles. Almost no evidence of physical erosion was found. Corrosion, deposition, heat transfer and ballistic performance are discussed in terms of physical and analytical models. The motor test results tend to confirm the original hypotheses concerning the beryllium nozzle erosion problem. Designs for the 500-pound grain motor tests and progress in the development of analytical design techniques are also discussed.

DD FORM 1 JAN 64 1473

UNCLASSIFIED
Security Classification

Unclassified
Security Classification

14. KEY WORDS	LINK A		LINK B		LINK C	
	ROLE	WT	ROLE	WT	ROLE	WT
Beryllium Solid Propellants Aluminum Analogs Rocket Motor Tests Corrosion Heat Transfer Rocket Nozzles						

INSTRUCTIONS

1. ORIGINATING ACTIVITY: Enter the name and address of the contractor, subcontractor, grantee, Department of Defense activity or other organization *(corporate author)* issuing the report.

2*a*. REPORT SECURITY CLASSIFICATION: Enter the overall security classification of the report. Indicate whether "Restricted Data" is included. Marking is to be in accordance with appropriate security regulations.

2*b*. GROUP: Automatic downgrading is specified in DoD Directive 5200.10 and Armed Forces Industrial Manual. Enter the group number. Also, when applicable, show that optional markings have been used for Group 3 and Group 4 as authorized.

3. REPORT TITLE: Enter the complete report title in all capital letters. Titles in all cases should be unclassified. If a meaningful title cannot be selected without classification, show title classification in all capitals in parenthesis immediately following the title.

4. DESCRIPTIVE NOTES: If appropriate, enter the type of report, e.g., interim, progress, summary, annual, or final. Give the inclusive dates when a specific reporting period is covered.

5. AUTHOR(S): Enter the name(s) of author(s) as shown on or in the report. Enter last name, first name, middle initial. If military, show rank and branch of service. The name of the principal author is an absolute minimum requirement.

6. REPORT DATE: Enter the date of the report as day, month, year; or month, year. If more than one date appears on the report, use date of publication.

7*a*. TOTAL NUMBER OF PAGES: The total page count should follow normal pagination procedures, i.e., enter the number of pages containing information.

7*b*. NUMBER OF REFERENCES: Enter the total number of references cited in the report.

8*a*. CONTRACT OR GRANT NUMBER: If appropriate, enter the applicable number of the contract or grant under which the report was written.

8*b*, 8*c*, & 8*d*. PROJECT NUMBER: Enter the appropriate military department identification, such as project number, subproject number, system numbers, task number, etc.

9*a*. ORIGINATOR'S REPORT NUMBER(S): Enter the official report number by which the document will be identified and controlled by the originating activity. This number must be unique to this report.

9*b*. OTHER REPORT NUMBER(S): If the report has been assigned any other report numbers *(either by the originator or by the sponsor)*, also enter this number(s).

10. AVAILABILITY/LIMITATION NOTICES: Enter any limitations on further dissemination of the report, other than those imposed by security classification, using standard statements such as:

(1) "Qualified requesters may obtain copies of this report from DDC."

(2) "Foreign announcement and dissemination of this report by DDC is not authorized."

(3) "U. S. Government agencies may obtain copies of this report directly from DDC. Other qualified DDC users shall request through
_______________________________________."

(4) "U. S. military agencies may obtain copies of this report directly from DDC. Other qualified users shall request through
_______________________________________."

(5) "All distribution of this report is controlled. Qualified DDC users shall request through
_______________________________________."

If the report has been furnished to the Office of Technical Services, Department of Commerce, for sale to the public, indicate this fact and enter the price, if known.

11. SUPPLEMENTARY NOTES: Use for additional explanatory notes.

12. SPONSORING MILITARY ACTIVITY: Enter the name of the departmental project office or laboratory sponsoring *(paying for)* the research and development. Include address.

13. ABSTRACT: Enter an abstract giving a brief and factual summary of the document indicative of the report, even though it may also appear elsewhere in the body of the technical report. If additional space is required, a continuation sheet shall be attached.

It is highly desirable that the abstract of classified reports be unclassified. Each paragraph of the abstract shall end with an indication of the military security classification of the information in the paragraph, represented as *(TS)*, *(S)*, *(C)*, or *(U)*.

There is no limitation on the length of the abstract. However, the suggested length is from 150 to 225 words.

14. KEY WORDS: Key words are technically meaningful terms or short phrases that characterize a report and may be used as index entries for cataloging the report. Key words must be selected so that no security classification is required. Identifiers, such as equipment model designation, trade name, military project code name, geographic location, may be used as key words but will be followed by an indication of technical context. The assignment of links, rules, and weights is optional.

Unclassified
Security Classification